

AN EXPERIMENTAL INVESTIGATION OF INTERACTING WING -TIP VORTEX PAIRS

by

Jeffrey S. Zsoldos

Thesis Submitted to the Faculty of the

Virginia Polytechnic Institute and State University

in partial fulfillment of the requirements for the degree of

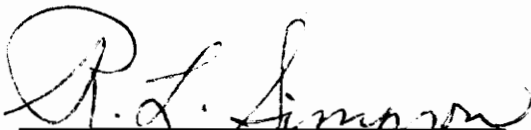
Master of Science


in

Aerospace Engineering

APPROVED:



Dr. W.J. Devenport

Dr. R.L. Simpson

Dr. S. Liapis

June, 1992

Blacksburg, Virginia

C.2

LD
5655
1855
1992
2764
C.2

AN EXPERIMENTAL INVESTIGATION OF INTERACTING WING -TIP VORTEX PAIRS

by

Jeffrey S. Zsoldos

William J. Devenport, Chairman

Aerospace Engineering

(ABSTRACT)

The interactions of trailing vortex pairs shed from the tips of two rectangular wings have been studied through helium bubble flow visualizations and extensive hot wire velocity measurements made between 10 and 30 chordlengths downstream. The wings were placed tip to tip at equal and opposite angles of attack, generating pairs of co-rotating and counter rotating vortices. Meaningful hot wire measurements could be made because the vortices were found to be insensitive to probe interference and experienced very small wandering motions.

The co-rotating pairs were observed to rotate around each other and merge. Upstream of the merging location, the vortices have approximately elliptical cores. These are surrounded by the two wing wakes which join together around the two cores. Flow in the vicinity of the cores appears fully developed. During the merging process, the cores rotate rapidly about each other, winding the wing wakes into a fine spiral structure. Merger roughly doubles the core size and appears to produce turbulence over a broad range of frequencies.

The counter rotating pairs move sideways under their mutual induction and slightly apart; their flow structure changing little with downstream location. These cores remain fairly circular and do not become fully developed within 30 chordlengths of the measurements.

Acknowledgements

I would like to thank Dr. William J. Devenport for his advice and instruction while completing this work. He made a great contribution to this thesis and to my understanding of fluid mechanics. I would also thank Dr. R. L. Simpson and Dr. S. Liapis for being committee members and for their contribution to this thesis.

Thanks to Mike Rife, Gautam Sharma and Ted Smith for their help in taking of the velocity measurements which was a great success. Also thanks to the Defense Advanced Research Projects Agency through the Office of Naval Research for making this project possible. Their support under project number N00014-91-J-1773 is gratefully acknowledged.

A very special thanks to my grandparents, Tom and Ruth Smull, for their encouragement and support without which none of this would have been possible. I am greatly indebted.

Table of Contents

List of Tables viii

List of Figures ix

List of Symbols xxv

1. Introduction 1

2. Experimental Apparatus And Techniques 8

 2.1 Facilities and Equipment 8

 2.1.1 Wind Tunnel 8

 2.1.2 Wings 9

 2.1.3 Traverse Mechanism 10

 2.1.4 Flow Visualization Equipment 11

 2.2 Hot Wire Anemometry 12

 2.2.1 Dummy Hot Wire Probe and Holder 14

 2.2.2 Single Hot Wire Probe 14

 2.2.3 Quad Hot Wire Probe 16

 2.2.3.1 Initial Estimates 17

 2.2.3.2 Corrections 19

3. Flow Visualization Results 21

 3.1 Co-rotating Vortex Pairs 22

3.1.1 Cases for Further Study	27
3.2 Counter Rotating Vortex Pairs	29
3.2.1 Cases for Further Study	32
4. Velocity Results	34
4.1 Wing Wake.....	35
4.1.1 Near Field Wing Wake	35
4.1.2 Farfield Wing Wake	40
4.2 Vortex Pairs Results.....	43
4.2.1 Co-Rotating Vortex Pairs	44
4.2.1.1 $x/c=10$	44
4.2.1.2 $x/c=15$	49
4.2.1.3 $x/c=22$	52
4.2.1.4 $x/c=30$	54
4.2.2 Counter Rotating Vortex Pairs.....	56
4.2.2.1 $x/c=10$	56
4.2.2.2 $x/c=30$	59
4.3 Further Analysis.....	61
4.3.1 Circulation.....	61
4.3.2 Spiral Wake.....	65
4.3.3 Triple Products.....	69
4.4 Vortex Motions and Core Region.....	71
4.4.1 Co-Rotating Pairs	71
4.4.2 Counter Rotating Pairs.....	72
4.4.3 Possible Sources of Vortex Motions	73
4.4.4 Filtered Results.....	77

5. Conclusions..... 81

6. References..... 84

Tables 88

Figures 93

Vita 407

List of Tables

Table 1. Flow conditions for visualizations 89

Table 2. Single hot wire uncertainties in measurements 90

Table 3. Quad hot wire uncertainties in measurements 90

Table 4. Wing trailing edge characteristics 91

Table 5. Locations of vortices in tunnel coordinates 92

List of Figures

Figure 1. Lancaster's model of the roll up of a single wing tip vortex	94
Figure 2. Tangential velocity and circulation distribution of an ideal vortex	94
Figure 3. Two different methods of vortex generation	95
Figure 4. General layout of the Virginia Tech Stability Wind Tunnel	96
Figure 5. Schematic of the wind tunnel test section	97
Figure 6. View of the two wings looking upstream	98
Figure 7. View of the test section looking upstream	98
Figure 8. Drawing of upper and lower wing mount hardware showing adjustments	99
Figure 9. Dummy hot wire probe with front part of probe holder	100
Figure 10. Velocity vector resolution of the single hot wire probe	100
Figure 11. Schematic of the quad hot wire probe showing dimensions and wire configuration in the measurement plane	101
Figure 12. Diagram of the probe holder and hot wire attachment	102
Figure 13. Contours of quad hot wire corrections as functions of the actual and estimated velocities	103
Figure 14. Sketch of an idealized co-rotating vortex pair	106

Figure 15. Helium bubble visualization looking upstream. $\Delta y=c/4$, $\alpha_o=5.0^\circ$, $Re_c=130,000$, 2 second exposure	106
Figure 16. Helium bubble visualization looking upstream. $\Delta y=c/4$, $\alpha_o=7.5^\circ$, $Re_c=130,000$, 2 second exposure	107
Figure 17. Helium bubble visualization looking upstream. $\Delta y=c/4$, $\alpha_o=10.0^\circ$, $Re_c=130,000$, 2 second exposure	107
Figure 18. Helium bubble visualization looking upstream. $\Delta y=3/8c$, $\alpha_o=5.0^\circ$, $Re_c=130,000$, 2 second exposure	108
Figure 19. Helium bubble visualization looking upstream. $\Delta y=3/8c$, $\alpha_o=7.5^\circ$, $Re_c=130,000$, 2 second exposure	108
Figure 20. Helium bubble visualization looking upstream. $\Delta y=3/8c$, $\alpha_o=10.0^\circ$, $Re_c=130,000$, 2 second exposure	109
Figure 21. Amplitude of lateral motions for co-rotating vortex pairs at $x/c=20$	109
Figure 22. Angle of rotation of co-rotating pairs as a function of α for different Δy	110
Figure 23. Angle of rotation of co-rotating pairs vs. $\Gamma x/\pi s^2 U_{ref}$	110
Figure 24. Angle of rotation of co-rotating pairs vs. $\Gamma x/\pi \Delta y^2 U_{ref}$	111
Figure 25. Co-rotating cases which merged within the length of the test section.....	111
Figure 26. Merging location of co-rotating pairs as a function of α for different Δy	112
Figure 27. Merging location of co-rotating pairs vs. $2\pi U_{ref} \Delta y^2/\Gamma c$	112
Figure 28. Photo-mosaics of co-rotating pairs at $\Delta y=3/8c$, $Re_c=130,000$	113
Figure 29. Photo-mosaic of co-rotating pair at $\Delta y=c/4c$, $Re_c=130,000$	114

Figure 30. Dummy hot-wire probe in core, $\Delta y=c/4c$, $Re_c=130,000$	115
Figure 31. Dummy hot-wire probe traversing through the core, $\Delta y=c/4c$, $Re_c=130,000$	115
Figure 32. Sketch of an idealized counter rotating vortex pair	116
Figure 33. Helium bubble visualization looking upstream. $\Delta y=c/4$, $\alpha_e=2.5^\circ$, $Re_c=130,000$, 2 sec exposure	116
Figure 34. Helium bubble visualization looking upstream. $\Delta y=c/4$, $\alpha_e=5.0^\circ$, $Re_c=130,000$, 2 sec exposure	117
Figure 35. Helium bubble visualization looking upstream. $\Delta y=c/4$, $\alpha_e=7.5^\circ$, $Re_c=130,000$, 2 sec exposure	117
Figure 36. Amplitude of lateral motions for counter rotating pairs at $x/c=20$	118
Figure 37. z/c location of counter rotating pairs as a function of α for different Δy at $x/c=20$	118
Figure 38. z/c location of counter rotating pairs vs. $\Gamma x/2\pi s U_{ref} c$ at $x/c=20$	119
Figure 39. Separation distance s/c of counter rotating pairs as a function of streamwise location x/c	119
Figure 40. Trajectory of counter rotating vortex pairs in the presence of a wall. Normalized with the separation distance at $x/c=20$	120
Figure 41. Photo-mosaics of co-rotating pairs at $\Delta y=3/8c$, $Re_c=130,000$	121
Figure 42. Photo-mosaic of co-rotating pair at $\Delta y=c/4c$, $Re_c=130,000$	122
Figure 43. Dummy hot-wire probe in core, $\Delta y=c/4c$, $Re_c=130,000$	123
Figure 44. Dummy hot-wire probe traversing through the core, $\Delta y=c/4c$, $Re_c=130,000$	123
Figure 45. Mean U profiles in the near field wing wake at various y/c locations for the co-rotating pairs	124

Figure 46. Mean U profiles in the near field wing wake at various y/c locations for the counter rotating pairs	125
Figure 47. Profiles of u^2 in the near field wing wake at various y/c locations for the co-rotating pairs.....	126
Figure 48. Profiles of u^2 in the near field wing wake at various y/c locations for the counter rotating pairs	127
Figure 49. Comparison of mean U profiles for both the co-rotating and counter rotating pairs	128
Figure 50. Comparison of u^2 profiles for both the co-rotating and counter rotating pairs	129
Figure 51. Representative u autospectra in the centerline of the near field wing wake for both the co-rotating and counter rotating pairs	130
Figure 52. Representative u autospectra measured on the suction side of the near field wing wake for both the co-rotating and counter rotating pairs	131
Figure 53. Representative u autospectra measured on the pressure side of the near field wing wake for both the co-rotating and counter rotating pairs	132
Figure 54. Comparison of u autospectra measured in the near filed wing wake for the suction, pressure and centerline locations.....	133
Figure 55. Mean U profiles of the far field upper wing wake for both the co-rotating and counter rotating pairs	134
Figure 56. u^2 profiles of the far field upper wing wake for both the co-rotating and counter rotating pairs	135
Figure 57. v^2 profiles of the far field upper wing wake for both the co-rotating and counter rotating pairs	136
Figure 58. w^2 profiles of the far field upper wing wake for both the co-rotating and counter rotating pairs	137
Figure 59. uv profiles of the far field upper wing wake for both the co-rotating and counter rotating pairs	138

Figure 60. vw profiles of the far field upper wing wake for both the co-rotating and counter rotating pairs	139
Figure 61. uw profiles of the far field upper wing wake for both the co-rotating and counter rotating pairs	140
Figure 62. Similarity profiles of the mean axial velocity deficit for the upper far field wing wakes	141
Figure 63. Similarity profiles of the normal stresses for the upper far field wing wakes	142
Figure 64. Similarity profiles of the shear stress uw for the upper far field wing wakes	143
Figure 65. u autospectra of the upper far field wing wake measured at the centerline of the wake.....	144
Figure 66. u autospectra of the upper far field wing wake measured at $(z-z_o)/c=-0.1$ of the wake.....	147
Figure 67. Autospectra normalized on similarity variables measured at the centerline of the far field wing wake	150
Figure 68. Autospectra normalized on similarity variables measured at $(z-z_o)/c=-0.1$ of the far field wing wake	151
Figure 69. Mean secondary flow vectors of the co-rotating pair at $x/c=10$	152
Figure 70. Contours of turbulent kinetic energy k/U_{ref}^2 for the co-rotating pair at $x/c=10$	153
Figure 71. Contours of v_x^2/U_{ref}^2 for the co-rotating pair at $x/c=10$	154
Figure 72. Core region showing mean secondary flows vectors for the upper co-rotating vortex at $x/c=10$	155
Figure 73. Core region showing contours of vorticity $\omega c/U_{ref}$ for the upper co-rotating vortex at $x/c=10$	156
Figure 74. Core region showing contours of turbulent kinetic energy k/U_{ref}^2 for the upper co-rotating vortex at $x/c=10$	157

Figure 75. Core region showing contours of v_x^2/U_{ref}^2 for the upper co-rotating vortex at $x/c=10$	158
Figure 76. Core region showing contours of v_θ^2/U_{ref}^2 for the upper co-rotating vortex at $x/c=10$	159
Figure 77. Core region showing contours of v_r^2/U_{ref}^2 for the upper co-rotating vortex at $x/c=10$	160
Figure 78. Core region showing contours of $v_x v_\theta/U_{ref}^2$ for the upper co-rotating vortex at $x/c=10$	161
Figure 79. Core region showing contours of $v_\theta v_r/U_{ref}^2$ for the upper co-rotating vortex at $x/c=10$	162
Figure 80. Core region showing contours of $v_x v_r/U_{ref}^2$ for the upper co-rotating vortex at $x/c=10$	163
Figure 81. Mean velocities and Reynolds stresses for profile Aa measured parallel to the line of antisymmetry for the upper co-rotating vortex at $x/c=10$	164
Figure 82. Mean velocities and Reynolds stresses for profile Bb measured perpendicular to the line of antisymmetry for the upper co-rotating vortex at $x/c=10$	167
Figure 83. Autospectra measured at representative radial locations along profile Aa for the upper co-rotating vortex at $x/c=10$	170
Figure 84. Autospectra measured at representative radial locations along profile Aa for the upper co-rotating vortex at $x/c=10$	173
Figure 85. Autospectra measured at representative radial locations along profile Bb for the upper co-rotating vortex at $x/c=10$	176
Figure 86. Autospectra measured at representative radial locations along profile Bb for the upper co-rotating vortex at $x/c=10$	179
Figure 87. Mean secondary flow vectors of the co-rotating pair at $x/c=15$	182
Figure 88. Contours of turbulent kinetic energy k/U_{ref}^2 for the co-rotating pair at $x/c=15$	183

Figure 89. Contours of v_x^2/U_{ref}^2 for the co-rotating pair at $x/c=15$	184
Figure 90. Core region showing mean secondary flows vectors for the upper co-rotating vortex at $x/c=15$	185
Figure 91. Core region showing contours of vorticity $\omega c/U_{ref}$ for the upper co-rotating vortex at $x/c=15$	186
Figure 92. Core region showing contours of turbulent kinetic energy k/U_{ref}^2 for the upper co-rotating vortex at $x/c=15$	187
Figure 93. Core region showing contours of v_x^2/U_{ref}^2 for the upper co-rotating vortex at $x/c=15$	188
Figure 94. Core region showing contours of v_θ^2/U_{ref}^2 for the upper co-rotating vortex at $x/c=15$	189
Figure 95. Core region showing contours of v_r^2/U_{ref}^2 for the upper co-rotating vortex at $x/c=15$	190
Figure 96. Core region showing contours of $v_x v_\theta/U_{ref}^2$ for the upper co-rotating vortex at $x/c=15$	191
Figure 97. Core region showing contours of $v_\theta v_r/U_{ref}^2$ for the upper co-rotating vortex at $x/c=15$	192
Figure 98. Core region showing contours of $v_x v_r/U_{ref}^2$ for the upper co-rotating vortex at $x/c=15$	193
Figure 99. Mean velocities and Reynolds stresses for profile Cc measured parallel to the line of antisymmetry for the upper co-rotating vortex at $x/c=15$	194
Figure 100. Mean velocities and Reynolds stresses for profile Dd measured perpendicular to the line of antisymmetry for the upper co-rotating vortex at $x/c=15$	197
Figure 101. Autospectra measured at representative radial locations along profile Cc for the upper co-rotating vortex at $x/c=15$	200
Figure 102. Autospectra measured at representative radial locations along profile Cc for the upper co-rotating vortex at $x/c=15$	203

Figure 103. Autospectra measured at representative radial locations along profile Dd for the upper co-rotating vortex at $x/c=15$	206
Figure 104. Autospectra measured at representative radial locations along profile Dd for the upper co-rotating vortex at $x/c=15$	209
Figure 105. Mean secondary flow vectors of the co-rotating pair at $x/c=22$	212
Figure 106. Contours of turbulent kinetic energy k/U_{ref}^2 for the co-rotating pair at $x/c=22$	213
Figure 107. Contours of v_x^2/U_{ref}^2 for the co-rotating pair at $x/c=22$	214
Figure 108. Core region showing mean secondary flows vectors for the co-rotating pair at $x/c=22$	215
Figure 109. Core region showing contours of vorticity $\omega c/U_{ref}$ for the co-rotating pair at $x/c=22$	216
Figure 110. Core region showing contours of turbulent kinetic energy k/U_{ref}^2 for the co-rotating pair at $x/c=22$	217
Figure 111. Core region showing contours of v_x^2/U_{ref}^2 for the co-rotating pair at $x/c=22$	218
Figure 112. Core region showing contours of v_θ^2/U_{ref}^2 for the co-rotating pair at $x/c=22$	219
Figure 113. Core region showing contours of v_r^2/U_{ref}^2 for the co-rotating pair at $x/c=22$	220
Figure 114. Core region showing contours of $v_x v_\theta/U_{ref}^2$ for the co-rotating pair at $x/c=22$	221
Figure 115. Core region showing contours of $v_\theta v_r/U_{ref}^2$ for the co-rotating pair at $x/c=22$	222
Figure 116. Core region showing contours of $v_x v_r/U_{ref}^2$ for the co-rotating pair at $x/c=22$	223

Figure 117. Mean velocities and Reynolds stresses for profile Ee for the co-rotating pair at $x/c=22$	224
Figure 118. Mean velocities and Reynolds stresses for profile Ff for the co-rotating pair at $x/c=22$	227
Figure 119. Autospectra measured at representative radial locations along profile Ee for the co-rotating pair at $x/c=22$	230
Figure 120. Autospectra measured at representative radial locations along profile Ee for the co-rotating pair at $x/c=22$	233
Figure 121. Autospectra measured at representative radial locations along profile Ee for the co-rotating pair at $x/c=22$	236
Figure 122. Autospectra measured at representative radial locations along profile Ee for the co-rotating pair at $x/c=22$	239
Figure 123. Mean secondary flow vectors of the co-rotating pair at $x/c=30$	242
Figure 124. Contours of turbulent kinetic energy k/U_{ref}^2 for the co-rotating pair at $x/c=30$	243
Figure 125. Contours of v_x^2/U_{ref}^2 for the co-rotating pair at $x/c=30$	244
Figure 126. Core region showing mean secondary flows vectors for the co-rotating pair at $x/c=30$	245
Figure 127. Core region showing contours of vorticity $\omega c/U_{ref}$ for the co-rotating pair at $x/c=30$	246
Figure 128. Core region showing contours of turbulent kinetic energy k/U_{ref}^2 for the co-rotating pair at $x/c=30$	247
Figure 129. Core region showing contours of v_x^2/U_{ref}^2 for the co-rotating pair at $x/c=30$	248
Figure 130. Core region showing contours of v_θ^2/U_{ref}^2 for the co-rotating pair at $x/c=30$	249
Figure 131. Core region showing contours of v_r^2/U_{ref}^2 for the co-rotating pair at $x/c=30$	250

Figure 132. Core region showing contours of $v_x v_\theta / U_{ref}^2$ for the co-rotating pair at $x/c=30$	251
Figure 133. Core region showing contours of $v_\theta v_r / U_{ref}^2$ for the co-rotating pair at $x/c=30$	252
Figure 134. Core region showing contours of $v_x v_r / U_{ref}^2$ for the co-rotating pair at $x/c=30$	253
Figure 135. Mean velocities and Reynolds stresses for profile Gg for the co-rotating pair at $x/c=30$	254
Figure 136. Mean velocities and Reynolds stresses for profile Hh for the co-rotating pair at $x/c=30$	257
Figure 137. Autospectra measured at representative radial locations along profile Gg for the co-rotating pair at $x/c=30$	260
Figure 138. Autospectra measured at representative radial locations along profile Gg for the co-rotating pair at $x/c=30$	263
Figure 139. Autospectra measured at representative radial locations along profile Hh for the co-rotating pair at $x/c=30$	266
Figure 140. Autospectra measured at representative radial locations along profile Hh for the co-rotating pair at $x/c=30$	269
Figure 141. Mean secondary flow vectors of the counter rotating pair at $x/c=10$	272
Figure 142. Contours of turbulent kinetic energy k/U_{ref}^2 for the counter co-rotating pair at $x/c=10$	273
Figure 143. Contours of v_x^2/U_{ref}^2 for the counter rotating pair at $x/c=10$	274
Figure 144. Core region showing mean secondary flows vectors for the upper counter rotating vortex at $x/c=10$	275
Figure 145. Core region showing contours of vorticity $\omega c/U_{ref}$ for the upper counter rotating vortex at $x/c=10$	276

Figure 146. Core region showing contours of turbulent kinetic energy k/U_{ref}^2 for the upper counter rotating vortex at $x/c=10$	277
Figure 147. Core region showing contours of v_x^2/U_{ref}^2 for the upper counter rotating vortex at $x/c=10$	278
Figure 148. Core region showing contours of v_θ^2/U_{ref}^2 for the upper counter rotating vortex at $x/c=10$	279
Figure 149. Core region showing contours of v_r^2/U_{ref}^2 for the upper counter rotating vortex at $x/c=10$	280
Figure 150. Core region showing contours of $v_x v_\theta/U_{ref}^2$ for the upper counter rotating vortex at $x/c=10$	281
Figure 151. Core region showing contours of $v_\theta v_r/U_{ref}^2$ for the upper counter rotating vortex at $x/c=10$	282
Figure 152. Core region showing contours of $v_x v_r/U_{ref}^2$ for the upper counter rotating vortex at $x/c=10$	283
Figure 153. Mean velocities and Reynolds stresses for profile Ii measured parallel to the line of symmetry for the upper counter rotating vortex at $x/c=10$	284
Figure 154. Mean velocities and Reynolds stresses for profile Jj measured perpendicular to the line of symmetry for the upper counter rotating vortex at $x/c=10$	287
Figure 155. Autospectra measured at representative radial locations along profile Ii for the upper counter rotating vortex at $x/c=10$	290
Figure 156. Autospectra measured at representative radial locations along profile Ii for the upper counter rotating vortex at $x/c=10$	293
Figure 157. Autospectra measured at representative radial locations along profile Jj for the upper counter rotating vortex at $x/c=10$	296
Figure 158. Autospectra measured at representative radial locations along profile Jj for the upper counter rotating vortex at $x/c=10$	299
Figure 159. Mean secondary flow vectors of the counter rotating pair at $x/c=30$	302

Figure 160. Contours of turbulent kinetic energy k/U_{ref}^2 for the counter rotating pair at $x/c=30$	303
Figure 161. Contours of v_x^2/U_{ref}^2 for the counter rotating pair at $x/c=30$	304
Figure 162. Core region showing mean secondary flows vectors for the upper counter rotating vortex at $x/c=30$	305
Figure 163. Core region showing contours of vorticity $\omega c/U_{ref}$ for the upper counter rotating vortex at $x/c=30$	306
Figure 164. Core region showing contours of turbulent kinetic energy k/U_{ref}^2 for the upper counter rotating vortex at $x/c=30$	307
Figure 165. Core region showing contours of v_x^2/U_{ref}^2 for the upper counter rotating vortex at $x/c=30$	308
Figure 166. Core region showing contours of v_θ^2/U_{ref}^2 for the upper counter rotating vortex at $x/c=30$	309
Figure 167. Core region showing contours of v_r^2/U_{ref}^2 for the upper counter rotating vortex at $x/c=30$	310
Figure 168. Core region showing contours of $v_x v_\theta/U_{ref}^2$ for the upper counter rotating vortex at $x/c=30$	311
Figure 169. Core region showing contours of $v_\theta v_r/U_{ref}^2$ for the upper counter rotating vortex at $x/c=30$	312
Figure 170. Core region showing contours of $v_x v_r/U_{ref}^2$ for the upper counter rotating vortex at $x/c=30$	313
Figure 171. Mean velocities and Reynolds stresses for profile Kk measured parallel to the line of symmetry for the upper counter rotating vortex at $x/c=30$	314
Figure 172. Mean velocities and Reynolds stresses for profile Ll measured perpendicular to the line of symmetry for the upper counter rotating vortex at $x/c=30$	317
Figure 173. Autospectra measured at representative radial locations along profile Kk for the upper counter rotating vortex at $x/c=30$	320

Figure 174. Autospectra measured at representative radial locations along profile Kk for the upper counter rotating vortex at $x/c=30$	323
Figure 175. Autospectra measured at representative radial locations along profile Ll for the upper counter rotating vortex at $x/c=30$	327
Figure 176. Autospectra measured at representative radial locations along profile Ll for the upper counter rotating vortex at $x/c=30$	329
Figure 177. Hoffmann and Joubert's circulation profiles.....	332
Figure 178. True circulation profiles for the co-rotating pairs at $x/c=10$ and 15 compared to Hoffmann and Joubert's circulation law	333
Figure 179. True circulation profiles for the co-rotating pairs at $x/c=22$ and 30 compared to Hoffmann and Joubert's circulation law	334
Figure 180. True circulation profiles for the counter rotating pairs at $x/c=10$ and 30 compared to Hoffmann and Joubert's circulation law	335
Figure 181. Turbulent kinetic energy contours showing shear layer coordinate system and stations for the co-rotating pairs	336
Figure 182. Turbulent kinetic energy in the wake centerline for the co-rotating pairs	337
Figure 183. Reynolds stresses for the co-rotating wake at $x/c=10$	338
Figure 184. Autospectra in the center of the wake for the co-rotating case at $x/c=10$	344
Figure 185. Autospectra in the center of the wake for the co-rotating case at $x/c=10$. Normalized by the local wake length scale L_0	347
Figure 186. Reynolds stresses for the co-rotating wake at $x/c=30$	348
Figure 187. Autospectra in the center of the wake for the co-rotating case at $x/c=30$	354
Figure 188. Autospectra in the center of the wake for the co-rotating case at $x/c=30$. Normalized by the local wake length scale L_0	357

Figure 189. Turbulent kinetic energy contours showing shear layer coordinate system and stations for the counter rotating pair at $x/c=10$	358
Figure 190. Turbulent kinetic energy in the wake centerline for the counter rotating pairs	359
Figure 191. Reynolds stresses for the counter rotating wake at $x/c=10$	360
Figure 192. Autospectra in the center of the wake for the counter rotating case at $x/c=10$	366
Figure 193. Autospectra in the center of the wake for the counter rotating case at $x/c=10$. Normalized by the local wake length scale L_0	367
Figure 194. Triple product vectors and turbulent kinetic energy contours for the co-rotating pair at $x/c=10$	370
Figure 195. Triple product vectors and turbulent kinetic energy contours for the co-rotating pair at $x/c=15$	371
Figure 196. Triple product vectors and turbulent kinetic energy contours for the co-rotating pair at $x/c=22$	372
Figure 197. Triple product vectors and turbulent kinetic energy contours for the co-rotating pair at $x/c=30$	373
Figure 198. Triple product vectors and turbulent kinetic energy contours for the counter rotating pair at $x/c=10$	374
Figure 199. Triple product vectors and turbulent kinetic energy contours for the counter rotating pair at $x/c=30$	375
Figure 200. Principal stress direction vectors in the core region for the upper co-rotating vortex at $x/c=10$	376
Figure 201. Principal stress direction vectors in the core region for the lower co-rotating vortex at $x/c=10$	377
Figure 202. Principal stress direction vectors in the core region for the upper co-rotating vortex at $x/c=15$	378
Figure 203. Principal stress direction vectors in the core region for the lower co-rotating vortex at $x/c=15$	379

Figure 204. Principal stress direction vectors in the core region for the co-rotating vortex at $x/c=22$	380
Figure 205. Principal stress direction vectors in the core region for the co-rotating vortex at $x/c=30$	381
Figure 206. Principal stress direction vectors in the core region for the upper counter rotating vortex at $x/c=10$	382
Figure 207. Principal stress direction vectors in the core region for the lower counter rotating vortex at $x/c=10$	383
Figure 208. Principal stress direction vectors in the core region for the upper counter rotating vortex at $x/c=30$	384
Figure 209. Principal stress direction vectors in the core region for the lower counter rotating vortex at $x/c=30$	385
Figure 210. Long time average autospectra measured in the core region of the upper co-rotating vortex at $x/c=10$	386
Figure 211. Long time average autospectra measured in the core region of the co-rotating vortex at $x/c=30$	387
Figure 212. Long time average autospectra measured in the core region of the upper counter rotating vortex at $x/c=10$	388
Figure 213. Profile Aa showing Reynolds stresses high passed filtered at a frequency of $fc/U_{ref}=1.5$ for the co-rotating pair at $x/c=10$	389
Figure 214. Profile Aa showing Reynolds stresses high passed filtered at a frequency of $fc/U_{ref}=7.0$ for the co-rotating pair at $x/c=10$	391
Figure 215. Profile Aa showing Reynolds stresses high passed filtered at a frequency of $fc/U_{ref}=20.0$ for the co-rotating pair at $x/c=10$	393
Figure 216. Profile Gg showing Reynolds stresses high passed filtered at a frequency of $fc/U_{ref}=1.5$ for the co-rotating pair at $x/c=30$	395
Figure 217. Profile Gg showing Reynolds stresses high passed filtered at a frequency of $fc/U_{ref}=7.0$ for the co-rotating pair at $x/c=30$	397

Figure 218. Profile Gg showing Reynolds stresses high passed filtered at a frequency of $fc/U_{ref}=20.0$ for the co-rotating pair at $x/c=30$	399
Figure 219. Profile Kk showing Reynolds stresses high passed filtered at a frequency of $fc/U_{ref}=1.5$ for the counter rotating pair at $x/c=30$	401
Figure 220. Profile Kk showing Reynolds stresses high passed filtered at a frequency of $fc/U_{ref}=7.0$ for the counter rotating pair at $x/c=30$	403
Figure 221. Profile Kk showing Reynolds stresses high passed filtered at a frequency of $fc/U_{ref}=20.0$ for the counter rotating pair at $x/c=30$	405

List of Symbols

c	wing chord
E_c	corrected hot wire voltage
E_m	measured hot wire voltage
G_{ii}	one sided auto spectral density function in the i th direction
h	hot wire yaw factor
k	hot wire pitch factor
L_o	length scale based on similarity solution
n	direction normal to wake width
n_d	number of distinct records
N	sample block length
Q	magnitude of mean velocities
Q_e	magnitude of estimated mean velocities
r	radial direction of cylindrical coordinate system
r_c	radius of curvature
Re_c	Reynolds number based on freestream velocity and wing chord
s	direction along spiral wake also used for separation distance between vortices

t	time
T_c	corrected temperature
T_m	measured temperature
u	fluctuating velocity in the x direction
U, V, W	mean velocity components in the x,y,z direction
U_e, V_e, W_e	hot wire estimates of mean velocities
U_{eff}	effective hot wire velocity
U_o	velocity scale based on similarity solution
U_n, U_t, U_s	velocities normal, tangential and spanwise to hot wire
u^2, v^2, w^2	turbulence normal stresses in x,y,z directions
uv, vw, uw	Reynolds shear stresses in x,y,z coordinate system
V_q, W_q	triple product transport vectors in y and z directions
V_r, V_θ, V_x	mean velocity components in r, θ ,x directions
v_r^2, v_θ^2, v_x^2	turbulence normal stresses in r, θ ,x directions
$v_x v_r, v_r v_\theta, v_\theta v_x$	Reynolds shear stresses in r, θ ,x coordinate system
x	streamwise direction
y	spanwise direction
z	transverse direction
z_o	center location of wing wake

Greek Symbols

α_e	angle of attack counter rotating vortex pairs
α_o	angle of attack co-rotating vortex pairs
δ	boundary layer thickness where $U/U_e=0.99$

δ^*	boundary layer displacement thickness
Δy	separation distance between two wings
ε_r	autospectra normalized random error
γ	hot wire over heat ratio (1.7 used)
Γ	closed loop circulation around vortex
Γ_o	wing root circulation
θ	angular direction about the x-axis
θ_i	quad hot wire effective wire angles $i=1....4$
ν	kinematic viscosity
ω	vorticity

1. Introduction

Vortical flows play an important role in aerodynamics and hydrodynamics. Of special interest is the interaction of vortices generated by lifting surfaces. The understanding of these interacting vortices is critical to the design and operation of both aircraft and naval vessels. Powerful vortex wakes produced by large military and commercial aircraft are extremely hazardous to smaller aircraft flying in the vicinity, resulting in countless accidents each year. This requires aircraft to be spaced a larger distance apart greatly reducing the efficiency of most airports. Also, vortices produced by the bow plane on a submarine interact with the rear of the vessel resulting in large acoustic signals. This increases the detection of the vessel and reduces its overall operational capability. In addition, helicopter blades produce vortices which interact with each other resulting in noise and vibration problems. With the recent development in large supercomputers and numerical schemes, solving these problems becomes much less time consuming and cost effective. However, before these flows can be successfully computed, the turbulent structure of vortical flows must be understood. Providing that understanding is the primary motivation of this experiment.

It is well known that a vortex sheet is produced from a finite lifting surface as a consequence of the nonuniform spanwise lift distribution on that surface. The roll up of

this sheet into a discrete vortex at the tip was recognized as far back as 1907 by Lancaster (see figure 1). Various models of the roll up process have been examined by Hackett and Evans (1971) and by Phillips (1981). The vortex produced at the wing-tip is characterized by two distinct regions of the flow. In the inner region called the core, the mean tangential velocity varies approximately proportionally with the radius from zero at the center to a maximum at the edge of the core. The circulation varies approximately proportionally with the radius squared until it reaches a maximum at the edge of the core. In the outer region, the mean tangential velocity varies approximately inversely with the radius and asymptotically approaches a value of zero. The circulation is much more constant with radius in the outer region. Figure 2 shows the velocity and circulation distribution for an ideal vortex.

A fair amount of research examining the mean velocity distributions of a single wing-tip vortex has been conducted by Hoffmann and Joubert (1963), Mason and Marchman (1972), Corsiglia et al (1973) and Barker et al (1974) and various other researchers over the last few decades. However, little work has been conducted on wing-tip vortex pairs and even less on the turbulent structure of these pairs. Previous research has concentrated on counter rotating vortex pairs produced by large aircraft and their interaction far down stream on other aircraft. Donaldson and Bilanin (1975) examined various aspects of vortices produced by large scale aircraft including the roll up process and lift distributions, interaction of tip vortices with each other and with flap and tail vortices, various ways to increase vortex decay, and atmospheric effects. Most of their results presented were produced computationally with some mean velocity measurements from full scale aircraft. Crow (1970) developed an inviscid stability theory for counter rotating vortices produced by large scale aircraft. He showed that for disturbances of

certain wavelengths, the vortex pair would undergo a symmetric sinusoidal instability that caused the pair to join and form a train of vortex rings.

Other work has concentrated on counter rotating vortices interacting with some type of wall or surface. Barker and Crow (1977) examined counter rotating vortices in a ground effect situation. Using two dimensional vortices, they compared the trajectories of the pairs against potential flow theory and to the results of full scale aircraft. They reported that relaminarization takes place in the core as the vortex pair is convected upwards. A large amount of work has been conducted between the interaction of three dimensional vortex pairs and a free surface. Workers such as Sarpkaya et al. (1988) and Willmarth et al. (1989) have compared the results to potential flow theory.

There appears to be little research conducted on the turbulence structure of an interacting wing-tip vortex pair. The main reason for this is that most workers have found it difficult to measure even a single vortex in the wind or water tunnel. Therefore it is of interest to discuss previous studies of a single wing-tip vortex. Vortices produced in the lab "meander" or "wander" in space, their core location downstream of the wing is a function of time. This meandering means that a stationary probe will measure velocities that are both a function of space and time. The motions will tend to smooth the measured mean velocity and turbulence intensity profiles in regions where they are changing rapidly. Also, turbulence stresses will be significantly over estimated where mean velocity gradients are significant. Baker et al. conducted experiments on a full wing in a water tunnel using laser doppler velocimeters. They found that vortex meandering decreased the maximum tangential velocities by 30% and increased the measured core radius by a factor of 2.2. Baker attributed the meandering to freestream

turbulence in the tunnel. Corsiglia et al (1973) conducted triple hot-wire measurements using a full wing in the NASA Ames 40x60 wind tunnel. They used a rapid rotating arm mechanism to fly the hot-wire through the core obtaining instantaneous mean velocity measurements. Maximum tangential velocities were increased by 50% using this approach as compared to a fixed hot-wire probe. Vortex meandering was 213% of the wing chord which they attributed to freestream turbulence. Singh and Uberoi (1976) measured the single vortex of a laminar flow half wing with hot-wires and concluded that the relatively high frequency unsteadiness of $fc/U_{ref}=2.1$, based on the wing chord and freestream velocity, was due to laminar flow instabilities associated with large axial velocity differences between the core and outer region. They inferred that these laminar flow instabilities had a symmetric and a helical mode with wavelengths of the same order as the core diameter. These helical modes were also observed in experiments by Sarpkaya (1992). Using both rectangular and swept half wings, he examined the interaction of a single vortex with its image and a free surface in the water tunnel. Sarpkaya noted that due to helical instabilities, the vortex peels off randomly and sheds vorticity along its length. He found that the core of the turbulent vortex is not a smooth axisymmetric solid body of rotation. Instead there is a transfer of momentum between the core and outer region. This leads to oscillations of the core and the various velocity components.

Another major problem in measuring wing-tip vortices is the effects of probe interference. Orloff (1971) and Gasperek (1960) reported that the trajectory of the vortex moved when a small diameter probe was inserted into the core. Stifle and Panton (1991) examined the effects of passing a wire through the core of a single vortex produced by a delta wing. They found that disturbances introduced into the vortex core

propagated both upstream and downstream with smaller disturbances produced by a slower moving wire.

However, some workers such as Mason and Marchman (1972) and Devenport and Sharma (1991) have showed that a relatively stable single vortex which is insensitive to probe interference can be generated in a large low turbulence wind tunnel, in their case the Virginia Tech Stability Tunnel. Mason and Marchman (1972) made farfield mean velocity measurements on a single vortex produced by a half wing. Using a five hole yaw head probe, they examined the mean structure and effects of mass injection. The vortex appeared very stable with no significant meandering present. They reported that there was a slight amount of probe interference but only when the probe was yawed. The most complete and detailed turbulence measurements to date on a single vortex are those by Devenport and Sharma (1991). They conducted similar experiments using Mason and Marchman's wing measuring the turbulent structure of the vortex with cross and triple hot-wire probes for a variety of Reynolds numbers and angles of attack. Using helium bubble flow visualizations and a dummy hot-wire probe, Devenport and Sharma showed how stable and insensitive their vortex was to probe interference. They reported that the maximum meandering was no greater than $\pm 4.7\%$ of the wing chord with frequencies on the order of $fc/U_{ref} = .005$.

To avoid the problems of meandering and probe interference, Green and Acosta (1991) used a novel approach to measure the instantaneous axial and tangential velocities produced by a swept half wing. They used double-pulsed holography of injected microbubbles which act as Lagrangian flow tracers. Also observed was a highly unsteady axial flow with large fluctuations on the order of the freestream velocity.

Vortex "kinks" were observed where the flow direction diverges quickly from the freestream direction, and then quickly recovers.

In an attempt to generate stable single vortices, some workers have used a split wing configuration. Here the vortex is generated at the junction of two wings placed at equal and opposite angles of attack. A small nacelle is often placed between the two wings and used to join the wing tips together. Although the split wing vortex is supposed to be more stable, it lacks the same initial turbulence or mean flow structure since it is from two wings as opposed to one. Figure 3 shows the difference between the split wing and full wing. Hoffmann and Joubert (1963) appear to be the first workers to use the split wing concept to generate a single vortex. They analyzed the circulation distribution of the vortex and found a region where the circulation is proportional to the logarithmic radius for various conditions. In addition they developed a circulation defect law in the inner region of the vortex analogous to a turbulent boundary layer. Leuchter and Solignac (1983) used a split wing to examine the effect of wind tunnel adverse pressure gradients on the decay of a vortex. Using laser doppler velocimeter, they obtained mean and turbulence quantities and found that with increased pressure gradients, vortex breakdown occurred much more rapidly. Bandyopadhyay et al.(1990) also made turbulence measurements using a split wing in various amounts of freestream turbulence. Using smoke flow visualizations and hot-wires, they observed that momentum transfer takes place between the core and outer region. They also discovered that turbulent fluid inside the core relaminarizes due to the rotational motion of the core. Phillips and Graham (1984) also used a split wing to generated a single trailing vortex. Using cross hot-wires they obtained mean velocities and Reynolds stresses for all three directions. Their vortex appeared to be axisymmetric with solid body rotation in the core region.

Ways to increase the decay rate were also examined by introducing jets and wakes into the core. In addition, Smits and Kumer (1985) examined a split wing vortex at various streamwise locations. They found that the two vortices of opposite sign rotated about each other and eventually merged to produce a dominant central vortex. Mean flow and turbulence quantities were obtained throughout the merging zone. Circulation profiles varied logarithmically with radius at all streamwise locations similar to those of Hoffmann and Joubert's (1963). The relationship between the mean flow gradients and shear stresses were also examined in applying first order turbulence models.

The aims of the present investigation are; to make detailed measurements of the mean flow and turbulence structure of co-rotating and counter rotating vortex pairs of equal strength; to use those measurements to deduce the true structure and physics of those flows by eliminating the vortex motions; to provide data for future computations. The investigation consists of two parts.

1. Helium bubble flow visualizations to examine qualitatively the overall characteristics of the interacting vortex pairs and to ensure their stability and insensitivity to probe interference over a wide range of conditions.
2. Detailed measurements of mean velocities, Reynolds stresses, spectra, and other turbulence quantities in two selected cases, one co-rotating and one counter rotating.

This report is organized into five chapters. Experimental equipment and measurements techniques are discussed in chapter two with the flow visualization results discussed in chapter three. Hot-wire measurements and results are presented in chapter four with conclusions made in chapter five.

2. Experimental Apparatus And Techniques

2.1 Facilities and Equipment

2.1.1 Wind Tunnel

Experiments were performed in the Virginia Tech Stability Wind Tunnel (figure 4 and 5). It is a continuous, single return, closed-circuit subsonic wind tunnel with various interchangeable test sections. It is powered by a 600 horse power d.c. motor allowing a maximum speed of 56 m/s. The test section used for the experiment is square with a cross section of 1.83m X 1.83m and a length of 7.33m. An air tight containing room is used to enclose the test section so that the pressure can be equalized between the test section and control room. Seven anti-turbulence screens are located in the settling chamber just ahead of the nozzle which has a contraction ratio of 9:1. The diffuser angle is 3 degrees with large vortex generators located at the entrance to prevent separation as the flow decelerates. Flow in the empty test section is closely uniform with a turbulence intensity of less than .03% at 20m/s (see Choi and Simpson (1987)). One side of the test section is made of plexiglass and glass panels through which observations are made.

2.1.2 Wings

Mason and Marchman's (1972) wing model was used along with an identical model produced on a numerical controlled milling machine. Each model has a rectangular planform, NACA 0012 airfoil section and a blunt wing tip. The chord and span are .203m and 1.22m respectively. Mason and Marchman's wing is made from solid brass while the other wing is made from solid aluminum. Surfaces of both wings are accurate to within $\pm .25\text{mm}$. The wings were mounted vertically at the mid span of the test section from opposite walls perpendicular to the freestream (figure 6). The end of each wing ran through a turntable mounted flush with each test section wall (figure 7 and figure 8). The turntables allowed the wings to be rotated to any angle of attack about the quarter chord location. The vertical location of each wing was varied by sliding it through the turntable and clamping it to the turntable outside of the test section (figure 8). The streamwise and lateral positions of the turntable and base plate holding the lower wing could be adjusted, enabling the two wings to be aligned. Once aligned, small gaps around the base plate were covered with tape to provide a flush surface with the test section wall. To eliminate flow induced vibration, the end of each wing outside of the test section was braced by running 4.0mm diameter steel cables stretched horizontally between steel supports. By varying the tension of each cable and allowing the wings to pivot at the turntables, the cables were also used to adjust the dihedral angle of each wing to 0° (i.e. to position the wings in the vertical plane). The cables were attached via a pin located at the axis of rotation (i.e. the quarter-chord location) and thus did not prevent the wing being rotated to angle of attack.

The wings were initially placed at zero angle of attack, with an accuracy of $\pm 0.2^\circ$ by using a removable wing tip holding 48 static pressure ports. The aluminum wing tip was 100mm wide with three rows of 16 pressure ports spaced equally on both sides located at 19mm, 44mm and 70mm from the outer edge. The pressure taps and wind tunnel pitot tube were both connected to a scanivalve system. Pressures were measured using a SETRA model 239 pressure transducer interfaced to an IBM AT computer through a Data Translation D2801-A A/D converter. The removable wing tip was first placed on the upper wing and used to position it at zero angle of attack by equalizing the pressures on both sides. The lower wing was then moved up through the turntable until its tip touched that of the upper wing. This wing was then rotated to the same angle. The lower wing was then slid down into position and clamped. Other angles of attack were measured relative to these locations. To eliminate possible unsteadiness and non-uniformity that might result from natural transition, the boundary layer on the wings were tripped. Glass beads with a diameter of .5mm were glued to the wings in a random pattern in a strip extending between the 20% to 40% chord locations. Average density was 200 beads/cm².

2.1.3 Traverse Mechanism

A traverse mechanism mounted in the test section was used to hold a dummy probe for flow visualizations and hot-wire probe for velocity measurements (figure 5 and 7). The location of the probe could be moved both vertically and horizontally in the test section. The streamwise location of the probe was changed by moving the traverse mechanism manually then securing it to the test section. Three RM series stepper motors produced by Compumotor were used to control both the vertical and horizontal axis. The motors

were connected to a SD drive system controlled by an IF1 controller also supplied by Compumotor. An IBM AT was used to send position locations through a RS-232 port to the IF1 controller. A Telebyte Model 268 optical isolator was inserted into the RS-232 line to reduce the amount of electrical noise received from the controller. This system allowed the probe location to be controlled by the data acquisition programs. Accuracy of the both the vertical and horizontal axis were within .025 mm

2.1.4 Flow Visualization Equipment

The flow visualizations were performed using a Sage Action Inc. Model 5 console helium bubble generator with two "plug in" heads. The generator produces helium filled bubbles by supplying Sage Action Inc. bubble film solution, helium and compressed air to the two heads. Micro-metering valves vary the amount of mixture supplied to the heads which effects the size and rate of helium bubbles produced. Valve settings were adjusted as specified in the Sage Action Operators Manual (1990), producing bubbles about 3.2mm in diameter . Bubbles generated by the heads are then passed through two filters designed to centrifuge out heavier than air bubbles. Bubbles leave the filters through two 12.7mm diameter plastic tubes which in this investigation were connected to two pieces of 4.8mm thick aluminum tubing of airfoil cross section. The airfoil tubing allowed bubbles to be injected into the flow with minimal interference (figure 6 and figure 7). Tubes were mounted 1.0m upstream of the wing tips. At no time did the bubble probes have any visible effects on the flow.

The helium bubbles were illuminated using a Varian arc lamp (Model p150S-7) supplied by Sage Action Inc. The arc lamp was mounted at the upstream end of the diffuser. It

was adjusted to produced a well defined narrow light beam aligned with the vortices. The amount of unnecessary scattered light was therefore minimized. The side of the test section opposite the plexiglass and glass panels was covered with flat black plastic sheet to improve the visibility of the helium bubbles.

Over 550 photographs were taken using a Nikon N6006 camera with ASA 1600 color film using 2 and 8 second exposure times and an aperture settings of f/1.8. Several hours of video film were also taken using a JVC camcorder with 1/60 second exposure times and 30Hz framing rate.

2.2 Hot Wire Anemometry

Velocity measurements were made using single and quad hot wire probes in conjunction with a Dantec anemometer system. This system consisted of a four Dantec 56C17 bridges and four Dantec 56C01 constant temperature anemometers housed in a Dantec 56B12 main frame. The output voltages from the anemometer bridges where then sent to a "buck and gain" amplifier system built in house with Burr-Brown integrated circuits. The amplifiers subtracted an offset voltage from the anemometer output voltage, typically 1.95 volts, and multiplied the result by a factor of 10. The frequency response of the amplifiers were flat out to 100kHz. Voltages were sent to an Analogic 12 bit HSDAS-12 A/D converter with a voltage range of 0-5.0 volts. The A/D converter can sample four channels simultaneously at a maximum rate of 100kHz per channel. In addition two other channels of the A/D converter were used for digitizing the free-stream pitot static pressure and the flow temperature. The resulting digitized signals were then sent to an IBM AT computer for processing. An 18-8 Laboratories PL1250 array

processor was used to linearize the hot-wire signals and present resulting velocities and stresses in real time. Optical disk cartridges holding up to 940 megabytes each were used to store the raw and processed data.

Both hot wire probes were calibrated before and after each traverse at a common calibration location to ensure accurate velocity measurements. King's law given below was used to relate the voltage of each wire to its effective velocity.

$$E^2 = A + BU_{\text{eff}}^n \quad (2.2.1)$$

where $n=0.45$. The constants A and B were determined from a least squares fit using 7 to 10 calibration points over a range of velocities. The actual velocity error from each calibration point was less than 1%. During a series of measurements the flow temperature inside the wind tunnel would vary a few degrees per hour due to outside temperature changes. Hot wire signals were corrected for temperature changes using the method of Bearman (1970) given by

$$E_c = E_m \sqrt{\frac{\gamma - 1}{\gamma - T_m / T_c}} \quad (2.2.2)$$

where γ is the over heat ratio (1.7 used) and E and T are the unlinearized voltage and temperature. Subscripts (m) and (c) stand for measured and corrected respectively. Frequency response of the hot-wire system was flat out to 50kHz for an over heat ratio of 1.7

2.2.1 Dummy Hot Wire Probe and Holder

Since one of the purposes of the flow visualization was to examine the effects of probe interference on the vortices, a dummy hot-wire probe was used during a few of the visualizations. The dimensions of the probe were matched to a Dantec cross hot wire probe and stem.

The probe holder (figure 9) was a 23.6mm diameter steel tube attached to the traverse mechanism and aligned with the flow. It positioned the tip of the dummy probe .7m upstream of the traverse mechanism. Two 6.2mm diameter rods were used to offset the dummy probe from the holder by 105mm. This arrangement allowed the dummy probe to be positioned in the core of one of the vortices with the large probe holder well outside it.

2.2.2 Single Hot Wire Probe

A TSI 1210T.5 single hot wire probe was used to measure velocity profiles at the trailing edge of the upper and lower wing. The single hot wire probe was mounted in a similar fashion as the dummy wire probe except that a 25.4mm diameter solid aluminum rod was used in place of the tube. The single hot wire was offset from the probe holder by 105mm using two 4.8mm diameter rods. The wire was positioned parallel to the wing 1 mm from the trailing edge.

According to Jorgenson (1971), the relationship between the effective cooling velocity of a wire U_{eff} and the velocities normal U_n , tangential U_t and spanwise U_s (figure 10) is given by

$$U_{\text{eff}}^2 = U_n^2 + k^2 U_t^2 + h^2 U_s^2 \quad (2.2.3)$$

where k and h are pitch and yaw factors respectively. Expressing these terms using velocity components U, V, W shown in figure 10, we obtain

$$U_{\text{eff}}^2 = U^2 + k^2 V^2 + h^2 W^2 \quad (2.2.4)$$

Splitting the velocity components in the mean and fluctuating parts and rearranging terms gives

$$U_{\text{eff}} + u = U \sqrt{1 + \frac{2u}{U} + \frac{u^2}{U^2} + k^2 \left(\frac{V^2}{U^2} + \frac{2Vv}{U^2} + \frac{v^2}{U^2} \right) + h^2 \left(\frac{W^2}{U^2} + \frac{2Ww}{U^2} + \frac{w^2}{U^2} \right)} \quad (2.2.5)$$

Assuming V, W, u, v, w are small compared to U and performing binomial expansion of the square root gives

$$U_{\text{eff}} + u_{\text{eff}} = U + u \quad (2.2.6)$$

Thus the single hot wire measures only the mean U and fluctuation u . The single wire probe was calibrated in the freestream against the wind tunnel pitot-static probe with the wire normal to the flow.

2.2.3 Quad Hot Wire Probe

A miniature quad hot wire probe produced by Auspex Corporation (model AVOP-4-100) was used to measure mean velocities and Reynolds stresses at various planes downstream of the wings. The quad hot wire probe consists of four wires arranged to form two orthogonal X-wire arrays with each wire inclined at a nominal angle of 45 degrees to the probe axis (figure 11). Eight prongs, 75 μ m in diameter at the tip, are used to position the wires 40mm upstream of the main part of the probe. A .9mm² sensing volume is used to achieve high spatial resolution and minimize probe interference effects. Each wire is made of tungsten and is 0.8mm in length and 5 μ m in diameter. The quad wire probe was mounted in a similar fashion as the single wire probe, using the aluminum probe holder as shown figure 12.

The quad hot wire is capable of simultaneous measurements of all 3 velocity components. These components were determined from the 4 instantaneous effective velocities output from the 4 sensors in a two stage process.

- (i) Initial estimates of the instantaneous velocity components were obtained using a Jorgenson (1971) type analysis taking into account the measured wire angles and pitch and yaw sensitivities.
- (ii) Corrections to these estimates were then applied.

2.2.3.1 Initial Estimates

According to Jorgenson (1971), the relationship between the effective cooling velocities of each wire and the normal, tangential and out of plane velocity components is given by

$$U_{\text{eff1}}^2 = (U \cos \theta_1 + V \sin \theta_1)^2 + k_1^2 (V \cos \theta_1 - U \sin \theta_1)^2 + h_1^2 W^2 \quad (2.2.7)$$

$$U_{\text{eff2}}^2 = (U \cos \theta_2 + W \sin \theta_2)^2 + k_2^2 (W \cos \theta_2 - U \sin \theta_2)^2 + h_2^2 V^2 \quad (2.2.8)$$

$$U_{\text{eff3}}^2 = (U \cos \theta_3 - V \sin \theta_3)^2 + k_3^2 (U \cos \theta_3 + V \sin \theta_3)^2 + h_3^2 W^2 \quad (2.2.9)$$

$$U_{\text{eff4}}^2 = (U \cos \theta_4 - W \sin \theta_4)^2 + k_4^2 (U \cos \theta_4 + W \sin \theta_4)^2 + h_4^2 V^2 \quad (2.2.10)$$

where wire 1 and wire 3 are in the UV plane and wire 2 and wire 4 are in the UW plane as shown in figure 11. The pitch and yaw factors k and h were estimated for each wire by making measurements over a range of yaw and pitch angles in a uniform flow of known direction. k was found to be approximately 0.0 and h was approximately 1.0 for all four wires. Effective wire angles were also determined using the angle calibration mechanism in the uniform flow. Angles obtained were $\theta_1=47^\circ$, $\theta_2=55^\circ$, $\theta_3=50^\circ$ and $\theta_4=51^\circ$ which were substantially different than their nominal values. Splitting the velocity components into the mean and fluctuating terms and ignoring higher order terms and assuming small W , we obtain for wire 1 and wire 3

$$U_{\text{eff1}} = \sqrt{A_1} U + \frac{D_1}{\sqrt{A_1}} V \quad (2.2.11)$$

$$U_{\text{eff3}} = \sqrt{A_3} U + \frac{D_3}{\sqrt{A_3}} V \quad (2.2.12)$$

where

$$\begin{aligned} A_1 &= 1 - \cos^2 \theta_1 & A_3 &= 1 - \cos^2 \theta_3 \\ D_1 &= \frac{\sin 2\theta_1}{2} & D_3 &= -\frac{\sin 2\theta_3}{2} \end{aligned}$$

assuming V is small and ignoring higher order terms we obtain for wire 2 and wire 4

$$U_{\text{eff}2} = \sqrt{A_2} U + \frac{D_2}{\sqrt{A_2}} W \quad (2.2.13)$$

$$U_{\text{eff}4} = \sqrt{A_4} U + \frac{D_4}{\sqrt{A_4}} W \quad (2.2.14)$$

where

$$\begin{aligned} A_2 &= 1 - \cos^2 \theta_2 & A_4 &= 1 - \cos^2 \theta_4 \\ D_2 &= \frac{\sin 2\theta_2}{2} & D_4 &= -\frac{\sin 2\theta_4}{2} \end{aligned}$$

The velocity components U, V, W can then be determined by

$$V = \frac{\frac{U_{\text{eff}3}}{\sqrt{A_3}} - \frac{U_{\text{eff}1}}{\sqrt{A_1}}}{\frac{D_3}{A_3} - \frac{D_1}{A_1}} \quad (2.2.15)$$

$$W = \frac{\frac{U_{\text{eff}4}}{\sqrt{A_4}} - \frac{U_{\text{eff}2}}{\sqrt{A_2}}}{\frac{D_4}{A_4} - \frac{D_2}{A_2}} \quad (2.2.16)$$

$$U = \frac{U_{\text{eff1}} - \frac{D_1}{\sqrt{A_1}} V}{\sqrt{A_1}} \quad (2.2.17)$$

2.2.3.2 Corrections

The corrections were determined in advance, by pitching and yawing the quad wire in a uniform flow of known velocity and direction. They were obtained by comparing the actual velocity components experienced by the probe, calculated from the flow velocity and pitch and yaw angles, with those obtained from the hot wire outputs using the Jorgenson method type analysis.

Corrections were initially determined, from a combination of 361 pitch and yaw angles between $\pm 45^\circ$, as functions of the actual components.

$$\begin{aligned} \frac{V - V_e}{Q} &= f_1\left(\frac{V}{Q}, \frac{W}{Q}\right) \\ \frac{W - W_e}{Q} &= f_2\left(\frac{V}{Q}, \frac{W}{Q}\right) \\ \frac{Q - Q_e}{Q} &= f_3\left(\frac{V}{Q}, \frac{W}{Q}\right) \end{aligned} \quad (2.2.18)$$

where $Q = \sqrt{U^2 + V^2 + W^2}$, U, V and W refer to the actual velocity components and subscript (e) identifies the estimates from the hot wire outputs derived above. Figure 13a through 13c show contours of f_1 , f_2 and f_3 . Note that even at moderate angles (e.g. 15° , $W/Q = .27$) the Jorgenson analysis requires significant if not substantial correction. To

make use of these corrections it is necessary to express them as functions of the estimated rather than the actual components i.e.

$$\begin{aligned}\frac{V - V_e}{Q_e} &= g_1\left(\frac{V_e}{Q_e}, \frac{W_e}{Q_e}\right) \\ \frac{W - W_e}{Q_e} &= g_2\left(\frac{V_e}{Q_e}, \frac{W_e}{Q_e}\right) \\ \frac{Q - Q_e}{Q_e} &= g_3\left(\frac{V_e}{Q_e}, \frac{W_e}{Q_e}\right)\end{aligned}\tag{2.2.19}$$

This was done by interpolating the corrections onto a square grid resulting in g_1 , g_2 , and g_3 in figure 13d through 13f. With increasing flow angles, the velocity estimates from the Jorgenson analysis increased to a maximum then decreased or "folded" toward lower estimates. These folded regions were ignored in the interpolation process resulting in corrections shown in figure 13. Thus the limits of the contoured regions shown in figures 13d through 13f represent the largest velocity estimates at which the quad wire probe can measure. g_1 , g_2 and g_3 were interpolated to obtain precise corrections for each set of estimated velocity components. The above procedure yielded instantaneous records of U, V, and W accurate to much larger values of instantaneous flow angles than the original estimates. Mean velocities, Reynolds stresses, triple products and spectra were then obtained from these records simply by applying their definitions.

3. Flow Visualization Results

The cartesian coordinate system (x,y,z) shown in figure 5 will be used in describing the results of the flow visualizations. The direction of the freestream flow is along the x axis with the wings aligned along the vertical y axis. The reference angle θ is measured about the x axis according to the right hand rule from the y axis. The origin of the coordinate system is located at the leading edges of the wings at zero angle of attack and is centered between the wing tips.

The bulk of the flow visualizations were performed at Reynolds numbers ($Re_c = U_{ref}c/\nu$) based on the freestream velocity and wing chord (.203m) of 130,000. A few visualizations were also performed at $Re_c=400,000$ to examine the sensitivity of selected flows to Reynolds number and probe interference. Visualizations were performed with the wings at equal (α_e) and at opposite (α_o) angles of attack, generating counter and co-rotating vortices of equal strength respectively. Angles of attack (α_e and α_o) were 2.5° , 5.0° , 7.5° and 10.0° . The separation distance between the wing-tips Δy was also varied. Separations of c , $c/2$, $3/8c$ and $c/4$ were studied. Photographs were taken at different streamwise locations through the transparent tunnel wall, ceiling and looking upstream from the diffuser. Video films were taken through the tunnel wall and from the diffuser,

looking upstream. Table 1 lists all the conditions at which visualizations were performed.

A selection of photographs taken from the diffuser looking upstream at $Re_c=130,000$ are shown in figure 15 through figure 20 for the co-rotating pairs and figure 33 through figure 35 for the counter rotating pairs. Photographs are grouped by wing-tip separation Δy and then by angle of attack. In all photographs the flow direction is from right to left. Note that the pictures presented are not an instantaneous view of the flow but are time averaged exposures. Therefore the paths followed by the bubbles appear as streaks. The center of the vortex cores are seen in the photographs as two bright streaks generated by the lighter-than-air helium bubbles trapped there. Note that both cores appear larger at the end of the test section due to the perspective view of the photographs.

3.1 Co-rotating Vortex Pairs

Before examining the photographs, it is important to note some properties of a co-rotating vortex pair. Figure 14 is a sketch of an idealized co-rotating vortex pair. Vortex (a) induces a velocity on the core of vortex (b) causing it to move to the left of the page. In turn, vortex (b) induces a velocity on the core of vortex (a) causing it to move to the right of the page. Since the velocities induced on the cores are equal and opposite, the pair tends to rotate clockwise about a common center. As the separation distance between the two decrease and/or the strength of both increase, the pair will experience a greater rotation rate about the common center.

Figure 15 shows the vortex pair generated with a wing-tip separation $\Delta y=c/4$ and an angle of attack $\alpha_o=5.0^\circ$. The wings are visible next to the circular reflection of the arc lamp beam on the right side of the photograph. The two vortex cores generated at the wing tips, rotate about each other as they move downstream. Over their first few chord lengths the vortex cores move slightly apart, presumably as a result of the same conservation theorems that cause an isolated wing tip vortex to initially move inboard. After reaching a maximum separation the cores begin moving towards each other, their rotation rate about each other increasing as they do. Ultimately, at about 20 chord lengths downstream of the wings, they merge and form a single vortex with a larger core. This merging process occurs over a distance of approximately 1.5 chord lengths and appears to be associated with it a significant amount of high frequency, small scale turbulent motion. The vortex pair rotate about each other approximately 1.25 to 1.5 times before merging occurs. At $\alpha_o=7.5^\circ$ and 10.0° (figure 16 and figure 17), the flow is quantitatively as at 5° angle of attack except that the vortices rotate the same amount more quickly and merge a shorter distance downstream of the wings. At $\alpha_o=2.5^\circ$, the visualization was far less clear either because of the centripetal forces experienced by the bubbles were too weak to hold them in the core, or because of substantial interaction between the vortex cores beginning at the wing tips.

Increasing Δy to $3/8c$ (figures 18 to 20), decreased the level of interaction between the vortices. As before, the cores are not clearly visible at $\alpha_o=2.5^\circ$. At $\alpha_o=5.0^\circ$ (figure 18), the vortex cores rotate about each other but do not merge within the length of the test section. Increasing angle of attack to $\alpha_o=7.5^\circ$ and 10.0° produces pairs that merge at $x/c=29.8$ and 20.0 respectively, (figures 19 and 20).

Increasing Δy to $c/2$ and c further decreased the level of interaction. In only one case at $\alpha_o=10^\circ$, $\Delta y=c/2$ did the vortices merge by the end of the test section, at $x/c=34.5$.

One feature of these flows not clearly visible in the photographs is small lateral motions of the vortex cores. For the most part the vortex cores moved simultaneously either in the same or opposite directions. Motions were quantified by direct observations and by examining the video tapes. In the most severe cases motions in the same directions had an amplitude of at most $\pm 20\text{mm}$ (10% chord) at $x/c=20$. In other cases (figure 21), especially those where the vortex pair merged, the amplitude was significantly lower. As evidenced by figure 21, we were able to find no other consistent variation of the amplitude with configuration. Though the difference was too small to quantify, the amplitude of these motions did appear, in all cases, to be slightly less in the z than in the y directions. Motions of the cores in opposite directions (which amount to changes in their angle of rotation about each other) did not appear to vary much from configuration to configuration. Their magnitude was at most $\pm 4^\circ$. The frequency of all motions was extremely low with the shortest period on the order of 5 seconds. Normalizing the frequency with the wing chord and freestream velocity, we obtain fc/U_{ref} of about .004, at least two orders of magnitude lower than any frequencies likely to result from turbulent structures. In the vicinity of the merging location, some much higher frequency smaller scale motions were present but these appeared to be part of the local turbulent structure.

Various properties of the co-rotating vortex pairs have been plotted. Figure 22 shows the angle of rotation of a line joining the vortex cores from the wing to $x/c=20$ as a function of angle of attack. Angles were determined from the photographs taken through the test

section wall and ceiling. The uncertainty in angles is about $\pm 10^\circ$. Note the almost linear relationship with angle of attack for each wing separation as might be expected. Crude estimates of the angle of rotation may be obtained if we model this flow using two infinite straight line vortices of strength equal to the total bound circulation on each wing Γ , as shown in figure 14. If we denote the distance between the vortices as s , then vortex (a) induces a velocity

$$\frac{\Gamma}{2\pi s} \quad (3.1.1)$$

on vortex (b). Vortex (b) of course, induces an equal and opposite velocity on (a). In the time t , therefore, a line joining (a) and (b) will rotate through an angle

$$\theta = \frac{\frac{\Gamma}{2\pi s} \times t}{s/2} = \frac{\Gamma t}{\pi s^2} \quad (3.1.2)$$

Substituting x/U_{ref} for t we have

$$\theta = \frac{\Gamma x}{\pi s^2 U_{\text{ref}}} \quad (3.1.3)$$

The present data are compared with the results of this analysis in figure 23. Values of s were obtained from the photographs at the points where the rotation angles were measured. Values of Γ were obtained using a lifting line theory calculation. Note the difference in slopes between theory and the data. This may be attributed to the

assumption that the vortices are infinitely long and two-dimensional, which of course they are not and also the implied assumption that the root circulation is entirely contained within their cores, which it is not. Also, downstream the separation distance between the vortex cores is decreasing resulting in a greater rotation angle compared to infinite line vortices. Surprisingly, the collapse of the data (though not its correlation with theory) is improved if Δy , the wing-tip separation, is used in place of s . θ vs $\Gamma x / \pi \Delta y^2 U_{ref}$ is plotted in figure 24.

In figure 25, the wing separation distance Δy has been plotted vs angle of attack for all sixteen cases tested. This plot shows the boundary between the pairs that merged and those that did not. Note the almost linear boundary between the two regions. In figure 26, the merging location x_m/c as a function of angle of attack has been plotted for the six flows that merged in the test section. The uncertainty level in x_m is about $\pm .5c$. The merging process must be associated with inviscid flow effects according to Rossow (1971) and Melander et al. (1988). Rossow conducted inviscid numerical calculations on interacting vortices by modeling the cores using concentric rings of point vortices. He discovered that when a vortex core was subjected to an induced velocity from another vortex, a shear was produced deforming the core. This deformation of the core allows vorticity to be transferred between the two cores resulting in merger. Rossow concluded that merger between the pairs depended entirely on the vortex strengths and their associated separation distance. Using this result, from equation 3.1.1 the induced velocity is given by

$$\frac{ds}{dt} = \frac{\Gamma}{2\pi s} \quad (3.1.4)$$

Substituting x/U_{ref} for t and solving for the merging location we have

$$x = \frac{2\pi s^2 U_{ref}}{\Gamma} \quad (3.1.5)$$

Because of the difficulty of defining a vortex separation distance s during the merging process we shall instead use the separation of the wings Δy which, in any case, better correlates the rotation angles. Normalizing by the wing chord c we obtain

$$\frac{x_m}{c} = \frac{2\pi \Delta y^2 U_{ref}}{\Gamma c} \quad (3.1.6)$$

As can be seen from figure 27, the data when plotted in these terms collapses fairly well to a straight line. There is a small additive constant present which causes the vortex pairs to merge faster than predicted from analysis. This may be attributed to viscous interaction from the shear layers which could slightly accelerate the merger process. Still, it is surprising to see such a good correlation of the results considering the assumption that transfer of vorticity causes merging to begin.

3.1.1 Cases for Further Study

The following four cases were selected for further study.

$\Delta y = 3/8c$	$\alpha_0 = 5.0^\circ$
$\Delta y = 3/8c$	$\alpha_0 = 7.5^\circ$
$\Delta y = 3/8c$	$\alpha_0 = 10.0^\circ$

$$\Delta y = c/4 \quad \alpha_0 = 5.0^\circ$$

These four cases were chosen because they displayed the greatest range of flow phenomenon, i.e., interaction of the separate vortex cores over a significant streamwise distance, merging, and formation of a single core.

In each case additional photographs were taken at $Re_c = 130,000$ through the transparent wind tunnel side wall enabling photo-mosaics of the complete flows to be constructed. One photo-mosaic was then taken at $Re_c = 400,000$ and compared, to examine the influence of Reynolds number on the flows (not shown). A decision as to which of these flows should be the subject of future hot-wire measurements and the location of those measurements, was then made. Finally photographs were taken in this case with the dummy probe and traverse located at the future measurement positions.

Photo-mosaics of the four flows at $Re_c = 130,000$ are presented in figures 28 and 29. Flow is from right to left with the wings appearing on the far right of the page. Those views more clearly show the interaction of the vortex cores in the vicinity of the merging location. The difference in size between the cores of the unmerged vortices and the core of the combined vortex is also noticeable, the later being almost twice the former. The increase in Re_c from 130,000 to 400,000 appeared to produce almost no change in the overall structure of these flows. The vortex cores as marked by the bubbles, did appear significantly thinner at the higher Reynolds number though. This may be partially due to the higher centripetal forces experienced by the helium bubbles confining them to a smaller region within the core. However, it is also indicative of the much smaller amplitude of the lateral motions at $Re_c = 400,000$. Motions no greater than $\pm 3.2\text{mm}$, 1.6% of the wing chord were observed. The frequency of these motions was higher than at

$Re_c=130,000$ suggesting that it may scale with velocity. Reliable estimates of the frequency could not be obtained at $Re_c=400,000$ due to the small magnitude of the lateral motions.

Visualizations with the dummy probe were made in the $\Delta y=c/4$, $\alpha_0=5^\circ$ case with the probe tip located at $x/c=10, 15, 22$ and 30 . This case was chosen for the hot-wire measurements because higher angles of attack create tangential velocities that are greater than what the hot-wire is able to measure accurately. These streamwise locations were chosen because it allowed measurements to be taken in both vortices upstream of the merging location, right before merging, right after merging and well downstream of the merging location in the combined vortex. Figure 30 shows the probe in the single vortex core at $x/c=22$. Note that there is no disturbance to the flow at the measurement point, only downstream of this location. Figure 31 shows the probe traversing through the core at a rate of 6.4mm/s in the same streamwise location. Again note that there is no disturbance to the flow at the measurement point. Other photographs taken with the probe at $x/c=10, 15$ and 30 also showed no evidence of probe interference at the measurement location. At no time did we observe any such interference by eye.

3.2 Counter Rotating Vortex Pairs

It is worth noting some properties of a counter rotating vortex pair before describing the resulting visualizations. Figure 32 shows a sketch of an idealized vortex pair. Vortex (a) induces a velocity on vortex (b) causing it to move to the right of the page. In turn, vortex (b) induces an equal velocity on vortex (a) causing it to also move to the right of

the page. As the separation distance between the pair decrease and/or their strength increase, the pair will move to the right of the page at a greater velocity.

Figure 33 shows the vortex pair generated at a wing-tip separation $\Delta y=c/4$ and angle of attack $\alpha_e=2.5^\circ$. The two vortex cores are clearly seen in the center of the photograph with the wings and arc lamp reflection located on the right. The vortex cores, generated at the wing tips, drift in the -z direction and move slowly apart with distance downstream. At the end of the test section, the separation distance between the cores is more than twice that of the original wing-tip separation. This is presumably a result of Betz's (1933) conservation theorems which causes each vortex to move inboard of the wing tip. At $\alpha_e=5.0^\circ$ and $\alpha_e=7.5^\circ$ (figure 34 and figure 35), the vortex cores move a greater distance in the -z direction. At $\alpha_e=10.0^\circ$ the two cores have moved such a large -z distance, that they leave the arc lamp beam and are thus not visible.

Increasing Δy to $3/8c$ decreased the amount of movement in the -z direction. As before, increasing angle of attack to 10.0° caused the two vortex cores to move out of the arc lamp beam. Increasing Δy to $c/2$ and c further decreased the amount of movement in the -z direction.

The counter rotating vortex pairs experienced small lateral motions of the same frequency as the co-rotating pairs. The vortex cores moved simultaneously in either the same or opposite directions. Figure 36 shows the magnitude of the motions for each case, the largest amplitude being again about $\pm 20\text{mm}$, 10% of the wing chord. The lateral motions are somewhat larger at higher angles of attack compared to the corresponding co-rotating pairs. As before, the motions appeared in general to be

slightly less in the z than in the y directions with no consistent variation between different configurations. As with the co-rotating pairs, the counter rotating pairs experienced a slight amount of rocking about each other of at most $\pm 4^\circ$. The frequency of all motions was very low with fc/U_{ref} typically .004.

Various properties have been plotted for the counter rotating vortex pairs. Figure 37 shows the z location of the vortex cores at $x/c=20$ as a function of angle of attack. The uncertainty in z is about $\pm 12\text{mm}$. Note the linear relationship for each Δy . Estimates of the movement in the -z direction may be obtained if we model the flow using two infinite straight line vortices of circulation $\pm\Gamma$. According to Lamb (1932), a two-dimensional vortex pair of opposite strength will propagate in the z direction at a velocity

$$\frac{dz}{dt} = \frac{\Gamma}{2\pi s} \quad (3.2.1)$$

Where s is the distance between the vortices. Substituting x/U_{ref} for t and dividing by c, we have

$$\frac{z}{c} = \frac{\Gamma x}{2\pi s U_{ref} c} \quad (3.2.2)$$

Figure 38 shows the measurements plotted in terms of these two variables, with s being taken as the vortex separation at $x/c=20$. Using those variables the data collapses to a single straight line, within the uncertainty limits. The correlation with infinite vortex line theory is good considering the assumptions involved.

In figure 39, the separation distance between the vortex cores as a function of streamwise location x/c is shown. As the flow traveled down the tunnel, the separation distance between the pair increased. The primary cause of increasing separation between the counter rotating pairs is attributed to the theory of Betz (1933) which is developed for a single trailing vortex. Even though Betz's theory is for a single vortex, it will give insight to the physical process of the vortex pair. According to Betz, the centroid of the shed vorticity remains at a constant distance from the wing root and the moment of inertia about the center of gravity is a constant. This implies in the case of the vortex pair, that the separation distance between the pair must increase downstream.

A possible secondary cause of this maybe due to interaction with an image pair in the tunnel wall of opposite sign. According to Lamb (1932), the resulting trajectory of a two-dimensional vortex pair near a wall is given by

$$\frac{s^2}{4}(y^2 + z^2) = y^2 z^2 \quad (3.2.3)$$

Figure 40 shows the inviscid flow trajectory for all cases in the y and $-z$ direction normalized by the separation distance s . The tunnel wall corresponds to $x/s=8$. As can be clearly seen, every pair is well out of the influence of its corresponding image pair in the wall with the case at $\Delta y=c$, $\alpha_o=10.0^\circ$ being the closest to the wall.

3.2.1 Cases for Further Study

The following four cases were selected for further study.

$$\Delta y=3/8c, \quad \alpha_c=5.0^\circ$$

$$\begin{array}{ll} \Delta y=3/8c, & \alpha_e=7.5^\circ \\ \Delta y=3/8c, & \alpha_e=10.0^\circ \\ \Delta y=c/4, & \alpha_e=5.0^\circ \end{array}$$

These cases were chosen to complement the corresponding co-rotating pairs.

Photo-mosaics of the four flows at $Re_c=130,000$ are presented in figures 41 and 42.

Flow is from right to left with the wings located on the right of the page. The increasing separation distance between the vortex cores can be clearly seen in the mosaics. There appeared to be no change in the overall structure of the flow between $Re_c=130,000$ and $Re_c=400,000$. The vortex cores at $Re_c=400,000$ appeared smaller as a result of higher centripetal forces experienced by the helium bubbles and also as a result of smaller lateral motions. Motions of $\pm 6.4\text{mm}$, 3.1% of the wing chord were observed. The frequency of these motions were higher than at $Re_c=130,000$ and appeared to scale with velocity. Estimates of the frequency could not be determined due to the small amplitude of the lateral motions.

The effect of the dummy hot-wire probe was also tested for $\Delta y=c/4$, $\alpha_e=5.0^\circ$. The probe tip was located at $x/c=10, 15, 22, 30$. This case and streamwise locations were chosen to complement the corresponding co-rotating case and measurement locations. Figure 43 shows the probe in the upper vortex core at $x/c=22$. Note that there is no disturbance to the flow at the measurement point. Figure 44 shows the probe traversing at 6.4mm/s through the top vortex core. Again note that there is no disturbance to the flow at the measurement point. Other photographs taken with the probe at $x/c=10, 15$ and 30 also showed no evidence of probe interference at the measurement point. These results are consistent with the findings for the co-rotating case.

4. Velocity Results

The following vortex pairs were selected for detailed velocity measurements based on the flow visualization results.

$\Delta y=c/4$	$\alpha_o=5.0^\circ$	$Re_c=260,000$	$x/c=10, 15, 22, 30$
$\Delta y=c/4$	$\alpha_e=5.0^\circ$	$Re_c=260,000$	$x/c=10, 30$

The Reynolds number based on the wing chord (.203m) was reduced from 400,000 discussed in the flow visualization results to 260,000, (20m/s) for velocity measurements due to vibration problems in the quad hot wire probe at the higher speed. The velocity results are presented in four separate sections, the wing wake, the vortex pairs, further analysis and finally the core region and motions . A large amount of data was taken in this experiment to get a detailed view of the physics of these flows. Over 70 traverses were made with an average of 70 points per traverse. At a sampling rate of 30kHz, with 100 blocks of 6144 samples being taken at each measurement point on the four quad wire channels, resulted in a total of over 33 Gigabytes of raw data taken for this experiment.

Uncertainties in the mean velocity components and Reynolds stresses measured with the single and quad hot wires, normalized on U_{ref} are presented in tables 2 and 3. These were calculated using the method of Kline and McClintock (1953) for 95% confidence limits. The following sources of uncertainty are included in these estimates: limited number of

samples taken to form averages, calibration drift, probe misalignment (pitch, yaw, roll), and pitch and yaw wire sensitivities. Electrical noise from the anemometer bridges and amplifiers was also determined and subtracted from the velocity measurements. This contribution to the turbulence stresses was determined from measurements made in the freestream where in the present work, the true velocity fluctuations were negligible.

4.1 Wing Wake

4.1.1 Near Field Wing Wake

The cartesian coordinate system shown in figure 5 will be used in describing the wing wake results. The near field wing wake was measured using a single hot wire probe placed 1mm downstream of the trailing edge of each airfoil. Since the probe location was so close to the wing trailing edge, these measurements are assumed similar to the wing's trailing edge boundary layer. Profiles of mean velocity, turbulence intensity and frequency spectra were measured at spanwise locations $y/c=1.3, .73, -.73$ and -1.3 for both the co-rotating and counter rotating cases. All velocities are normalized by the freestream velocity U_{ref} with distances normalized by the wing chord 'c'. During measurements, the hot wire output was sampled at a rate of 30kHz. At each point, 50 blocks of 3072 points were taken over a total period of about 1 minute.

It is well known that the roll up of a vortex sheet from a finite wing induces a velocity in the downward direction along the span of that wing. This downwash velocity has the effect of reducing the local angle of attack near the wing tip. This results in a variation in lift and circulation along the span of the wing. Moving two wings close together as in

the case of this experiment, greatly affects the downwash velocity felt by each wing. In the counter rotating case with the wings at equal angles of attack, each wing feels an upwash velocity from the other which reduces its own downwash velocity. This implies that the root circulation is greater for the counter rotating wings compared to that of a single wing. In the case of the co-rotating wings, the opposite is true. Each wing feels a downwash velocity from the other which increases its own downwash velocity. This implies that the root circulation of the co-rotating wings is lower compared to the single wing and counter rotating wings. These effects are important as they affect the development of the flow downstream of the wings.

The thickness of each half wake δ , was estimated from the trailing edge measurements from the value of z where the r.m.s. axial turbulence intensity was 1.0%. At this location, the value of the mean axial velocity was assumed to be equal to the edge velocity U_e . The displacement thickness δ^* and momentum thickness θ , for each half of the wing wake is defined by

$$\delta^* = \int_0^{\delta} (1 - U / U_e) dy \quad (4.1.1)$$

$$\theta = \int_0^{\delta} (1 - U / U_e) U / U_e dy \quad (4.1.2)$$

The integration was performed using the trapezoidal rule. Table 4 lists these parameters for both the suction and pressure side of each wing wake. In both cases the boundary layers on the two wings appeared similar with thickness between $0.038c$ and $0.063c$. The

counter rotating spanwise location $y/c=-1.3$ is not presented due to a computer malfunction that occurred during measurements.

Profiles of U and u^2 vs $(z-z_o)/c$ are shown in figure 45 through figure 50. z_o is defined as the center location of each wing wake. The data in these figures show that at the trailing edge the wing wake is similar to a two dimensional fully turbulent boundary layer. In figures 45 and 46, all of the velocity profiles show that the boundary layer is not separated near the wing trailing edge. The increased thickness of the wake on the suction side compared to the pressure side can be seen in the mean velocity profiles and in the displacement and momentum thickness in table 4. These profiles are in qualitative agreement with those from Simpson (1981) for a two dimensional boundary layer in an adverse pressure gradient. In figures 47 and 48, the maximum normal stress occurs on the suction side of each wing very near to the wake centerline where there is a dip in the normal stress profile. There is a slight difference in the stress peaks on the suction side between the upper and lower wing. The upper wing has a small peak while the lower wing does not. This may be caused by small differences in the trailing edge, the upper wing having a slightly sharper trailing edge than the bottom wing. On the suction side, the stress profile of both wings is fuller due to the greater adverse pressure gradient. This is also indicated in table 4 which shows a larger displacement and momentum thickness for the suction side of both cases. Spanwise variations in boundary layer properties due to variations in the local angle of attack appear to be small with table 4 showing less than a 5% difference for each case. The present results are similar to those of Yu (1981) and Nakayama (1984) for a two dimensional airfoil.

Figures 49 and 50 compare the profiles measured at different spanwise locations for the two wings. The mean profiles show the flows over the two wings to be very similar and almost two dimensional. The maximum velocity deficit for all cases is 80%. In figure 50, the normal stress profiles illustrate the similarity between the two wings. The thickness of the wing wake and maximum stresses is similar for all cases. On the suction side, the counter rotating cases have fuller profiles compared to the co-rotating cases as a result of the larger local angle of attack produced by the interaction of the two wings. This is also indicated in table 4 which shows about a 10% larger displacement and momentum thickness for the counter rotating case. From the similarity in the stress profiles, it appears the wing trip is producing a uniform turbulent flow along both wings. The difference in the normal stress profiles due to the sharper trailing edge of the upper wing appears to be small.

To analyze the frequency content of the velocity fluctuations, raw data was transformed into the frequency domain using fast fourier transforms. Block lengths of 2048 points with 50% overlap were used resulting in 100 averages for each autospectra. Hanning windows were also used in the calculation of all frequency data. The frequency data obtained was used to estimate the one sided autospectral density function given by

$$G_{xx}(f) = \frac{2\Delta t}{N} [\overline{X(f)}]^2 \quad (4.1.3)$$

where $X(f)$ is the raw FFT, Δt the sampling period and N the block length. Uncertainties were computed for the autospectral density function using the method of Bendat and

Piersol (1986). The normalized random error for autospectral density functions is given by

$$\epsilon_r[G_{xx}(f)] = \frac{1}{\sqrt{n_d}} \quad (4.1.4)$$

where $\epsilon_r[G_{xx}(f)]$ is the random error in the autospectral density function and n_d is the number of distinct records. In the case of the near field wing wake measurements, $n_d=50$; therefore $\epsilon_r[G_{xx}(f)]=.141$ or 14.1%.

In figures 51 through 54, representative frequency spectra at $y/c=\pm .73$ are shown for the centerline, suction and pressure sides. The spectra are normalized on the freestream velocity U_{ref} and wing chord 'c'. Figure 51 shows u autospectra for the centerline location where $(z-z_o)/c=0.0$. Each spanwise location has a constant region of spectral energy up to a frequency of $fc/U_{ref}=2.0$. It then follows close to a power law with -1 slope up to $fc/U_{ref}=24$. After that it decreases towards dissipation through a -4 slope. The energy distribution across all frequencies appears to be the same for the two wings. Figures 52 and 53 are autospectra at $(z-z_o)/c$ locations of .02 and -.02 respectively. These two figures show an almost constant energy level up to $fc/U_{ref}=5$ then they fall off without any distinct inertial subranges for both the suction and pressure sides. Comparing the centerline, pressure and suction autospectra, figure 54 shows the difference in the energy distribution. At low frequencies, the suction side contains most of the energy. This may indicate the presence of larger scale structures due to the greater adverse pressure gradient and thicker boundary layer. At frequencies greater than $fc/U_{ref}=5$, both the pressure and suction sides fall off towards dissipation with out any distinct inertial subrange unlike the center line case which has a slope of approximately -

1. This reflects the large velocity gradients that are present in the near wall region of the trailing edge boundary layer. This is similar to Klebanoff (1954) for autospectra in the near wall region of a boundary layer. At higher frequencies, both the pressure and suction side spectra contain more energy than those of the centerline location which is consistent with the normal stress profiles in figure 50.

4.1.2 Farfield Wing Wake

Velocity measurements were performed in the farfield wing wake at $x/c=10, 15, 22$ and 30 for the co-rotating case and $x/c=10$ and 30 for the counter rotating case using the quad hot wire probe. The measurements were made only for the top wing wake in both the co and counter rotating cases at $y/c=2.5$. All velocities are normalized by the freestream velocity U_{ref} with distances normalized by the wing chord ' c '. During measurements, the hot wire output was sampled at a rate of 30kHz. At each point, 100 records of 6144 points were taken over a total period of about 2 minutes. This resulted in uncertainties in the autospectra of 10.0%.

Figures 55 through 61 show the mean velocity U , normal stresses u^2, v^2, w^2 and the shear stresses $-uv, -vw$ and $-uw$. Values of mean V and W were negligible compared to U and thus are not presented. Figure 55 shows the mean velocity U at the different streamwise locations. At $x/c=10$, the velocity deficit in the wake is 5% and reduces to 2% at $x/c=30$. Also notice how the wake width increases with downstream location as a result of the entrainment process. The mean velocity distribution appears to be symmetric about the wake center line at all streamwise locations. In figure 56 the normal stress u^2 is shown. With increasing distance downstream, the turbulence stress reduces by 60% and the wake width increases by 30%. Notice the higher stress values on the suction side of the wing

for the co-rotating streamwise locations compared to the counter rotating locations. This is probably a result of the local angle of attack affecting the normal stresses downstream. The counter rotating pair has a more uniform lift distribution, thus the stresses appear more two dimensional downstream. The normal stresses v^2 and w^2 shown in figures 57 and 58 behave similar to u^2 at all downstream locations. Notice that w^2 is constant across the inner part of the wake compared to u^2 and v^2 . This is typical for a two dimensional wake as shown by Wygnanski et al (1986). As with the normal stresses, the shear stresses decreased with downstream location. The most dominant stress $-uw$ is much larger than both $-vw$ and $-uv$. At the center of the wake uw is zero since there is no rate of strain $\partial U / \partial Z$ to produce this stress (figure 61). Near $(z-z_0)/c=0.1$, the greatest $-uw$ value exists which results in a large rate of strain and new large scale vortices formed which produce much of the turbulence energy.

It is well known that a turbulent wake can be expressed as a self-similar flow solution where all velocities and lengths can be normalized on a velocity scale $U_0(x)$ and $L_0(x)$. U_0 is defined as the velocity deficit in the center of the wake ($U_{ref}-U$) and varies as $\sqrt{L_0/x}$. L_0 is defined as the value of $(z-z_0)$ where the velocity deficit is $1/2U_0$ and varies as \sqrt{x} . Applying this concept to the resulting wakes, figure 62 shows the velocity deficit normalized by these scales. Note the overall collapse using similarity variables. Figure 63 shows u^2 , v^2 , and w^2 normalized on the two scales. Collapse of the profiles is good except for v^2 where there is a small difference in the velocity scaling. This may be attributed to the uncertainties involved on U_0 and L_0 . Figure 64 shows the shear stress profile uw normalized on these scales. There is good collapse for both the velocity and length scales. These results are consistent with Wygnanski et al (1986).

Representative autospectra are shown in figure 65 at the center of the wing wakes and in figure 66 at $(z-z_o)/c=0.1$, near the location where uw is a maximum. Autospectra and frequency are normalized on the freestream velocity U_{ref} and wing chord ' c '. Spectra were calculated using equation 4.1.3 with a block length of 4096, 50% overlap and 200 averages. Figure 65a shows G_{uu} for all six streamwise measurement locations. As x/c increases, the energy across all frequencies decreases proportionally. The energy level is constant out to $fc/U_{ref}=2.5$ then slowly falls off with out any distinct slopes. In figure 65b, the G_{vv} energy level decreases downstream at all frequencies similar to the G_{uu} . There is a slight increase in energy levels up to $fc/U_{ref}=2.5$ then it slowly falls off also without any distinct slopes. The autospectra of w shown in figure 65c clearly has a dominant frequency near $fc/U_{ref}=5$ at $x/c=10$ which reduces to $fc/U_{ref}=2$ at $x/c=30$. This is presumably the result of fairly regular large scale coherent structures in the wake. After this peak, the autospectra falls off with a $-5/3$ slope up to $fc/U_{ref}=18$, then the slope decreases toward dissipation. The overall decrease in energy with downstream location is similar to u and v autospectra. Figure 66 shows autospectra near the location of the maximum shear stress uw . These results are similar to the centerline results except G_{uu} shows a clear inertial subrange with a $-5/3$ slope.

Because of the self preserving nature of the flow, the autospectra can be compared using the similarity variables discussed above. Figures 67 and 68 show G_{uu} , G_{vv} and G_{ww} for $(z-z_o)/c=0.0$ and -0.1 respectively plotted in terms of $G_{uu}U_{ref}/u^2L_o$ vs fL_o/U_{ref} . Notice how the length scale L_o shifts the peaks from the large scale structures in the w autospectra to the same frequency for all streamwise locations. There is some variation in the energy level at $fc/U_{ref} > 50$ but the overall collapse is good. These results are also consistent with Wygnanski et al (1986).

4.2 Vortex Pairs Results

Velocity measurements were performed in the co-rotating and counter rotating vortex pairs using the quad hot wire probe. During measurements, the hot wire outputs were sampled at a rate of 30kHz. At each point 100 blocks of 6144 points were taken over a total period of 2 about minutes. This results in uncertainties in the autospectra of 10.0% for 95% confidence levels. Point measurements were made in a number of radial traverses through the core of each vortex producing a polar grid. In planes where two vortices were present, an additional traverse was made perpendicular to the line connecting the cores. During the experiment, the vortex centers were located in advance of the traverse measurements as the locations of minimum tangential velocities. Care was taken to eliminate the possibility of probe interference effects. Before each traverse, the probe holder was rotated about its axis to position the offsetting rods holding the quad wire probe normal to the traverse direction. This ensured that the probe holder was always as far away as possible from the vortex core, reducing interference effects.

All velocity measurements will be normalized by the freestream U_{ref} with distances normalized by the wing chord 'c'. Table 5 gives the center location of each vortex core in tunnel coordinates. In the single merged vortices, the center location is defined as the point of minimum tangential velocities. In the case of two vortices, a similar location was used but first the induced velocity from the other vortex was calculated assuming a linear variation across the core. This induced velocity was then subtracted allowing the center of each vortex to be determined from the location of the minimum tangential velocities.

In presenting the results an important question is raised, what coordinate system is most appropriate to represent the physics of the flow? Various types of coordinate systems were examined such as cartesian coordinates, flow direction coordinates and cylindrical coordinates but these lacked the ability to present the vortex pairs. A variation of cylindrical coordinates (r, θ, x) is used to present results. At locations where a merged single vortex was present, standard cylindrical coordinates are used. At locations where two vortices are present, the measurement plane is divided in half with a cylindrical coordinate system located at each core.

4.2.1 Co-Rotating Vortex Pairs

Measurements of the co-rotating pairs were taken at streamwise locations $x/c=10, 15, 22$, and 30 (see figure 29 to visualize these locations). It was shown from the flow visualization results that the co-rotating pairs rotate about their common center and then merge to form a single vortex at x/c about 20 . At $x/c=10$ and 15 the flow contains two separate vortices, whereas at locations at $x/c=22$ and 30 there is only a merged single vortex.

4.2.1.1 $x/c=10$

Figure 69 shows a plot of mean secondary flow vectors for the co-rotating vortex pair at $x/c=10$. The length of each vector and the size of its head are proportional to the magnitude of the secondary flow velocity vector. By this streamwise location, the vortices have rotated about their common center through an angle of 135° . They are separated by a distance of $0.29c$, slightly more than the wing tip separation. The vectors

show the strong rotational flows generated by the vortices and their mean interaction on the outer edge of each core away from the center of the figure 69. In the center of the flow midway between the vortex cores a cross flow stagnation point exists.

Contours of turbulent kinetic energy k , $(v_x^2 + v_\theta^2 + v_r^2)/2$ and the normal stress v_x^2 , in figure 69 and 70 clearly show the wing wakes that surround the vortex cores. The wing wakes have merged along a line midway between the two cores. They are rolled into spirals about each core both by rotational velocity fields of each vortex and by the rotation of the pair about their common center. The resulting shear and distortion may be responsible for the reduction of peak turbulence levels as the wake approaches the core, from $k=0.00061$ in the outer region to $k=0.00044$ close to the core. The wake width away from the cores is approximately $0.39c$.

Figure 72 through 80 show in detail the core region of the upper vortex, the flow being antisymmetric. Figure 72 shows the mean secondary flow velocity vectors. Note that all the profiles do not intersect each other in the same location. This is the result of corrections to the absolute traverse positions applied after the measurements were completed. It is estimated that these profiles are positioned with an accuracy of $\pm 1\text{mm}$ ($\pm 0.005c$). The core edge shown by the solid line, was determined as the location of maximum V_θ for each profile. It is slightly elliptical with its major axis normal to a line connecting the two cores. The diameters of the major axis is $0.08c$ with a minor axis of $0.075c$. Distorted cores are seen in inviscid computational results presented by Rossow (1971) and Melander et. al. (1988). They examined the merging process of two co-rotating vortices and found with decreased distance between the cores, each core deformed into an elliptical shape. In the present flows the tangential velocities at the

edge of the core vary substantially from 10.3% U_{ref} on the side closest to the line of antisymmetry to 20.4% U_{ref} on the opposite edge.

The mean vorticity defined as

$$\omega = \frac{V_\theta}{r} + \frac{\partial V_\theta}{\partial r} - \frac{1}{r} \frac{\partial V_r}{\partial \theta} \quad (4.2.1)$$

was computed for the core region of the vortex pairs. Contours of normalized vorticity $\omega c/U_{ref}$ presented in figure 73 are slightly elliptical in the core region being concentric with the core. They show a maximum normalized vorticity of 18.0 in the center of the core. Contours also show the wing wake wrapping around the core and a small island of positive vorticity located between the cores around the line of antisymmetry. Figures 74 through 80 show turbulence kinetic energy, and the Reynolds stresses in the core region. Part of the wing wake can clearly be seen in figure 74 as it merges into the flow structure surrounding the core. Velocity fluctuations increase in the vicinity of the core region, a maximum being reached in the center of the core in all the normal stresses, here $k=0.0095$, $v_x^2=0.0019$, $v_\theta^2=.0072$ and $v_r^2=.010$. Note that v_x^2 is at least 70% lower than both v_θ^2 and v_r^2 . It appears that the large stresses in the core are at least partly a result of the vortex wandering and large mean velocity gradients in the core. Notice that v_x^2 is the least affected normal stress in the center of the vortex due to the wandering the of core in the r - θ plane. The fact that v_r^2 is not equal to v_θ^2 may indicate the vortex wandering is not isotropic but has a preferred direction. The shear stresses $v_x v_\theta$ and $v_x v_r$ in figures 78 and 80 have two lobes in this region which could be partly due to the motions and or

partly due to the fact that the core axis lies at an angle to the freestream direction. $v_\theta v_r$ is the dominant shear stress in and around the core at ± 0.0020 , 60% greater than $v_x v_\theta$.

To better illustrate the flow structure, selected radial profiles of the mean velocities and Reynolds stresses are shown in figure 81 and 82. These profiles are labeled Aa and Bb in figure 72. The capital letter 'A' donates the location of a positive direction in figure 81 with the lower letter 'a' signifying a -r direction. Profile Aa shows the structure of the flow parallel to the line of antisymmetry with Bb taken perpendicular to this line. In the mean V_x velocity profile (figure 81a) small velocity deficits (2.5 % U_{ref}) are present in Aa at the outer edges of the profile resulting from the wakes of the two wings. As the flow spirals around the vortex core, these axial deficits are negligible in profile Bb (figure 82a). In the core region, the effect of the interaction between the pair on V_θ is clearly seen along Bb. Closest to the plane of antisymmetry, the tangential velocities are 50% lower than on the opposite side of the core. The large radial velocity is attributed to the profile not passing exactly through the vortex center. Parallel to the antisymmetry line profile Aa, V_θ is symmetric across the core with V_r present resulting from the induced velocity of the neighboring vortex. The axial velocity deficit in the center of the core created by the rotation of the flow is 11% U_{ref} .

The presence of the wing wake can be seen in the Reynolds stresses in figure 81b and 82b. In Aa (figure 81b), large turbulent fluctuations at $r/c=0.75$ ($k=0.0006$) and $r/c=-0.6$ ($k=0.00051$) mark the center of each wake. Across the wake width, the both $v_x v_\theta$ and $v_x v_r$ change sign with $v_\theta v_r$ having a constant sign. Moving around the core to profile Bb (figure 82b), the wing wake spirals closer to the vortex core and is barely visible at $r/c=0.25$. In the center of the core the effect of the vortex wandering can be clearly seen.

Fluctuations in v_r^2 and v_θ^2 are much larger than v_x^2 in the center of the core. Also in the shear stresses (figure 82c) the effect of the motions can be seen by the fact that $v_\theta v_r$ changes sign across the core.

An alternative view of the turbulence structure in and around the vortex core may be gained from velocity spectra at various representative radial locations. Figure 83 and 84 show autospectra $G_{v_{xx}}/U_{ref}c$, $G_{v_\theta v_\theta}/U_{ref}c$ and $G_{v_r v_r}/U_{ref}c$ vs fc/U_{ref} , where f is frequency in hertz, for profile Aa. These radial locations are marked in figure 81. The spectrum at $r/c=0.48$ and 0.26 show velocity fluctuations and some electrical noise in the low turbulent region between the core and wing wake. Those at $r/c=0.15$ and 0.09 show fluctuations in the region adjacent to the core with large peaks at $fc/U_{ref}=4$ in $G_{v_r v_r}$. A distinct inertial subrange in $G_{v_\theta v_\theta}$ with a $-5/3$ slope is seen in figure 83b. Moving closer to the core, these peaks around $fc/U_{ref}=4$ at $r/c=0.09$ then disappear by $r/c=0.04$ in $G_{v_r v_r}$. However, this peak begins to appear in $G_{v_{xx}}$ close to the center of the core around $fc/U_{ref}=4$ at $r/c=0.01$. This may be the result of some type of axial instability in the core region which will be discussed later in this section. On the other side of the profile in figure 84, large peaks are seen at $r/c=-0.09$ around $fc/U_{ref}=4$. Moving away from the core, these peaks disappear by $r/c=-0.16$ and -0.25 . At $r/c=-0.53$, this peak reappears in the spiral wake around $fc/U_{ref}=3$. Assuming Taylor's hypothesis, the frequency at $fc/U_{ref}=3$ implies a length scale of 0.33 chordlengths. This is a probable size of large scale structures in the wake which away from the vortex core is 0.39 chordlengths in width. Close to the center of the core, the spectral energy level at lower frequencies rises and reaches a maximum in $G_{v_\theta v_\theta}$ and $G_{v_r v_r}$. This is presumably a partial result of the velocity fluctuations produced by vortex wandering. Notice that in the center of the core, $G_{v_{xx}}$ has much less energy than $G_{v_\theta v_\theta}$ and $G_{v_r v_r}$ in the lower frequencies since it is less

affected by the vortex wandering. At higher frequencies $fc/U_{ref} > 20$, spectral energy levels change little between $r/c = \pm 0.09$ and ± 0.04 and then slightly decrease in the core. This latter result, which implies that velocity fluctuations in the core are only slightly lower than elsewhere is surprising considering the strong stabilizing nature of the flow.

Autospectra taken along profile Bb (figure 85 and 86) show similar features as profile Aa. Peaks associated with large scale structures from the spiral wake are visible at $fc/U_{ref} = 4$ at radial locations $r/c = \pm 0.16$ and ± 0.24 in $G_{vr/r}$. Approaching the core, these peaks disappear by $r/c = 0.04$ but reappear in the core in $G_{vx/vx}$ at about the same frequency. On the opposite side of the core, the wake structures are visible at $r/c = -0.15$ and -0.09 . At low frequencies vortex wandering appears to cause a large increase in spectral energy levels (about an order of magnitude) in $G_{v\theta/v\theta}$ and $G_{vr/r}$ compared with $G_{vx/vx}$. At high frequencies $fc/U_{ref} > 20$, there is a slight decrease in spectral energy levels in the core compared to the elsewhere in the flow.

4.2.1.2 $x/c=15$

By $x/c=15$ the co-rotating vortex pairs have rotated about their common center through an angle of about 252° and moved closer together to a separation of $0.2c$ (figure 87). The contours of turbulent kinetic energy and v_x^2 in figure 88 and 89, show the distortion of the wing wakes caused by the further rotation of the vortices about their common center. Notice the decrease in peak turbulence kinetic energy as the wakes approach the cores from $k=.00038$ to $k=.00024$. This is also about a 32% reduction of the peak turbulence energy in the wake from $x/c=10$. The wake width at the maximum t.k.e is $0.42c$, a 7% increase from $x/c=10$

Detailed cross flow velocity vectors of the vortex core originating from the lower wing are shown in figure 90. The velocity field is even less axisymmetric than at $x/c=10$. In both mean velocity vectors and vorticity contours (figure 91), the core is even more elliptical than at $x/c=10$ with major and minor axes diameters of $0.115c$ and $0.08c$ respectively. This implies a core area 50% greater than at $x/c=10$. Peak tangential velocities at the edge of the core, vary from $6.7\% U_{ref}$ closest to the line of antisymmetry to $16.1\% U_{ref}$ on the opposite side. The vorticity contours are approximately concentric with the core and have a maximum in the center of 15.7 , 13% less than at $x/c=10$. Near the plane of antisymmetry, a small island of positive vorticity exists as a result of the interaction between the pair, again similar to the upstream location. Contours of t.k.e and Reynolds stresses (figures 92 through 98), show variations consistent with convoluted wakes at this location. The vortex wandering causes the turbulence levels to rise to a maximum in the core with $k=.0114$ (17% increase from $x/c=10$), $v_x^2=.0019$ (0% increase from $x/c=10$), $v_\theta^2=.01$ (39% increase from $x/c=10$) and $v_r^2=.011$ (10% increase from $x/c=10$) implying motions that are slightly greater than at $x/c=10$.

Representative profiles of the top vortex core are shown in figures 99 and 100 and are labeled profile Cc and Dd in figure 90. Profile Cc is parallel to the line of antisymmetry, and shows very little effect of the wing wake on the axial velocity profile in figure 99a. The decreased distance between the pair causes a greater induced velocity on each vortex core partly resulting in the large radial velocities present in profile Cc. The effect of the wing wake on the axial velocity can be seen as a small deficit ($2\%U_{ref}$) near $r/c=0.55$ in profile Dd. The normal stresses (figures 99b and 100b) clearly show the two wing wakes at $r/c=0.4$ (peak $k=0.00023$) and at $r/c=-0.4$ (peak $k=0.00022$) in profile Cc and at $r/c=0.5$

(peak $k=0.00062$) in profile Dd. In the center of the core the effect of the wandering is seen on the turbulent fluctuations. As with $x/c=10$ v_x^2 is much lower than v_θ^2 and v_r^2 . The shear stresses (figures 99c and 100c) show a similar increase in stress levels in the core region. Outside the core, the shear stress levels in the wake can be seen to increase further out from the core.

Velocity spectra along representative radial locations in profile Cc are shown in figures 101 and 102. The radial locations are marked in figures 99 and 100. These spectra are similar to those at $x/c=10$ with peaks present at $r/c=0.3$ and -0.32 in G_{vr} and $G_{v\theta}$ but at a lower frequency of $fc/U_{ref}=2.5$ implying a larger scale. Similar peaks are also seen in G_{vxx} (figure 101a) in the center of the core at the same frequency. It is possible that these spectral peaks in the core are some type of axial instability stimulated by the large scale structures in the wake. Again at low frequencies G_{vxx} is much less than $G_{v\theta}$ and G_{vr} as a result of the vortex wandering. At high frequencies $fc/U_{ref}>20$, the turbulent fluctuations in the core region are higher than other parts of the flow and at $x/c=10$. This may imply that with increased aging of the vortices, the turbulent fluctuations in the core may also increase. Perpendicular to the antisymmetry line in profile Dd (figures 103 and 104) the outer region of the flow is similar to profile Cc, with peaks at $r/c=0.6$ with a frequency $fc/U_{ref}=3$. These peaks are also seen at $r=0.11$ and 0.31 with slightly lower frequencies. Closer to the line of antisymmetry, the intensity of these peaks increase around $fc/U_{ref}=3$ in figure 110. This is presumably associated with the passage of large scale wake structures between the vortices as the wake spirals around the core. These peaks can be clearly seen in G_{vxx} and G_{vr} at $r/c=-0.10$ and -0.15 . Also there is higher energy levels at $fc/U_{ref}>20$ in the region between the vortices as a result of the spiral wake merging with surrounding core region.

4.2.1.3 $x/c=22$

By $x/c=22$ the vortex cores appear to have merged to form a single vortex with an approximately axisymmetric velocity field about a single center (figure 105). The t.k.e and v_x^2 contours, figures 106 and 107, show the wing wakes well wrapped up around the center of rotation forming a large turbulent region $1.25c$ in diameter at the minimum. The t.k.e in the wakes decreases from $k=0.00022$ in the outer region to $k=0.00010$ close to the core. This is a 55% reduction in peak t.k.e. from $x/c=15$. The maximum wake width increases by 17% from $x/c=15$ to $0.49c$. The core of the combined flow, shown in figure 108 is not circular but has an outline like that of two overlapping ellipses. It has diameters of $0.21c$ and $0.17c$ in the y and z directions respectively, about twice the size of each of the unmerged cores. V_θ at the edge of the core is not axisymmetric but varies by $\pm 1.3\% U_{ref}$ with an average value of $12.6\% U_{ref}$. The contours of vorticity (figure 109) are similar in shape of the vortex core with a maximum in the center of 9.0. Further out from the core, the contours are not concentric but appear affected by the merging of the wakes into the surrounding core region. This is also seen in the t.k.e and Reynolds stress contours (figures 110 through 116) in particular those of $v_x v_r$ (figure 116). The contours are non-axisymmetric well into the core implying that even in the core the merging process is not complete. This is clearly seen in $v_x v_r$ which shows a number of spirals in and around the core. Peak turbulence levels in the center of the core are $k=0.0021$ which is 4 times smaller than the peak levels in the unmerged vortices, $v_x^2=0.0011$, $v_\theta^2=0.0015$ and $v_r^2=0.0015$. Note how all three normal stresses are approximately equal. It appears that most of the turbulence levels in the core are not affected by the vortex wandering.

To better illustrate the flow structure across the vortex at $x/c=22$, profiles in figure 108 Ee and Ff are shown in figure 117 through 118. The mean velocity profiles (figures 117a and 118a) clearly show the incomplete merging process of the two vortices as dips and valleys in both the axial and tangential velocity profiles. These dips and valleys are part of the wake structure extending right up to the core edge. On either side of the core, there appears to be at least 3 separate half turns of the wing wake around the flow. This is also confirmed by the normal and shear stresses in figures 117b and 118b. The normal stresses show 3 peaks on either side of the core in profile Ee, one large peak ($k=0.00022$) at $r/c=0.65$ and two smaller ones at $r/c=0.4$ and 0.2 closer to the core. This is also seen in the shear stress $-v_x v_r$ (figure 117c) which changes sign 3 different times on either side of the core. The axial velocity deficit in the core is $7.3\% U_{ref}$. Note the zero V_θ at the vortex center and negligible V_r in figure 117a and figure 118a.

The spectral structure of the flow at this streamwise location is illustrated in figures 119 and 120 for profile Ee. As with the unmerged vortices, the spectra measured in the wing wake outside the core ($r/c=0.53, 0.35 -0.37$ and -0.57) show broad peaks at frequencies likely to be associated with the passage of large wake structures at $fc/U_{ref}=2$. Moving closer to the core, the frequency of these structures increase to $fc/U_{ref}=3$ ($r/c=\pm 0.19$) implying a decrease in size as the core is approached. Moving into the core, energy levels at all frequencies rise. At lower frequencies, however, the rise is less dramatic than in the unmerged cores with $G_{v_{xv_x}}$ approximately equal to $G_{v_{rv_r}}$ and $G_{v_{\theta v_\theta}}$ implying that there is less of an effect associated with the vortex wandering. This is consistent with the approximately equal normal stresses levels in the center of the core. In the center of the core, the spectra look qualitatively similar to those of a boundary layer implying that the merging process generates turbulence in the core region over a board

range of scales. Notice that there are no peaks in $G_{v_{xx}}$ at the center of the core as was the case for the unmerged vortices. This implies that the merging process may drastically change the core structure allowing it to be unaffected by the wake. Spectra of profile Ff (figures 121 and 122) also show similar results suggesting large scale structures in the spiral wake at $f c/U_{ref}=2$ ($r/c=0.55, 0.37, -0.35, -0.55$) and an increase in the spectral energy across all frequencies in the center of the core. At very low frequencies, the spectral energy for all 3 autospectra are approximately equal again implying a lack of any significant vortex wandering.

4.2.1.4 $x/c=30$

At $x/c=30$, the most downstream location measured, the turbulence and mean flow measurements, figures 123 through 125, show a somewhat similar structure to that at $x/c=22$. The large turbulent region surrounding the core has grown to a width of $1.5c$ at minimum. The maximum t.k.e in the wake has decreased to $k=0.00015$ from $x/c=22$. The wake width has slightly increased to $0.51c$. Detailed views of the core region show a core that is much more circular with a diameter of $0.2c$ (figure 126). The tangential velocities at the edge of the core are at $12.9\% U_{ref}$ and vary no more than $.38\% U_{ref}$. The further development of the flow and merging of the wake structure around the core can be clearly seen in the vorticity contours (figure 127). The contours are closely circular in the core with a maximum normalized vorticity of 5.6 in the center. Contours of turbulence kinetic energy and normal stresses (figures 128 through 131) are slightly out of round. In the center of the core values of $k=0.0018$, $v_x^2=0.00063$, $v_y^2=0.0014$ and $v_z^2=0.0015$ similar to those at $x/c=22$. These out of round t.k.e contours are presumably the effect of the two wing wakes merging into the flow surrounding the core. It is

questionable if the interaction of the wing wakes allows the vortex to really obtain an axisymmetric turbulence region surrounding the core. This is also seen in the shear stress in figures 132 through 134.

Profiles along the lines Gg and Hh indicated in figure 126 are presented in figures 135 and 136. In the outer regions of the flow, the mean velocity profiles show the small dips and valleys resulting from the wing wakes. The axial deficit in the core has decreased to $7.0\%U_{ref}$, a 4% decrease from $x/c=22$. The Reynolds stresses figures 135b and 136b clearly show 2 distinct half spirals of the wing wake around the core region. The maximum t.k.e in the wake region for profile Gg is $k=0.00015$ ($r/c=0.7$) and $k=0.00018$ ($r/c=-0.8$). As the wake spirals round the core, profile Hh shows a reduction in these levels by about 35% with decreasing radius. The most dominant shear stress in the wake $-v_x v_r$ (figure 135c) can be seen to decrease in a similar manner as the wake spirals around the core.

The spectra shown in figures 137 through 140 for profiles Gg and Hh show a similar structure to that of $x/c=22$. Peaks in those spectra suggest the presence of large wake structures in the outer regions of the flow at $fc/U_{ref}=2$, for example at $r/c=0.62$ in figure 137c, but with lower energy levels compared to $x/c=22$. These spectra appear to have a more pronounced inertial subrange following -1 power law than the upstream locations possibly as a result of the larger vortex Reynolds number $Re_\Gamma=\Gamma_1/\nu$ where subscript 1 is at the core edge. At low frequencies, the spectral energy for all three autospectra are approximately equal (figures 137 and 138) implying that there is little if any vortex wandering present. At high frequencies, the spectral energy in and immediately around

the core is lower than at $x/c=22$. The implication of this is that the rotation of the core may have a stabilizing effect on the turbulence generated in the merging process.

4.2.2 Counter Rotating Vortex Pairs

Measurements were also made in the counter rotating vortex pairs at streamwise locations $x/c=10$ and 30 (see figure 42 to visualize these locations).

4.2.2.1 $x/c=10$

Figures 141 through 143 show the flow structure of the counter rotating vortex pair at $x/c=10$. In contrast to the co-rotating pair, this structure does not change significantly with downstream distance. The vectors shown in figures 141 like the flow visualizations, show the vortices moving slowly apart with distance downstream and in the $-z$ direction as a result of their mutual induction. The core separation distance is approximately $0.45c$ (compared to a wing tip separation of $0.25c$) and the cores are centered at $z=-0.66c$. This z -wise movement stretches the wing wakes as seen in figure 142 and 143 forcing them into contact between the vortices. Approaching the cores, this distortion process causes an increase in the peak turbulence levels in the wing wake with k reaching a maximum value of 0.00075 between the vortices. This is in contrast to the co-rotating vortex pairs which at most locations show a decrease in t.k.e. as the cores are approached. In the outer region, the wake width is approximately $0.42c$ similar to the co-rotating case at $x/c=10$.

A detailed view of the mean velocity field of the upper vortex core is shown in figure 144. This shows a fairly circular core having a radius of $0.088c$. Peak tangential

velocities vary from 34% U_{ref} at the edge of the core closest to the line of symmetry to 48% U_{ref} on the outer edge. On the whole, these velocities are much larger than in the co-rotating unmerged pairs at least partly because of the difference in the velocity field the vortices impose on each other. It may also be partly due to the fact that the root circulation for the counter rotating vortices is 40% greater because of the mutual interference of the wings. The vorticity contours (figure 145), shows the circular vortex core surrounded by approximately circular regions of positive vorticity. Away from the core and line of symmetry, the interaction from the other vortex causes regions of low negative vorticity to exist. Peak normalized vorticity in the core is 35.1, considerably higher than the co-rotating cases as a result of the increased wing root circulation. Contours of turbulent kinetic energy and the normal stresses (figures 146 through 149) are also fairly circular in the core with large fluctuations levels in the core center. These maximum values in the center are $k=0.010$, $v_x^2=.0011$, $v_\theta^2=0.010$, and $v_r^2=0.009$ similar to those of the co-rotating pair at the same streamwise location. As with the co-rotating pairs, these large stress levels are mostly due to vortex wandering implying motions which are similar. The effect of wandering can also be seen in the shear stresses (figures 150 through 152) with various lobes present in the core region.

To better illustrate the flow structure in the upper vortex, profile Ii, parallel to the line of symmetry and profile Jj perpendicular to the line of symmetry in figure 144 are presented in figures 153 and 154. The mean axial velocity (figure 153a) shows a small dip in the profile at $r/c=0.6$ resulting from the upper wing wake. In the core region profile Jj, large tangential velocities are evident closest to the line of symmetry resulting from the induced velocity field of the other vortex. In profile Ii, large radial velocities are also present as a result of the induced velocity from the other vortex. One interesting point that is visible

is the small bump in the axial velocity of the core. Note how this phenomenon is symmetric about the y axis and not about the z axis. Some possible explanations for this are secondary vortices present from the roll up of the vortex sheet, or an imperfection in the wing tip which causes an axial instability in the core. This phenomenon is not seen in any of the other vortex cores measured. The normal and shear stress profile Ii (figure 153) shows 3 distinct half rolls of the wing wake in the region surrounding the core. The fluctuations in the outer wake are at $r/c=0.6$ figure 153b with $k=0.00020$. The effect of the vortex wandering on the normal stresses can be seen with v_r^2 and v_θ^2 much larger than v_x^2 . The shear stresses also show the effect of wandering with the different lobes in the core region.

The spectral structure of the counter rotating flow for profile Ii is shown in figures 155 and 156. The spectrum at $r/c=0.47$ shows a large peak in G_{vrvr} and $G_{v\theta v\theta}$ at $fc/U_{ref}=3$, possibly resulting from the large scale structures in the wake similar to those conjectured in the co-rotating pairs. Moving closer to the core, these structures are visible at $r/c=0.15$ and $r/c=0.08$ but at a slightly higher frequency of $fc/U_{ref}=5$ suggesting a reduction in size of the wake structures as they near the core. The presence of these large scale structures are also seen in G_{vrvr} (figure 156c) at $r/c=-0.23$ and $r/c=-0.15$. Moving in towards the core these peaks become much more distinct at $r/c=\pm 0.01$ and ± 0.04 with a frequency of $fc/U_{ref}=5$ and a harmonic at $fc/U_{ref}=10$. These large peaks in the core are seen in all three autospectra, which may indicate that the large scale wake structures are affecting the stability of the flow inside of the core. At lower frequencies $fc/U_{ref}<1$, there is a larger rise in the spectral energy of both G_{vrvr} and $G_{v\theta v\theta}$ compared with G_{vxvx} . As with the co-rotating pairs, this is presumably the result of the vortex wandering increasing the energy levels in the θ and r direction at low frequencies. At high frequencies, the spectral

energy at $r/c=\pm 0.04$ and $r/c=\pm 0.01$ is more than an order of magnitude lower than other parts of the flow, which may suggest very little small scale turbulent motion at the core center. The spectra for profile Jj in figures 157 and 158 show qualitatively the same spectral energy for that of profile Ii. Near the plane of symmetry, at $r/c=-0.29$ and -0.24 larger peaks are present in $G_{v_{rr}}$ (figure 158c) around $fc/U_{ref}=4$ indicating the passage of the large scale wake structure as the two wing wakes contact together at the plane of symmetry.

4.2.2.2 $x/c=30$

At $x/c=30$, the counter rotating pairs have moved further in the $-z$ directions and are centered at $z=-1.7c$ (figure 159). The separation distance between the cores is $0.52c$. This further z wise movement stretches the wing wakes which are less inclined with the z axis than at $x/c=10$ as shown in the t.k.e. and v_x^2 contours of figures 160 and 161. As at $x/c=10$, there is an increase in the peak t.k.e as the wake approaches the core with a maximum value of $k=0.00058$. This is a 22% decrease in peak turbulence energy in the wake from $x/c=10$. Detailed core vectors (figure 162) and vorticity contours (figure 163) show a circular core with slightly oval shape vorticity contours surrounding the core. As at $x/c=10$, there is a region of low negative vorticity away from the core and line of symmetry. The core diameter is $0.108c$ with peak tangential velocities at the core edge that vary from $36\%U_{ref}$ closest to the plane of symmetry to $25\%U_{ref}$ on the other side of the core. The peak vorticity in the core is 33.1 slightly lower than at $x/c=10$. The contours on turbulence kinetic energy (figure 164) are also fairly circular in the core with large fluctuations in the center of $k=0.0366$, over 2 times greater than at $x/c=10$. The maximum normal stresses (figures 165 through 167) are $v_\theta^2=.0380$, $v_r^2=.033$ with v_x^2

much lower at 0.0022. These results imply a vortex wandering which is over 3 times larger than at $x/c=10$. This relatively large amplitude may have smoothed some parts of the measured mean velocity field in figure 162. The shear stresses (figures 168 through 170) also show the effects of the motions with increased stress levels in the core.

Profiles Kk and Ll in figure 162 are shown in figures 171 and 172. Overall the profiles are very similar to those of $x/c=10$. The velocity deficit in the core has decreased to 14.1% U_{ref} . The turbulence levels in the wing wake have also decreased downstream with $k=0.00011$ at $r/c=1.1$ in figure 171b. Closer to the core, two more half spirals can be seen. In the core region there are much larger Reynolds stresses as a consequence of the increased wandering (figure 171c).

The vortex wandering is also seen to effect the spectral energy levels in figures 173 through 176. At $fc/U_{ref}<2$ in figure 173c notice how there is about an order of magnitude increase in spectral energy compared to $x/c=10$ for all three autospectra in the core region. Outside of the core large peaks are seen at $fc/U_{ref}=3$ which may contribute to the increase in motions. Inside the core, there are still peaks in all three autospectra around $fc/U_{ref}=4$ presumably resulting from some type of core instability. At high frequencies, the turbulent fluctuations are much less in the core similar to the spectra at $x/c=10$. Overall these spectra are qualitatively identical to those at $x/c=10$.

4.3 Further Analysis

4.3.1 Circulation

Using the results presented above, the development of the vortex pairs can be analyzed at the various downstream locations. The theory for vortex development was first analyzed by Hoffmann and Joubert (1963) and is analogous to a two dimensional turbulent boundary layer. In the core region of the vortex, solid body rotation will exist such that the circulation Γ varies as r^2 . The shear stresses in this region are small since the rate of strain is negligible. Tangential inertial forces dominate the core region and right outside of it as a result of rapidly changing tangential velocities as well as changing radial velocities due to axial velocity deficits. This region is similar to the viscous sublayer of a boundary layer. In the region of maximum tangential velocities, tangential inertial forces are small compared to the shear stresses. Therefore, it is expected in this region that a logarithmic distribution of circulation will exist in the form

$$\frac{\Gamma}{\Gamma_1} = \frac{1}{H} \log_{10} \left(\frac{r}{r_1} \right) + 1 \quad (4.3.1)$$

where Γ_1 and r_1 are the core circulation and core radius respectively. $1/H$ is a universal constant whose value is determined experimentally. Connecting these two regions is a small buffer region similar to a turbulent boundary layer.

Using equation 4.3.1, Hoffmann and Joubert observed two different circulation distributions from their experimental results. Figure 177 shows the difference between

the two basic types. The first type figure 177a has a logarithmic circulation distribution intersecting the core circulation. They showed that this type of distribution was dependent on viscosity. The second type figure 177b has no intersection of the logarithmic and core region. They showed that profiles of this type were independent of viscosity and fully developed. Using this fact, they produced a universal inner region for a fully turbulent vortex. The core region is given as

$$\frac{\Gamma}{\Gamma_1} = 1.83 \left(\frac{r}{r_1} \right)^2 \quad (4.3.2)$$

and the logarithmic region is given by

$$\frac{\Gamma}{\Gamma_1} = 2.14 \log_{10} \left(\frac{r}{r_1} \right) + 1 \quad (4.3.3)$$

From their results, the condition for complete independence of viscosity appeared to be $U_{ref}x/\Gamma_o > 150$ for their isolated split wing vortex, where Γ_o is the wing root circulation. Devenport et al (1992) also observed a value greater than 150 for the same relation for fully developed isolated single wing vortices.

Using these results, the state of the vortex pairs can be determined at the various streamwise locations. The true circulation for each vortex was calculated using the integral definition

$$\Gamma(r) = \oint_c \mathbf{V}_\theta(r) \cdot d\mathbf{s} \quad (4.3.4)$$

This integral was applied along circular paths concentric with the core with radii extending up to the symmetry or antisymmetry line in the case where two vortices were present.

Figure 178 shows the circulation distribution for the co-rotating pairs at $x/c=10$ and 15. In the core region there is good agreement with the theory of Hoffmann and Joubert. The log region matches fairly well with their universal distribution considering that each vortex is affected by an induced velocity field from its neighboring vortex. From their circulation distribution, the state of the vortices at $x/c=10$ and 15 appear to be fully developed. However, the value for $U_{ref}x/\Gamma_o$ at $x/c=10$ and 15 is 52.3 and 78.4 respectively, with Γ_o equal to the root circulation for one wing. This result is surprising because $U_{ref}x/\Gamma_o$ is much lower than Hoffmann and Joubert's value of 150 for a fully developed flow. It appears that the interaction of the pair has accelerated the development process of the vortices. This indication is also confirmed by the autospectra measured in the core presented in section 4.2.1.1. At high frequencies of $fc/U_{ref} > 20$ (figures 83c and 101c), the turbulence levels in the core are approximately equal to else where in the flow. Devenport et al (1992) also have reported high turbulence levels in the core for fully developed single wing vortices.

At $x/c=22$ and 30, the results shown in figure 179 are in good agreement with the universal law for a fully developed vortex. It is surprising that the vortex at $x/c=22$ is fully developed considering incomplete merging process. After merging of the two

vortices it appears that the mean velocity field quickly assumes an equilibrium state. There is much better agreement in the log region than locations at $x/c=10$ and 15 presumably due to the lack of an induced velocity acting on the core. Notice the slight dips and bumps in the log region which are a result of the spiral wake in the outer region. Again $U_{ref}x/\Gamma_o$ is much lower than Hoffmann Joubert's value at 57.5 and 78.4 for $x/c=22$ and 30 respectively. As with the unmerged cores, the merged cores have high turbulence levels in core autospectra shown in figures 120c and 137c. This confirms the fully developed state of the vortices at $x/c=22$ and $x/c=30$.

The circulation profiles of the counter rotating pairs at $x/c=10$ and 30 are shown in figure 180. These profiles show good agreement at the beginning of the log region out to the edge of the core. However, outside of the core the results deviate from the log region suggesting that the flow is still dependent on viscosity and not fully developed. These circulation profiles are similar to the underdeveloped viscosity dependent case shown in figure 177a. $U_{ref}x/\Gamma_o$ for $x/c=10$ and 30 is 36.4 and 109.1 respectively. This underdeveloped state is also indicated by the autospectra (figures 155c and 173c) which show low turbulence levels in the core above $fc/U_{ref}>20$ compared to the surrounding locations. These spectra are also similar to underdeveloped single wing vortices presented by Devenport et al (1992). Notice that at $x/c=30$, $U_{ref}x/\Gamma_o$ for the under developed vortex is 109.1 which is about 40% greater than the co-rotating vortices at $x/c=15$.

4.3.2 Spiral Wake

One interesting feature of the vortex pairs is the development of the spiral wake as it approaches the core region. Representative locations for the co-rotating pairs at $x/c=10$ and 30 and the counter rotating pair at $x/c=10$ were analyzed. Since the spiral wakes in each of these flows are not aligned with any of the above coordinate systems, a flow direction system following the spiral wake with coordinates (x,s,n) . Where x is the x -axis as before, s is the direction along the wake centerline with the positive direction taken from the core to the outer region, and n completes the right hand coordinate system. From the above velocity results, it was shown that as the spiral wake approaches the core, it is stretched and distorted which changes the turbulence fluctuations along its length. The two primary processes involved in this change are shear due to the mean velocity field defined as

$$\varepsilon = \frac{\partial V_\theta}{\partial r} - \frac{V_\theta}{r} \quad (4.3.5)$$

and flow curvature due to the roll up of the wake defined as

$$r_c = \left(1 + \frac{V_x^2}{V_\theta^2} \right) r \quad (4.3.6)$$

where r_c is the radius of curvature, and r is the wake width. Using the counter rotating pair at $x/c=10$ which has the largest tangential velocities close to the line of symmetry, we can calculate the radius of curvature at the edge of the core with $U=1.0$ and $V_\theta=0.48$.

r_c turns out to be 5 times the width of the wake, implying that the flow curvature will probably be significant close to the core region.

Figure 181 shows the centerline of the spiral wake for the co-rotating pairs at $x/c=10$ and 30. From the results in section 4.2.1, it was shown that turbulence kinetic energy decreased as the wake approached the core. However, this is not the case for the whole wake, as shown in figure 182. θ is defined as the angle that the upper wing wake takes about its respective vortex center (figure 5). The first measurement location close to 0° is the farfield wing wake from section 4.1.2. Notice that all four streamwise locations, there is an increase in t.k.e from the far field wing wake to the beginning measurements surrounding the vortex. At $x/c=10$, the peak t.k.e occurs at $\theta=45^\circ$. This increases to $\theta=90^\circ$ at $x/c=30$. One possible explanation for this increases is due to the increase in vorticity closer to the wing tip. Since the wing is shedding vorticity along its span, the wing wake also contains some of this shed vorticity close to the wing tip and vortex center. This shed vorticity increases the t.k.e. as the wing wake moves from a mostly two dimensional state to a 3D one closer to the vortex. Closer to the vortex the mean shear increases, reducing the t.k.e. in the wing wake as it moves closer to the core. Near the core, the t.k.e increases resulting from the vortex wandering.

Figure 183 shows the Reynolds stresses along the spiral wake of the co-rotating case at $x/c=10$. The farfield wing wake is also shown for comparison. The representative stations 1-5 are labeled in figure 181. At station 1, the turbulence kinetic energy is almost 50% larger with $k=0.00059$ compared to $k=0.00032$ for the wing wake. All three directions show an increase in fluctuations with v_n^2 having the greatest increase. There is also a large increase in all three shear stress $v_x v_s$, $v_s v_n$ and $v_x v_n$ compared to the farfield

wing wake. The increase in $v_s v_n$ is a result of the tangential velocities imposing a shear on the spiral wake structure. The shear stress $v_x v_n$, which is influenced by the axial velocity deficits, is only slightly larger than the farfield wake. Moving closer to the vortex core, the turbulence kinetic energy decreases up to station 4 then slightly increases close to the core as a result of the vortex wandering. This can be seen in figure 183a where there is a large increase in v_x^2 at station 5. However, the normal stress v_n^2 increases to a maximum at station 3 then decreases towards the core. This increase is also seen in $v_x v_n$ at station 3.

An alternative view of the flow structure is shown by the autospectra in figure 184. Large peaks are seen in G_{vsvs} at $fc/U_{ref}=3$ at stations 1 and 2. The intensity of these peaks is seen to decrease as the core is approached. By station 4, none of the peaks are visible. This may be the result of the increased shear breaking up the large scale structures as the core is approached. In figure 184c, G_{vnvn} also shows large peaks which increase in frequency from $fc/U_{ref}=3$ to $fc/U_{ref}=4$ close to the core. This may suggest that closer to the core these large structures are broken into smaller ones which have a higher frequency. At high frequencies, all three autospectra have approximately the same energy indicating that the small scale turbulence levels are similar. Using the similarity analysis discussed section 4.1.2, the autospectra can be scaled on the width of the wake at the various stations. Figure 185 shows the autospectra, where L_o is the local length scale at each station. There is good collapse of both G_{vxx} and G_{vnvn} above $fL_o/U_{ref}>.1$. In G_{vsvs} stations 4 and 5 do not collapse well since they have no pronounced peaks around $fL_o/U_{ref}=.25$.

Moving downstream to $x/c=30$, figure 186 shows the Reynolds stresses in the spiral wake for stations 1-8 labeled in figure 181. Approaching the core along the spiral wake, the turbulence kinetic energy increases from $k=0.00010$ in the far field wake to $k=0.000161$ at station 1. The t.k.e. then decreases up to station 8 where presumably the vortex wandering increases the fluctuations. The shear stresses are also similar to the stress at $x/c=10$, with an increase in $v_s v_n$ resulting from the shear of the tangential velocities. Also, $v_x v_n$ remains fairly constant up to station 3 until it begins to decrease due to the lack of a mean axial velocity deficit.

The spectra for $x/c=30$, figure 187, also are quantitatively similar to those at $x/c=10$. Large peaks resulting from the large scale wake structures are seen in G_{vsvs} at $fc/U_{ref}=2.5$, which reduce in intensity as the core is approached. These peaks are also seen in G_{vnvn} at $fc/U_{ref}=2.5$, but unlike $x/c=10$ they do not increase in frequency as the core is approached. This could be due to the larger radial distance station 8 is located from the core resulting in lower damping of the large scale structures. Figure 188 shows similarity scaling of the autospectra based on the local length scale L_o . There is good collapse for all nine locations across all frequencies.

The location of the spiral wing wake is shown in figure 189 for the counter rotating pair at $x/c=10$. In these pairs, the t.k.e in the wake increases from the far field wing wake to a location between the two cores (figure 190). In contrast to the co-rotating pairs, there is no increase in the t.k.e in the outer region of the vortex. This probably results from lower amounts of vorticity shed away from the tips for the counter rotating wings as compared to the co-rotating wings.

At $x/c=10$, the t.k.e. from the farfield wake ($k=0.00037$) increases to station 4 ($k=0.00072$) located directly between the cores. At this location, there is a large shear from both vortices in the 's' direction which is partly responsible for the increased fluctuations. Also partly responsible for the increased fluctuations is the vortex wandering shown by the large stresses at the edge of the station 4 wake in figure 191a. This large increase is also seen in the shear stress v_{svn} in figure 191e.

The spectra in figure 192 also show pronounced peaks in G_{vsvs} at the farfield wake and station 1 locations. Moving closer to the core, the large scale structures increase in frequency and decrease in intensity. In figure 192c, G_{vnnn} show very large peaks centered around $fc/U_{ref}=4$ for all of the spiral locations. The intensity of these peaks reach a maximum at station 4 corresponding to the large t.k.e., then decrease further along the spiral. Figure 193 shows the autospectra scaled on L_o . There is a fairly good collapse above $fL_o/U_{ref}>.1$ for all three autospectra. Below $fL_o/U_{ref}<.1$, there are large differences between the various stations possibly resulting from the vortex wandering which increases the energy at low frequencies.

4.3.3 Triple Products

Triple products are a quantity that is both difficult to measure and interpret . One way to analyze these results is the triple product contribution to transverse diffusion of turbulent kinetic energy. This discussion is taken from Nasseri (1990) who measured a vortex interacting with a boundary layer.

According to Nasseri, the y component transport velocity is defined as

$$V_q = (u^2v + v^3 + vw^2) / (u^2 + v^2 + w^2) \quad (4.3.7)$$

with the z component defined as

$$W_q = (u^2w + w^3 + v^2w) / (u^2 + v^2 + w^2) \quad (4.3.8)$$

Actually these definitions should include pressure fluctuation terms, but these terms are difficult to measure so that the pressure diffusion has been ignored. Note that the diffusion velocity vectors in the y-z plane require 9 turbulence quantities - 6 triple products and 3 normal stresses. Figures 194 through 199 show the transport velocity vectors for the 6 streamwise locations measured. The triple products appear fairly consistent at all streamwise locations which is surprising considering the uncertainties of these quantities. If turbulent diffusion of the Reynolds stresses and t.k.e. were both pure gradient diffusion processes, then the triple product vectors would be normal to the contours of t.k.e. and their magnitude proportional to the gradient of turbulent energy. Clearly from figures 194 through 199, the vectors are close to being normal to the t.k.e. contours and proportional to the gradient in the wake and outer region of the vortex. Near the vortex core, this is not true suggesting that gradient transport of Reynolds stress is not an accurate approximation for the core region.

4.4 Vortex Motions and Core Region

4.4.1 Co-Rotating Pairs

From the velocity results in section 4.2, it was shown that the core region of the vortex pairs is dominated by large Reynolds stresses which are attributed to wandering of the pairs about the tunnel. This was confirmed by the flow visualization results in section 3.0 which showed low frequency motions to be present. The direction of this wandering can be estimated by determining the direction of the principal stresses using a Mohr's circle analysis. If we assume that most if not all of the stresses in the core are associated with this wandering, we can estimate, using the measured mean velocity gradient, an upper bound for the amplitude of the core motions.

At $x/c=10$ the r.m.s. amplitude of the motions for the upper and lower vortex is $0.023c$ and $0.021c$ respectively. This length is marked on figure 75 to give a qualitative idea of the degree to which wandering may have smoothed the measured mean velocity field. Figures 200 and 201 show the principal stress directions in the core region which only represent the direction and not the magnitude of the principal stress. Outside of the core, the principal direction appears to be closely aligned with the radial direction in most locations. However, in the center of the core, the vectors are clearly aligned along a certain direction for both vortices. The vectors in the upper vortex appear aligned at 140° with the lower vortex vectors aligned at 160° . This alignment indicates surprisingly, that the motions are not isotropic but have a preferred direction. This direction is similar to the line connecting the two cores which is at 135° .

Moving downstream to $x/c=15$, the magnitude of the Reynolds stresses inside the core increase presumably as a result of the increased vortex wandering. This implies motions with an r.m.s amplitude less than $0.031c$ for the upper vortex and $0.030c$ for the lower vortex. The direction of these non-isotropic motions can be seen in figures 202 and 203 for both vortices. The upper and lower core vectors appear to be aligned approximately 80° and 95° respectively. Notice that at this streamwise location, the line connecting the two cores has rotated to about 70° similar to the direction of the principal stress vectors.

By $x/c=22$, the merged single vortex has stresses in the core which are 4 times smaller than the unmerged cores. These stress levels imply motions with an r.m.s. amplitude of $0.016c$. Figure 204 shows the direction of the principal stress vectors in the core. It appears there is no alignment of the vectors indicating the motions have no preferred direction and are isotropic. At $x/c=30$, the motions have slightly increased to an amplitude of $0.021c$. However unlike $x/c=22$, the principal stress vectors are aligned at about a 110° angle to the y axis indicating non-isotropic motions. This is surprising since there is no influence from other vortices at this streamwise location.

4.4.2 Counter Rotating Pairs

In the core region of the flow, the counter rotating pairs experience increased stress levels similar to the co-rotating pairs. Overall these levels were much larger than the co-rotating cases probably as a result of the larger velocity gradients present in the core. Using this fact we can obtain an estimate of the wandering for the pairs at $x/c=10$. The r.m.s amplitude for the upper and lower vortices are $0.021c$ and $0.020c$ respectively. These motions are similar to the co-rotating pairs at the same streamwise location. The

principal stress vectors are shown in figures 206 and 207 for the upper and lower vortices. Around the outer edge of the core, the vectors are mostly aligned with the radial direction. Inside the core however, most of the vectors appeared aligned in similar directions implying non-isotropic motions. The directions are approximately 130° for the upper vortex and 60° for the lower vortex. Notice that these directions do not lie along a line connecting the two cores as was the case for the co-rotating pairs.

At $x/c=30$, there are large increases in stress levels in the core implying an increase in the vortex wandering. The estimate of the r.m.s amplitude is $0.058c$ and $0.055c$ for the upper and lower vortex respectively. These relatively large amplitudes may have smoothed some parts of the measured mean velocity field which is marked on figure 162. The principal stress directions are shown in figures 208 and 209 for the upper and lower vortices with the upper vortex aligned at 130° and the lower vortex aligned at 50° . These directions of the non-isotropic motions are similar to those at $x/c=10$.

4.4.3 Possible Sources of Vortex Motions

Several explanations are suggested for the wandering of vortices generated in the wind tunnel. From the above results it appears there are three main types of motions that may be responsible for the increased stress levels in the center of the vortex core. These are classified by (i) wind tunnel induced motions which are below frequencies $fc/U_{ref} < 0.05$ (ii) self induced instabilities between frequencies $0.05 < fc/U_{ref} < 1.0$ and (iii) vortex wave instabilities between $1.0 < fc/U_{ref} < 10$. Above $fc/U_{ref} > 10$ the measured autospectra showed no indication of any dominant frequencies and it appears that most of the energy is due to "true" turbulent fluctuations.

Figures 210 through 212 show representative long time average autospectra taken in the core region for the co-rotating case at $x/c=10$ and 30, and the counter rotating case at $x/c=10$. At frequencies below $fc/U_{ref}<0.05$, there is almost two orders of magnitude increase in energy levels which primarily occurs in $G_{v\theta v\theta}$ and $G_{vr vr}$. From video tape taken during the flow visualization results, low frequency motions around $fc/U_{ref}=.004$ were observed in all cases. The movement of the vortex pairs were closely correlated (i.e. they almost always move in tandem). Since the wing wake essentially forms a mass boundary, this implies that the entire flow field in the test section must move as a whole to cause motions. The low frequency motions may therefore be due to small flow direction changes in the test section with time. Possible sources of the flow direction changes are wind gusts (which may effect the flow inside the tunnel, since the Stability Tunnel is vented to the outside). We discount this source since the unsteadiness appeared to scale with velocity and all cases experienced the same movement regardless of weather.

Another source of tunnel induced motions is viscous effects such as transient separation in the contraction and possibly in the diffuser. This is supported by the fact that the magnitude of the lateral motions appear to be a strong effect of Reynolds number. This implies that a greater length to diameter ratio (l/d), test section would reduce the lateral motions by straightening the flow. The Virginia Tech Stability Tunnel has a $l/d=4.0$, compared to most tunnels which are around 2.0 perhaps explaining why our vortices are more stable than those studied by other workers.

Yet another possibility was suggested by Baker et al. (1974). They conducted laser anemometer experiments on a single vortex generated in a water tunnel and argued that freestream turbulence was the cause of the unsteadiness. Since the Stability Tunnel has freestream turbulence levels less than .05% this seems an unlikely cause.

Increasing in frequency to $0.05 < fc/U_{ref} < 1.0$, motions due to vortex pair self induction may be responsible. One example of this instability is reported by Crow (1970). Crow developed a stability theory for counter-rotating vortex pairs which demonstrated that such pairs are unstable to disturbances of certain wavelengths. In Crow's non-dimensional terms the most unstable wave number and its amplification rate, β_{max} and α_{max} , are about 0.7 and 0.85 respectively for the counter rotating vortex pairs.

Assuming these disturbances to be convected at the freestream velocity, $\beta_{max}=0.7$ implies frequencies of $fc/U_{ref} = 0.44$. The corresponding amplification factor of this disturbance over the length of the test section is 215. Relative to the wing span these disturbances act in planes which are at equal and opposite angles for each vortex. These directions are clearly seen in the principal stress vectors in figures 206 through 209 for $x/c=10$ and 30. The autospectra at $x/c=30$ figure 173c also show a dominant peak at $fc/U_{ref}=0.35$ suggesting that the counter rotating pairs may suffer from Crow instability. These peaks are not seen at $x/c=10$ presumably as a result of the low amplitude disturbances.

This raises an interesting question in the case of the co-rotating pairs at $x/c=10$ and 15. If the counter rotating pairs suffer from instabilities brought about by self induction, why should not the co-rotating pairs suffer from a similar process? The direction of the principal stress vectors in figures 201 through 203 appear to be aligned with the line

joining the two cores. It is unlikely this is due to wind tunnel induced motions since the direction of the principal stress changes from $x/c=10$ to $x/c=15$. The only mention of this instability is discussed by Leonard (1985). He showed that when curved, an ideal vortex induces velocities of itself that makes it unstable. However in figure 86c, no large peaks are present in the autospectra at frequencies between $0.05 < fc/U_{ref} < 1.0$. One possible reason such peaks are not observed is that the merging process may damp out any amplified disturbances which might be seen in the autospectra.

In the range of frequencies $1.0 < fc/U_{ref} < 10$, there is the possibility of motions as a result of vortex wave instabilities. The theory of these instabilities is discussed in Marshall (1991). Since the vortex core is essentially one continuous column of fluid, waves can travel along the core at velocities different from that of the freestream. Marshall discusses the two most dominant types of instabilities, the axisymmetric and helical modes. The axisymmetric instability appears as bulging of the vortex core where the core increases and decreases in area as it travels downstream. The helical instability is where the vortex core follows a helical path around a central axis. Both of these modes are unstable and increase in amplitude with downstream distance. Singh and Uberoi (1975) appear to have the best measurements of these two types of instabilities. Using two probe spatial correlations, they found that both these modes existed in their vortex core. The helical mode was observed at a frequency of $fc/U_{ref}=2.1$ and the axisymmetric mode at $fc/U_{ref}=4.9$.

Spectral peaks in this frequency range are seen in the co-rotating pairs at $x/c=10$ in figure 86a at $fc/U_{ref}=3.2$. Since this frequency is between Singh and Uberoi's helical and axial mode, it is difficult to suggest which one it could be. By $x/c=15$, this peak has

disappeared which may suggest that the interaction of the pair has a damping effect on these instabilities. Viewing video tapes taken during the flow visualizations, it was also seen that the core "buckles" at various times. Marshall (1992) also discusses this phenomenon which may influence some of the core motions. However it appears unlikely that this buckling would occur at a specific frequency which could be determined from the autospectra. At $x/c=22$ and 30, there are no indications of any instabilities in the core which probably results from the increased turbulence in the core.

The counter rotating case at $x/c=10$, figure 156a shows two sharply defined peaks at $f_c/U_{ref}=5.0$ and 9.0 in the core region. The second peak is likely a harmonic of the first suggesting that the frequency is nonsinusoidal. The high frequency of these peaks suggest that they may result from an axisymmetric instability rather than an helical instability. However by $x/c=30$, the spectral peaks appear to decrease to $f_c/U_{ref}=4.0$ again at a similar frequency to that of Singh and Uberoi. According to Singh and Uberoi, these instabilities were brought about by the large axial velocity differences ($50\%U_{ref}$) between the outer and core region of the vortex. However, the velocity deficit in the counter rotating pairs is at most $15\%U_{ref}$. Possible explanations due to these instabilities are the under developed state of the vortices which may make them more susceptible to small disturbances. Also, the large scale structures from the spiral wake may "beat" on the core producing disturbances which lead to these instabilities.

4.4.4 Filtered Results

One way to examine the flow structure surrounding the core region with reduced effects from the vortex wandering is to high pass filter the data at various cut off frequencies. A

square filter was used to high pass representatives profiles at frequencies $fc/U_{ref}=1.5, 7.0$ and 20.0 . This technique does not reduce any of the effects of smoothing in the mean velocity field, therefore mean velocities are not presented.

At $x/c=10$ the representative profile for the co-rotating case from section 4.2.1 is shown in figure 81. This profile is labeled Aa in figure 72 and is parallel to the line of antisymmetry. In the center of the core, the maximum t.k.e is $k=0.0058$ with the maximum t.k.e in the wake of $k=0.0006$. The filtered data with a cut off frequency of $fc/U_{ref}=1.5$ is shown in figure 213. Overall the shape of the profile is similar to the unfiltered data with decreased levels of turbulence energy. The maximum t.k.e in the center of the core has reduced to $k=0.0030$ a 48% reduction from the unfiltered data. The maximum t.k.e. in the wake also has been reduced to $k=0.00053$. This suggests that almost 50% of the fluctuation levels in the core are due to wind tunnel induced motions and or self induction of the vortex pair. Increasing the filter frequency to $fc/U_{ref}=7.0$, figure 214 shows a large decrease in the center of the core with $k=0.00053$, a 91% decrease compared to the unfiltered data. The t.k.e energy in the wake reduces to $k=0.00013$, a 78% reduction compared to the unfiltered data. This indicates that 43% of the energy lies in the frequency range $1.5 < fc/U_{ref} < 7.0$. Increasing the filtering frequency to $fc/U_{ref}=20.0$, the true structure of the core region becomes visible in figure 215. Surrounding the outer edge of the core, is a region of increased turbulence fluctuations. This region does not appear to be part of the wing wake but appears associated with the core itself. Other profiles through the vortex show that this region is concentric surrounding the core. Inside the core, $k=0.00005$, accounting for about 1% of the measured fluctuations. This suggests that 8% of the measured turbulence energy lies in the frequency range $7.0 < fc/U_{ref} < 20$.

Moving downstream to $x/c=30$, figure 135 shows the unfiltered data for profile Gg marked in figure 126. In the core and wake regions $k=0.00145$ and 0.00018 respectively. Increasing the filter frequency to $fc/U_{ref}=1.5$, (figure 216) reduces the t.k.e in the core by 65% to $k=0.0005$ and in the wake to $k=0.00012$, a 35% reduction. This large reduction in the core energy suggests that the merged co-rotating pairs may be effected by wind tunnel induced motions. Since there are no neighboring vortices, it seems unlikely the motions are caused by mutual induction. Increasing the filtering frequency to $fc/U_{ref}=7.0$, figure 217 shows the true structure around the core beginning to appear. In the core $k=0.00007$, indicating that 30% of the turbulence energy lies in the range $1.5 < fc/U_{ref} < 7.0$. At a filter frequency of $fc/U_{ref}=20$, figure 218 shows a similar core structure with a larger diameter compared to $x/c=10$. Other profiles confirm that this region is concentric about the core and not associated with spiral wake. In the center of the core the t.k.e has reduced to $k=0.00001$, implying that 4% of the energy lies between $7.0 < fc/U_{ref} < 20$.

In the counter rotating case at $x/c=30$, figure 171 shows the unfiltered data for profile Kk parallel to the line of symmetry. In the center, the effect of the motions are clearly seen by the large v_θ^2 and v_r^2 with $k=0.029$. In the wake region, the t.k.e. is much lower with $k=0.00011$. Using a filter frequency of $fc/U_{ref}=1.5$, figure 219 shows a 95% decrease in energy at the center of the core. From previous results, it appears that most of this energy reduction is due to the elimination of the effects from the Crow instability which occurs at $fc/U_{ref}=0.44$. Increasing fc/U_{ref} to 7.0 shows a reduction in t.k.e in the center of the core with $k=0.00030$. This indicates that 3% of the measured energy lies in the range $1.5 < fc/U_{ref} < 7$. Increasing fc/U_{ref} even further to 20, figure 220 shows the true turbulent

structure surrounding the core similar to the co-rotating vortices. Other profiles indicate that the turbulence structure seen in figure 221 is of similar magnitude and concentric with the core. In figure 221a, a small increase in v_θ^2 can be seen at $r/c=-0.4$ which may result from the spiral wake surrounding the core. This is not seen in the co-rotating pairs which may result from the under developed state of the counter rotating vortices. In the center of the core $k=0.00005$ indicating that 1% of the measured energy lies between $7.0 < fc/U_{ref} < 20.0$.

5. Conclusions

The flow structure produced by co-rotating and counter rotating trailing vortex pairs has been studied through helium bubble visualizations and detailed three component hot wire velocity measurements. The vortices were generated by two rectangular wings placed tip to tip at equal and opposite angles of attack. Velocity measurements were made at a chord Reynolds number of 260,000 with a wing tip separation of $0.25c$. The wings were placed at equal and opposite angles of attack producing counter rotating and co-rotating pairs respectively. Quad hot wire measurements were taken at streamwise locations $x/c=10, 15, 22$, and 30 for the co-rotating pairs, and at $x/c=10$, and 30 for the counter rotating pairs.

The main conclusions to be drawn from the flow visualizations are:

1. The co-rotating pairs were seen to rotate about each other, and if the wing separation was sufficiently small ($\leq 0.375c$) and the angle of attack sufficiently large ($\geq 5.0^\circ$), merging occurred within the 30 chordlengths of the test section.
2. The counter rotating pairs moved slightly apart and across the test section under their mutual induction changing little with streamwise location.
3. The vortex pairs showed no significant effects of a 3:1 change in Reynolds number.

4. At all conditions the vortices appeared completely insensitive to probe interference and were subject only to very small wandering at low frequencies.

The main conclusions to be drawn from the velocity measurements are:

5. Upstream of the merging location, the co-rotating pairs have approximately elliptical cores. Contours of vorticity are also elliptical being concentric with the core.

6. Autospectra and true circulation profiles suggest that the flow in the vicinity of the cores is fully developed (i.e. viscosity independent). This is surprising, since the ageing of the pairs ($U_{ref}x/\Gamma_0$) are only one third to one half of that required for fully developed flow in isolated vortices.

7. The turbulence levels in the wing wakes increase, moving from the two dimensional wake to the outer regions of the vortices presumably as a result of the shed vorticity from the wings. Approaching the cores, the wakes become wrapped up into spirals reducing the turbulence levels as a result of the accompanying distortion.

8. During the merging process, the vortex cores roll about one another rapidly winding up the wing wakes into a fine spiral structure that remains visible for some distance downstream. Merging roughly doubles the size of the core and produces turbulence over a broad range of frequencies.

9. After merging the core region recovers rapidly to a fully developed state.

10. In the center of the cores, large stresses exist as a consequence of the small amplitude wandering. Principal stress directions indicated that motions are not isotropic but have a preferred direction.

11. In contrast to the co-rotating pairs, the counter rotating pairs move across the test section stretching the wing wakes and forcing them into contact between the cores. As

the wakes are forced between the vortices, the turbulence levels increase then decrease as they move further around the cores.

12. The cores of these vortices remain fairly circular despite the strong velocity fields they impose on each other.

13. Autospectra and true circulation profiles suggest that the counter rotating pairs do not become fully developed within the 30 chordlengths of the measurements.

14. Autospectra and principal stress directions in the core suggest that the counter rotating pairs are effected by Crow instability, especially at 30 chordlengths.

6. References

- Baker G R, Barker S J, Bofah K K and Saffman P G, 1974, "Laser anemometer measurements of trailing vortices in water", *Journal of Fluid Mechanics*, vol 65, pp. 325-336.
- Bandyopadhyay P, Stead D and Ash R, 1990, "The organized nature of a turbulent trailing vortex", *AIAA 21st Fluid Dynamics, Plasma Dynamics and Lasers Conference*, June 18-20, Seattle, WA. AIAA paper 90-1625.
- Barker S J and Crow S C, 1977, "The motions of two-dimensional vortex pairs in a ground effect", *Journal of Fluids Mechanics*, vol 82, pp. 659-671.
- Bendat J S and Piersol A G, 1986, Random Data Analysis and Measurement Procedures, pp. 361-424, John Wiley & Sons, New York, 1986.
- Betz D, 1933, "Behavior of vortex systems", NACA TM 713.
- Chigier N A and Corsiglia V R, 1972, "Wind tunnel studies of wing wake turbulence", *Journal of Aircraft*, vol 9, pp. 820-825.
- Choi K and Simpson R L, 1987, "Some mean-velocity, turbulence, and unsteadiness characteristics of the VPI&SU Stability Wind Tunnel", Report VPI-AOE-161, VPI&SU, Blacksburg, VA.
- Corsiglia V R, Schwind R G, and Chigier N A, 1973, "Rapid scanning, three-dimensional hot-wire anemometer surveys of wing-tip vortices", *Journal of Aircraft*, vol 10, pp. 752.-757
- Crow S C 1970, "Stability theory for a pair of trailing vortices", *AIAA Journal*, vol 8, pp. 2172-2179.

- Devenport W J and Sharma G, 1991, "Far-field turbulence structure of the tip vortex shed by a single rectangular wing", Eighth Symposium on Turbulent Shear Flows.
- Devenport W J, Glegg S A L and Sharma G, 1992, "Measurements in trailing vortices for BWI noise prediction. Part 1. Measurements", AOE Dept., VPI&SU.
- Donaldson C duP and Bilanin A J, 1975, "Vortex wakes of conventional aircraft", AGARD AG-204.
- Gasperek E, 1960, "Viscous decay of a vortex", Master Thesis, Syracuse University, NY.
- Green S I and Acosta A J, 1991, "Unsteady flow in trailing vortices", Journal of Fluid Mechanics, vol 227, pp 107-134.
- Hackett J E and Evans M R, "Vortex wakes behind high lift wings", Journal of Aircraft, May 1971, pp. 334-343.
- Hoffmann E R and Joubert P N, 1963, "Turbulent line vortices", Journal of Fluid Mechanics, vol 16, pp. 395-411.
- Jorgenson F E, 1971, "Directional sensitivity of wire and fiber-film probes", DISA Information, No.11, pp. 6-10.
- Klebanoff F S, 1975, "Characteristics of turbulence in a boundary layer with zero pressure gradient", NACA Technical Report 1247.
- Kline S J and McClintock, F A, 1953, "Describing uncertainty in single sample experiments", Mechanical Engineering, January, pp. 3-8.
- Lamb H, 1932, "Hydrodynamics", 6th edn, Dover, pp. 223-230.
- Leanord A, 1985, "Computing three-dimensional incompressible flows with vortex elements", Annual Review of Fluid Mechanics, vol 17, pp. 523-559.
- Lee H, and Schetz J A, 1985, "Experimental results for Reynolds number effects on trailing vortices", Journal of Aircraft, vol 22, pp. 158-160.
- Leuchter O and Solignac J L, 1983, "Experimental investigation of the turbulence structure of vortex wakes", Proceedings of the 5th Symposium on Turbulent Shear Flows, Ithaca, NY, pp. 5.31-5.36.
- Marshall J S, 1991, "A general theory of curved vortices with circular cross section and variable core area", Journal of Fluid Mechanics, vol. 229 pp. 311-338.

- Mason W H and Marchman J F, 1972, "Far-field structure of an aircraft trailing vortex, including effects of mass injection", NASA CR 62078.
- Maxworthy T, Hopfinger E J and Redekopp L G, 1985, "Wave motions on vortex cores", *Journal of Fluid Mechanics*, vol. 151, pp 141-165.
- Melander M V, Zabusky M J and McWilliams J C, 1988, "Symmetric vortex merger in two dimensions; cause and conditions", *Journal of Fluid Mechanics*, vol 195, pp. 303-340.
- Naaseri M, 1990, "Studies in Complex 3D Turbulent Flows", PhD Thesis, Aero. Dept., Imperial College, University of London.
- Nakayama A, 1983, "Measurements of attached and separated turbulent flows in the trailing- edge regions of airfoils", 2nd Symposium of Numerical and Physical Aspects of Aerodynamic Flows, California State University, Long Beach.
- Orloff K L, 1971, "Experimental investigation of upstream influence in a rotating flowfield", PhD thesis, University of California, Santa Barbara.
- Phillips W R C, 1981, "The turbulent trailing vortex during roll-up", *Journal of Fluid Mechanics*, vol. 105, pp. 451-467.
- Phillips W R C and Graham J A H, 1984, "Reynolds stress measurements in a turbulent trailing vortex", *Journal of Fluid Mechanics*, vol 147, pp. 353-371.
- Rossow V J, 1977, "Convective merging of vortex cores in lift generated wakes", *Journal of Aircraft*, vol 14, #3, pp. 283-290.
- Sarpkaya T, Elnitsky J and Leeker R E, 1988, "Wake of a vortex pair on the free surface", *Proceedings of the 17th Symposium on Naval Hydrodynamics*, 1988, National Academy Press, Washington DC, pp. 47-54.
- Sarpkaya T, 1992, "Three dimensional interactions of vortices with a free surface", *AIAA 30th Aerospace Sciences Meeting*, Jan 6-9, Reno, NV. Paper AIAA-92-0059.
- Schlichting H, 1965, "Boundary Layer Theory", 6th edn, McGraw-Hill, pp. 686-690.
- Simpson R L, Chew Y T and Shivaprasad B G, 1981, "The structure of a separated turbulent boundary layer", *Journal of Fluid Mechanics*, vol. 113, pp. 319-339.

- Singh P I and Uberoi M S, 1976, "Experiments on vortex stability", *Physics of Fluids*, vol 19, p 1858-1863.
- Smits A J and Kummer R P, 1985, "The interaction and merging of two turbulent line vortices", AIAA paper 85-0046.
- Stifle K E and Panton R L, "Experiments concerning the theories of vortex breakdown", AIAA 29th Aerospace Sciences Meeting, Reno, NV, Jan 6-9. Paper AIAA-91-0736.
- Tryggvason G, Abdollahi-Alibeik J, Willmarth W and Hirs A, 1990, "Collision of a vortex pair with a contaminated free surface", Report 90-1, University of Michigan.
- Willmarth W W, Tryggvason G, Hirs A, and Yu D, 1989, "Dynamics of vortex interaction with a density interface", Report No. MSM-8707646-88-01, The University of Michigan Ann Arbor, Michigan.
- Wynanski I, Champagne F and Marasli B, "On the large-scale structures in two-dimensional, small-deficit, turbulent wakes", *Journal of Fluids*, vol 168, pp. 31-71.
- Yu J C, 1981, "Trailing edge boundary layer measurements of a two dimensional airfoil", NASA TP-1845.
- Zsoldos J S and Devenport W J, 1991, "Flow visualization of interacting wing-tip vortex pairs", Report VPI-AOE-177, AOE Dept., VPI&SU, Blacksburg, VA.
- Zsoldos J S and Devenport W J, 1992, "An experimental investigation of interacting trailing vortex pairs", 19th Symposium on Naval Hydrodynamics Seoul, South Korea, August 1992.

Tables

Table 1. Flow conditions for visualizations.

Wing Separation Δy	Angle of Attack α_o, α_e	Reynolds Number Re_c	Dummy Probe
c	$\pm 2.5^\circ$	130,000	
c	± 5.0	130,000	
c	± 7.5	130,000	
c	± 10.0	130,000	
c/2	± 2.5	130,000	
c/2	± 5.0	130,000	
c/2	± 7.5	130,000	
c/2	± 10.0	130,000	
3/8c	± 2.5	130,000	
3/8c	± 5.0	130,000	yes
3/8c	± 7.5	130,000	yes
3/8c	± 10.0	130,000	yes
c/4	± 2.5	130,000	
c/4	± 5.0	130,000	yes
c/4	± 7.5	130,000	
c/4	± 10.0	130,000	
3/8c	± 5.0	400,000	yes
3/8c	± 7.5	400,000	yes
3/8c	± 10.0	400,000	yes
c/4	± 5.0	400,000	yes

Table 2. Typical uncertainties in measurements made with the single hot wire probe.

	Wake edge		Wake center	
Quantity	Value	Uncert.	Value	Uncert.
U/U_e	9.8×10^{-1}	1.9×10^{-2}	2.1×10^{-1}	2.5×10^{-3}
u^2/U_e^2	5.5×10^{-5}	6.5×10^{-7}	5.8×10^{-3}	7.5×10^{-5}

Table 3. Typical uncertainties in measurements made with the quad hot wire probe.

	Wake region		Core edge		Core center	
Quantity	Value	Uncert.	Value	Uncert.	Value	Uncert.
U/U_e	9.7×10^{-1}	1.5×10^{-2}	9.4×10^{-1}	1.5×10^{-2}	9.0×10^{-1}	1.4×10^{-2}
V/V_e	-3.6×10^{-2}	2.5×10^{-2}	-1.3×10^{-1}	2.5×10^{-2}	-6.4×10^{-2}	2.4×10^{-2}
W/U_e	1.9×10^{-2}	2.5×10^{-2}	9.6×10^{-2}	2.4×10^{-3}	-4.6×10^{-2}	2.3×10^{-2}
u^2/U_e^2	3.5×10^{-4}	3.1×10^{-6}	8.5×10^{-4}	1.4×10^{-5}	1.3×10^{-3}	4.3×10^{-5}
v^2/U_e^2	2.6×10^{-4}	9.5×10^{-6}	6.1×10^{-4}	1.5×10^{-5}	5.7×10^{-3}	1.7×10^{-4}
w^2/U_e^2	3.7×10^{-4}	9.9×10^{-6}	1.1×10^{-3}	2.0×10^{-5}	4.5×10^{-3}	1.6×10^{-4}
uv/U_e^2	1.8×10^{-5}	4.3×10^{-6}	-2.7×10^{-5}	1.4×10^{-5}	-7.7×10^{-4}	1.2×10^{-4}
vw/U_e^2	1.1×10^{-4}	4.5×10^{-6}	1.6×10^{-4}	2.3×10^{-5}	-1.8×10^{-3}	5.2×10^{-5}
uw/U_e^2	5.4×10^{-5}	2.9×10^{-6}	-2.6×10^{-4}	8.5×10^{-6}	-1.3×10^{-4}	1.0×10^{-4}

Table 4. Wing trailing edge characteristics.

Case	δ/c	δ^*/c	θ/c	Re_θ
$\alpha_o y/c=1.3$ pressure	.03564	.00797	.00453	1060.0
$\alpha_o y/c=1.3$ suction	.05482	.01349	.00732	1712.6
$\alpha_o y/c=.73$ pressure	.04028	.00958	.00533	1289.1
$\alpha_o y/c=.73$ suction	.05631	.01344	.00742	1796.1
$\alpha_o y/c=-.73$ pressure	.04770	.01005	.00615	1486.9
$\alpha_o y/c=-.73$ suction	.06275	.01500	.00835	1953.9
$\alpha_o y/c=-1.3$ pressure	.04889	.01066	.00618	1445.9
$\alpha_o y/c=-1.3$ suction	.06378	.01568	.00856	2004.15
$\alpha_e y/c=1.3$ pressure	.03364	.00734	.00419	979.76
$\alpha_e y/c=1.3$ suction	.05843	.01477	.00778	1819.7
$\alpha_e y/c=.73$ pressure	.03834	.00850	.00488	1180.1
$\alpha_e y/c=.73$ suction	.05949	.01535	.00822	1986.4
$\alpha_e y/c=-.73$ pressure	.04544	.00960	.00579	1400.2
$\alpha_e y/c=-.73$ suction	.06232	.01552	.00857	2072.4

Table 5. Locations of vortices in tunnel coordinates.

Case	Wing	x/c	y/c	z/c
α_o	upper	10	-.0711	.1473
α_o	lower	10	.1289	-.0590
α_o	upper	15	-.0038	-.0515
α_o	lower	15	.0600	.1423
α_o	both	22	.0700	.0441
α_o	both	30	.0868	.0445
α_e	upper	10	.2425	-.6690
α_e	lower	10	-.1975	-.6609
α_e	upper	30	.2656	-1.7403
α_e	lower	30	-.2553	-1.7265

Figures

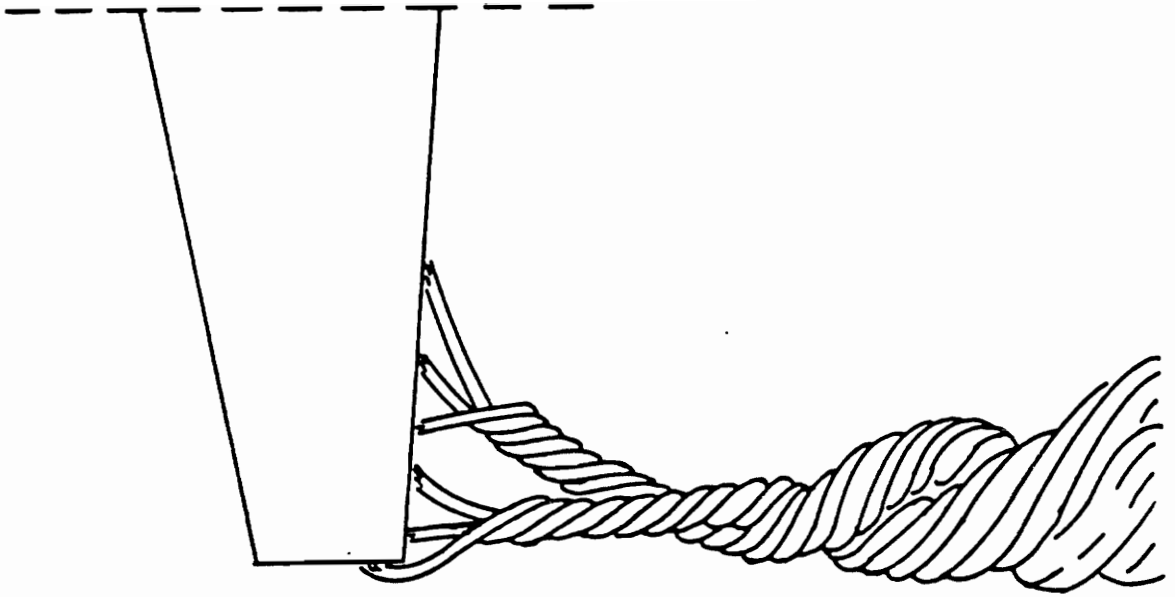


Figure 1. Lancaster's model of the roll up of a single wing tip vortex.

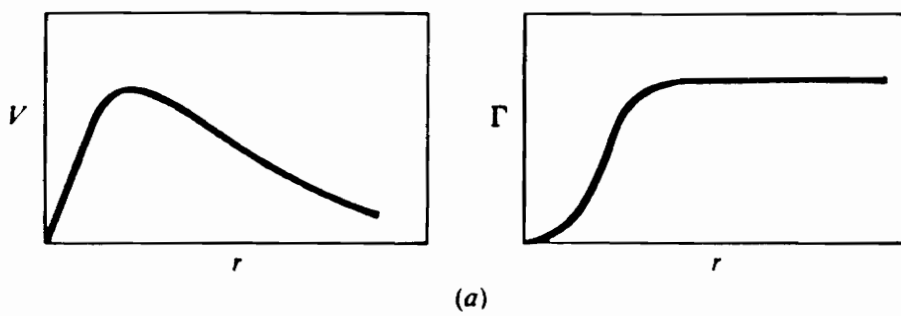


Figure 2. Tangential velocity and circulation distribution of an ideal vortex.

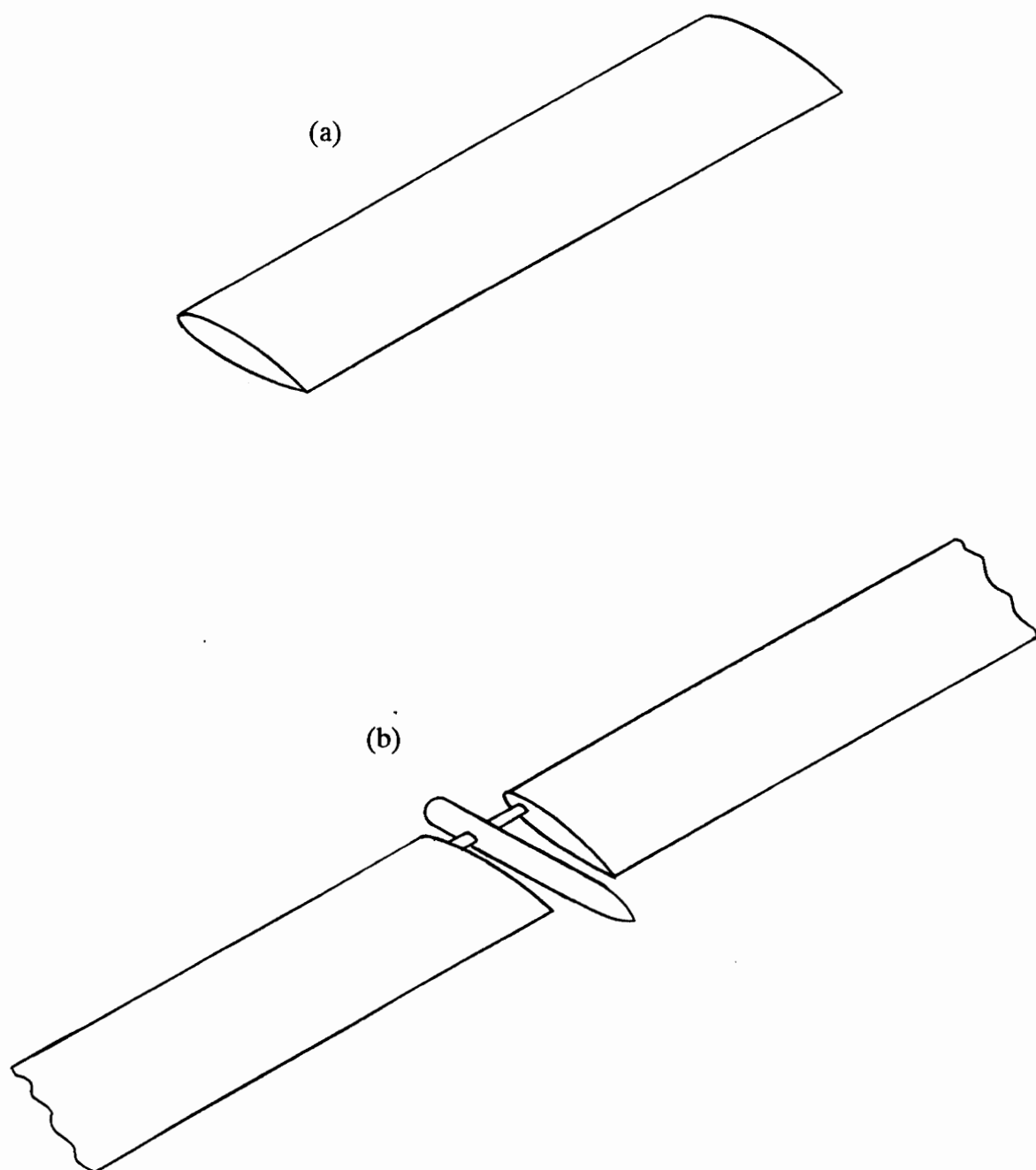


Figure 3. Two different methods of vortex generation. (a) Full wing producing a single vortex from each wing-tip. (b) Split wing producing a single vortex at the junction of two wings.

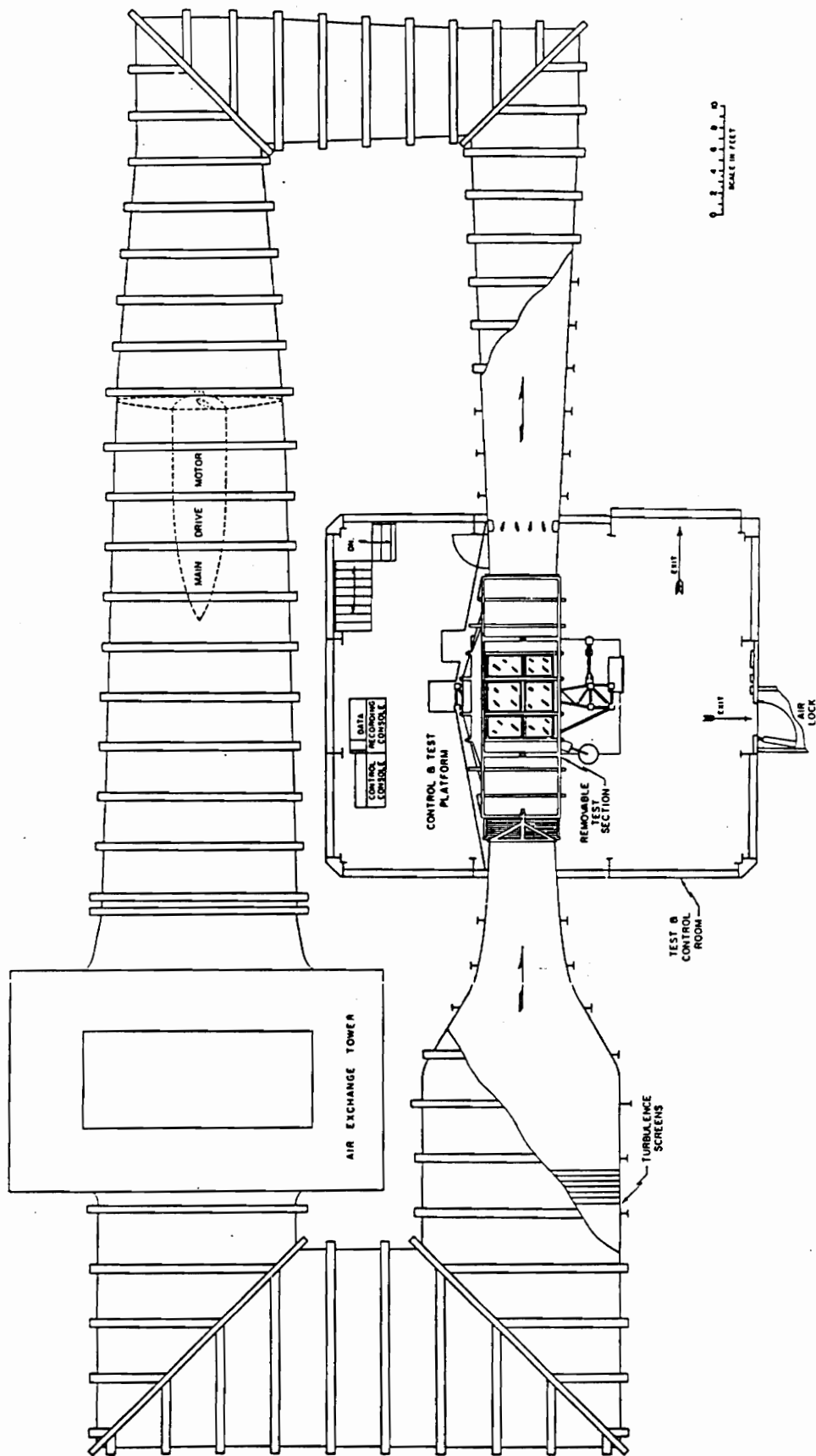


Figure 4. General layout of the Virginia Tech Stability Wind Tunnel.

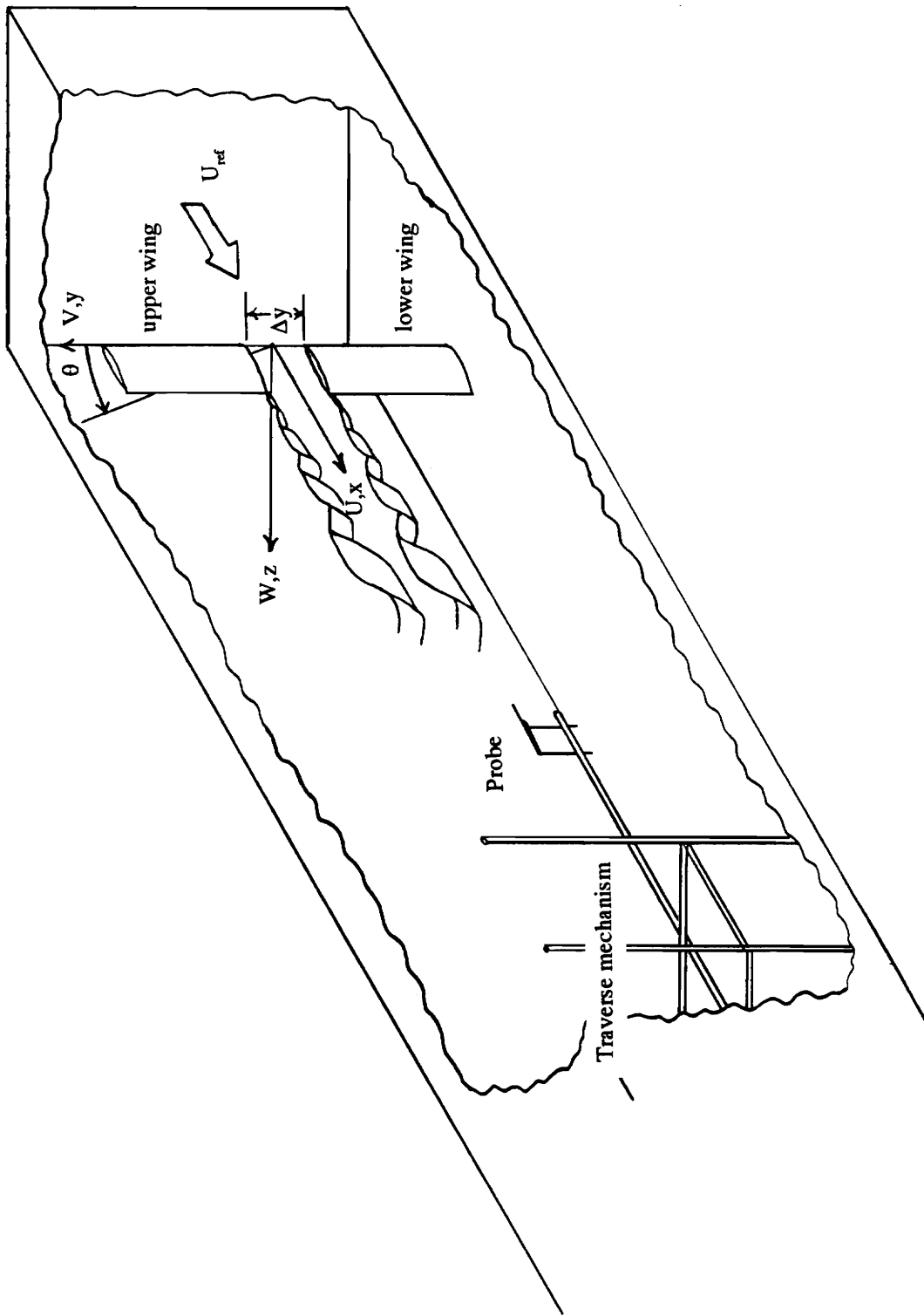


Figure 5. Schematic of the test section showing the coordinate system, the two NACA 0012 wings, and traverse mechanism.

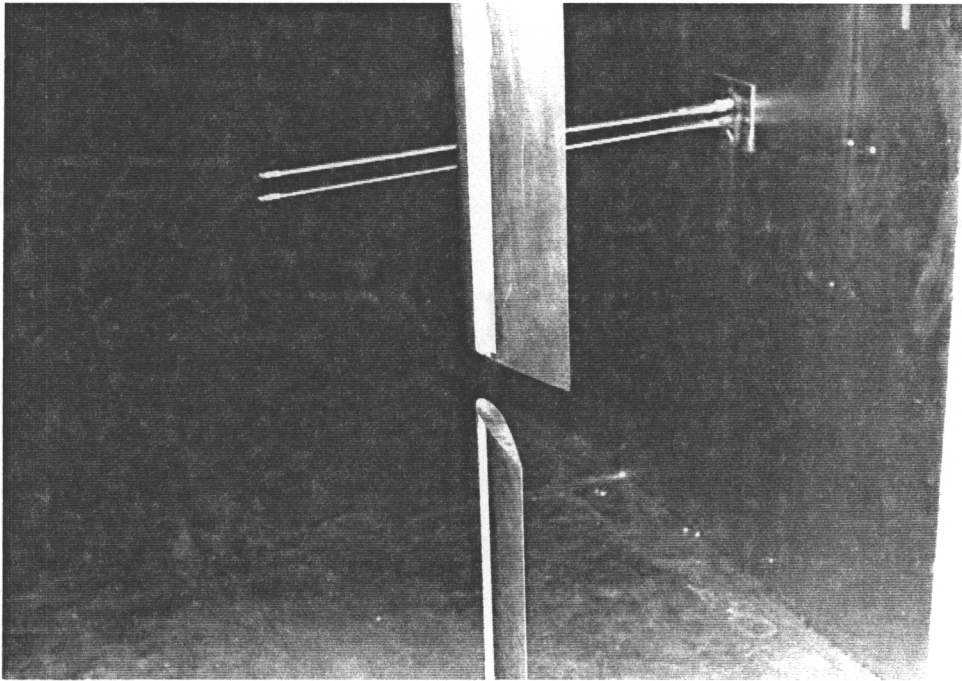


Figure 6. View of the two wings looking upstream. Note bubble probe in background and wings at opposite angle of attack.

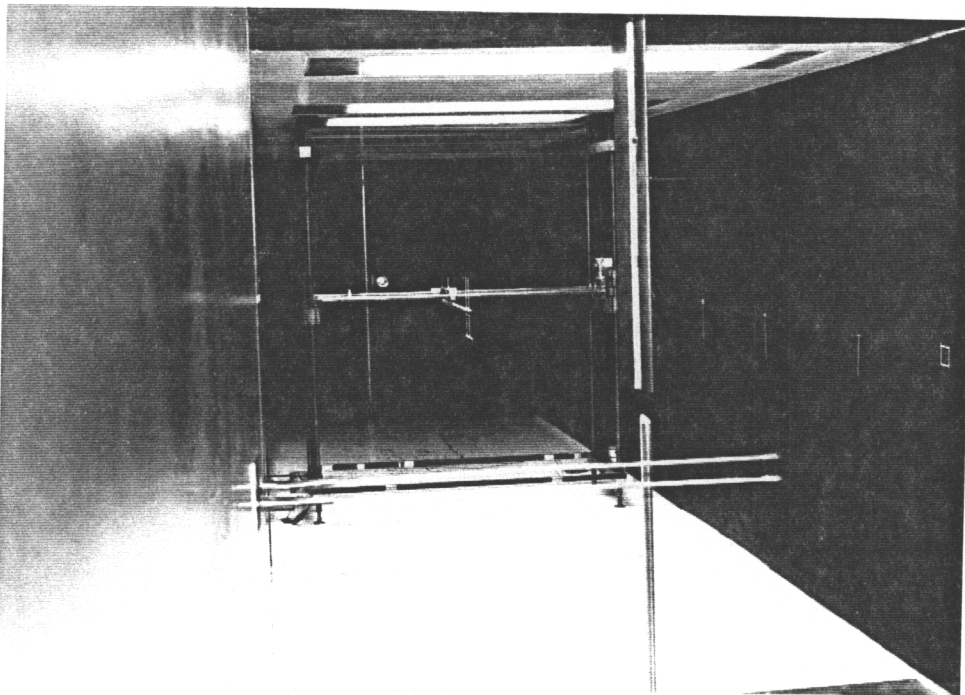


Figure 7. View of the test section looking upstream. Note traverse system and quad hot wire probe in background.

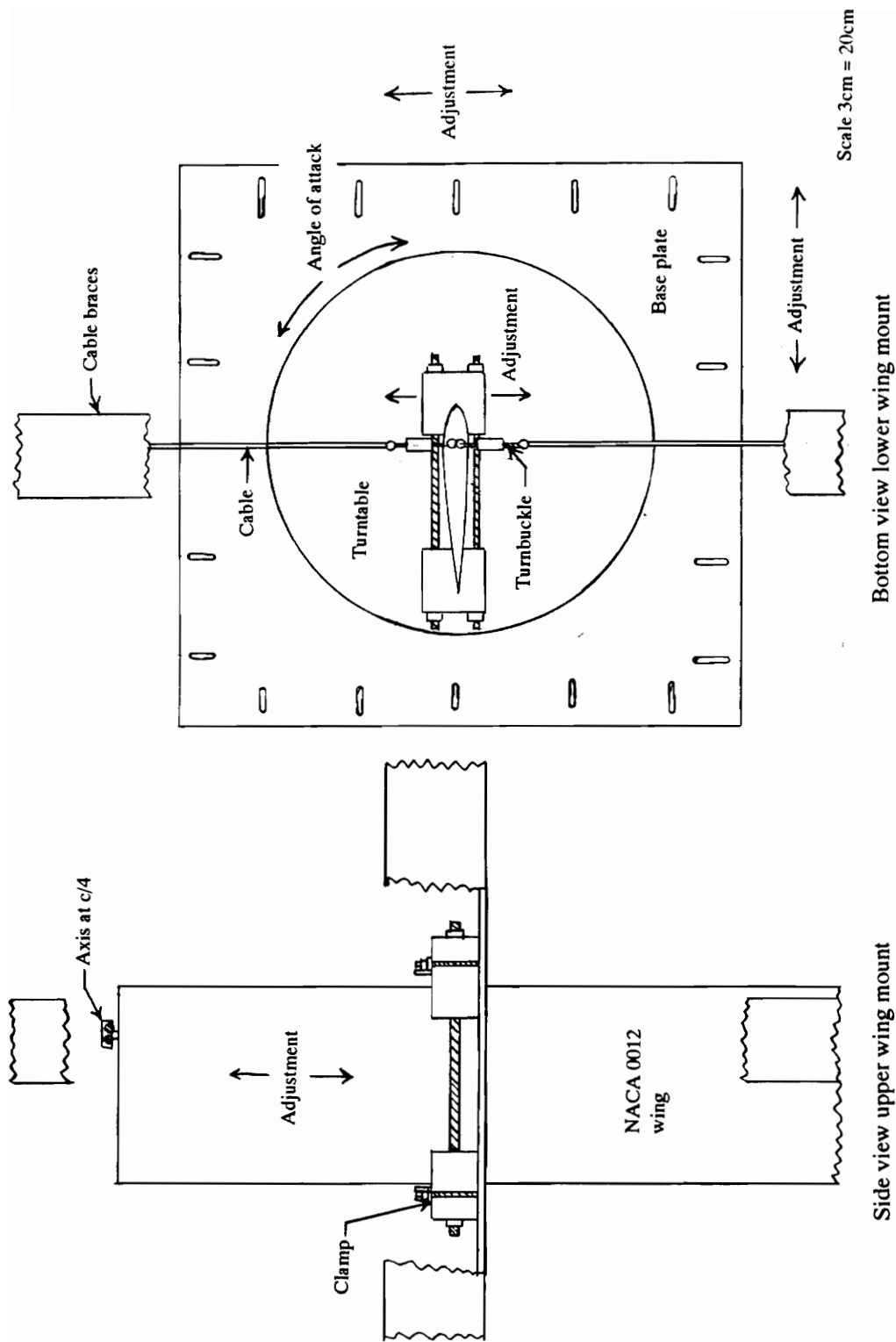


Figure 8. Drawing of upper and lower wing mount hardware showing adjustments.

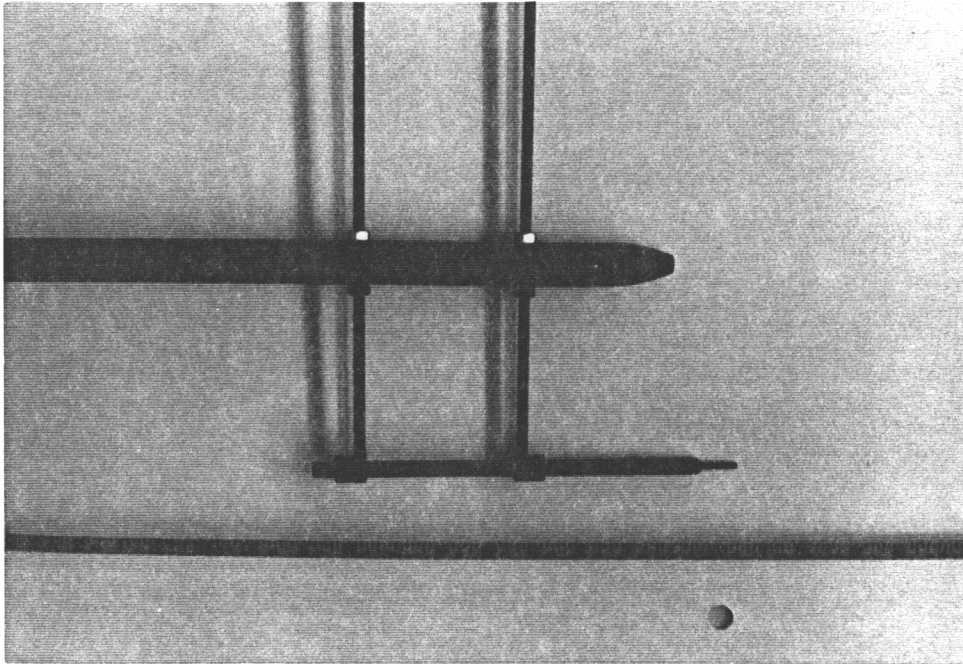


Figure 9. Dummy hot wire probe (bottom, horizontal) with front part of probe holder (top, horizontal).

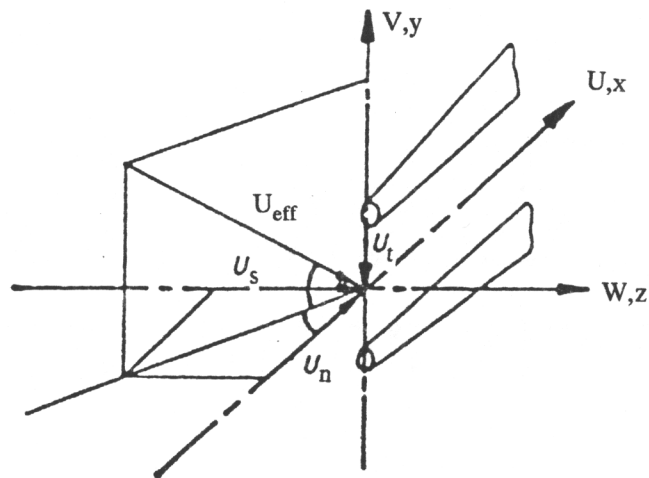


Figure 10. Velocity vector resolution at prong-sensor plane of the single hot wire probe.

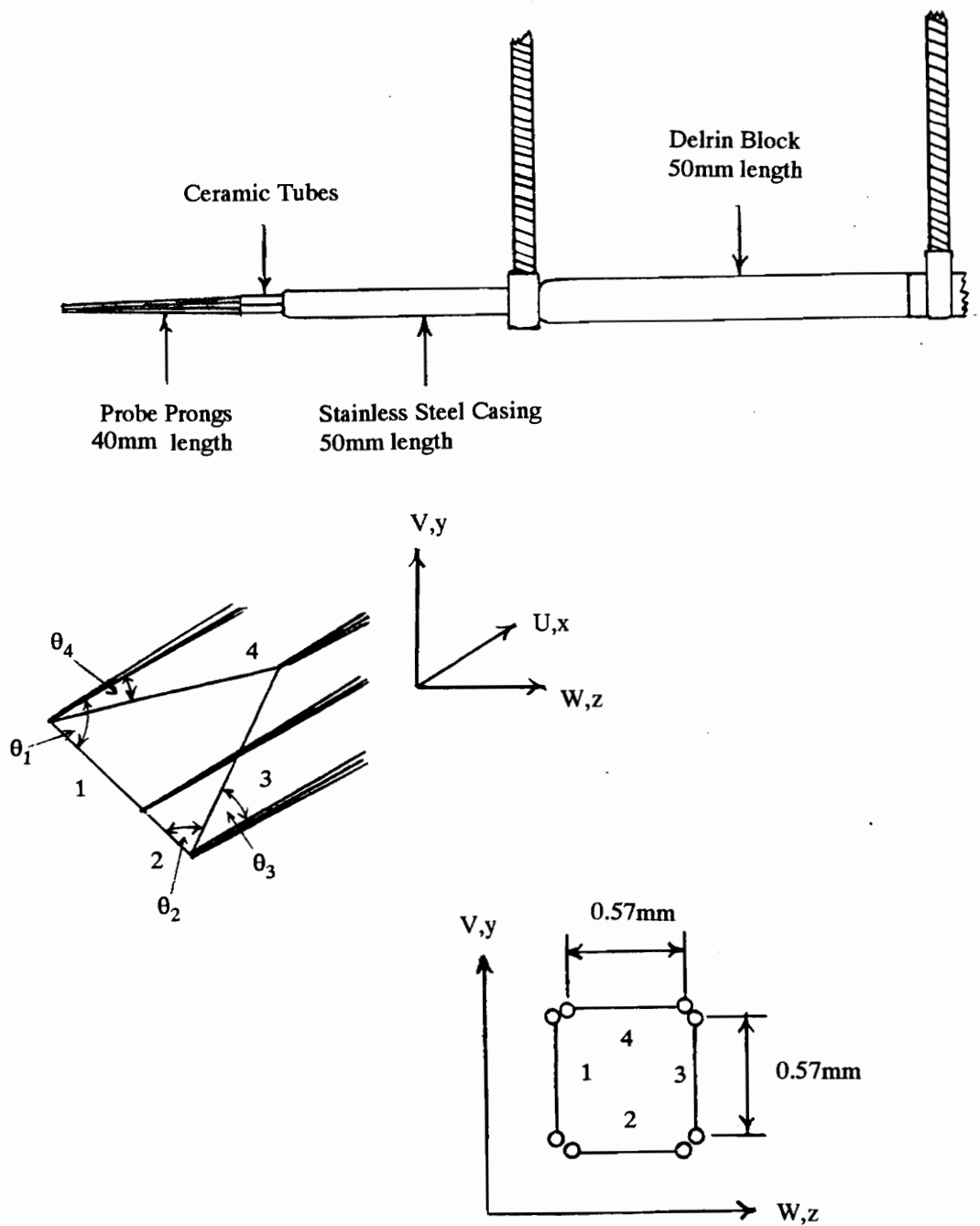
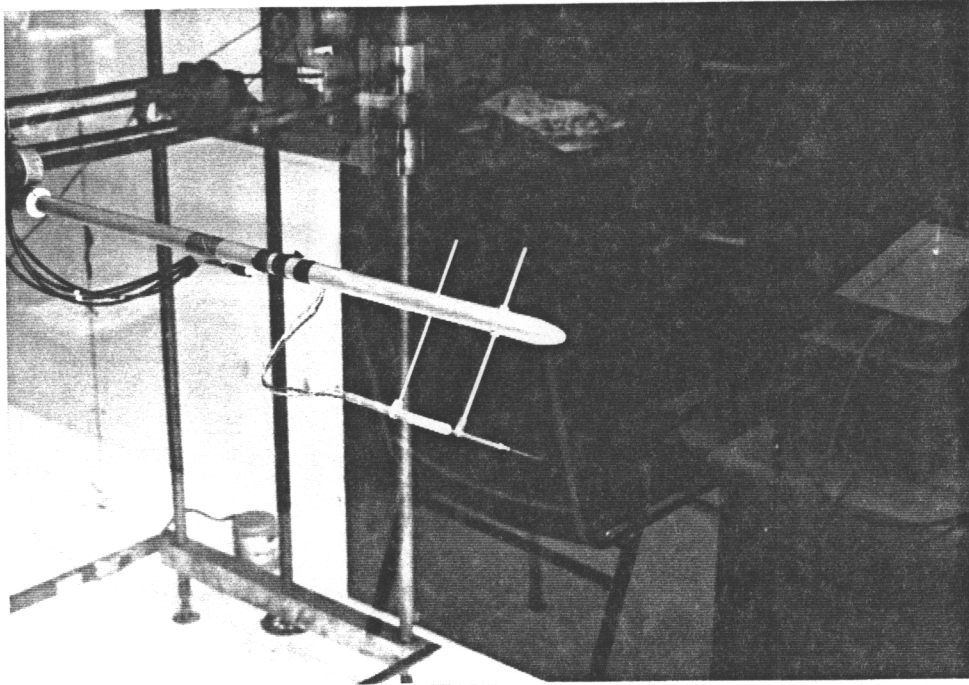
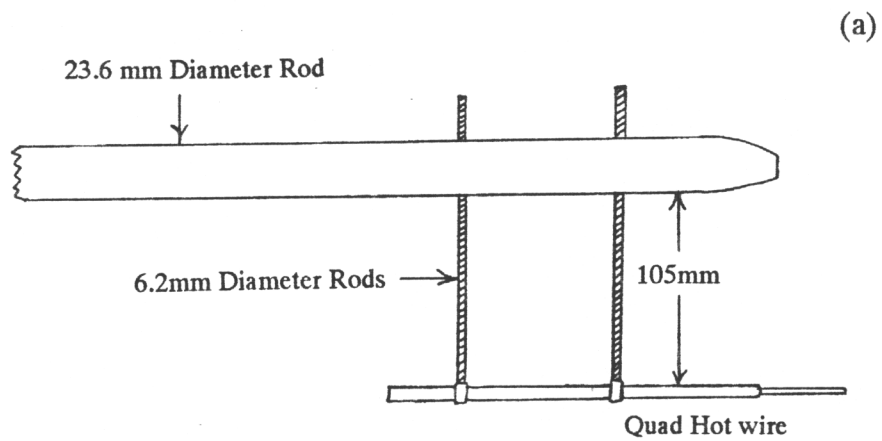


Figure 11. Schematic of the quad hot wire probe showing dimensions and wire configuration in the measurement plane.



(b)



(a)

Figure 12. (a) Diagram of the probe holder and hot wire attachment. (b) View of the probe holder and quad hot wire attached to the traverse mechanism. Note the probe holder rotated about its axis.

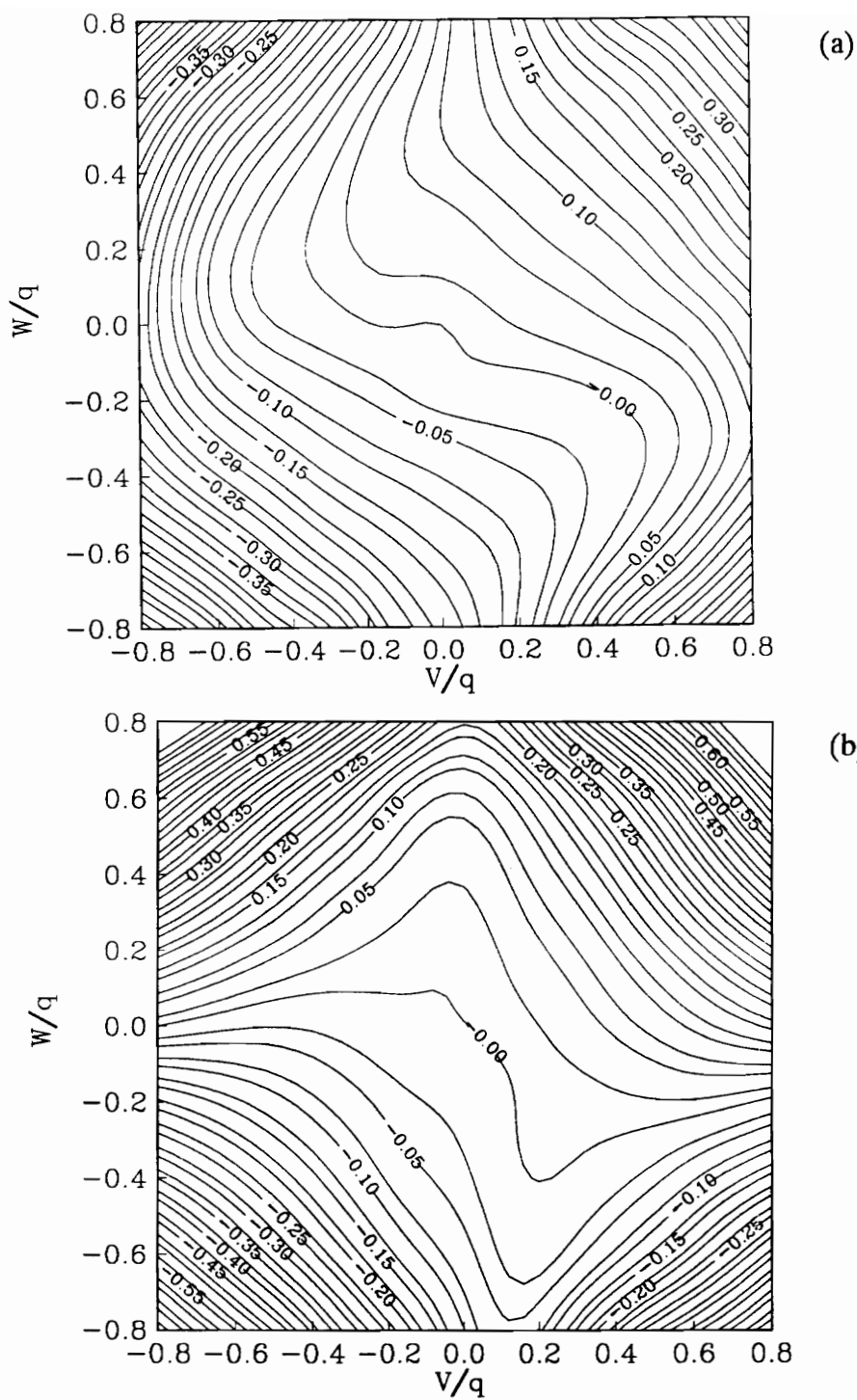


Figure 13. Contours of quad hot wire corrections (a) V corrections f_1 as a function of the actual velocities (b) W corrections f_2 as a function of the actual velocities.

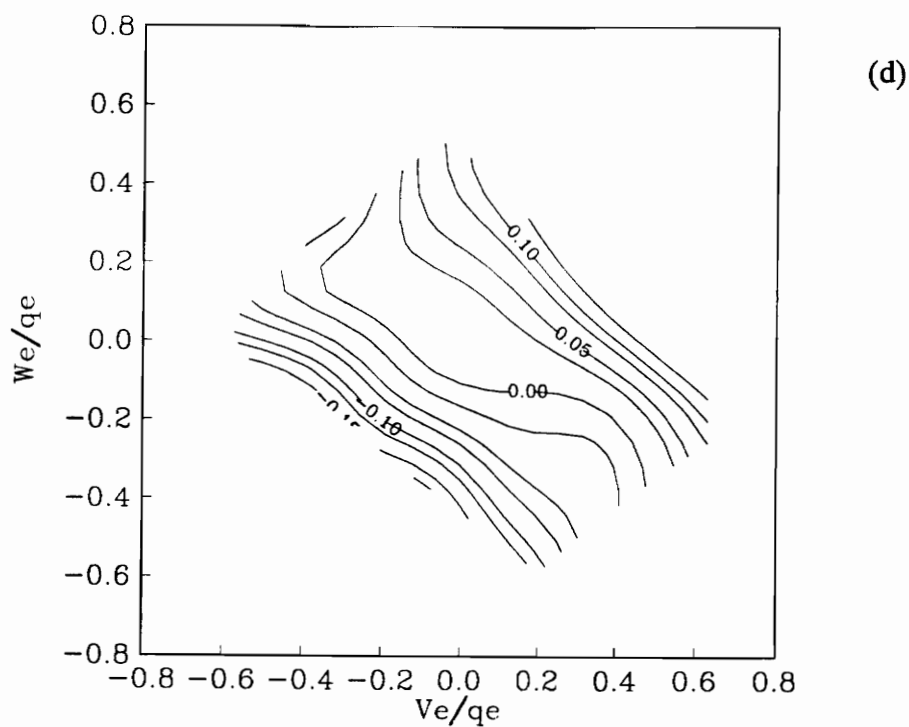
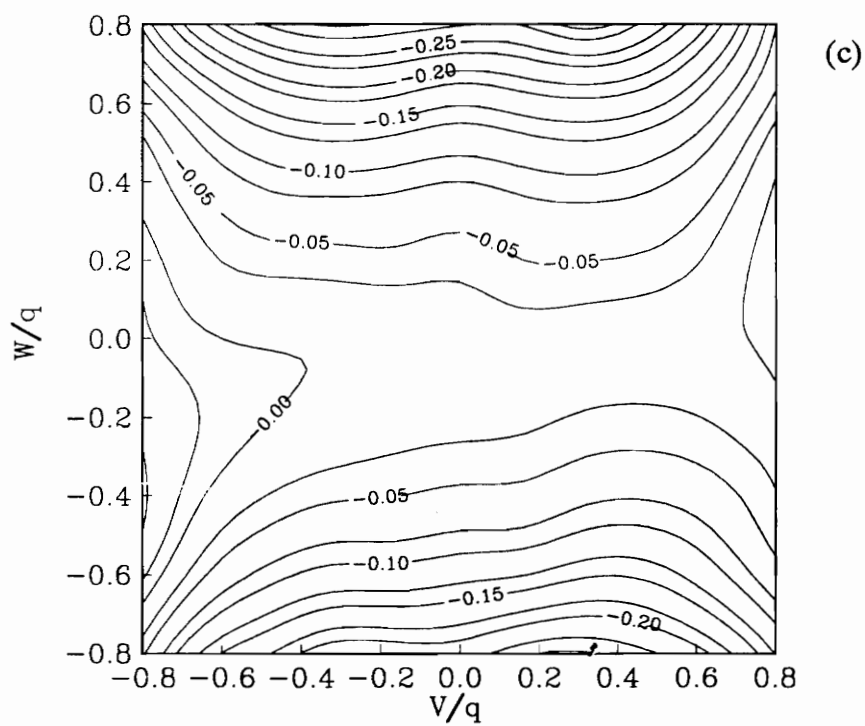
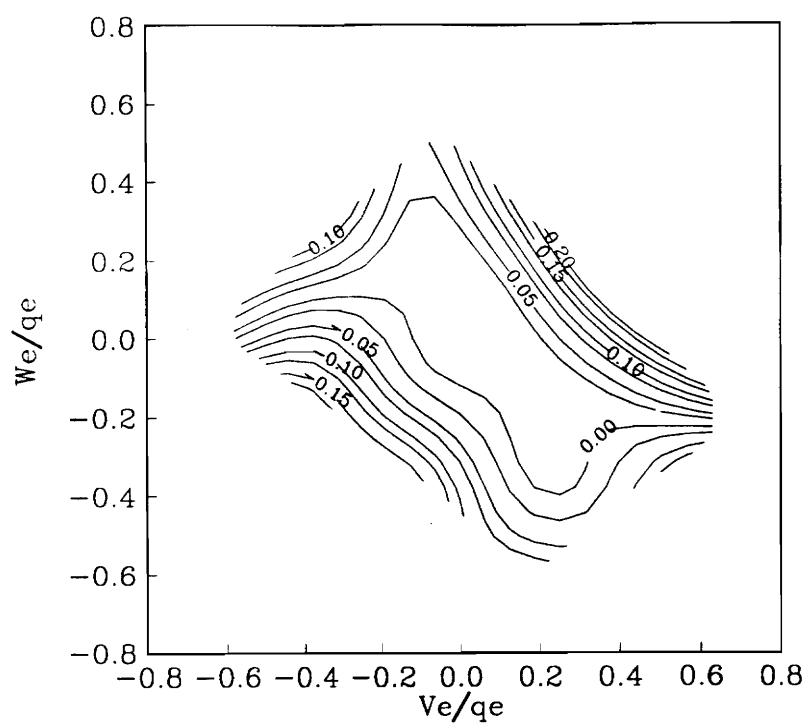
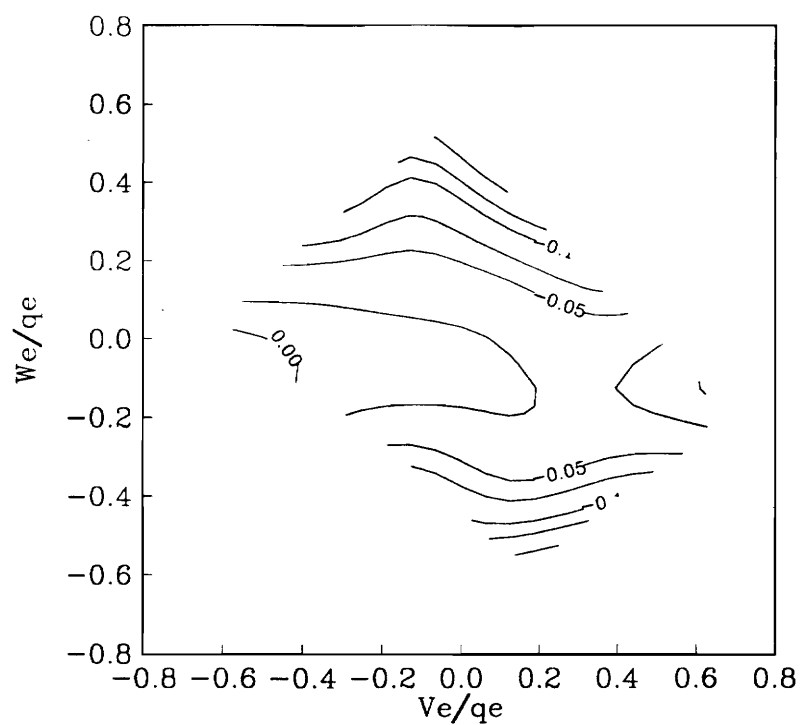


Figure 13. Contours of quad hot wire corrections (c) Q corrections f_3 as a function of the actual velocities (d) V corrections g_1 as a function of the estimated velocities.



(e)



(f)

Figure 13. Contours of quad hot wire corrections (e) W corrections g_2 as a function of the estimated velocities (f) Q corrections g_3 as a function of the estimated velocities.

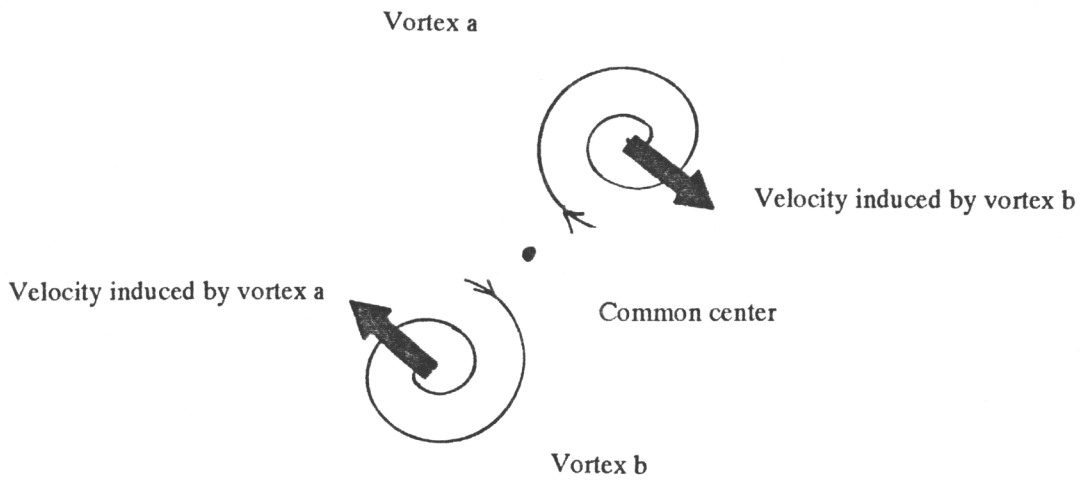


Figure 14. Sketch of an idealized co-rotating vortex pair.

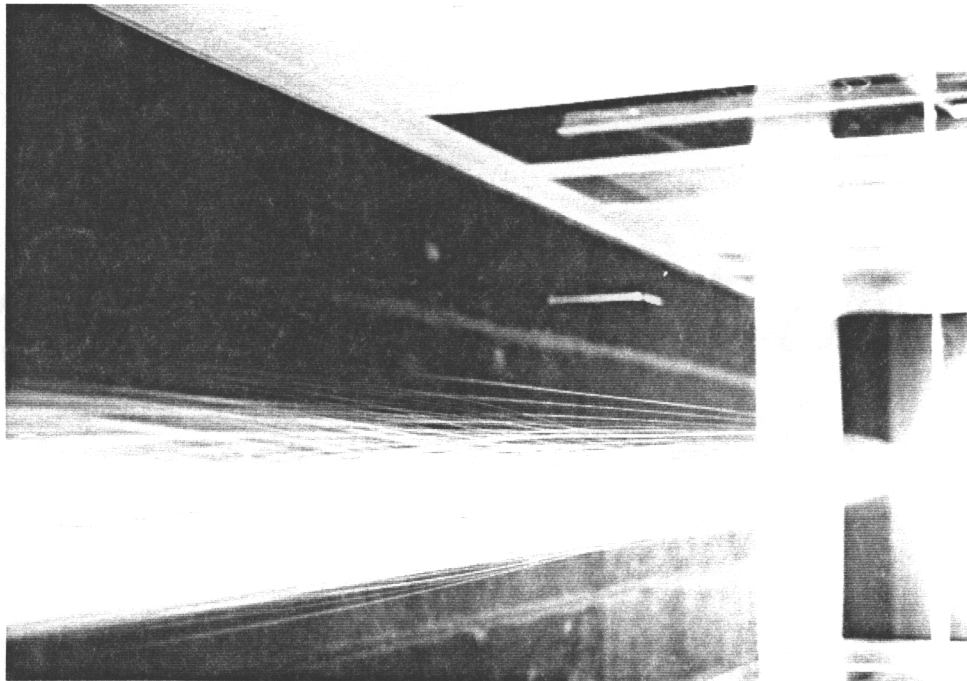


Figure 15. Helium bubble visualization looking upstream. $\Delta y=c/4$, $\alpha_o=5.0^\circ$, $Re_c=130,000$, 2 second exposure.

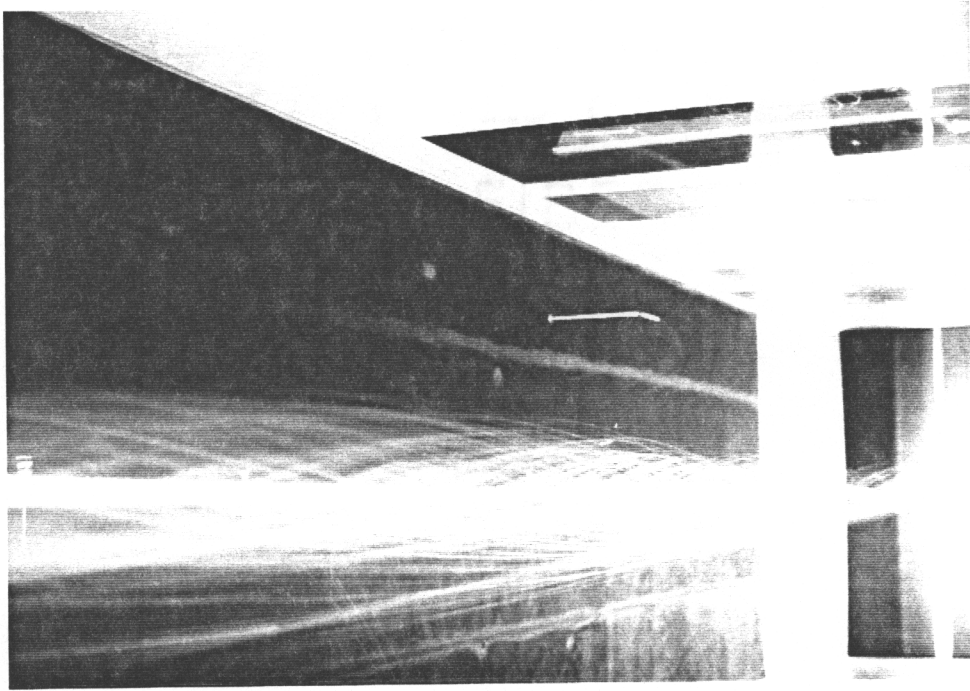


Figure 16. Helium bubble visualization looking upstream. $\Delta y=c/4$, $\alpha_0=7.5^\circ$, $Re_c=130,000$, 2 second exposure.



Figure 17. Helium bubble visualization looking upstream. $\Delta y=c/4$, $\alpha_0=10.0^\circ$, $Re_c=130,000$, 2 second exposure.

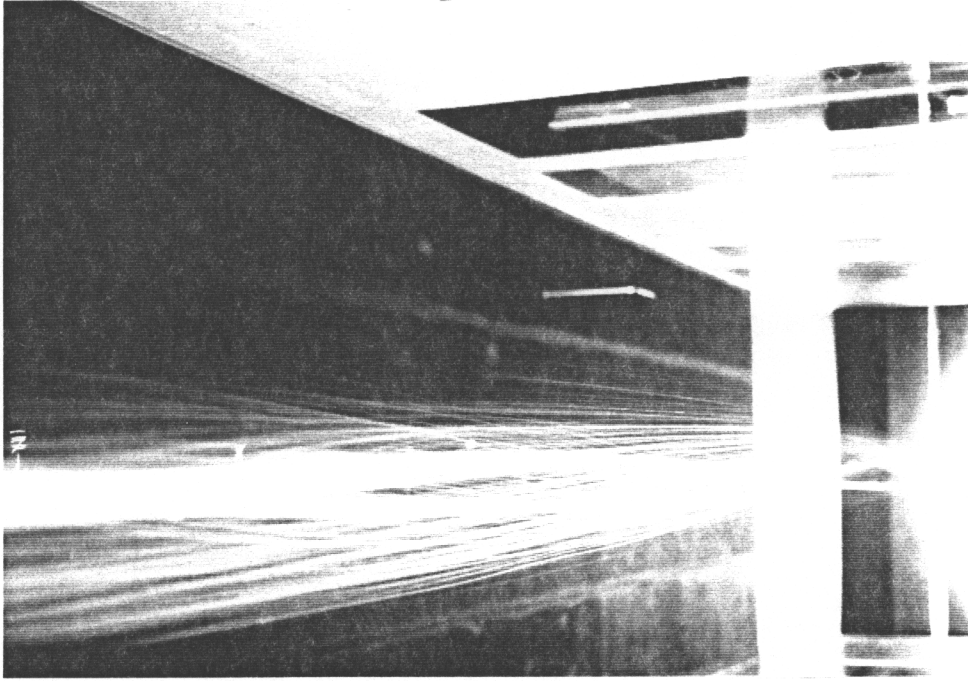


Figure 18. Helium bubble visualization looking upstream. $\Delta y = 3/8c$, $\alpha_0 = 5.0^\circ$, $Re_c = 130,000$, 2 second exposure.

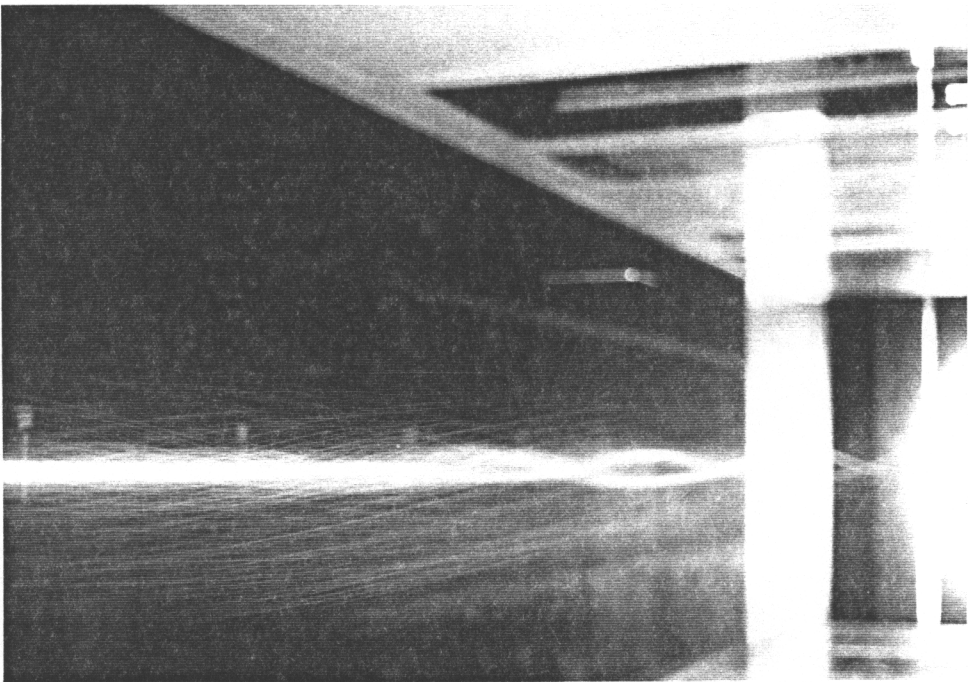


Figure 19. Helium bubble visualization looking upstream. $\Delta y = 3/8c$, $\alpha_0 = 7.5^\circ$, $Re_c = 130,000$, 2 second exposure.

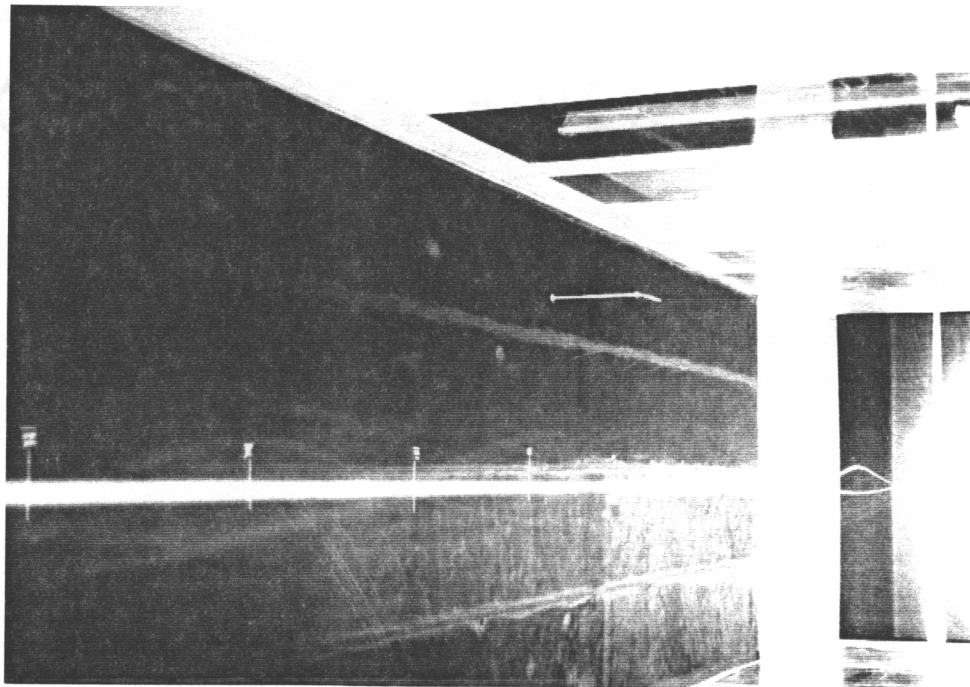


Figure 20. Helium bubble visualization looking upstream. $\Delta y=3/8c$, $\alpha_0=10.0^\circ$, $Re_c=130,000$, 2 second exposure.

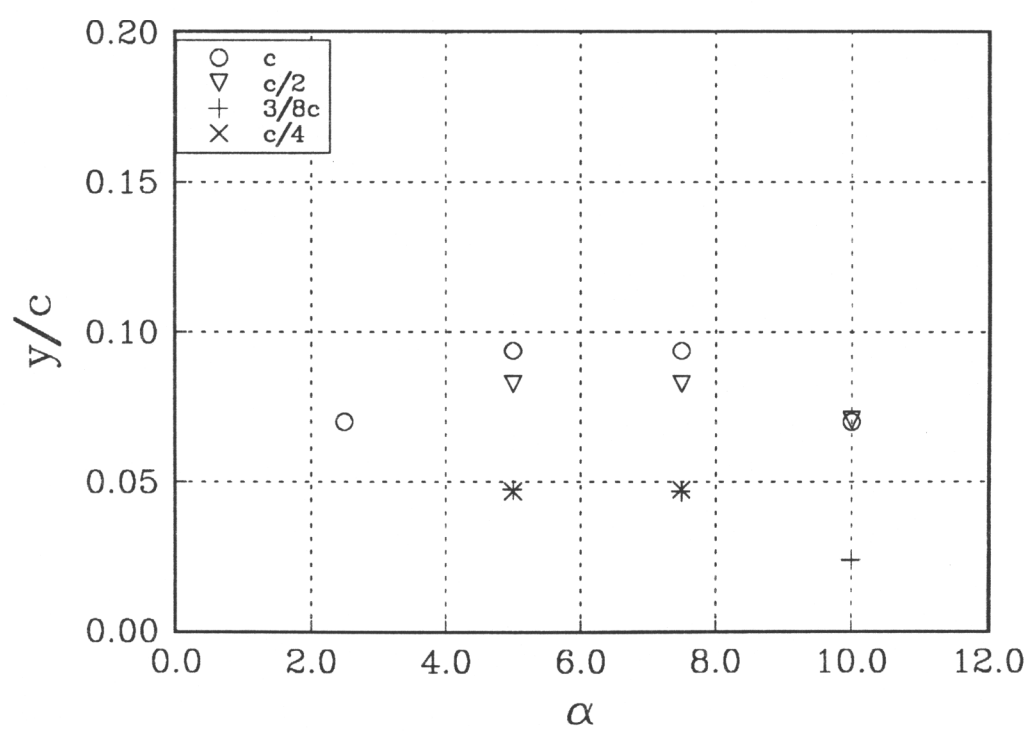


Figure 21. Amplitude of lateral motions for co-rotating vortex pairs at $x/c=20$.

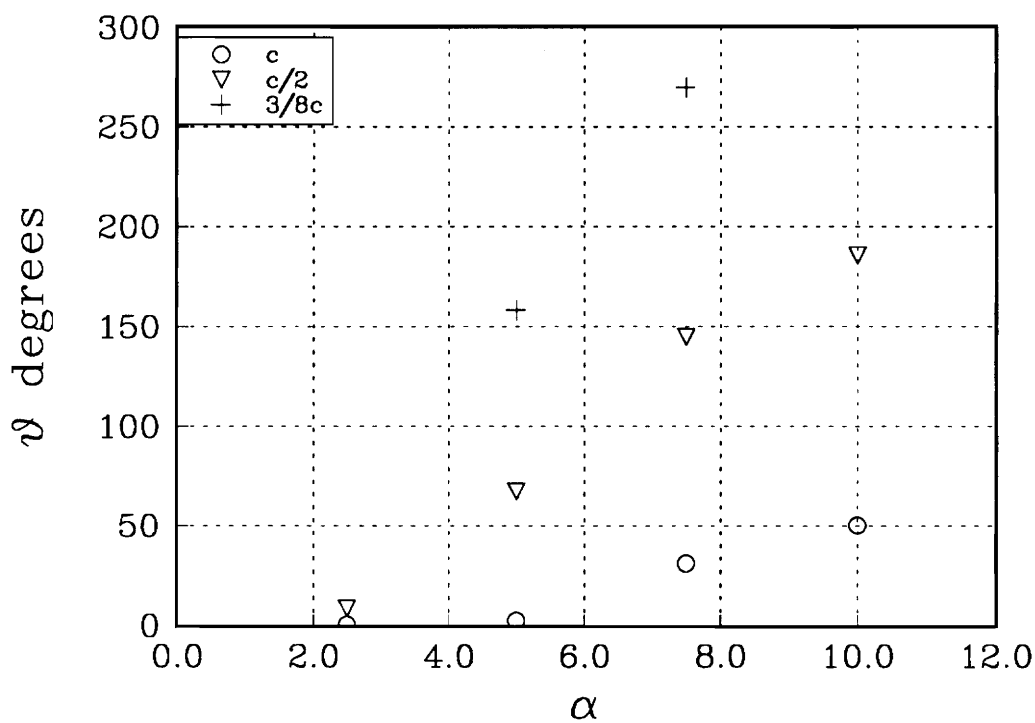


Figure 22. Angle of rotation of co-rotating pairs as a function of α for different Δy .

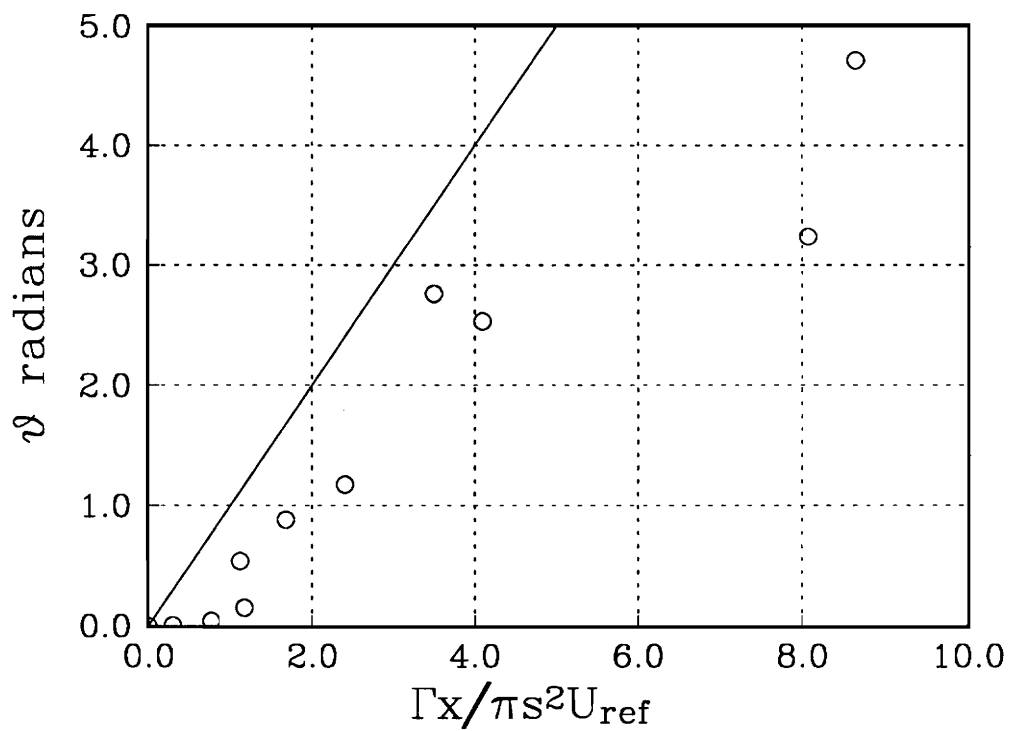


Figure 23. Angle of rotation of co-rotating pairs vs. $\Gamma_X / \pi S^2 U_{ref}$.

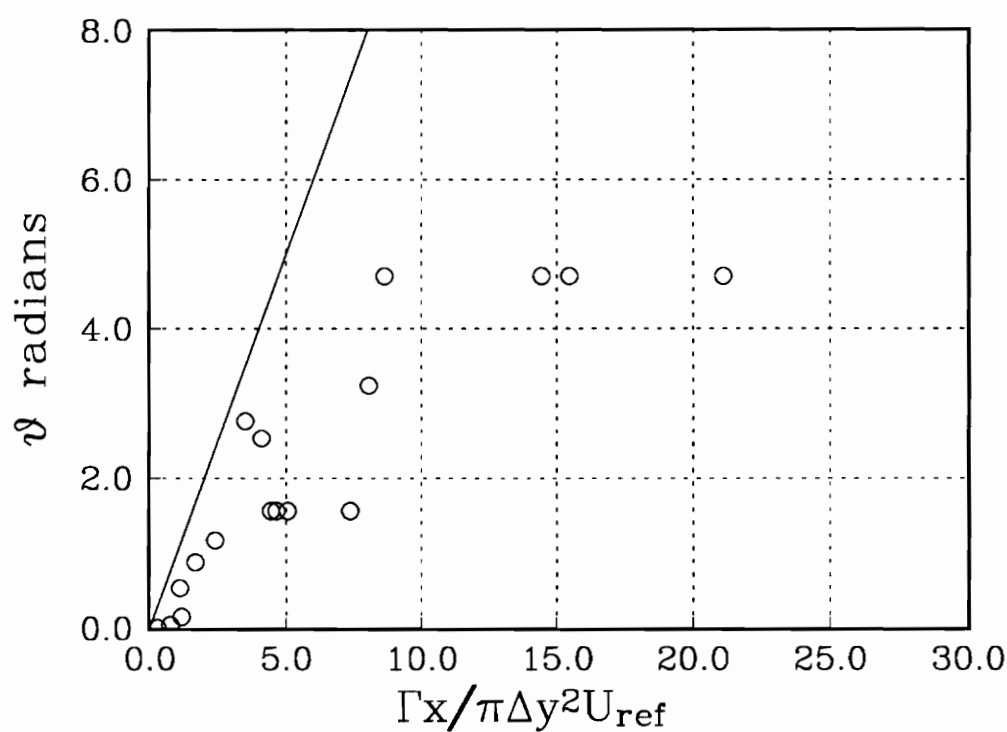


Figure 24. Angle of rotation of co-rotating pairs vs. $\Gamma x / \pi \Delta y^2 U_{ref}$.

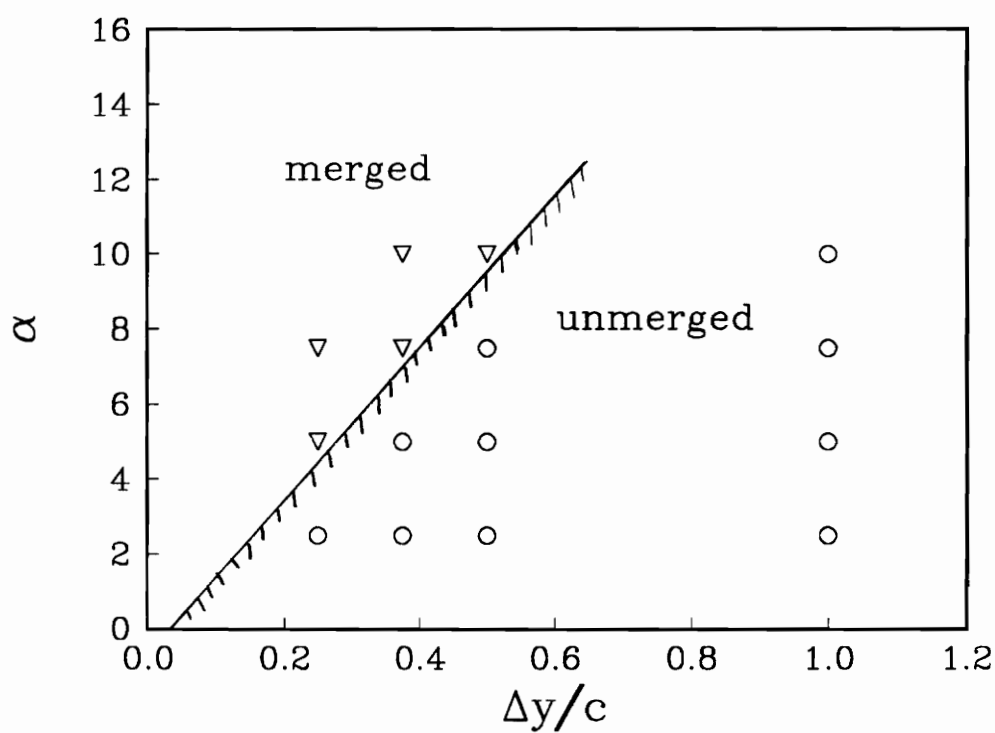


Figure 25. Co-rotating cases which merged within the length of the test section.

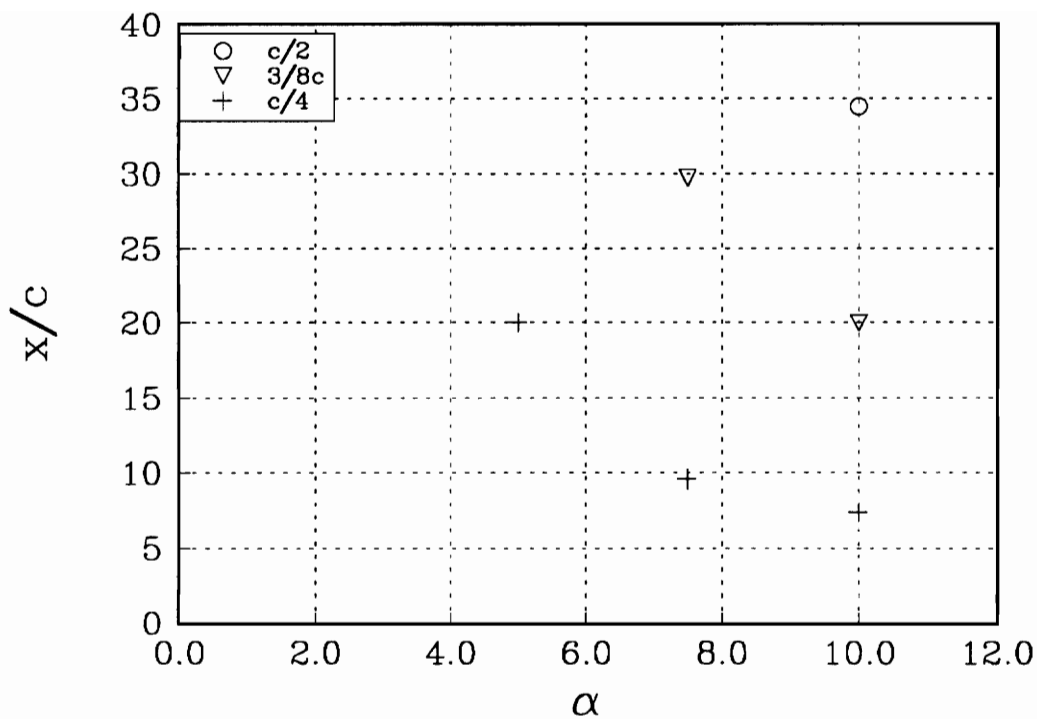


Figure 26. Merging location of co-rotating pairs as a function of α for different Δy .

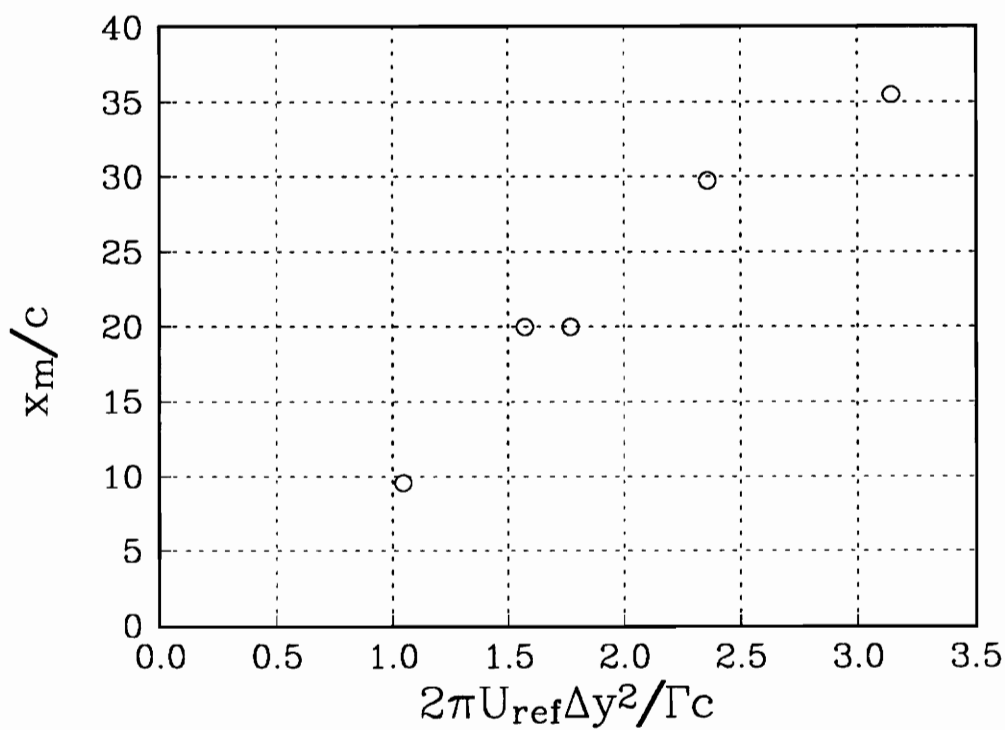


Figure 27. Merging location of co-rotating pairs vs. $2\pi U_{\text{ref}} \Delta y^2 / \Gamma c$.

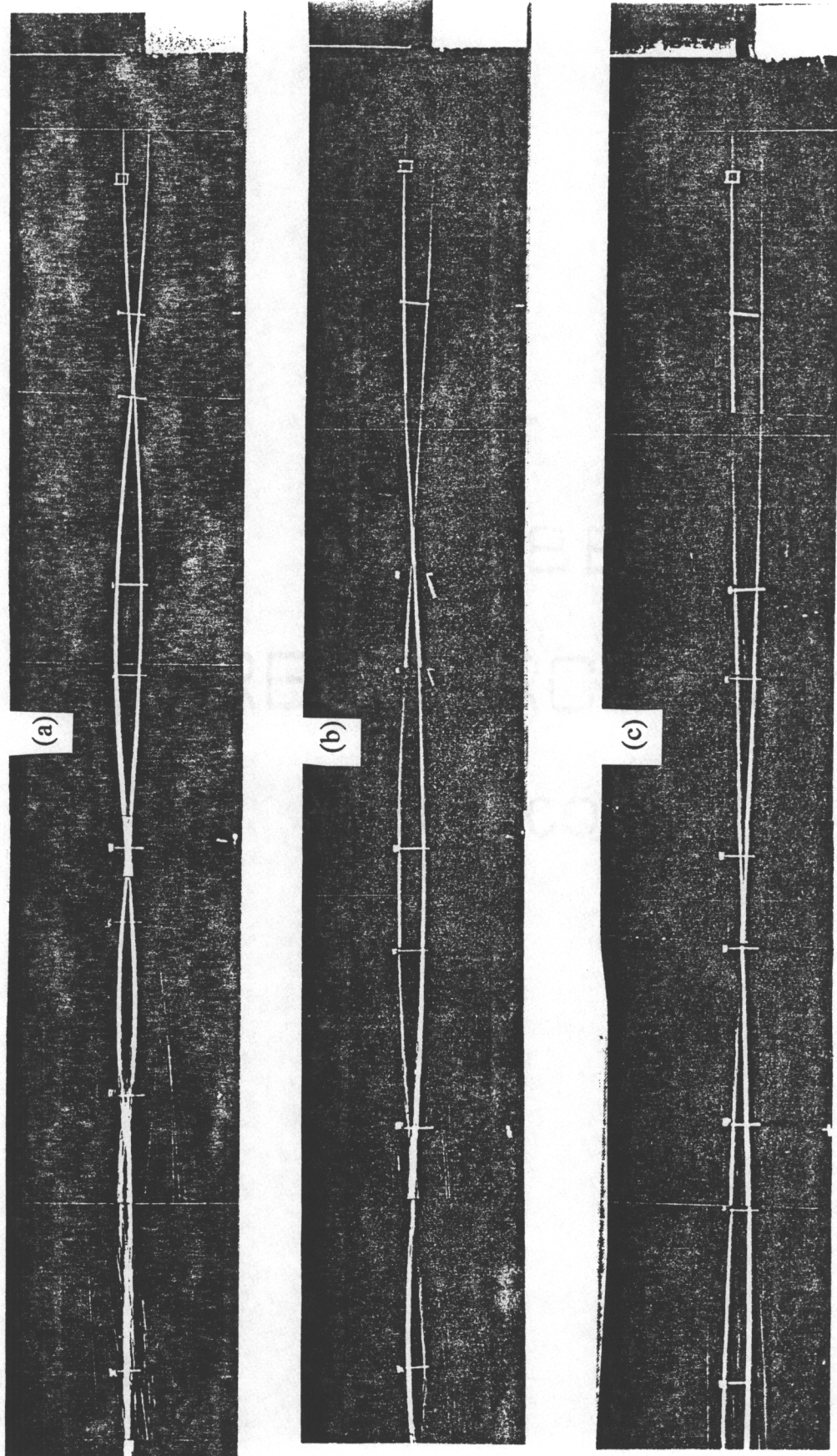


Figure 28. Photo-mosaics of co-rotating pairs at $\Delta y = 3/8c$, $Re_c = 130,000$, (a) $\alpha_0 = 10.0^\circ$, (b) $\alpha_0 = 7.5^\circ$, (c) $\alpha_0 = 5.0^\circ$. 8 sec exposures.

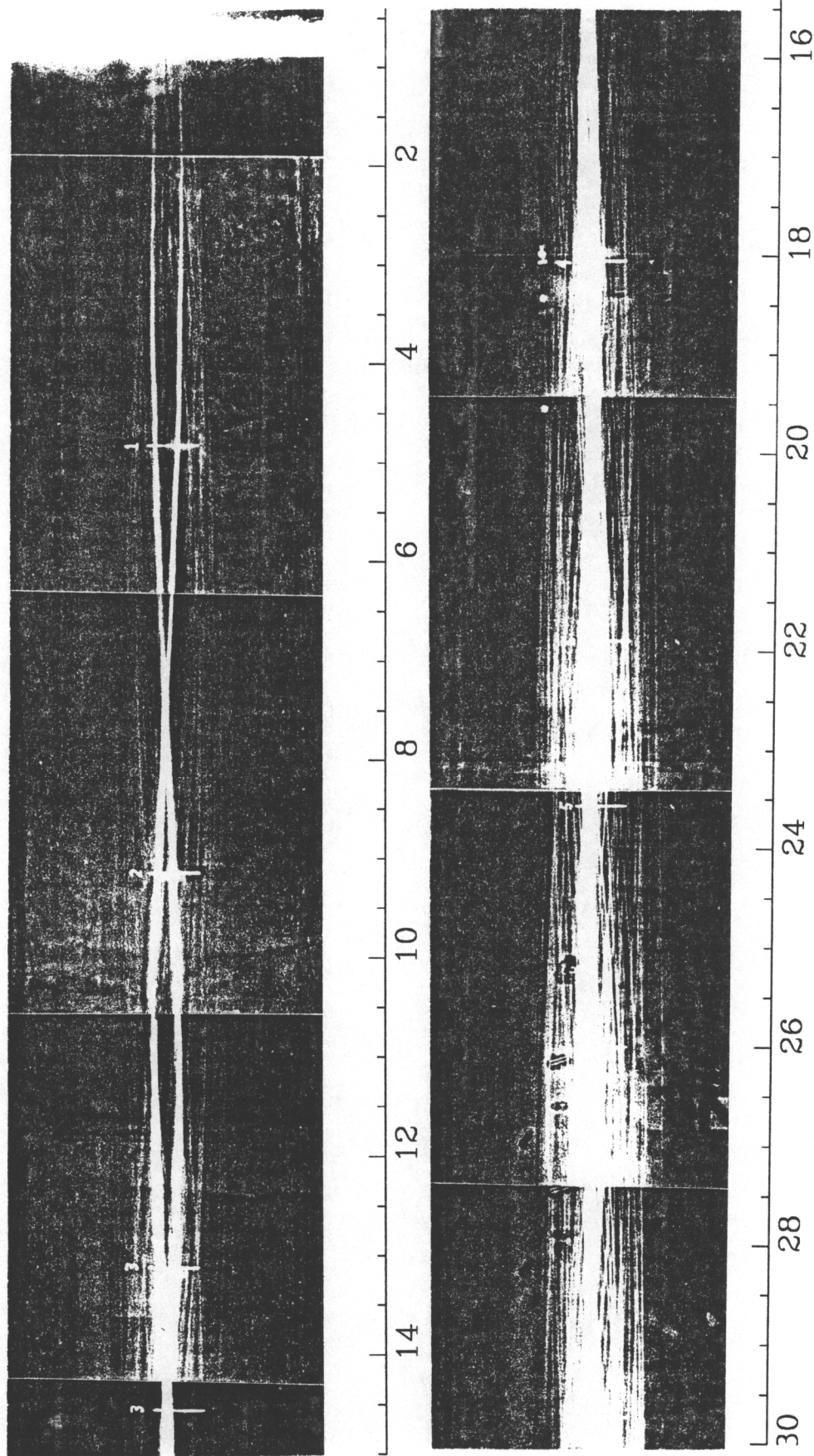


Figure 29. Photo-mosaic of co-rotating pair at $\Delta y=c/4c$, $Re_c=130,000$, $\alpha_o=5.0^\circ$. 8 sec exposure.

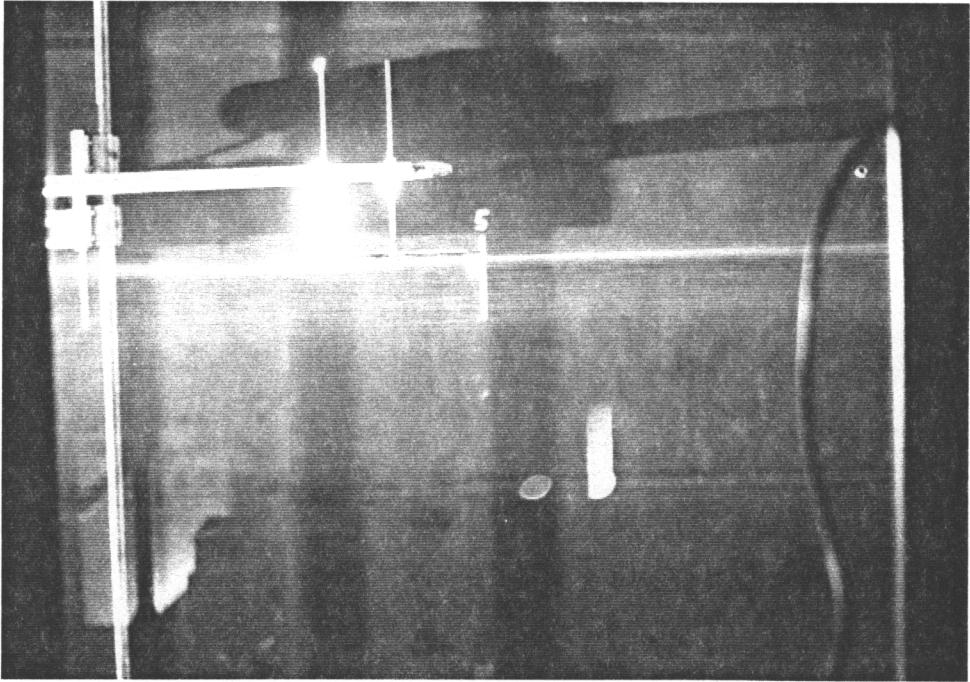


Figure 30. Dummy hot-wire probe in core, $\Delta y=c/4c$, $Re_c=130,000$, $\alpha_o=5.0^\circ$ at streamwise location $x/c=22$. 8 sec exposure.

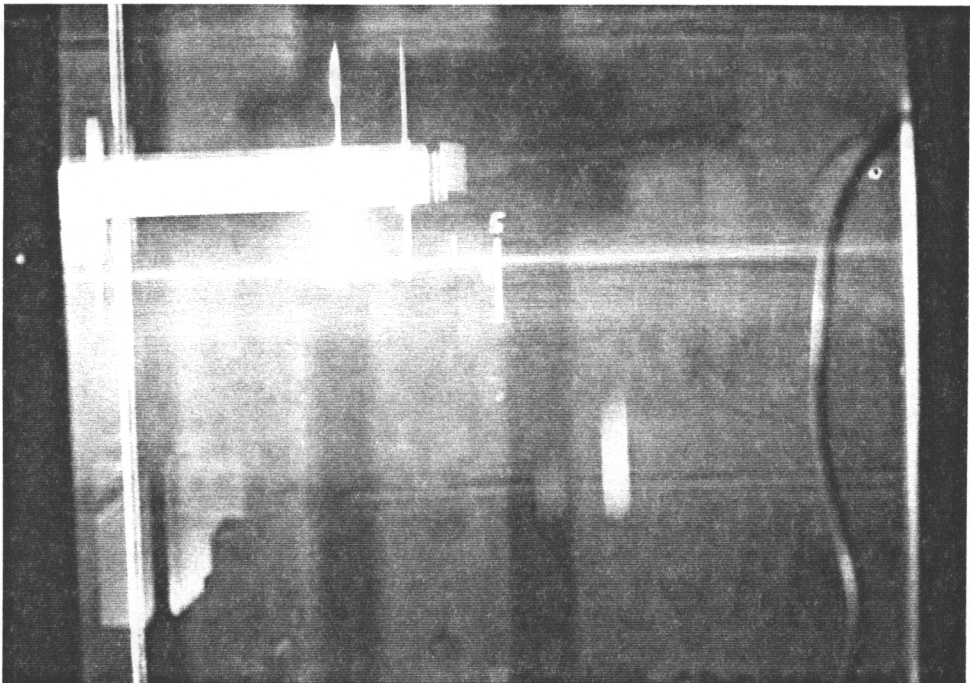


Figure 31. Dummy hot-wire probe traversing through the core, $\Delta y=c/4c$, $Re_c=130,000$, $\alpha_o=5.0^\circ$ at streamwise location $x/c=22$. 8 sec exposure.

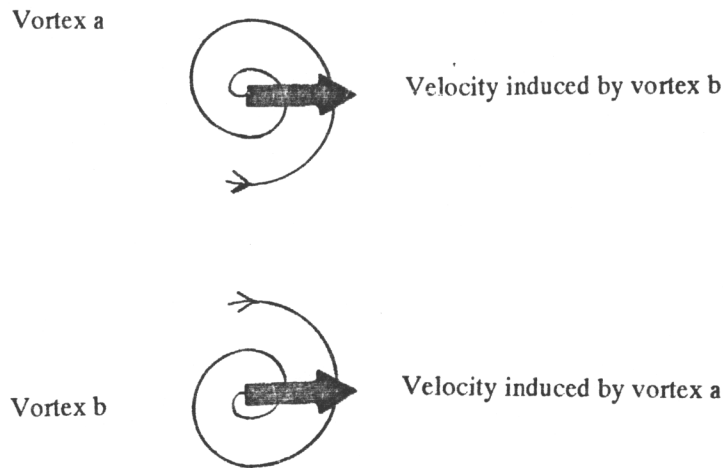


Figure 32. Sketch of an idealized counter rotating vortex pair.

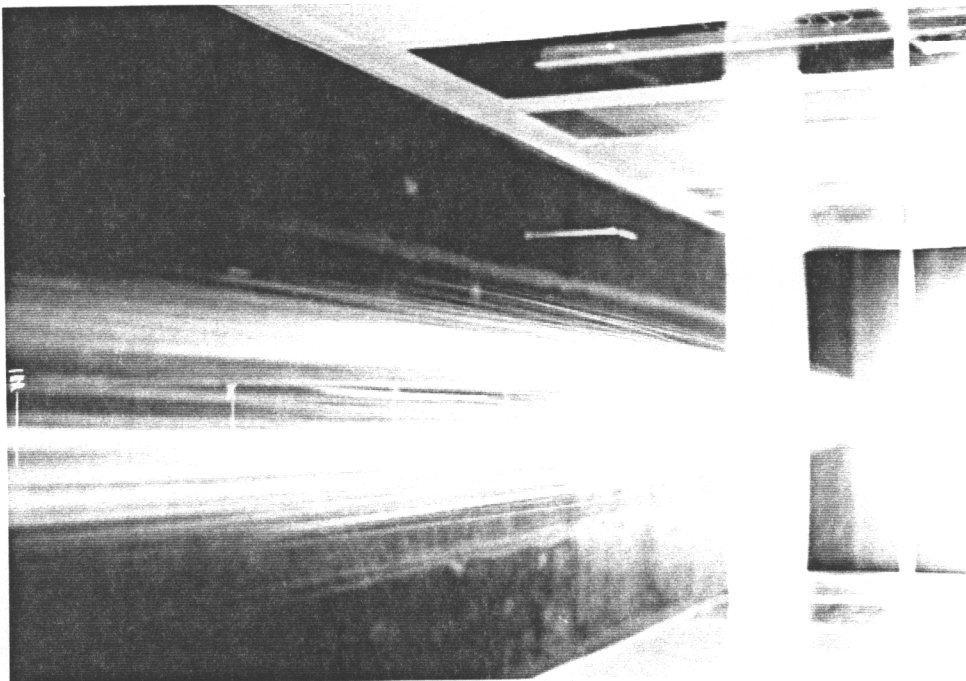


Figure 33. Helium bubble visualization looking upstream. $\Delta y=c/4$, $\alpha_e=2.5^\circ$, $Re_c=130,000$, 2 sec exposure.

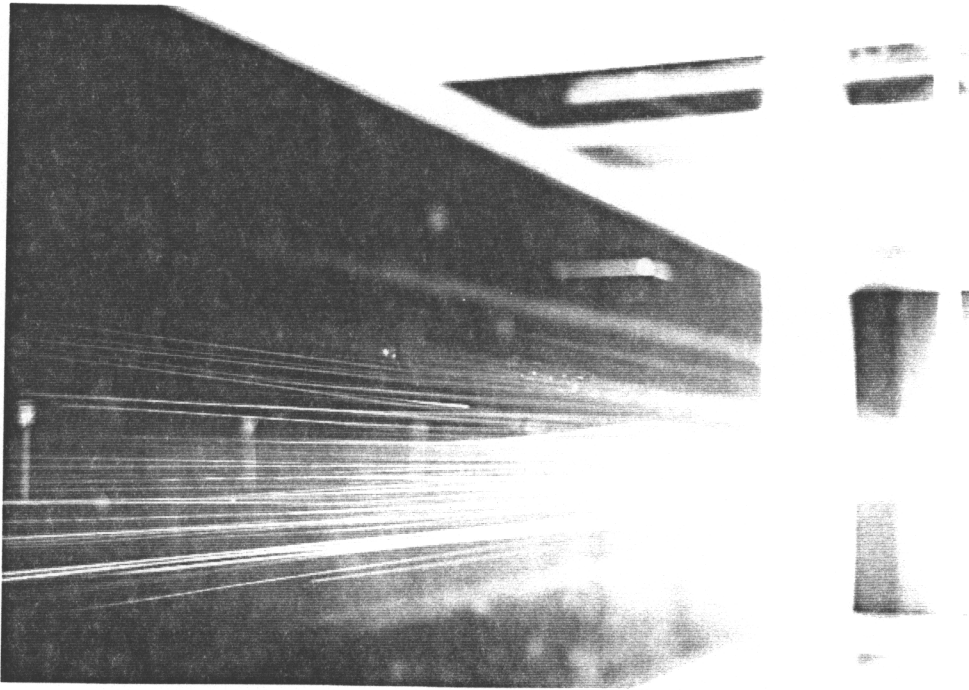


Figure 34. Helium bubble visualization looking upstream. $\Delta y=c/4$, $\alpha_e=5.0^\circ$, $Re_c=130,000$, 2 sec exposure.

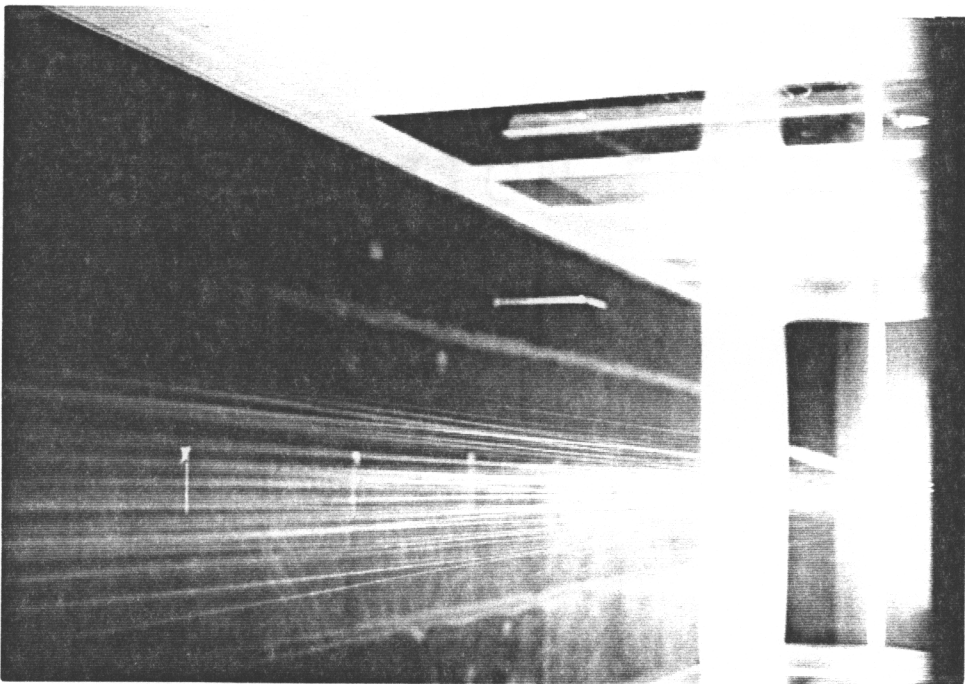


Figure 35. Helium bubble visualization looking upstream. $\Delta y=c/4$, $\alpha_e=7.5^\circ$, $Re_c=130,000$, 2 sec exposure.

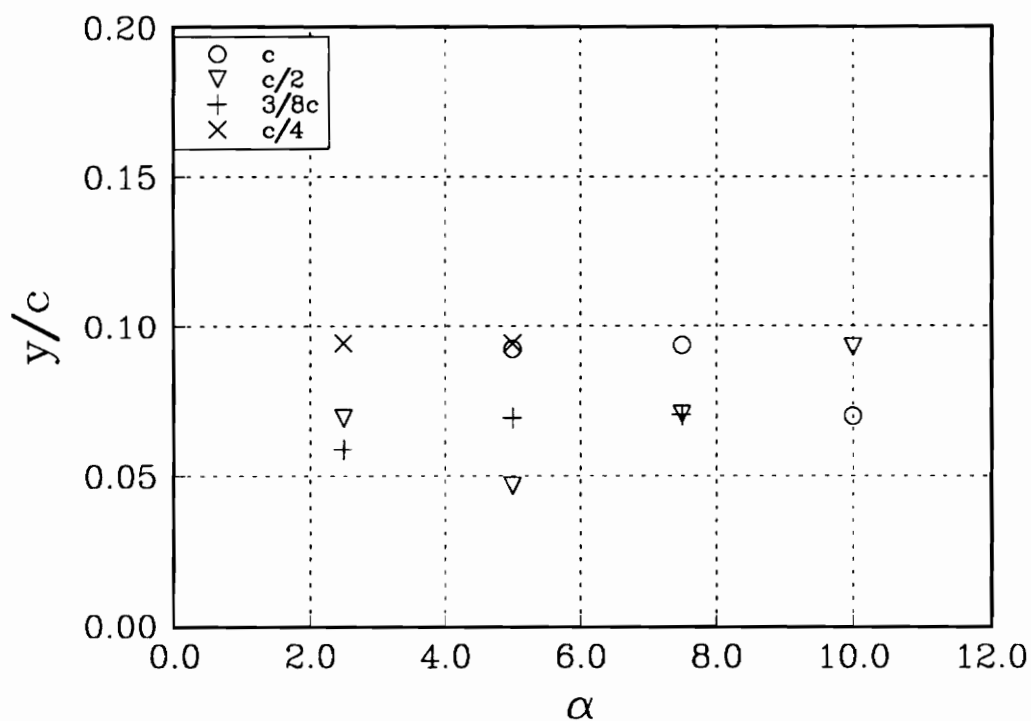


Figure 36. Amplitude of lateral motions for counter rotating pairs at $x/c=20$.

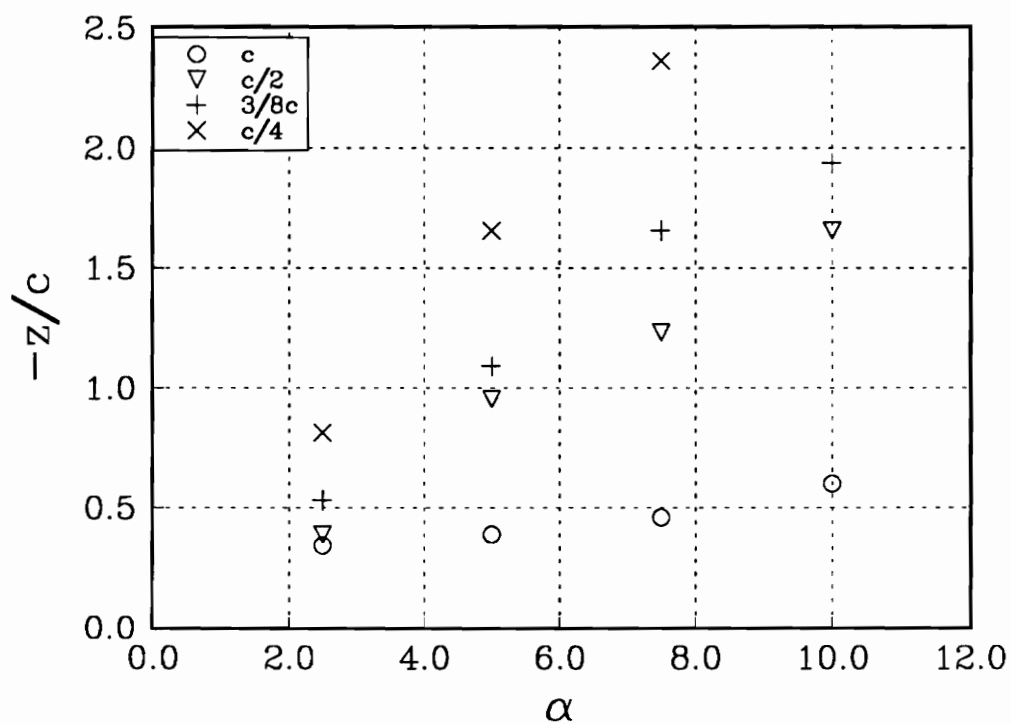


Figure 37. z/c location of counter rotating pairs as a function of α for different Δy at $x/c=20$.

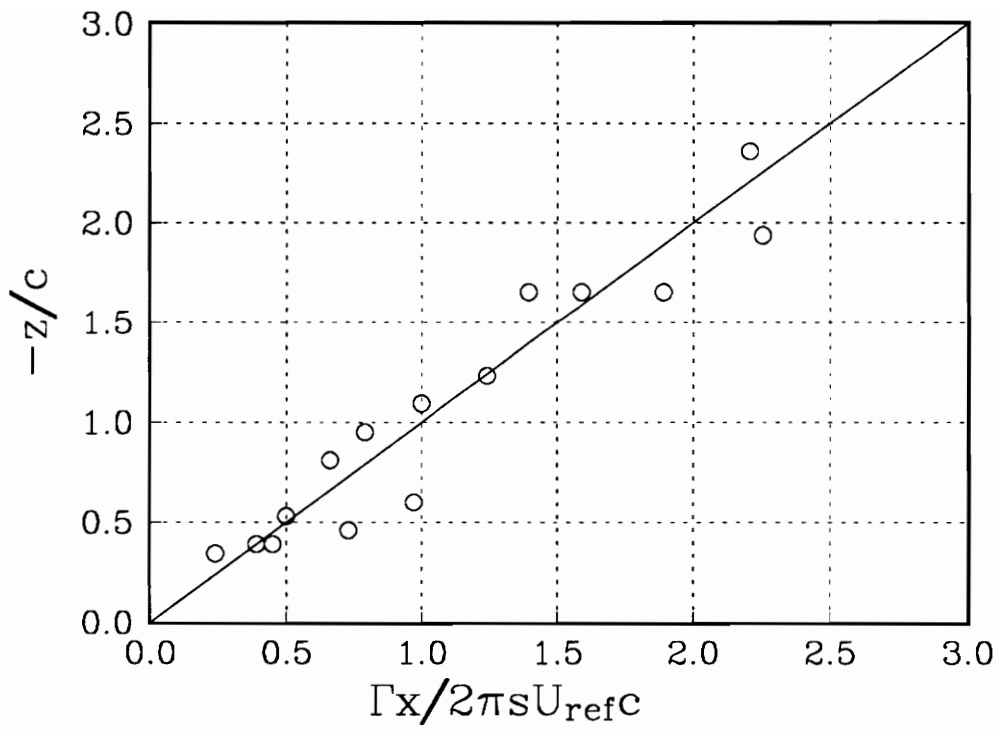


Figure 38. z/c location of counter rotating pairs vs. $\Gamma x / 2\pi s U_{ref} c$ at $x/c=20$.

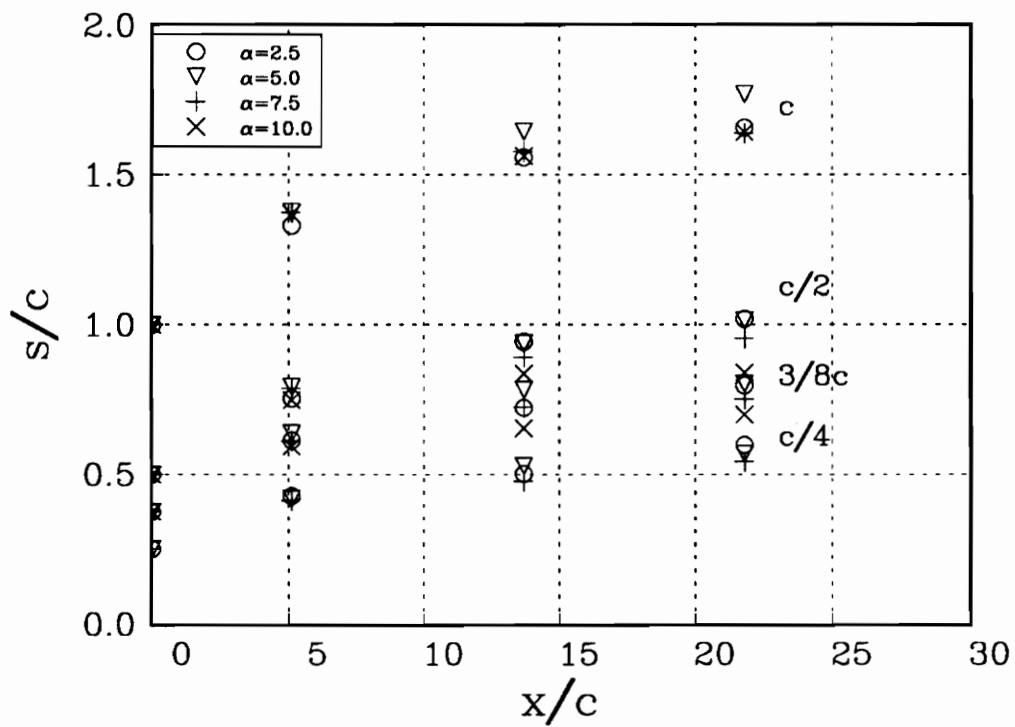


Figure 39. Separation distance s/c of counter rotating pairs as a function of streamwise location x/c .

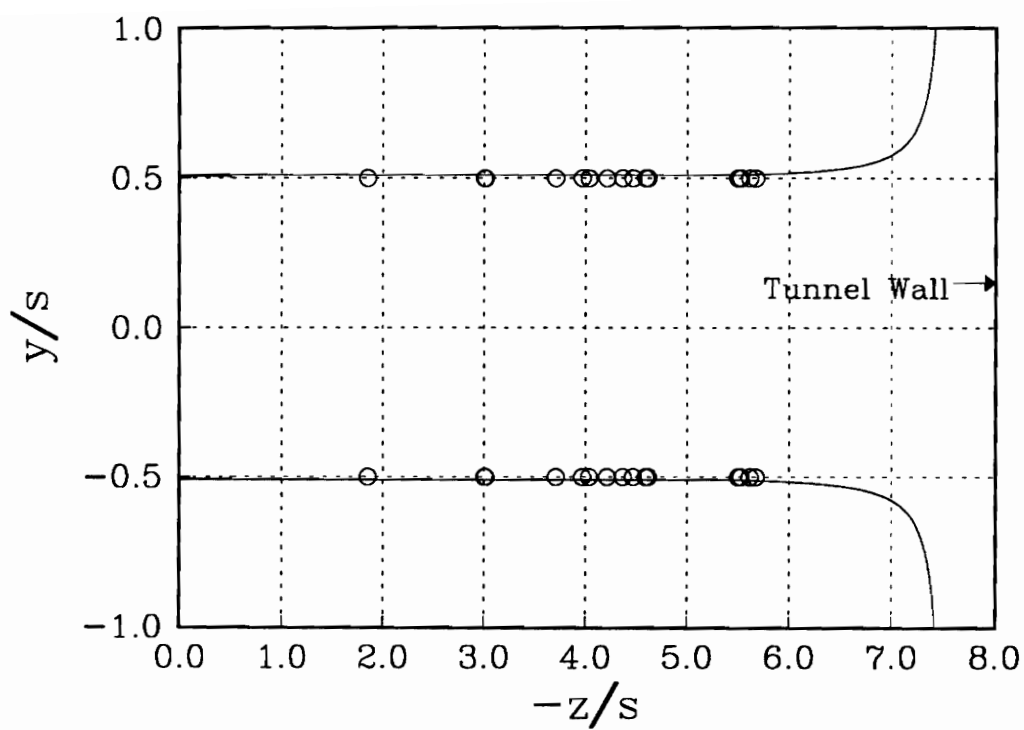


Figure 40. Trajectory of counter rotating vortex pairs in the presence of a wall. Normalized with the separation distance at $x/c=20$.

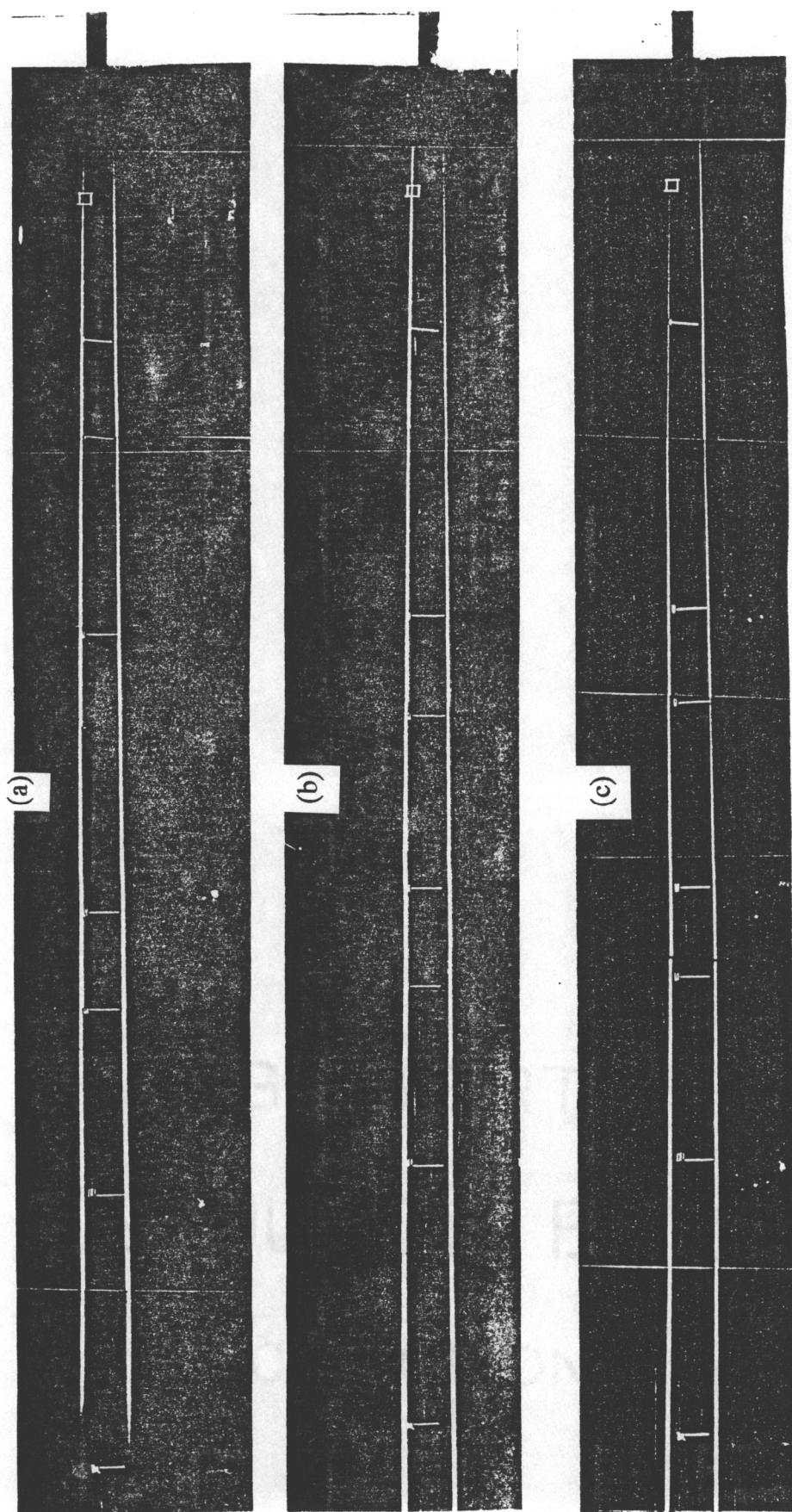


Figure 41. Photo-mosaics of co-rotating pairs at $\Delta y=3/8c$, $Re_c=130,000$, (a) $\alpha_e=10.0^\circ$,
 (b) $\alpha_e=7.5^\circ$, (c) $\alpha_e=5.0^\circ$. 8 sec exposures.

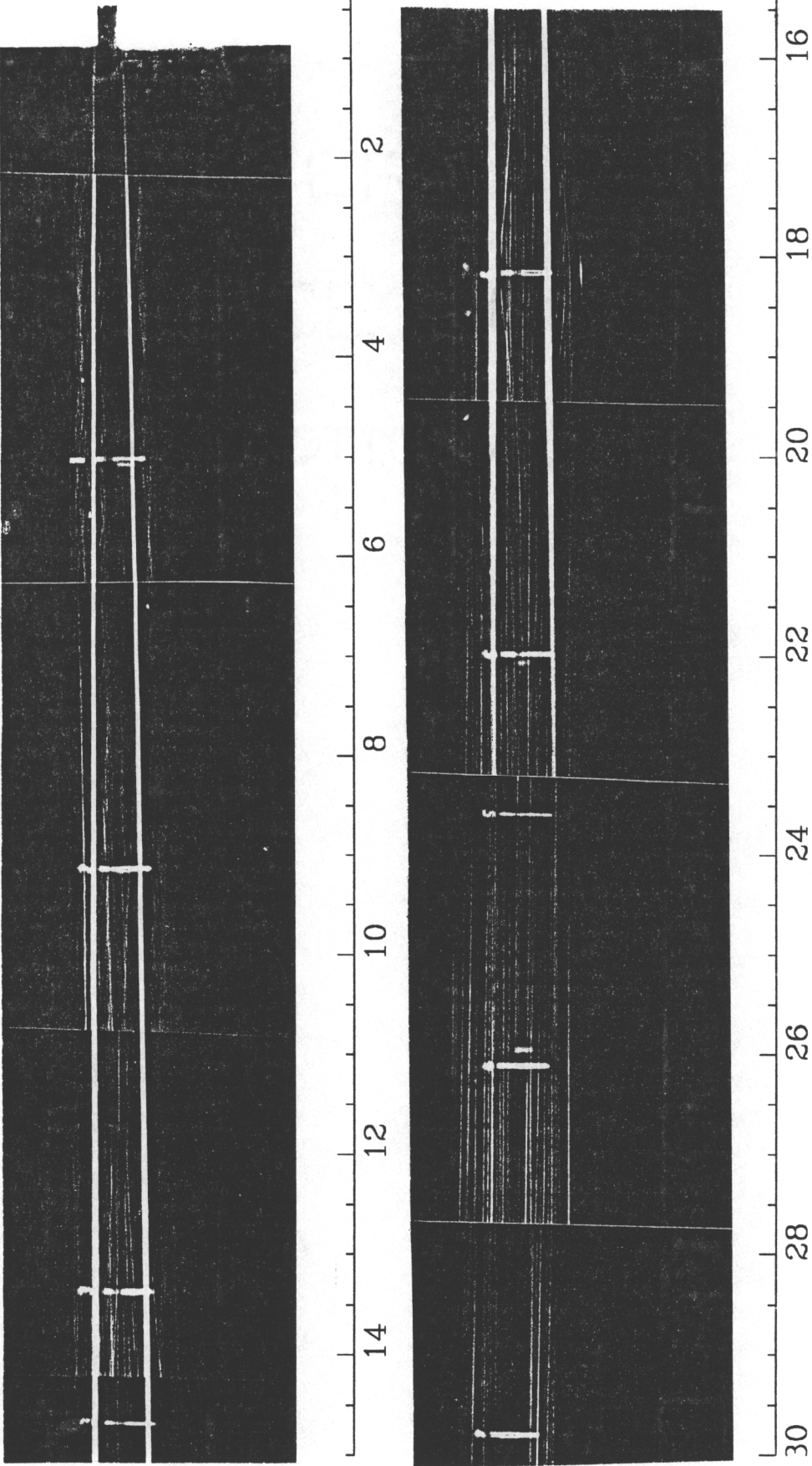


Figure 42. Photo-mosaic of co-rotating pair at $\Delta y=c/4c$, $Re_c=130,000$, $\alpha_e=5.0^\circ$. 8 sec exposure.

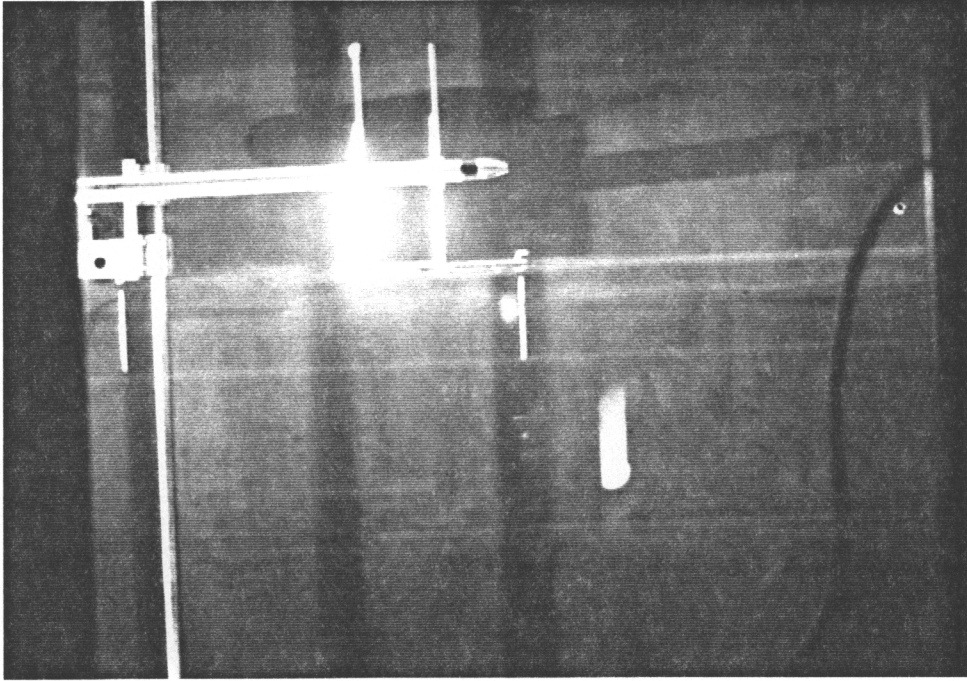


Figure 43. Dummy hot-wire probe in core, $\Delta y=c/4c$, $Re_c=130,000$, $\alpha_e=5.0^\circ$ at streamwise location $x/c=22$. 8 sec exposure.

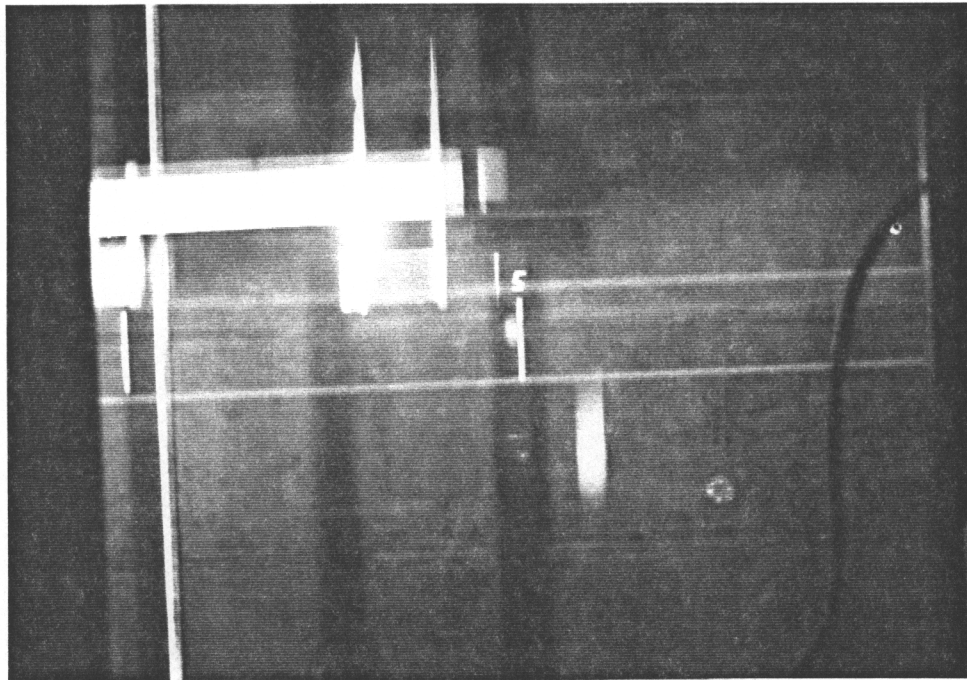


Figure 44. Dummy hot-wire probe traversing through the core, $\Delta y=c/4c$, $Re_c=130,000$, $\alpha_e=5.0^\circ$ at streamwise location $x/c=22$. 8 sec exposure.

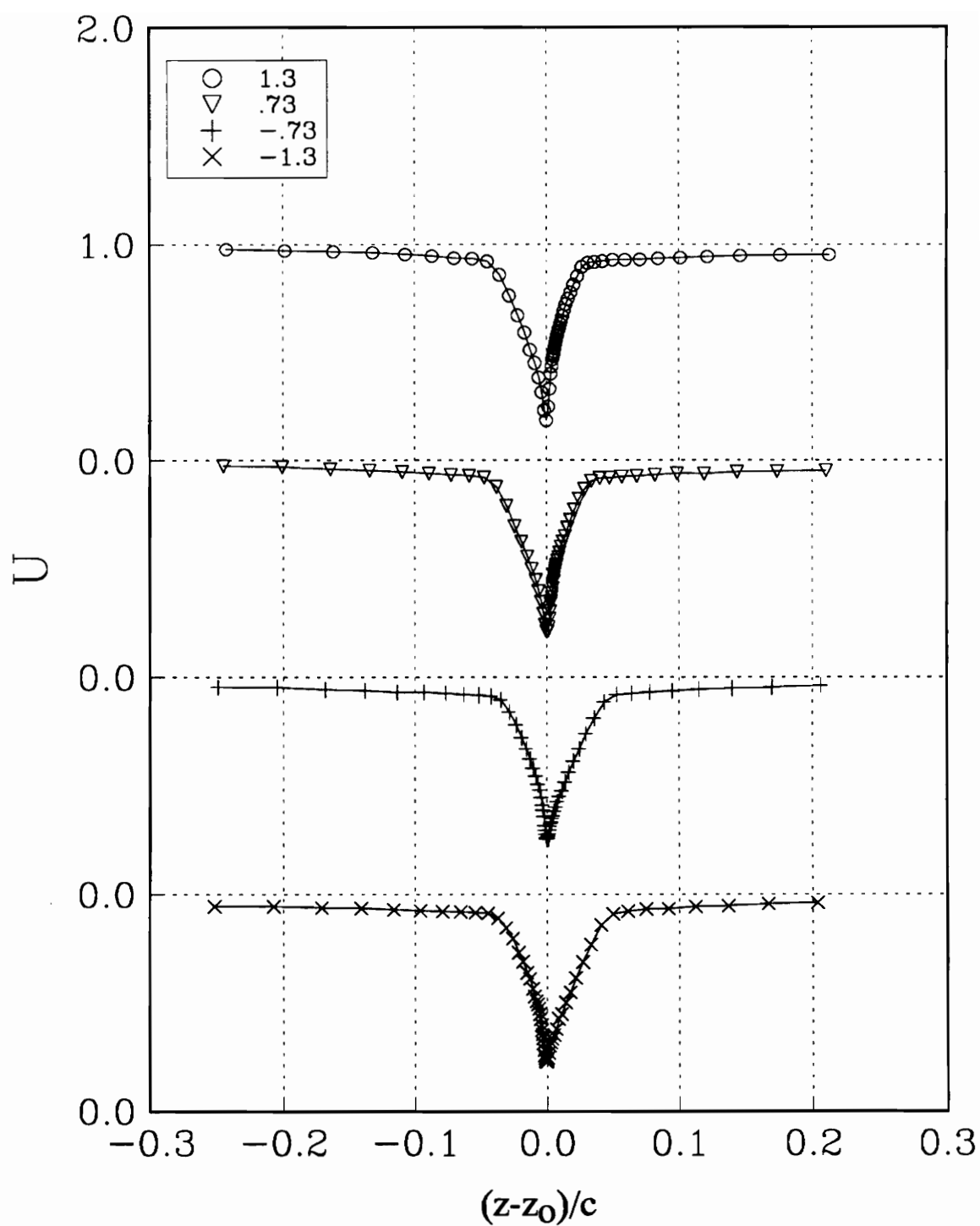


Figure 45. Mean U profiles in the near field wing wake at various y/c locations for the co-rotating pairs.

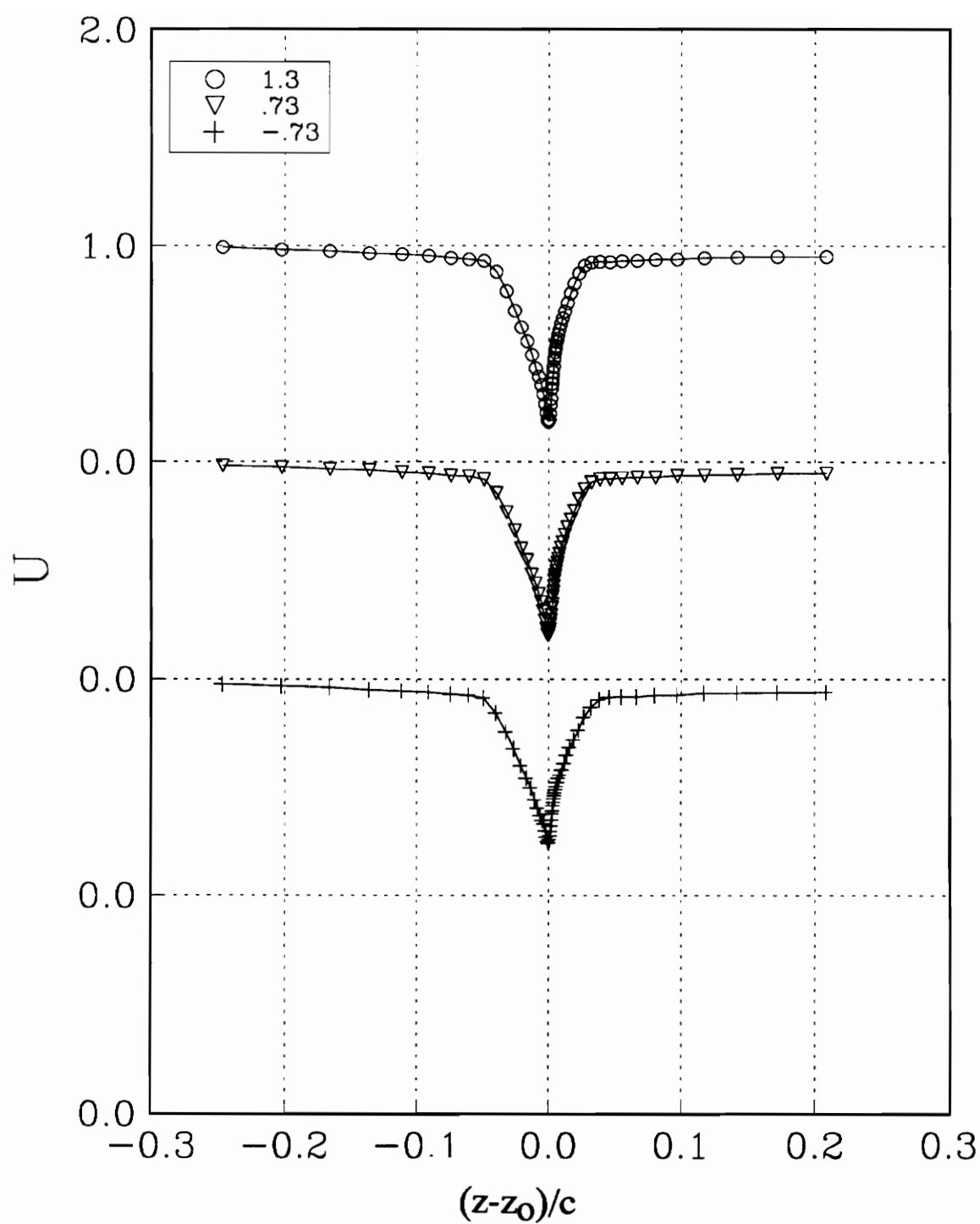


Figure 46. Mean U profiles in the near field wing wake at various y/c locations for the counter rotating pairs.

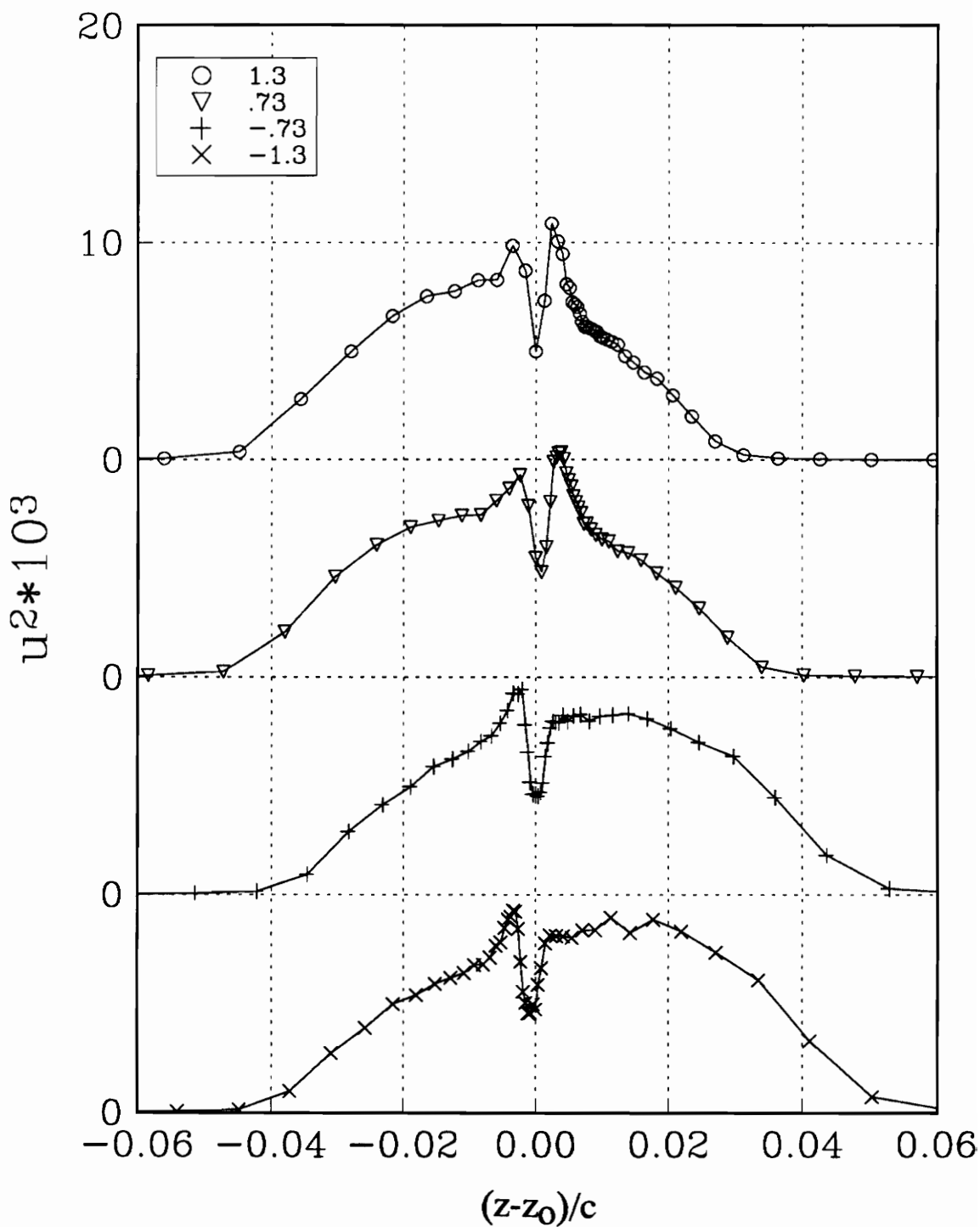


Figure 47. Profiles of u^2 in the near field wing wake at various y/c locations for the co-rotating pairs.

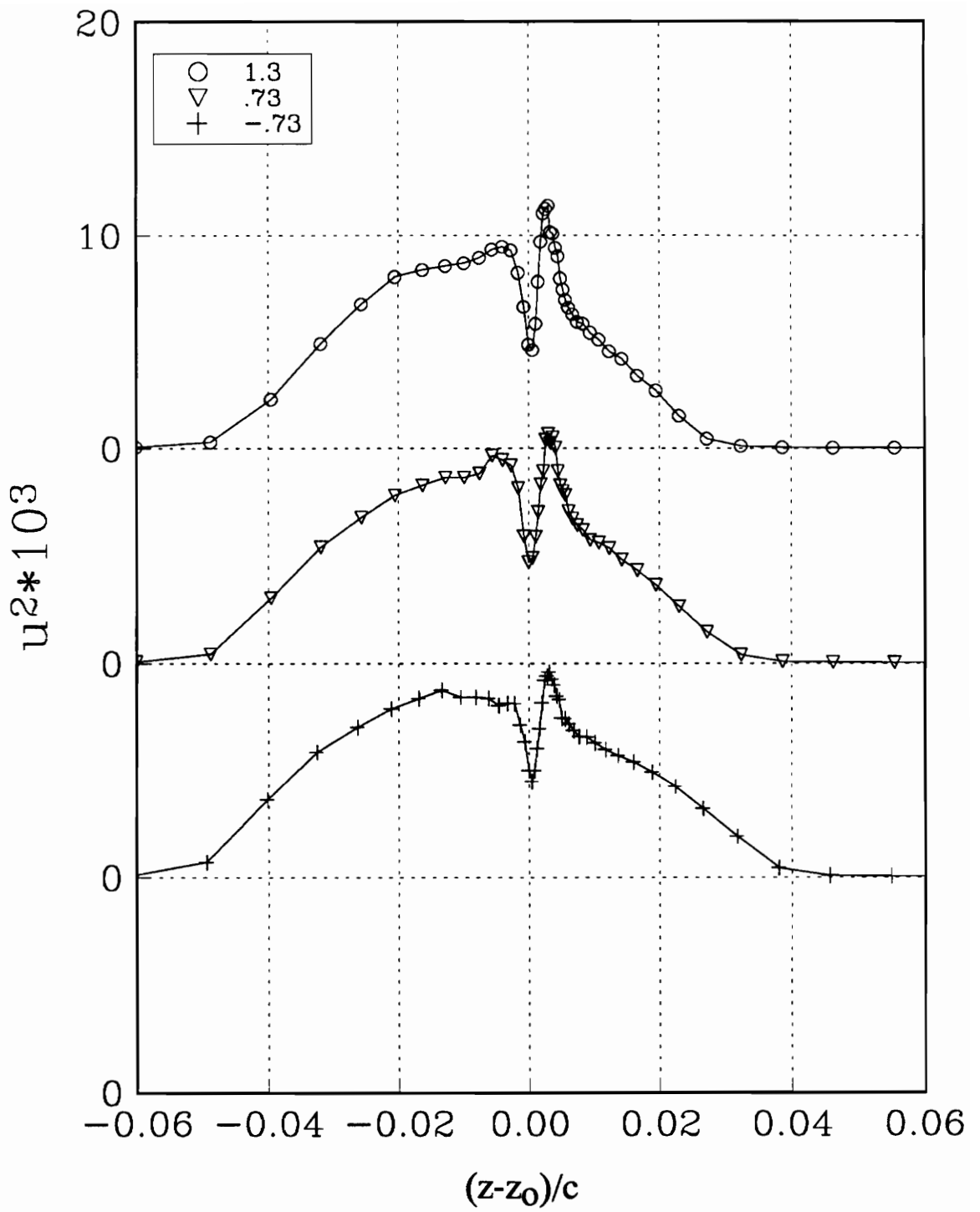


Figure 48. Profiles of u^2 in the near field wing wake at various y/c locations for the counter rotating pairs.

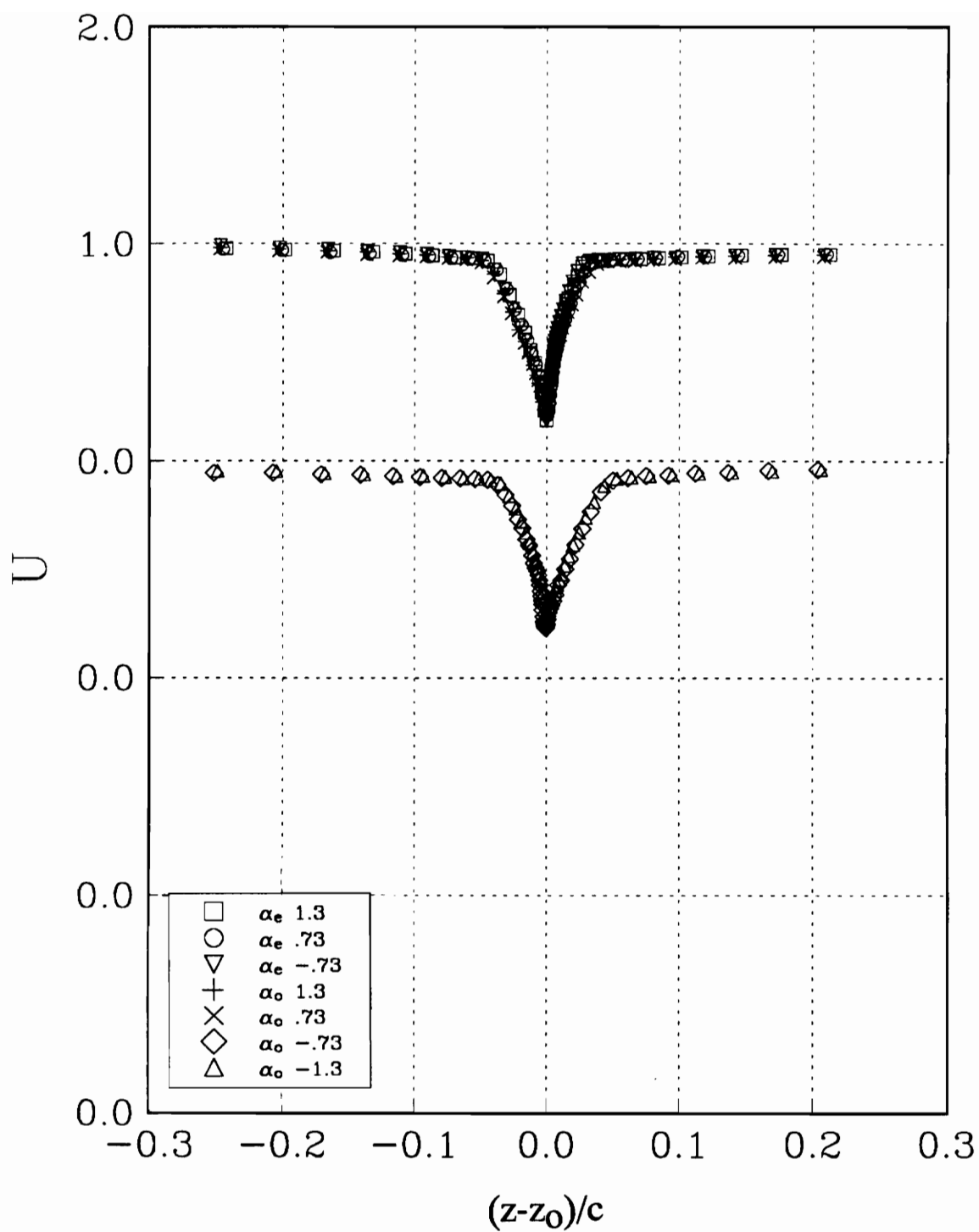


Figure 49. Comparison of mean U profiles for both the co-rotating and counter rotating pairs.

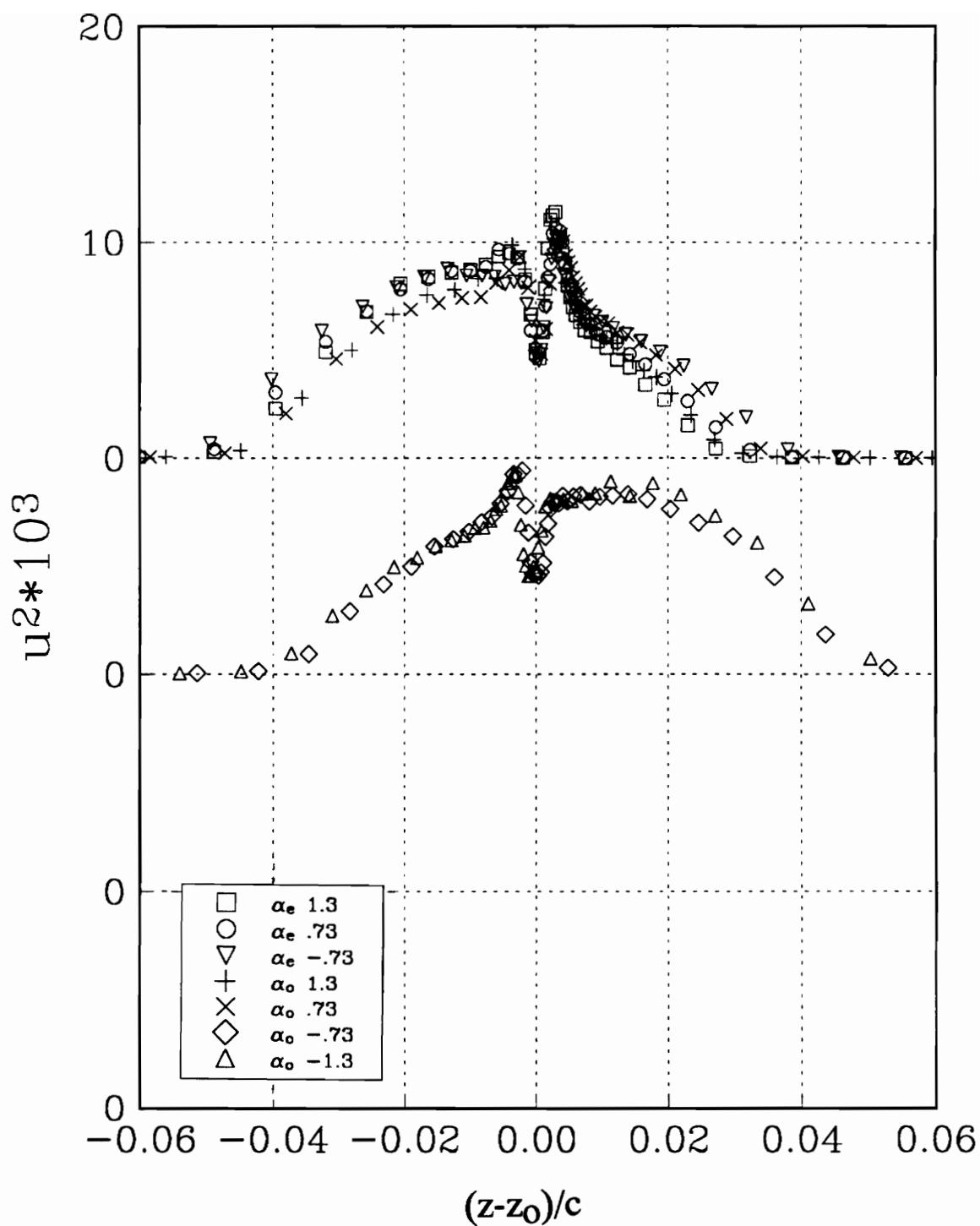


Figure 50. Comparison of u^2 profiles for both the co-rotating and counter rotating pairs.

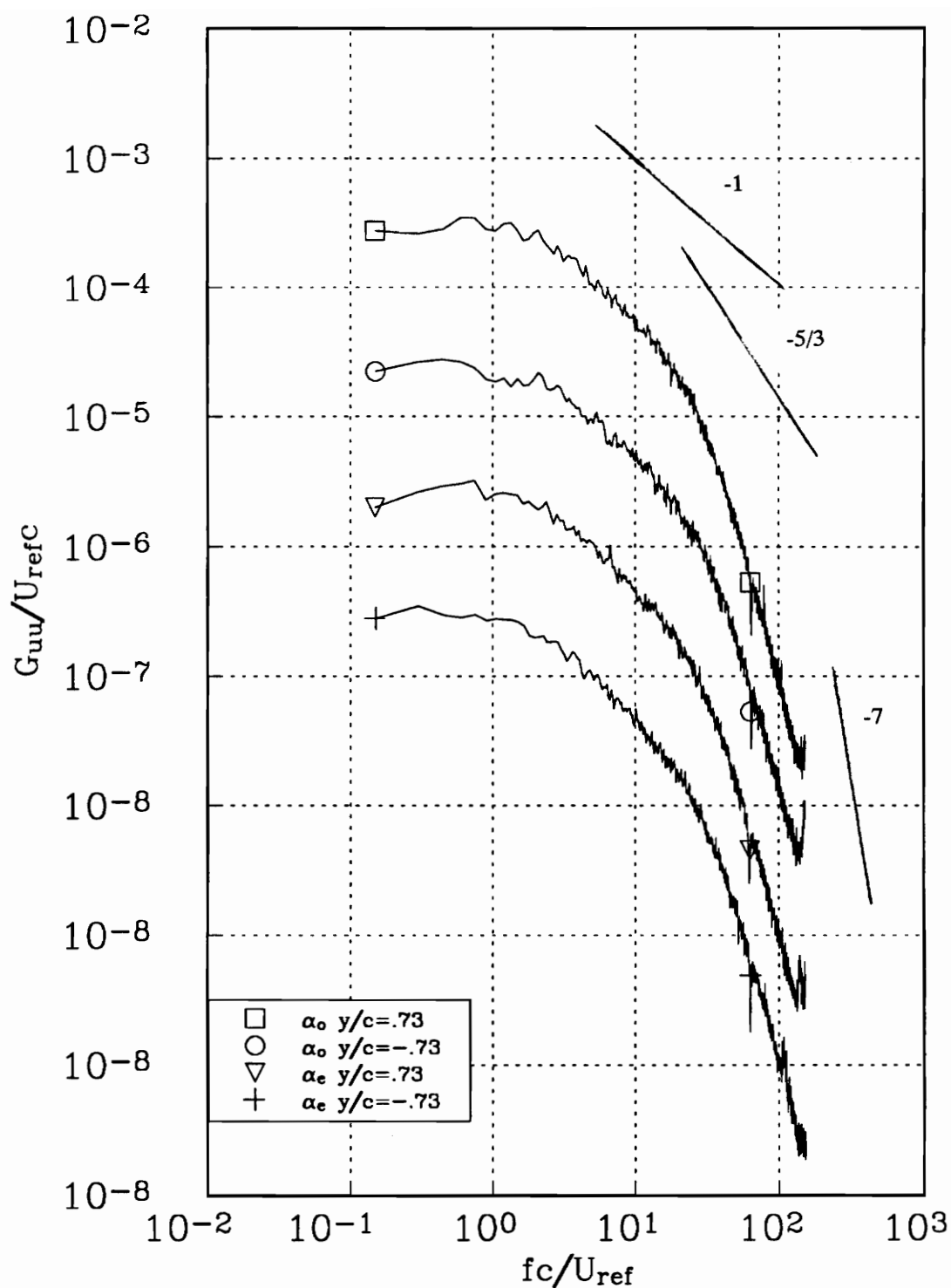


Figure 51. Representative u autospectra in the centerline of the near field wing wake for both the co-rotating and counter rotating pairs.

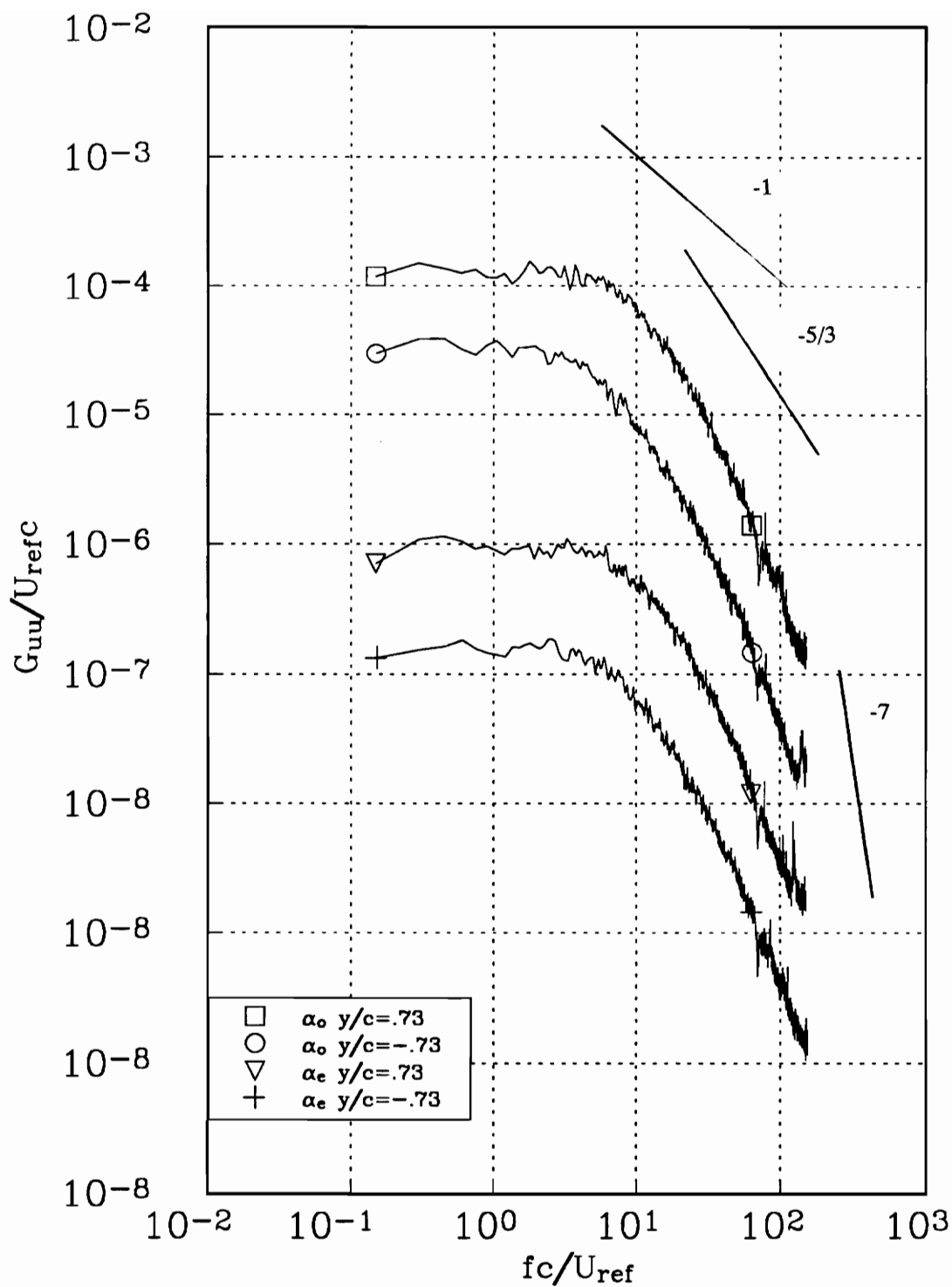


Figure 52. Representative u autospectra measured on the suction side of the near field wing wake for both the co-rotating and counter rotating pairs.

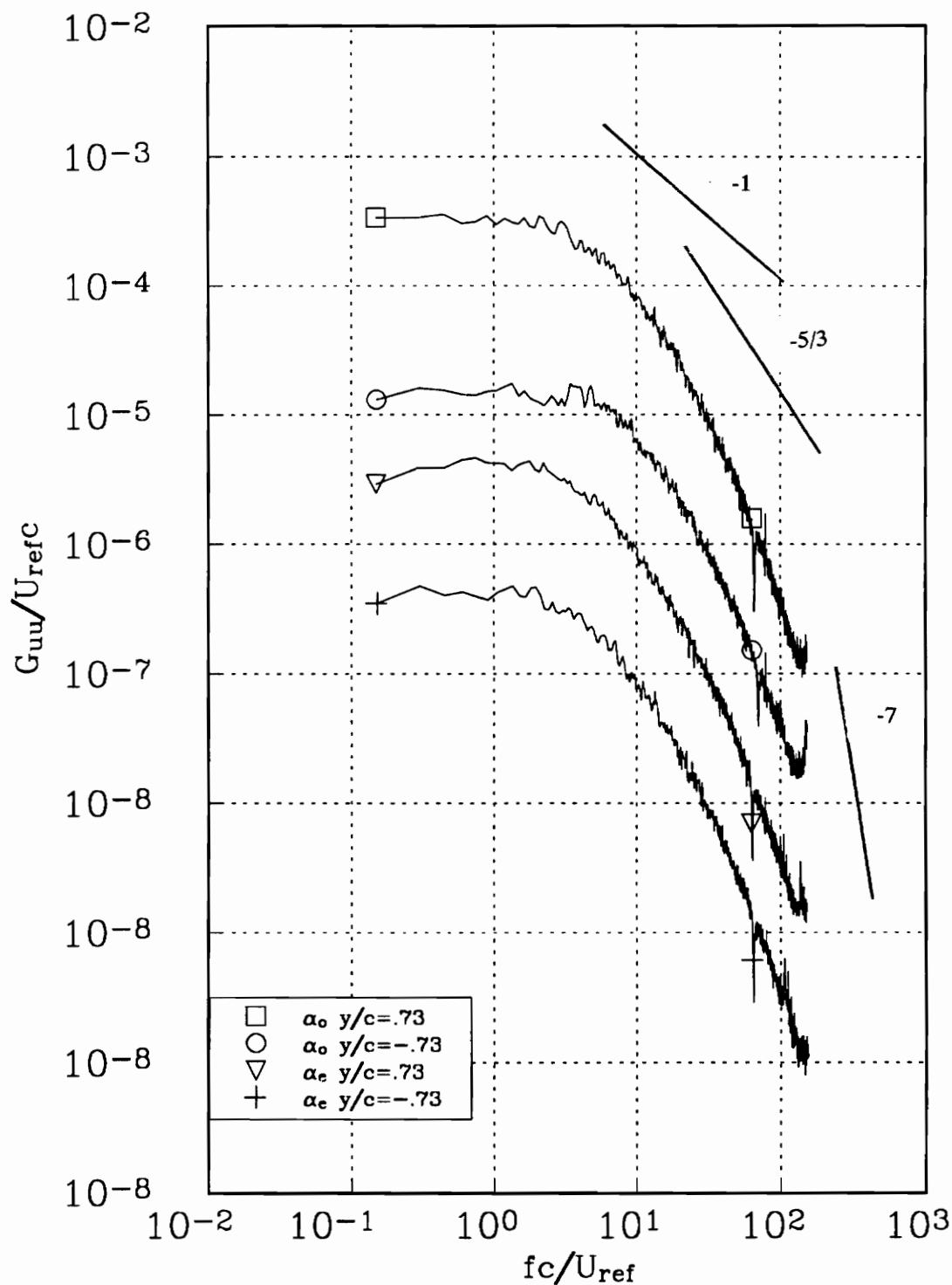


Figure 53. Representative u autospectra measured on the pressure side of the near field wing wake for both the co-rotating and counter rotating pairs.

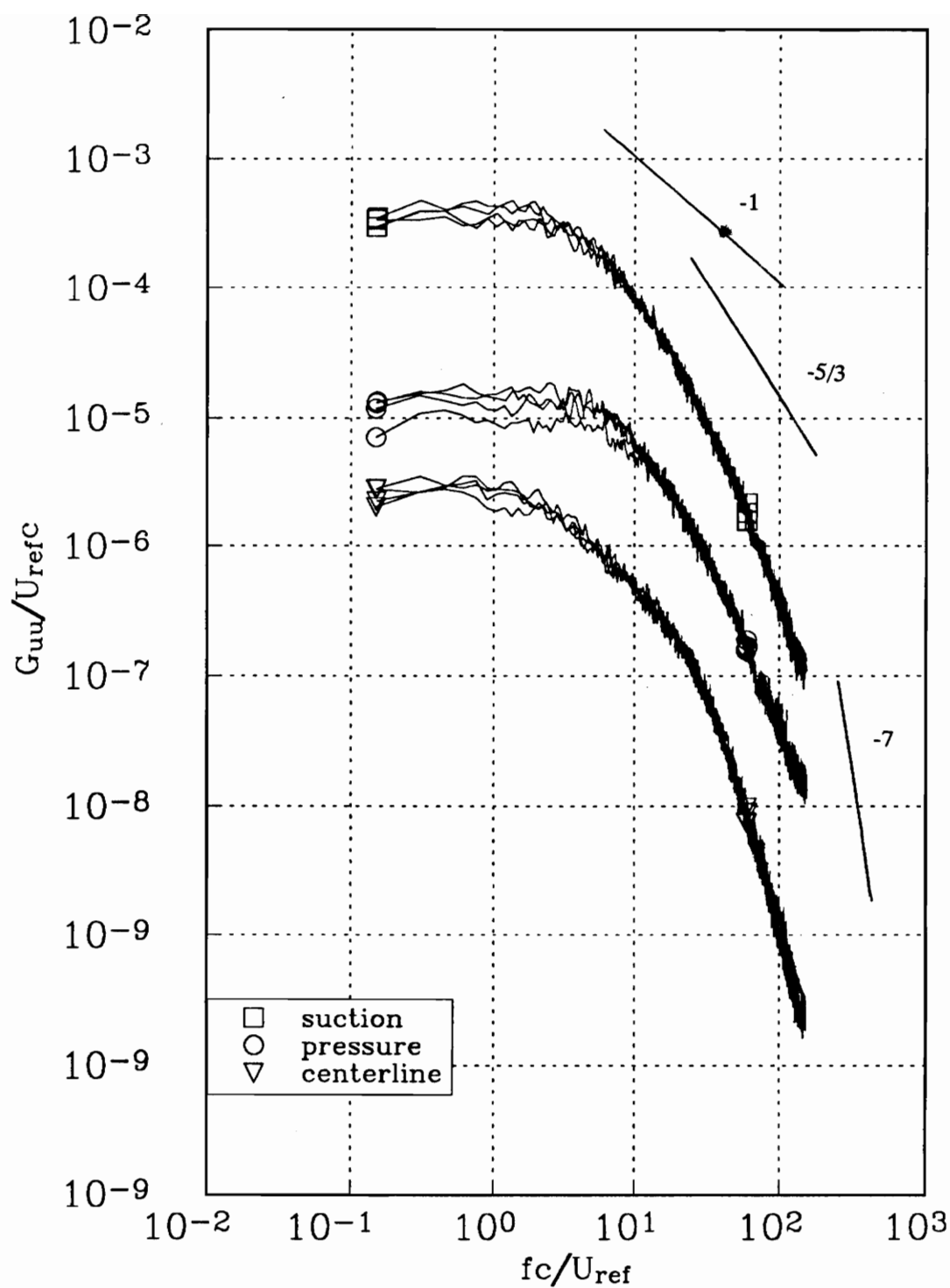


Figure 54. Comparison of u autospectra measured in the near filed wing wake for the suction, pressure and centerline locations.

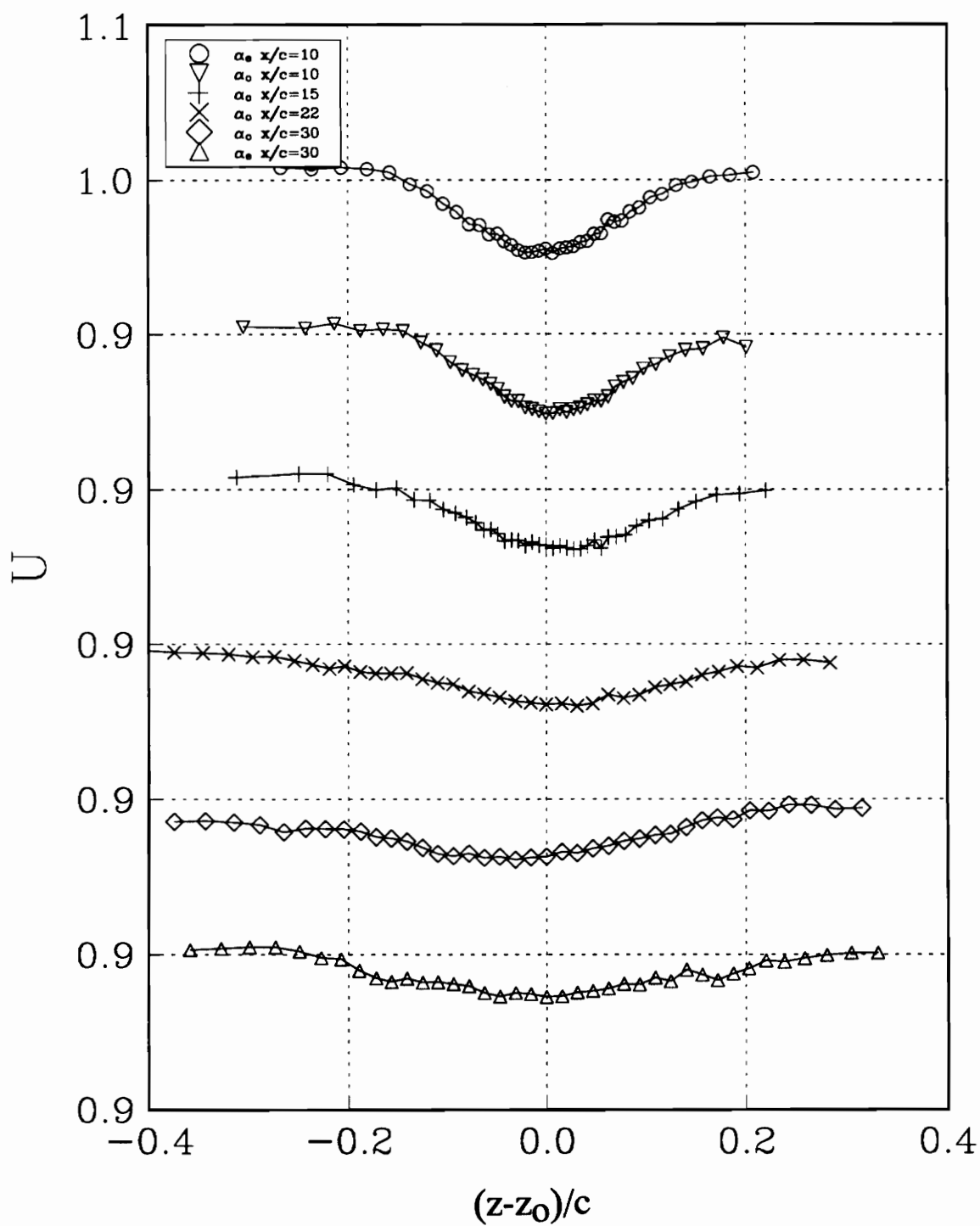


Figure 55. Mean U profiles of the far field upper wing wake for both the co-rotating and counter rotating pairs.

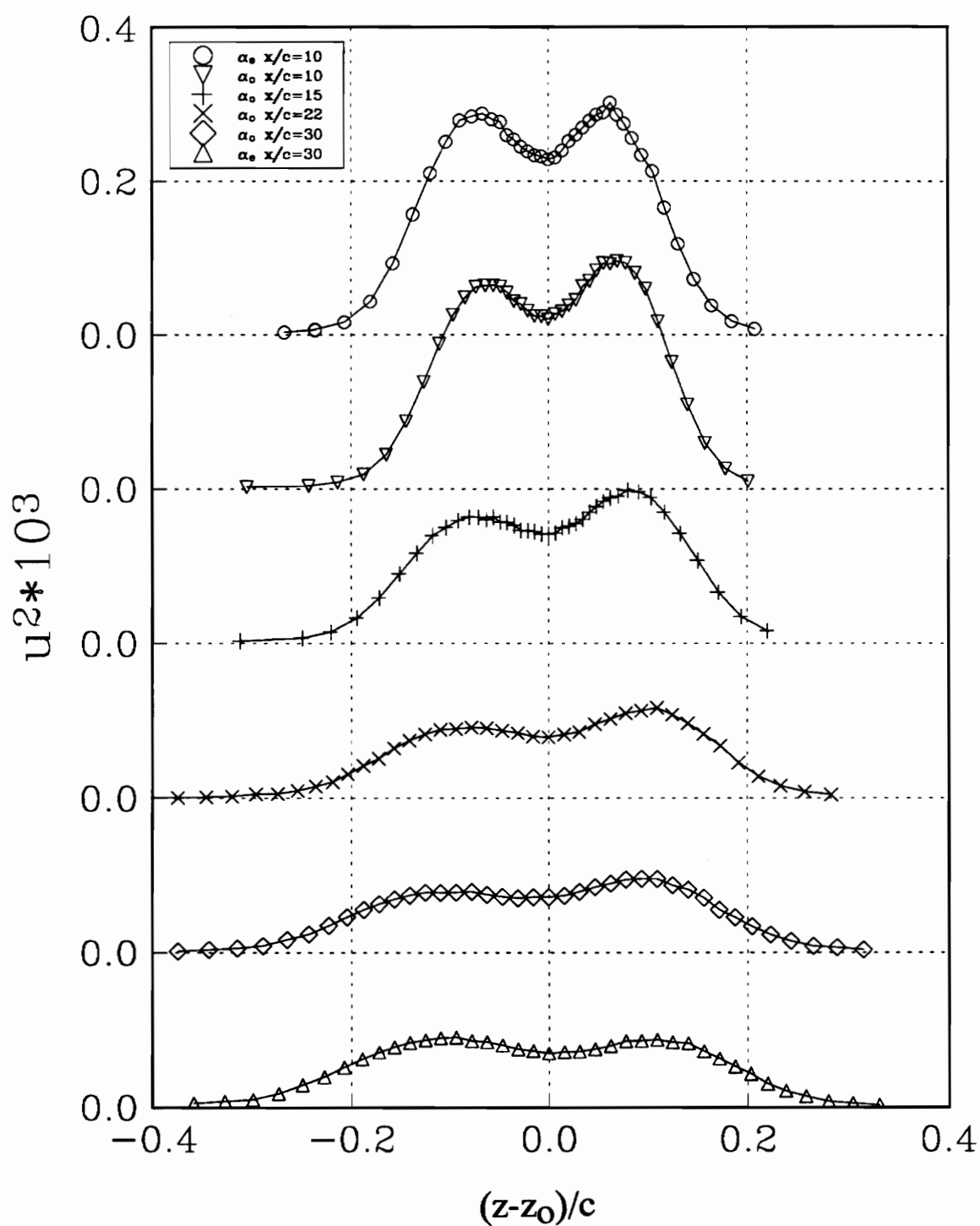


Figure 56. u^2 profiles of the far field upper wing wake for both the co-rotating and counter rotating pairs.

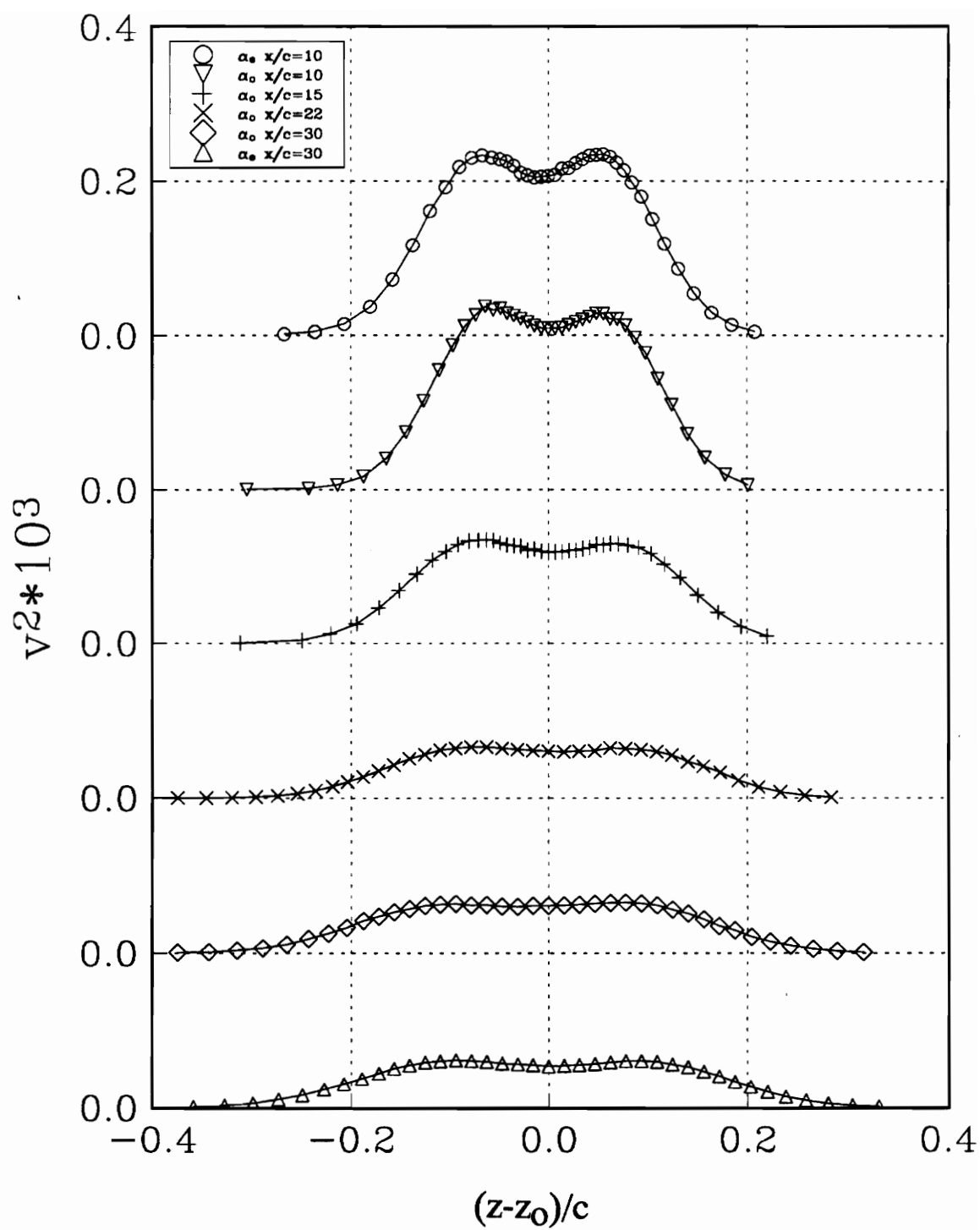


Figure 57. v^2 profiles of the far field upper wing wake for both the co-rotating and counter rotating pairs.

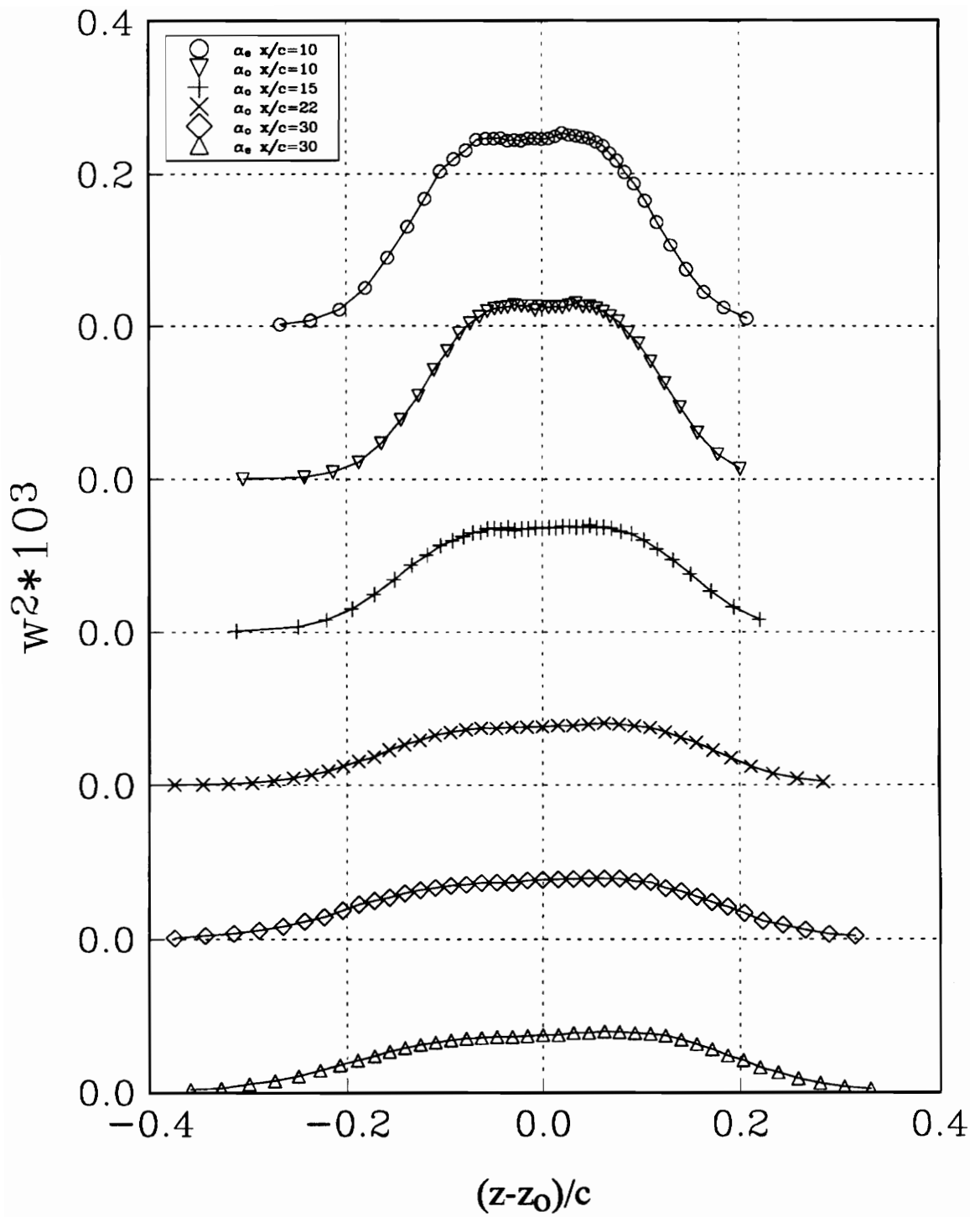


Figure 58. w^2 profiles of the far field upper wing wake for both the co-rotating and counter rotating pairs.

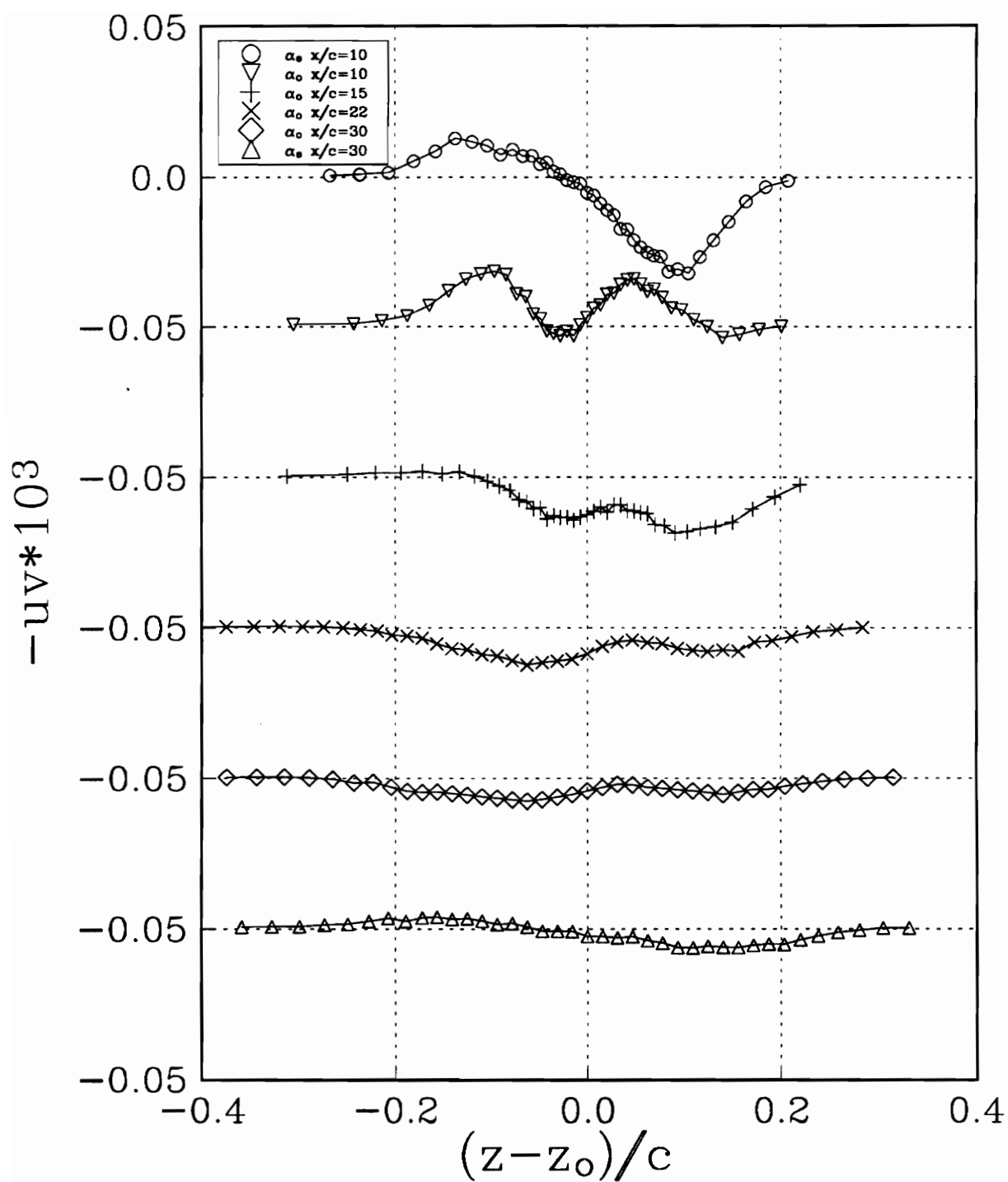


Figure 59. uv profiles of the far field upper wing wake for both the co-rotating and counter rotating pairs.

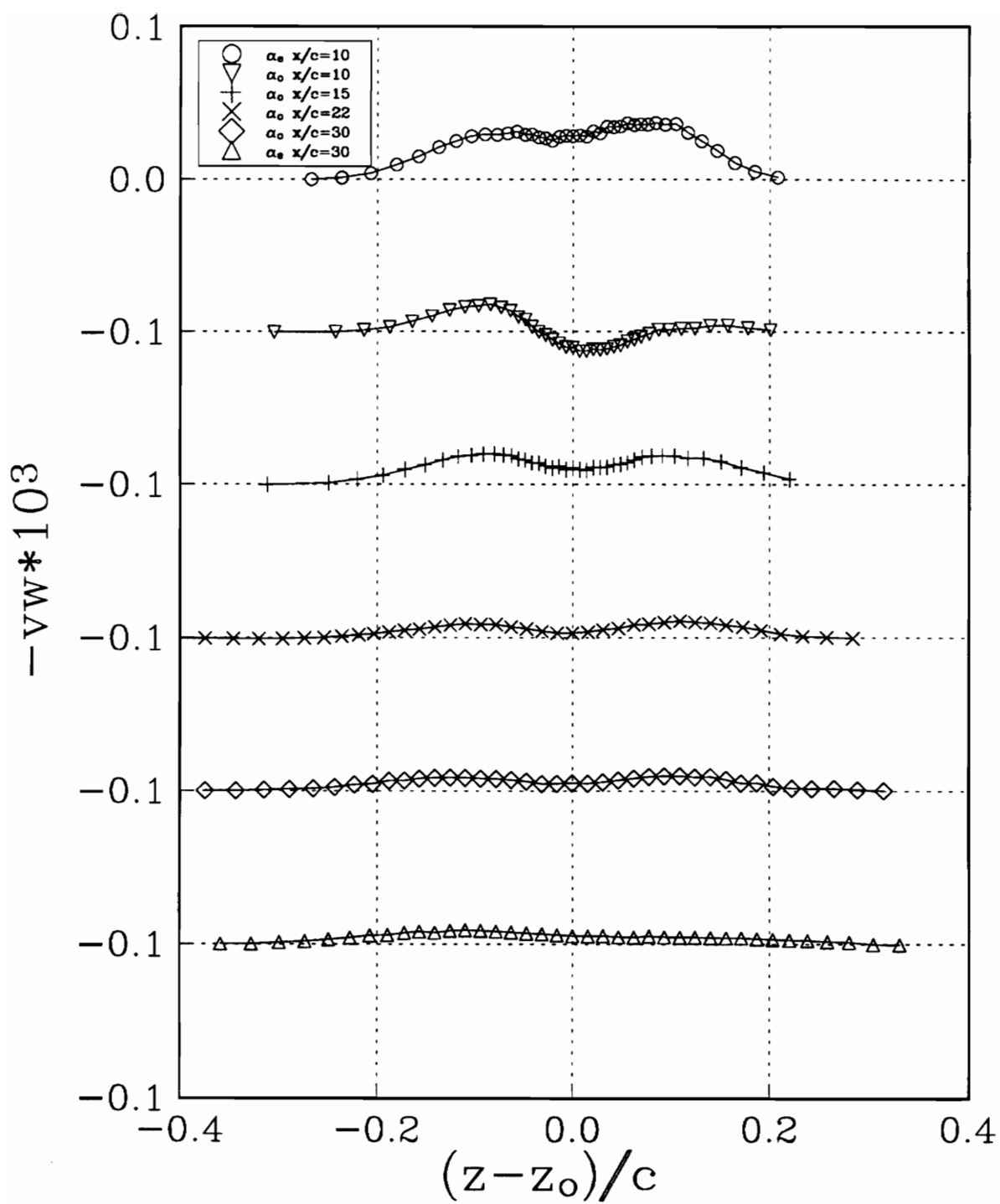


Figure 60. v_w profiles of the far field upper wing wake for both the co-rotating and counter rotating pairs.

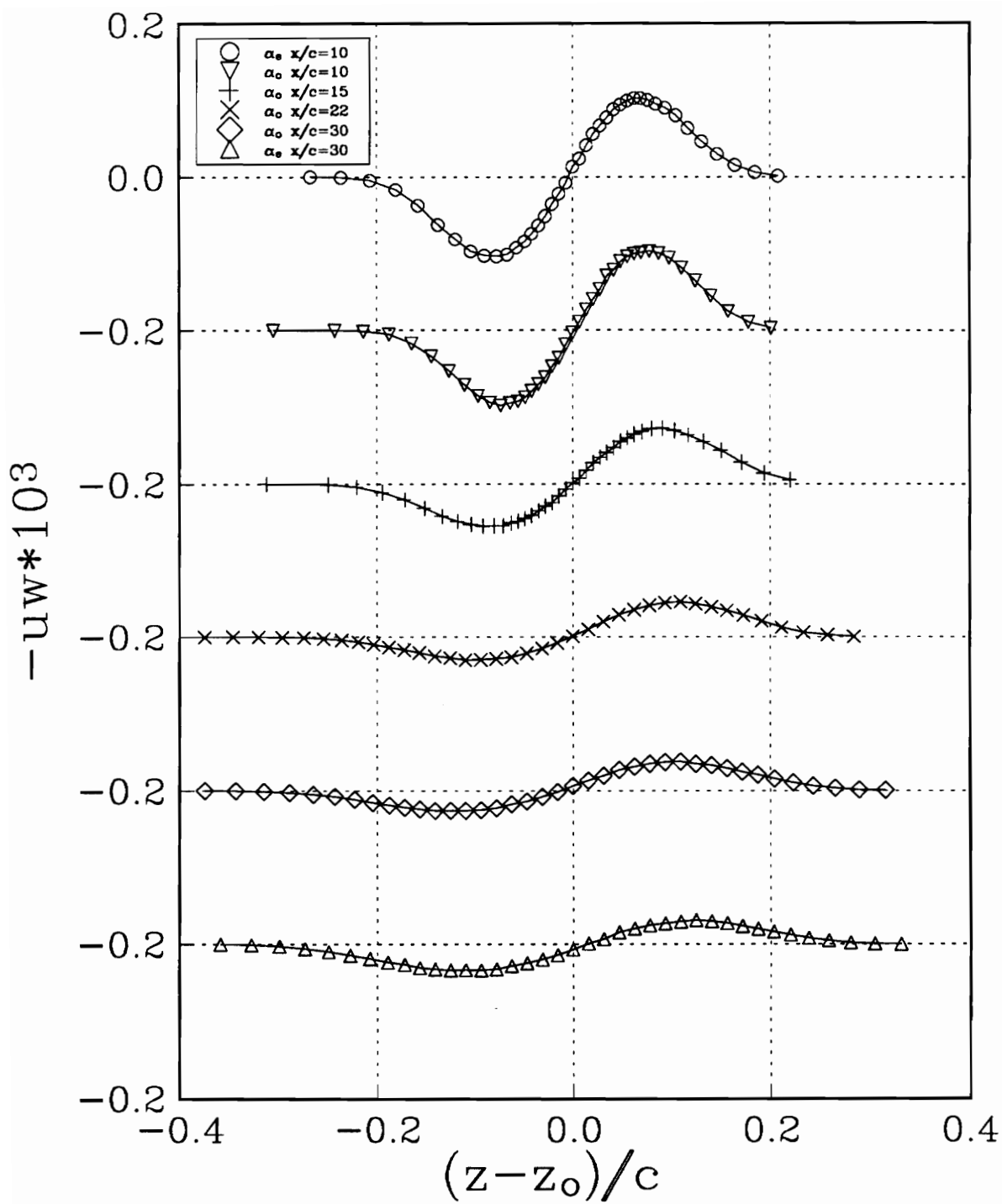


Figure 61. uw profiles of the far field upper wing wake for both the co-rotating and counter rotating pairs.

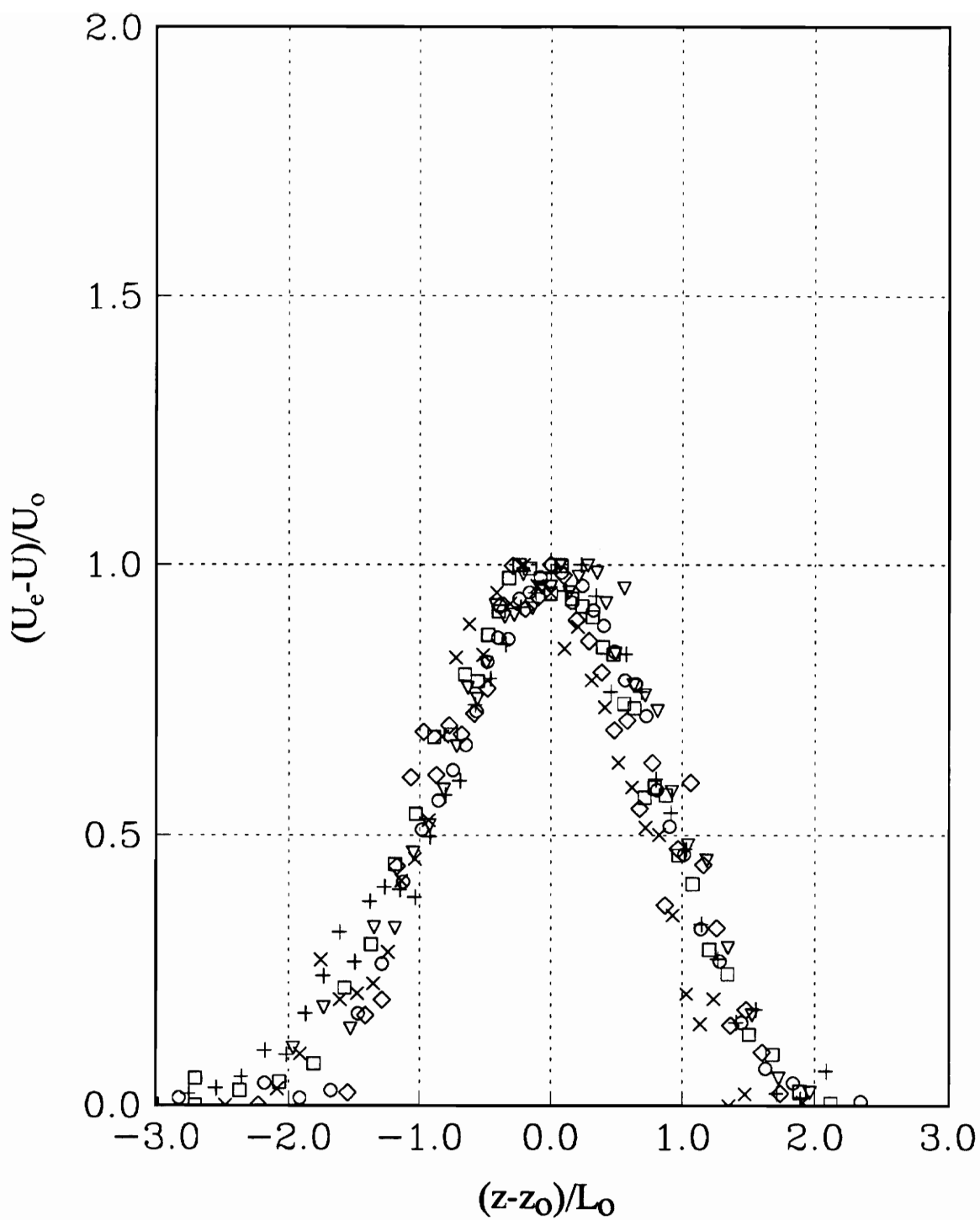


Figure 62. Similarity profiles of the mean axial velocity deficit for the upper far field wing wakes for both the co-rotating and counter rotating pairs.

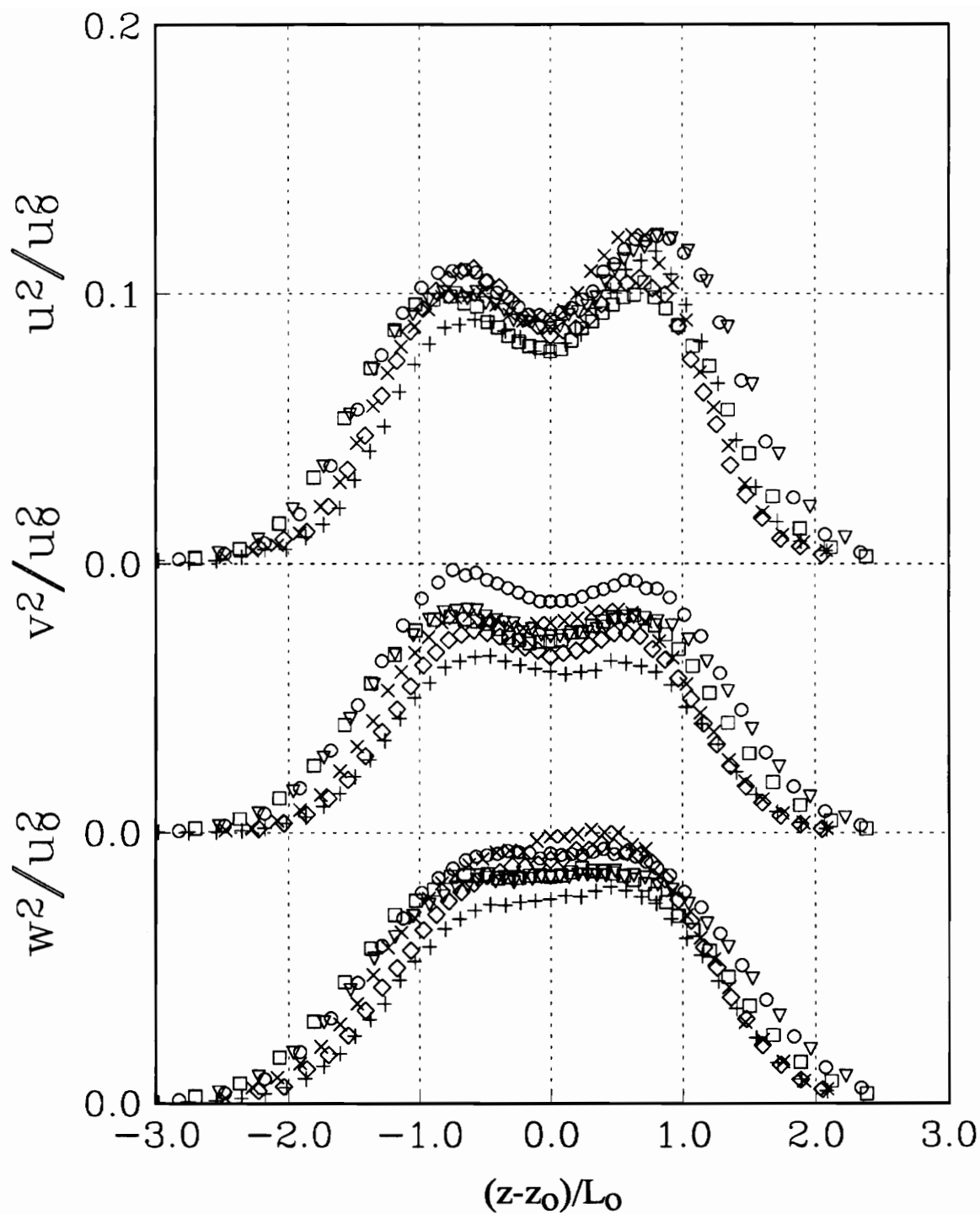


Figure 63. Similarity profiles of the normal stresses for the upper far field wing wakes for both the co-rotating and counter rotating pairs.

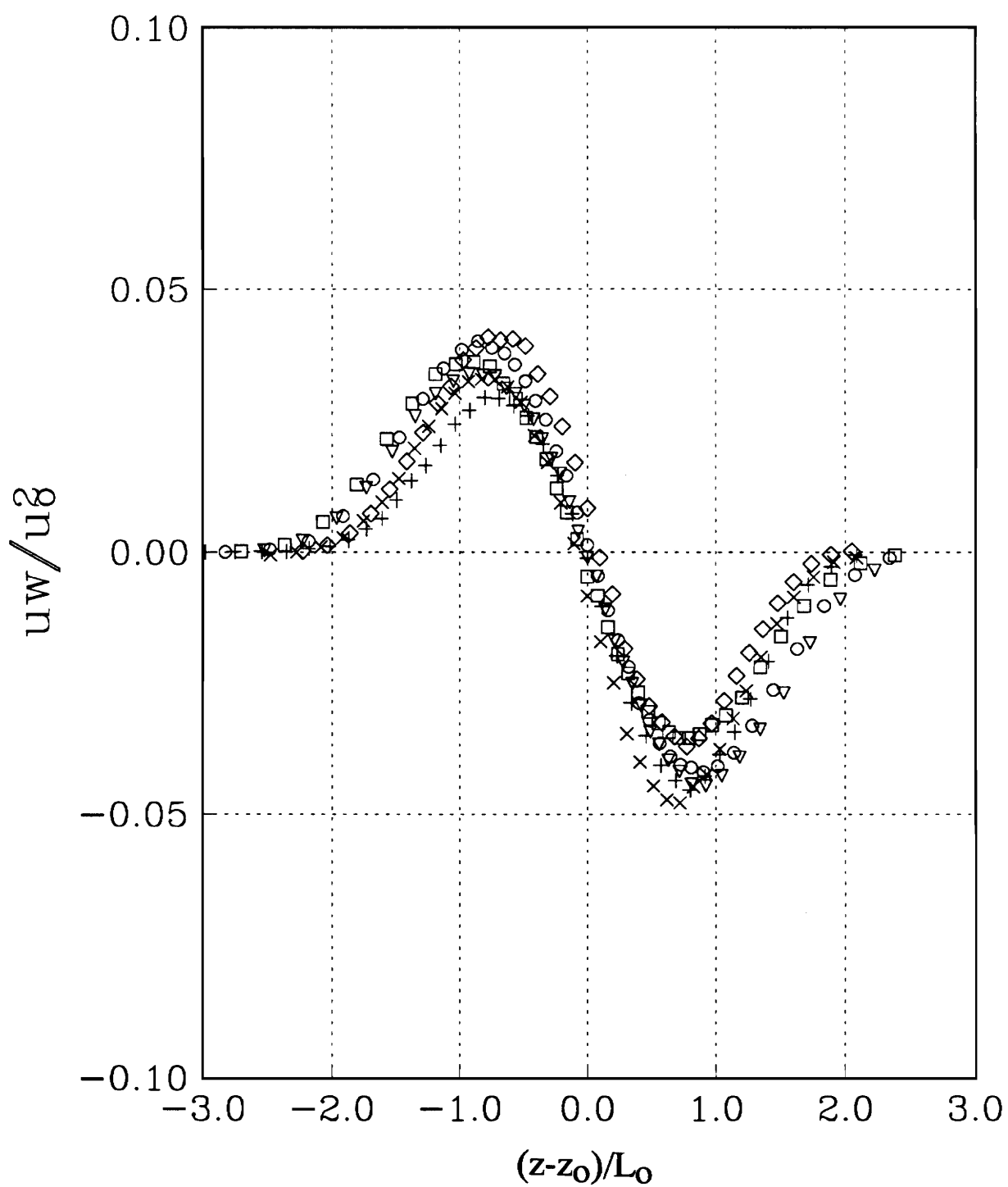


Figure 64. Similarity profiles of the shear stress uw for the upper far field wing wakes for both the co-rotating and counter rotating pairs.

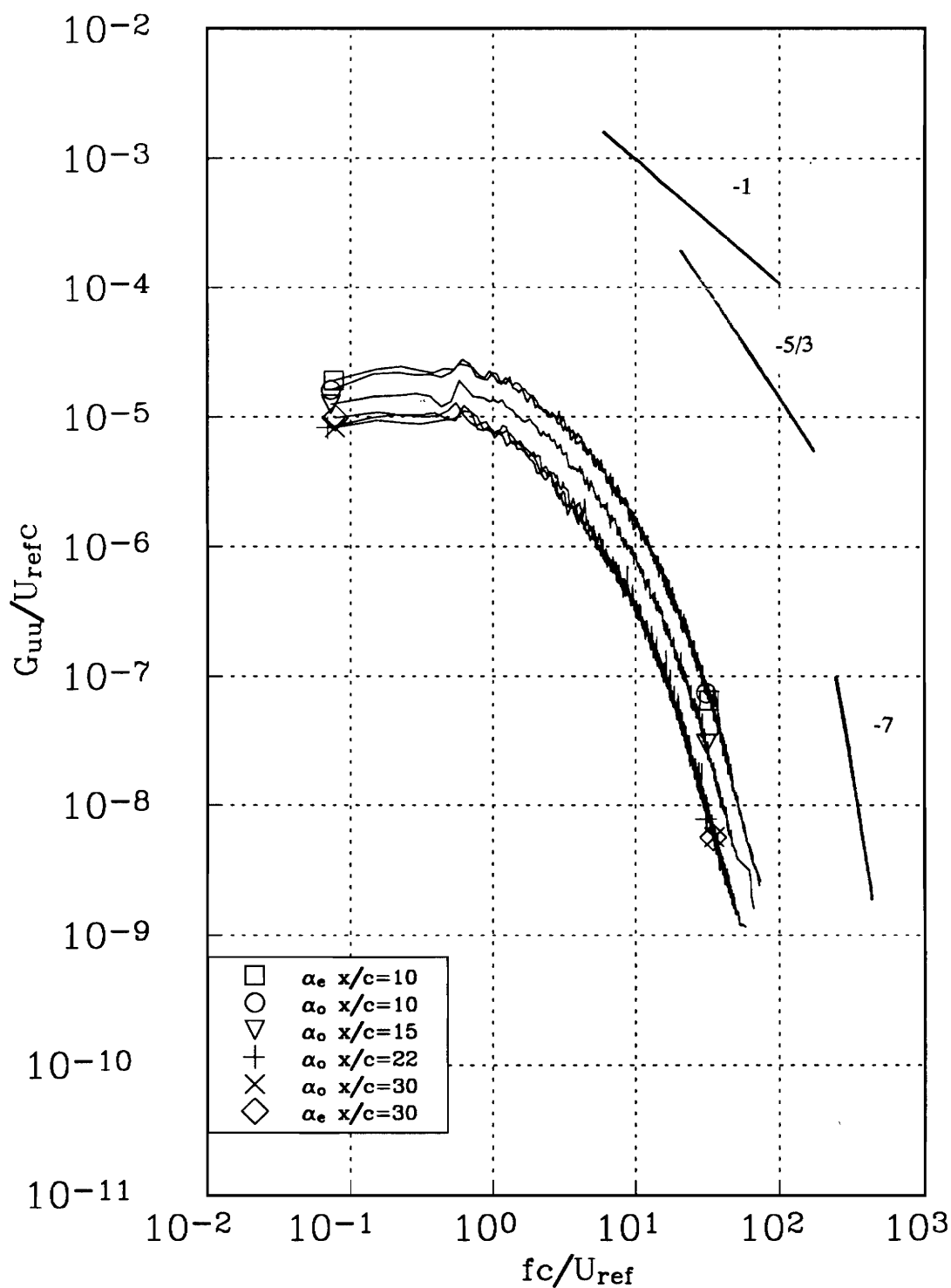


Figure 65a. u autospectra of the upper far field wing wake measured at the centerline of the wake for both the co-rotating and counter rotating pairs.

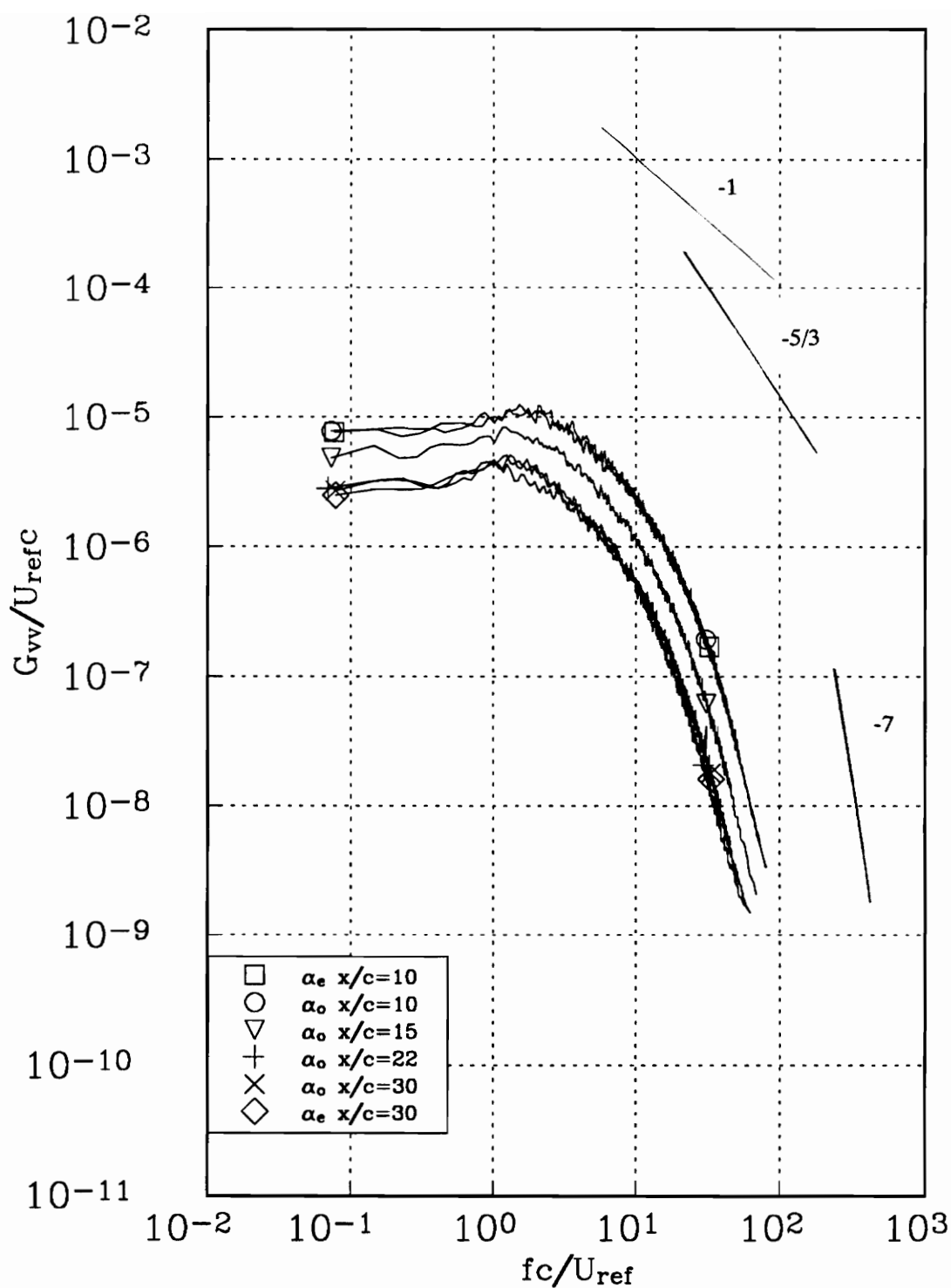


Figure 65b. v autospectra of the upper far field wing wake measured at the centerline of the wake for both the co-rotating and counter rotating pairs.

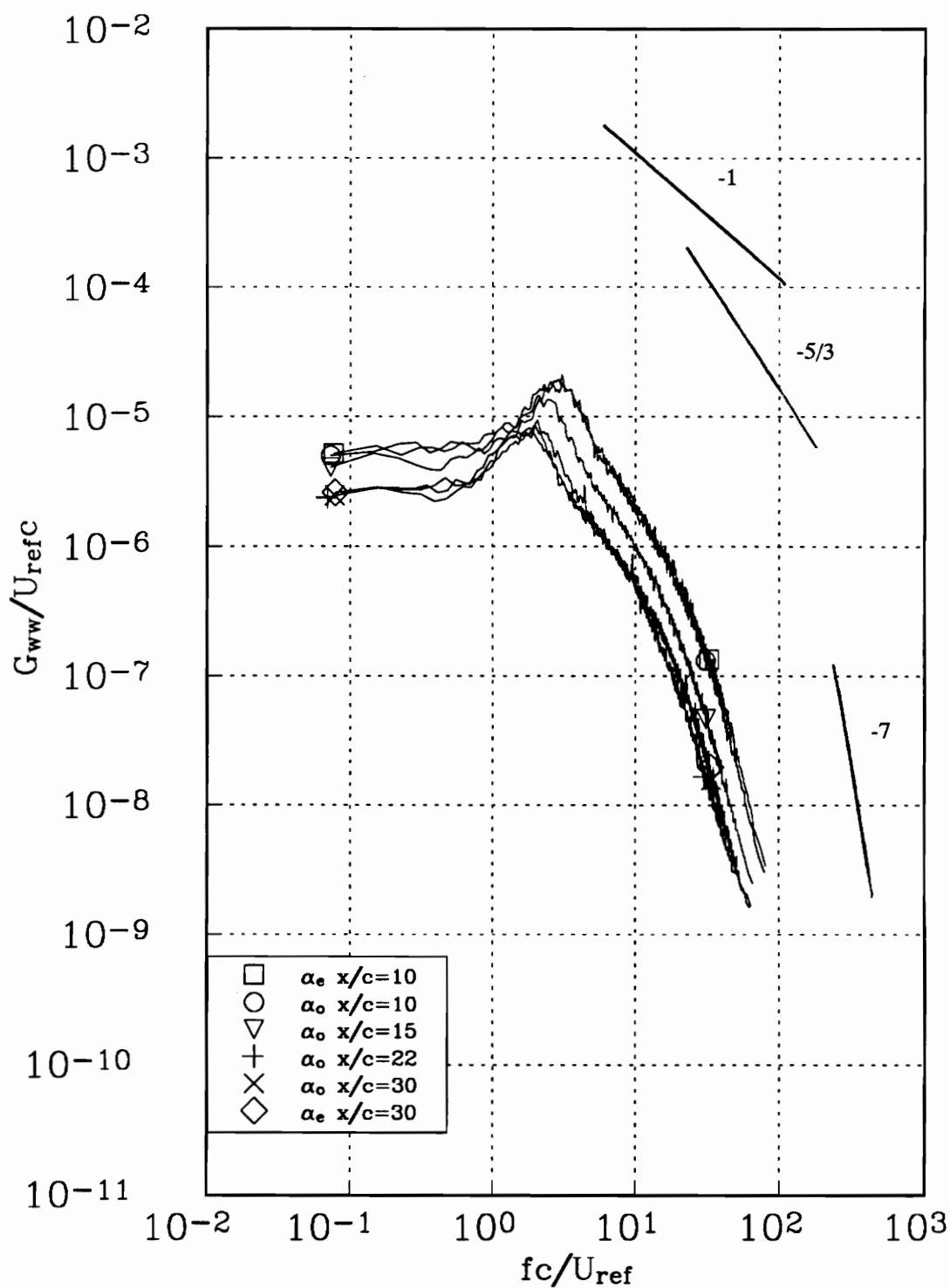


Figure 65c. w autospectra of the upper far field wing wake measured at the centerline of the wake for both the co-rotating and counter rotating pairs.

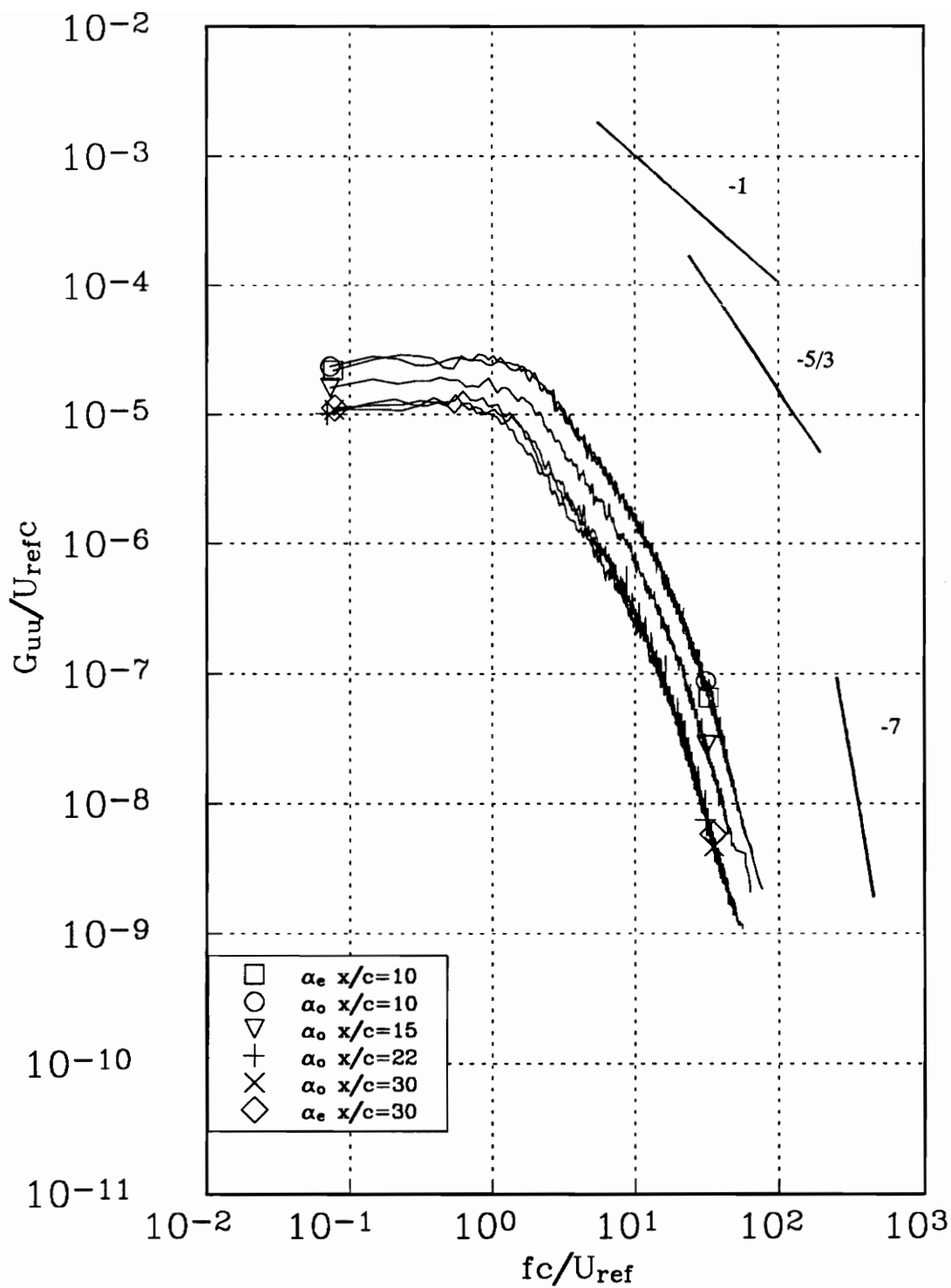


Figure 66a. u autospectra of the upper far field wing wake measured at $(z-z_o)/c=-0.1$ of the wake for both the co-rotating and counter rotating pairs.

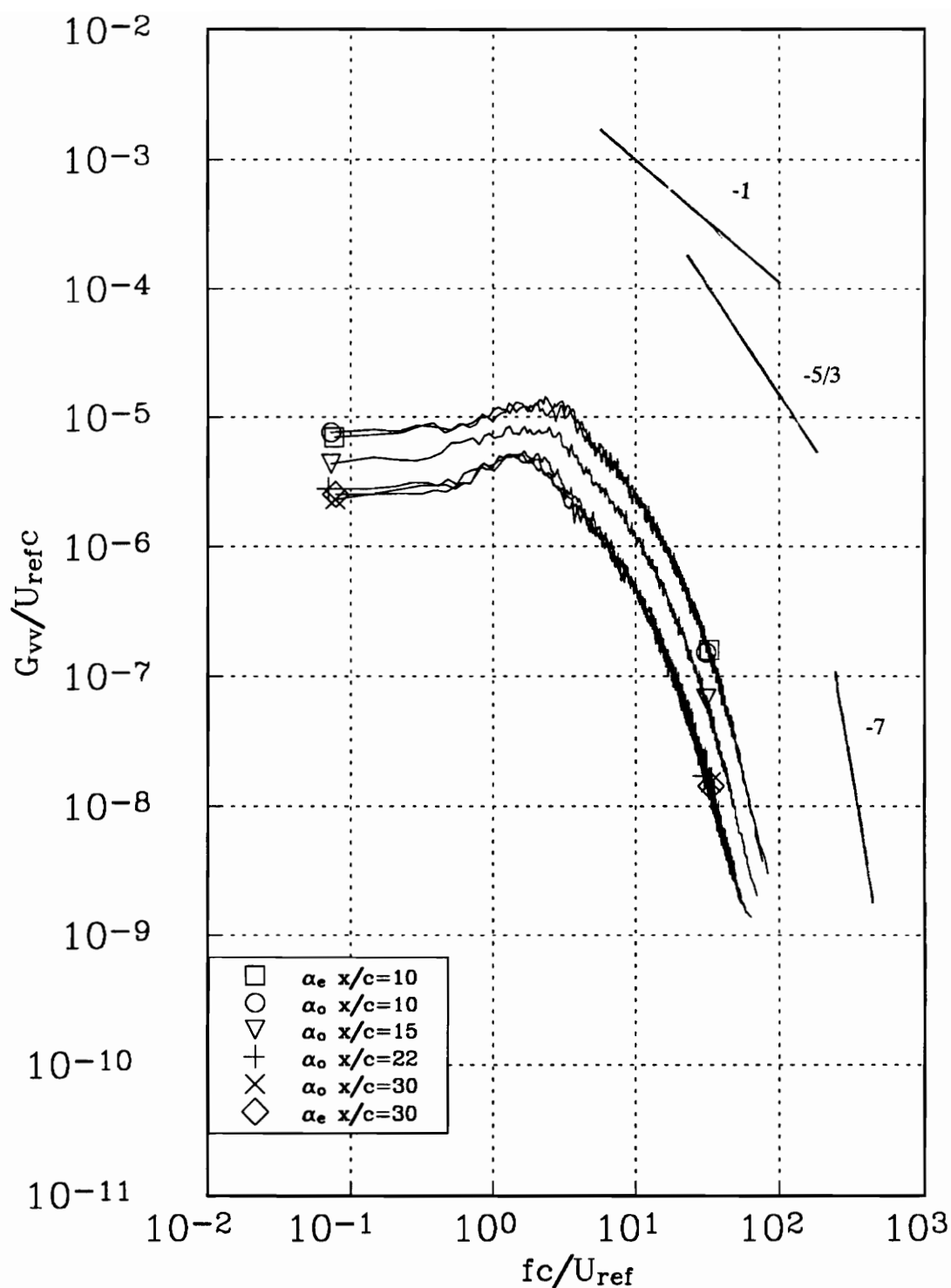


Figure 66b. v autospectra of the upper far field wing wake measured at $(z-z_o)/c=-0.1$ of the wake for both the co-rotating and counter rotating pairs.

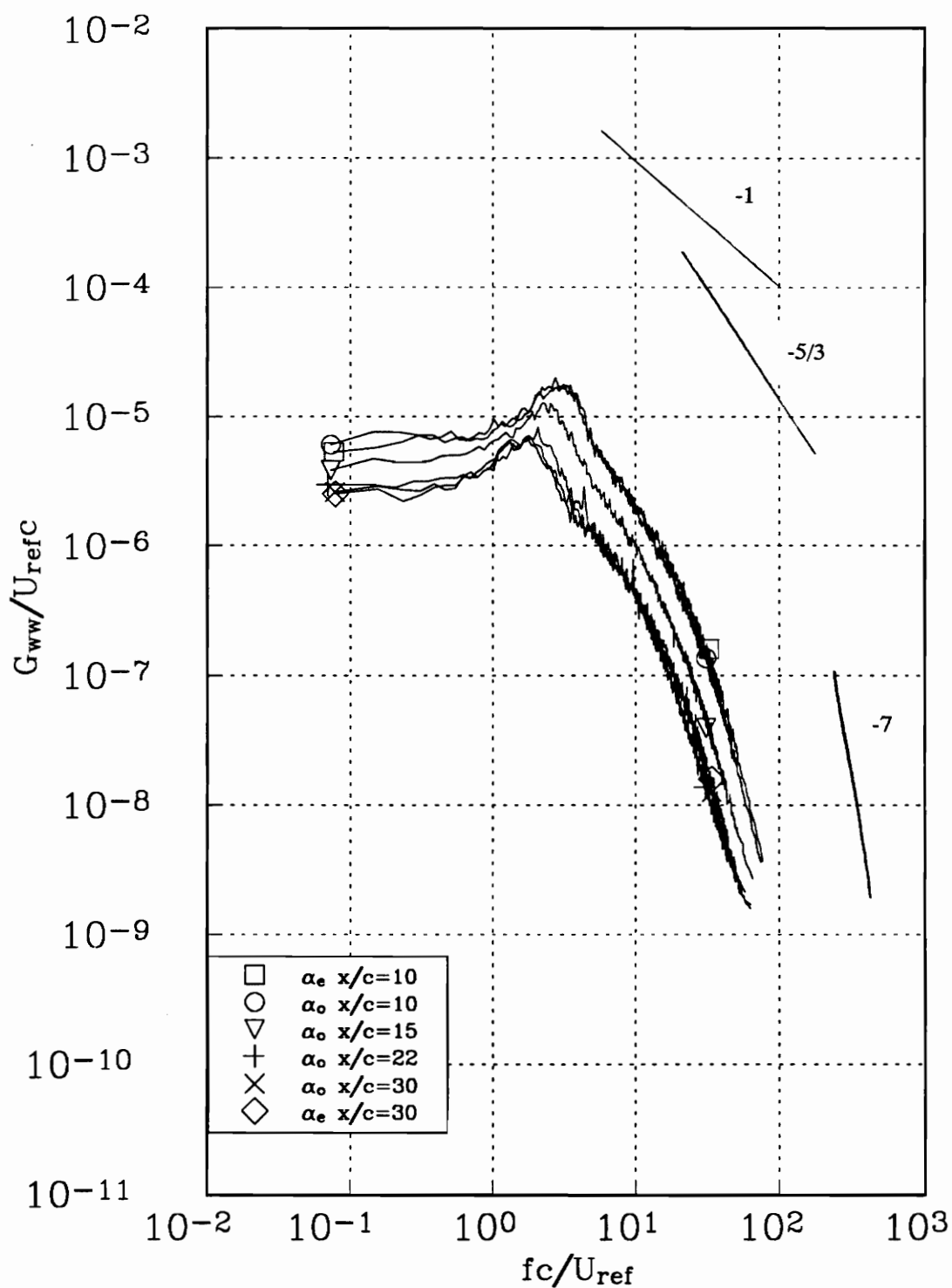


Figure 66c. w autospectra of the upper far field wing wake measured at $(z-z_o)/c=-0.1$ of the wake for both the co-rotating and counter rotating pairs.

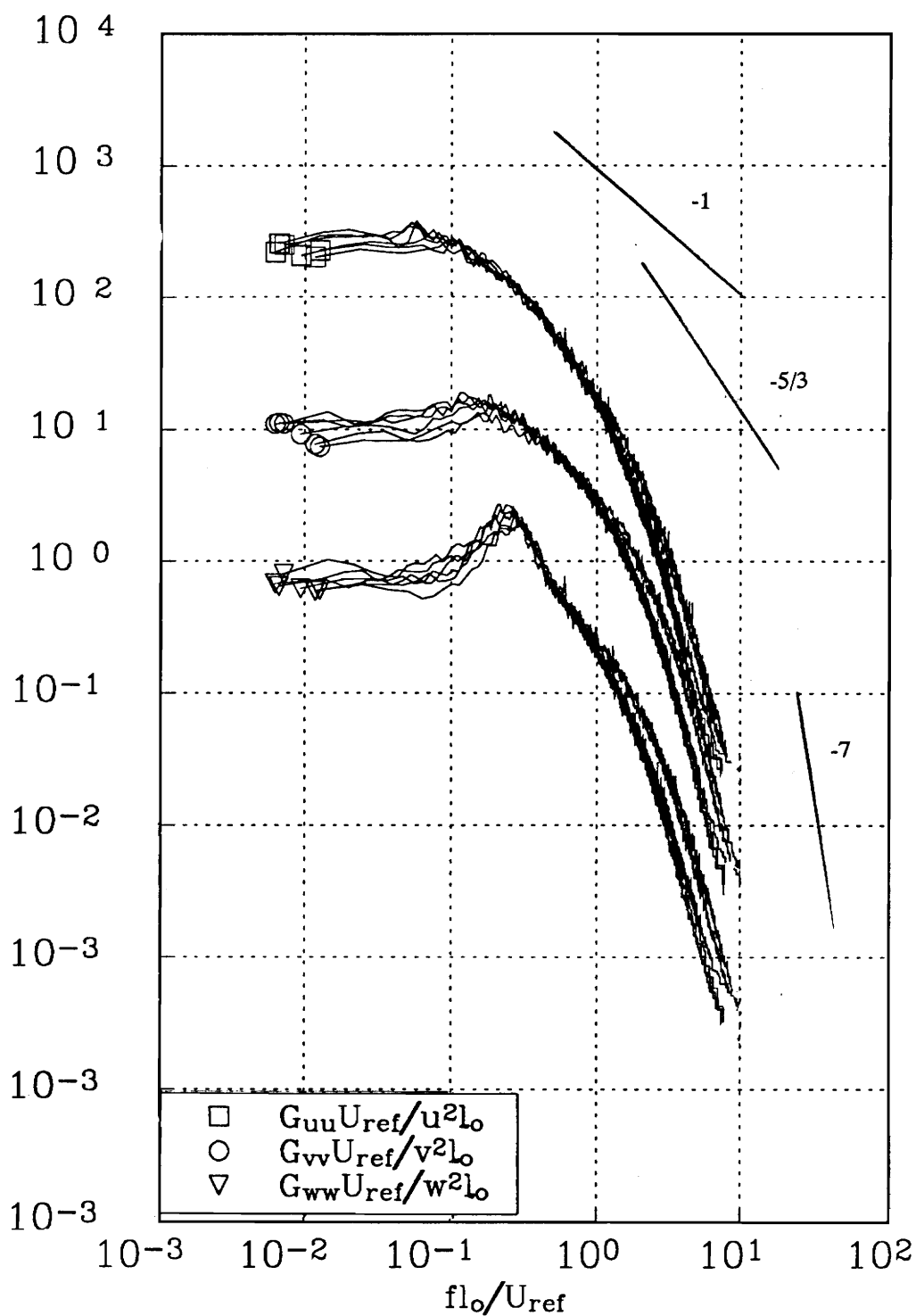


Figure 67. Autospectra normalized on similarity variables measured at the centerline of the far field wing wake for both the co-rotating and counter rotating pairs.

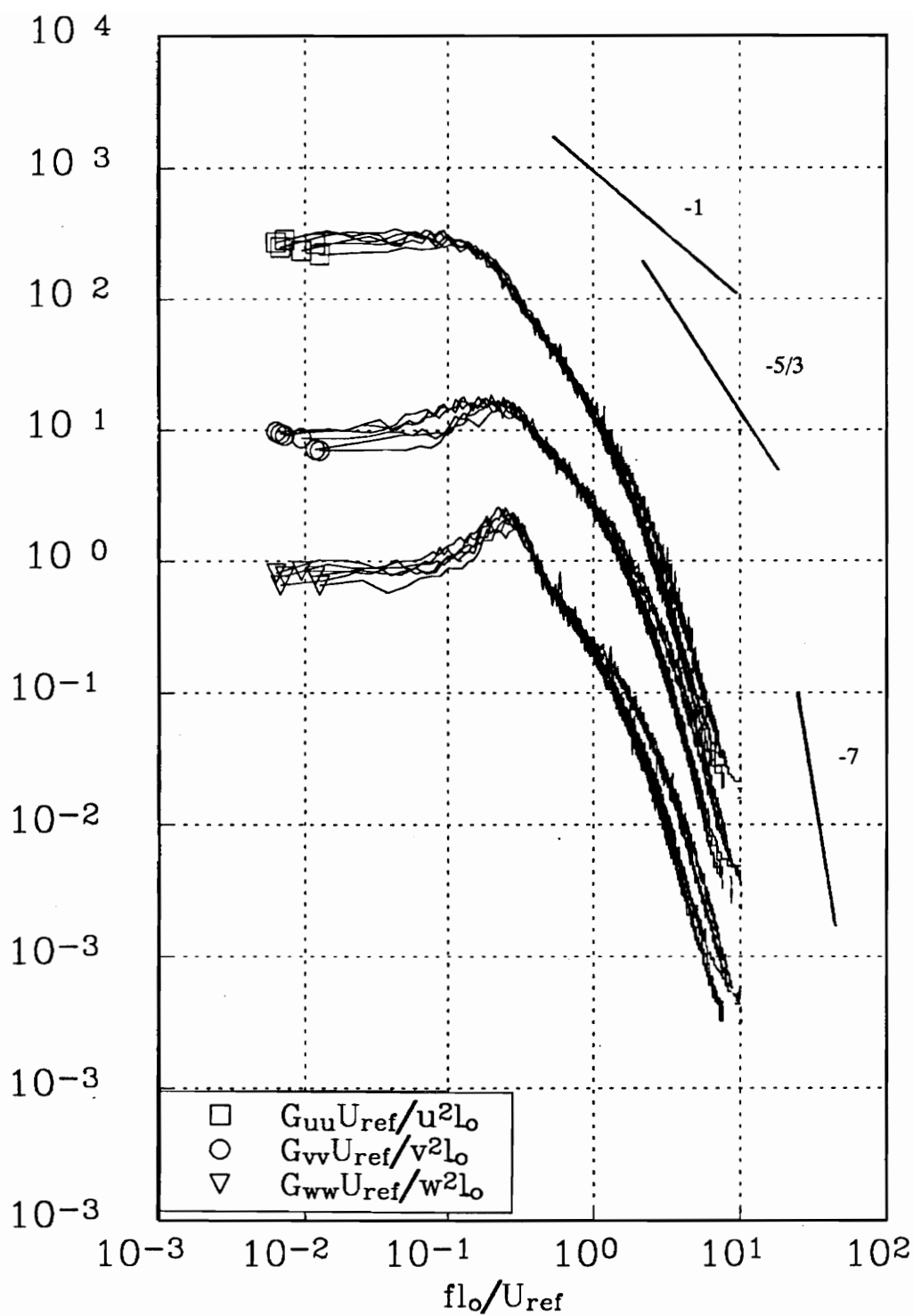


Figure 68. Autospectra normalized on similarity variables measured at $(z-z_o)/c=-0.1$ of the far field wing wake for both the co-rotating and counter rotating pairs.

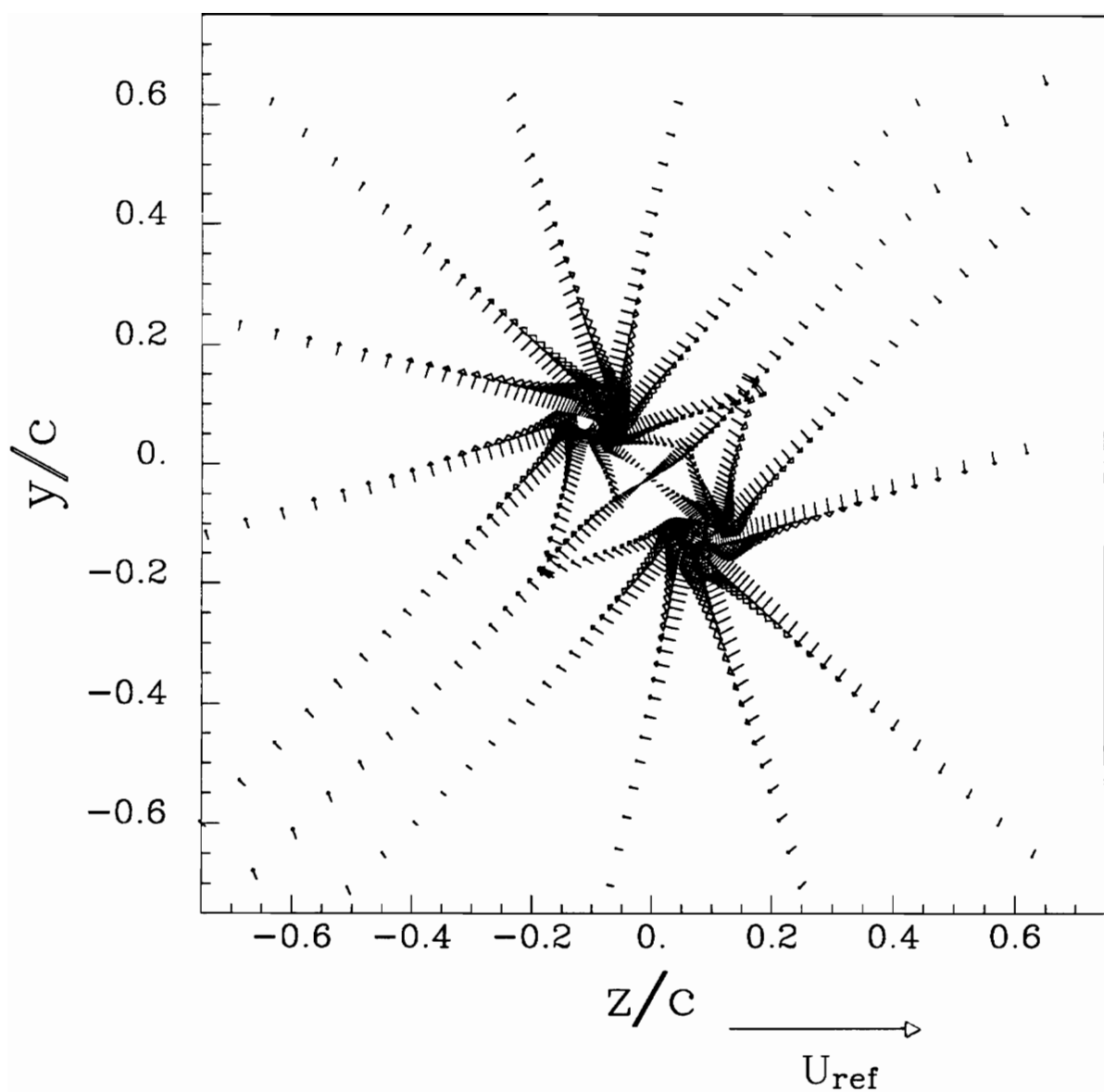
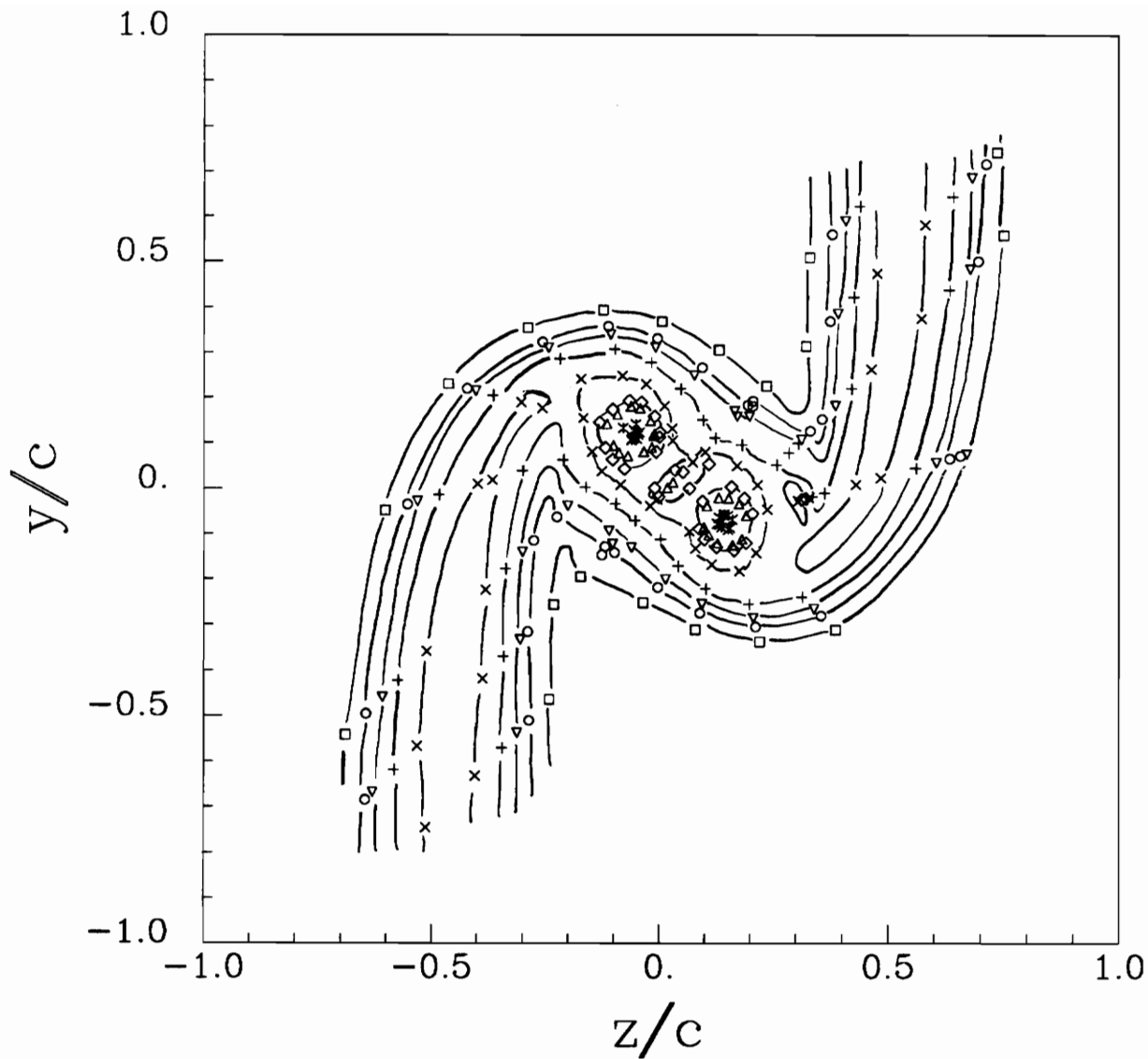
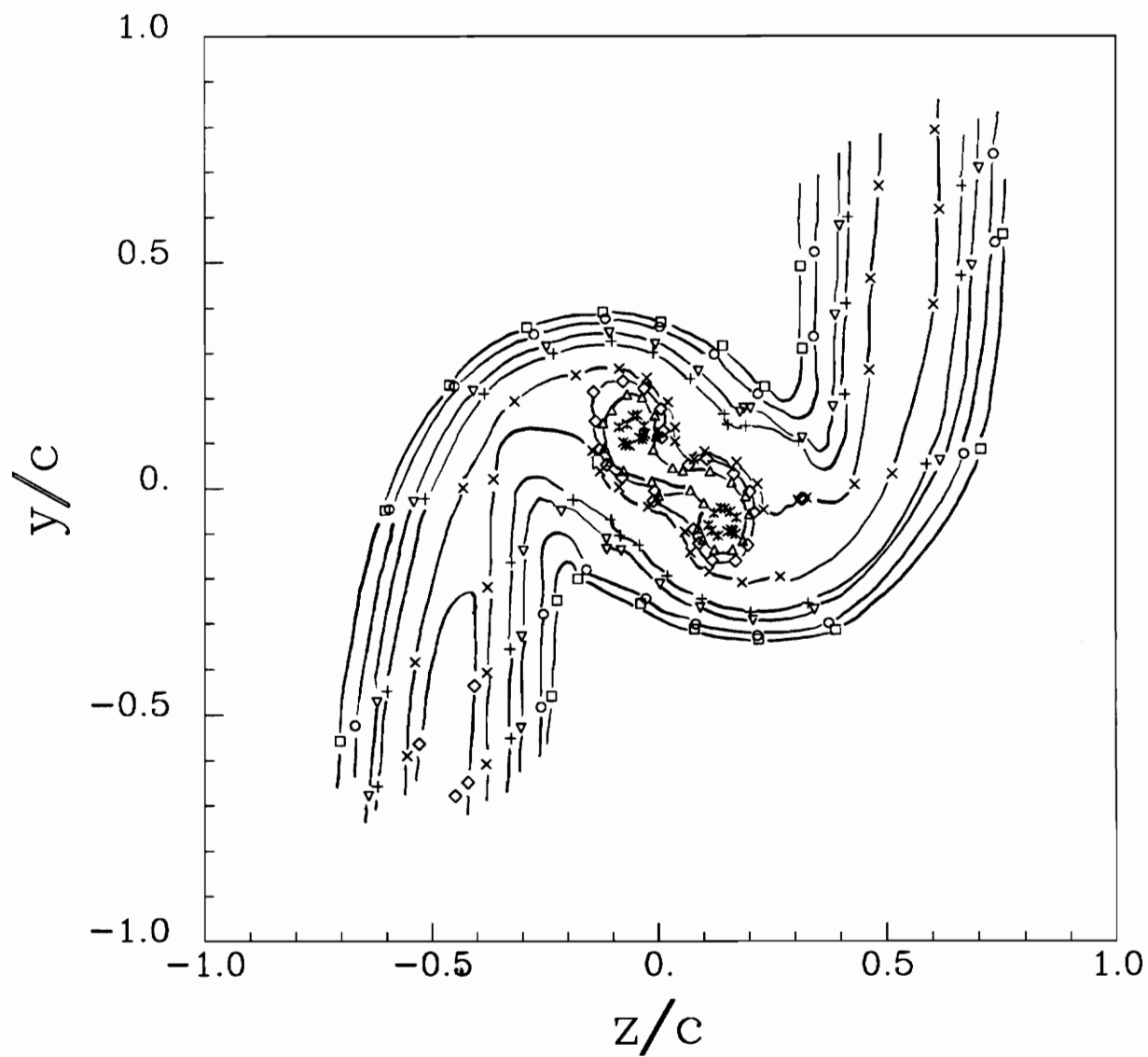


Figure 69. Mean secondary flow vectors of the co-rotating pair at $x/c=10$, angle of attack 5° , $Re_c=260,000$.



□	0.000010
○	0.000050
▽	0.000100
+	0.000250
×	0.000500
◇	0.000750
△	0.001000
⋈	0.005000

Figure 70. Contours of turbulent kinetic energy k/U_{ref}^2 for the co-rotating pair at $x/c=10$, angle of attack 5° , $Re_c=260,000$.



□	0.000005
○	0.000010
▽	0.000050
+	0.000100
×	0.000300
◇	0.000400
△	0.000500
*	0.001000

Figure 71. Contours of v_x^2/U_{ref}^2 for the co-rotating pair at $x/c=10$, angle of attack 5° , $Re_c=260,000$.

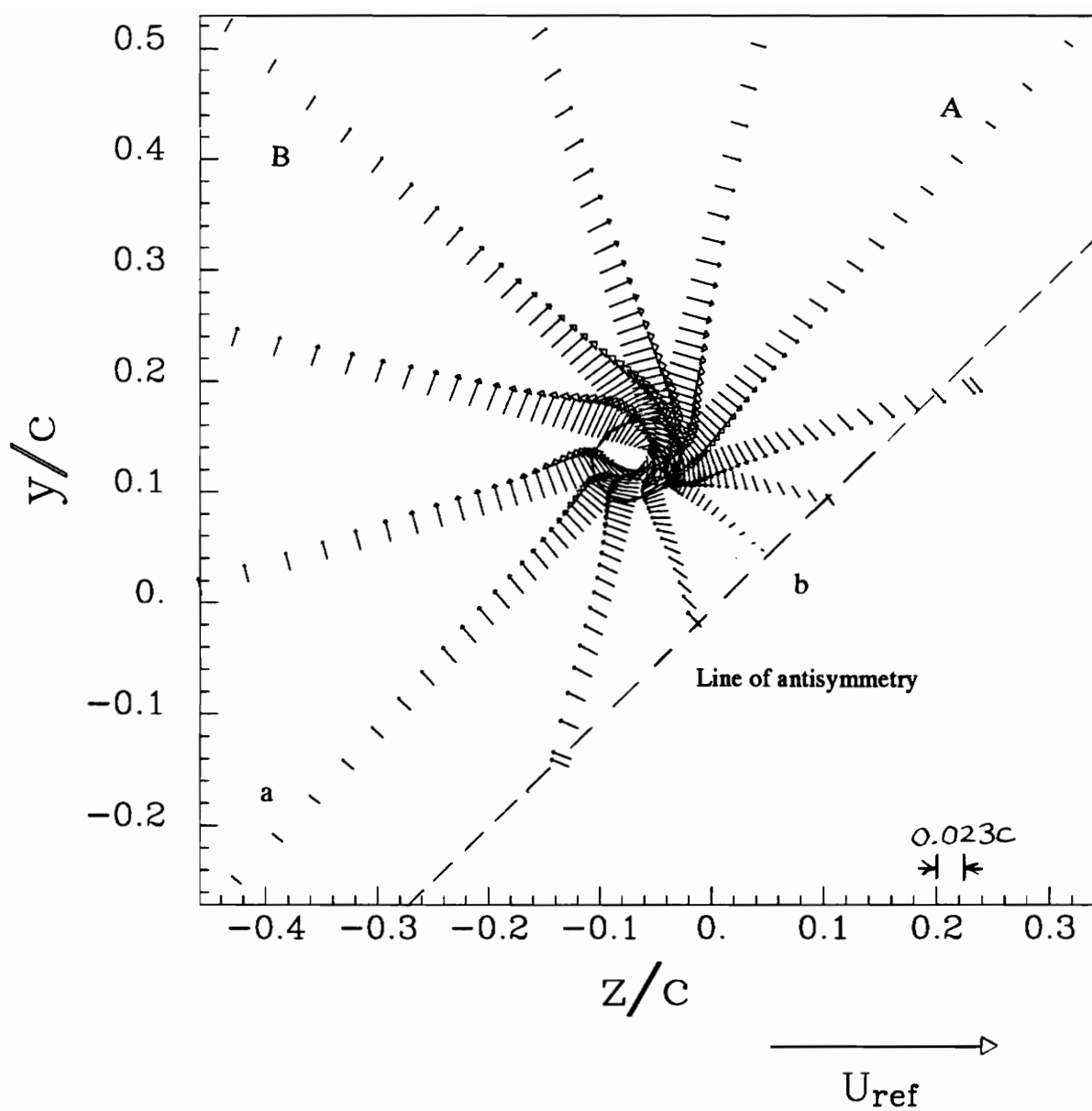


Figure 72. Core region showing mean secondary flows vectors for the upper co-rotating vortex at $x/c=10$, angle of attack= 5° , $Re_c=260,000$. Dotted line indicates core edge.

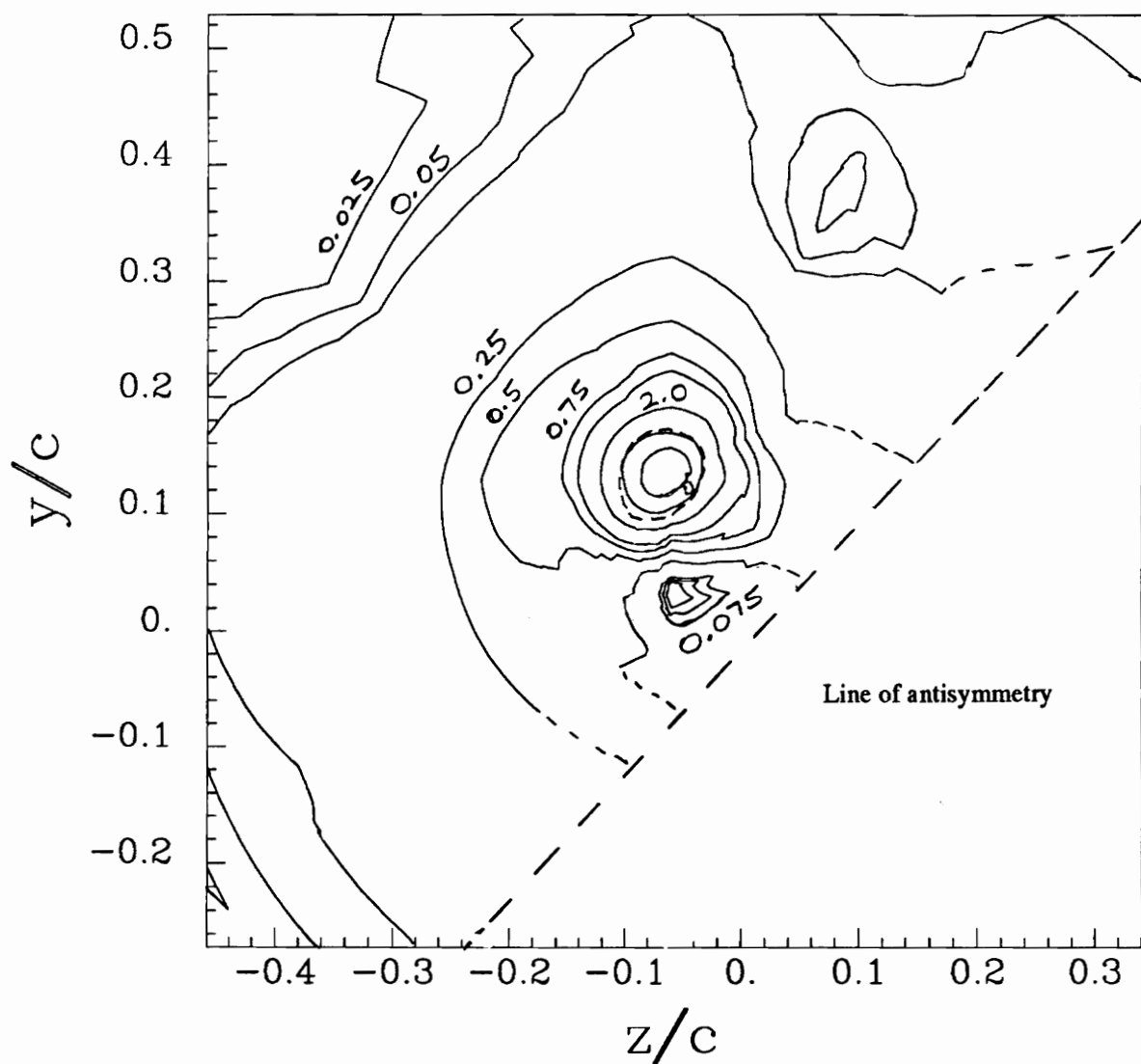


Figure 73. Core region showing contours of vorticity $\omega c/U_{\text{ref}}$ for the upper co-rotating vortex at $x/c=10$, angle of attack= 5° , $Re_c=260,000$. Dotted line indicates core edge.

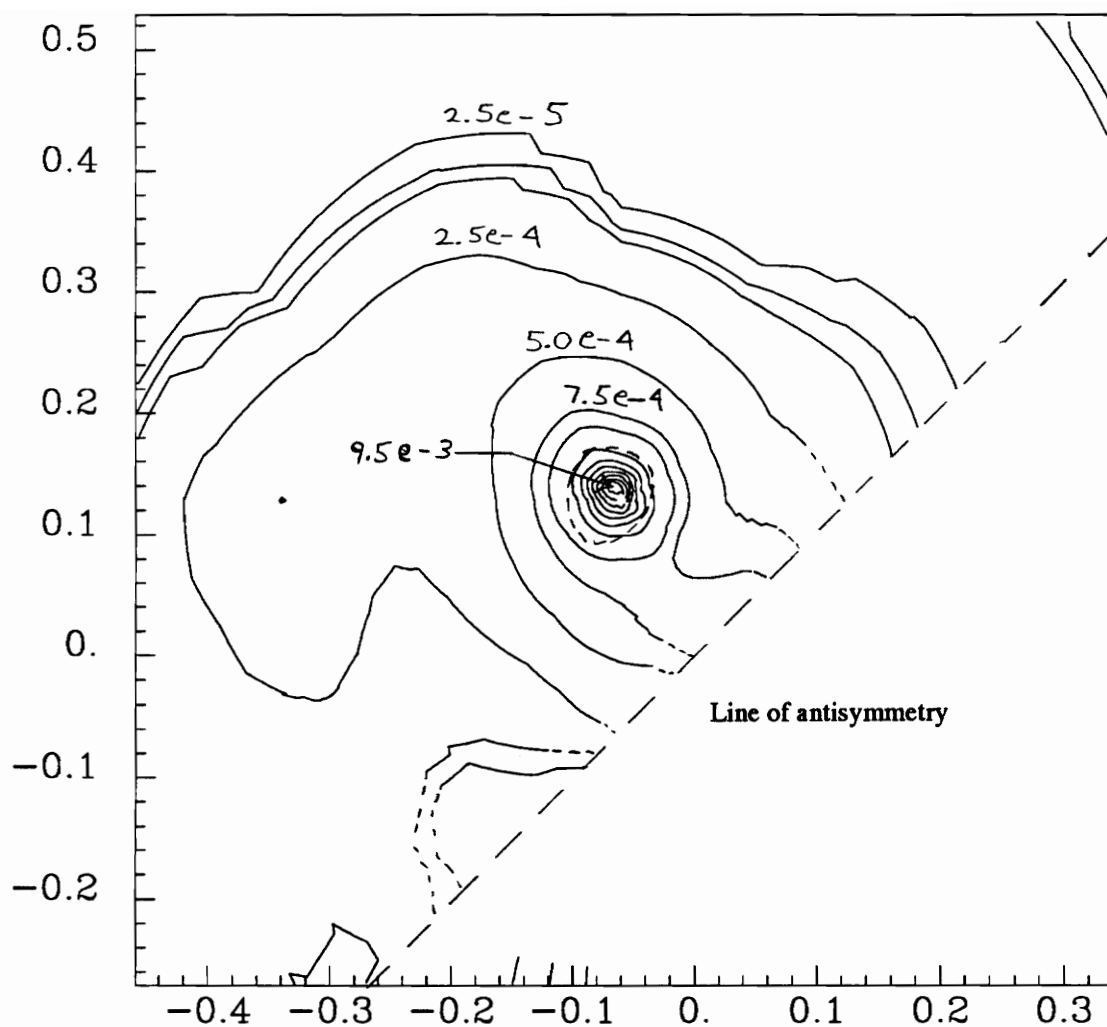


Figure 74. Core region showing contours of turbulent kinetic energy k/U_{ref}^2 for the upper co-rotating vortex at $x/c=10$, angle of attack $=5^\circ$, $Re_c=260,000$. Dotted line indicates core edge.

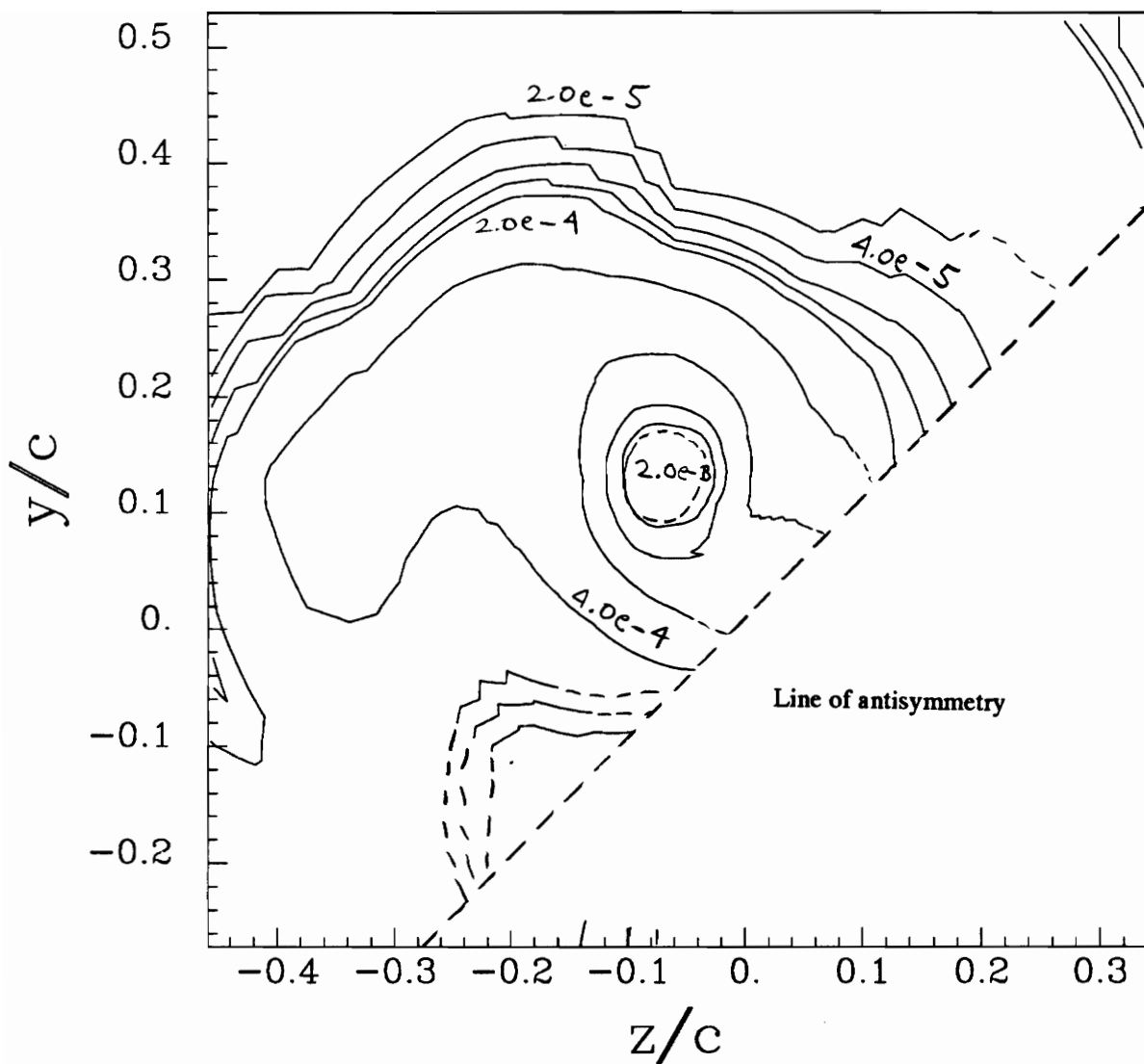


Figure 75. Core region showing contours of v_x^2/U_{ref}^2 for the upper co-rotating vortex at $x/c=10$, angle of attack= 5° , $Re_c=260,000$. Dotted line indicates core edge.

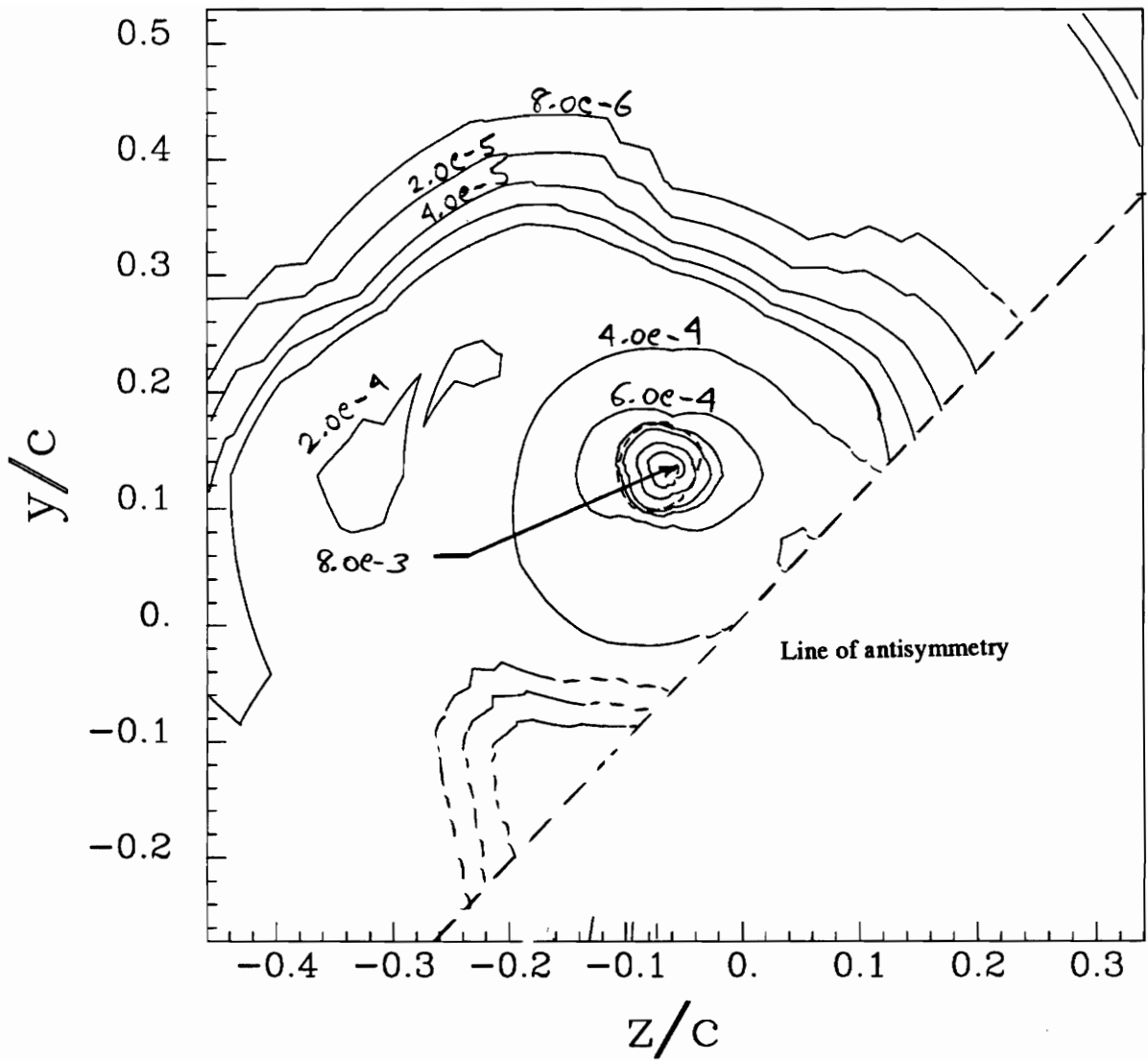


Figure 76. Core region showing contours of v_θ^2/U_{ref}^2 for the upper co-rotating vortex at $x/c=10$, angle of attack= 5° , $Re_c=260,000$. Dotted line indicates core edge.

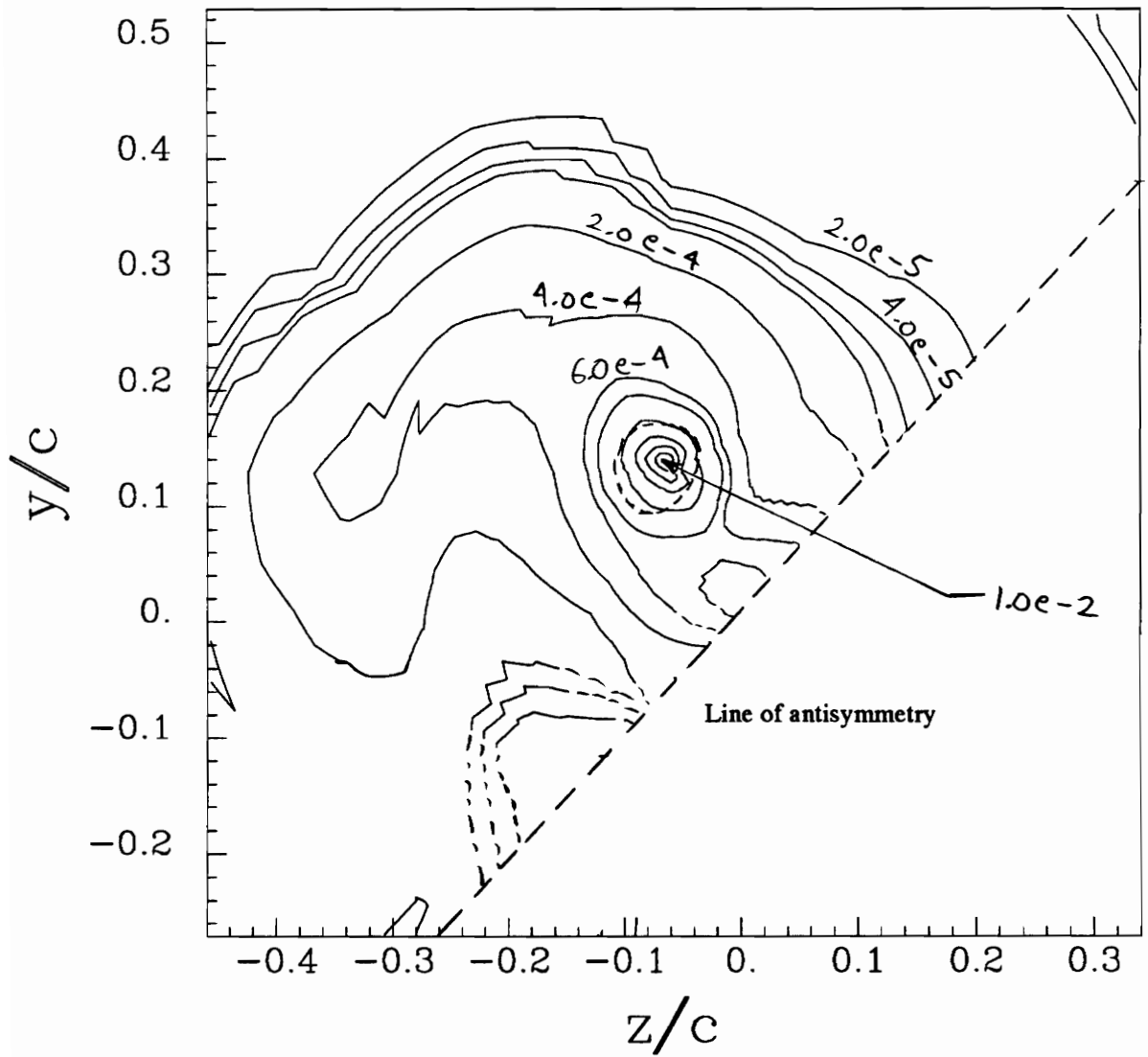


Figure 77. Core region showing contours of v_r^2/U_{ref}^2 for the upper co-rotating vortex at $x/c=10$, angle of attack= 5° , $Re_c=260,000$. Dotted line indicates core edge.

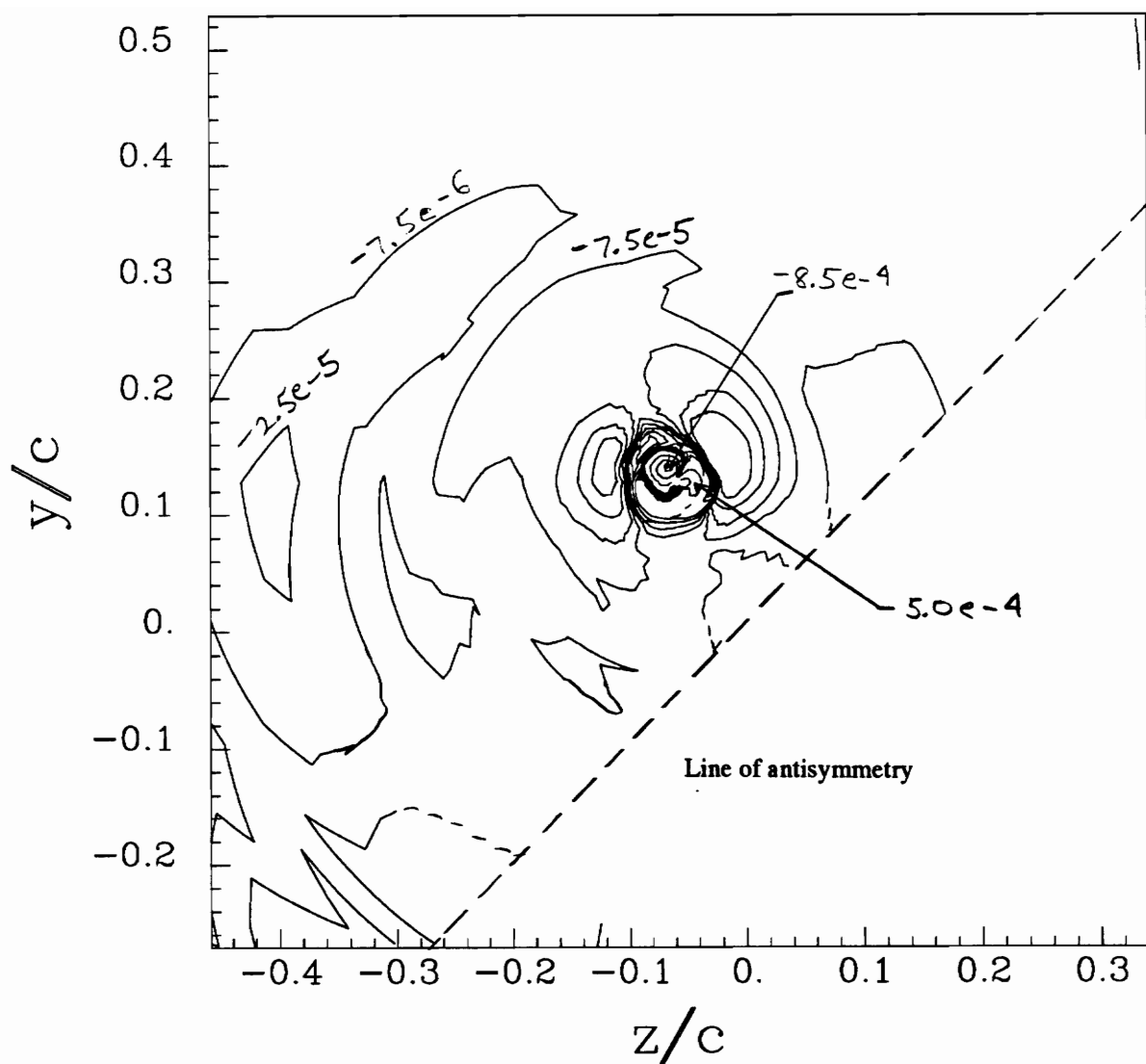


Figure 78. Core region showing contours of $v_x v_\theta / U_{ref}^2$ for the upper co-rotating vortex at $x/c=10$, angle of attack $=5^\circ$, $Re_c=260,000$. Dotted line indicates core edge.

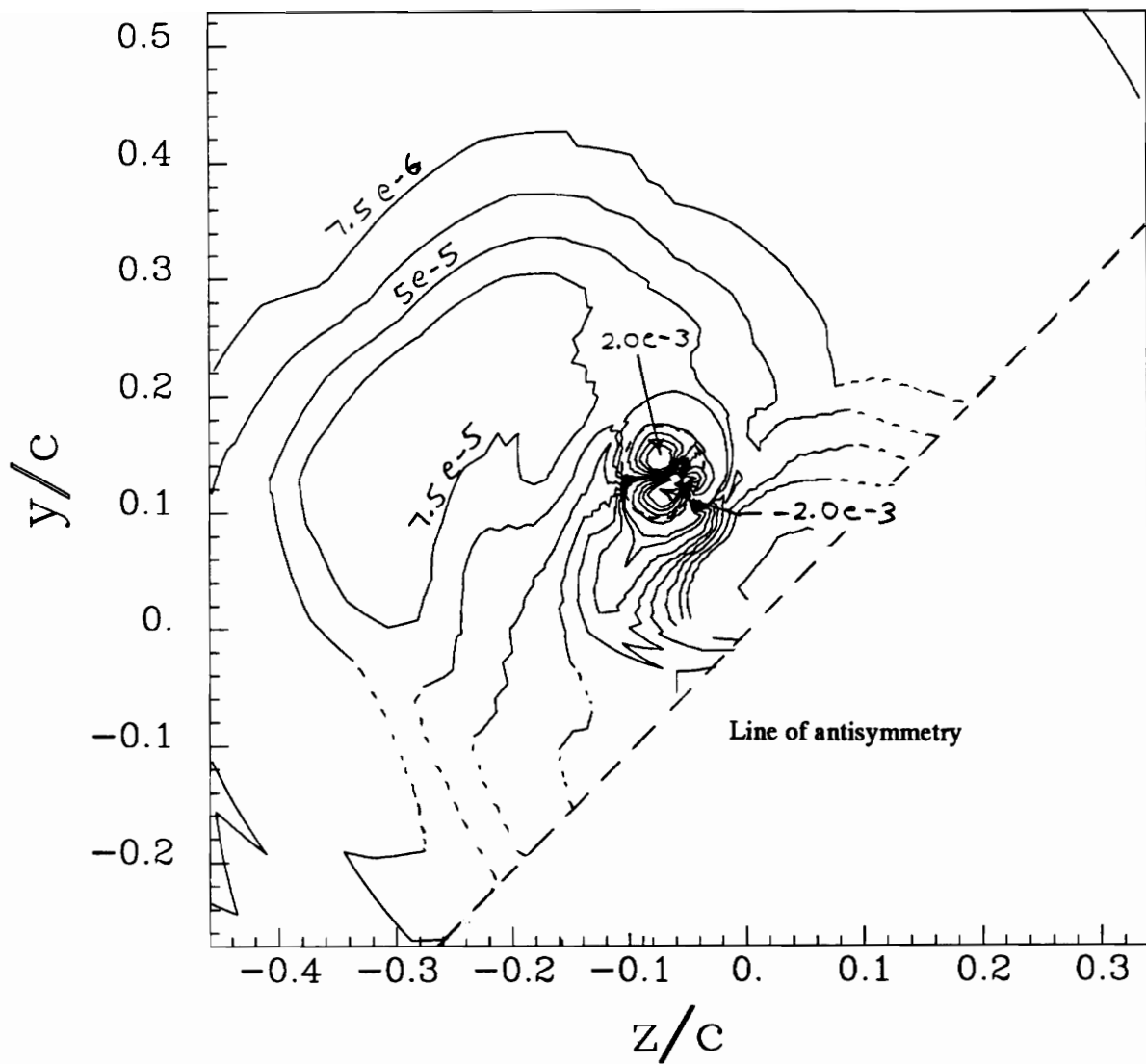


Figure 79. Core region showing contours of $v_{\theta}v_r/U_{ref}^2$ for the upper co-rotating vortex at $x/c=10$, angle of attack= 5° , $Re_c=260,000$. Dotted line indicates core edge.

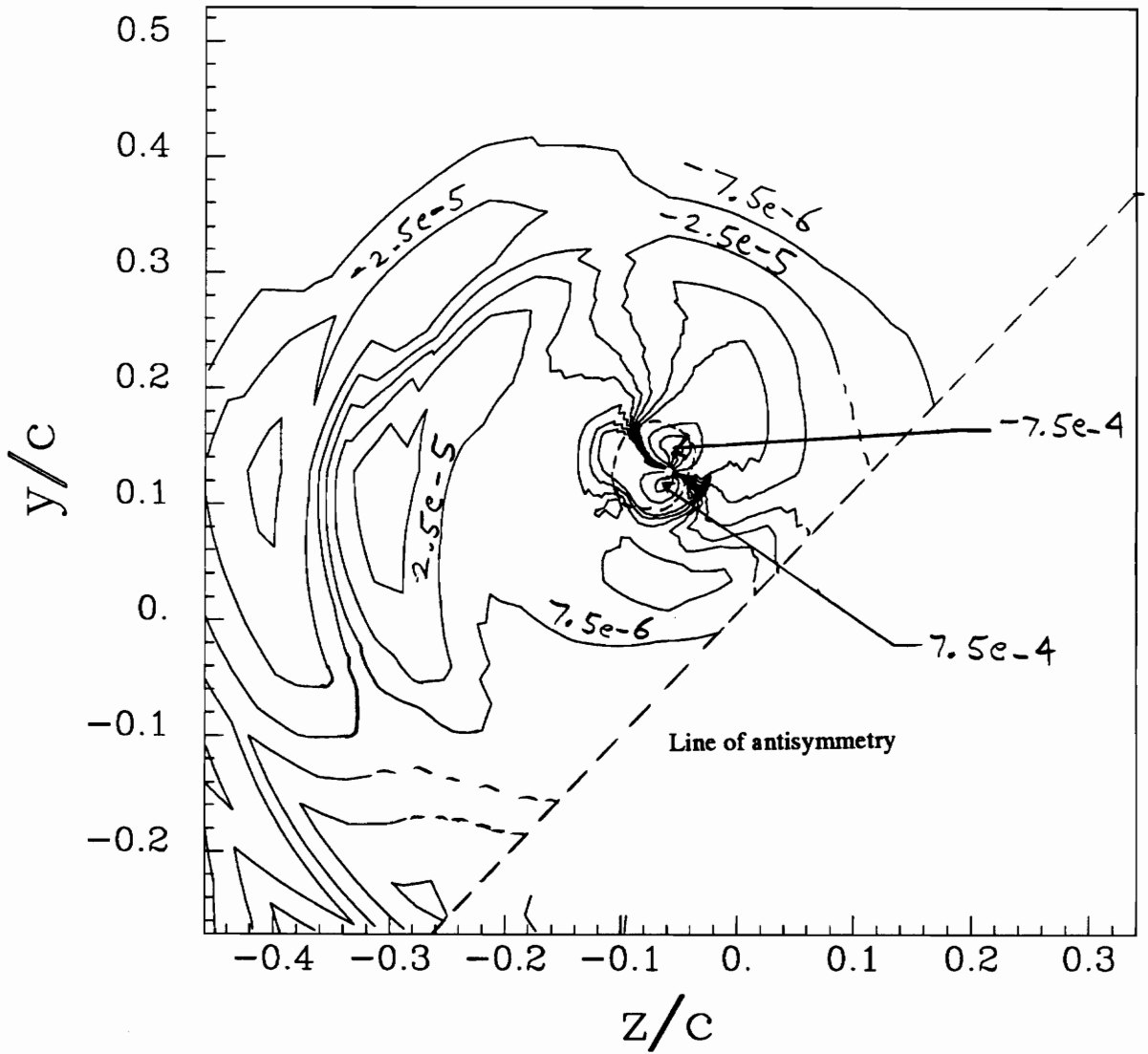


Figure 80. Core region showing contours of $v_x v_r / U_{ref}^2$ for the upper co-rotating vortex at $x/c=10$, angle of attack= 5° , $Re_c=260,000$. Dotted line indicates core edge.

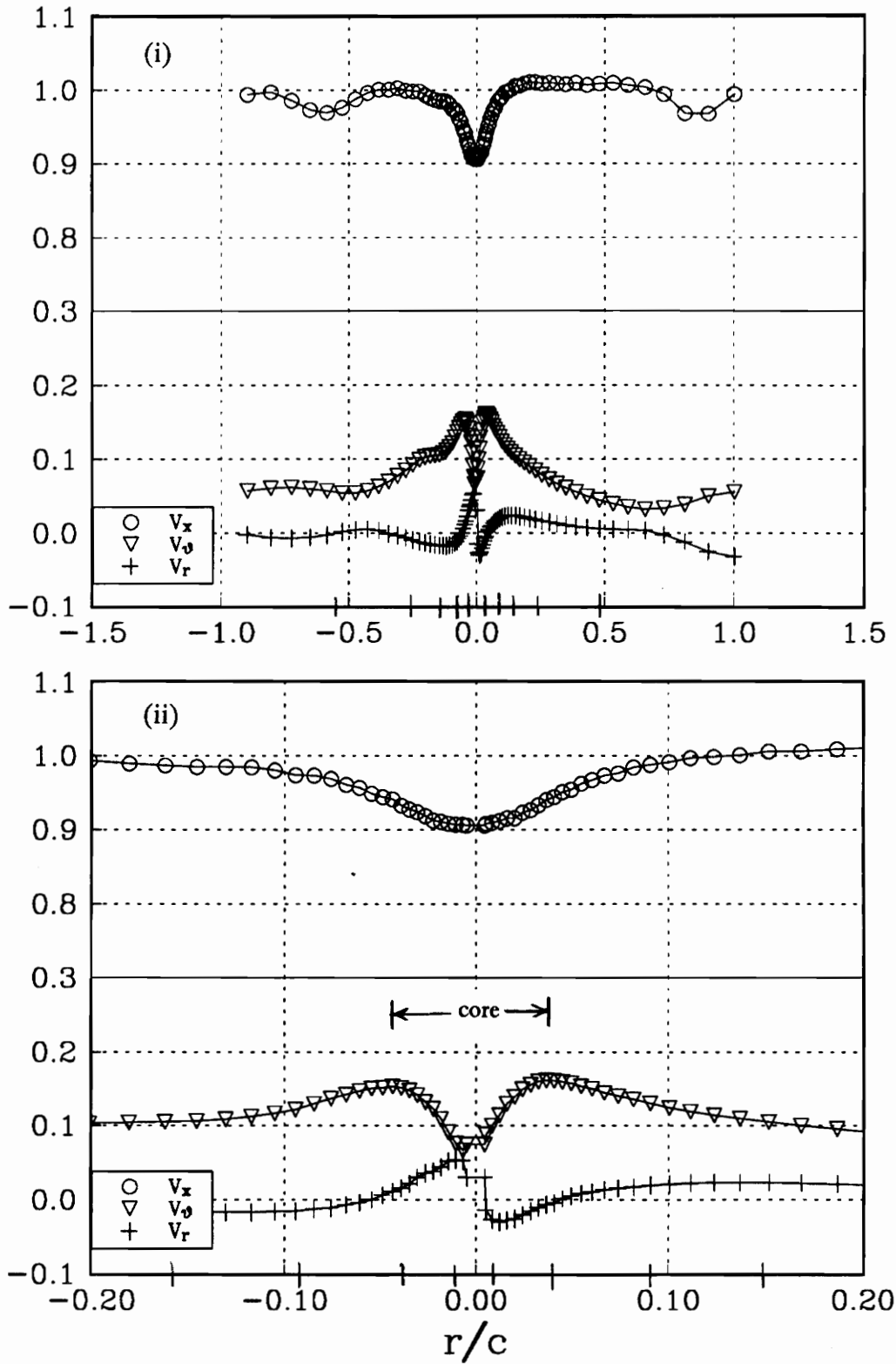


Figure 81a. Profile Aa mean velocities, measured parallel to the line of antisymmetry for the upper co-rotating vortex at $x/c=10$. (i) wake region, (ii) core region.

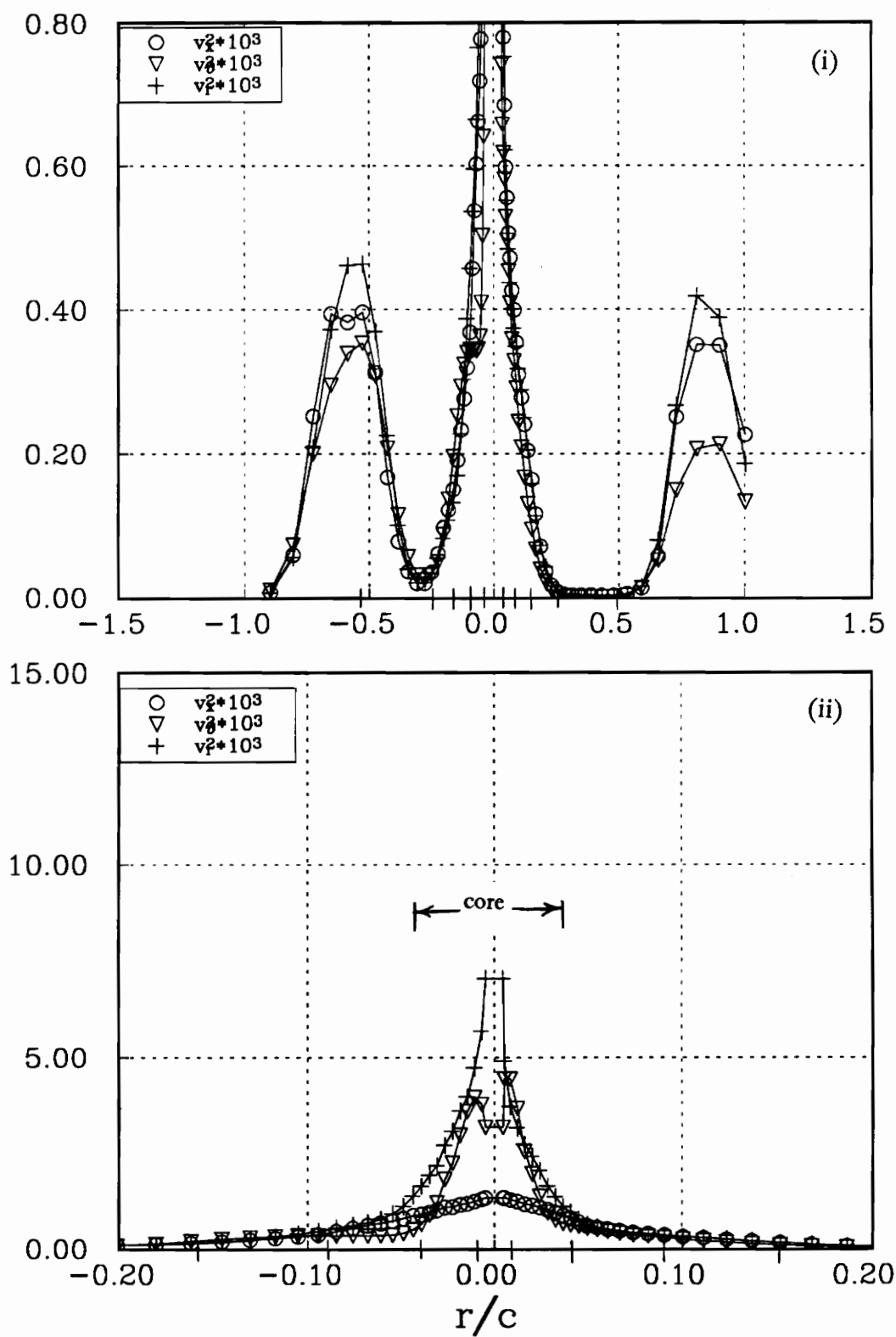


Figure 81b. Profile Aa normal stresses, measured parallel to the line of antisymmetry for the upper co-rotating vortex at $x/c=10$. (i) wake region, (ii) core region.

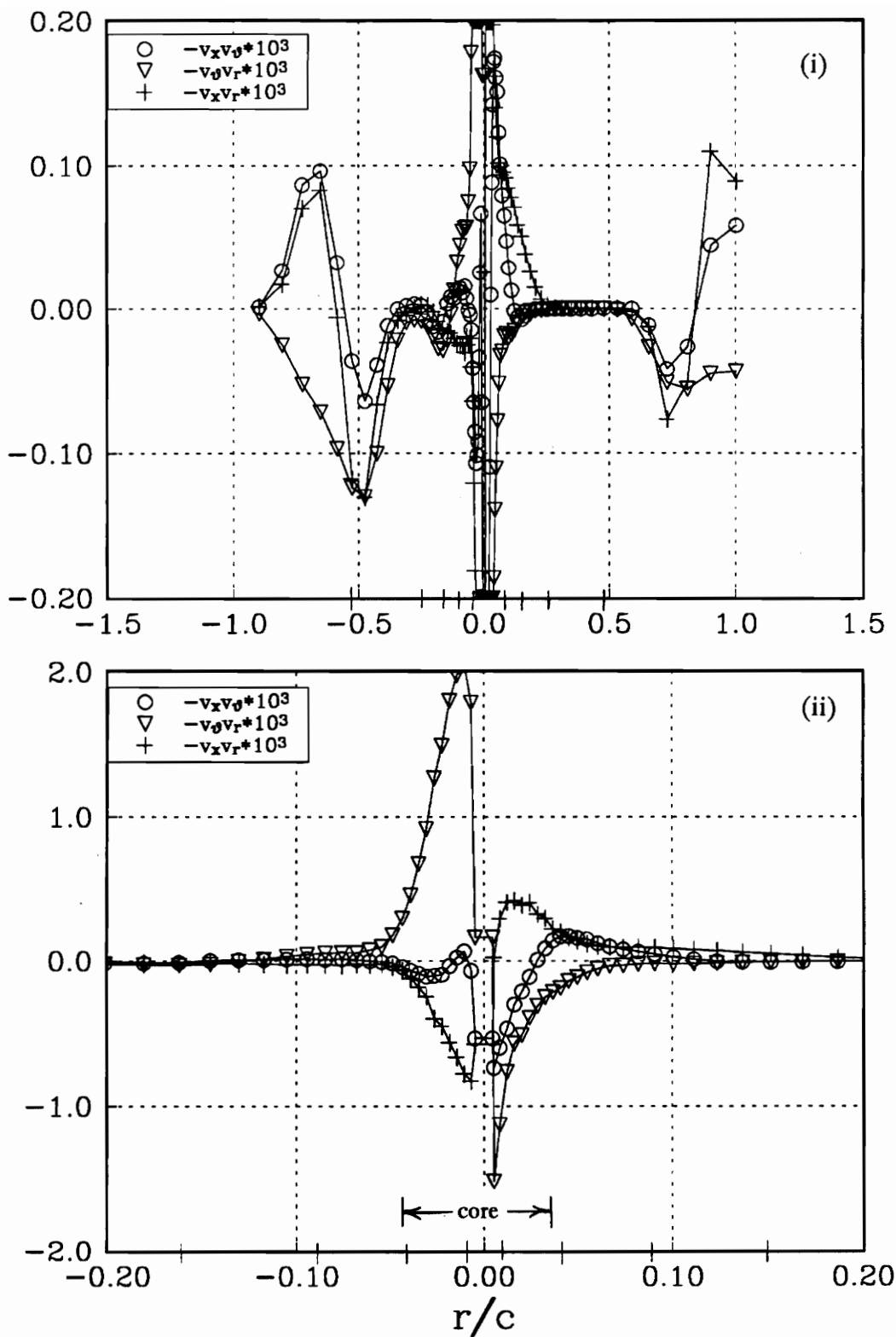


Figure 81c. Profile Aa shear stresses, measured parallel to the line of antisymmetry for the upper co-rotating vortex at $x/c=10$. (i) wake region, (ii) core region.

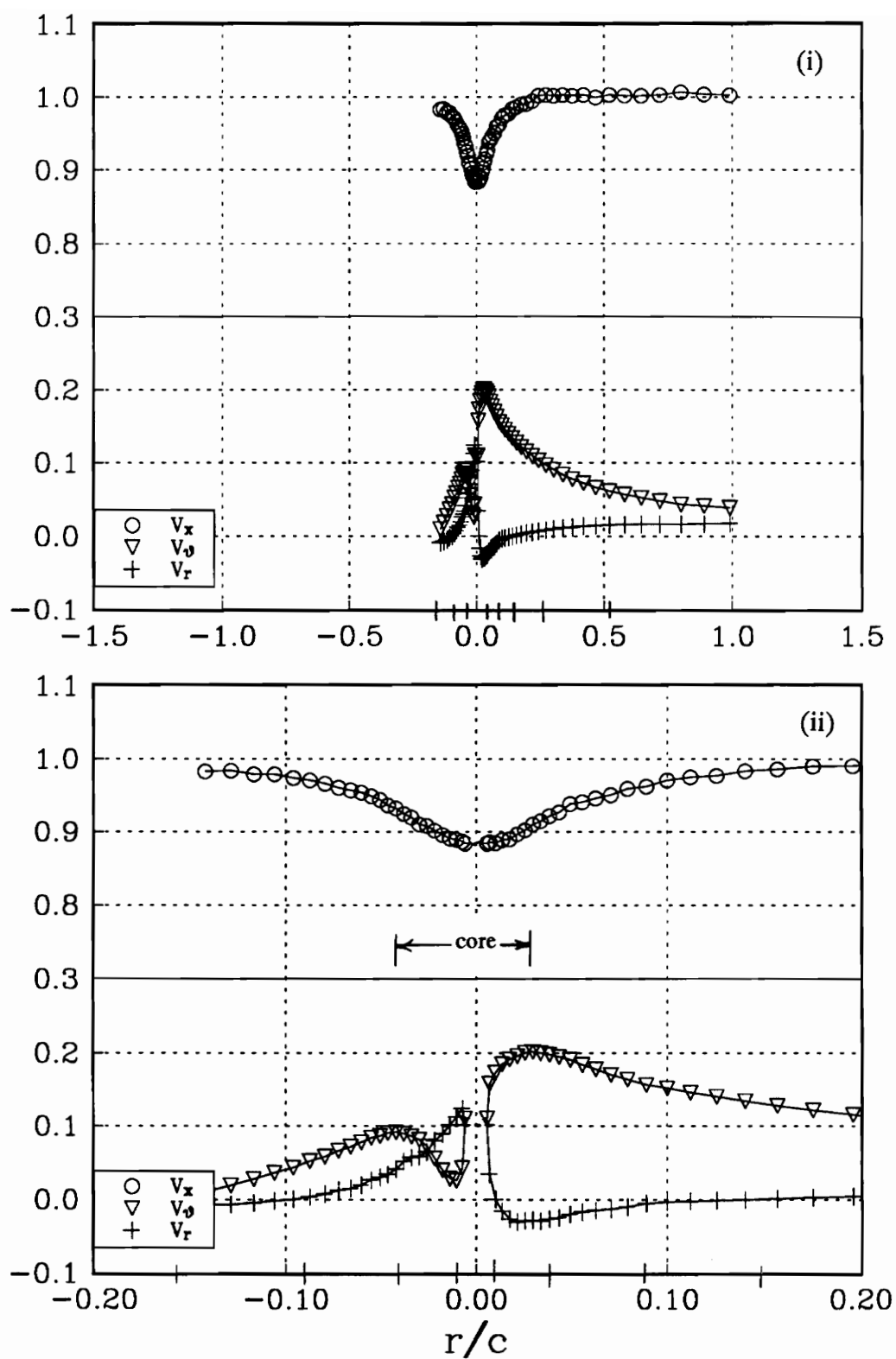


Figure 82a. Profile Bb mean velocities, measured perpendicular to the line of antisymmetry for the upper co-rotating vortex at $x/c=10$. (i) wake region, (ii) core region.

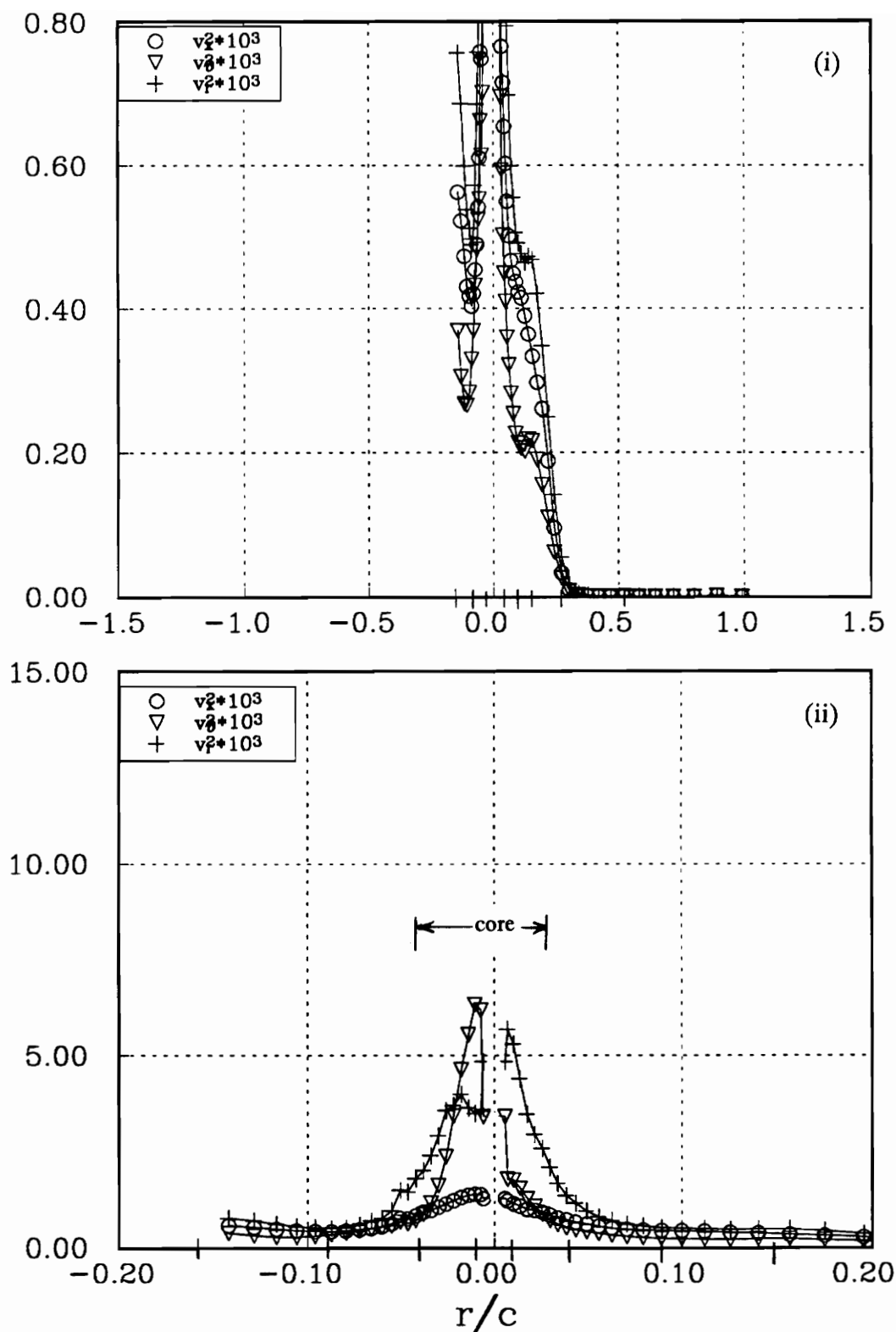


Figure 82b. Profile Bb normal stresses, measured perpendicular to the line of antisymmetry for the upper co-rotating vortex at $x/c=10$. (i) wake region, (ii) core region.

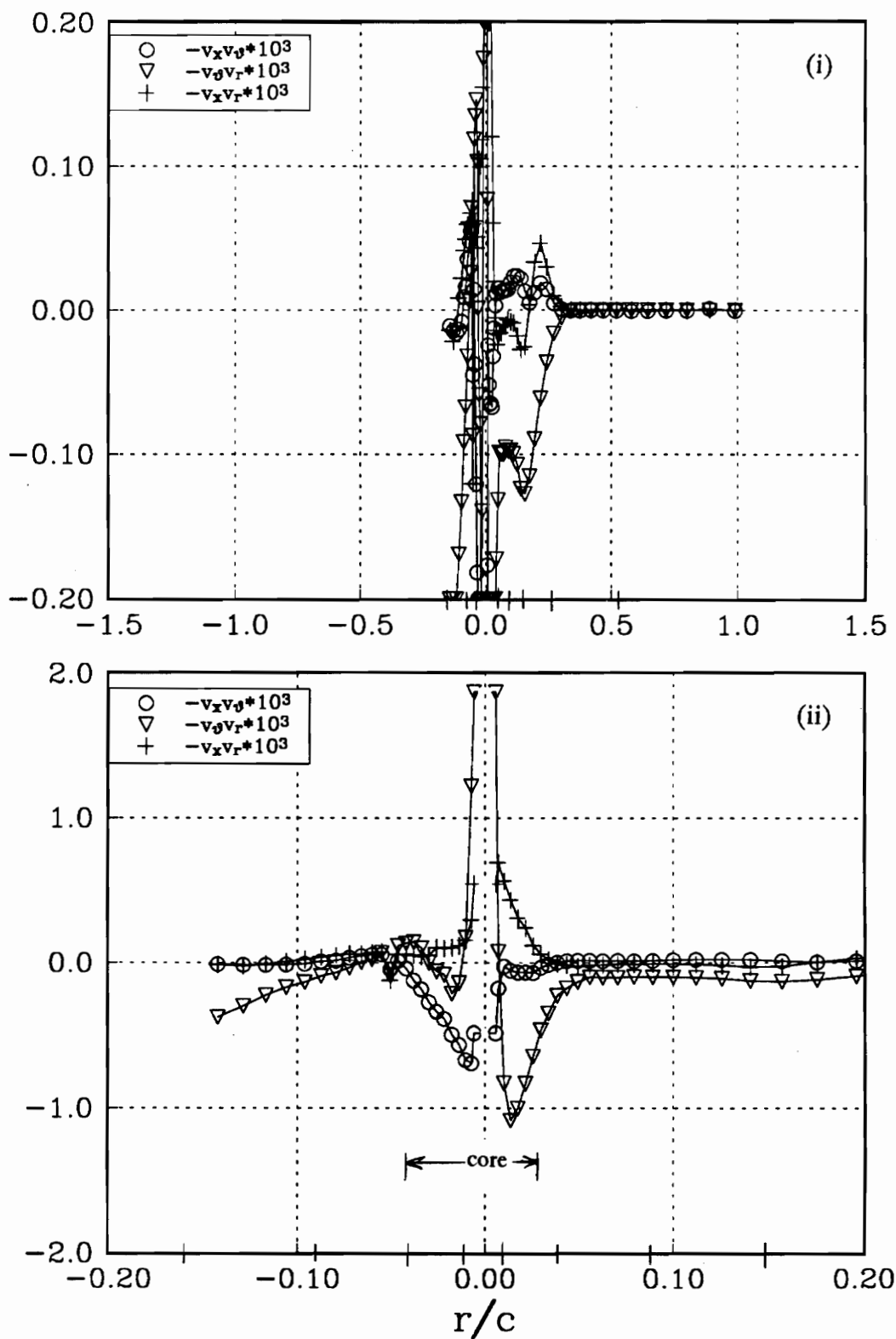


Figure 82c. Profile Bb shear stresses, measured perpendicular to the line of antisymmetry for the upper co-rotating vortex at $x/c=10$. (i) wake region, (ii) core region.

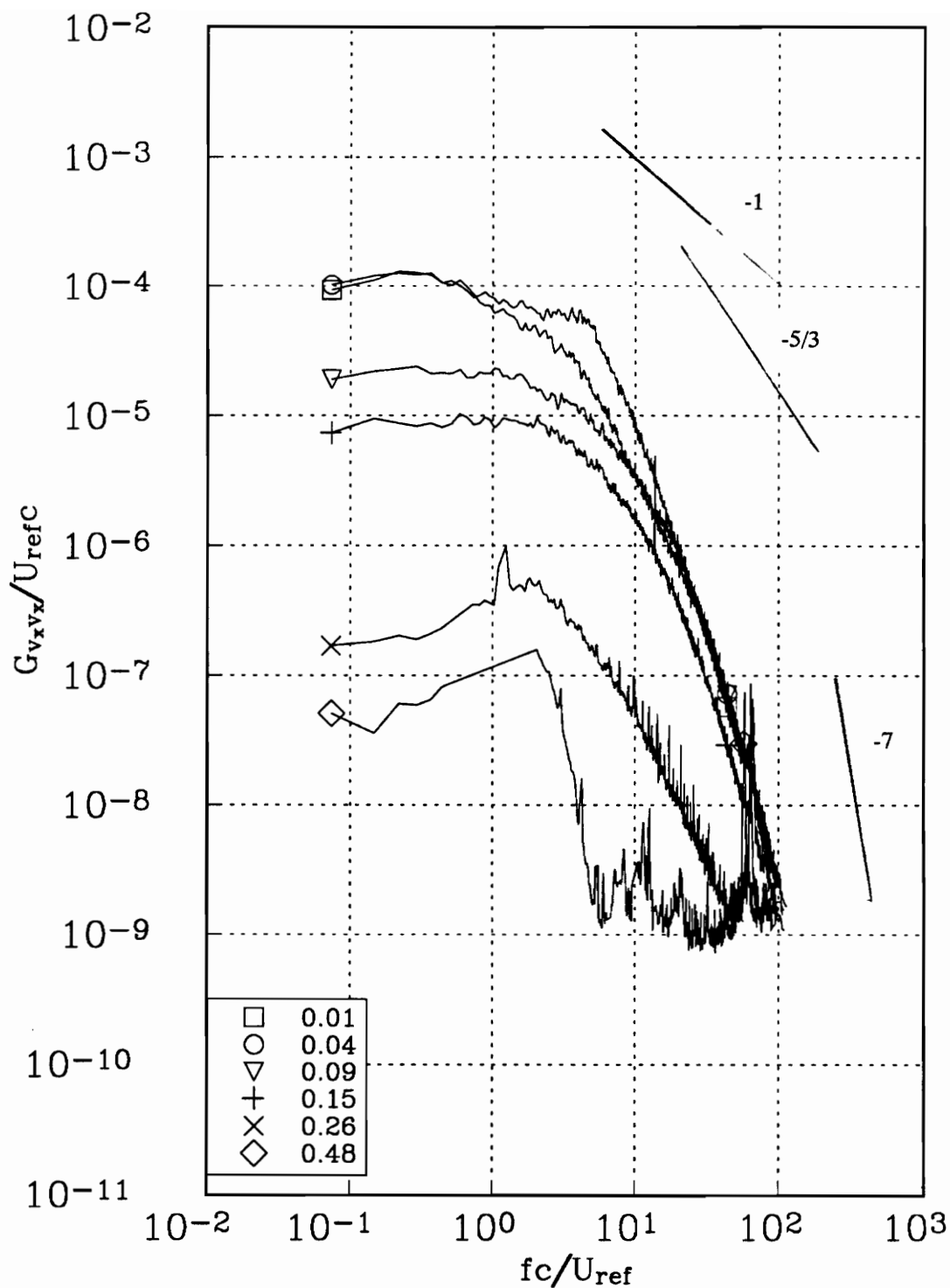


Figure 83a. v_x autospectra measured at representative radial locations along profile Aa for the upper co-rotating vortex at $x/c=10$. Tic marks in figure 81 indicate measured r/c locations.

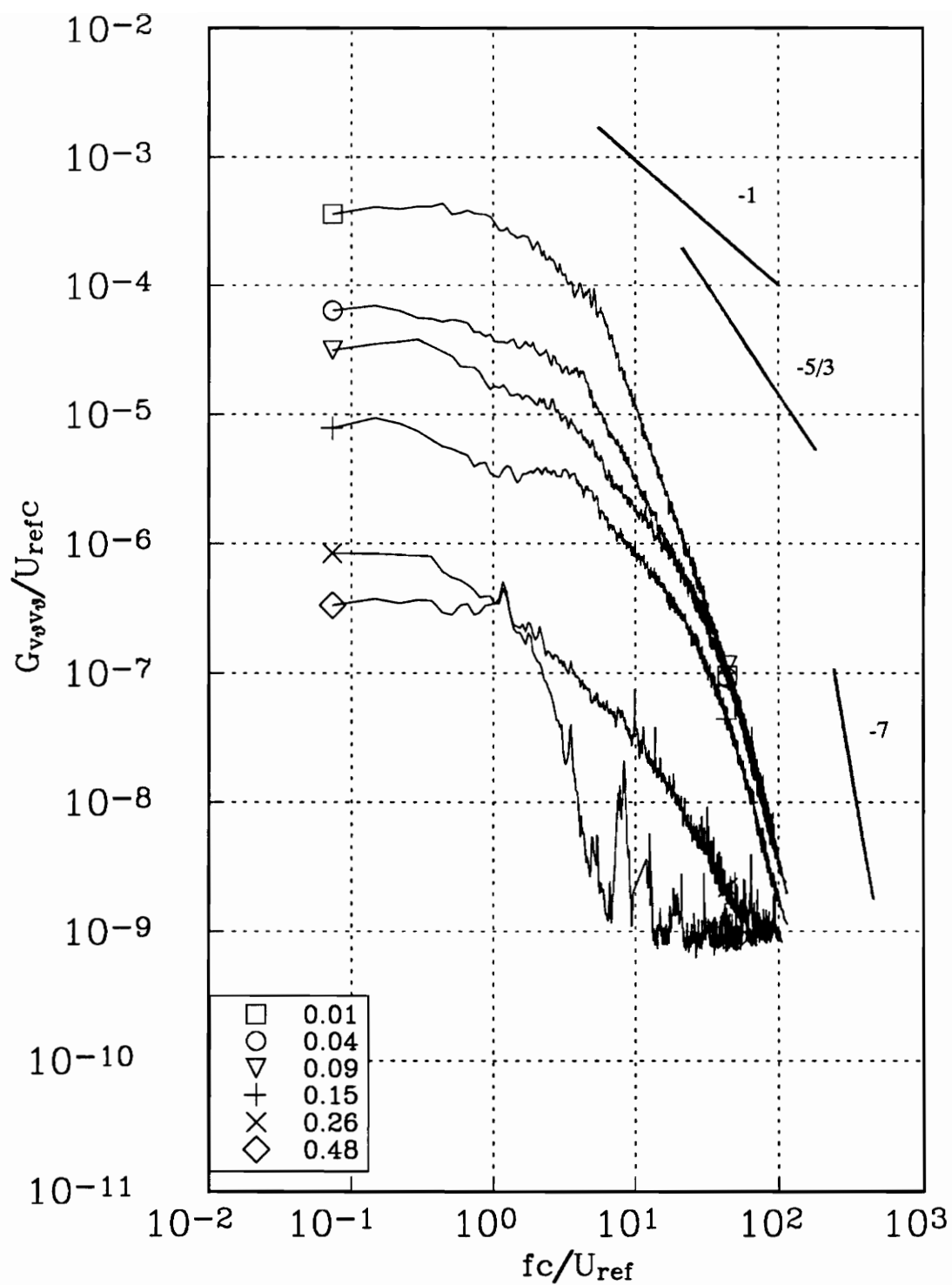


Figure 83b. v_{θ} autospectra measured at representative radial locations along profile Aa for the upper co-rotating vortex at $x/c=10$. Tic marks in figure 81 indicate measured r/c locations.

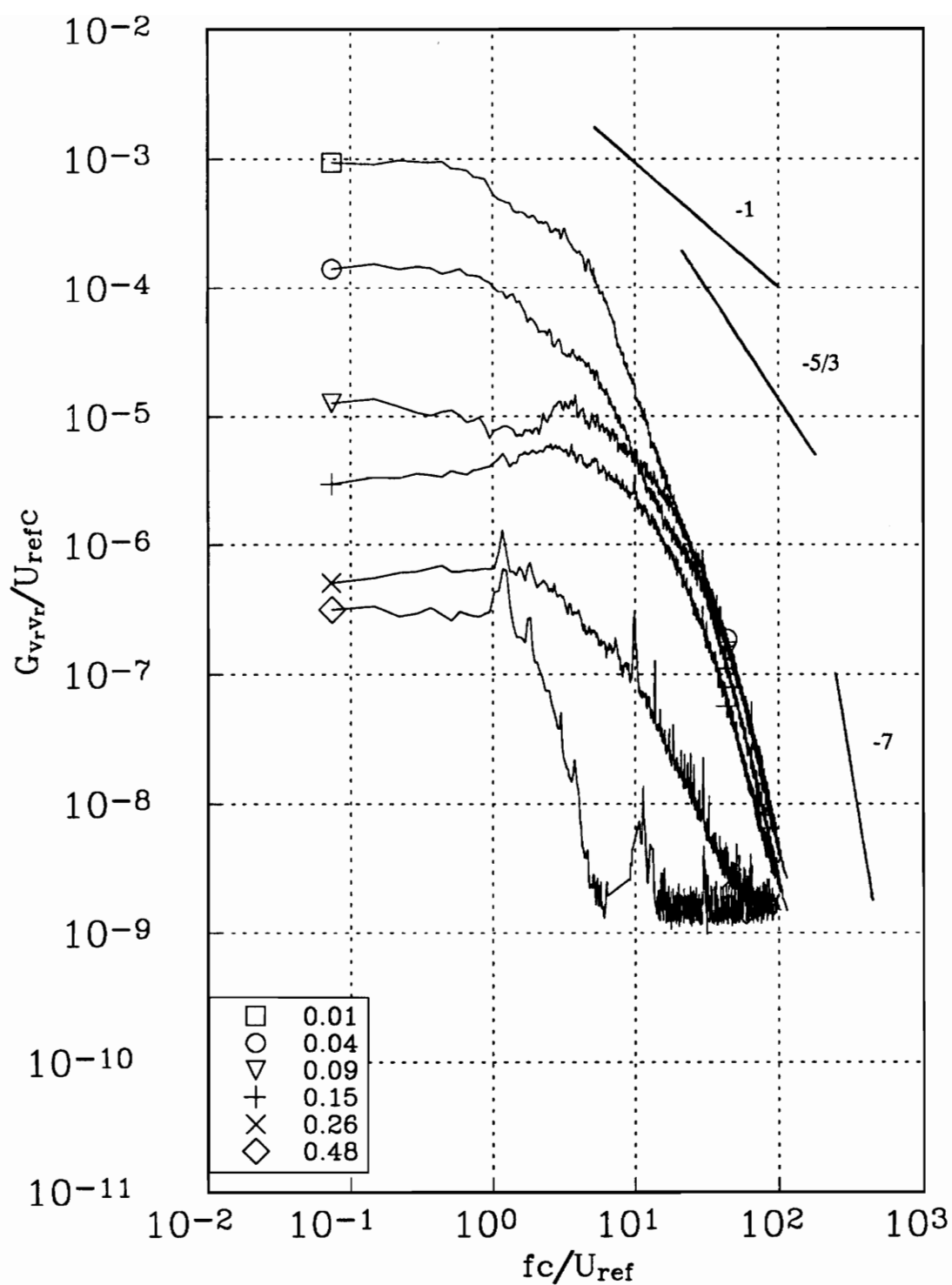


Figure 83c. v_r autospectra measured at representative radial locations along profile Aa for the upper co-rotating vortex at $x/c=10$. Tic marks in figure 81 indicate measured r/c locations.

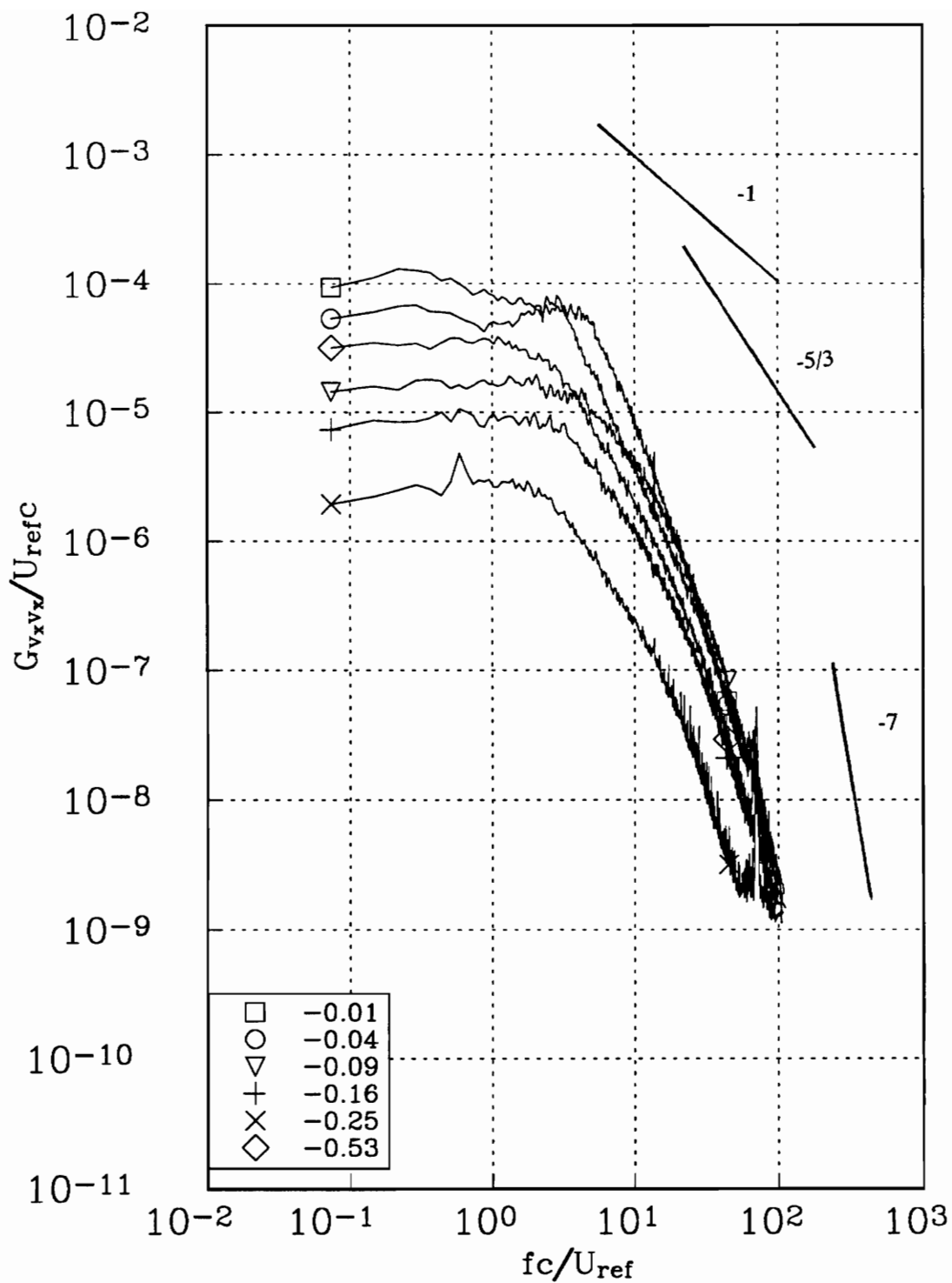


Figure 84a. v_x autospectra measured at representative radial locations along profile Aa for the upper co-rotating vortex at $x/c=10$. Tic marks in figure 81 indicate measured r/c locations.

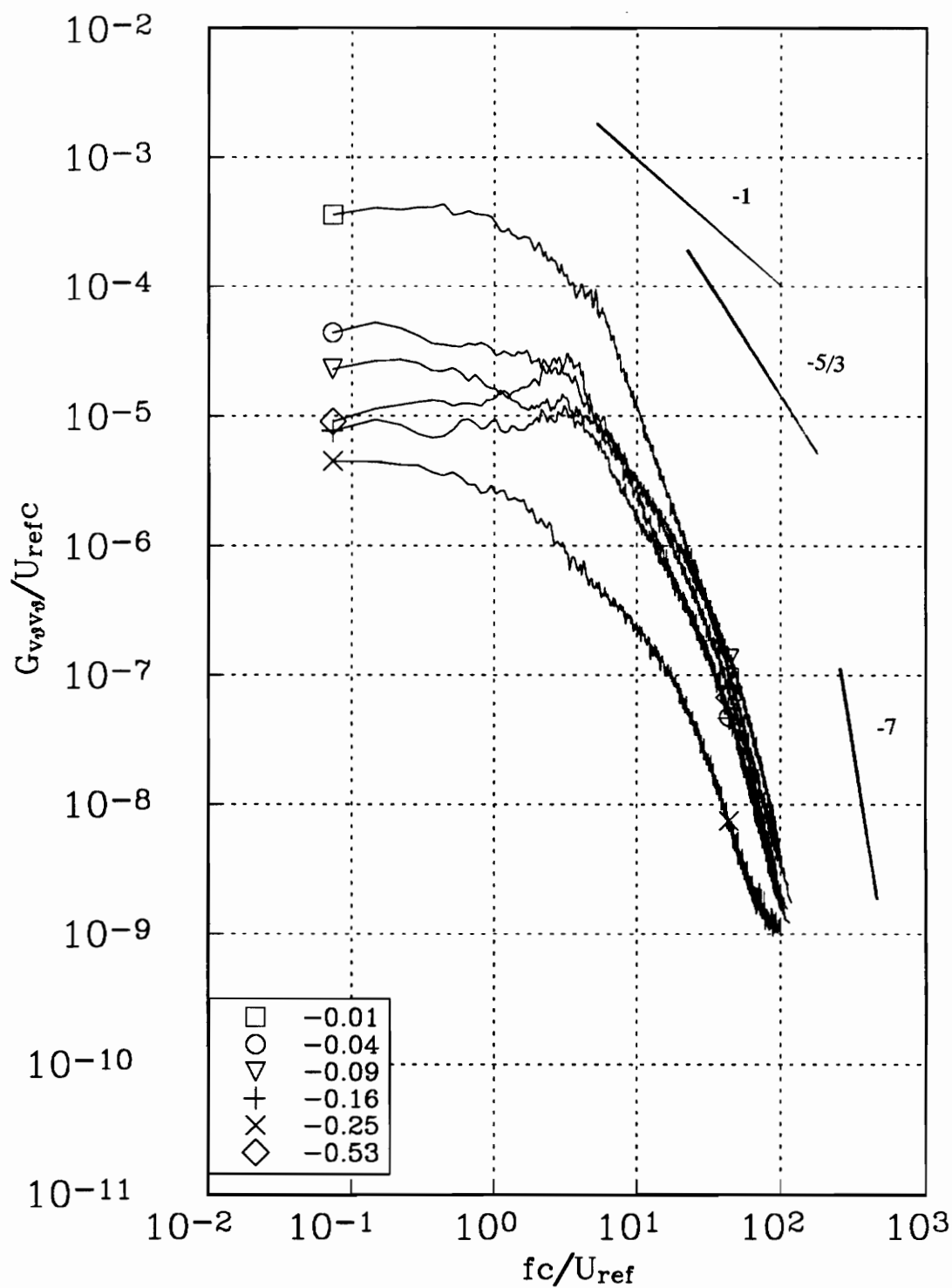


Figure 84b. v_θ autospectra measured at representative radial locations along profile Aa for the upper co-rotating vortex at $x/c=10$. Tic marks in figure 81 indicate measured r/c locations.

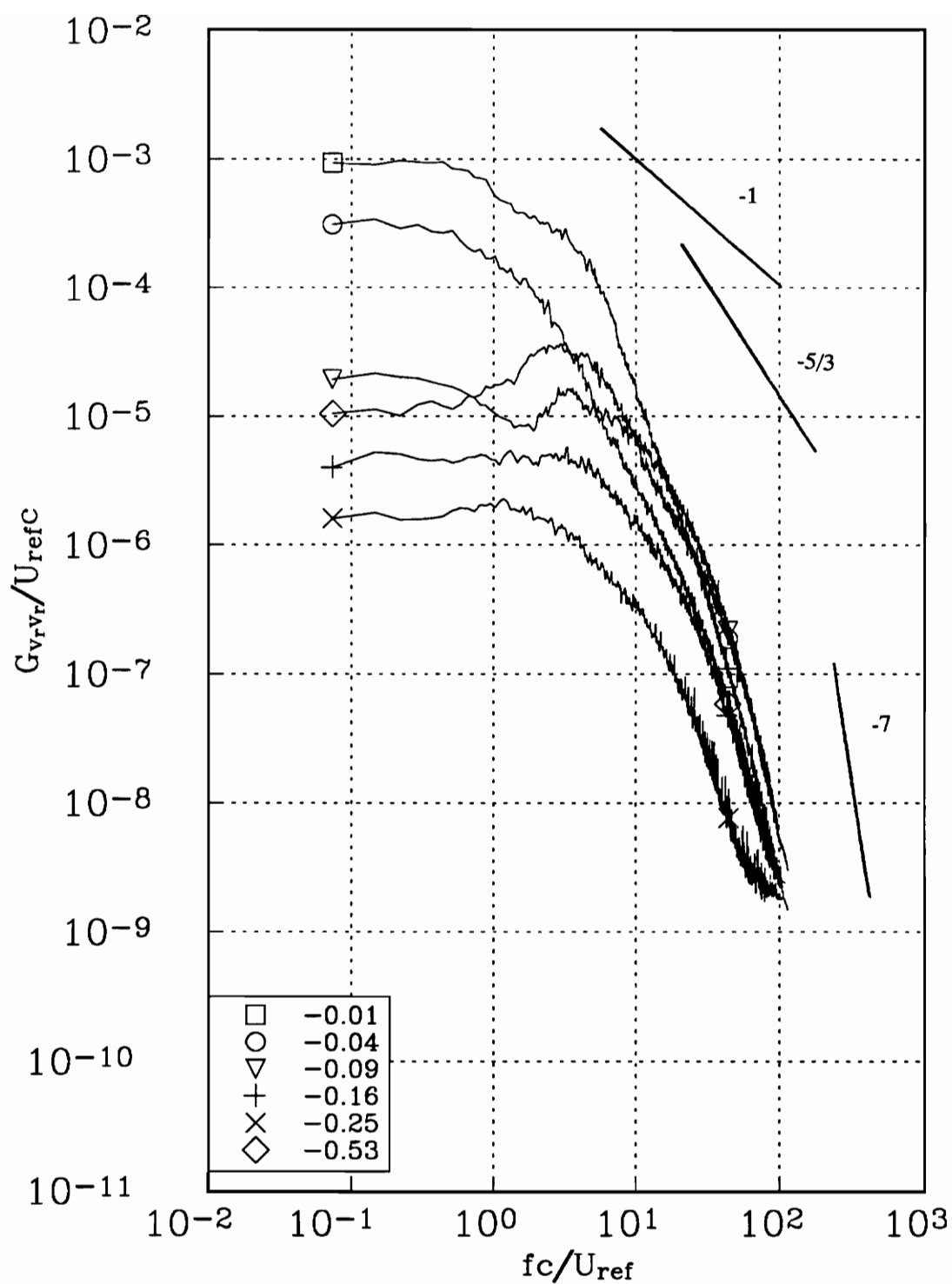


Figure 84c. v_r autospectra measured at representative radial locations along profile Aa for the upper co-rotating vortex at $x/c=10$. Tic marks in figure 81 indicate measured r/c locations.

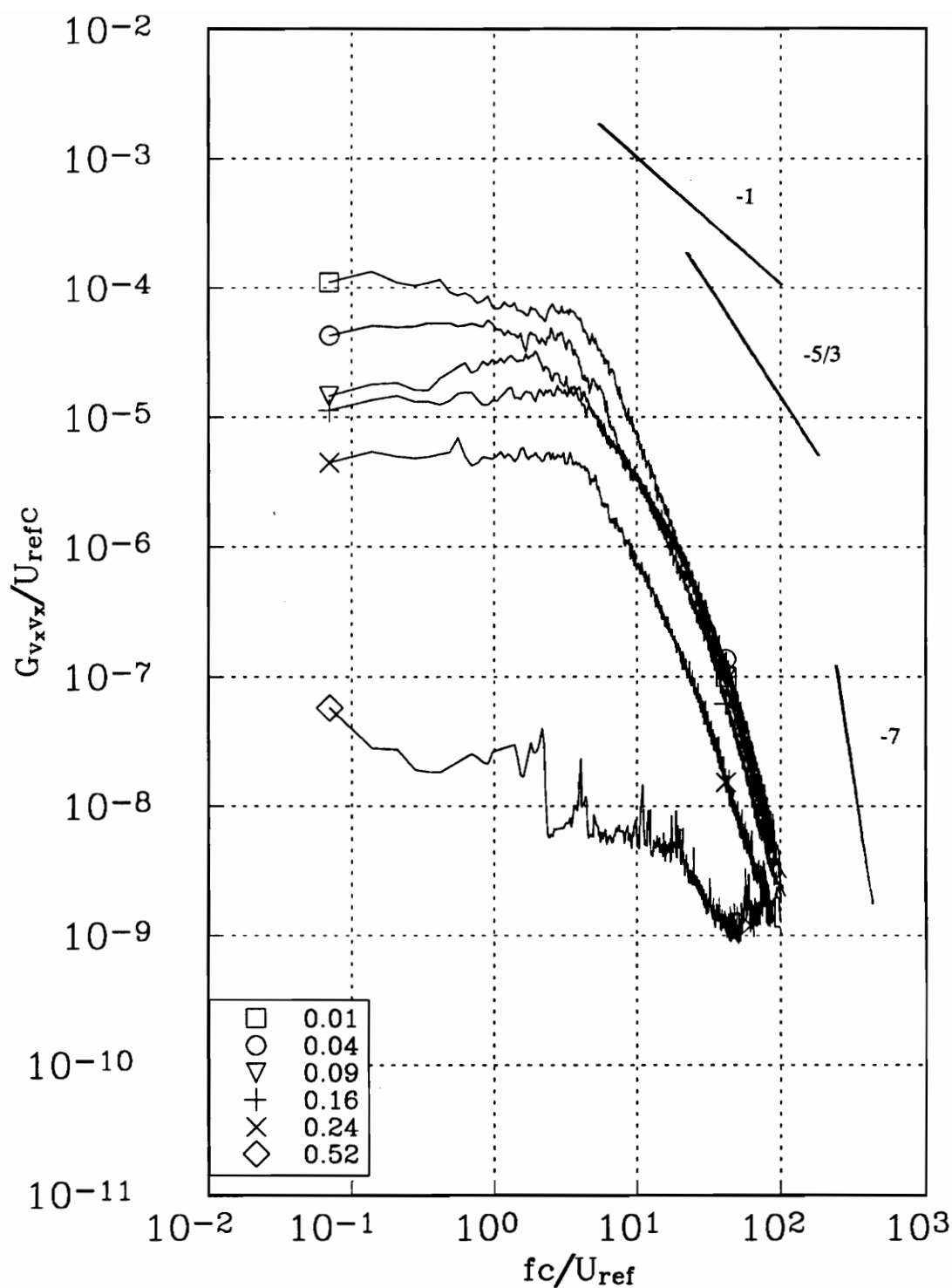


Figure 85a. v_x autospectra measured at representative radial locations along profile Bb for the upper co-rotating vortex at $x/c=10$. Tic marks in figure 82 indicate measured r/c locations.

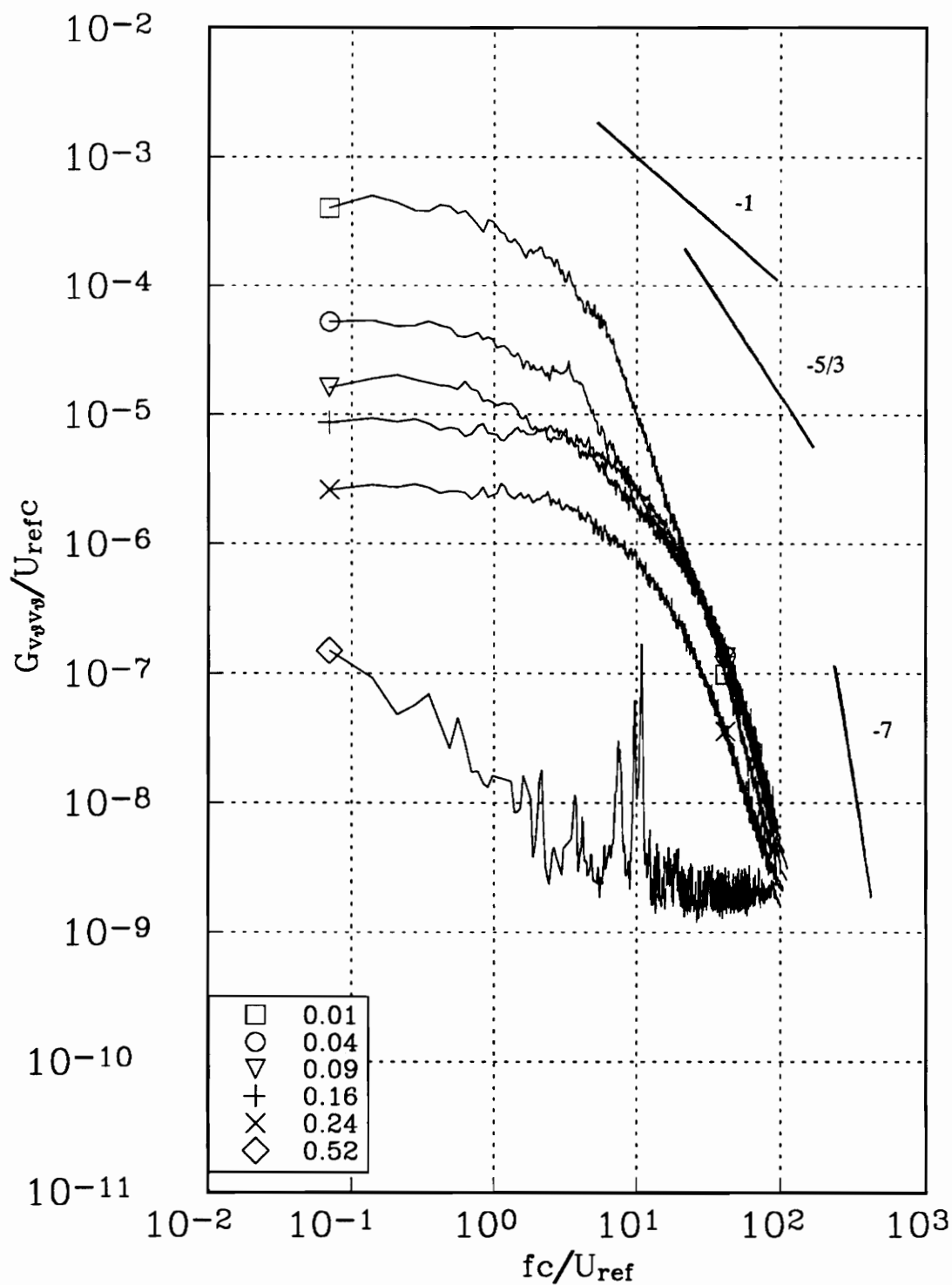


Figure 85b. v_θ autospectra measured at representative radial locations along profile Bb for the upper co-rotating vortex at $x/c=10$. Tic marks in figure 82 indicate measured r/c locations.

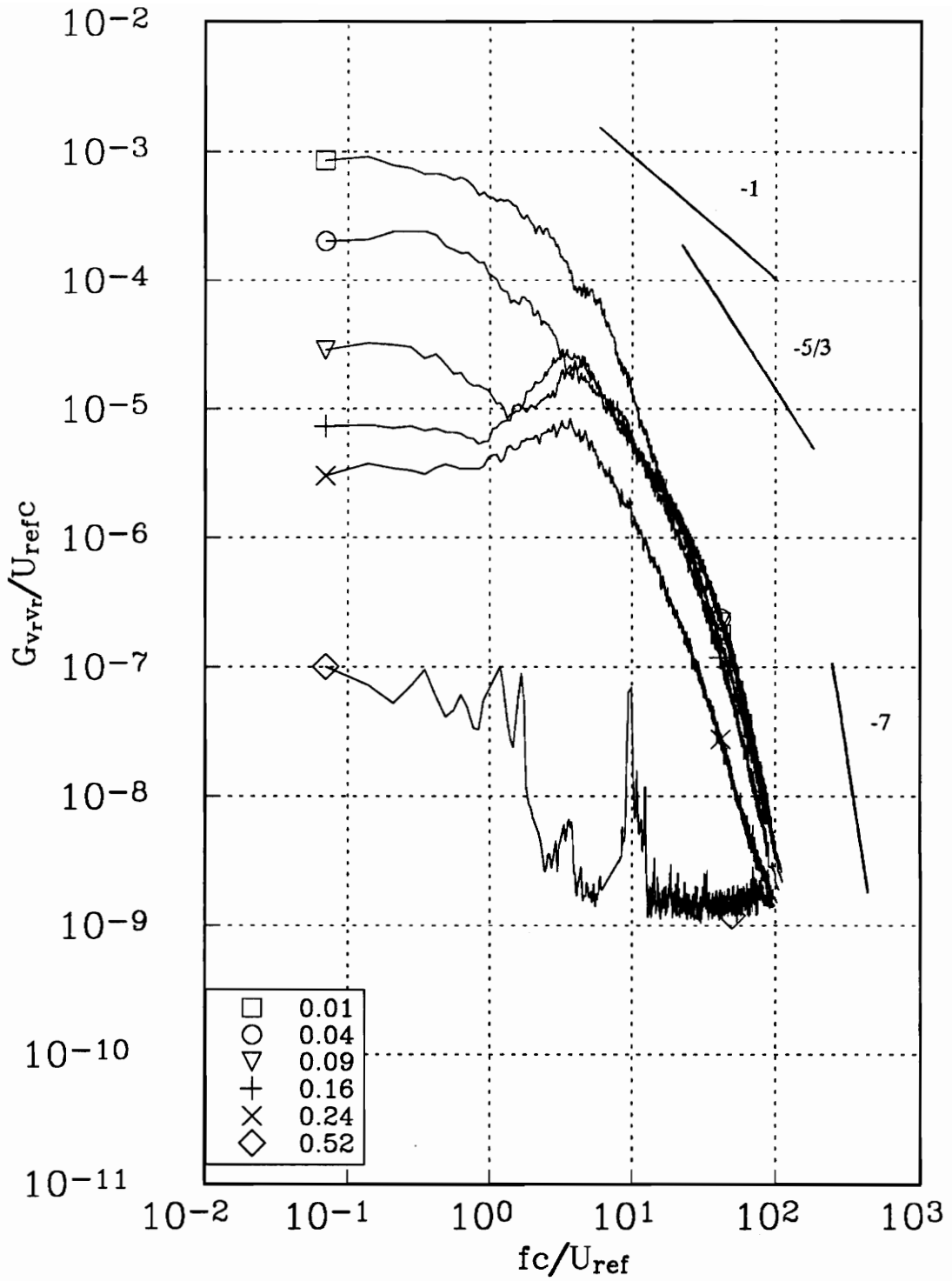


Figure 85c. v_r autospectra measured at representative radial locations along profile Bb for the upper co-rotating vortex at $x/c=10$. Tic marks in figure 82 indicate measured r/c locations.

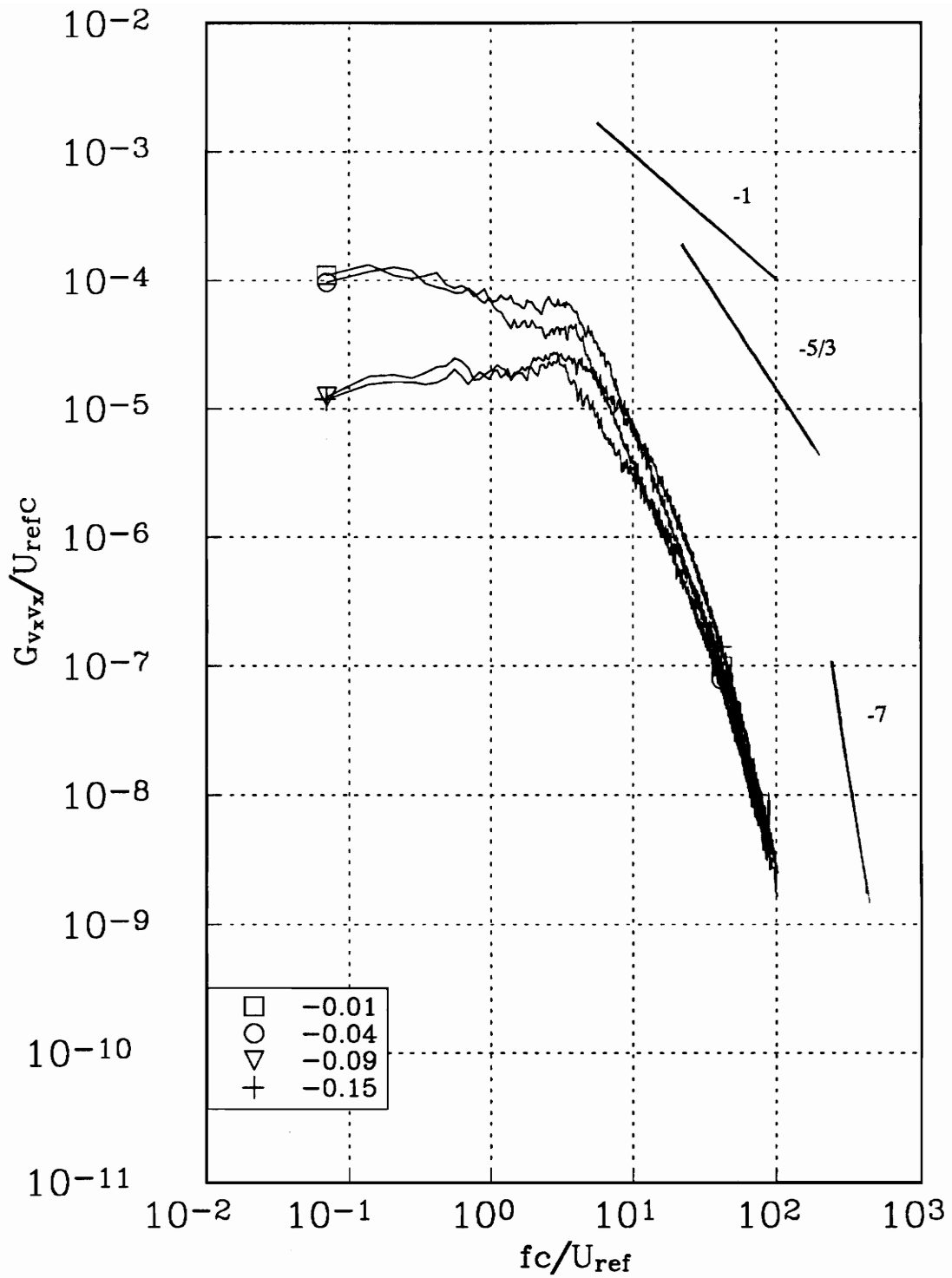


Figure 86a. v_x autospectra measured at representative radial locations along profile Bb for the upper co-rotating vortex at $x/c=10$. Tic marks in figure 82 indicate measured r/c locations.

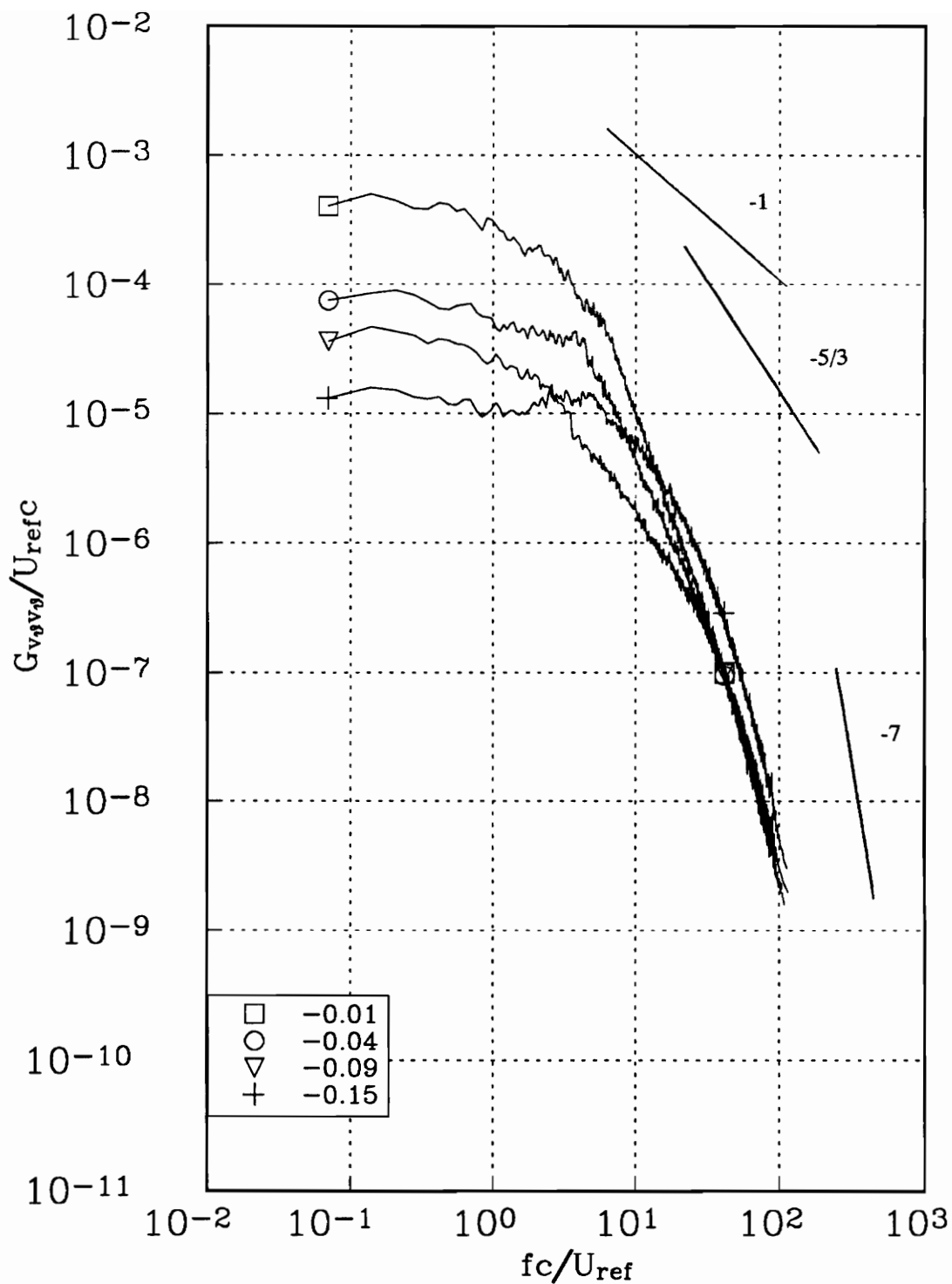


Figure 86b. v_θ autospectra measured at representative radial locations along profile Bb for the upper co-rotating vortex at $x/c=10$. Tic marks in figure 82 indicate measured r/c locations.

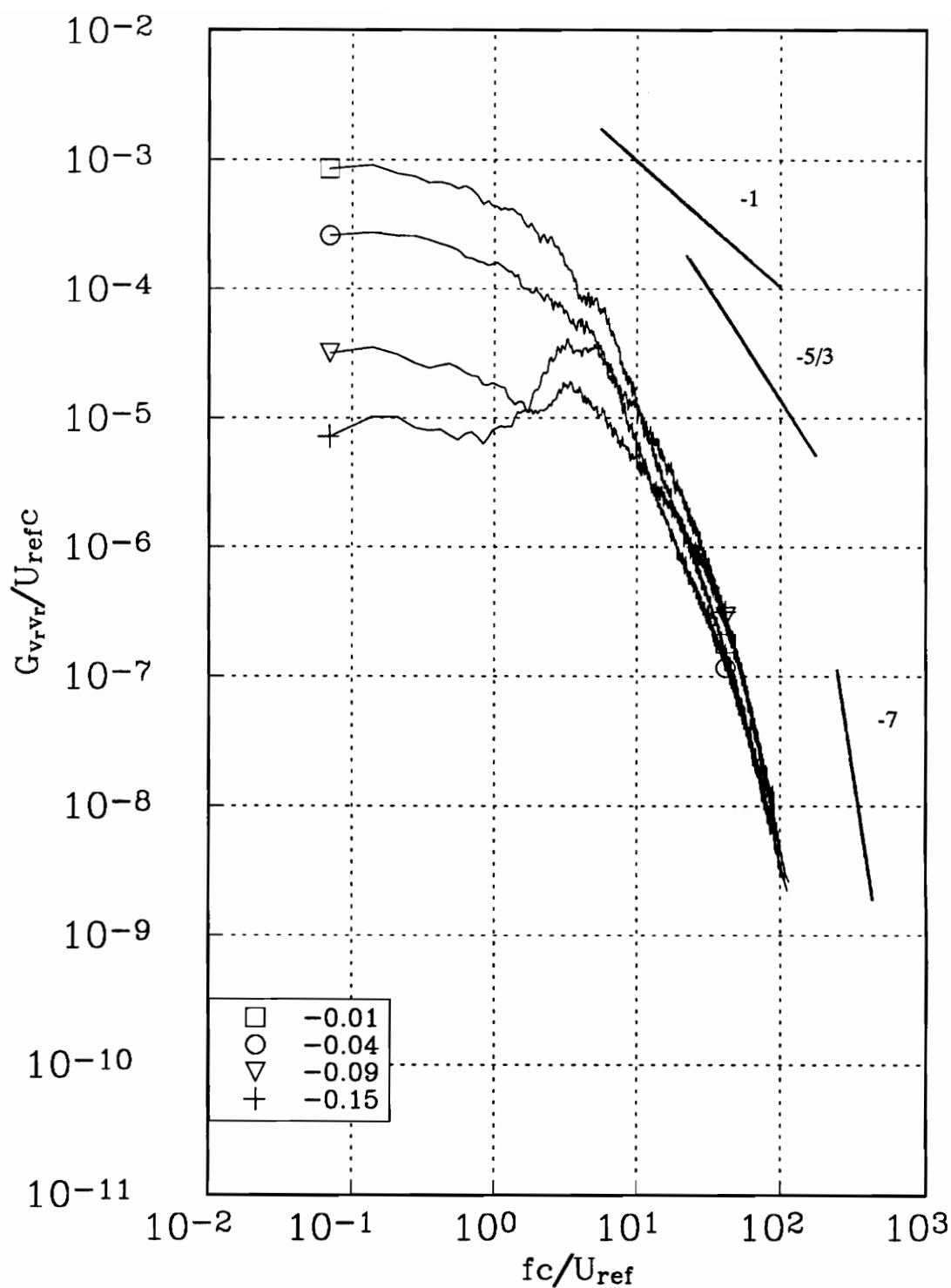


Figure 86c. v_r autospectra measured at representative radial locations along profile Bb for the upper co-rotating vortex at $x/c=10$. Tic marks in figure 82 indicate measured r/c locations.

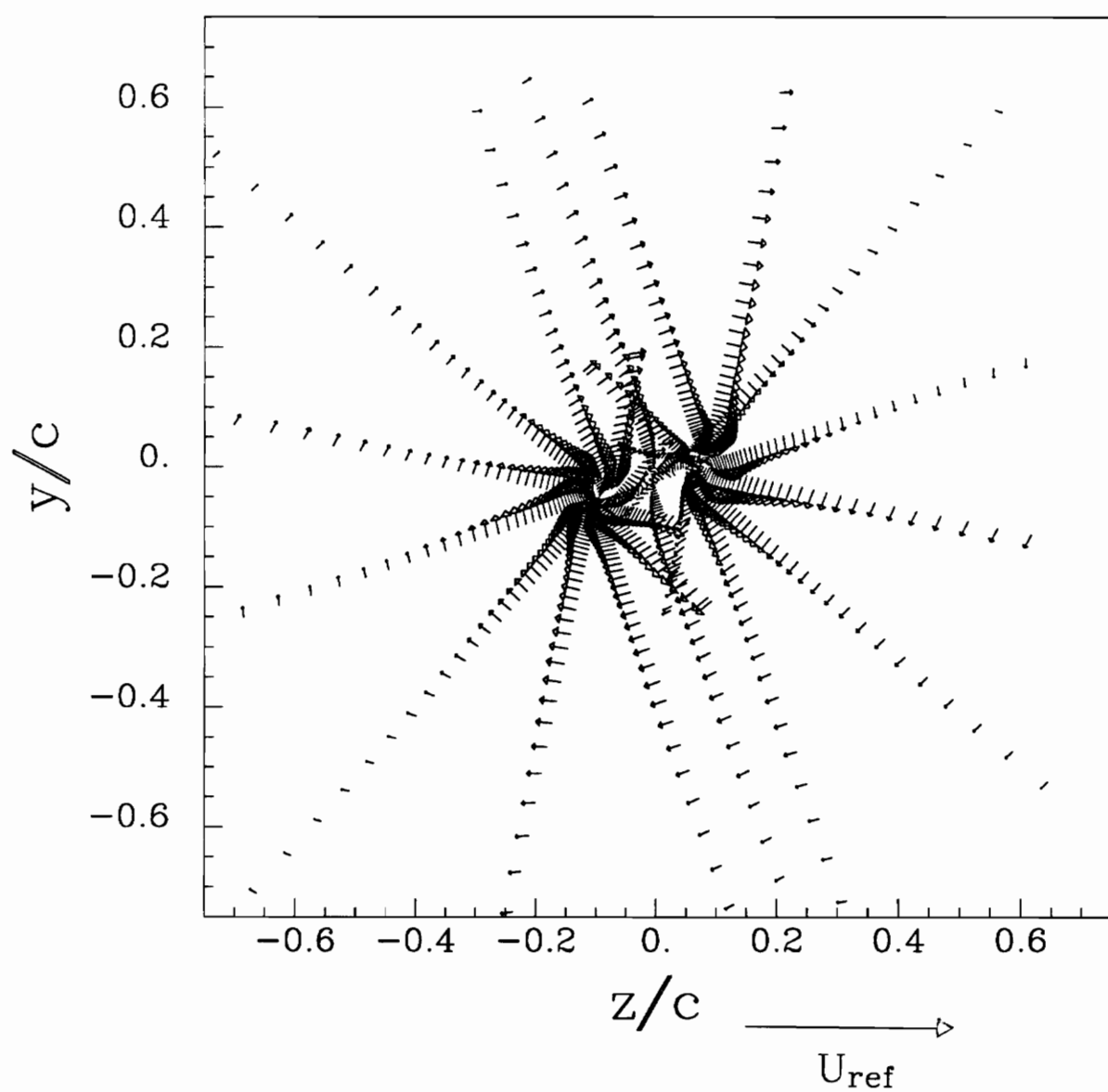
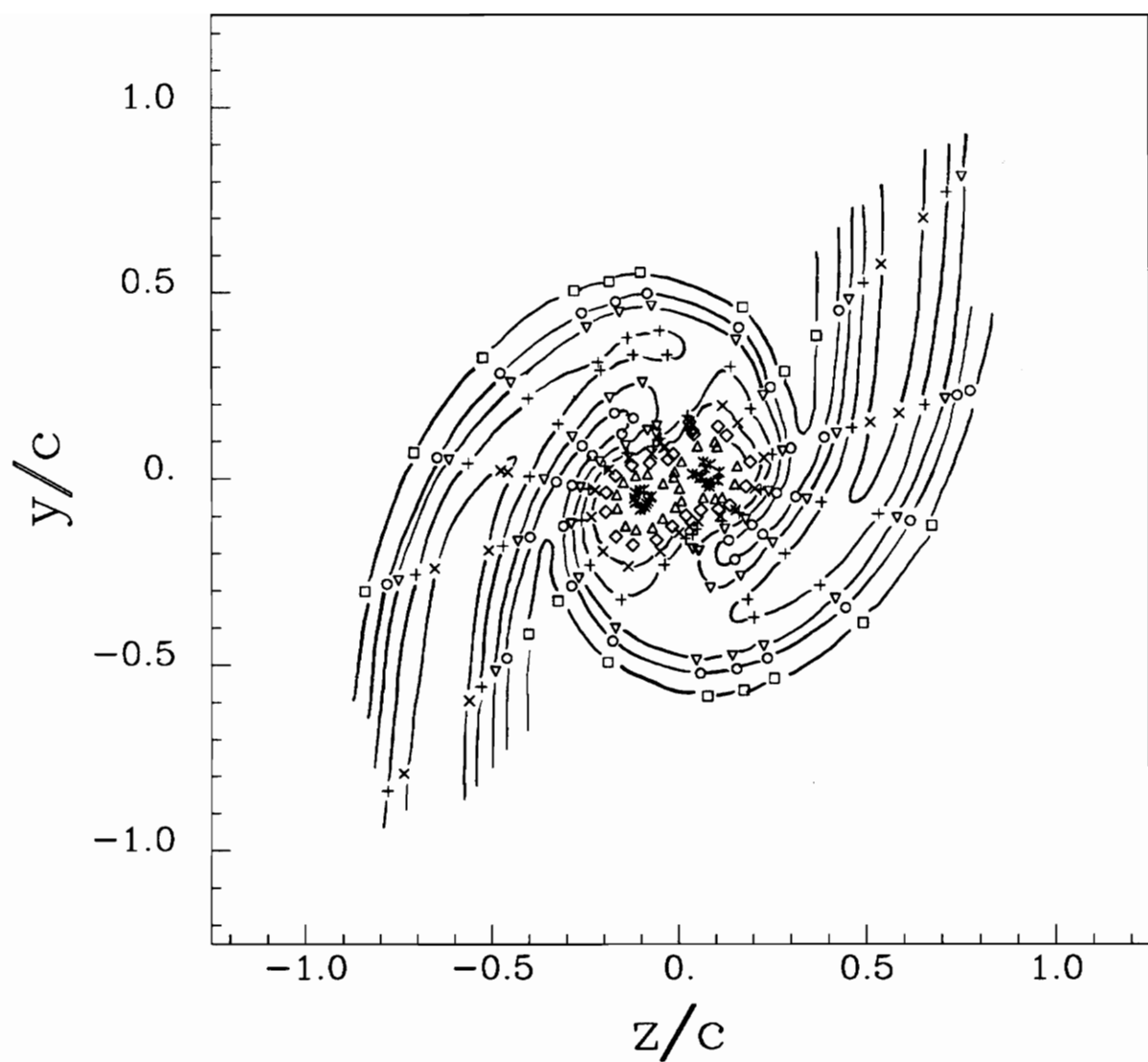


Figure 87. Mean secondary flow vectors of the co-rotating pair at $x/c=15$, angle of attack 5° , $Re_c=260,000$.



□	0.000010
○	0.000050
▽	0.000100
+	0.000200
×	0.000300
◇	0.000500
△	0.001000
✱	0.005000

Figure 88. Contours of turbulent kinetic energy k/U_{ref}^2 for the co-rotating pair at $x/c=15$, angle of attack 5° , $Re_c=260,000$.

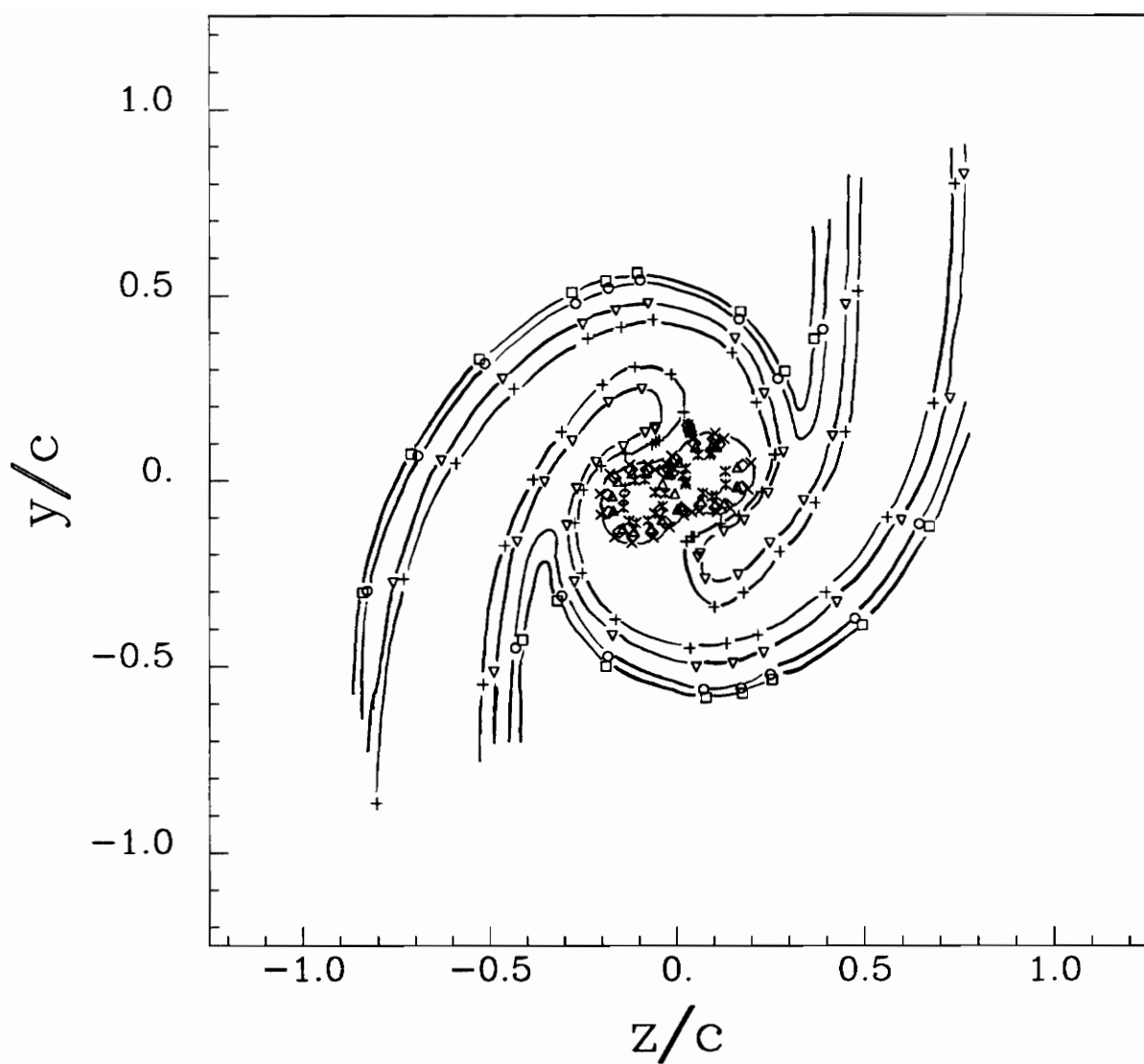


Figure 89. Contours of v_x^2/U_{ref}^2 for the co-rotating pair at $x/c=15$, angle of attack 5° , $Re_c=260,000$.

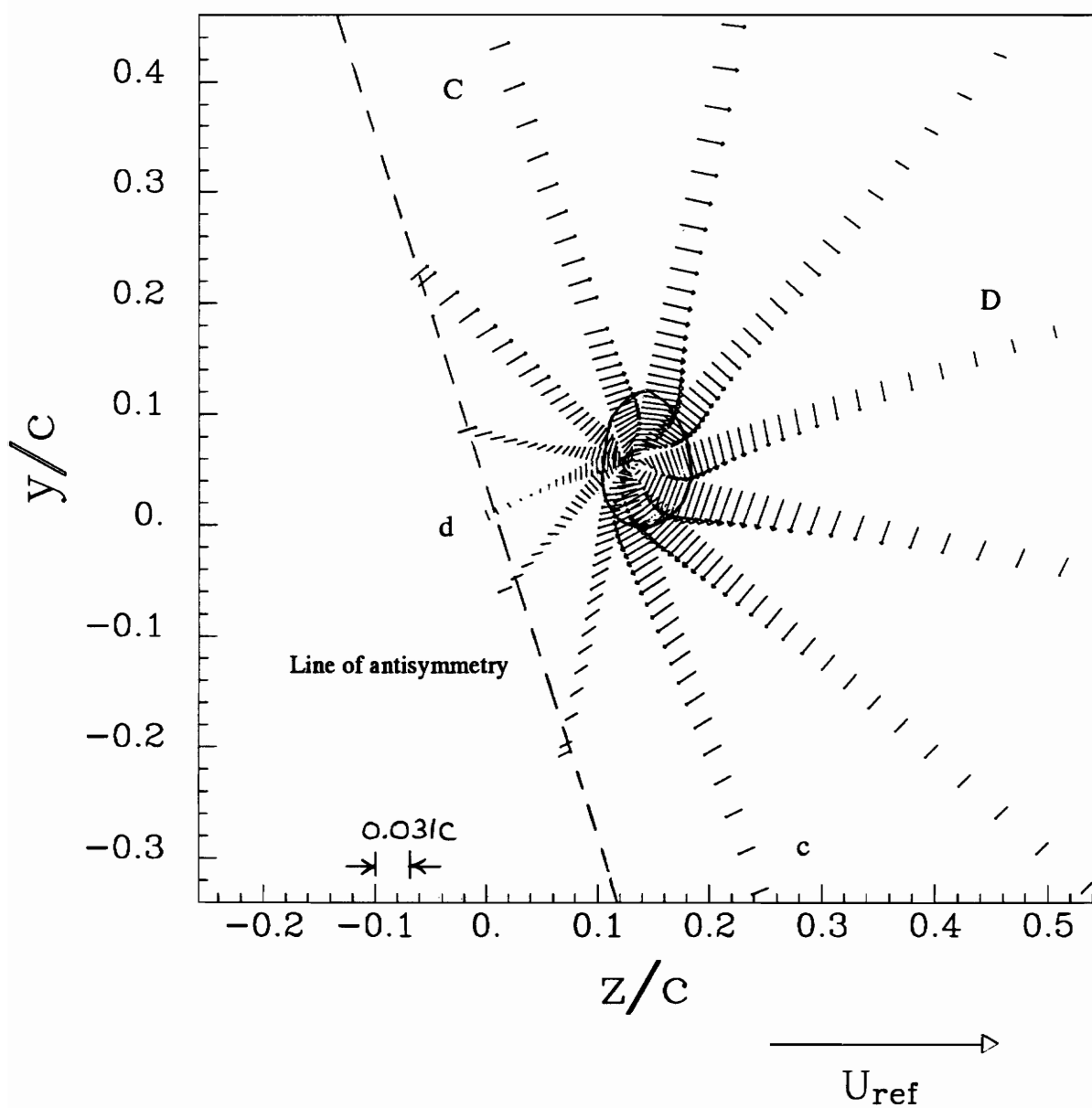


Figure 90. Core region showing mean secondary flows vectors for the upper co-rotating vortex at $x/c=15$, angle of attack= 5° , $Re_c=260,000$. Dotted line indicates core edge.

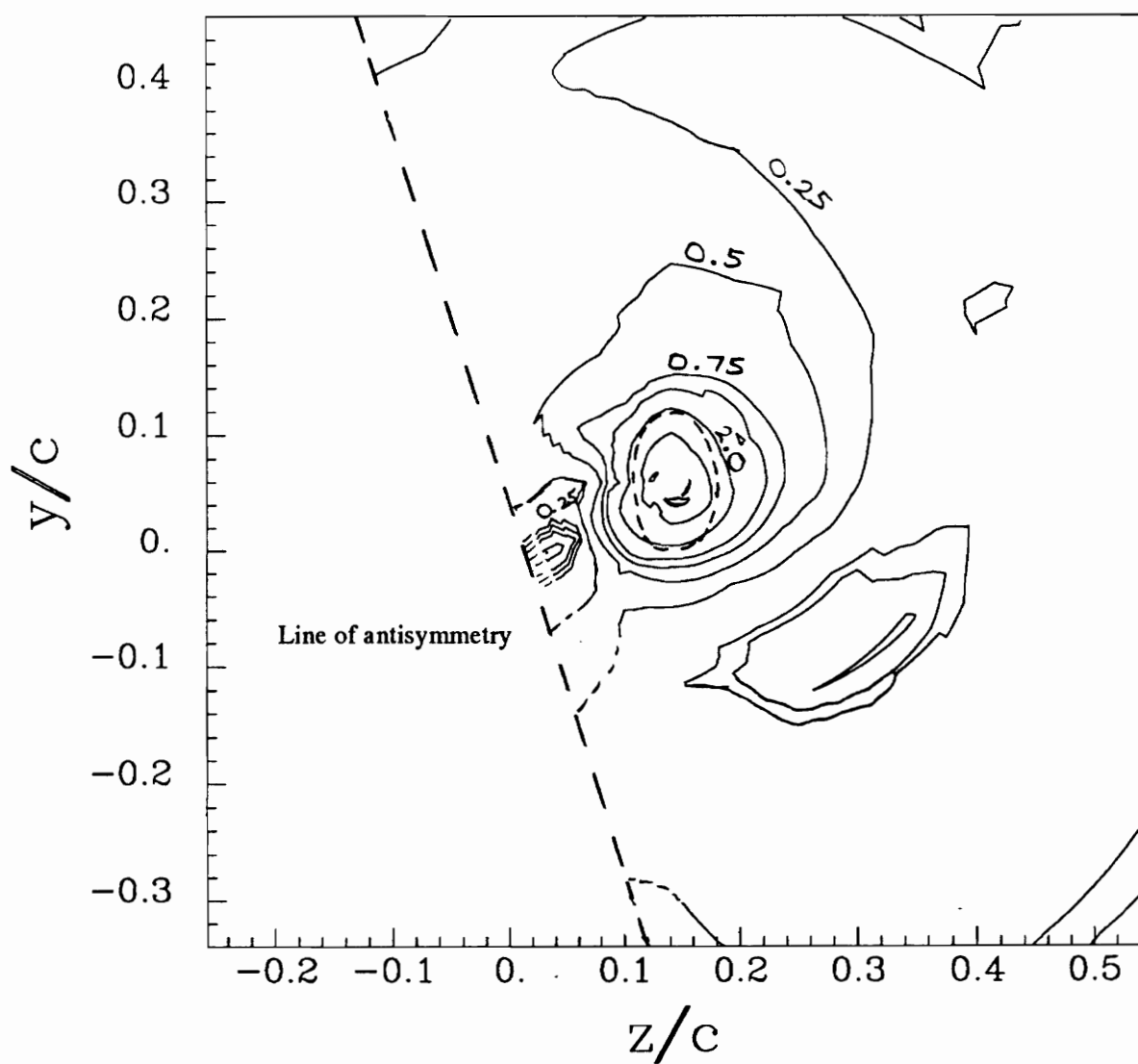


Figure 91. Core region showing contours of vorticity $\omega c/U_{\text{ref}}$ for the upper co-rotating vortex at $x/c=15$, angle of attack= 5° , $Re_c=260,000$. Dotted line indicates core edge.

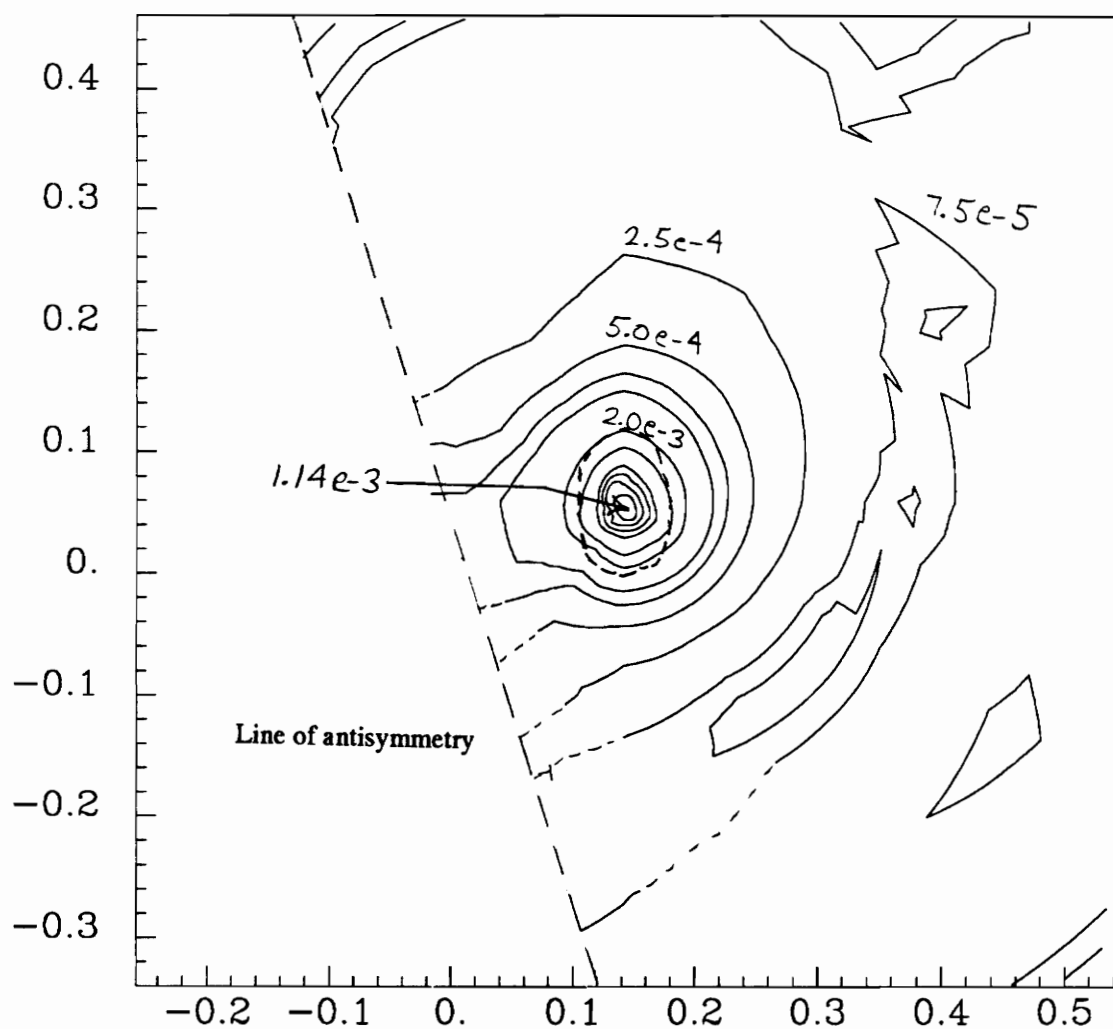


Figure 92. Core region showing contours of turbulent kinetic energy k/U_{ref}^2 for the upper co-rotating vortex at $x/c=15$, angle of attack= 5° , $Re_c=260,000$. Dotted line indicates core edge.

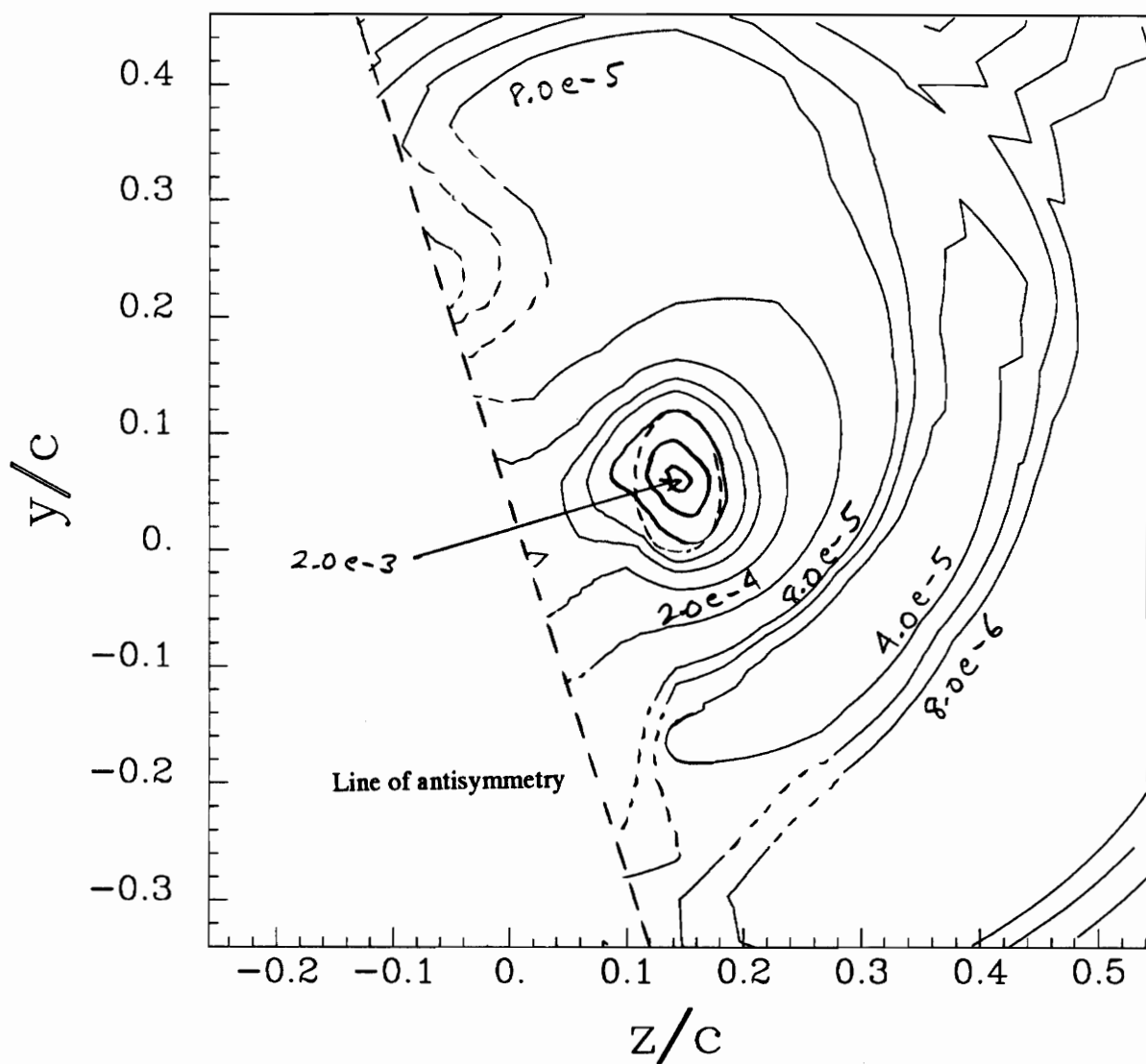


Figure 93. Core region showing contours of v_x^2/U_{ref}^2 for the upper co-rotating vortex at $x/c=15$, angle of attack= 5° , $Re_c=260,000$. Dotted line indicates core edge.

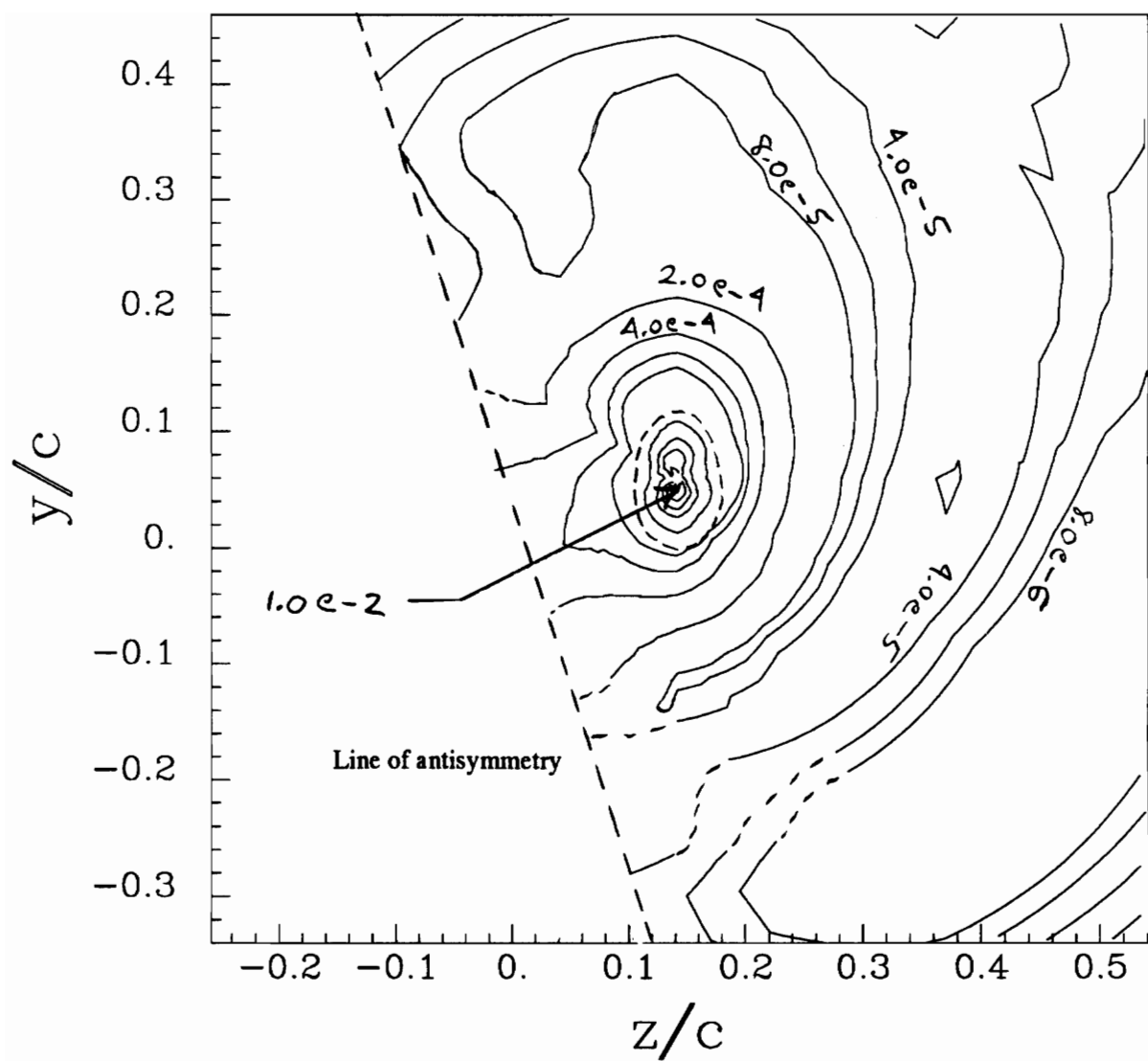


Figure 94. Core region showing contours of v_{θ}^2/U_{ref}^2 for the upper co-rotating vortex at $x/c=15$, angle of attack= 5° , $Re_c=260,000$. Dotted line indicates core edge.

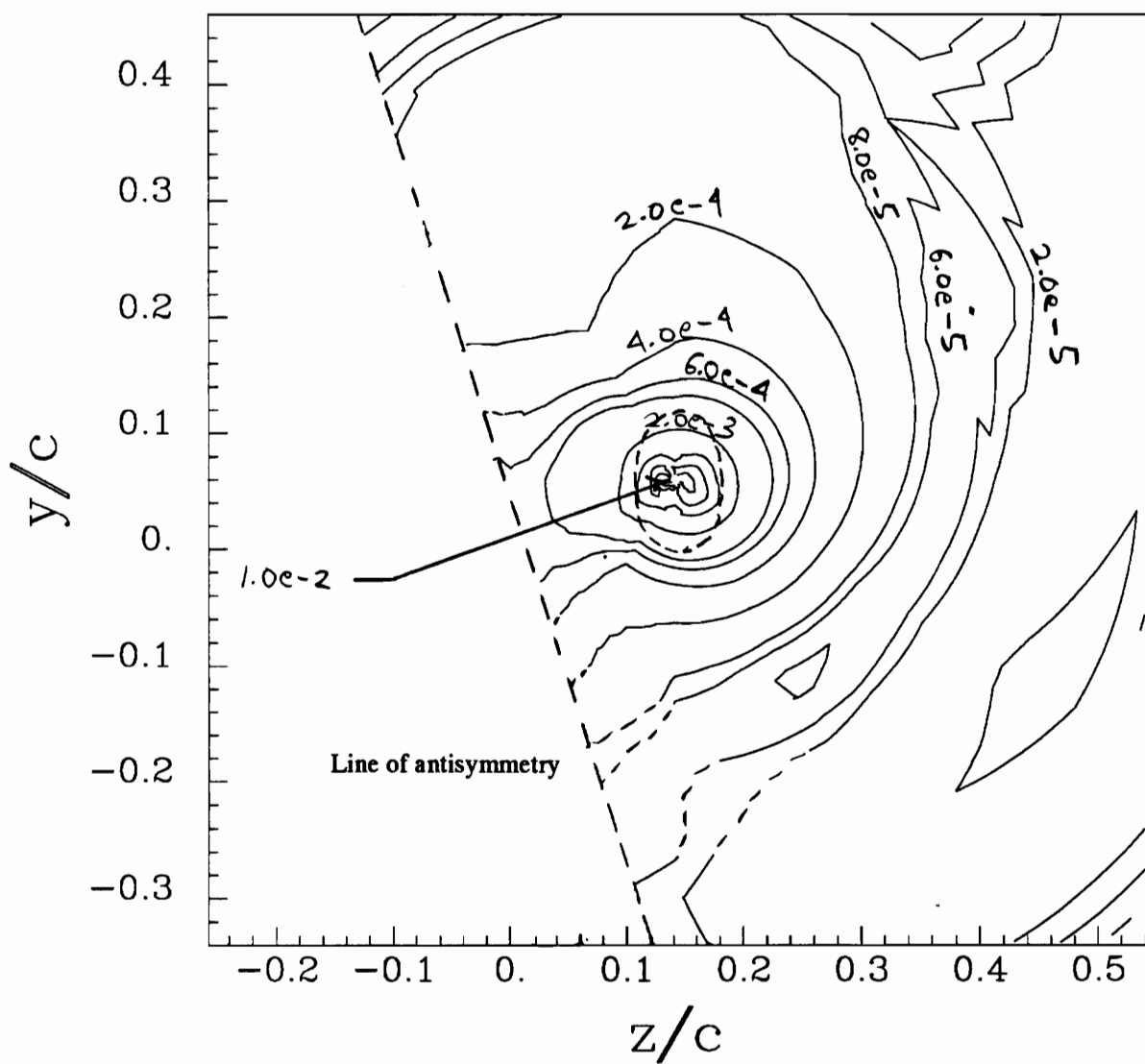


Figure 95. Core region showing contours of v_r^2/U_{ref}^2 for the upper co-rotating vortex at $x/c=15$, angle of attack= 5° , $Re_c=260,000$. Dotted line indicates core edge.

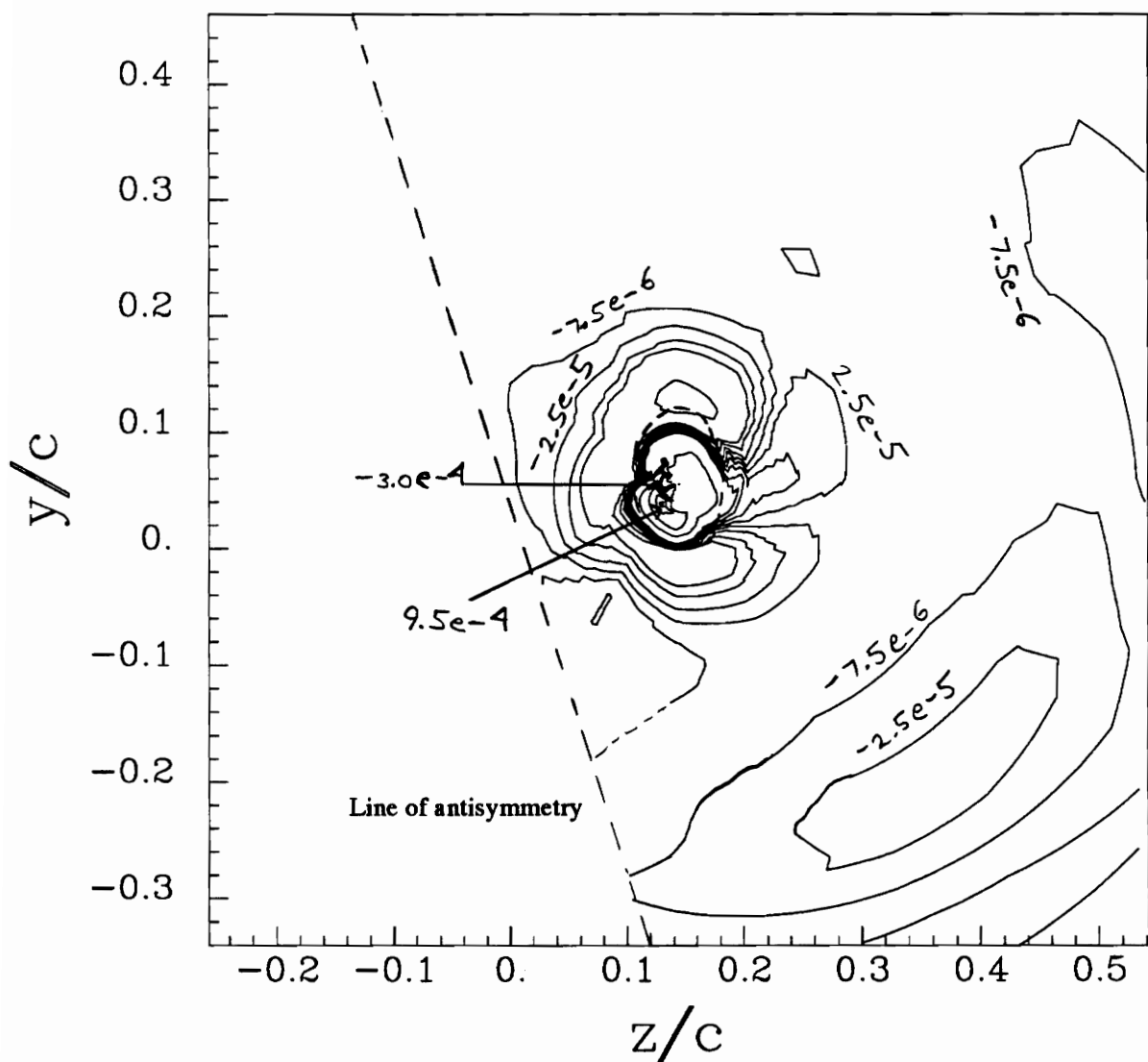


Figure 96. Core region showing contours of $v_x v_\theta / U_{ref}^2$ for the upper co-rotating vortex at $x/c=15$, angle of attack= 5° , $Re_c=260,000$. Dotted line indicates core edge.

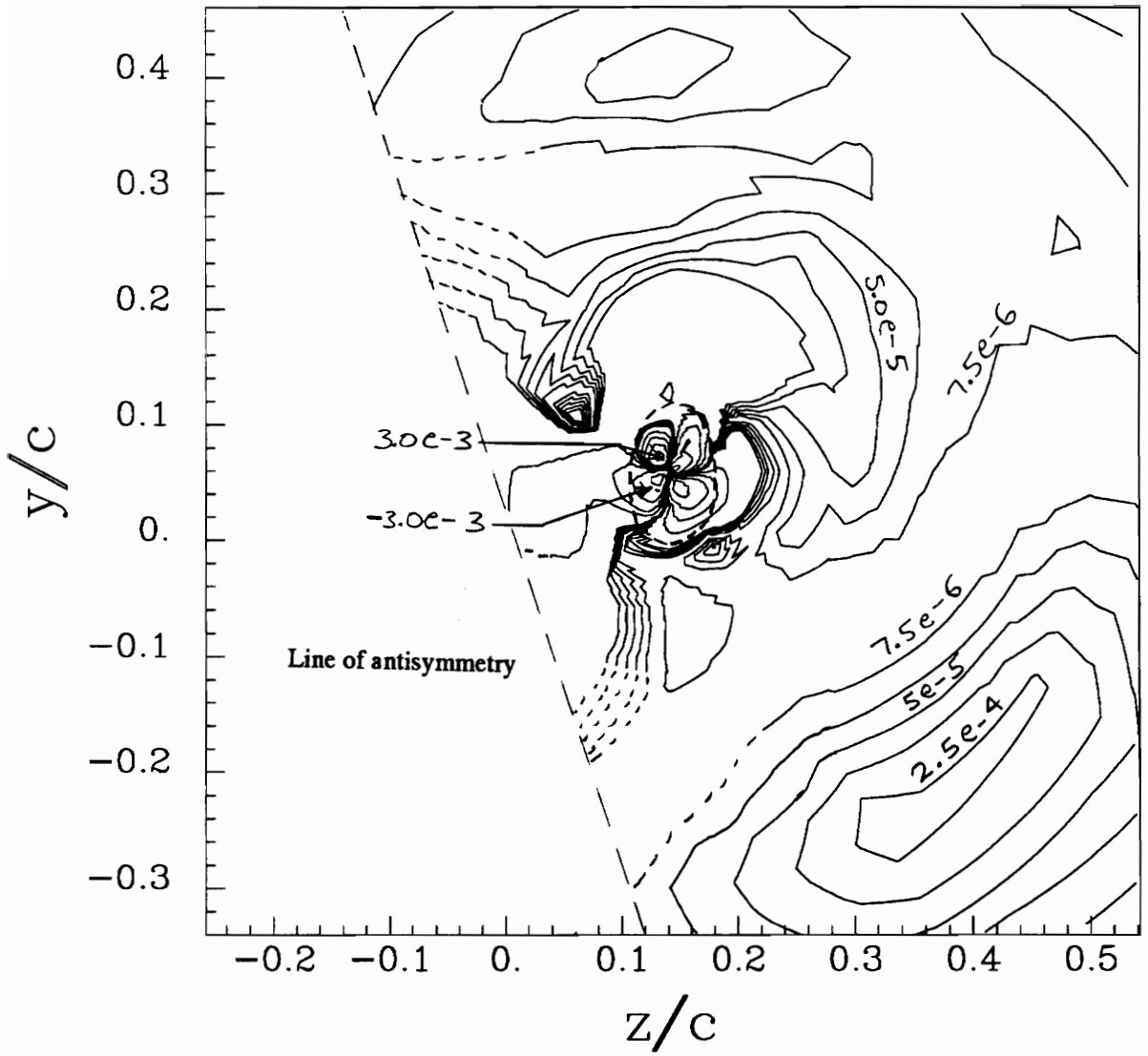


Figure 97. Core region showing contours of $v_\theta v_r / U_{ref}^2$ for the upper co-rotating vortex at $x/c=15$, angle of attack= 5° , $Re_c=260,000$. Dotted line indicates core edge.

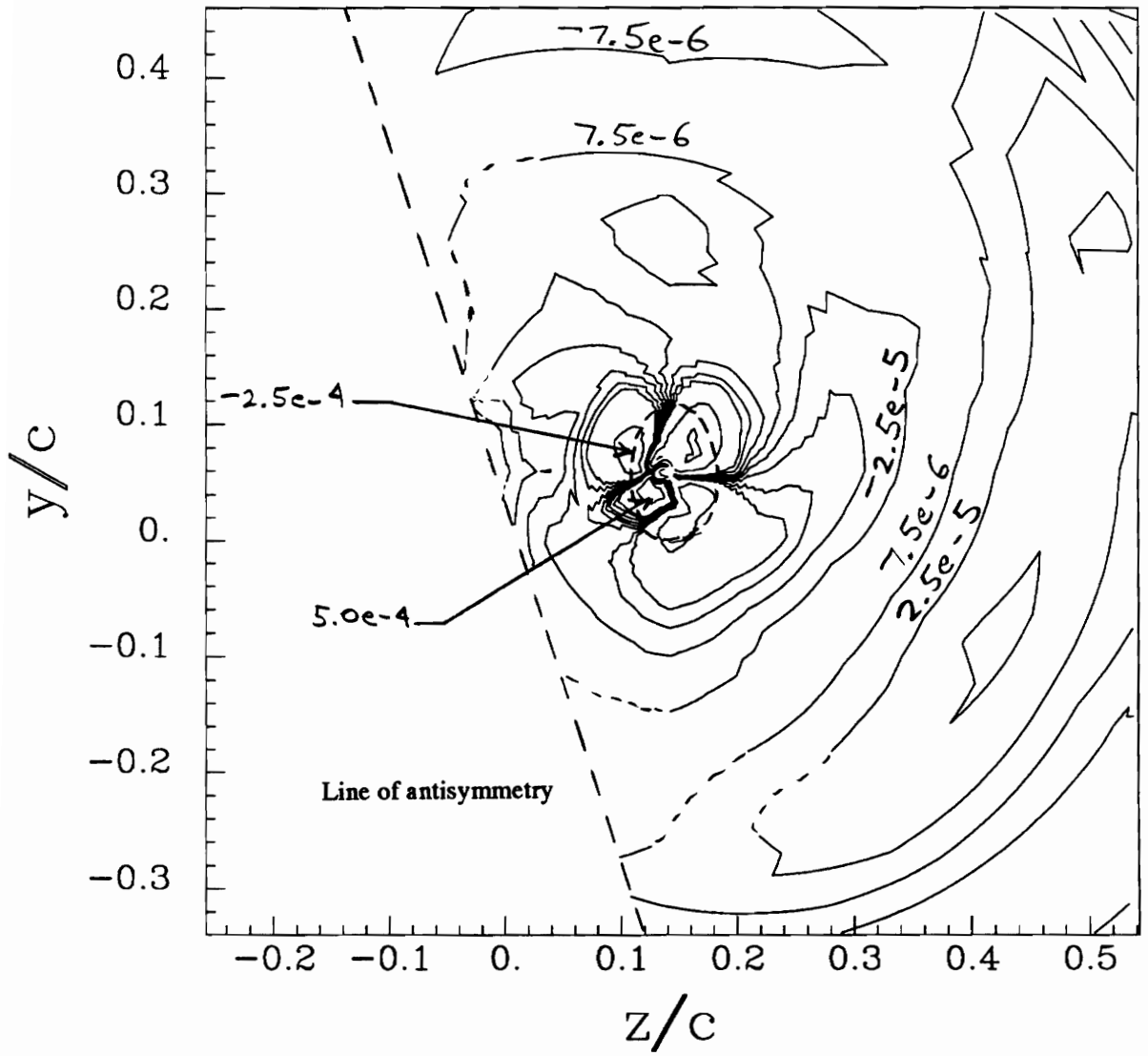


Figure 98. Core region showing contours of $v_x v_r / U_{ref}^2$ for the upper co-rotating vortex at $x/c=15$, angle of attack= 5° , $Re_c=260,000$. Dotted line indicates core edge.

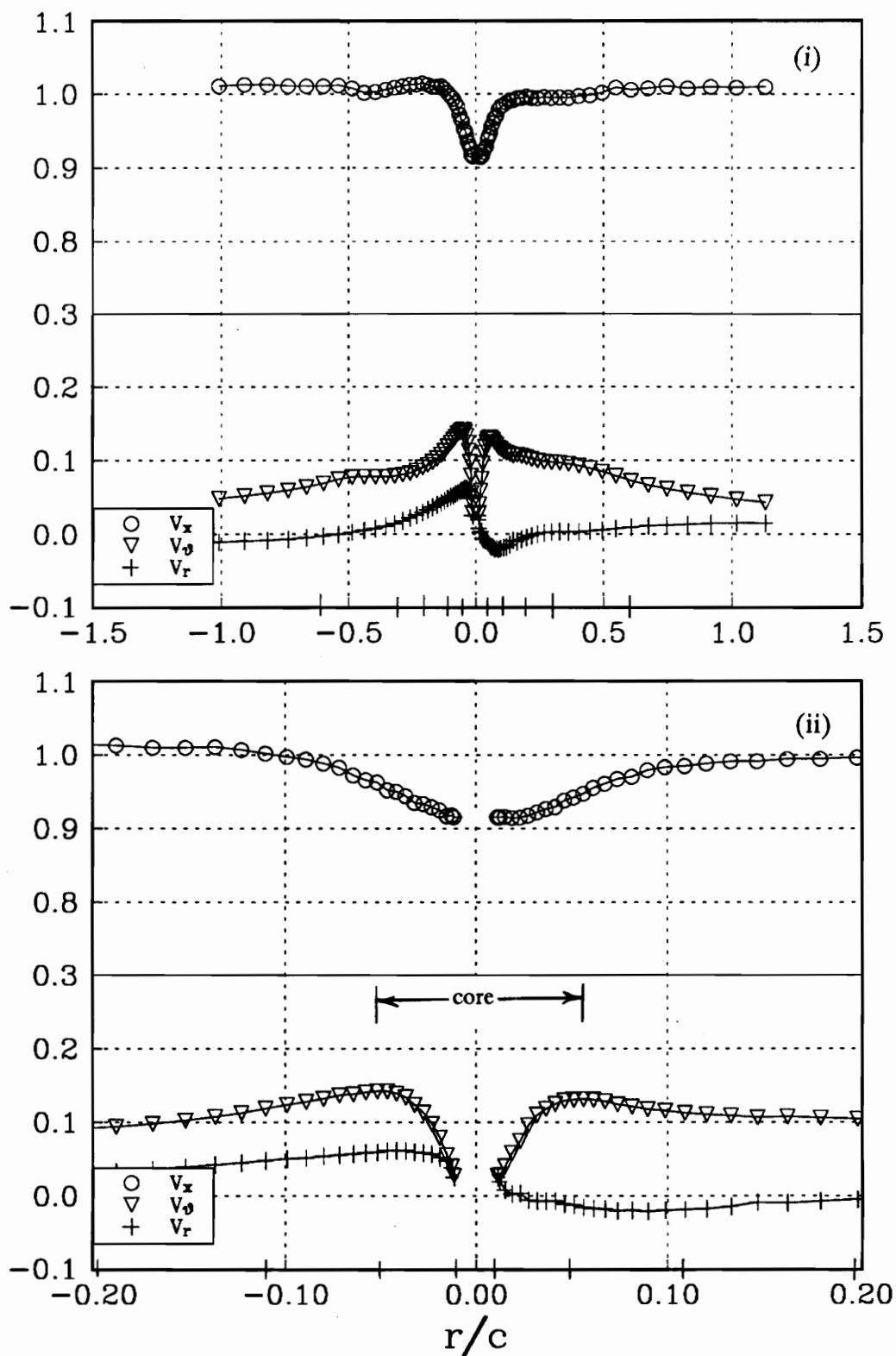


Figure 99a. Profile Cc mean velocities, measured parallel to the line of antisymmetry for the upper co-rotating vortex at $x/c=15$. (i) wake region, (ii) core region.

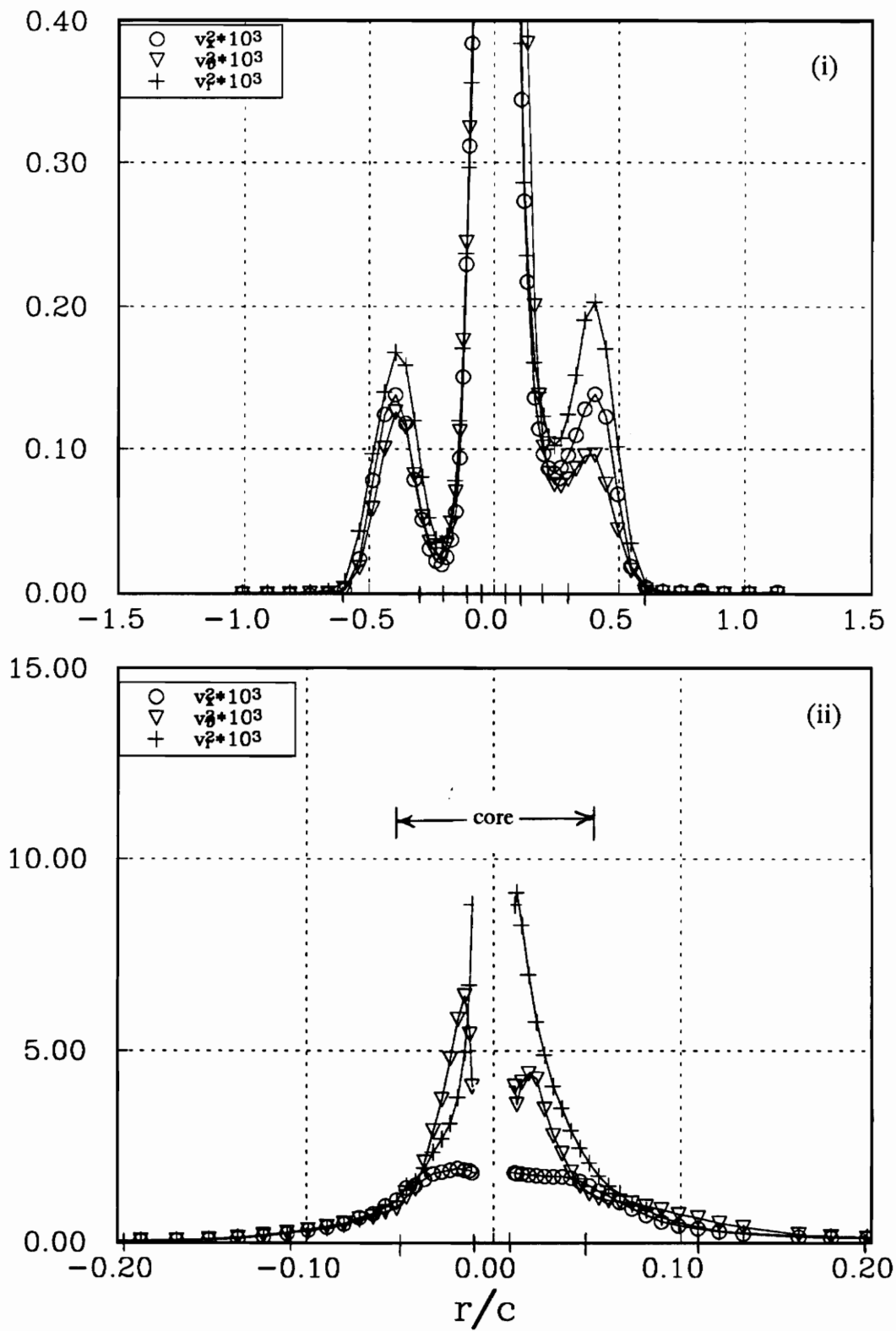


Figure 99b. Profile Cc normal stresses, measured parallel to the line of antisymmetry for the upper co-rotating vortex at $x/c=15$. (i) wake region, (ii) core region.

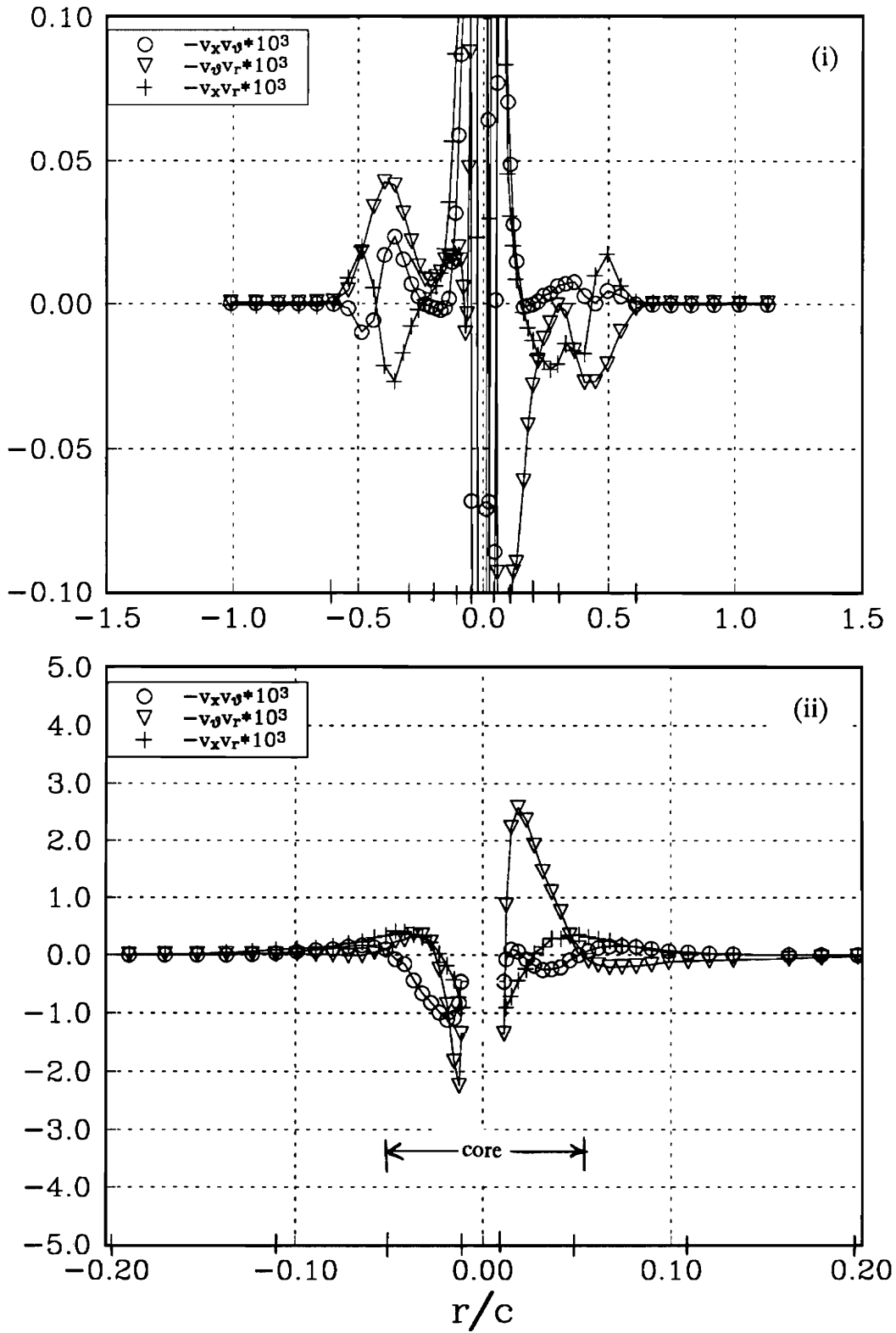


Figure 99c. Profile Cc shear stresses, measured parallel to the line of antisymmetry for the upper co-rotating vortex at $x/c=15$. (i) wake region, (ii) core region.

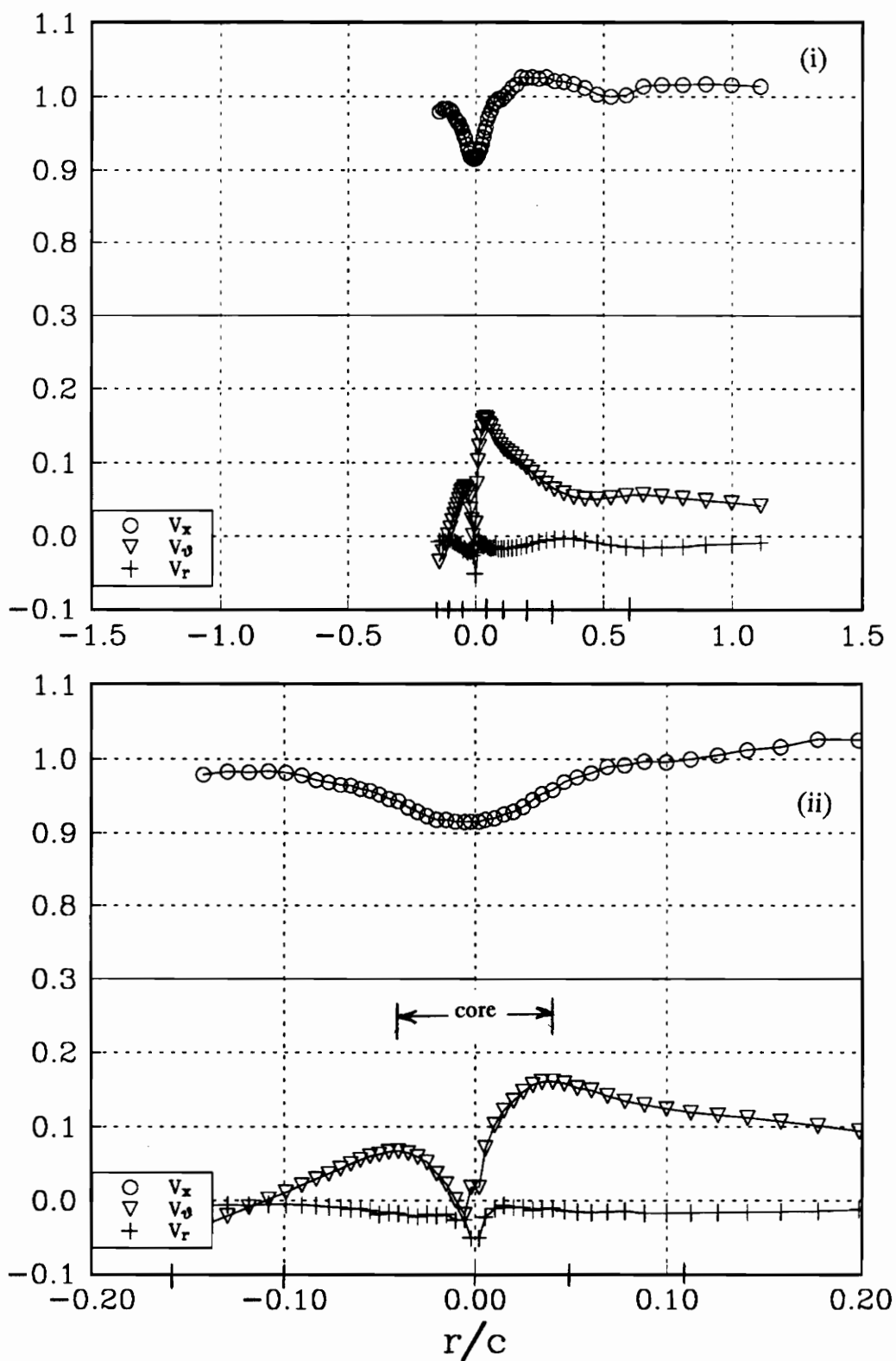


Figure 100a. Profile Dd mean velocities, measured perpendicular to the line of antisymmetry for the upper co-rotating vortex at $x/c=15$. (i) wake region, (ii) core region.

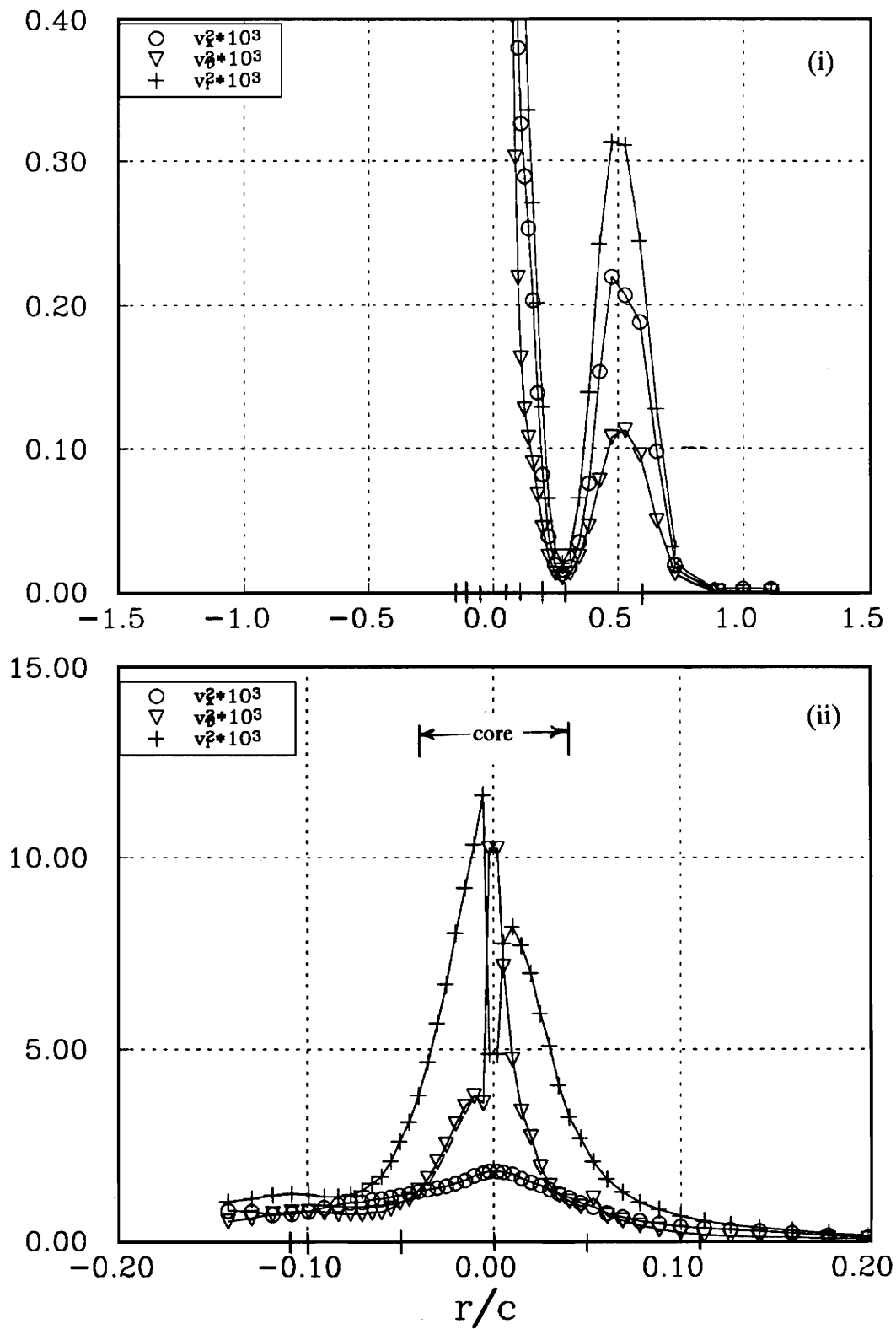


Figure 100b. Profile Dd normal stresses, measured perpendicular to the line of antisymmetry for the upper co-rotating vortex at $x/c=15$. (i) wake region, (ii) core region.

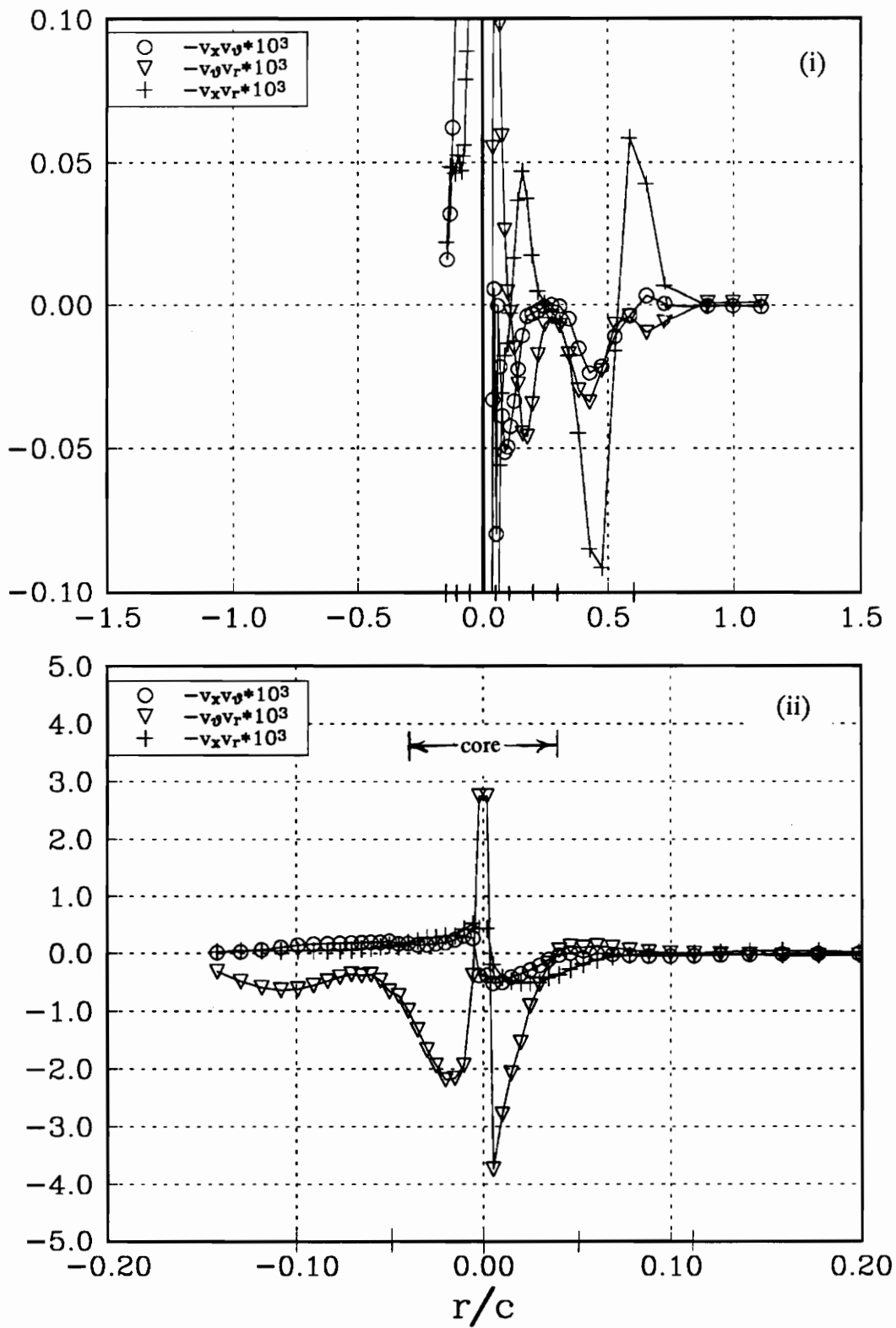


Figure 100c. Profile Dd shear stresses, measured perpendicular to the line of antisymmetry for the upper co-rotating vortex at $x/c=15$. (i) wake region, (ii) core region.

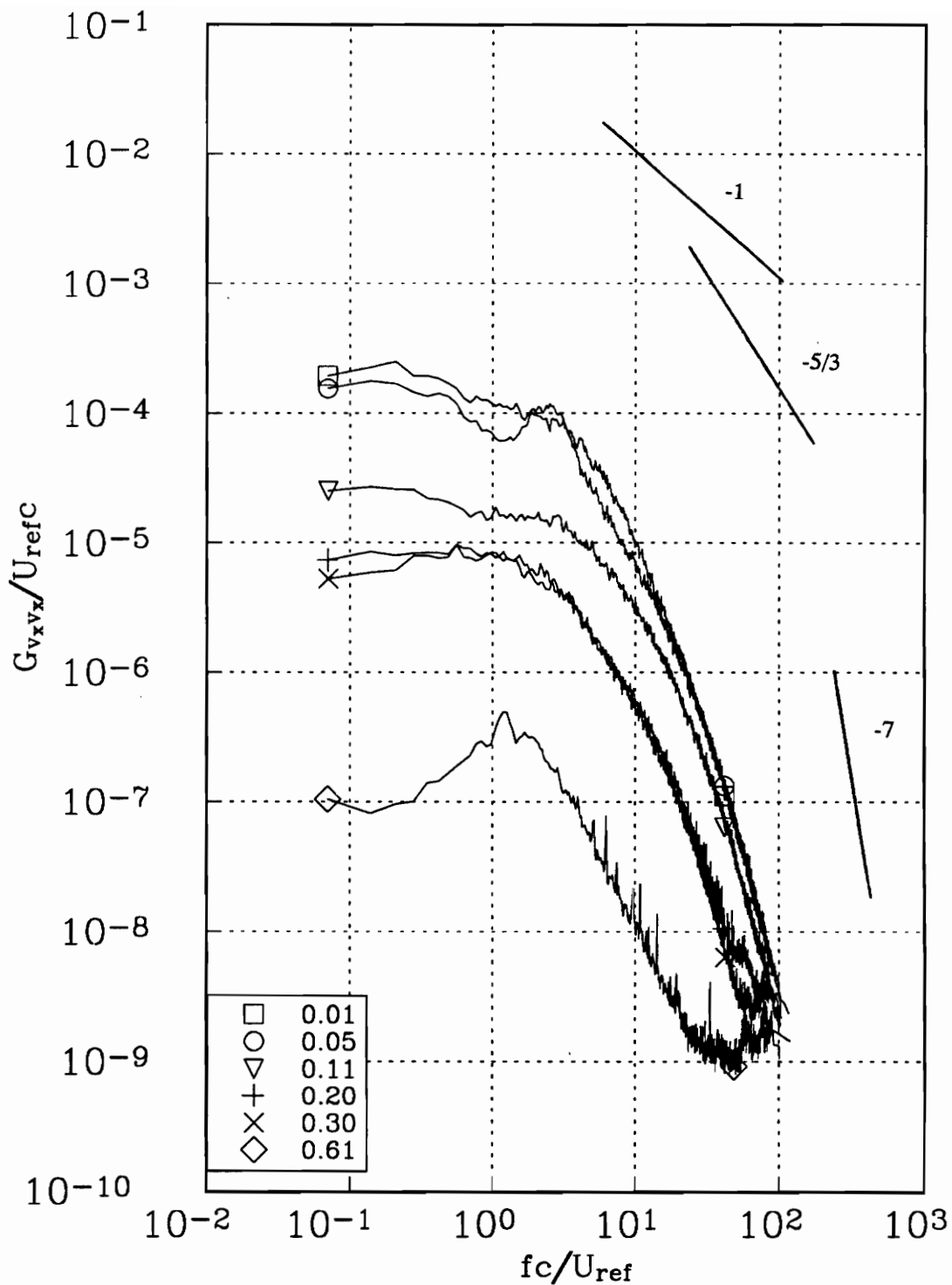


Figure 101a. v_x autospectra measured at representative radial locations along profile Cc for the upper co-rotating vortex at $x/c=15$. Tic marks in figure 99 indicate measured r/c locations.

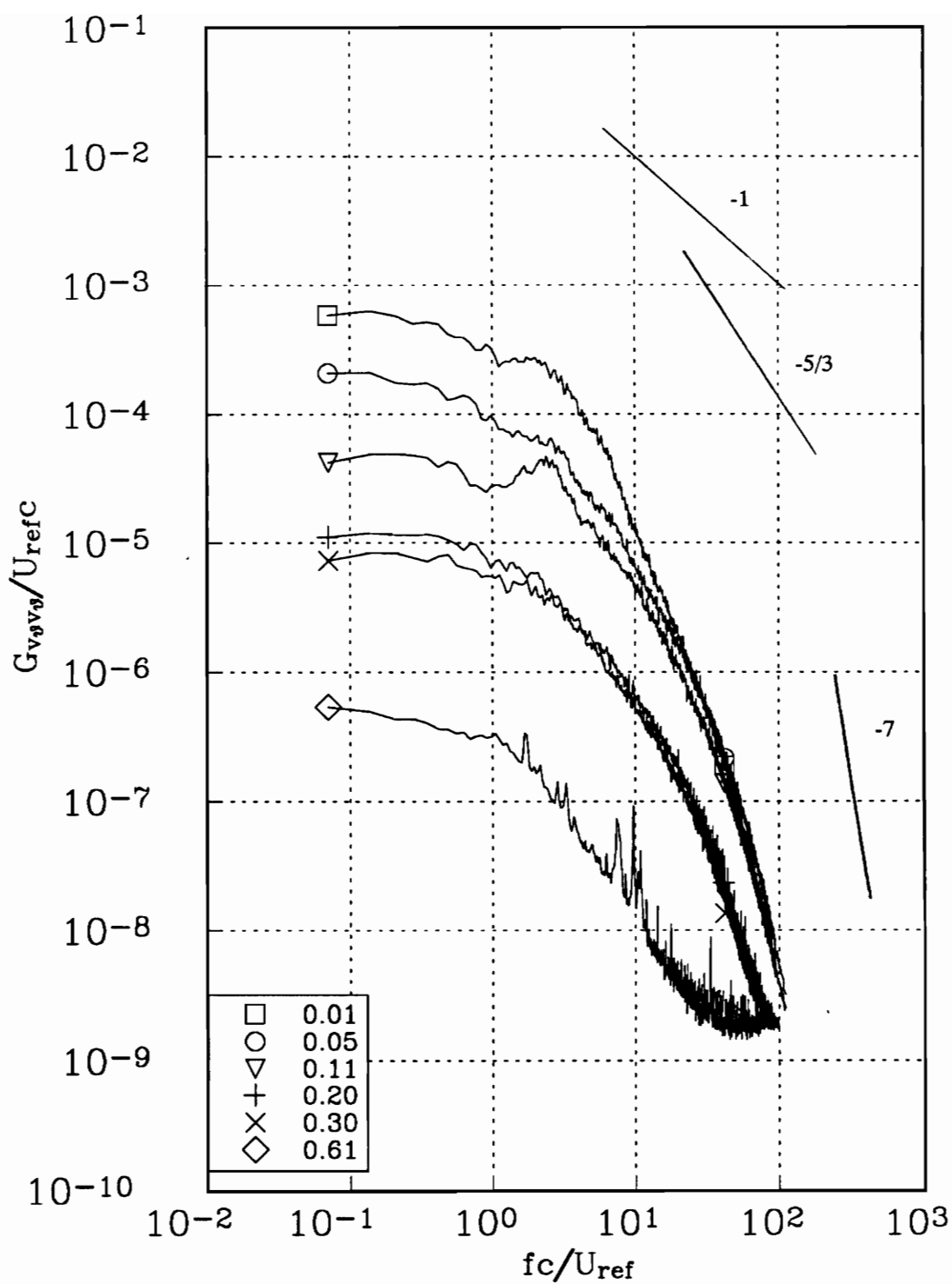


Figure 101b. v_θ autospectra measured at representative radial locations along profile Cc for the upper co-rotating vortex at $x/c=15$. Tic marks in figure 99 indicate measured r/c locations.

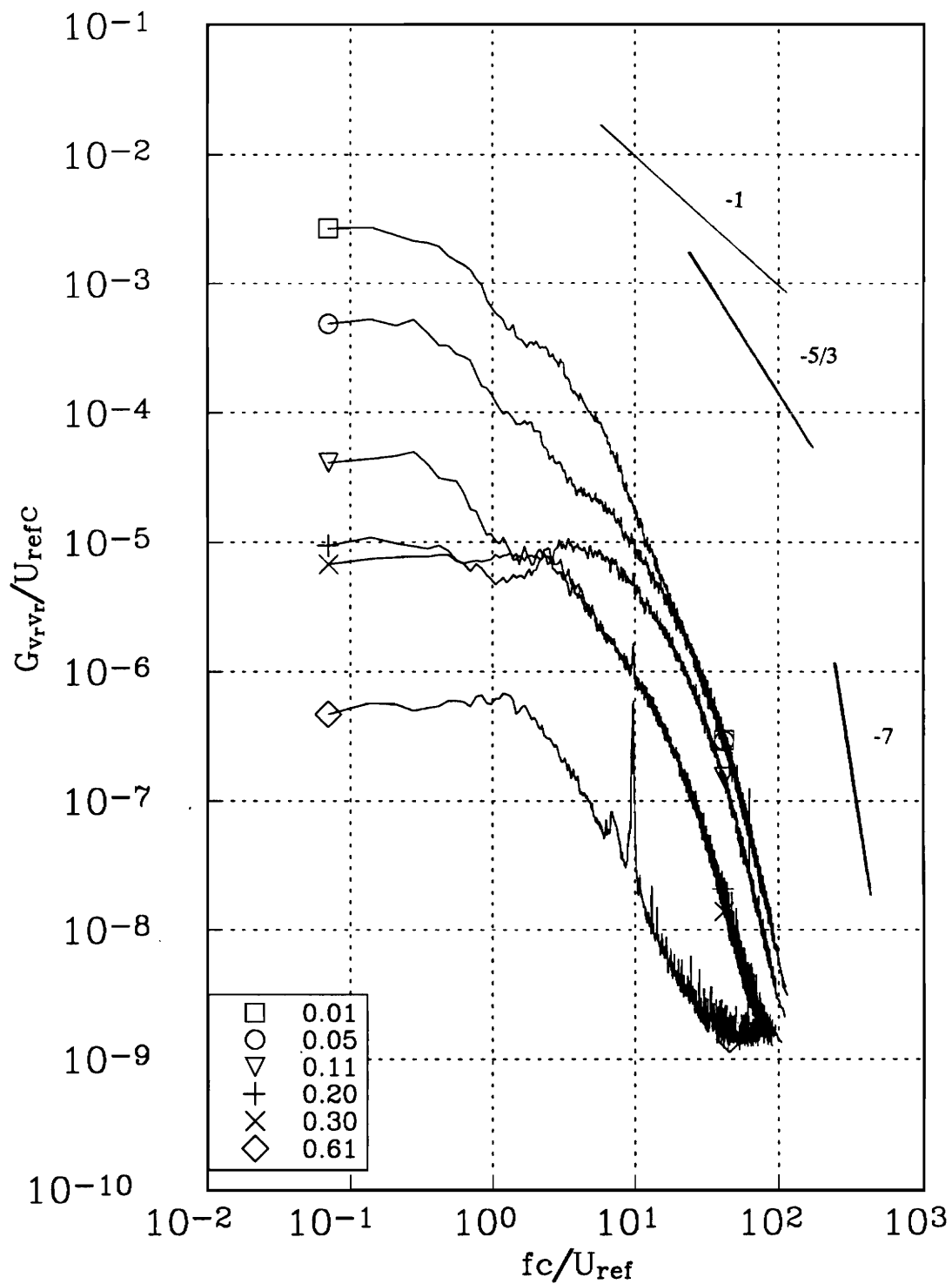


Figure 101c. v_r autospectra measured at representative radial locations along profile Cc for the upper co-rotating vortex at $x/c=15$. Tic marks in figure 99 indicate measured r/c locations.

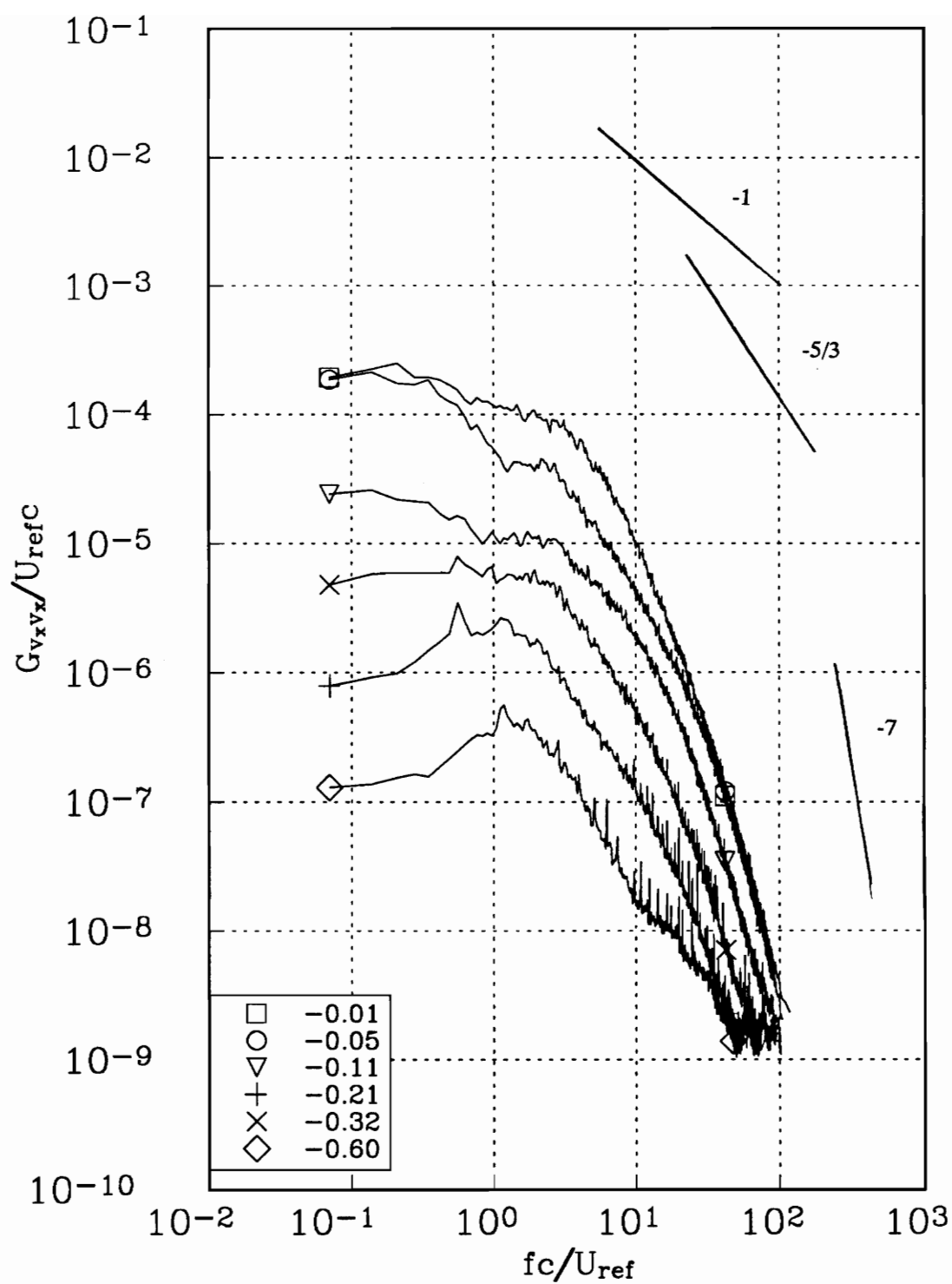


Figure 102a. v_x autospectra measured at representative radial locations along profile Cc for the upper co-rotating vortex at $x/c=15$. Tic marks in figure 99 indicate measured r/c locations.

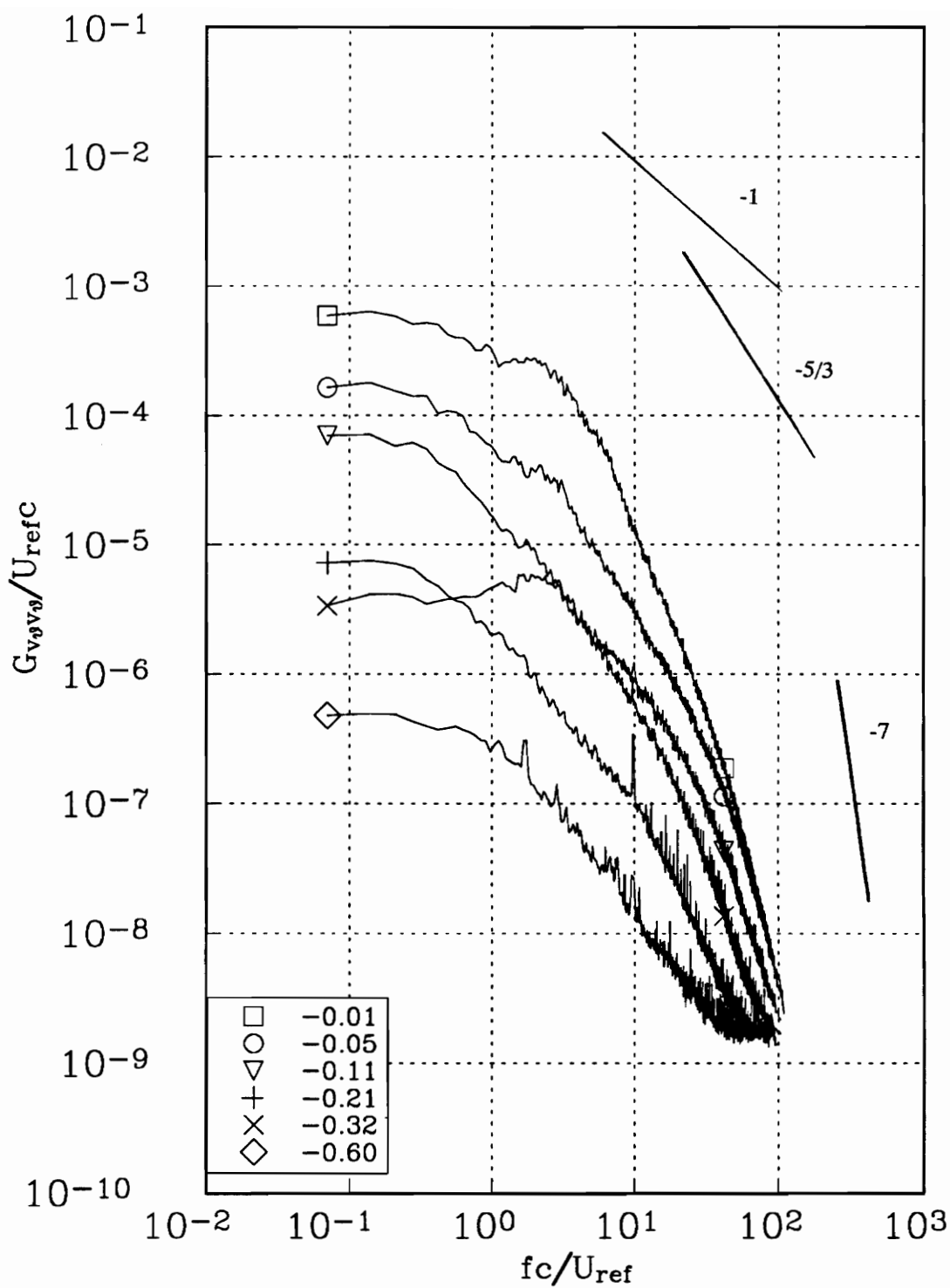


Figure 102b. v_θ autospectra measured at representative radial locations along profile Cc for the upper co-rotating vortex at $x/c=15$. Tic marks in figure 99 indicate measured r/c locations.

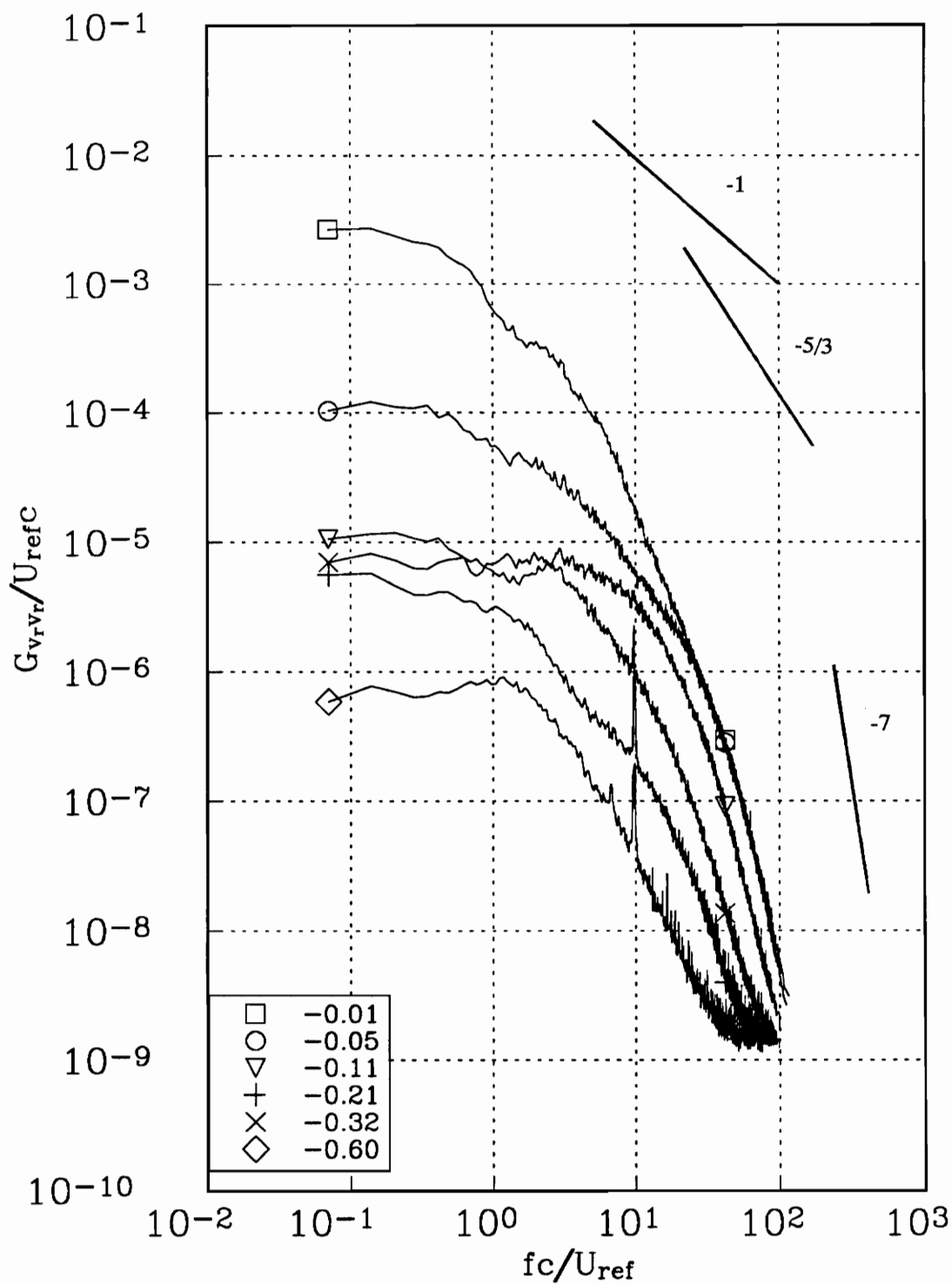


Figure 102c. v_r autospectra measured at representative radial locations along profile Cc for the upper co-rotating vortex at $x/c=15$. Tic marks in figure 99 indicate measured r/c locations.

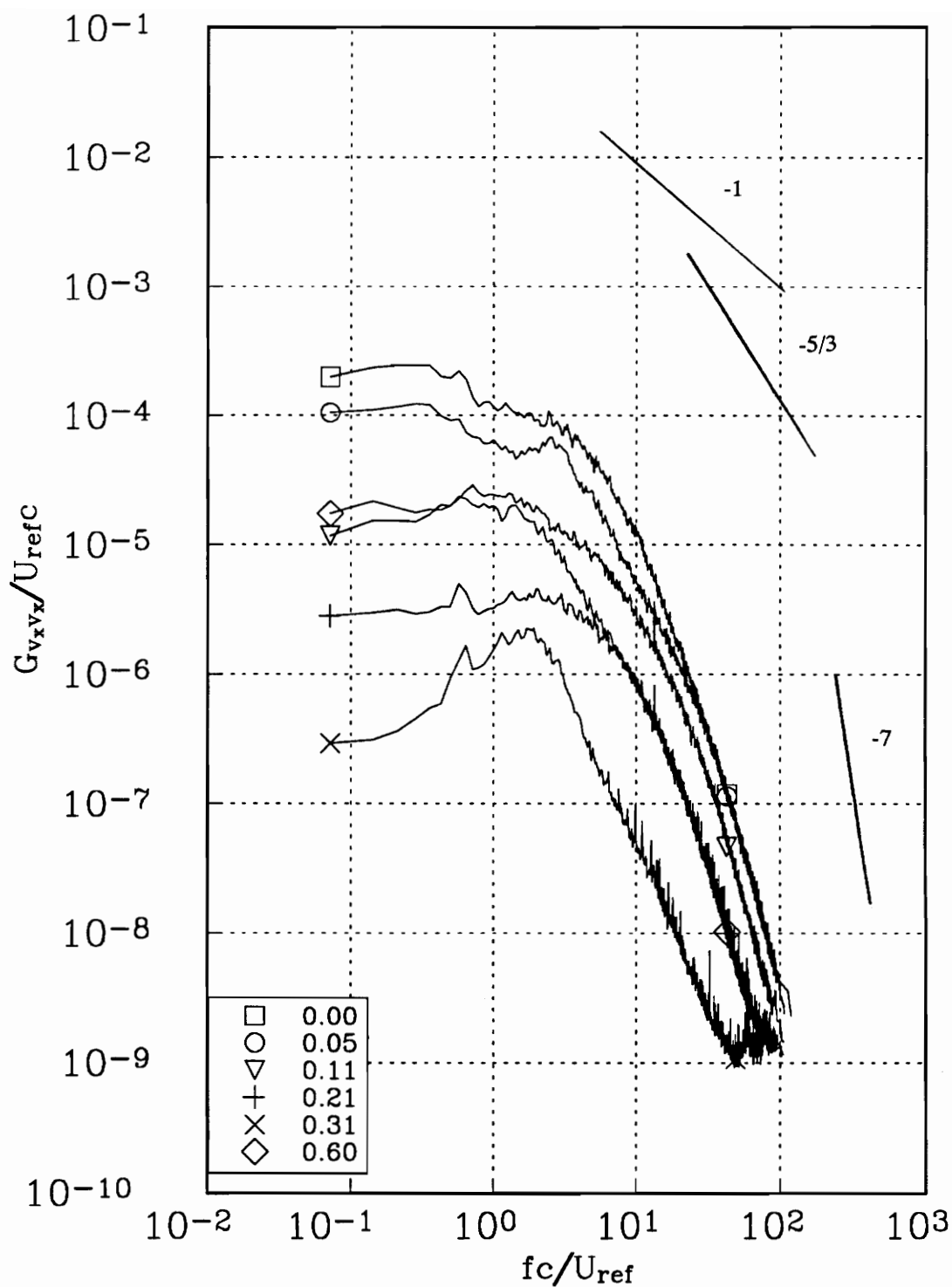


Figure 103a. v_x autospectra measured at representative radial locations along profile Dd for the upper co-rotating vortex at $x/c=15$. Tic marks in figure 100 indicate measured r/c locations.

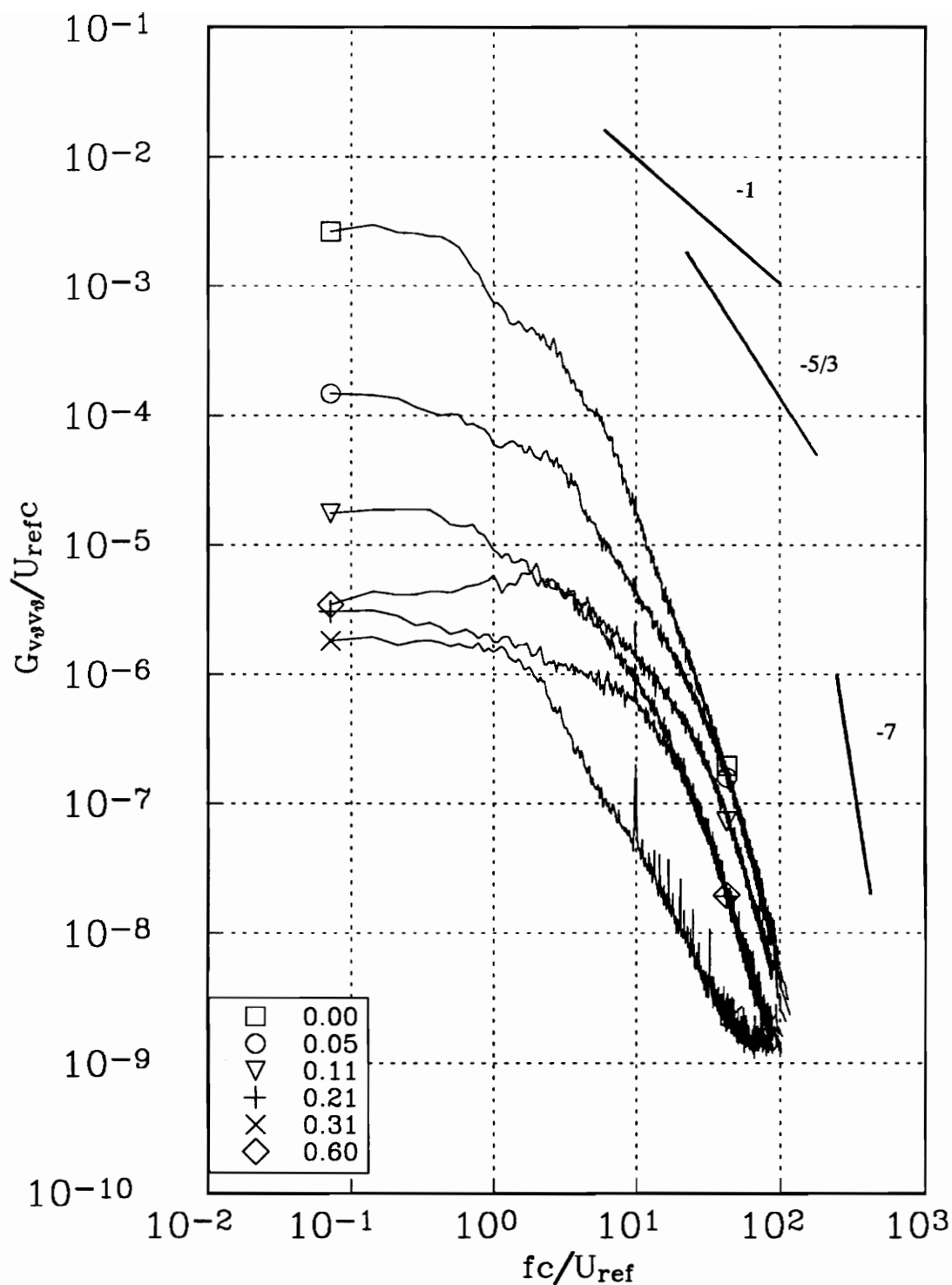


Figure 103b. v_θ autospectra measured at representative radial locations along profile Dd for the upper co-rotating vortex at $x/c=15$. Tic marks in figure 100 indicate measured r/c locations.

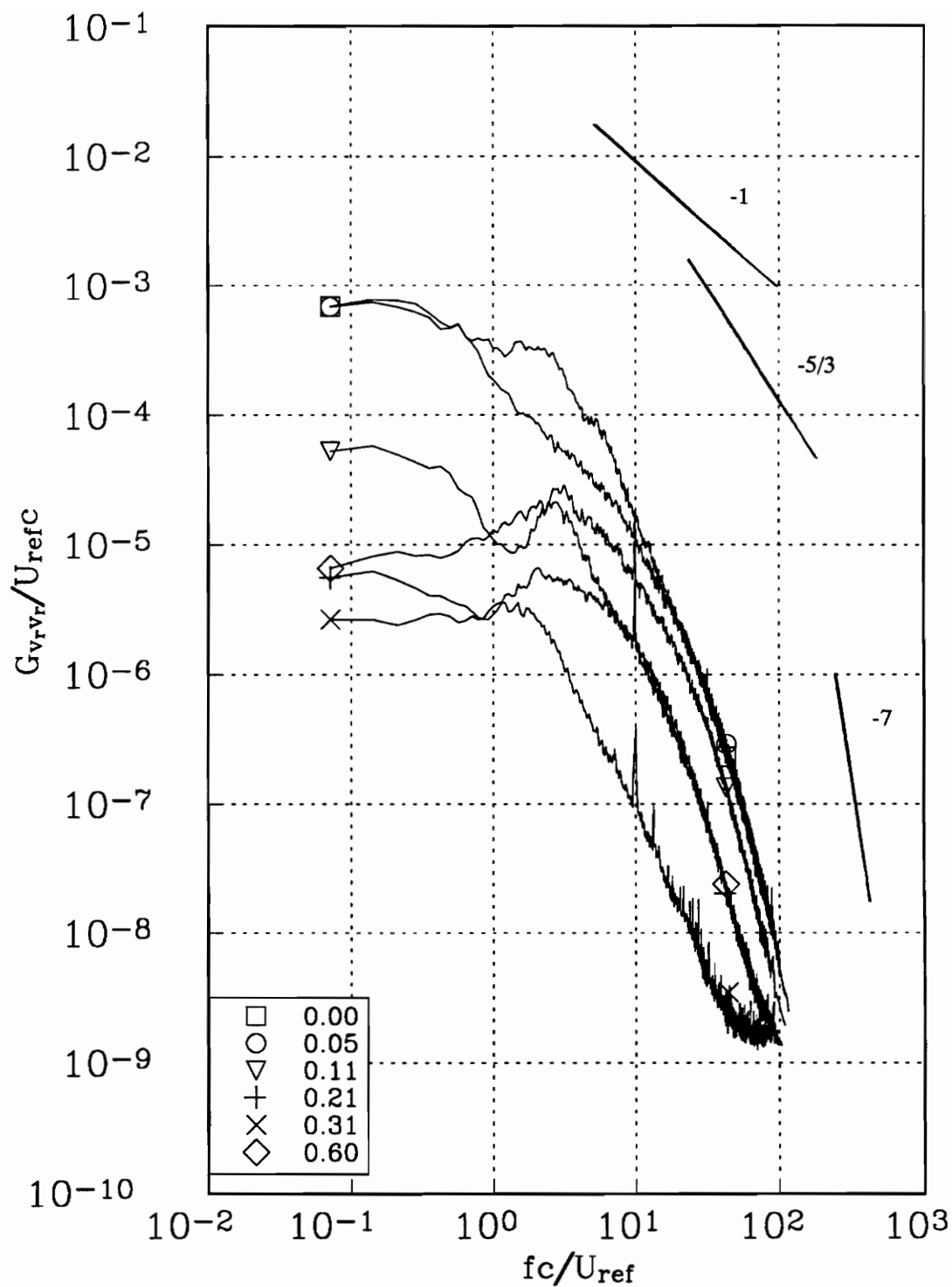


Figure 103c. v_r autospectra measured at representative radial locations along profile Dd for the upper co-rotating vortex at $x/c=15$. Tic marks in figure 100 indicate measured r/c locations.

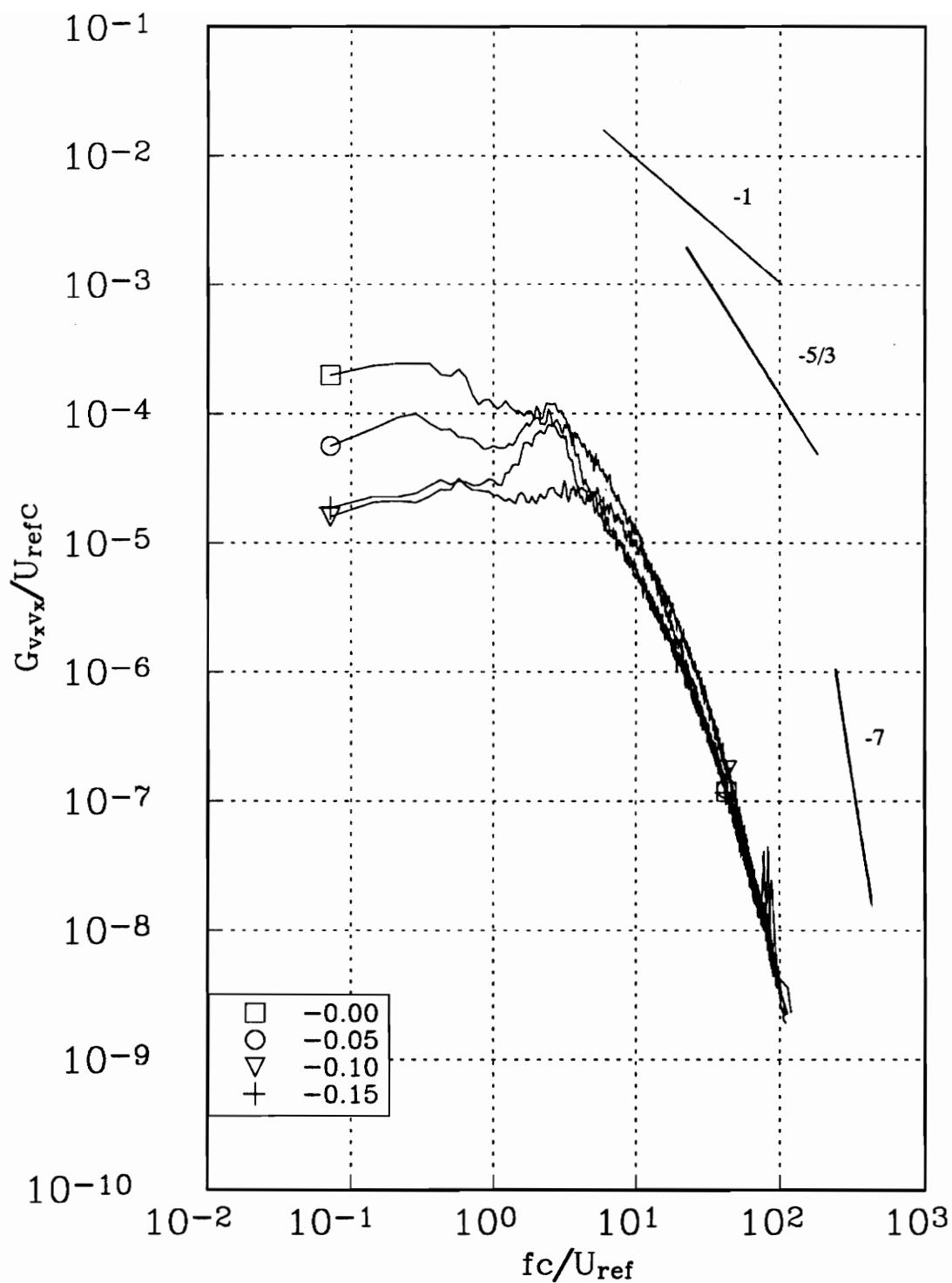


Figure 104a. v_x autospectra measured at representative radial locations along profile Dd for the upper co-rotating vortex at $x/c=15$. Tic marks in figure 100 indicate measured r/c locations.

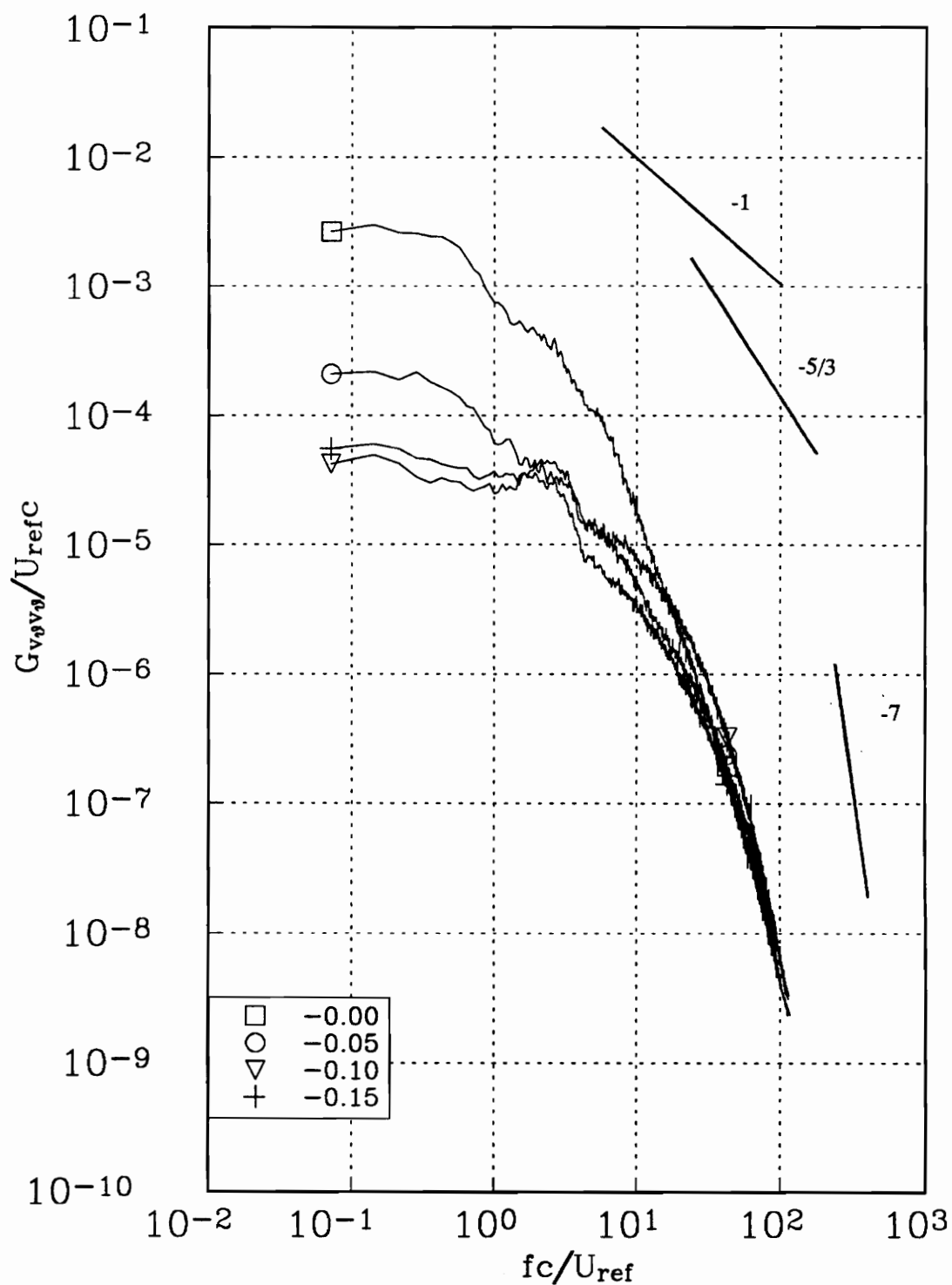


Figure 104b. v_θ autospectra measured at representative radial locations along profile Dd for the upper co-rotating vortex at $x/c=15$. Tic marks in figure 100 indicate measured r/c locations.

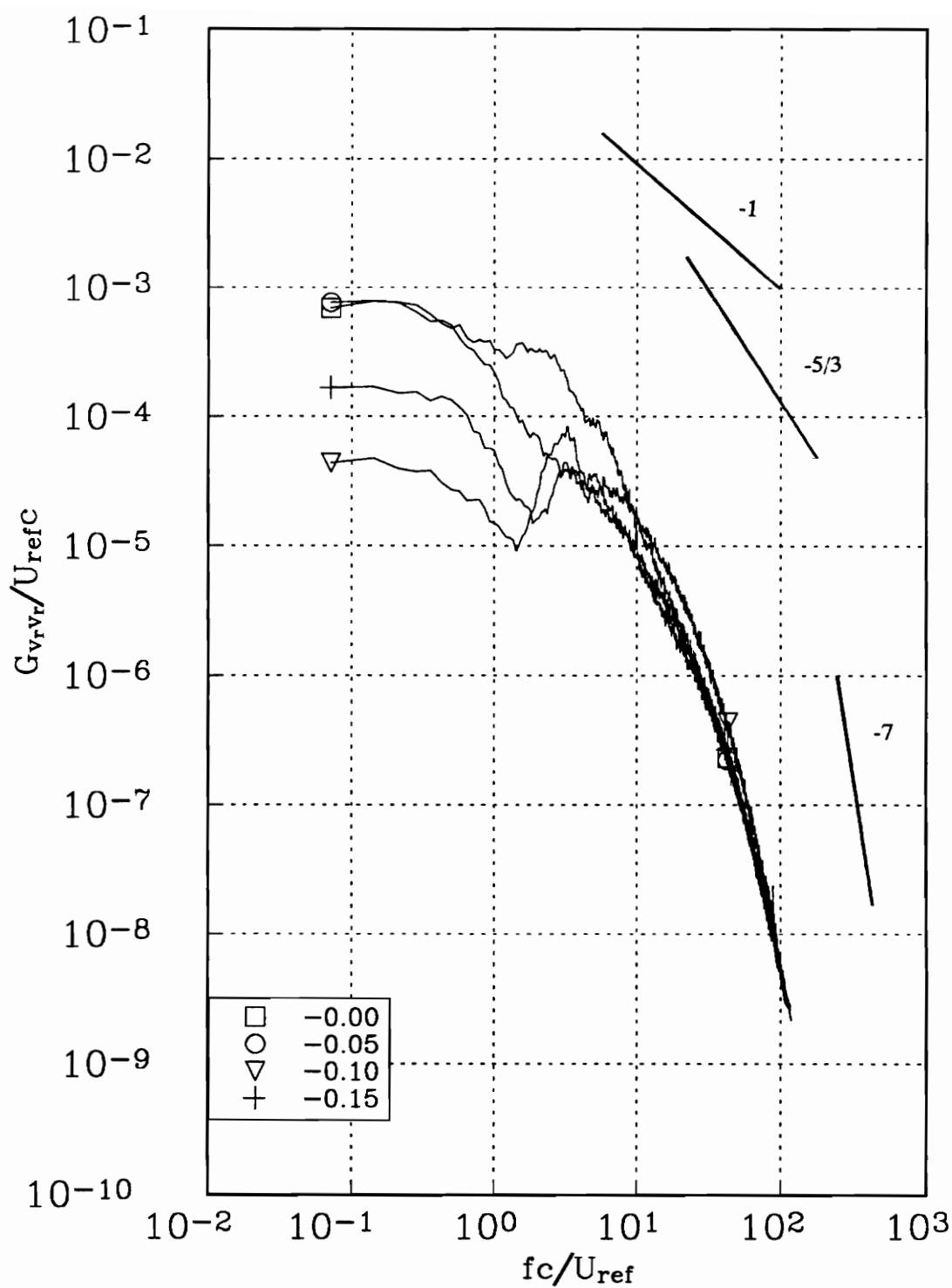


Figure 104c. v_r autospectra measured at representative radial locations along profile Dd for the upper co-rotating vortex at $x/c=15$. Tic marks in figure 100 indicate measured r/c locations.

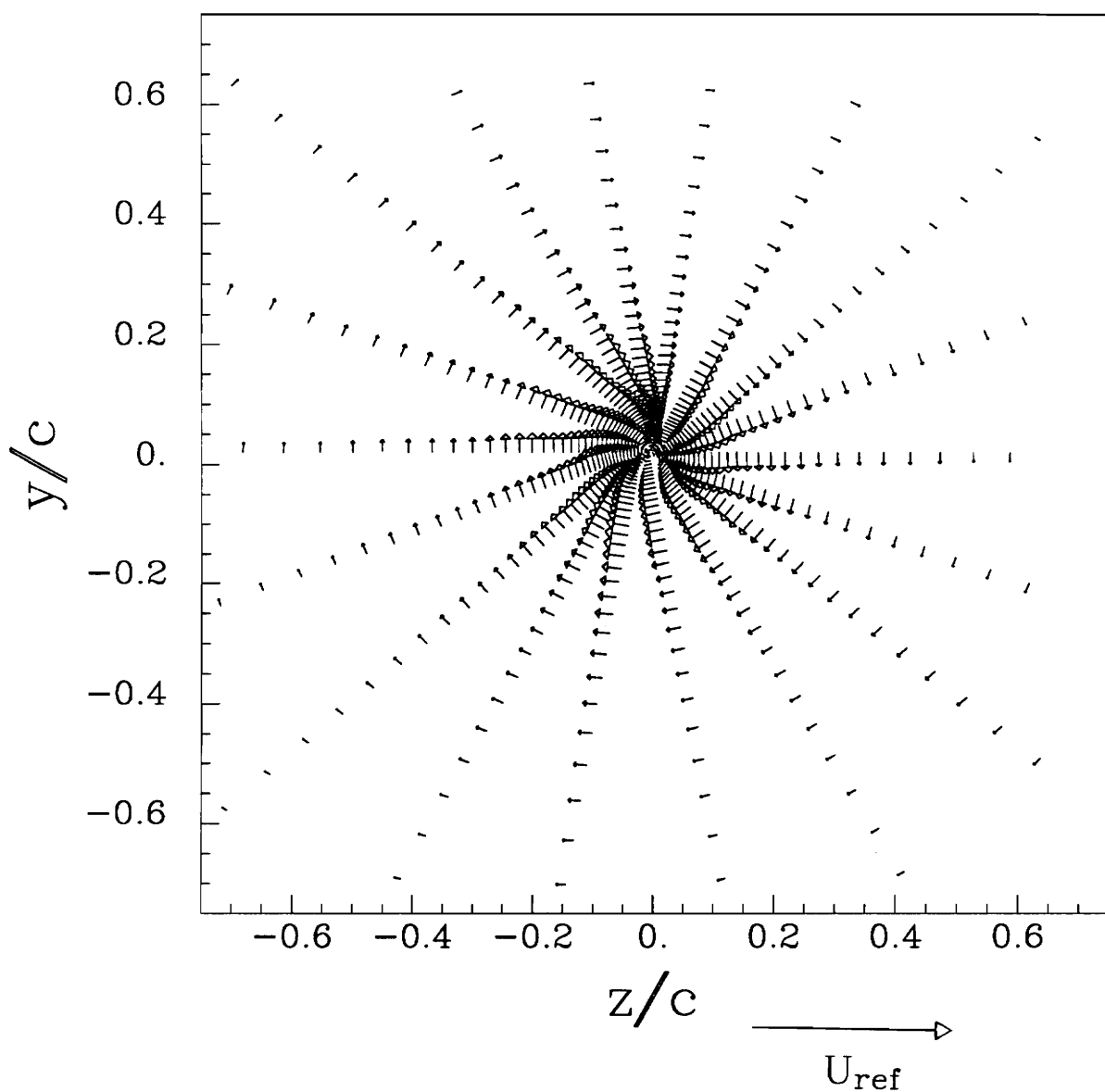
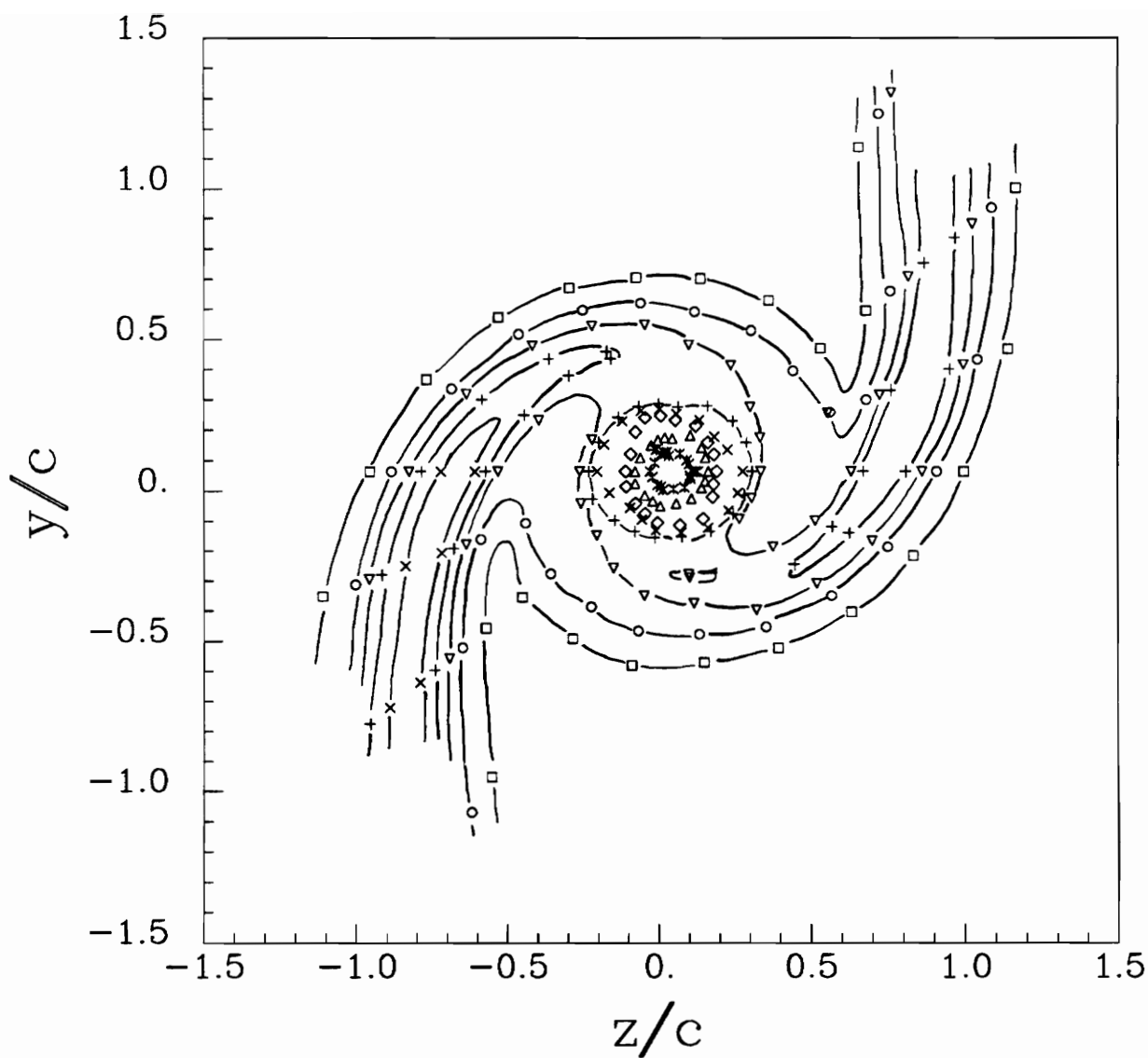
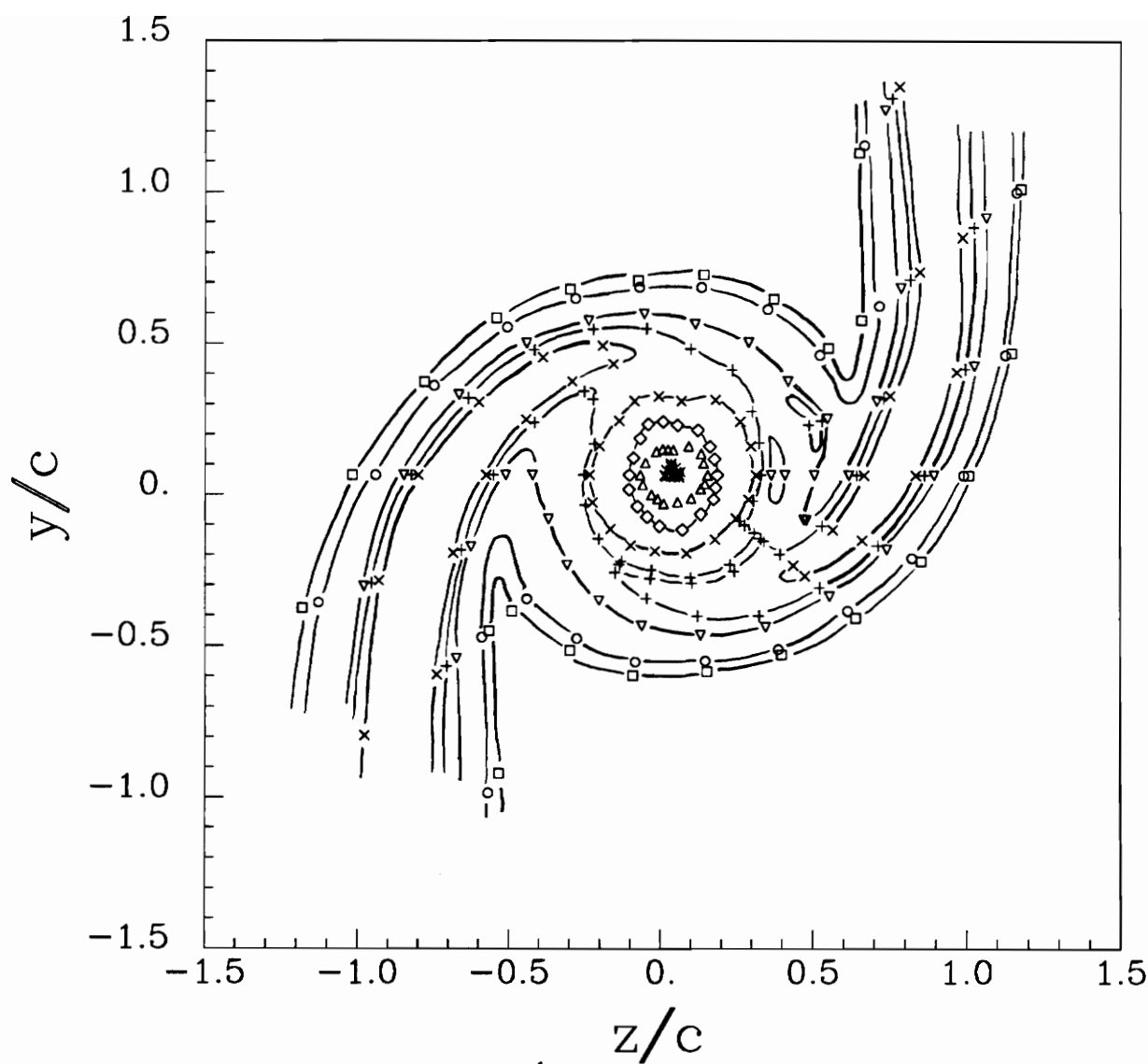


Figure 105. Mean secondary flow vectors of the co-rotating pair at $x/c=22$, angle of attack 5° , $Re_c=260,000$.



□	0.000010
○	0.000050
▽	0.000100
+	0.000150
×	0.000200
◇	0.000300
△	0.000500
✱	0.001000

Figure 106. Contours of turbulent kinetic energy k/U_{ref}^2 for the co-rotating pair at $x/c=22$, angle of attack 5° , $Re_c=260,000$.



□	0.000005
○	0.000010
▽	0.000050
+	0.000075
×	0.000100
◇	0.000250
△	0.000500
⋈	0.001000

Figure 107. Contours of v_x^2/U_{ref}^2 for the co-rotating pair at $x/c=22$, angle of attack 5° , $Re_c=260,000$.

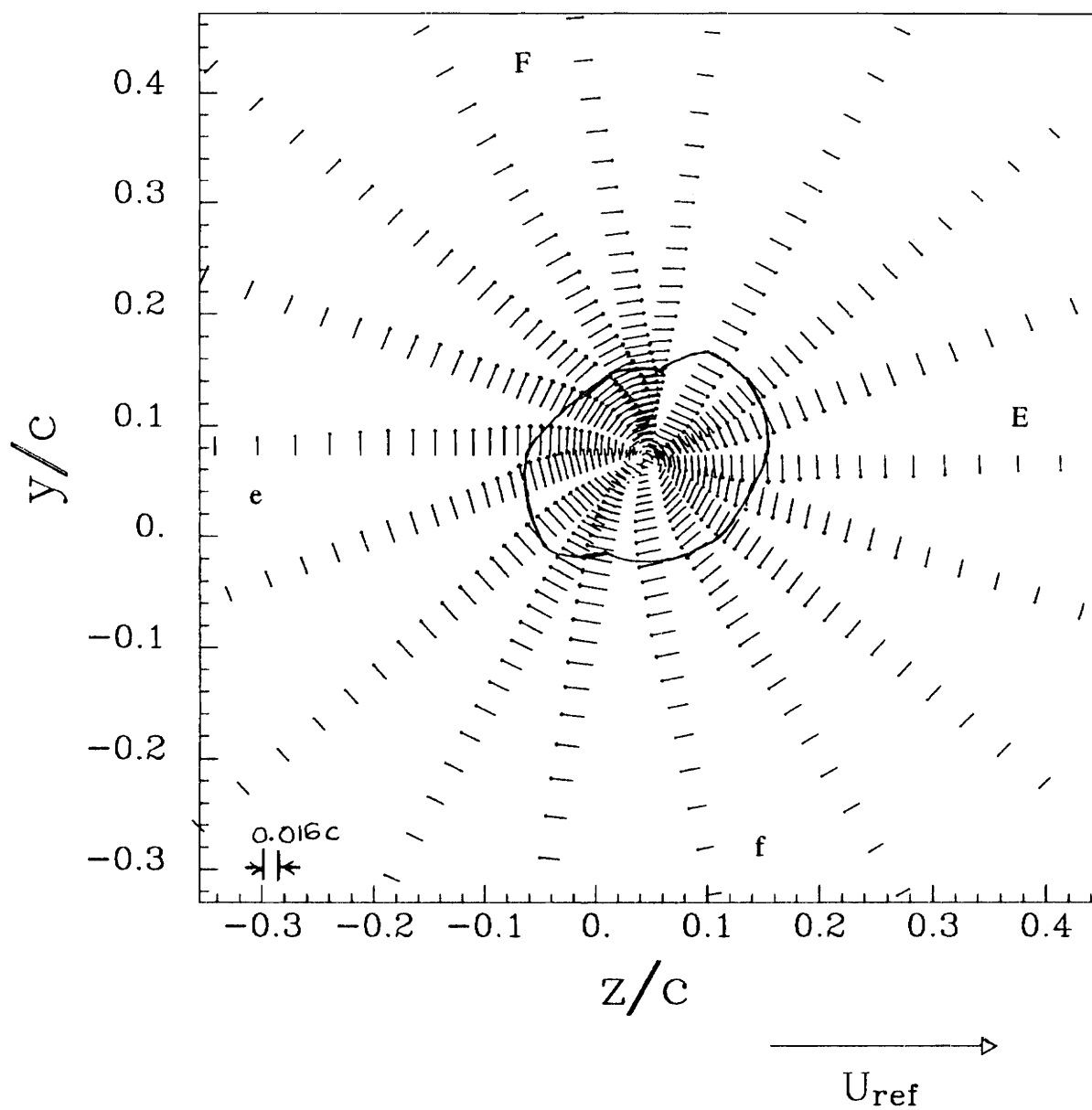


Figure 108. Core region showing mean secondary flows vectors for the co-rotating pair at $x/c=22$, angle of attack= 5° , $Re_c=260,000$. Dotted line indicates core edge.

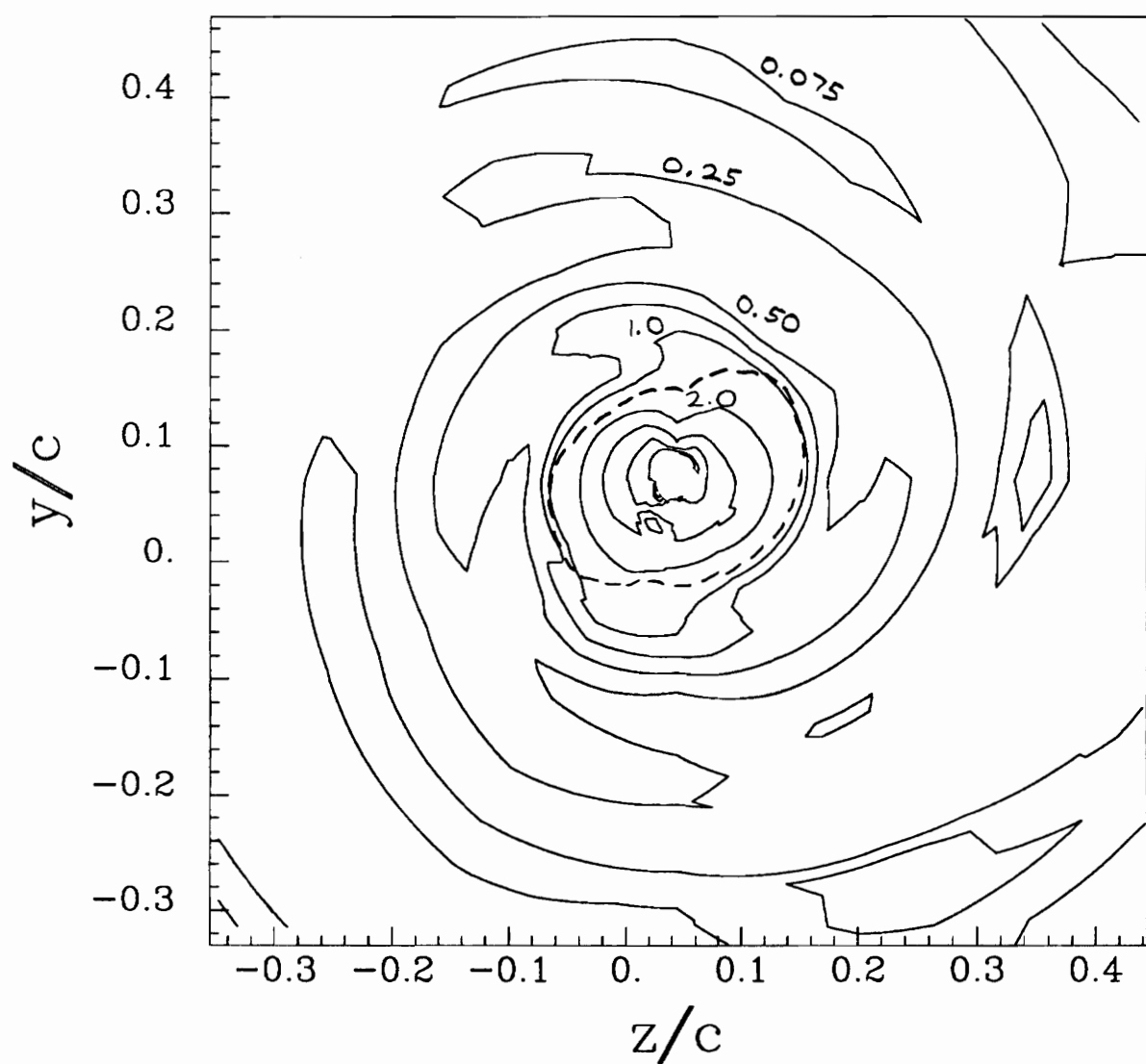


Figure 109. Core region showing contours of vorticity $\omega c/U_{\text{ref}}$ for the co-rotating vortex at $x/c=22$, angle of attack= 5° , $Re_c=260,000$. Dotted line indicates core edge.

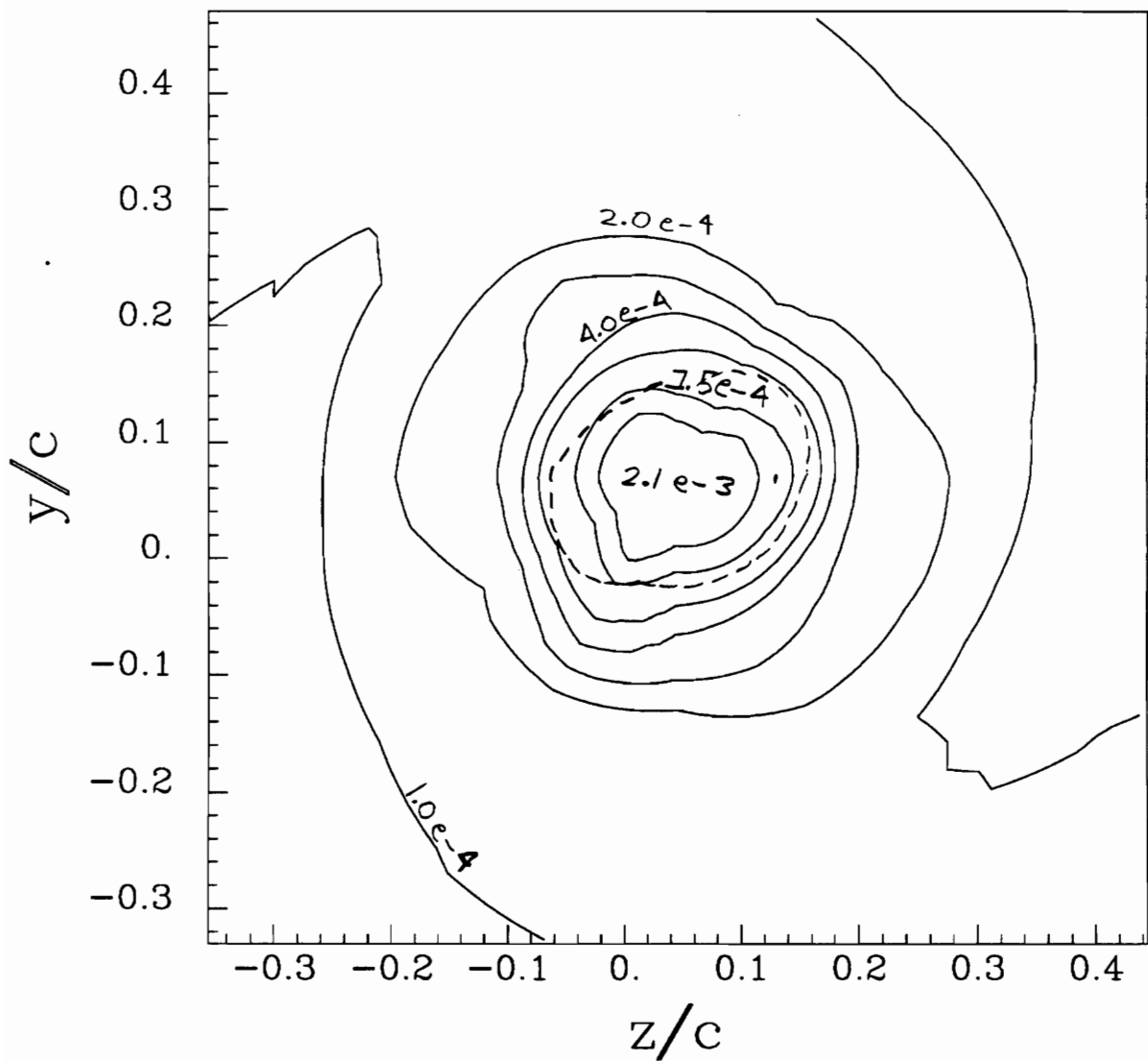


Figure 110. Core region showing contours of turbulent kinetic energy k/U_{ref}^2 for the co-rotating pair at $x/c=22$, angle of attack= 5° , $Re_c=260,000$. Dotted line indicates core edge.

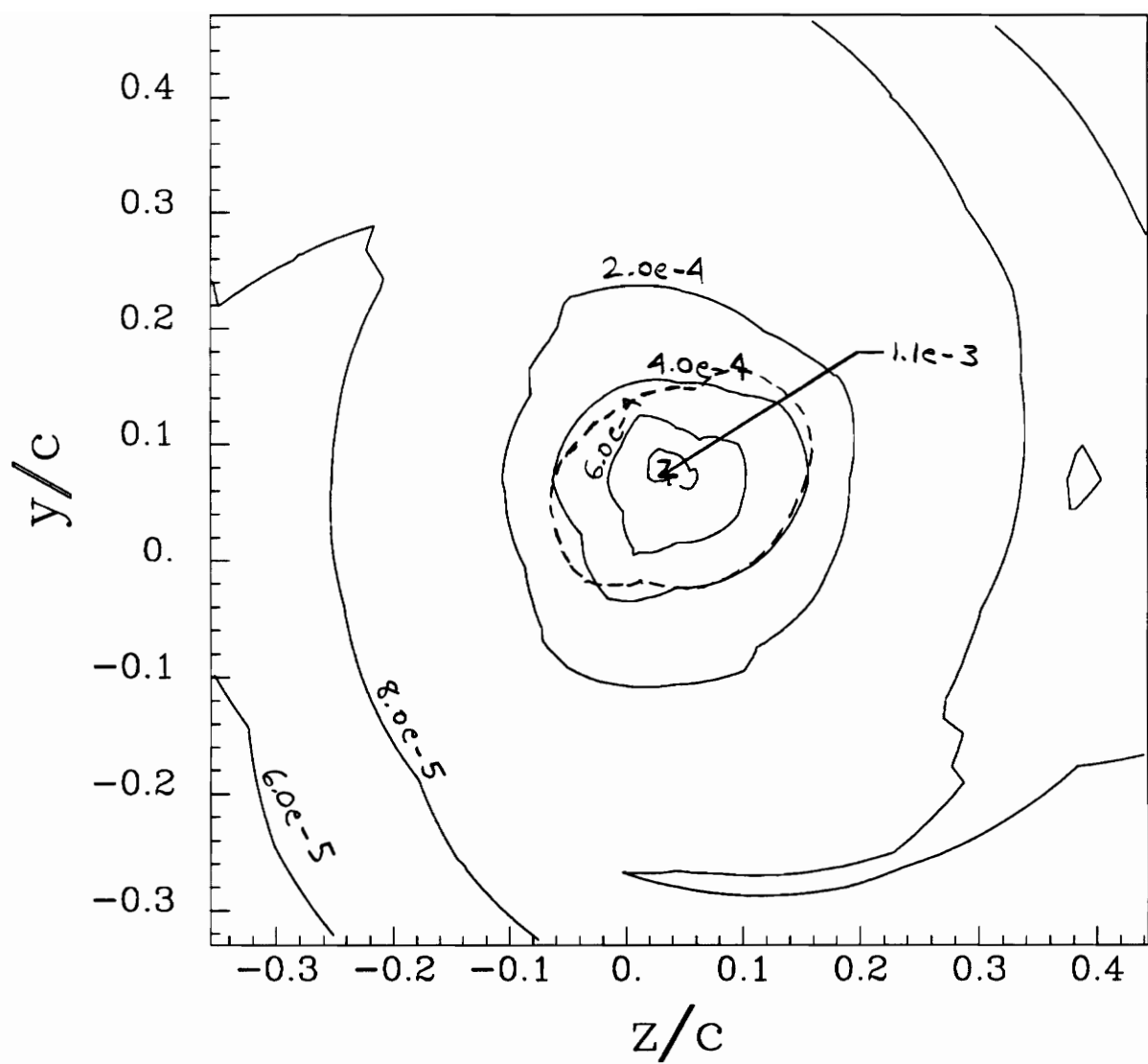


Figure 111. Core region showing contours of v_x^2/U_{ref}^2 for the co-rotating pair at $x/c=22$, angle of attack= 5° , $Re_c=260,000$. Dotted line indicates core edge.

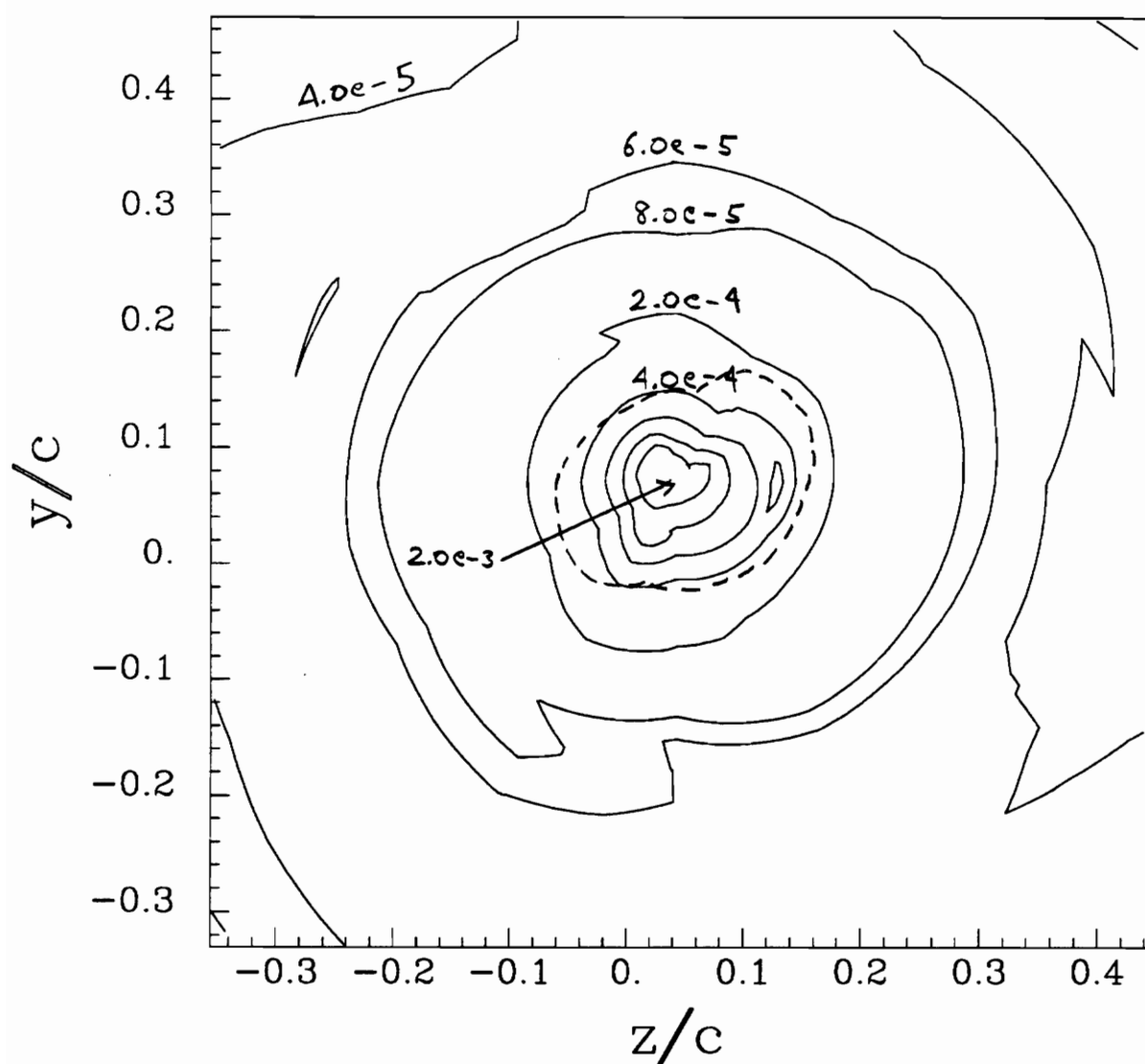


Figure 112. Core region showing contours of v_θ^2/U_{ref}^2 for the co-rotating pair at $x/c=22$, angle of attack= 5° , $Re_c=260,000$. Dotted line indicates core edge.

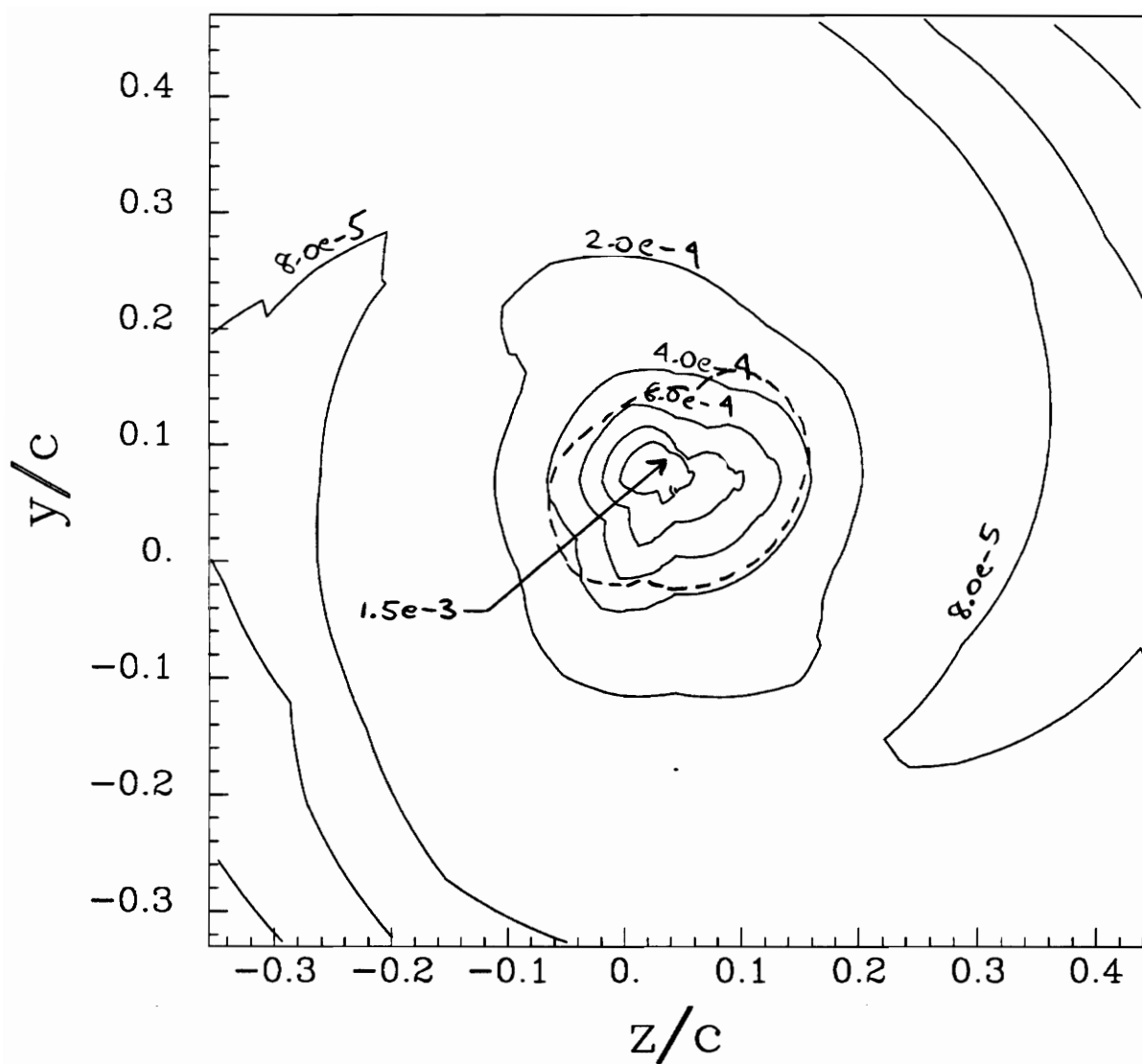


Figure 113. Core region showing contours of v_r^2/U_{ref}^2 for the co-rotating pair at $x/c=22$, angle of attack= 5° , $Re_c=260,000$. Dotted line indicates core edge.

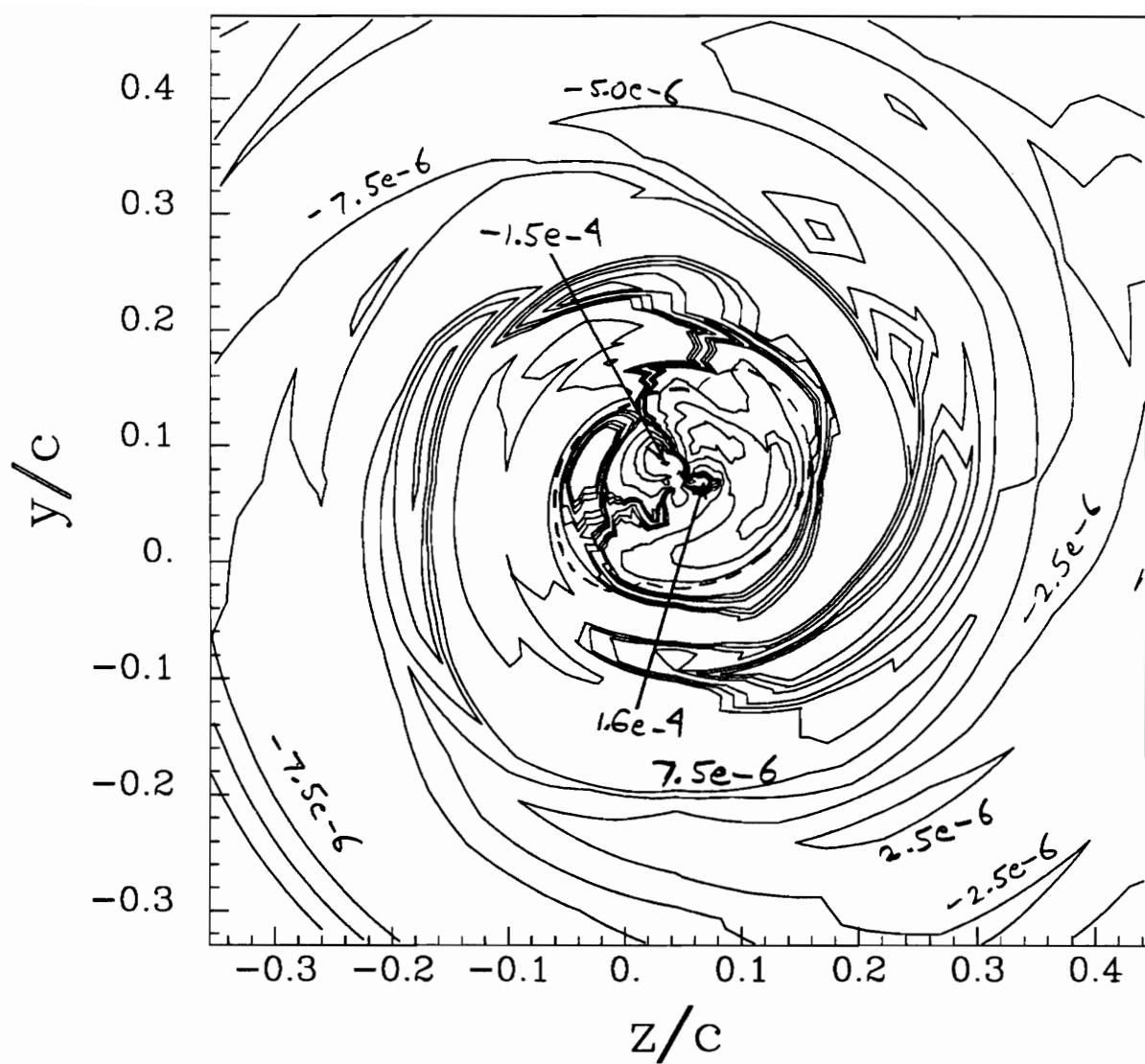


Figure 114. Core region showing contours of $v_x v_\theta / U_{ref}^2$ for the co-rotating pair at $x/c=22$, angle of attack= 5° , $Re_c=260,000$. Dotted line indicates core edge.

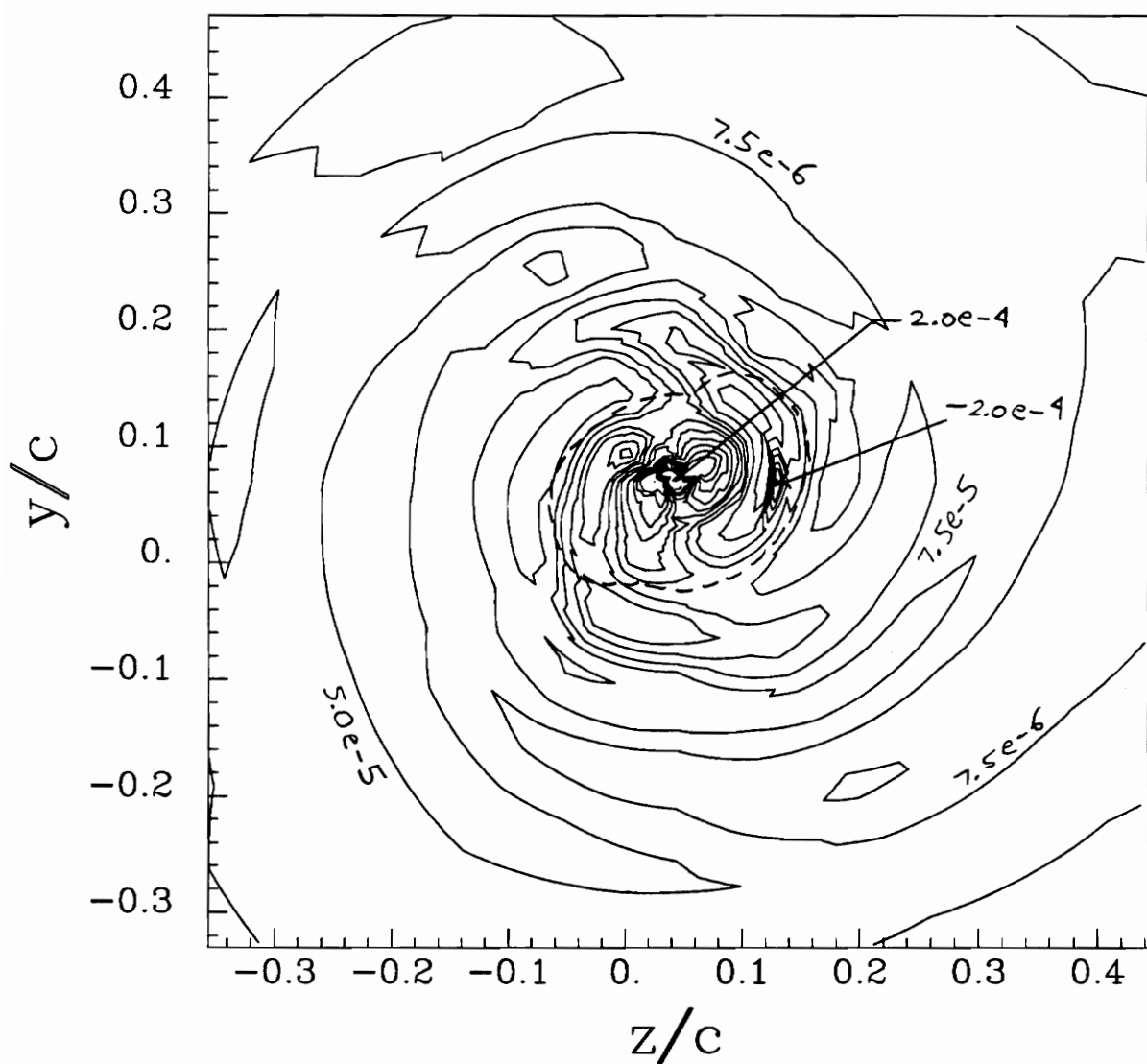


Figure 115. Core region showing contours of $v_\theta v_r / U_{\text{ref}}^2$ for the co-rotating pair at $x/c=22$, angle of attack= 5° , $Re_c=260,000$. Dotted line indicates core edge.

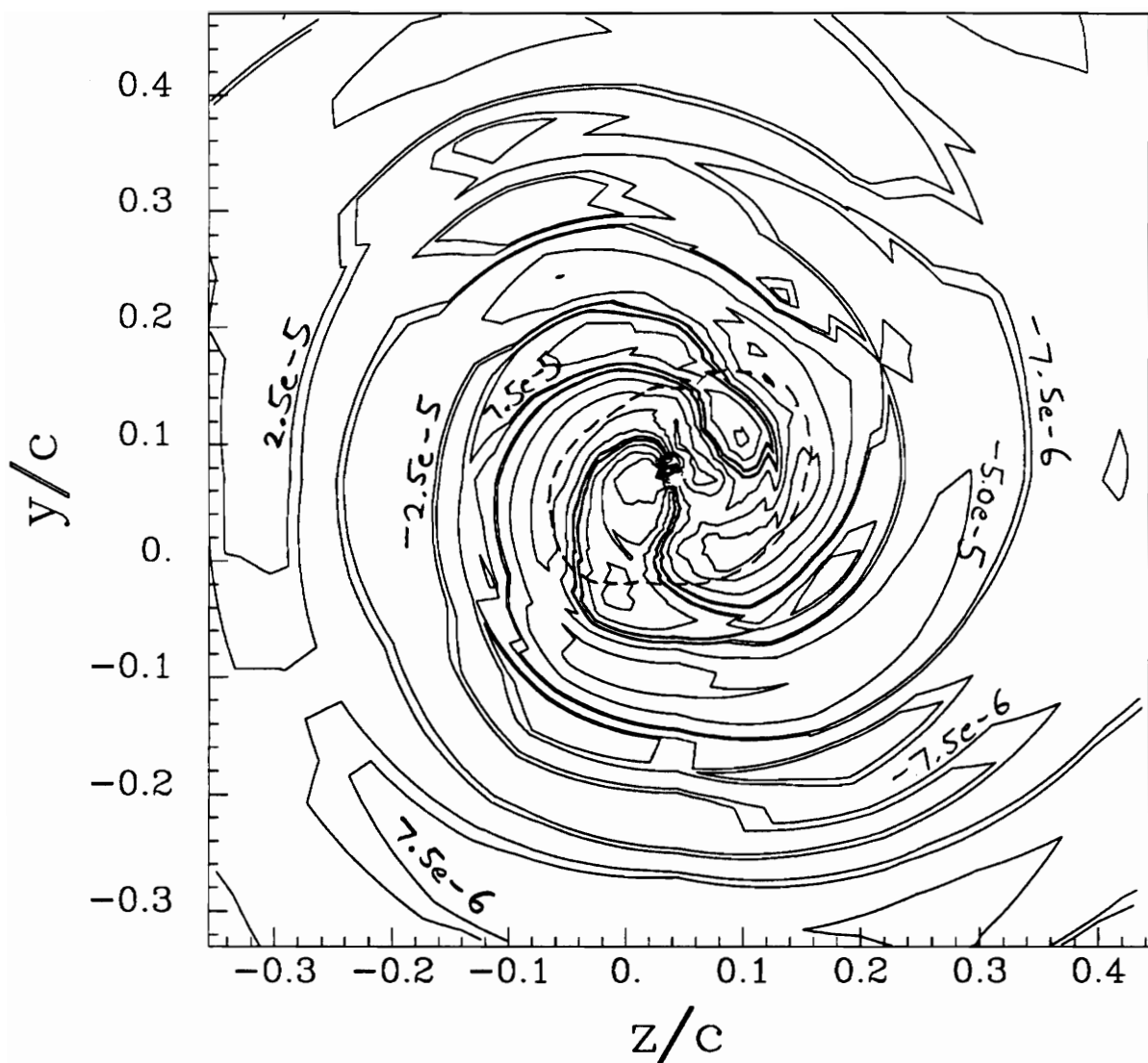


Figure 116. Core region showing contours of $v_x v_r / U_{ref}^2$ for the co-rotating pair at $x/c=22$, angle of attack= 5° , $Re_c=260,000$. Dotted line indicates core edge.

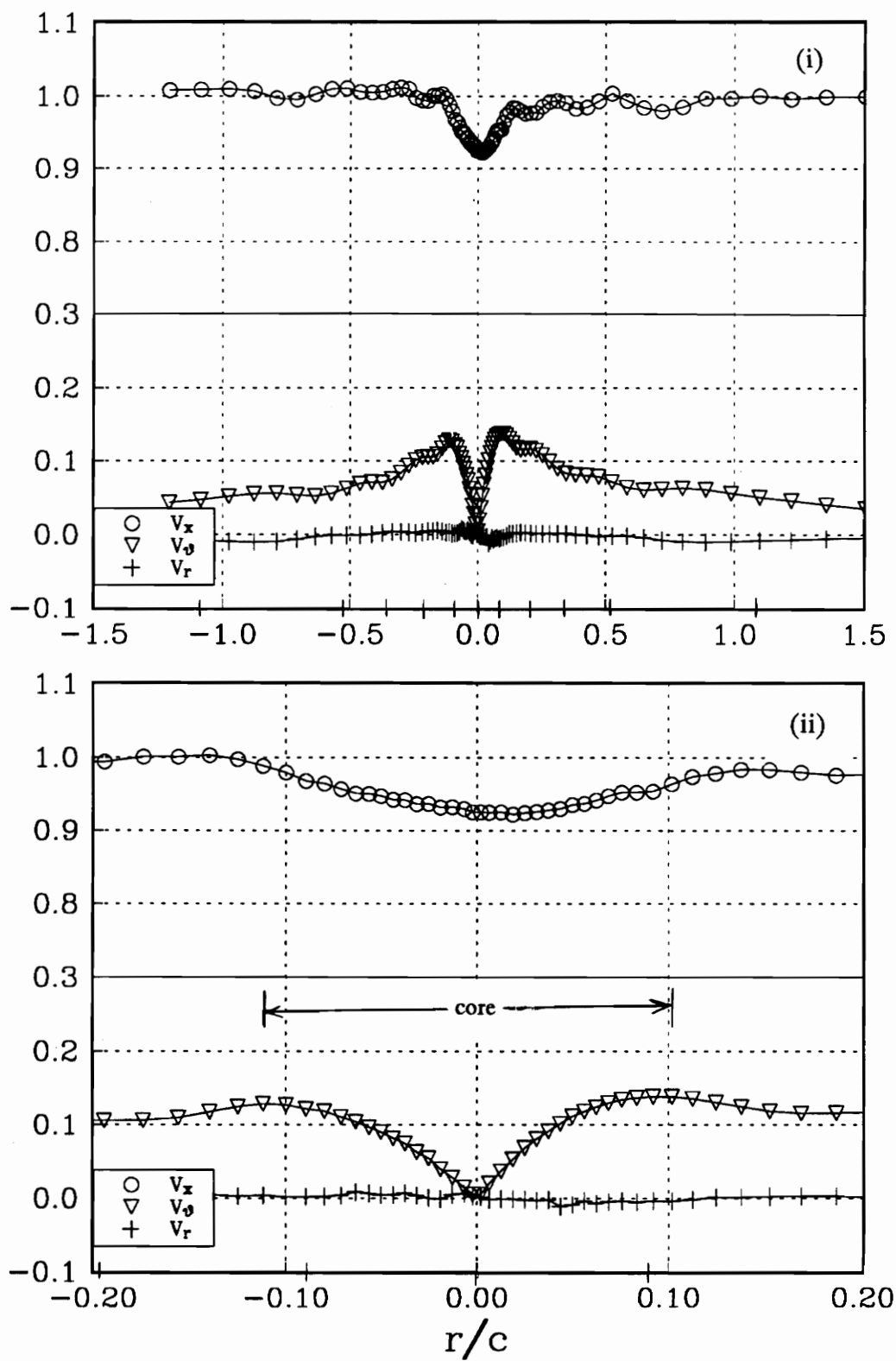


Figure 117a. Profile Ee mean velocities for the co-rotating pair at $x/c=22$. (i) wake region, (ii) core region.

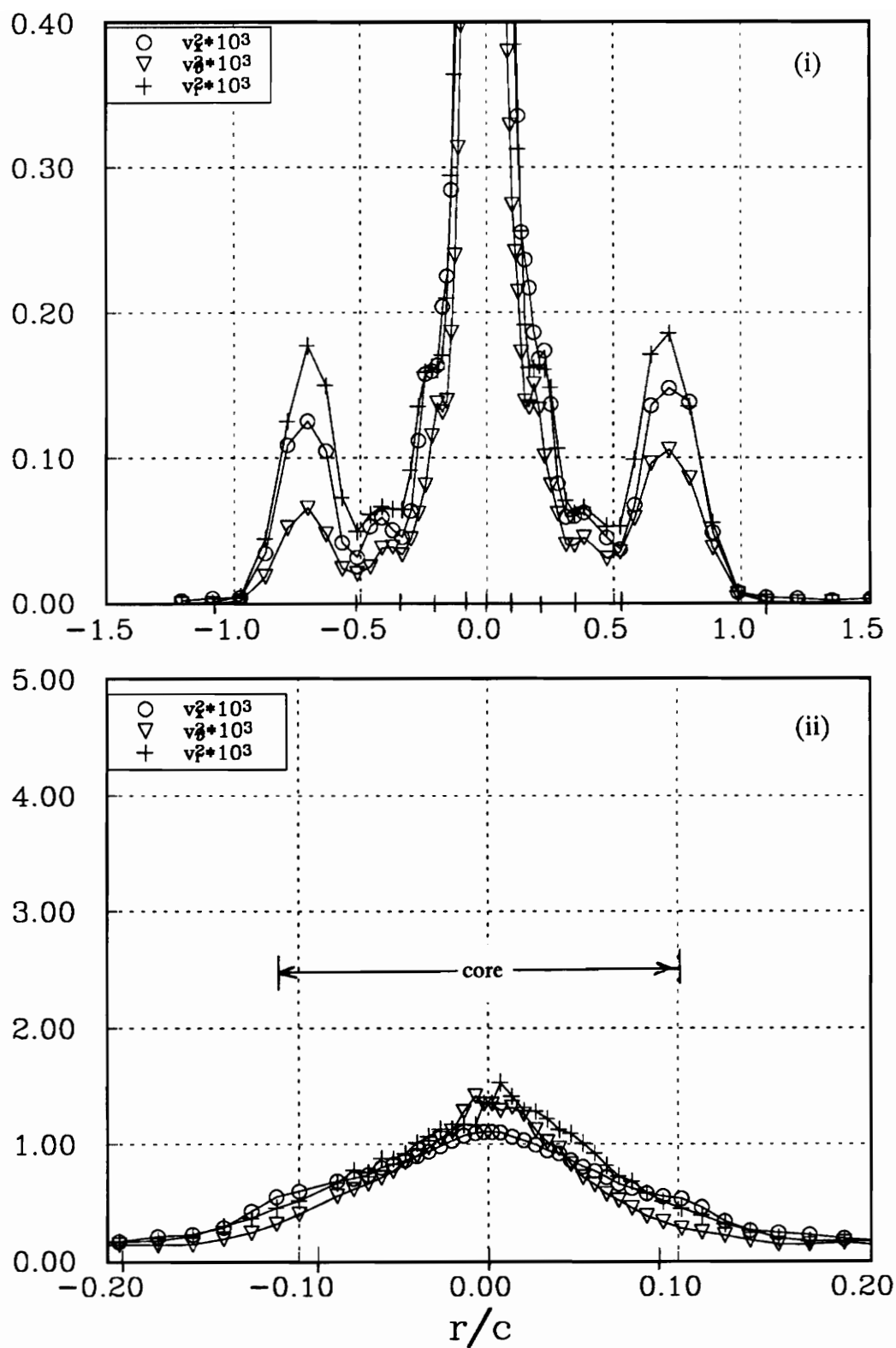


Figure 117b. Profile σ_{rr} normal stresses for the co-rotating pair at $x/c=22$. (i) wake region, (ii) core region.

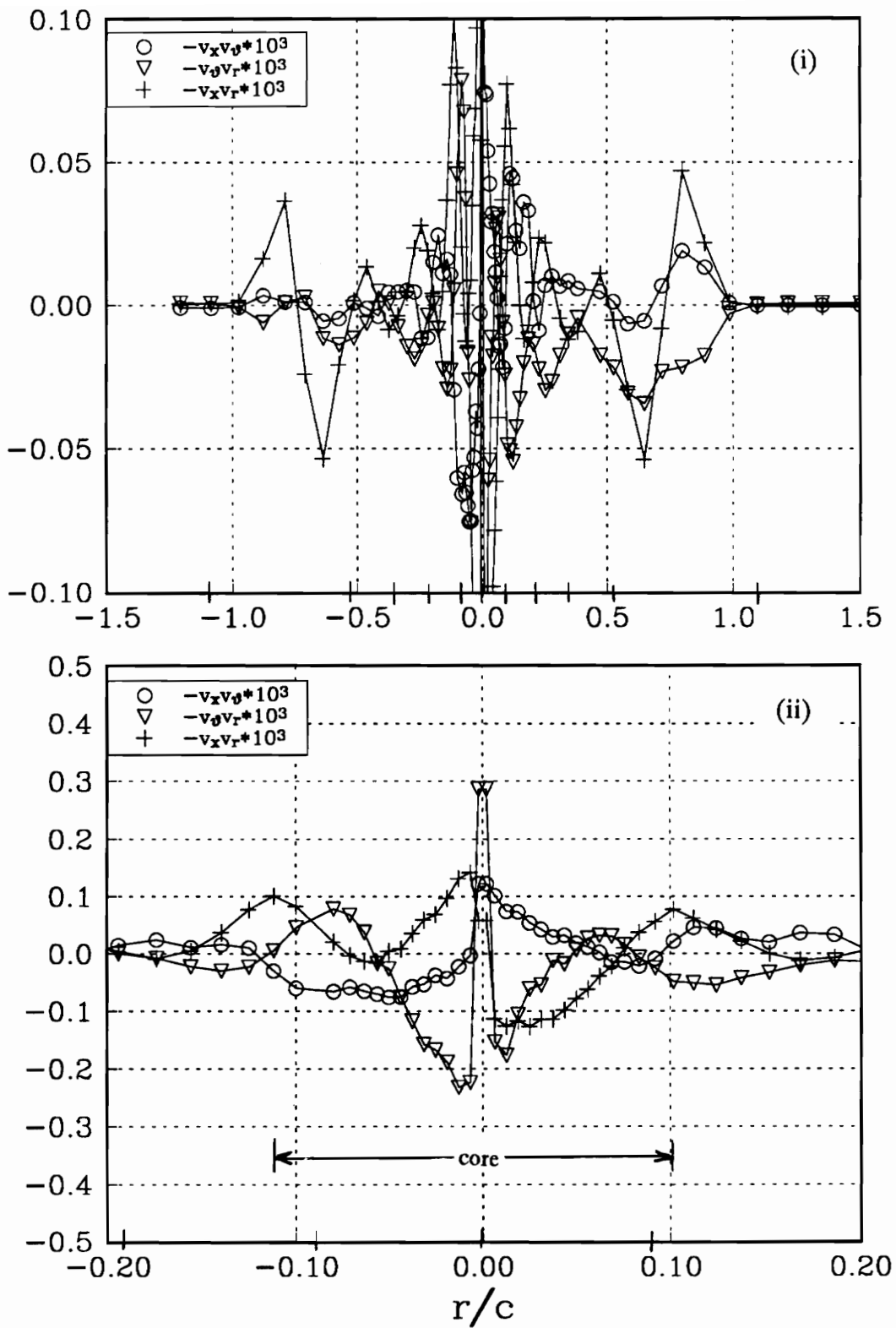


Figure 117c. Profile E_e shear stresses for the co-rotating pair at $x/c=22$. (i) wake region, (ii) core region.

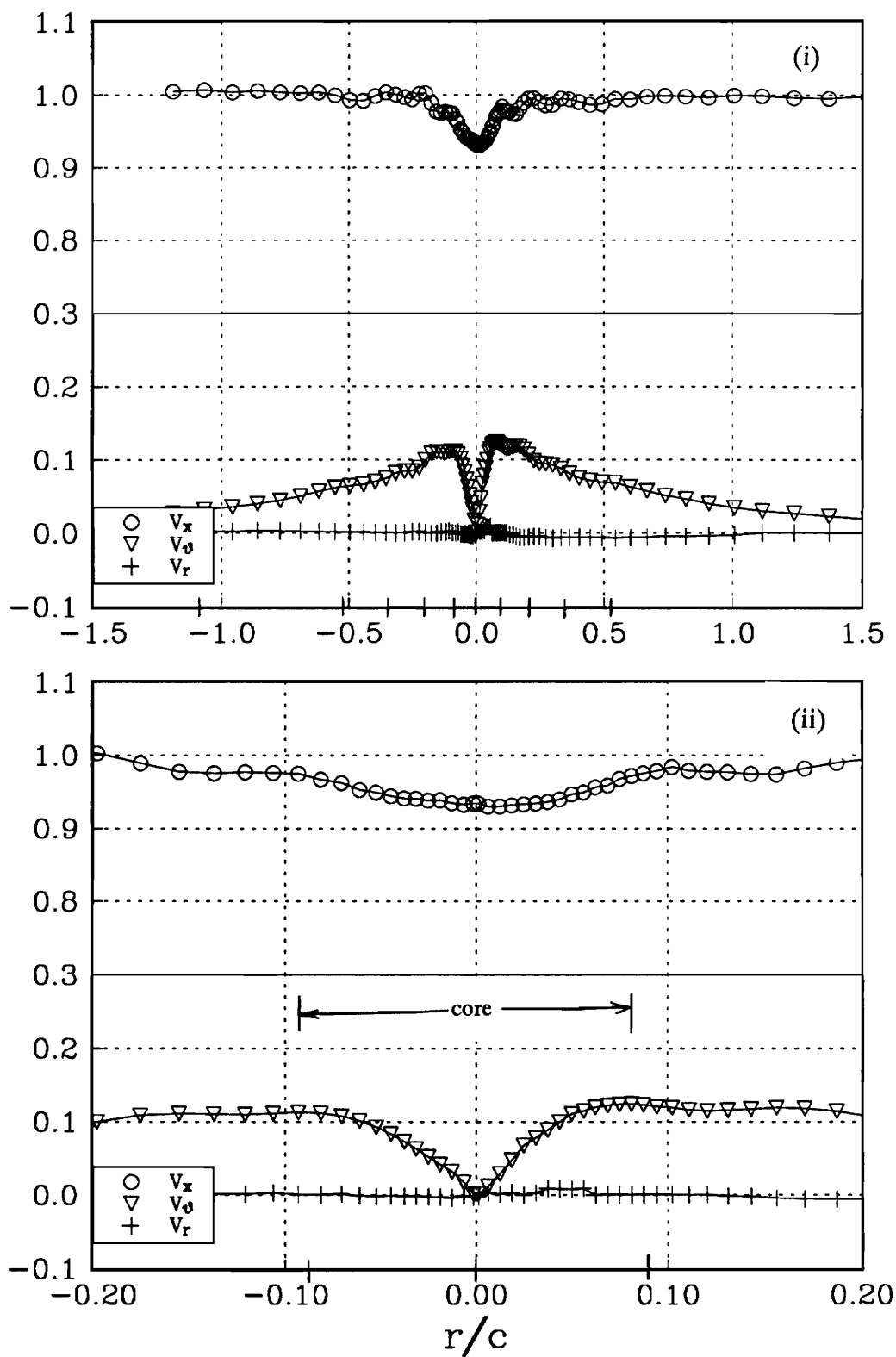


Figure 118a. Profile of mean velocities for the co-rotating pair at $x/c=22$. (i) wake region, (ii) core region.

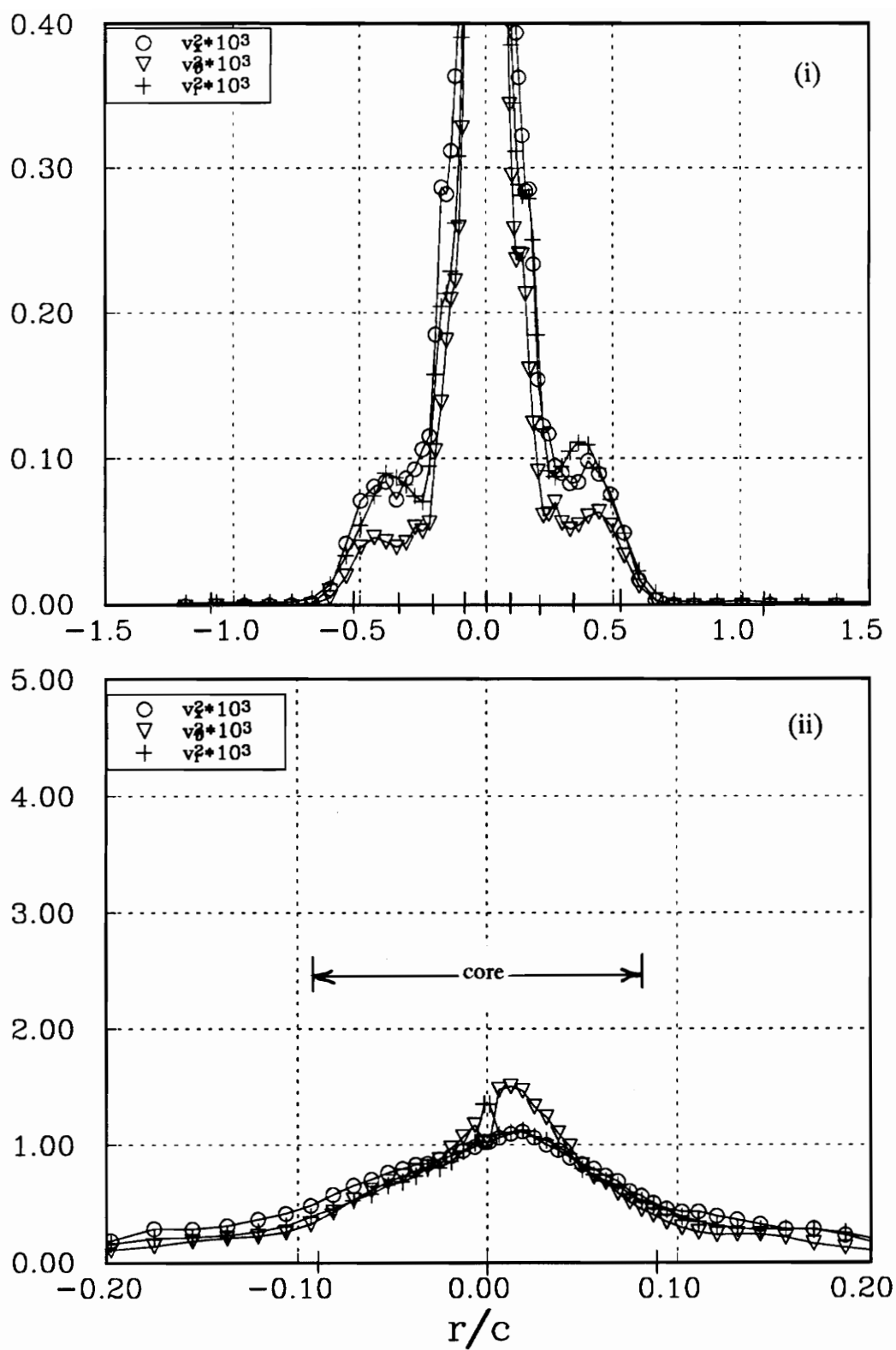


Figure 118b. Profile Ff normal stresses for the co-rotating pair at $x/c=22$. (i) wake region, (ii) core region.

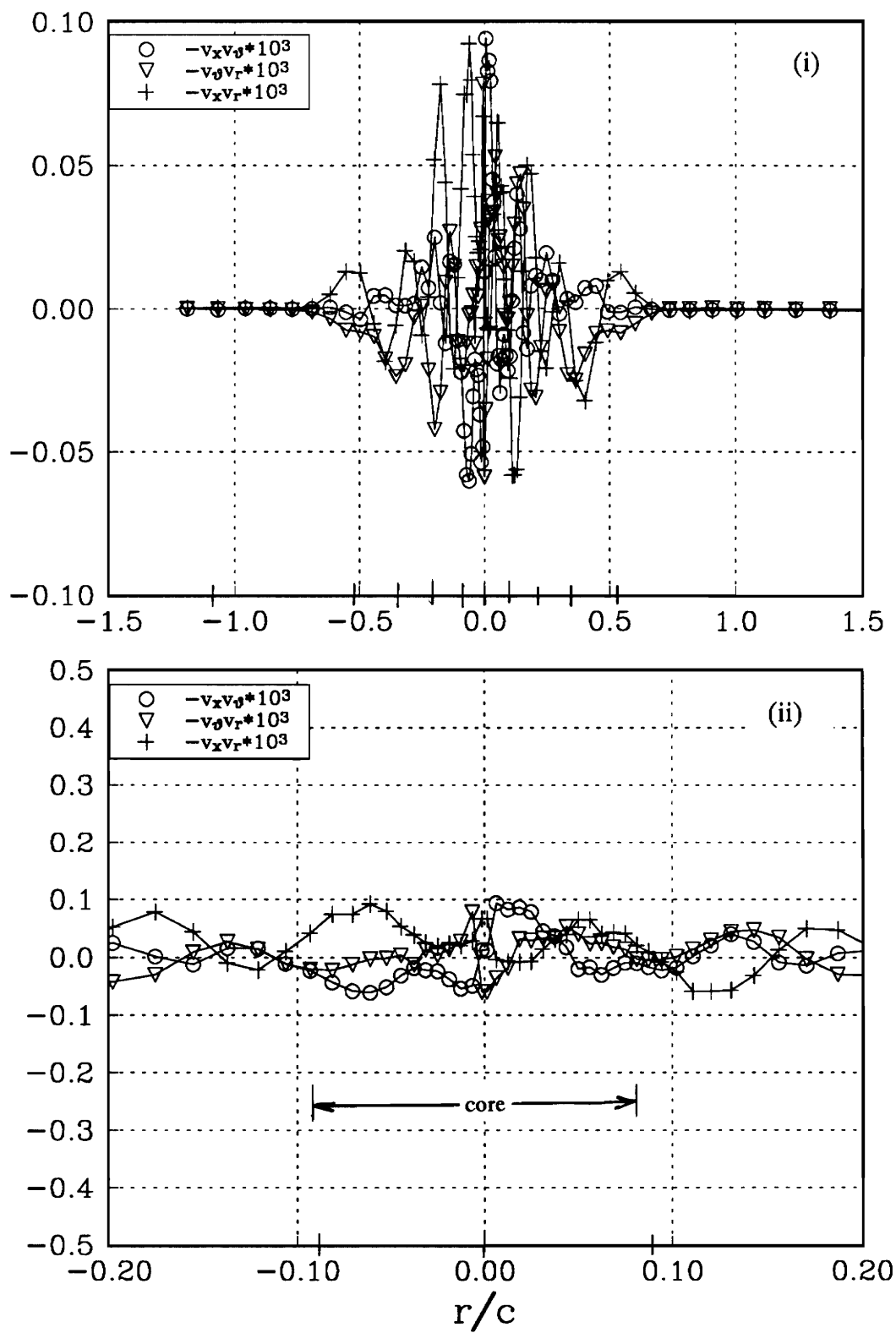


Figure 118c. Profile Ff shear stresses for the co-rotating pair at $x/c=22$. (i) wake region, (ii) core region.

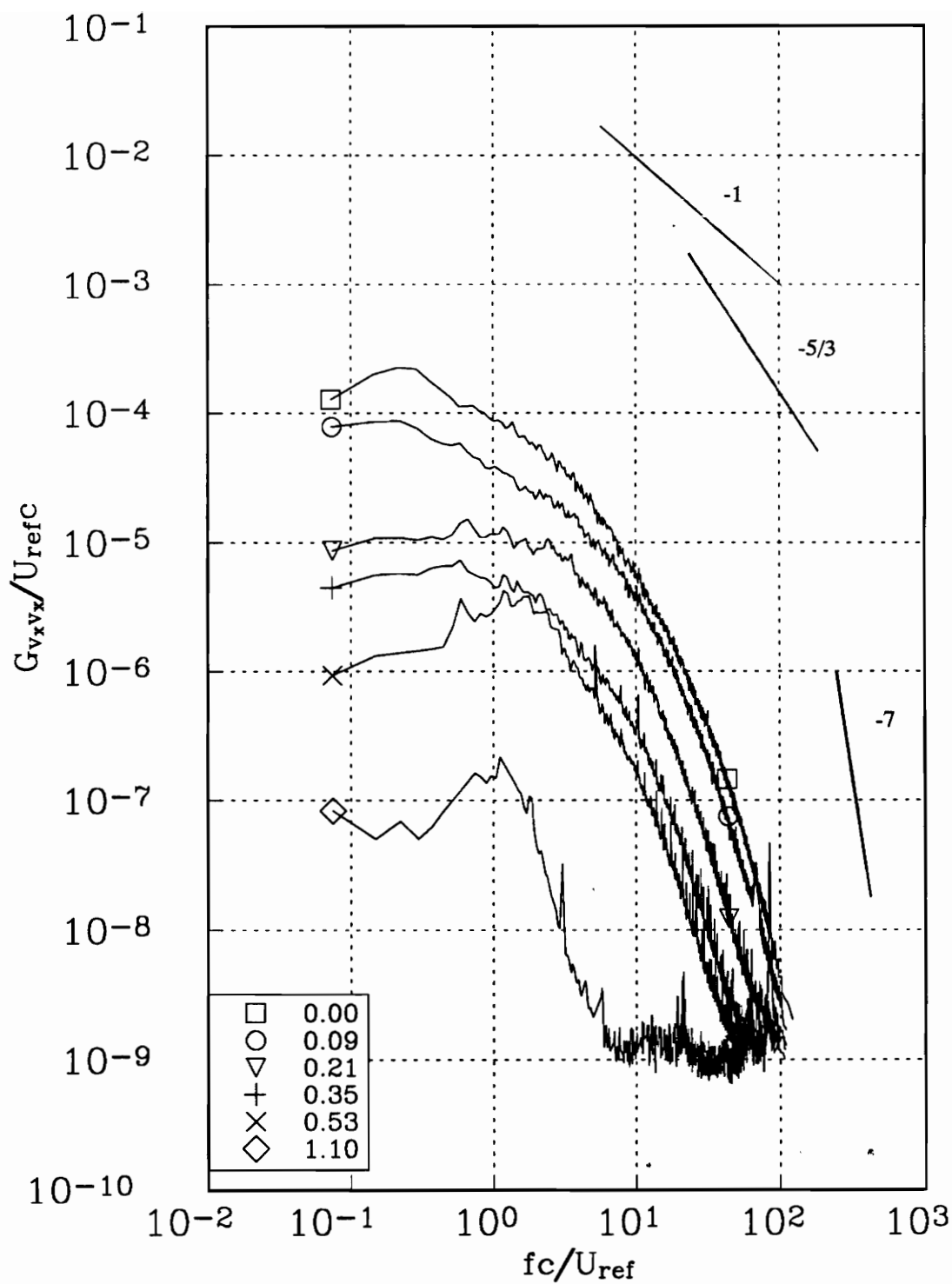


Figure 119a. v_x autospectra measured at representative radial locations along profile Ee for the co-rotating pair at $x/c=22$. Tic marks in figure 117 indicate measured r/c locations.

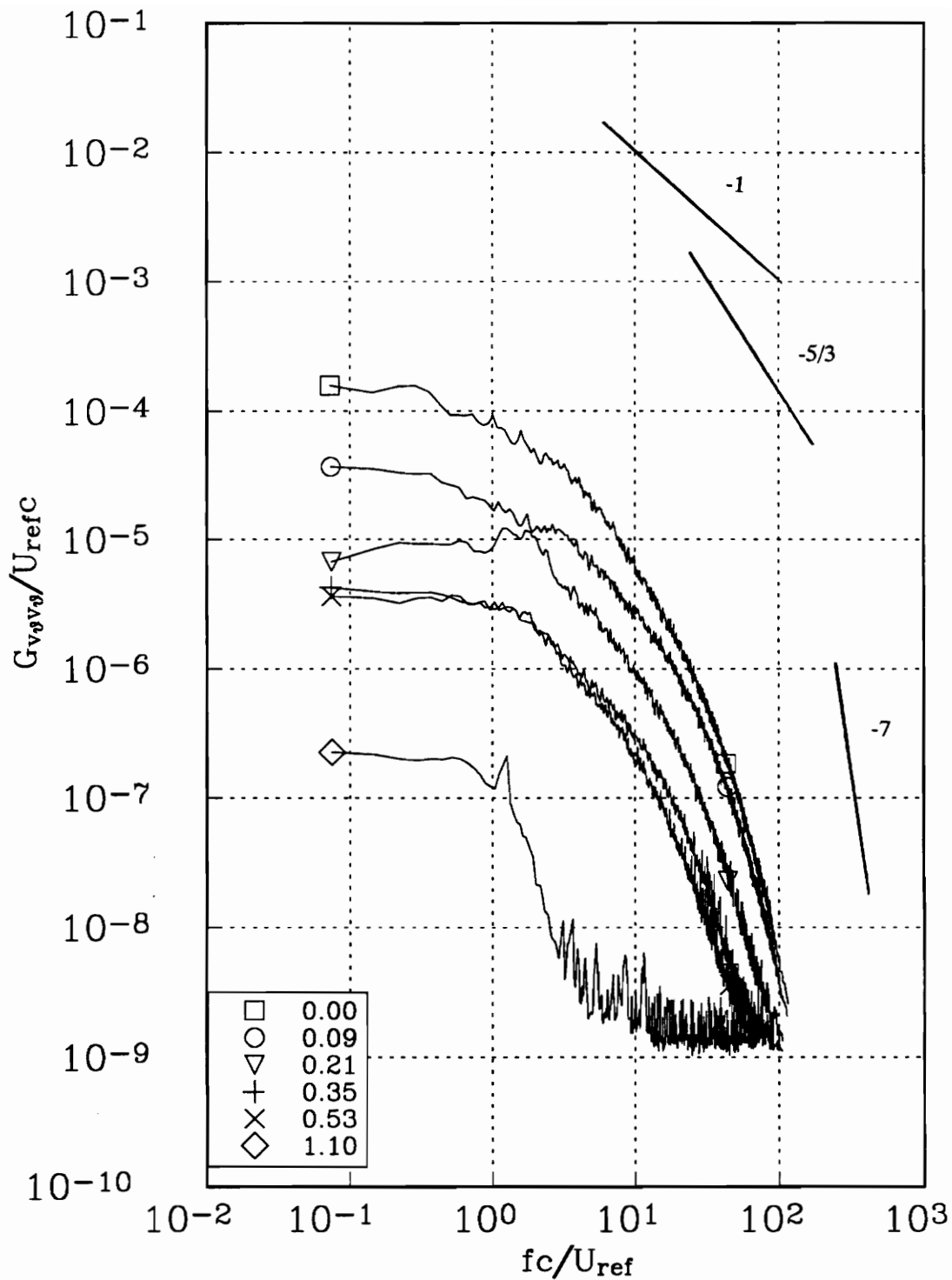


Figure 119b. v_θ autospectra measured at representative radial locations along profile Ee for the co-rotating pair at $x/c=22$. Tic marks in figure 117 indicate measured r/c locations.

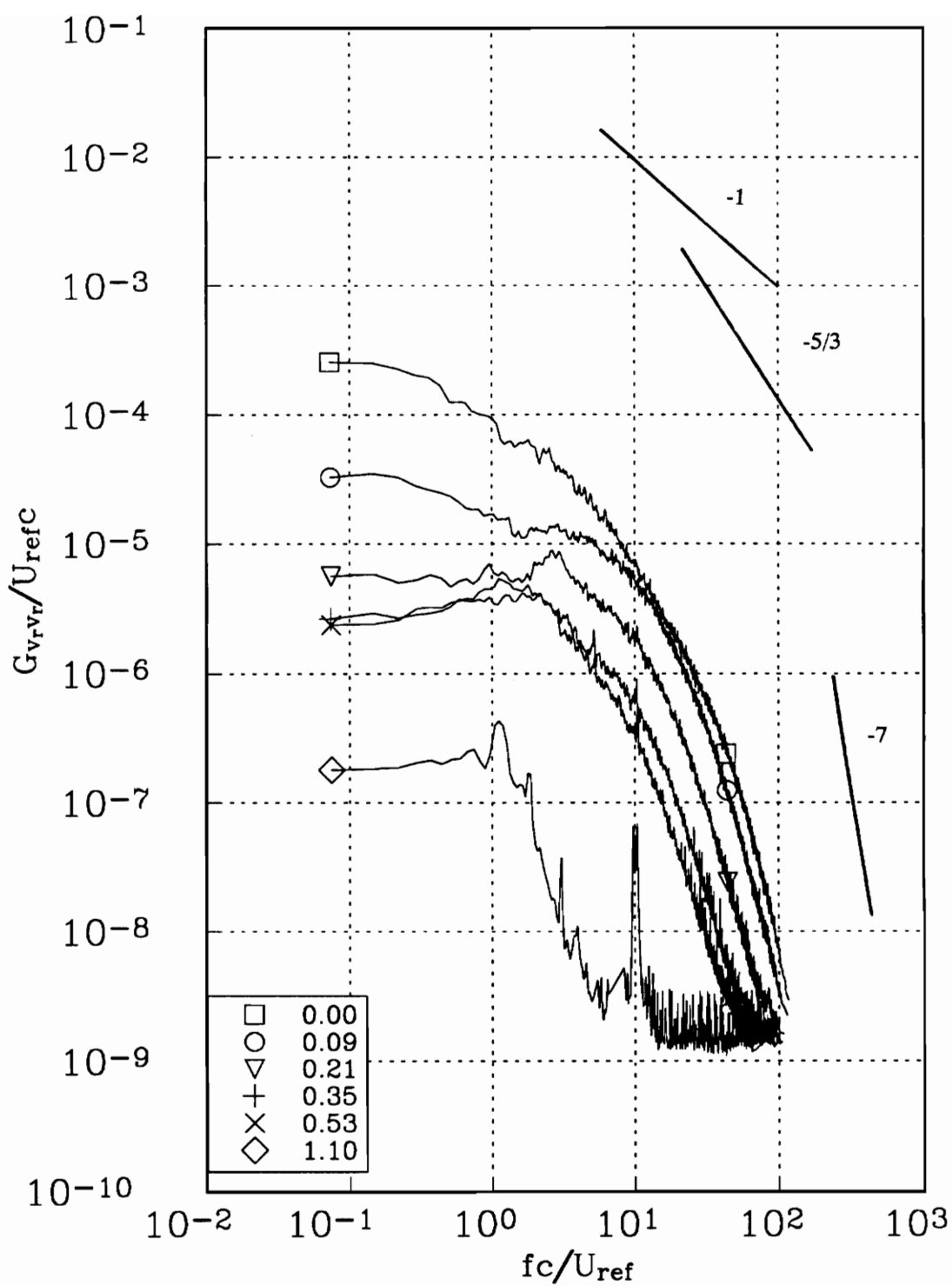


Figure 119c. v_r autospectra measured at representative radial locations along profile Ee for the co-rotating pair at $x/c=22$. Tic marks in figure 117 indicate measured r/c locations.

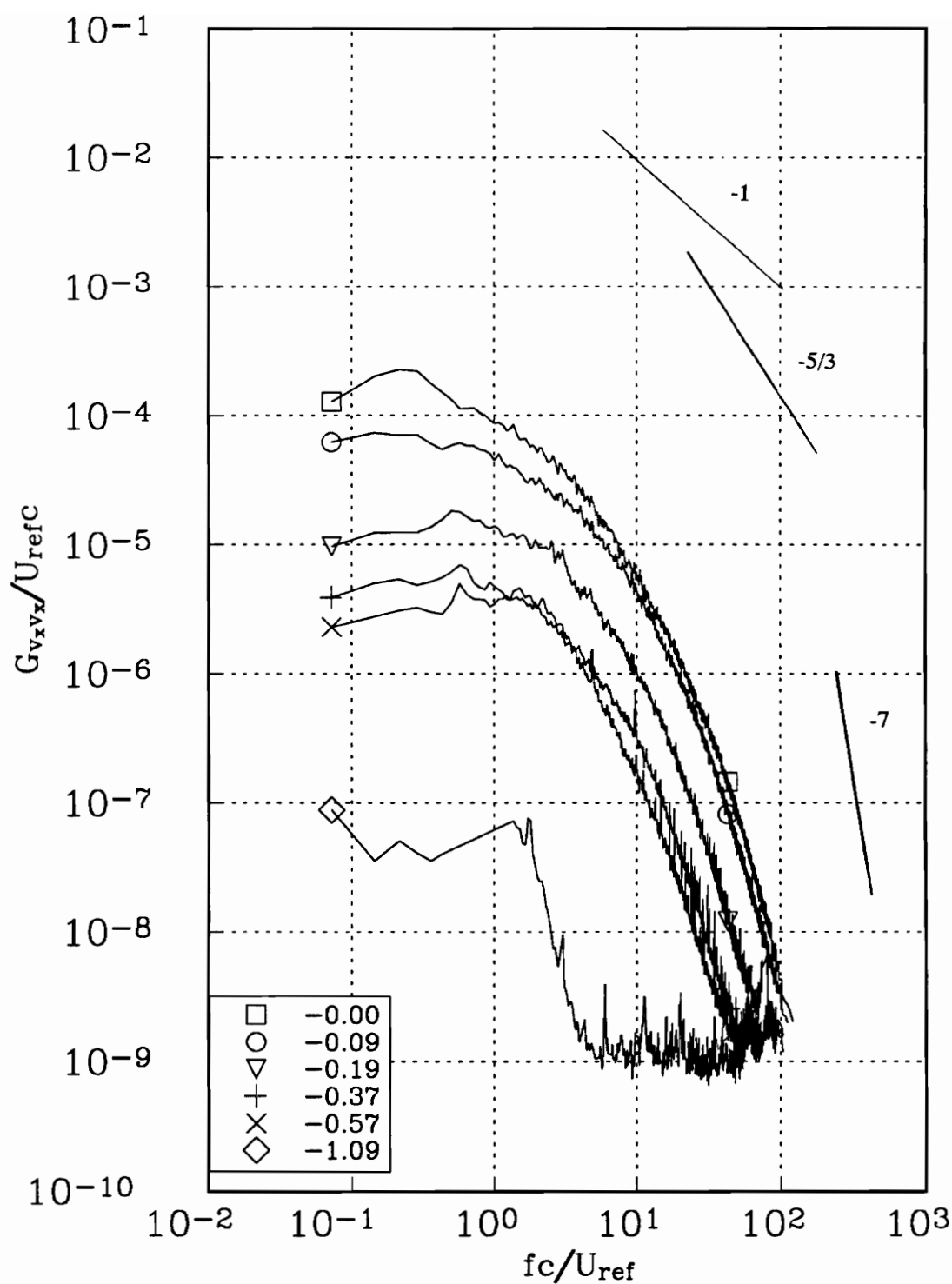


Figure 120a. v_x autospectra measured at representative radial locations along profile Ee for the co-rotating pair at $x/c=22$. Tic marks in figure 117 indicate measured r/c locations.

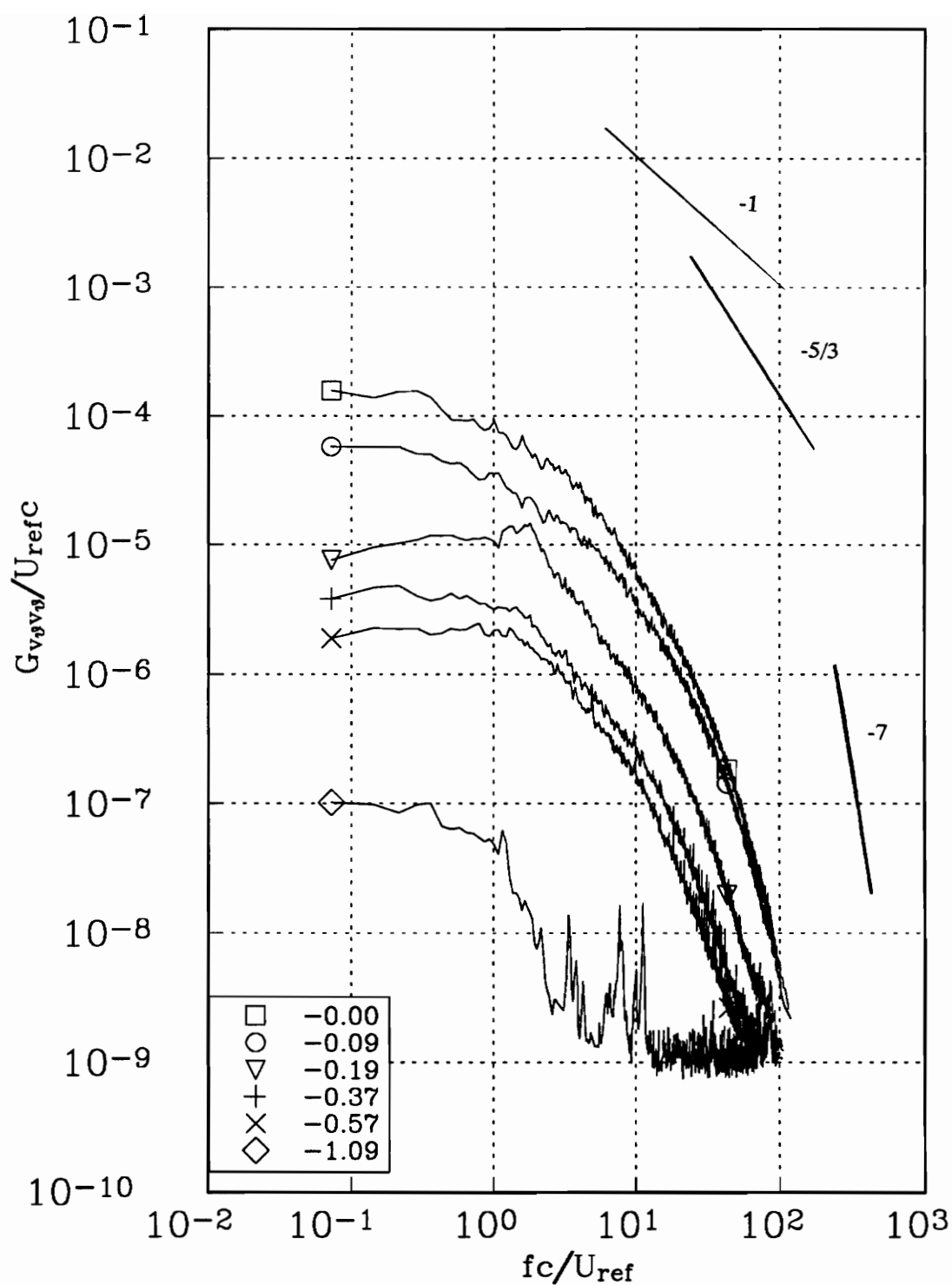


Figure 120b. v_θ autospectra measured at representative radial locations along profile Ee for the co-rotating pair at $x/c=22$. Tic marks in figure 117 indicate measured r/c locations.

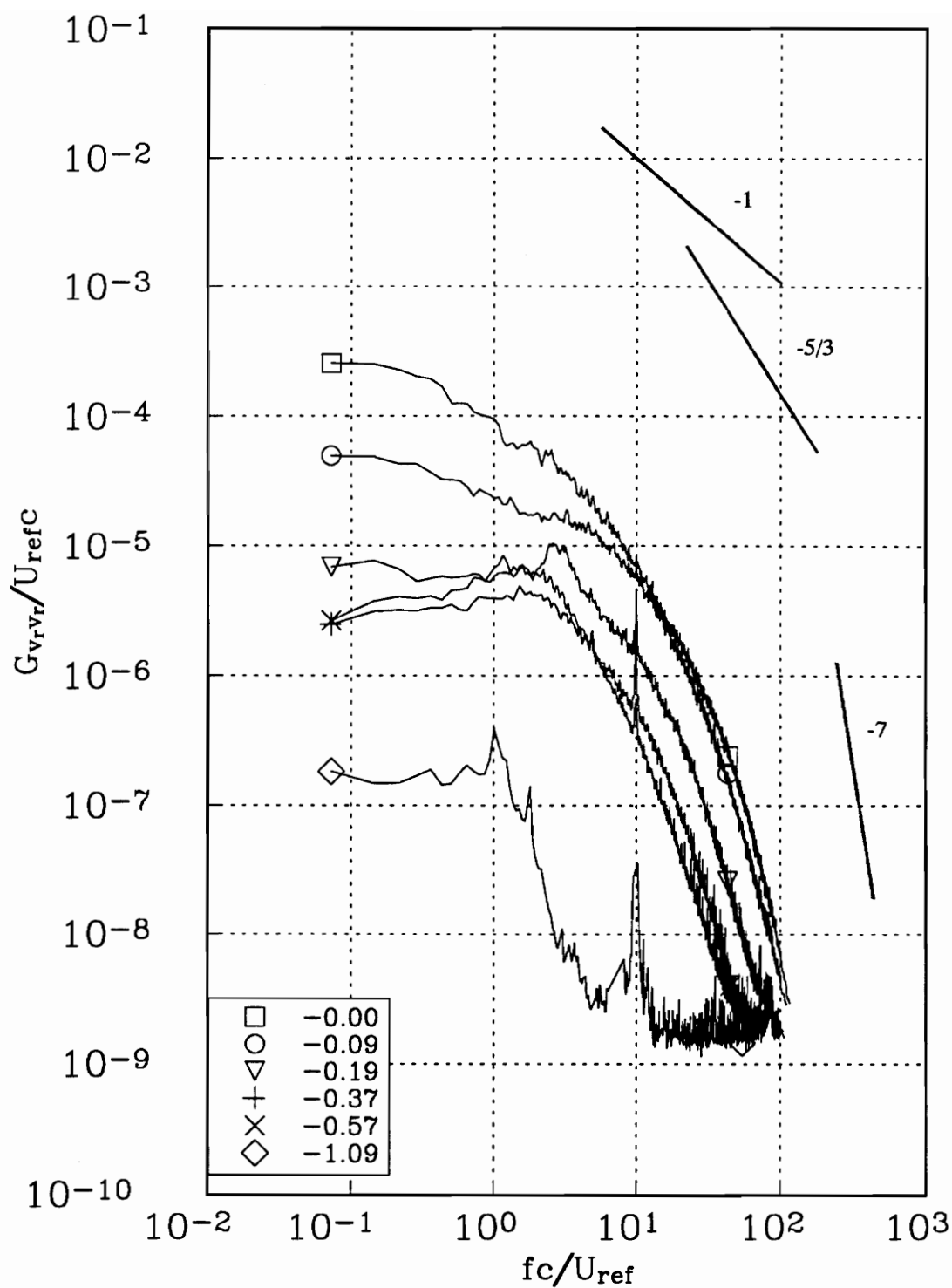


Figure 120c. v_r autospectra measured at representative radial locations along profile Ee for the co-rotating pair at $x/c=22$. Tic marks in figure 117 indicate measured r/c locations.

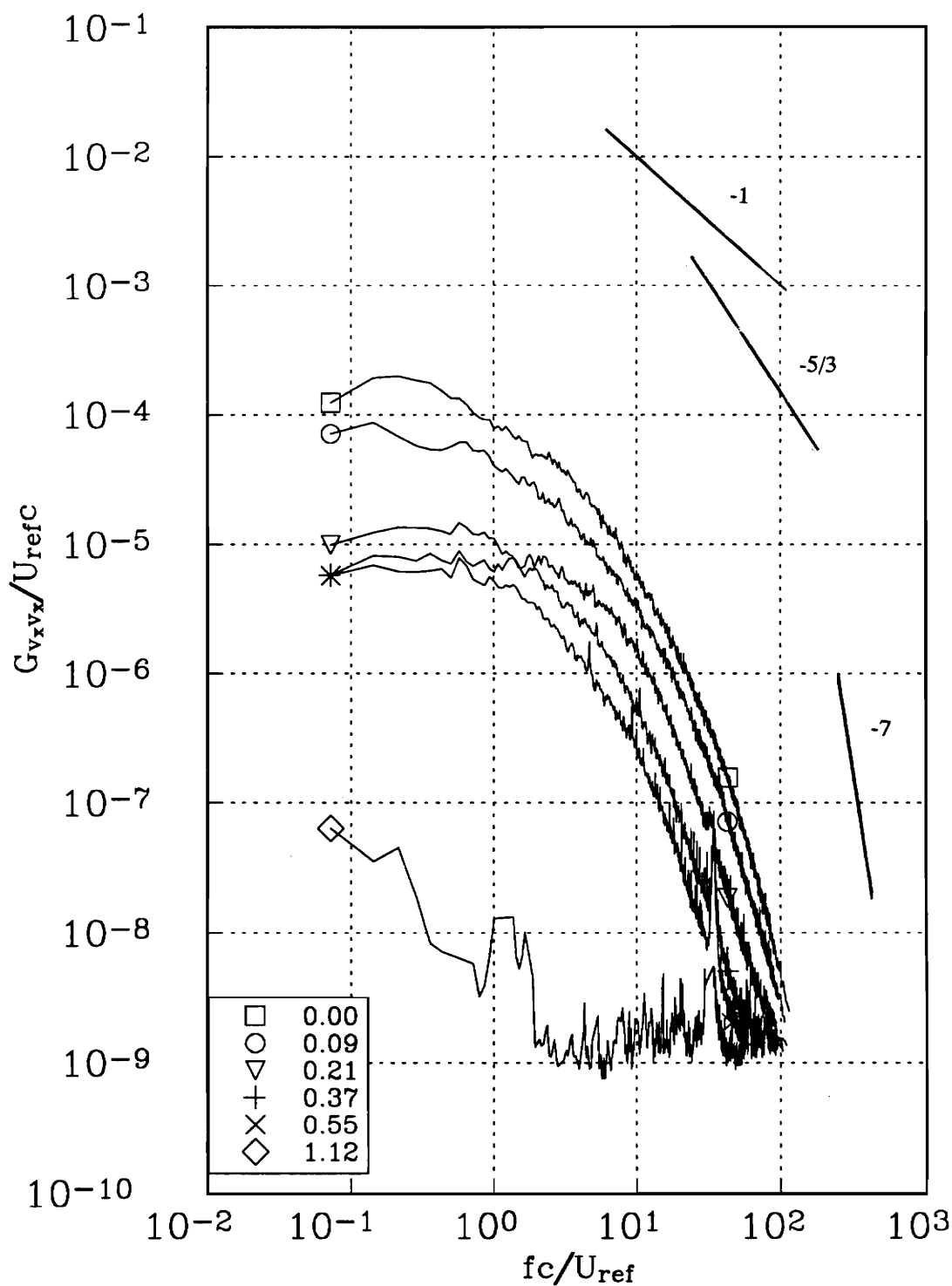


Figure 121a. v_x autospectra measured at representative radial locations along profile Ff for the co-rotating pair at $x/c=22$. Tic marks in figure 118 indicate measured r/c locations.

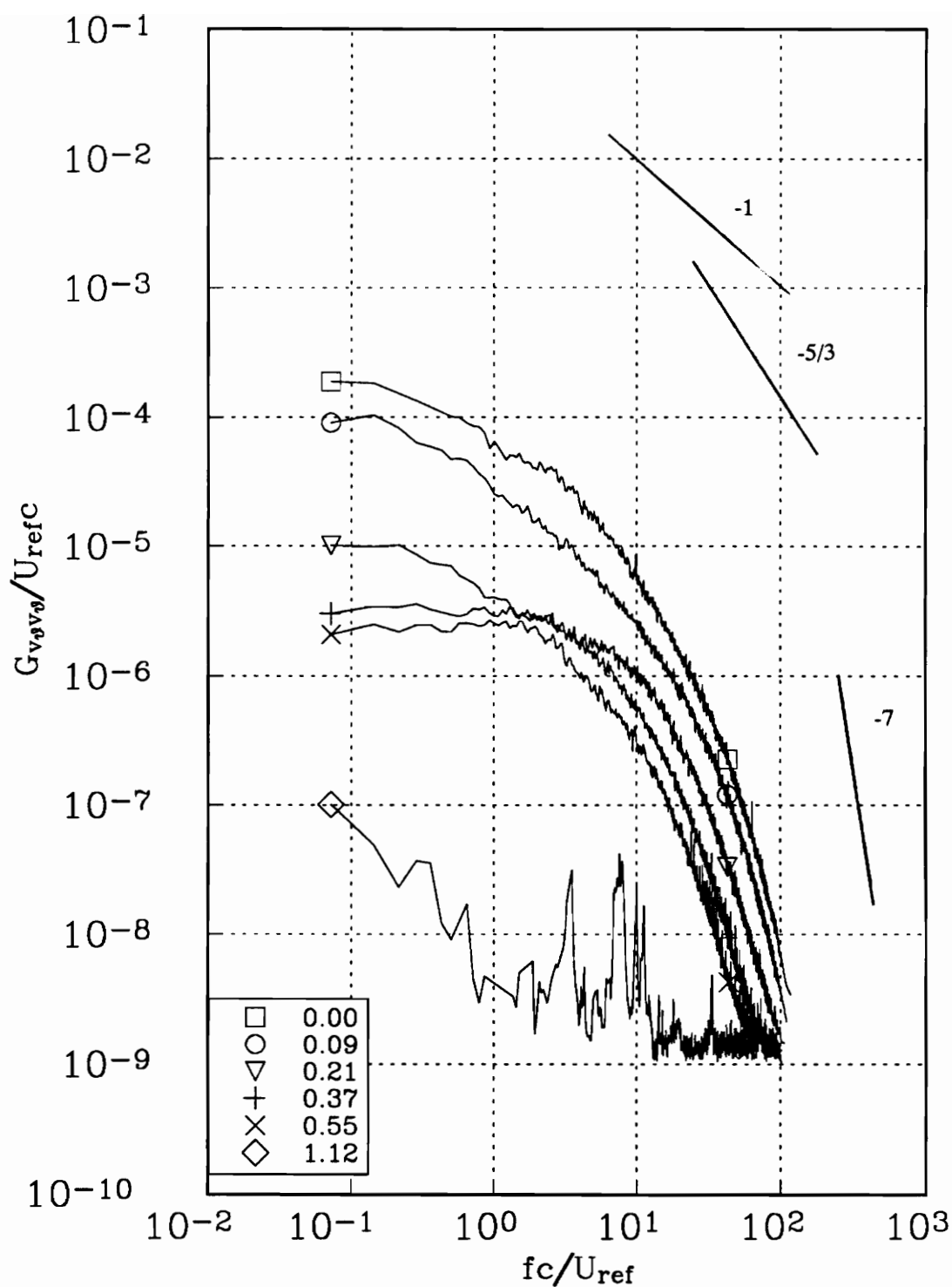


Figure 121b. v_{θ} autospectra measured at representative radial locations along profile Ff for the co-rotating pair at $x/c=22$. Tic marks in figure 118 indicate measured r/c locations.

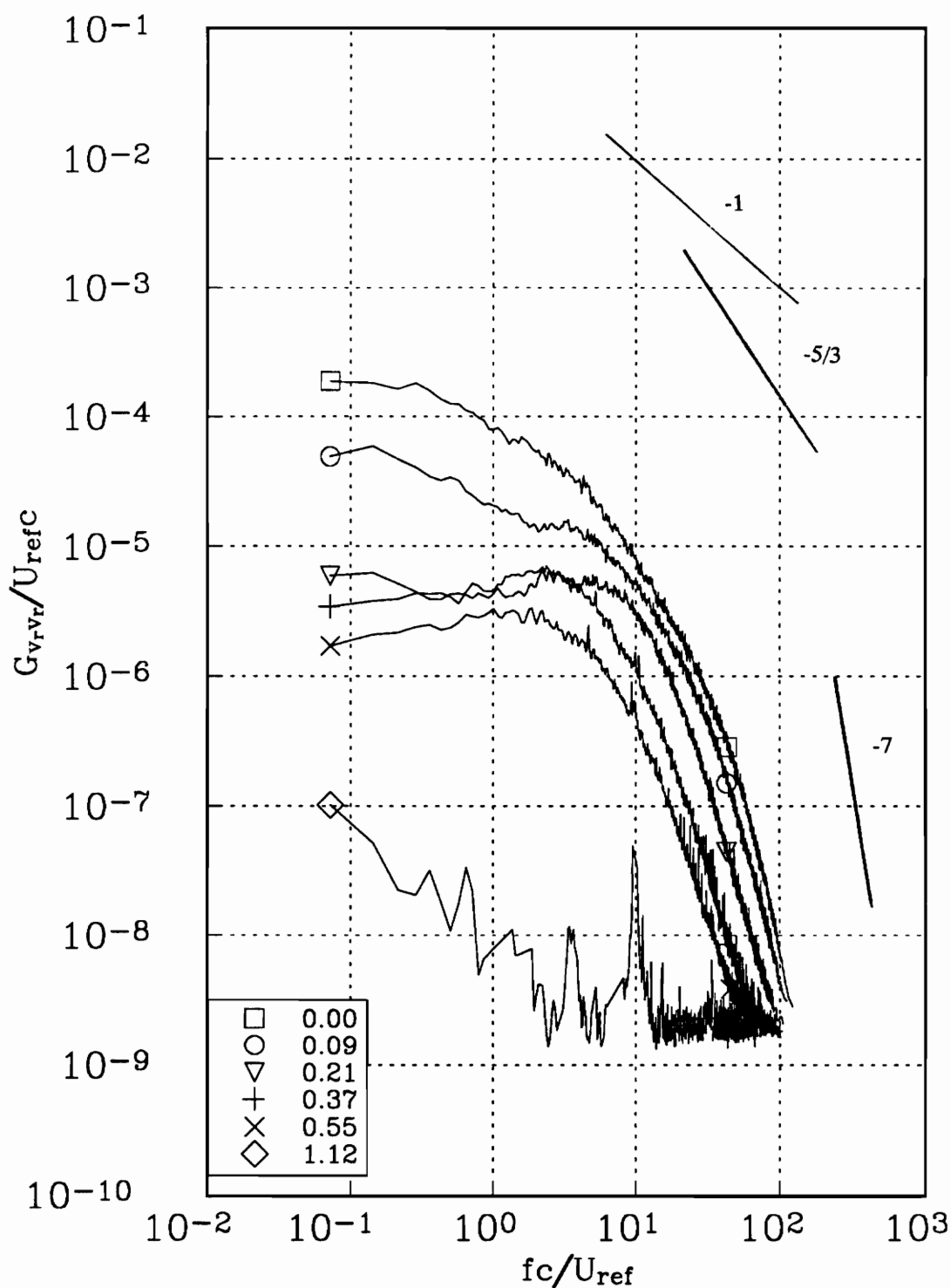


Figure 121c. v_r autospectra measured at representative radial locations along profile Ff for the co-rotating pair at $x/c=22$. Tic marks in figure 118 indicate measured r/c locations.

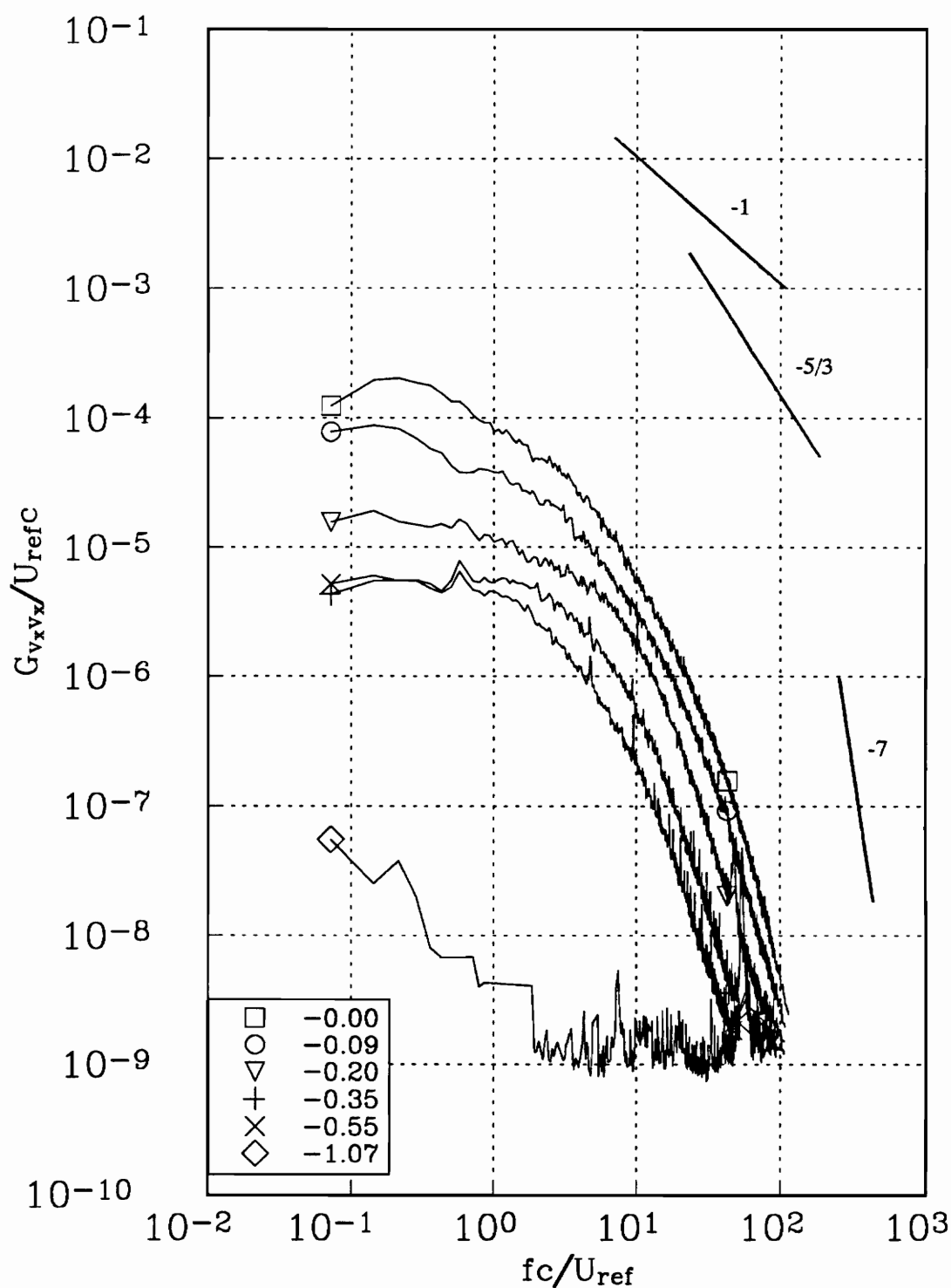


Figure 122a. v_x autospectra measured at representative radial locations along profile Ff for the co-rotating pair at $x/c=22$. Tic marks in figure 118 indicate measured r/c locations.

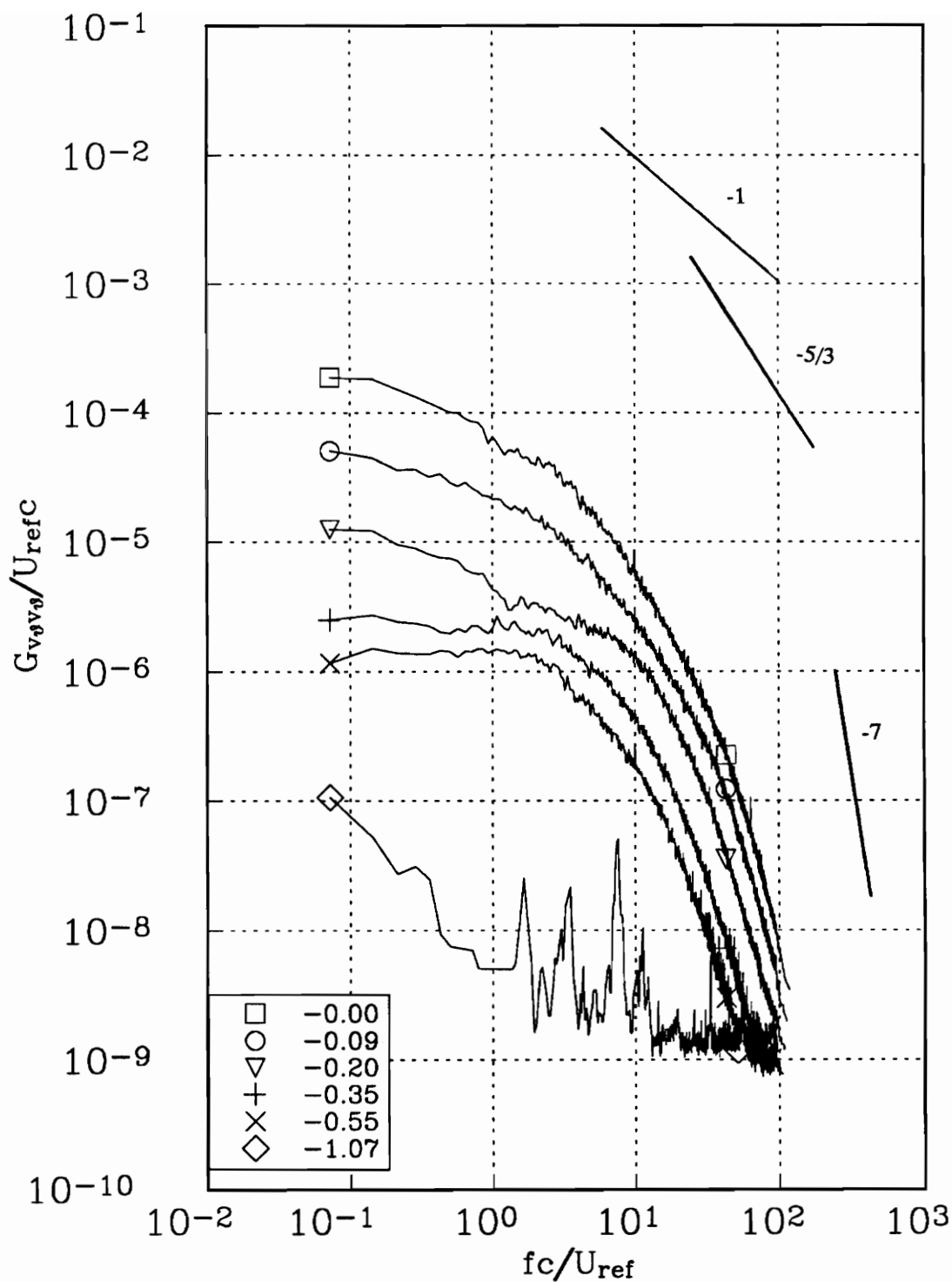


Figure 122b. v_θ autospectra measured at representative radial locations along profile Ff for the co-rotating pair at $x/c=22$. Tic marks in figure 118 indicate measured r/c locations.

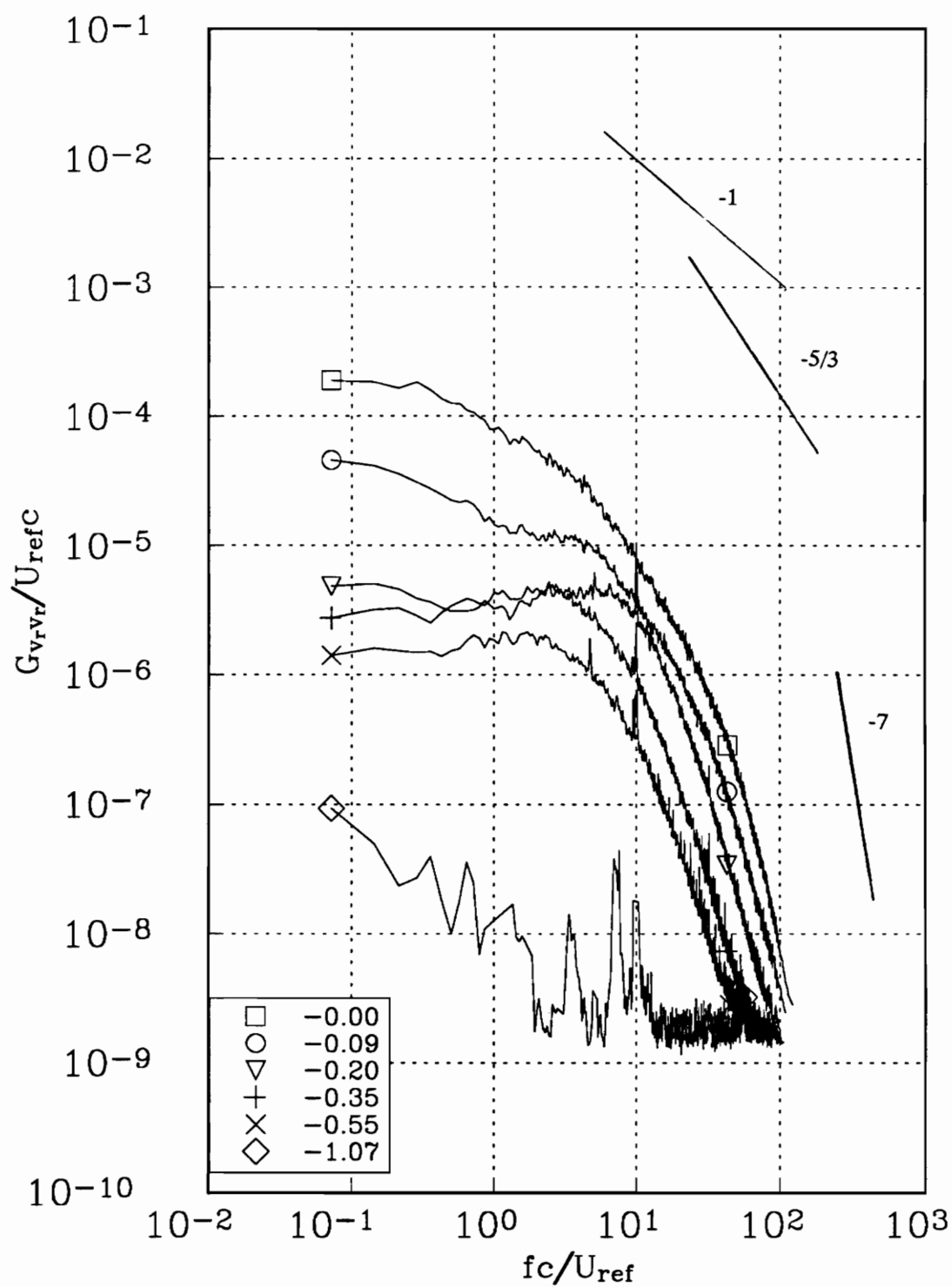


Figure 122c. v_r autospectra measured at representative radial locations along profile Ff for the co-rotating pair at $x/c=22$. Tic marks in figure 118 indicate measured r/c locations.

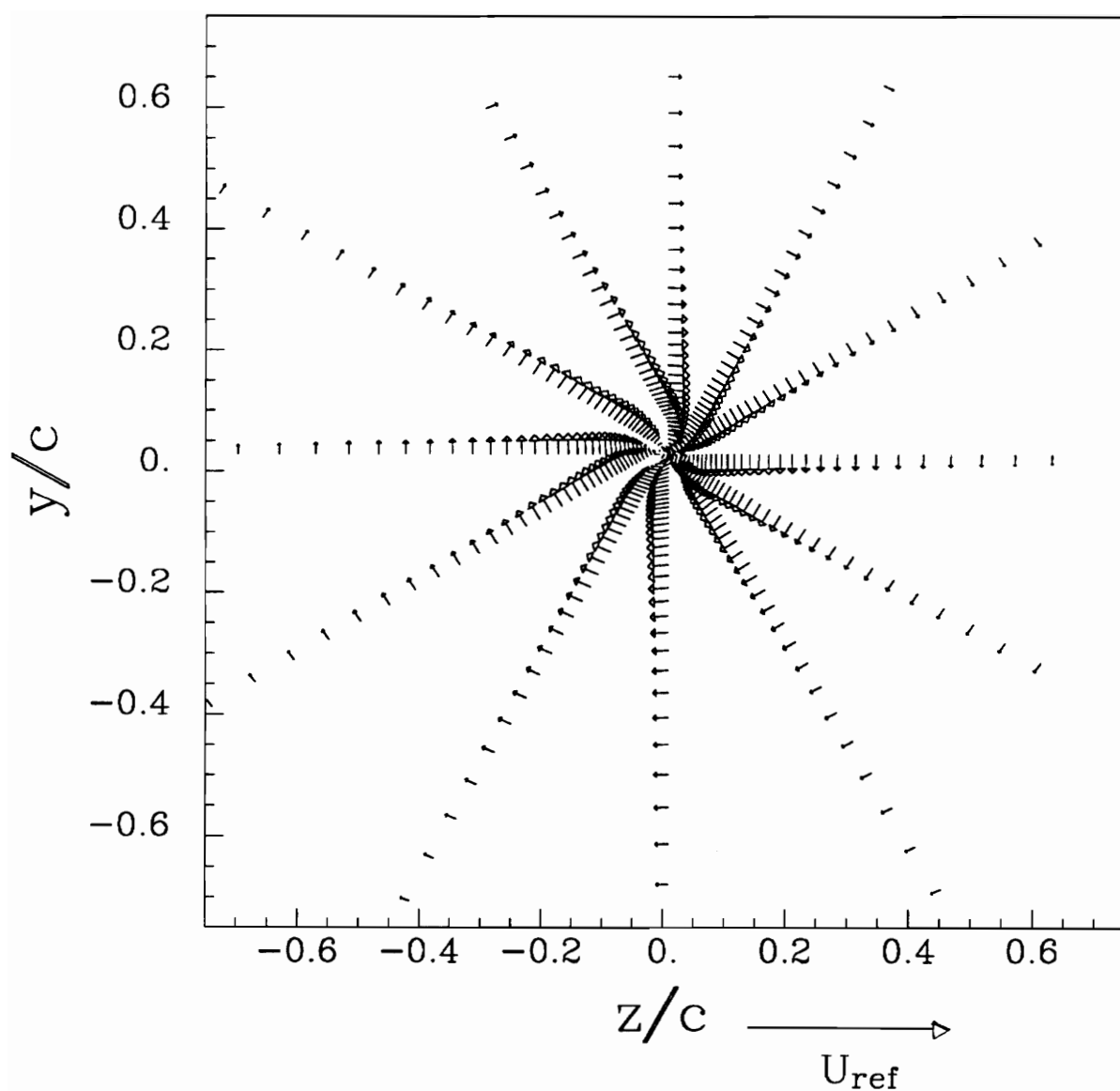
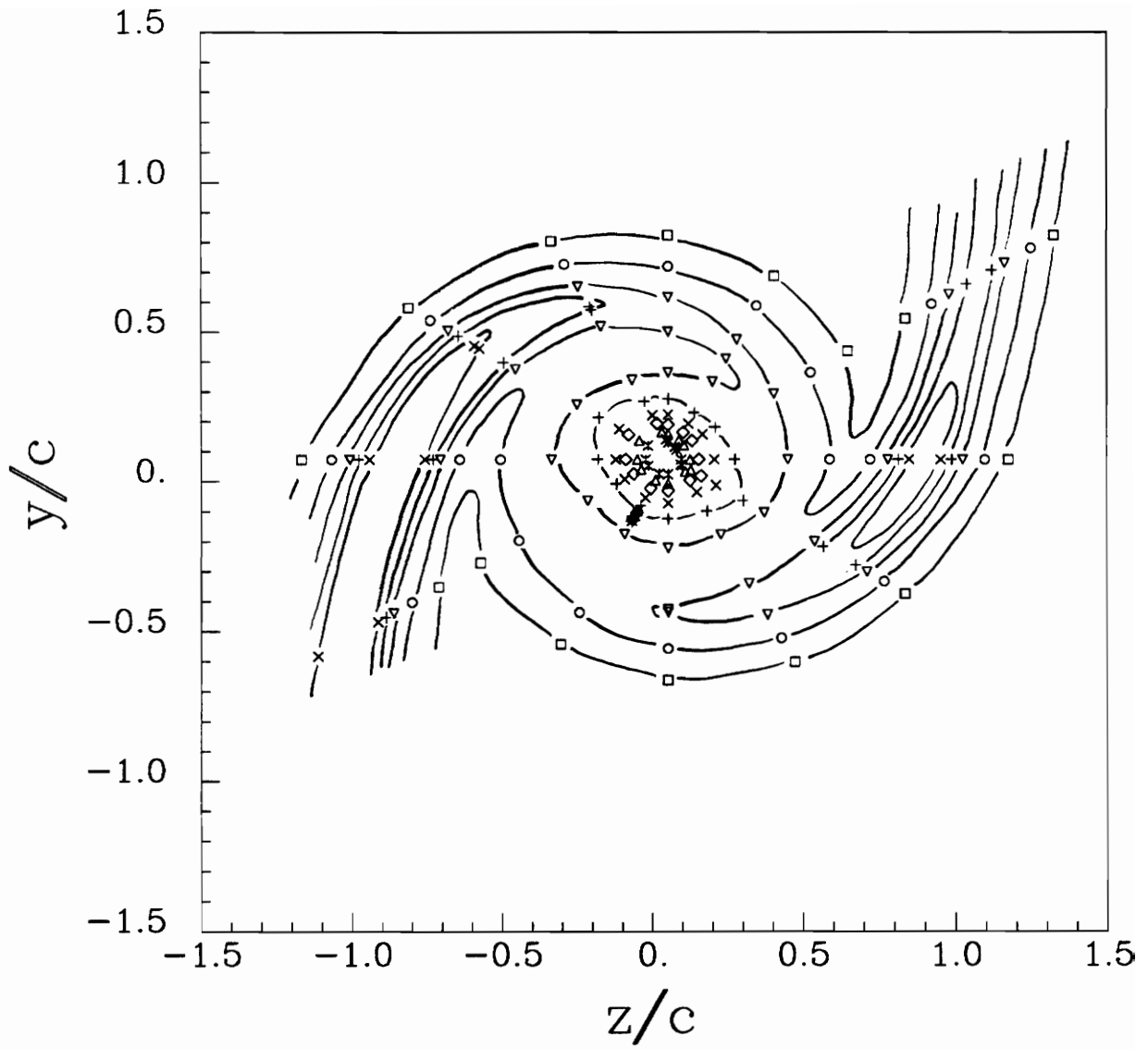
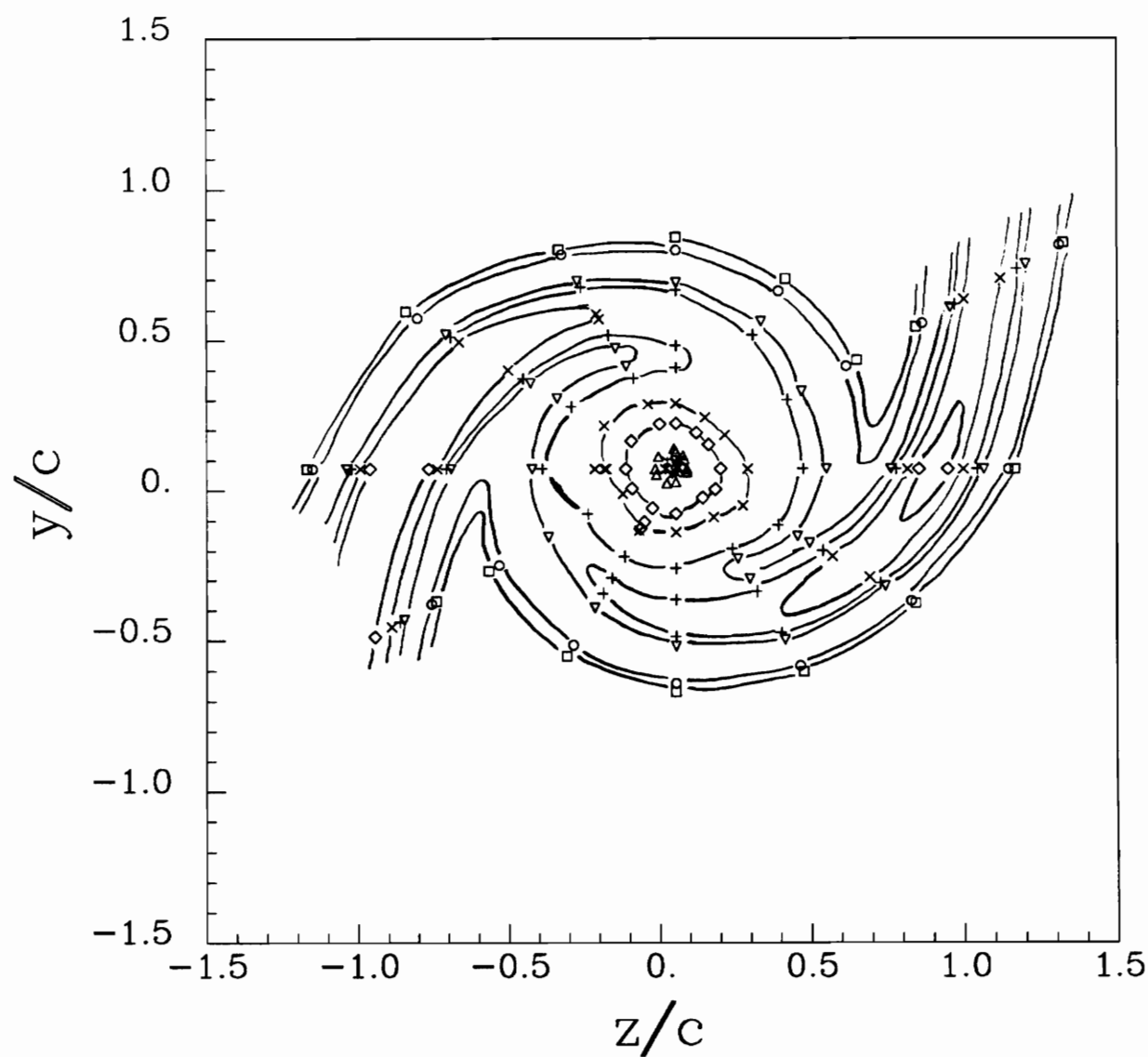


Figure 123. Mean secondary flow vectors of the co-rotating pair at $x/c=30$, angle of attack 5° , $Re_c=260,000$.



□	0.000010
○	0.000050
▽	0.000100
+	0.000125
×	0.000150
◇	0.000200
△	0.000300
✱	0.000500

Figure 124. Contours of turbulent kinetic energy k/U_{ref}^2 for the co-rotating pair at $x/c=30$, angle of attack 5° , $Re_c=260,000$.



□	0.000005
○	0.000010
▽	0.000050
+	0.000060
×	0.000080
◇	0.000100
△	0.000250
✱	0.000500

Figure 125. Contours of v_x^2/U_{ref}^2 for the co-rotating pair at $x/c=30$, angle of attack 5° , $Re_c=260,000$.

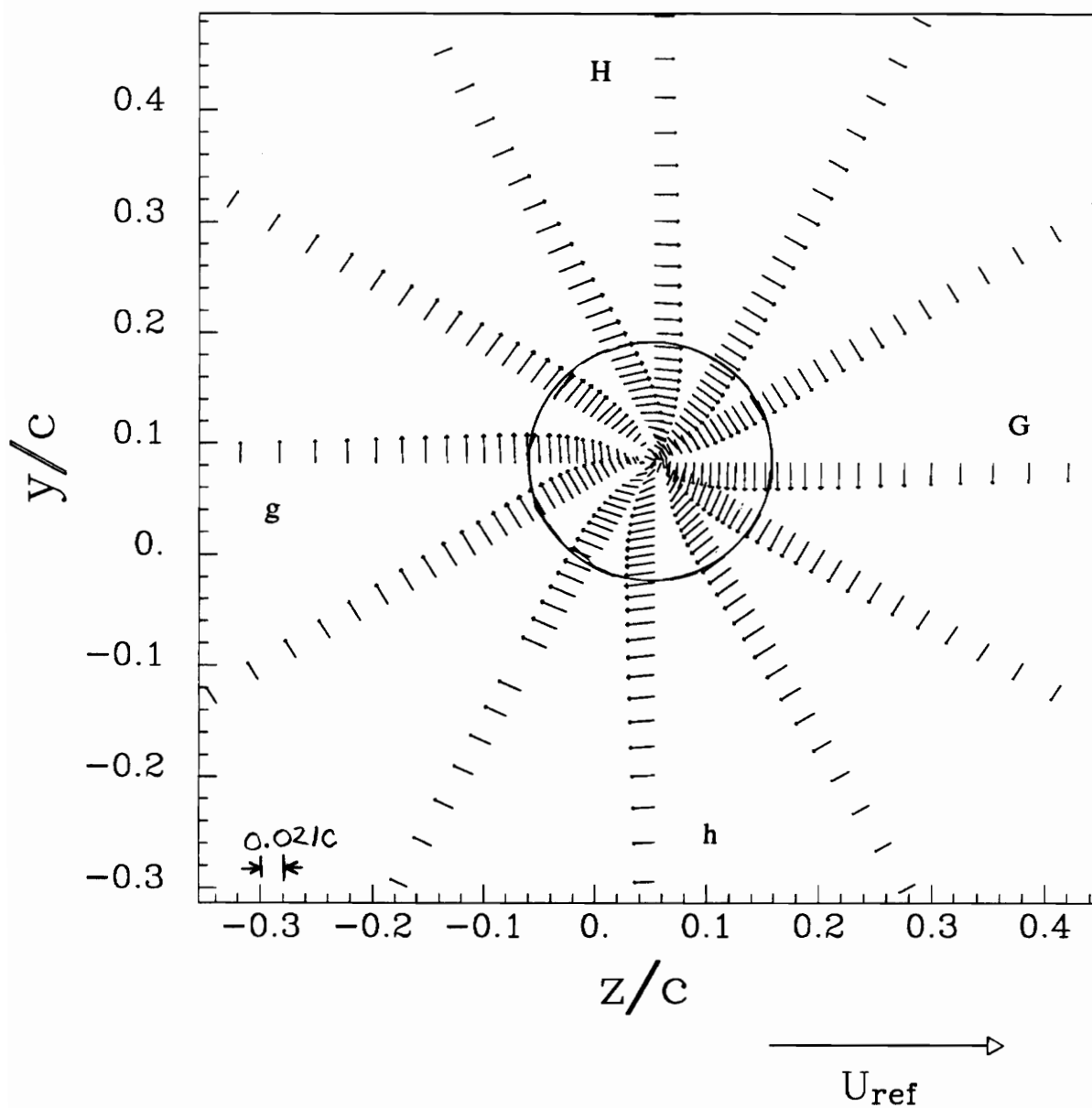


Figure 126. Core region showing mean secondary flows vectors for the co-rotating pair at $x/c=30$, angle of attack= 5° , $Re_c=260,000$. Dotted line indicates core edge.

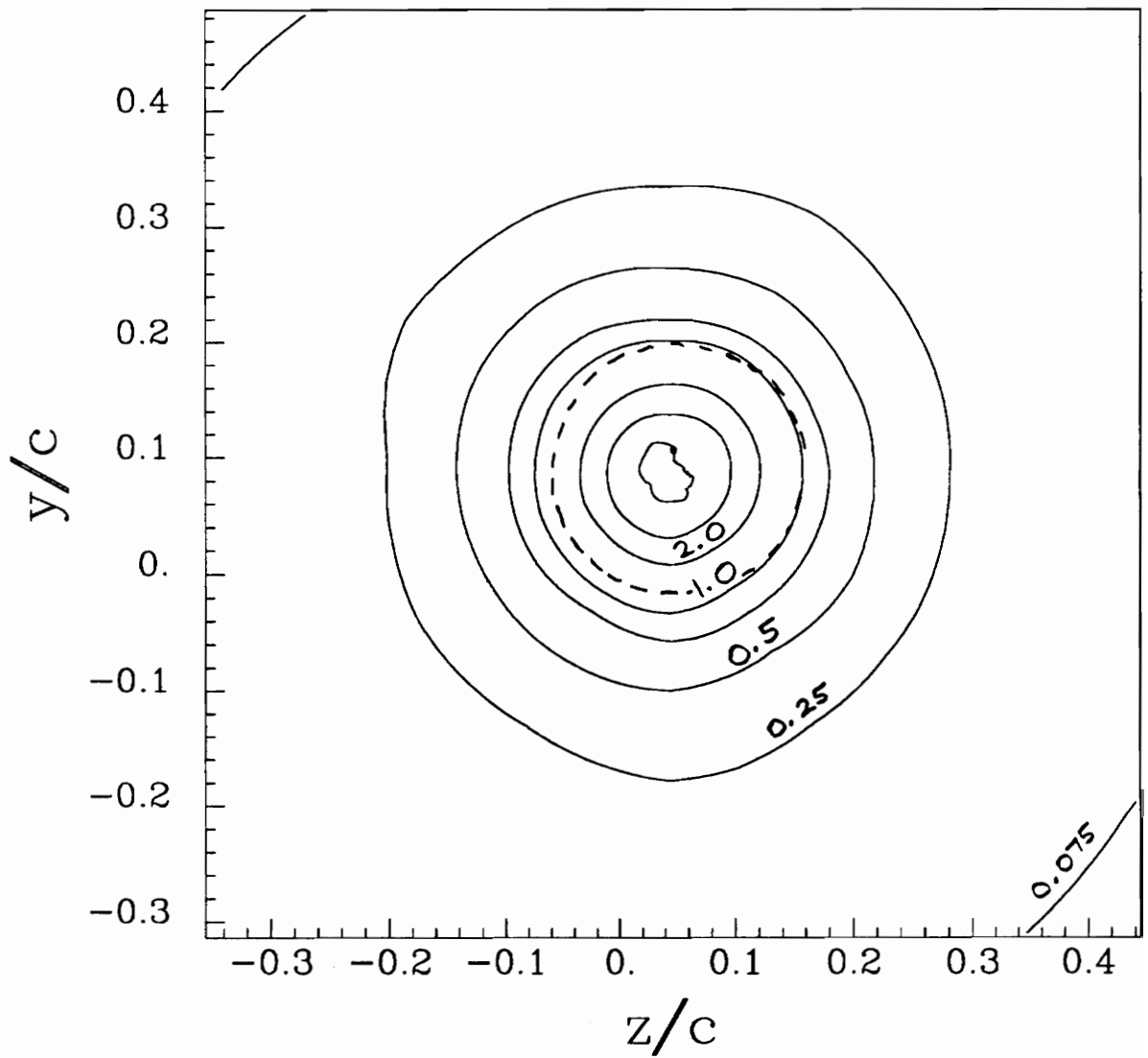


Figure 127. Core region showing contours of vorticity $\omega c/U_{ref}$ for the co-rotating vortex at $x/c=30$, angle of attack= 5° , $Re_c=260,000$. Dotted line indicates core edge.

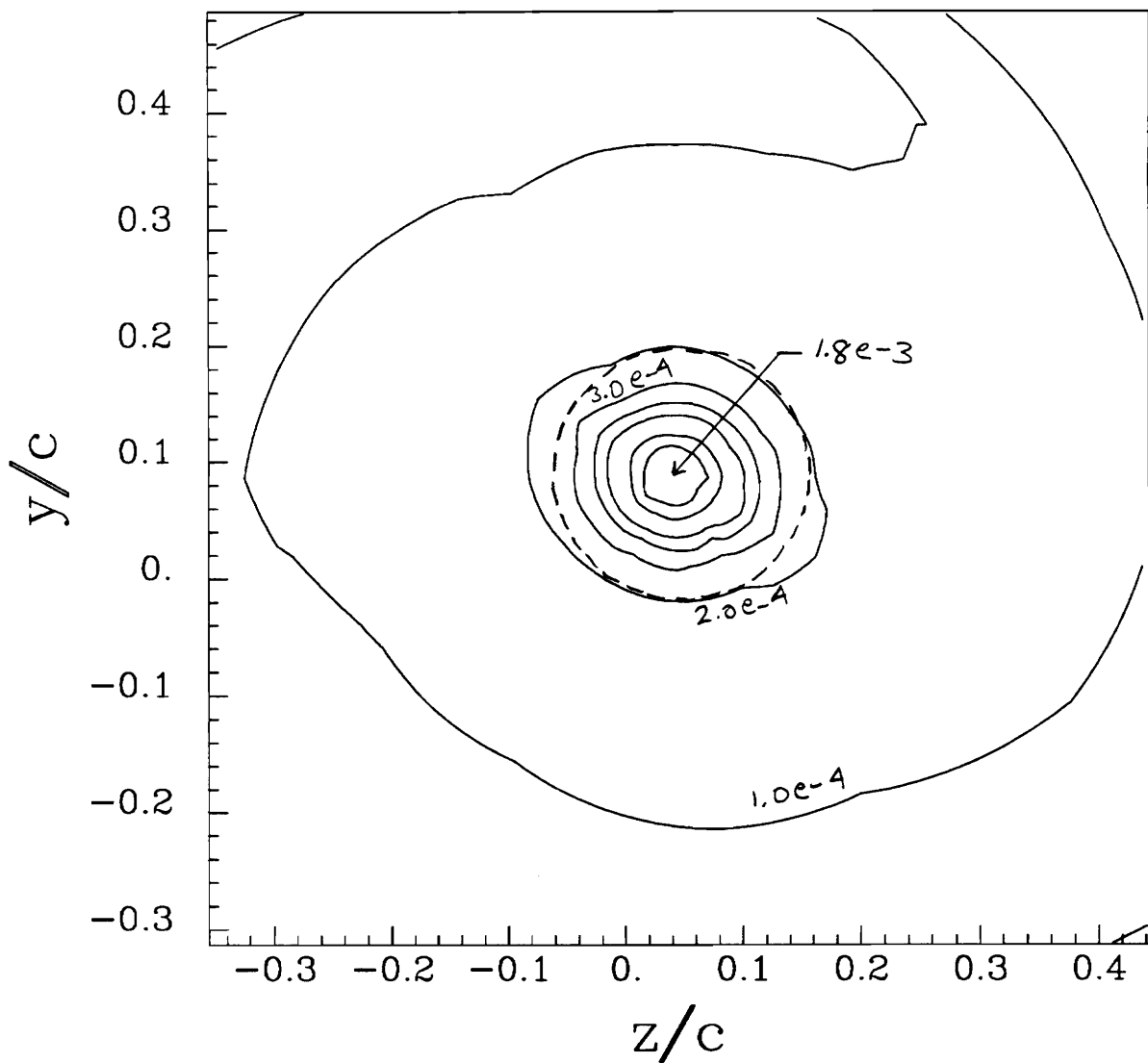


Figure 128. Core region showing contours of turbulent kinetic energy k/U_{ref}^2 for the co-rotating pair at $x/c=30$, angle of attack= 5° , $Re_c=260,000$. Dotted line indicates core edge.

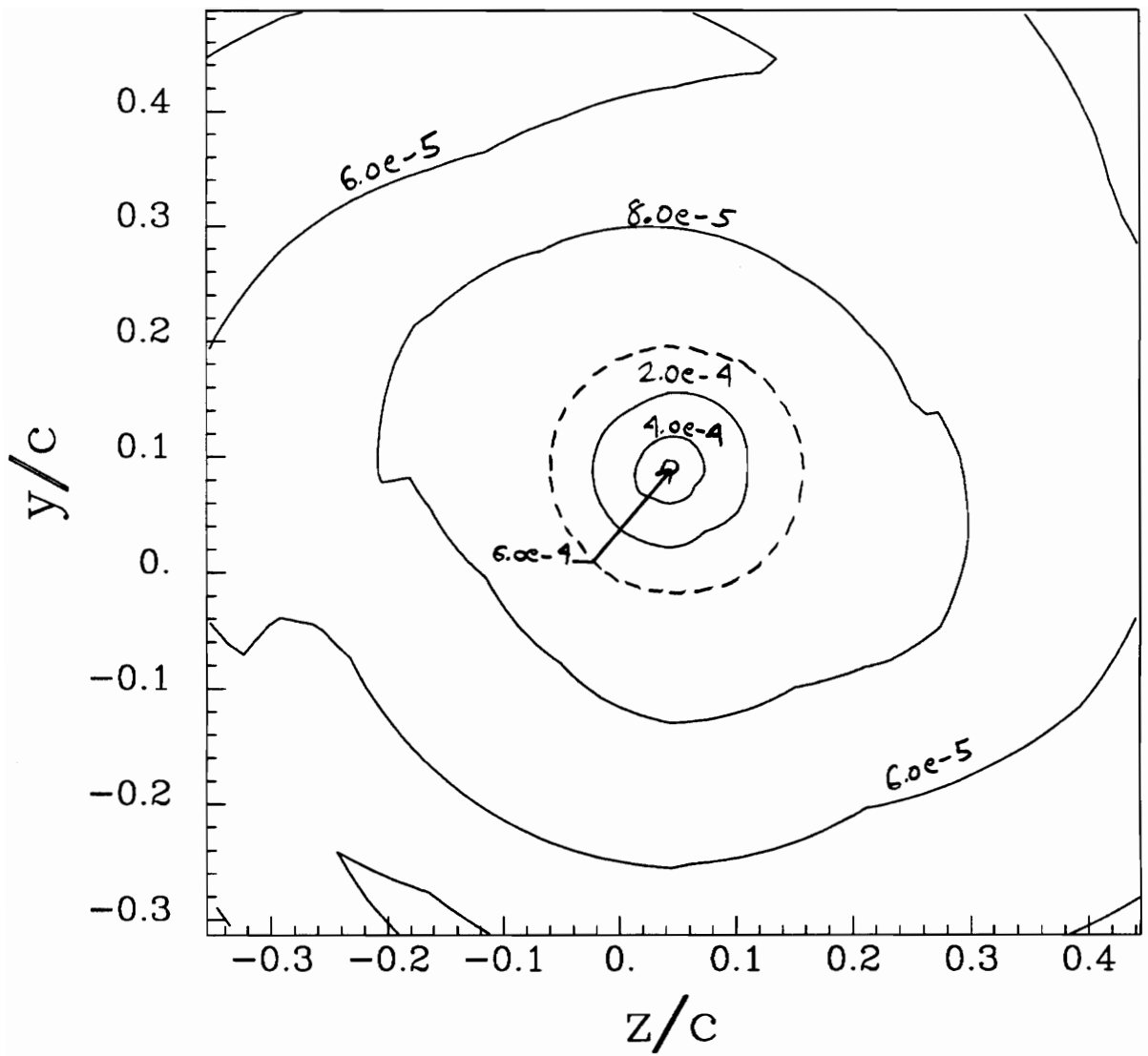


Figure 129. Core region showing contours of v_x^2/U_{ref}^2 for the co-rotating pair at $x/c=30$, angle of attack= 5° , $Re_c=260,000$. Dotted line indicates core edge.

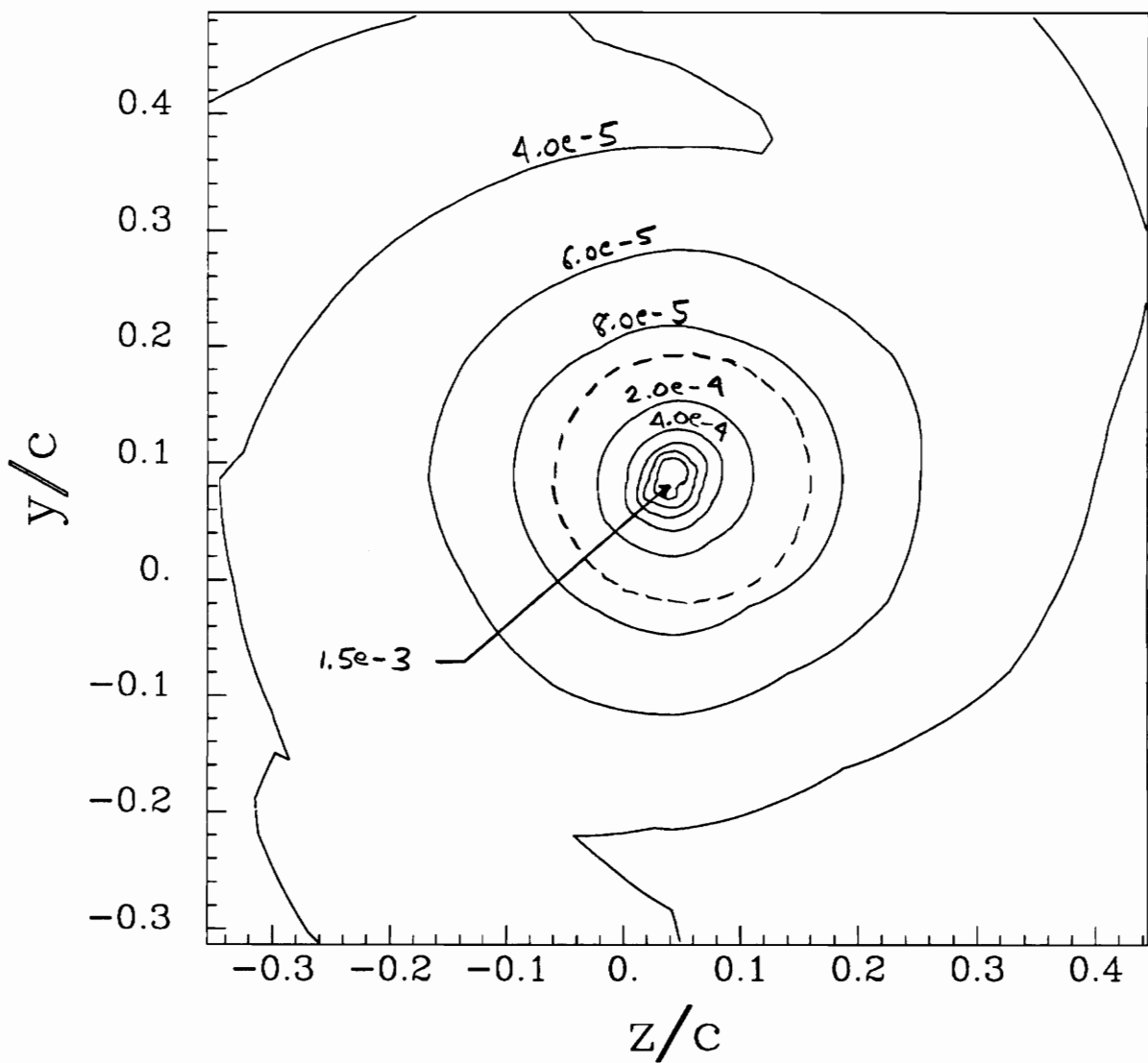


Figure 130. Core region showing contours of v_{θ}^2/U_{ref}^2 for the co-rotating pair at $x/c=30$, angle of attack= 5° , $Re_c=260,000$. Dotted line indicates core edge.

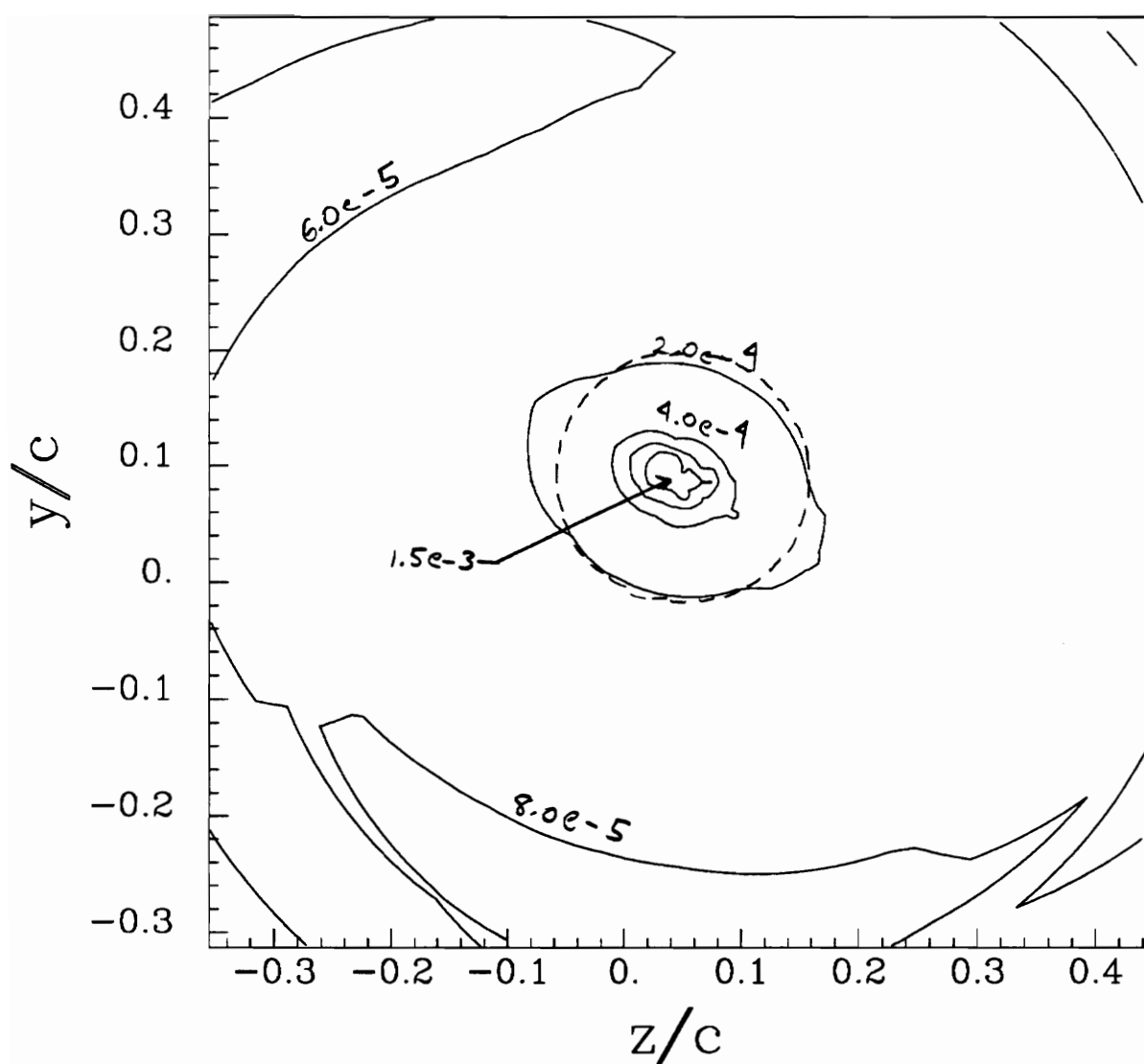


Figure 131. Core region showing contours of v_r^2/U_{ref}^2 for the co-rotating pair at $x/c=30$, angle of attack= 5° , $Re_c=260,000$. Dotted line indicates core edge.

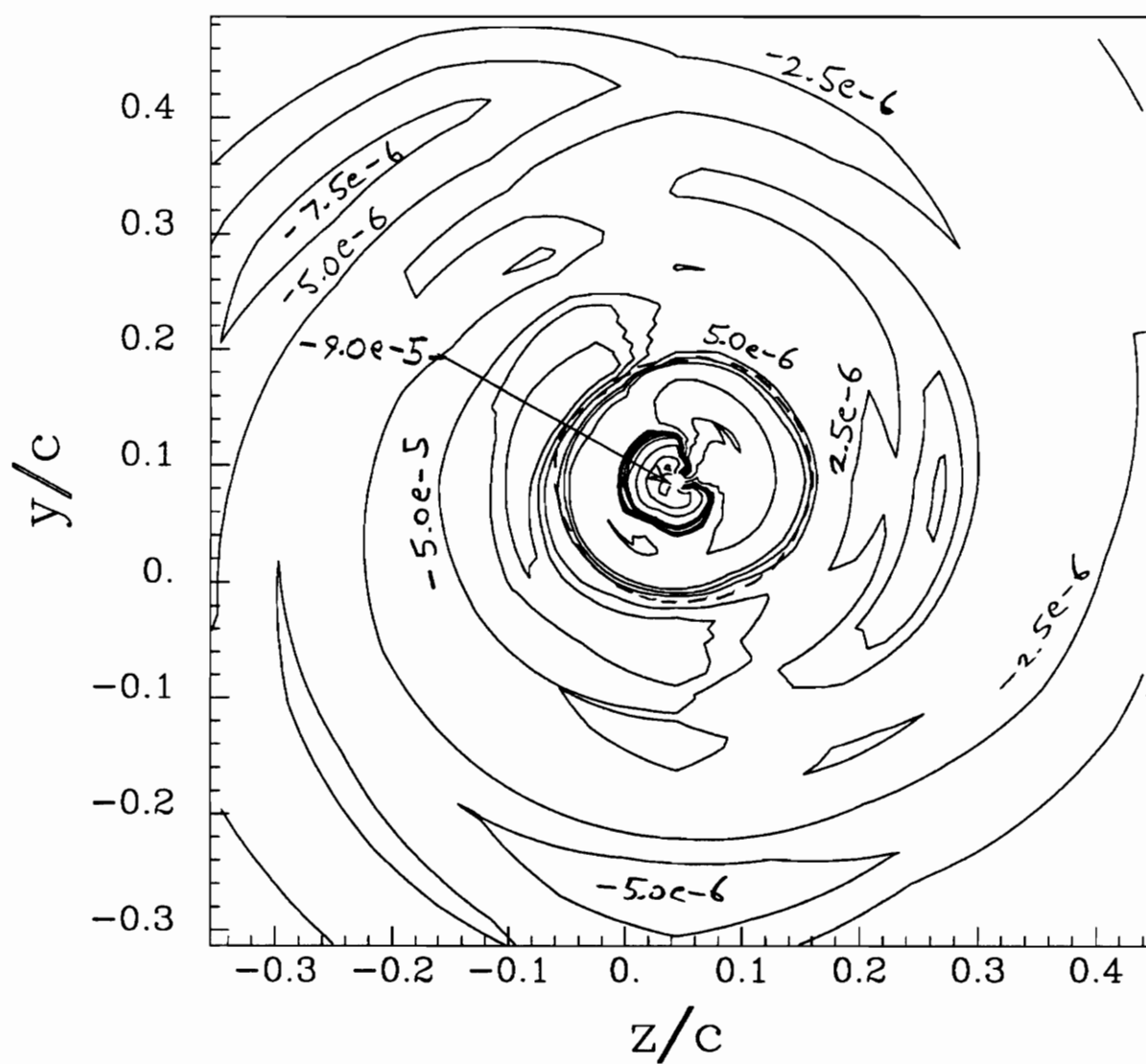


Figure 132. Core region showing contours of $v_x v_\theta / U_{ref}^2$ for the co-rotating pair at $x/c=30$, angle of attack= 5° , $Re_c=260,000$. Dotted line indicates core edge.

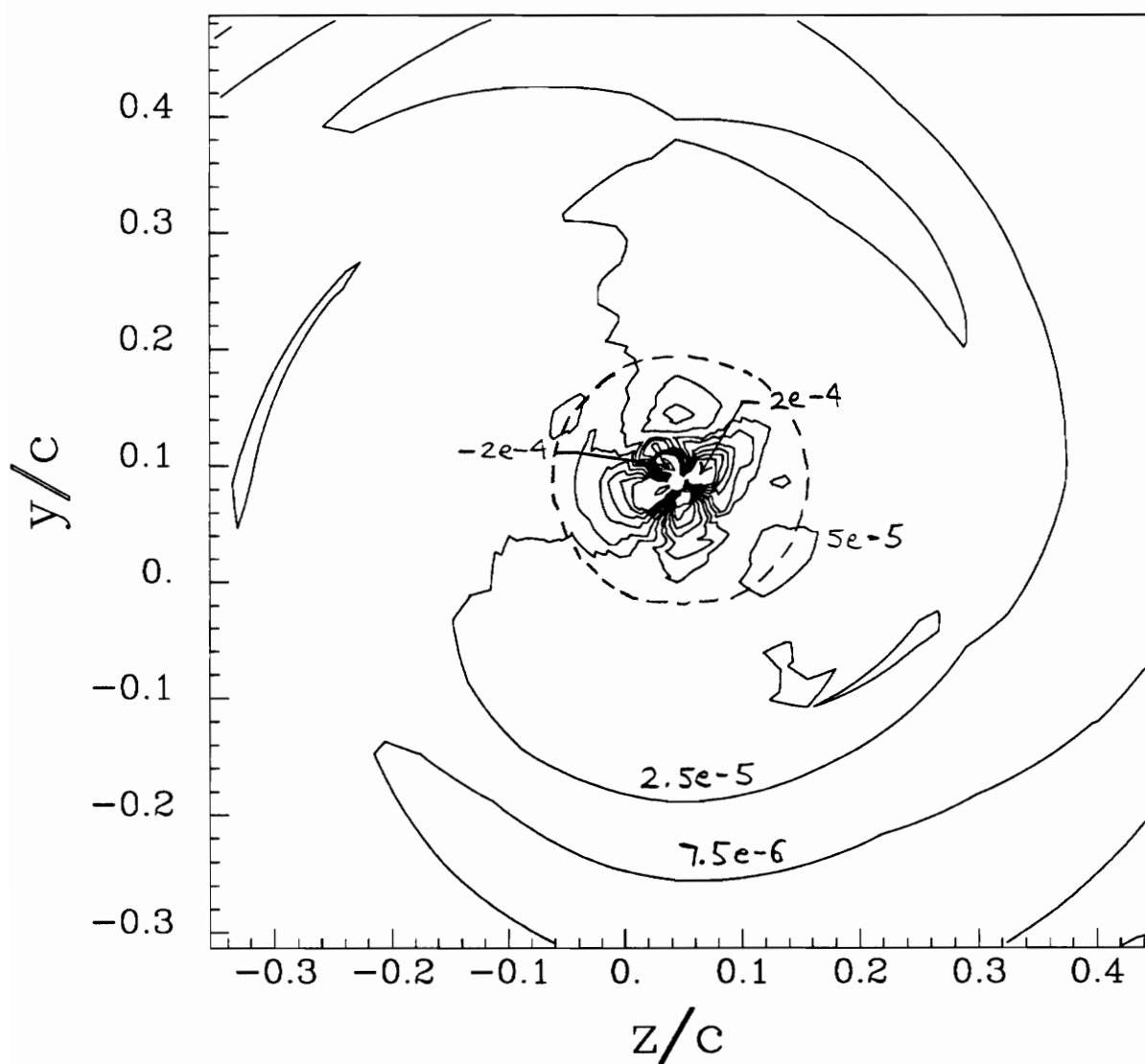


Figure 133. Core region showing contours of $v_{\theta}v_r/U_{ref}^2$ for the co-rotating pair at $x/c=30$, angle of attack= 5° , $Re_c=260,000$. Dotted line indicates core edge.

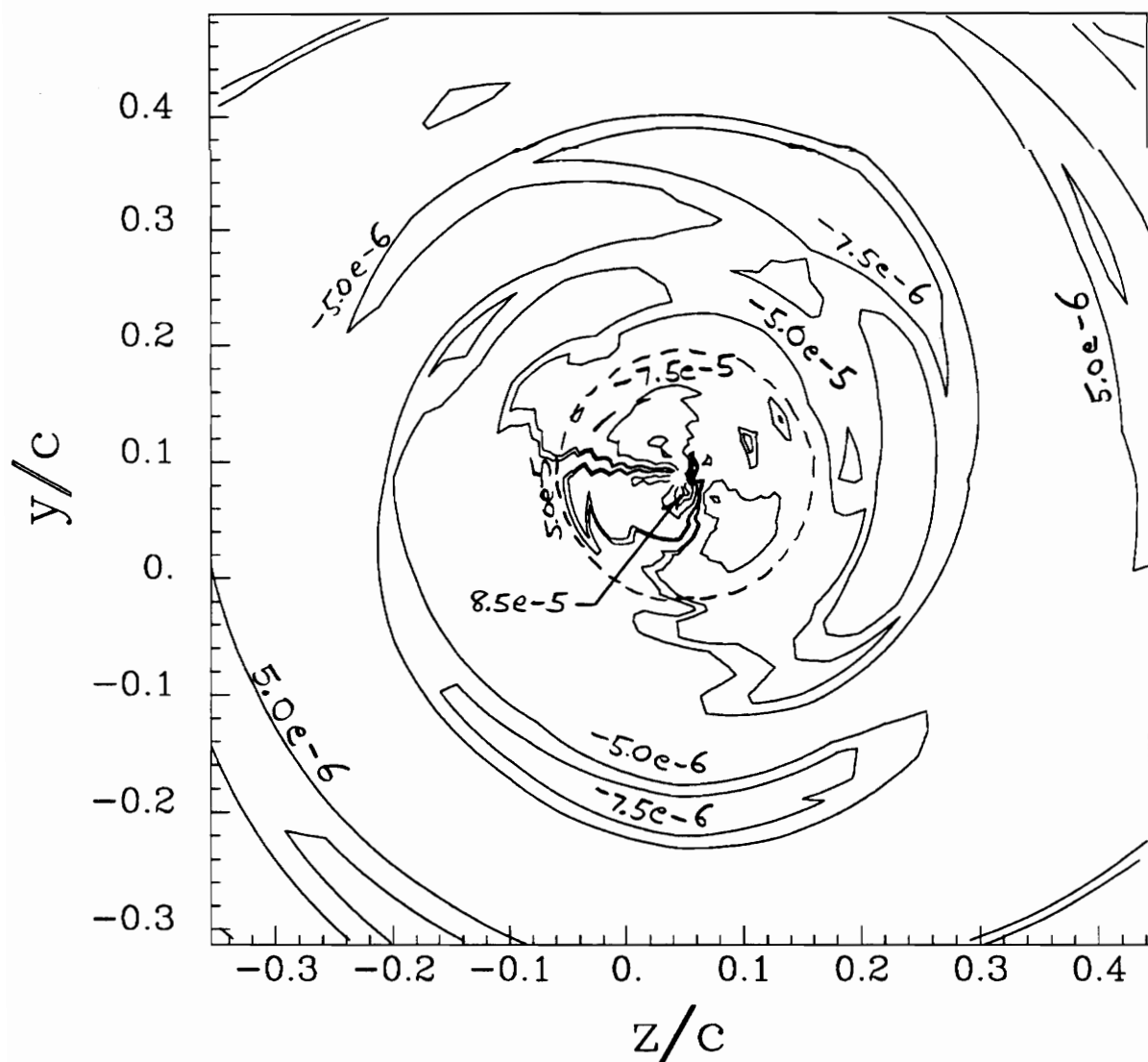


Figure 134. Core region showing contours of $v_x v_r / U^2_{ref}$ for the co-rotating pair at $x/c=30$, angle of attack= 5° , $Re_c=260,000$. Dotted line indicates core edge.

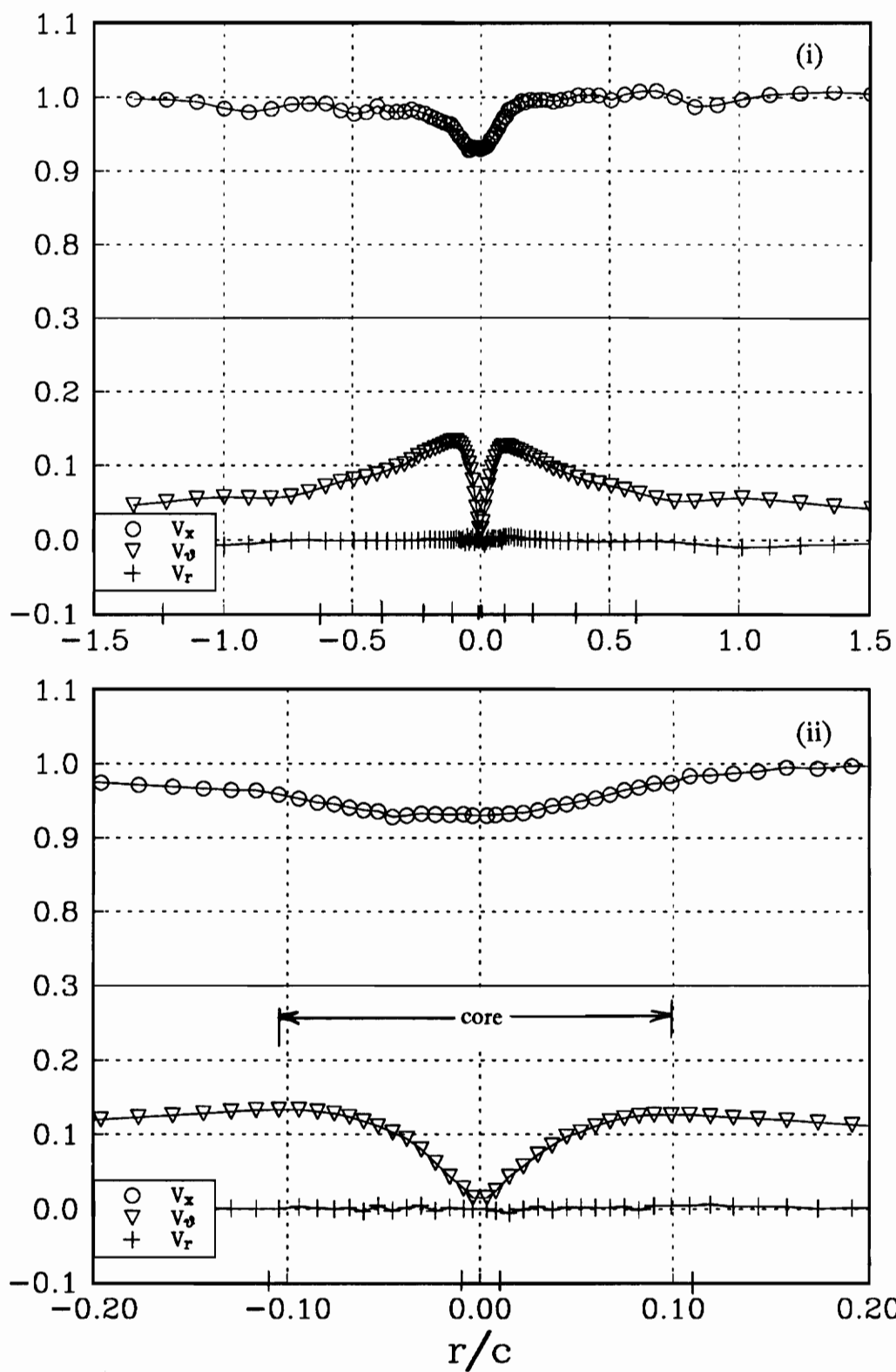


Figure 135a. Profile Gg mean velocities for the co-rotating pair at $x/c=30$. (i) wake region, (ii) core region.

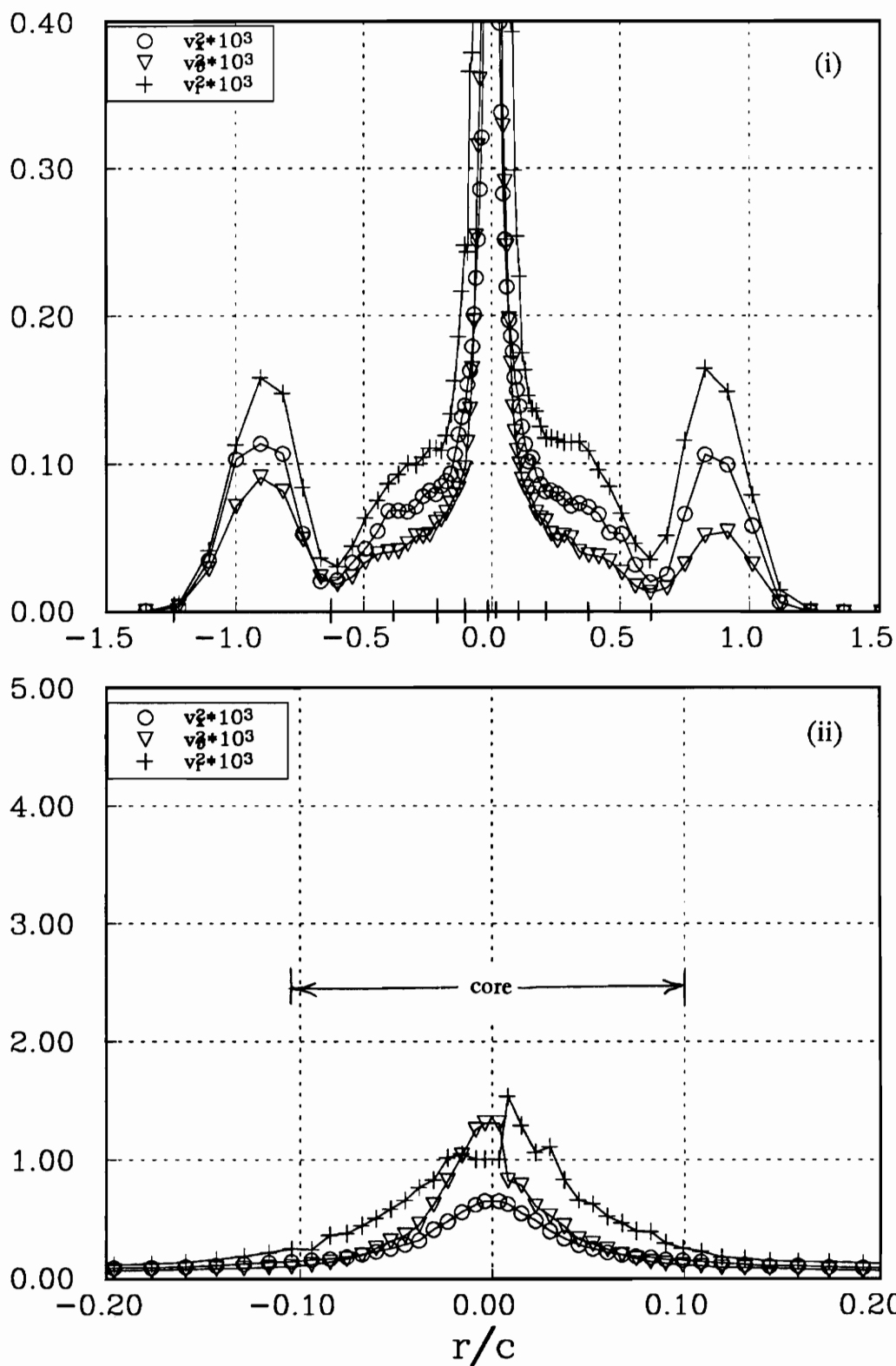


Figure 135b. Profile Gg normal stresses for the co-rotating pair at $x/c=30$. (i) wake region, (ii) core region.

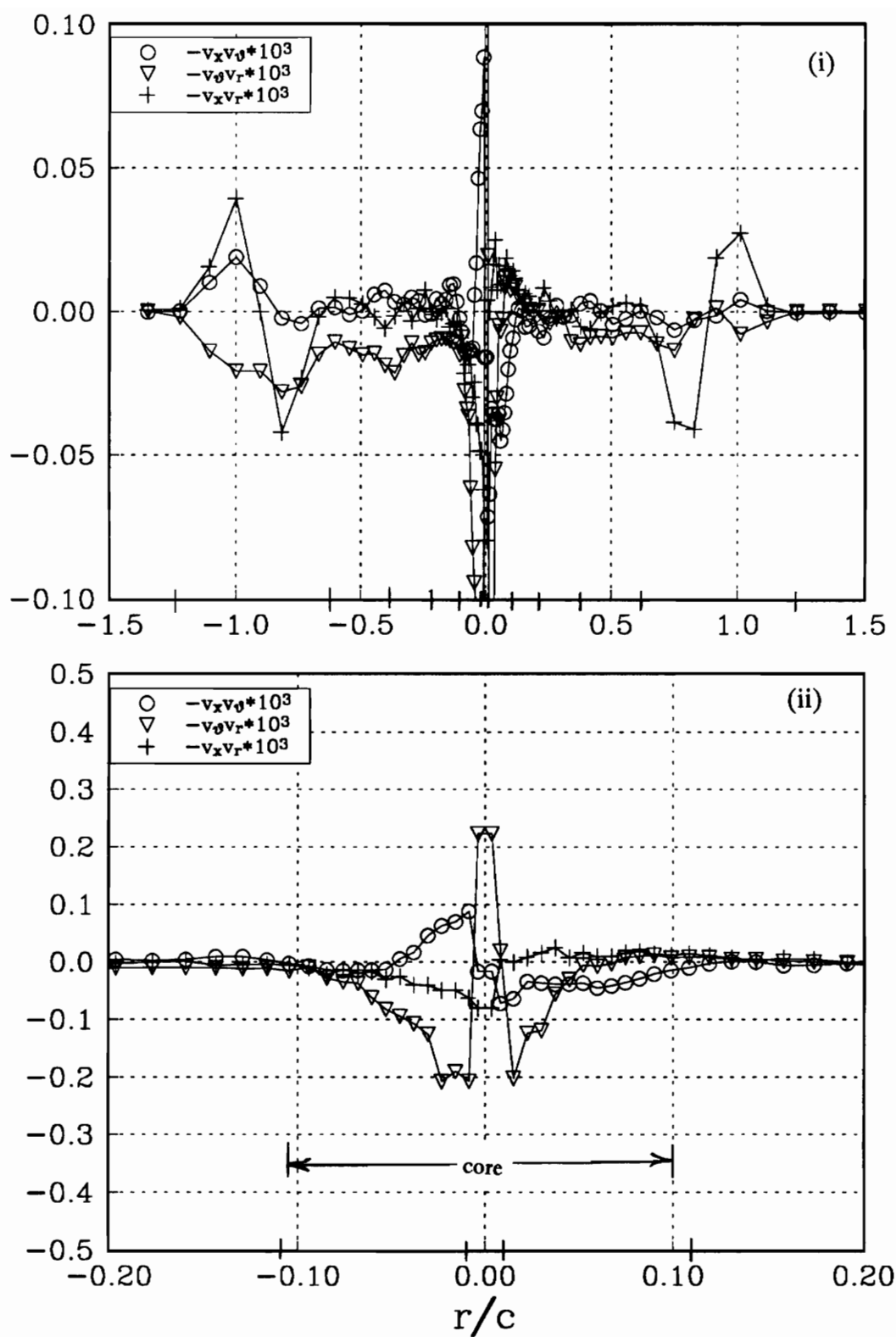


Figure 135c. Profile Gg shear stresses for the co-rotating pair at $x/c=30$. (i) wake region, (ii) core region.

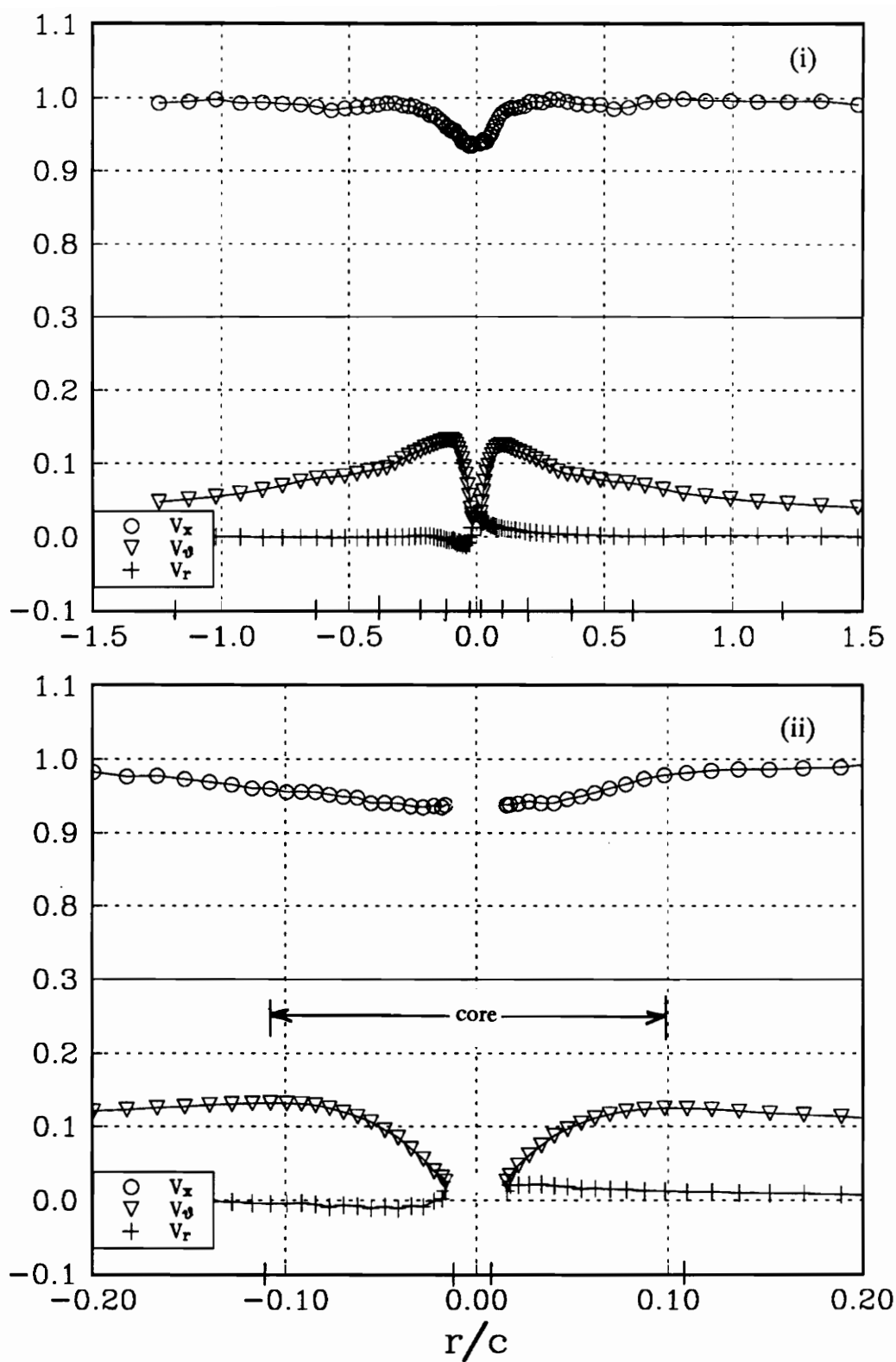


Figure 136a. Profile Hh mean velocities for the co-rotating pair at $x/c=30$. (i) wake region, (ii) core region.

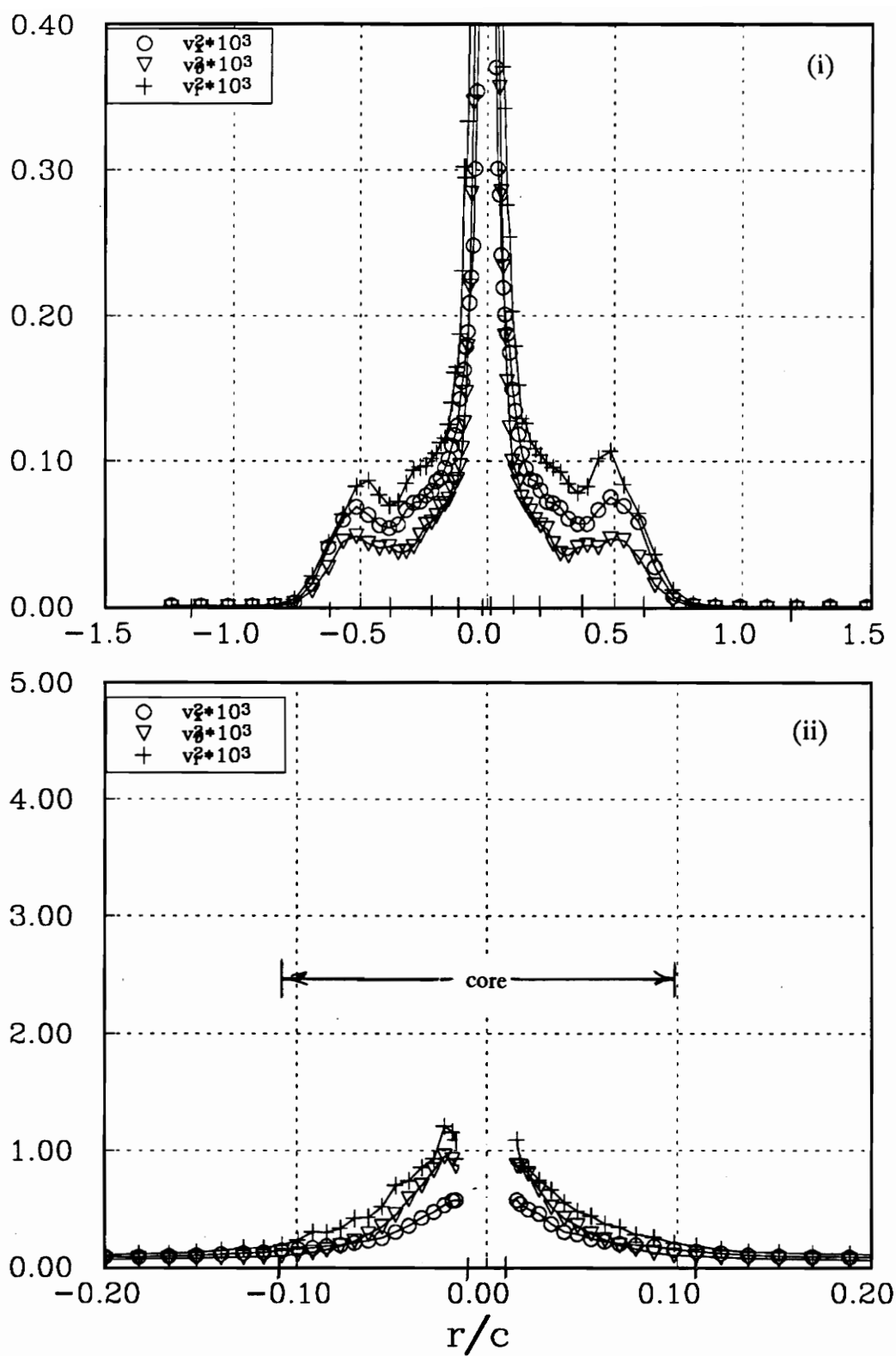


Figure 136b. Profile Hh normal stresses for the co-rotating pair at $x/c=30$. (i) wake region, (ii) core region.

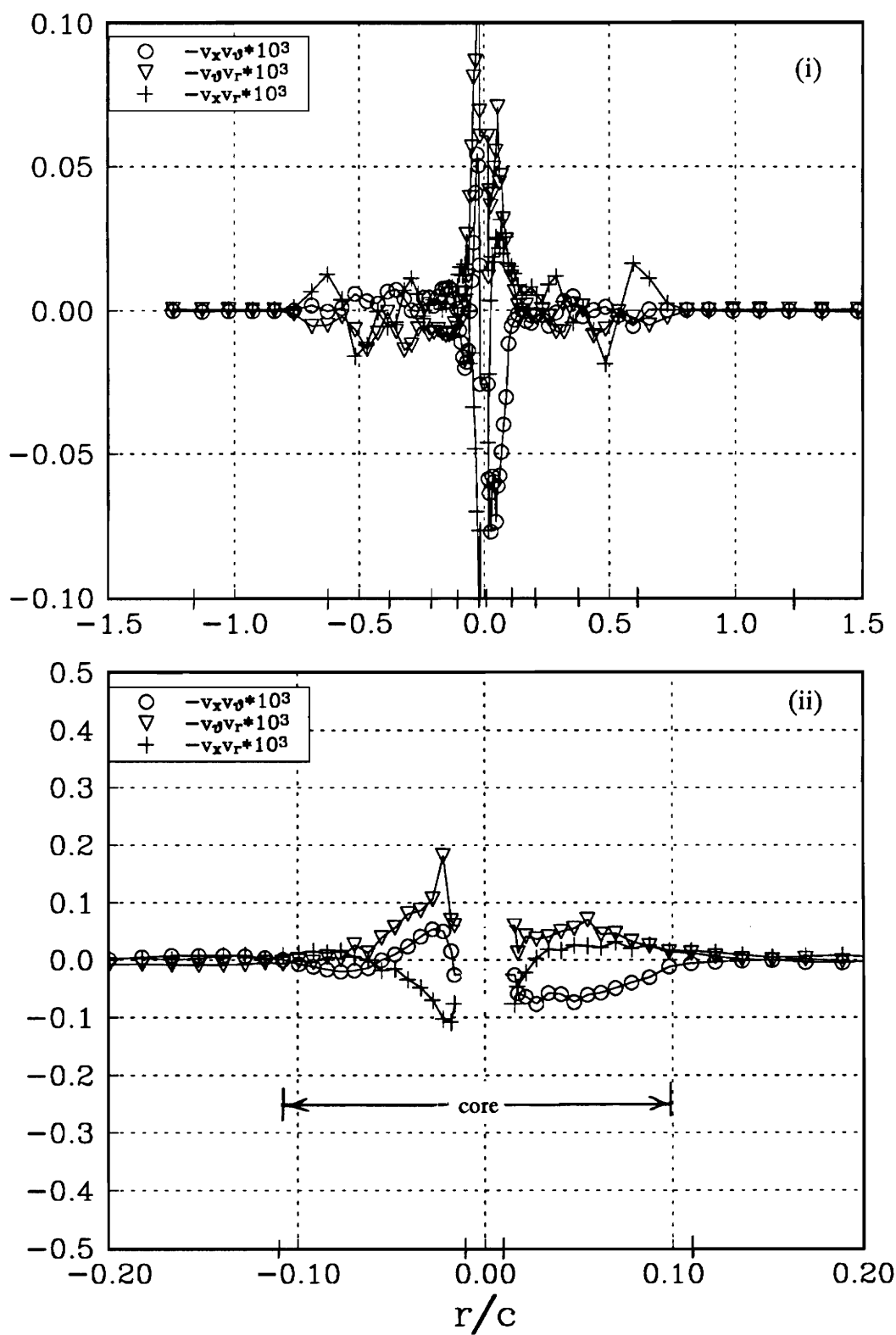


Figure 136c. Profile Hh shear stresses for the co-rotating pair at $x/c=30$. (i) wake region, (ii) core region.

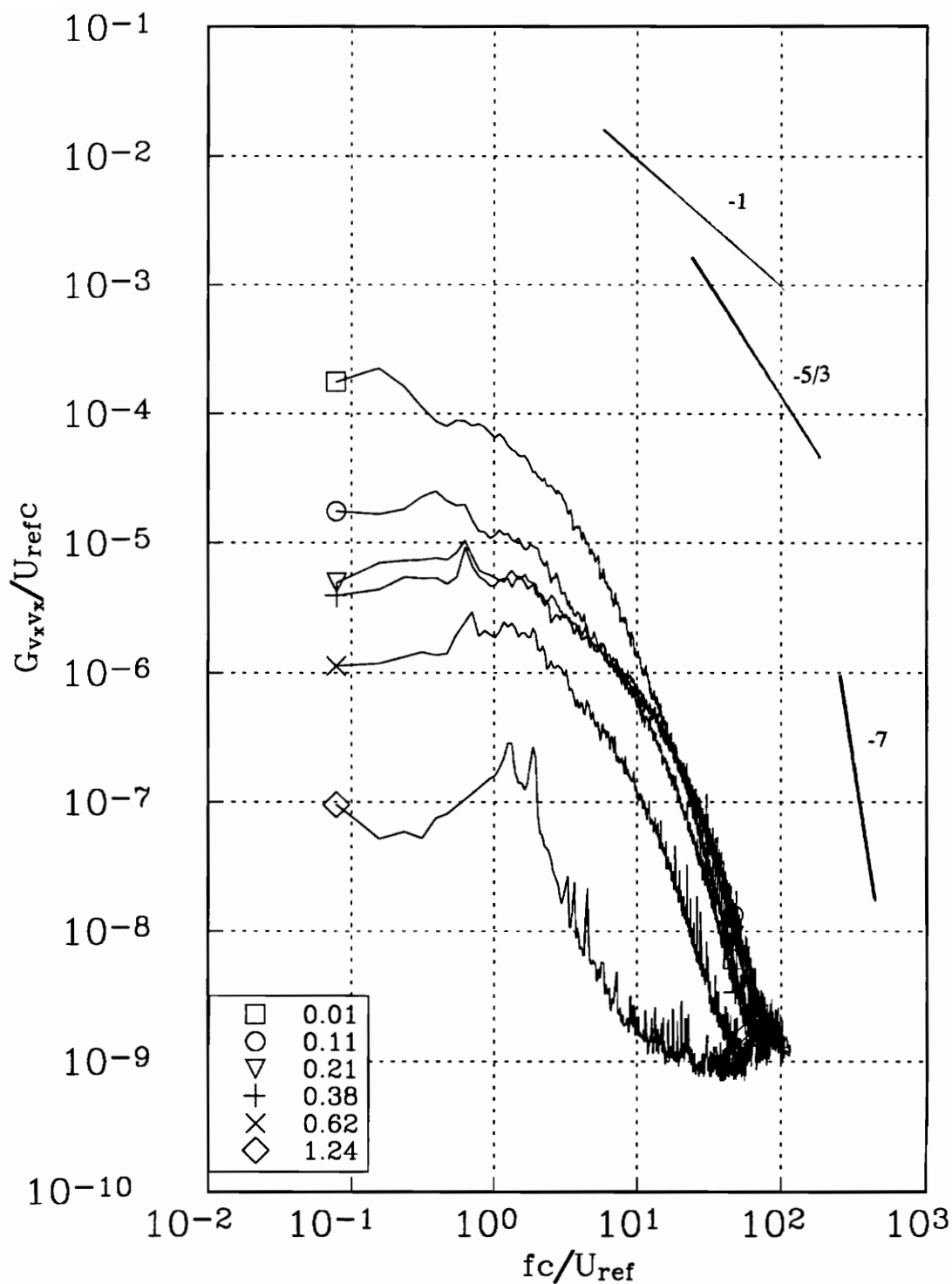


Figure 137a. v_x autospectra measured at representative radial locations along profile Gg for the co-rotating pair at $x/c=30$. Tic marks in figure 135 indicate measured r/c locations.

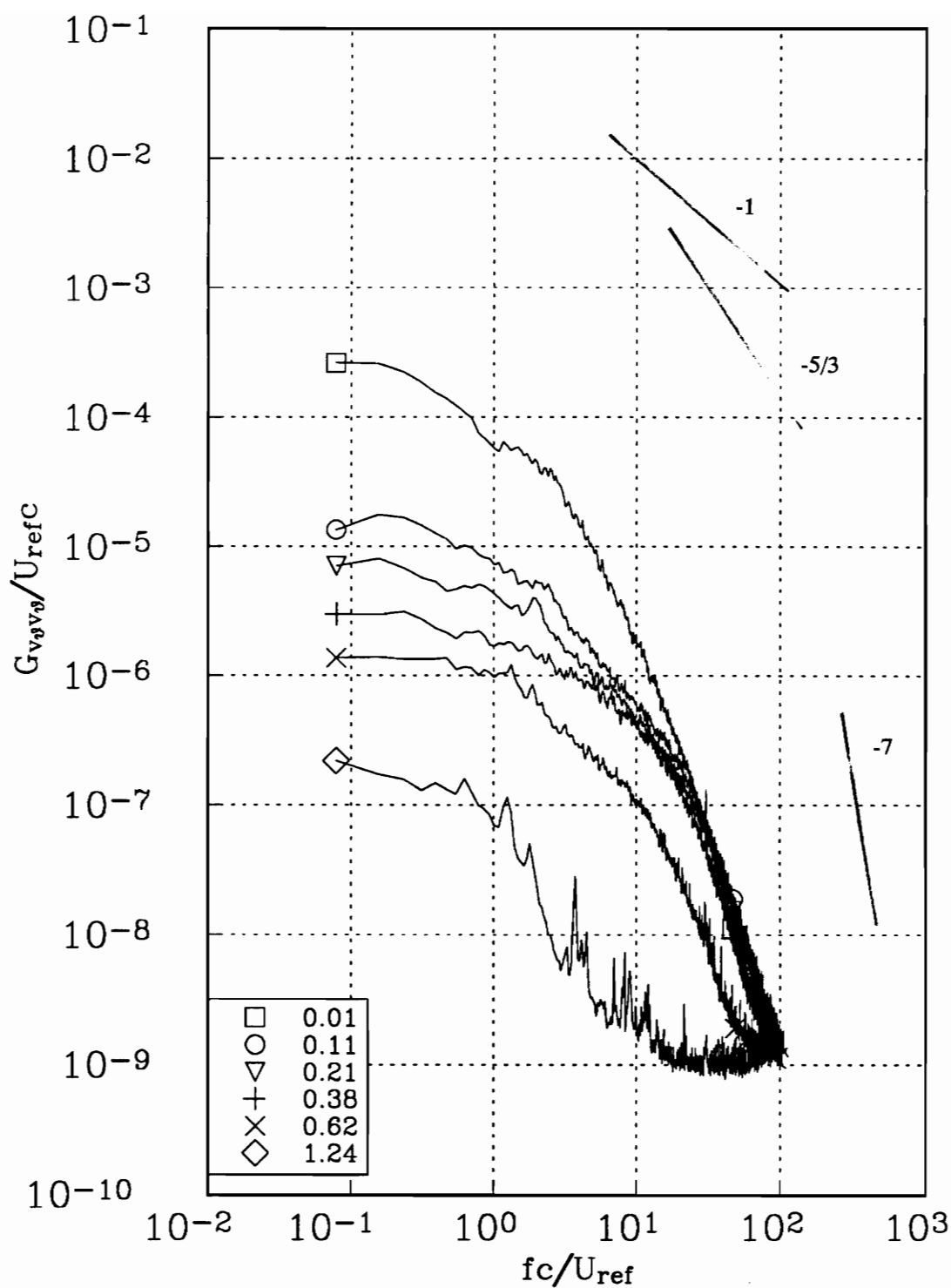


Figure 137b. v_θ autospectra measured at representative radial locations along profile Gg for the co-rotating pair at $x/c=30$. Tic marks in figure 135 indicate measured r/c locations.

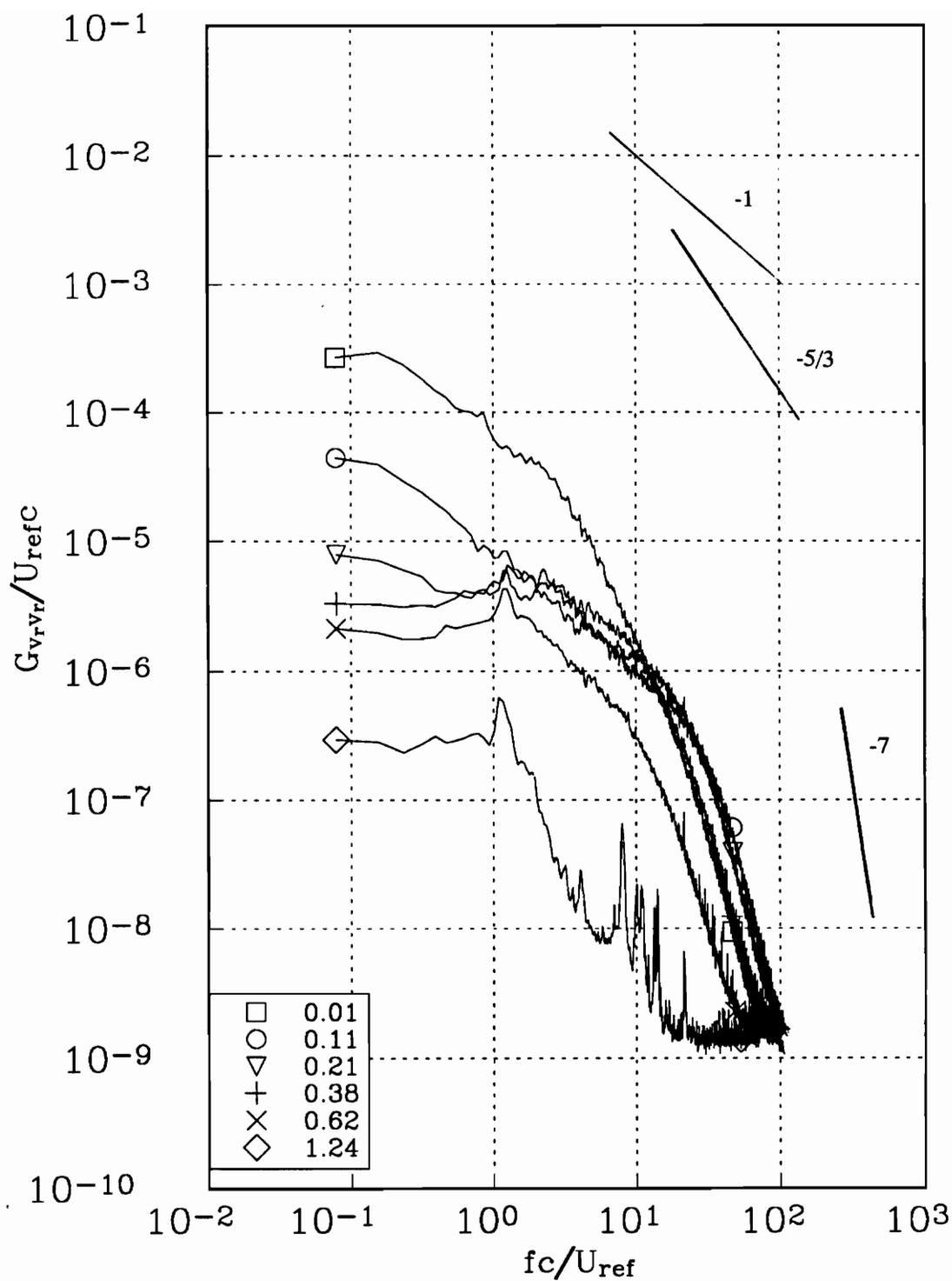


Figure 137c. v_r autospectra measured at representative radial locations along profile Gg for the co-rotating pair at $x/c=30$. Tic marks in figure 135 indicate measured r/c locations.

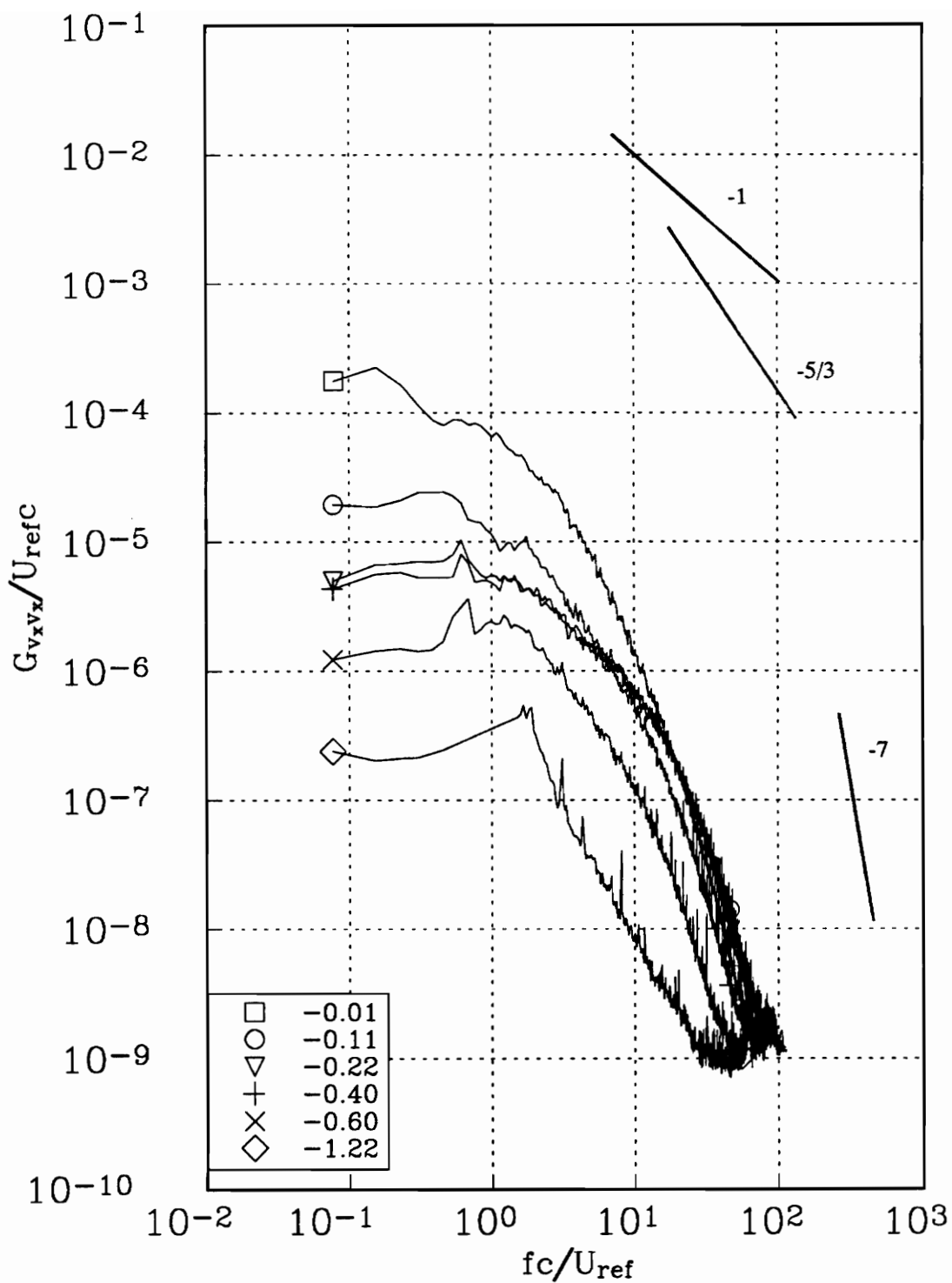


Figure 138a. v_x autospectra measured at representative radial locations along profile Gg for the co-rotating pair at $x/c=30$. Tic marks in figure 135 indicate measured r/c locations.

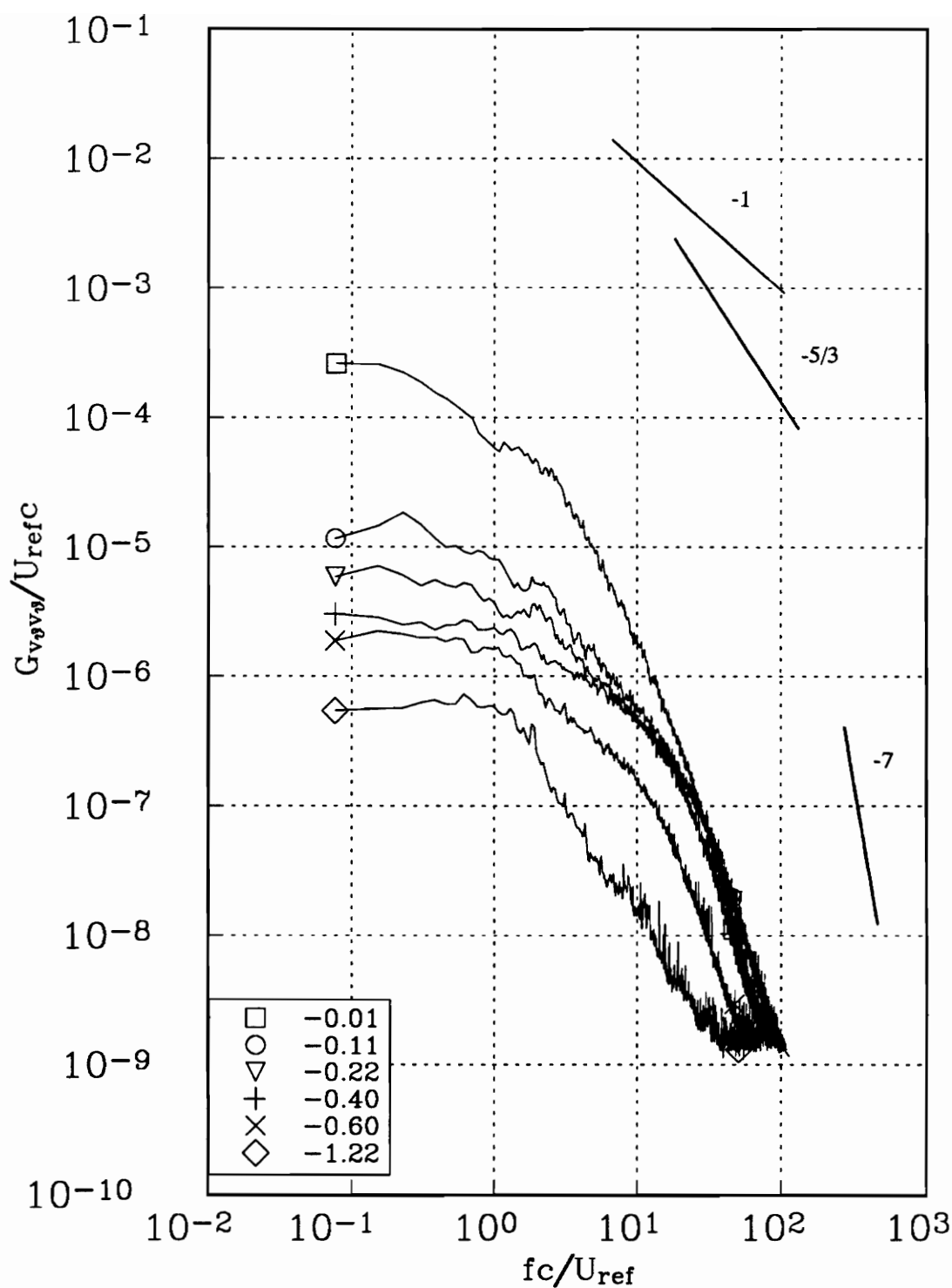


Figure 138b. v_θ autospectra measured at representative radial locations along profile Gg for the co-rotating pair at $x/c=30$. Tic marks in figure 135 indicate measured r/c locations.

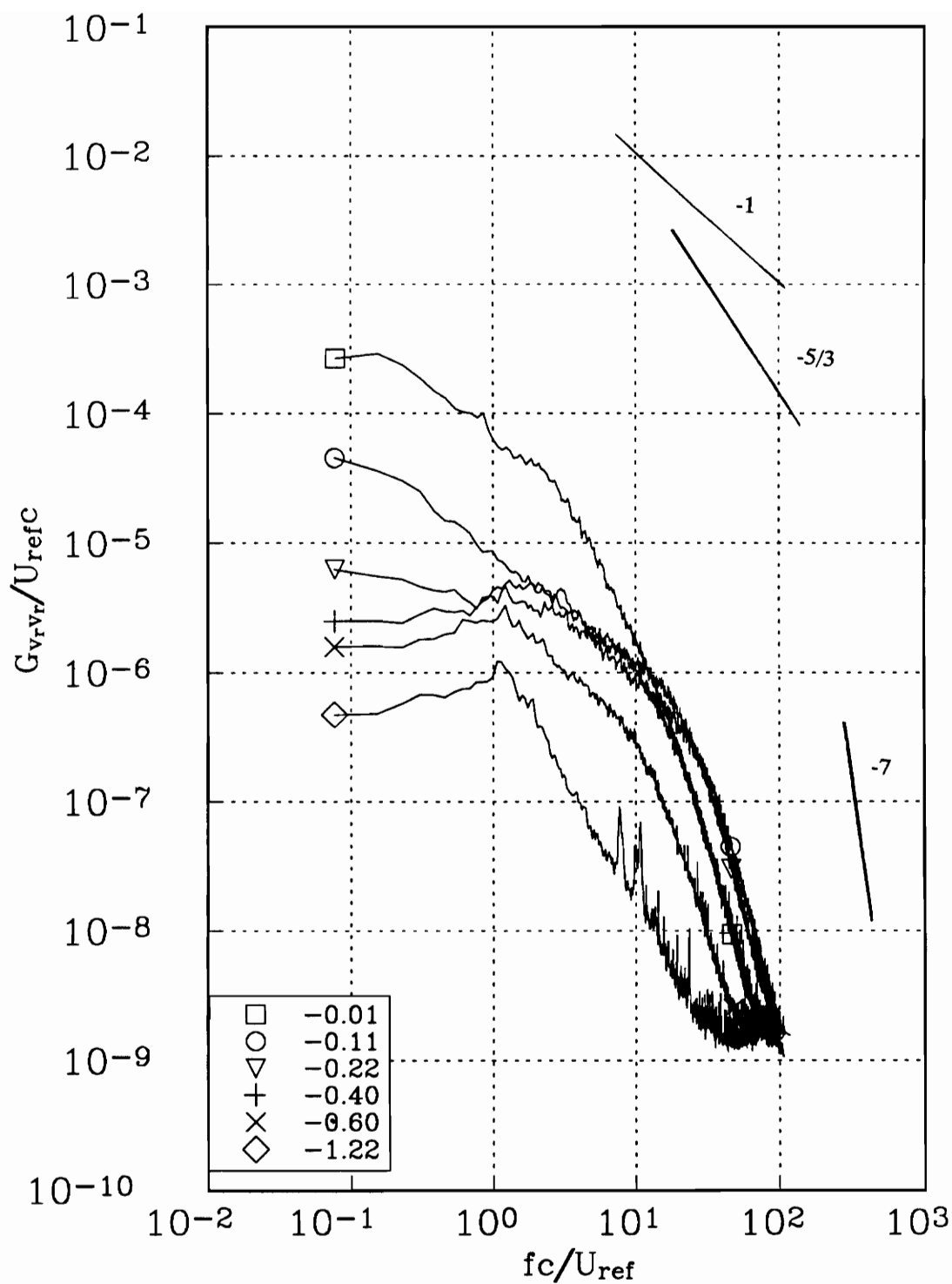


Figure 138c. v_r autospectra measured at representative radial locations along profile Gg for the co-rotating pair at $x/c=30$. Tic marks in figure 135 indicate measured r/c locations.

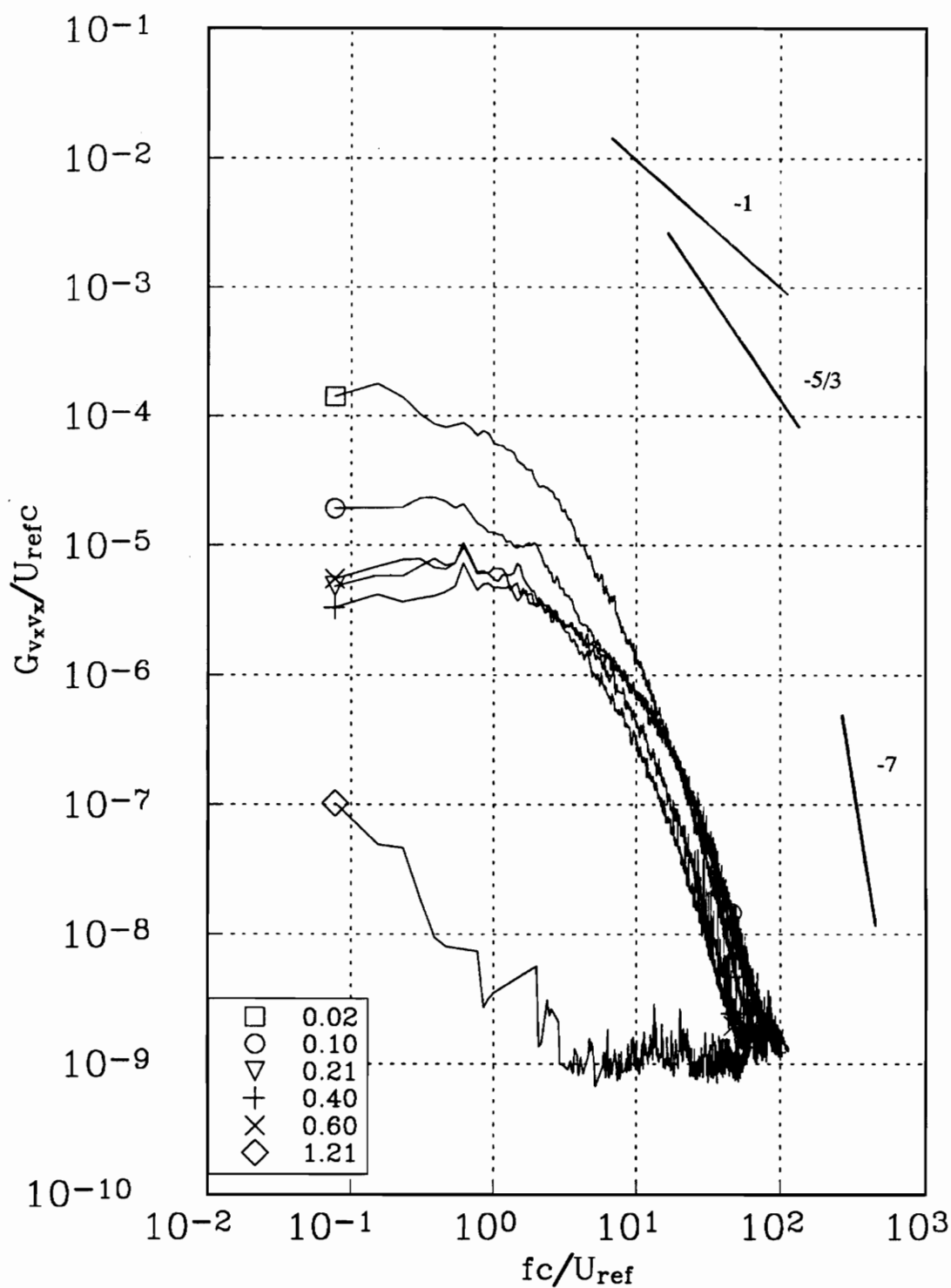


Figure 139a. v_x autospectra measured at representative radial locations along profile Hh for the co-rotating pair at $x/c=30$. Tic marks in figure 136 indicate measured r/c locations.

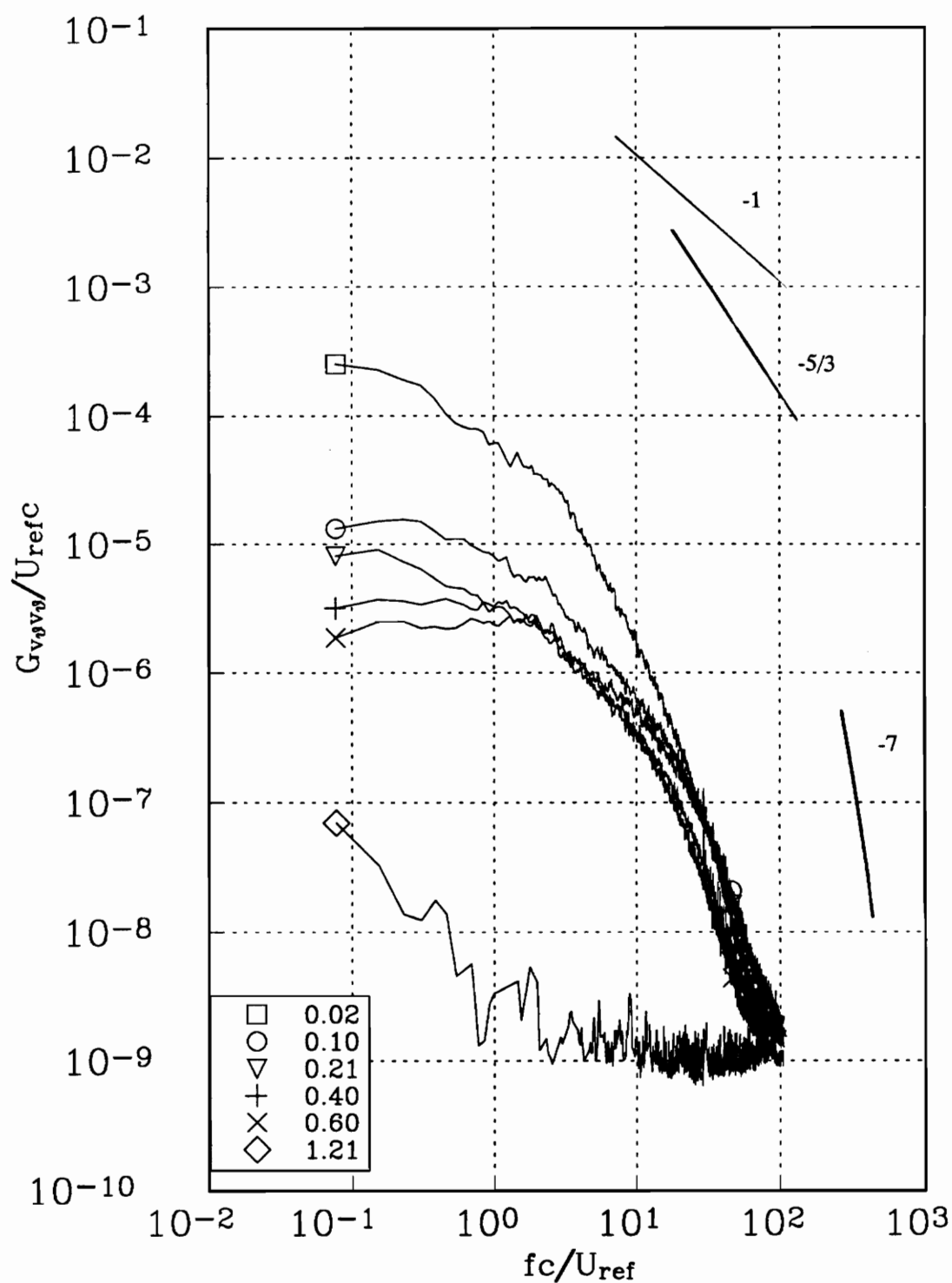


Figure 139b. v_θ autospectra measured at representative radial locations along profile Hh for the co-rotating pair at $x/c=30$. Tic marks in figure 136 indicate measured r/c locations.

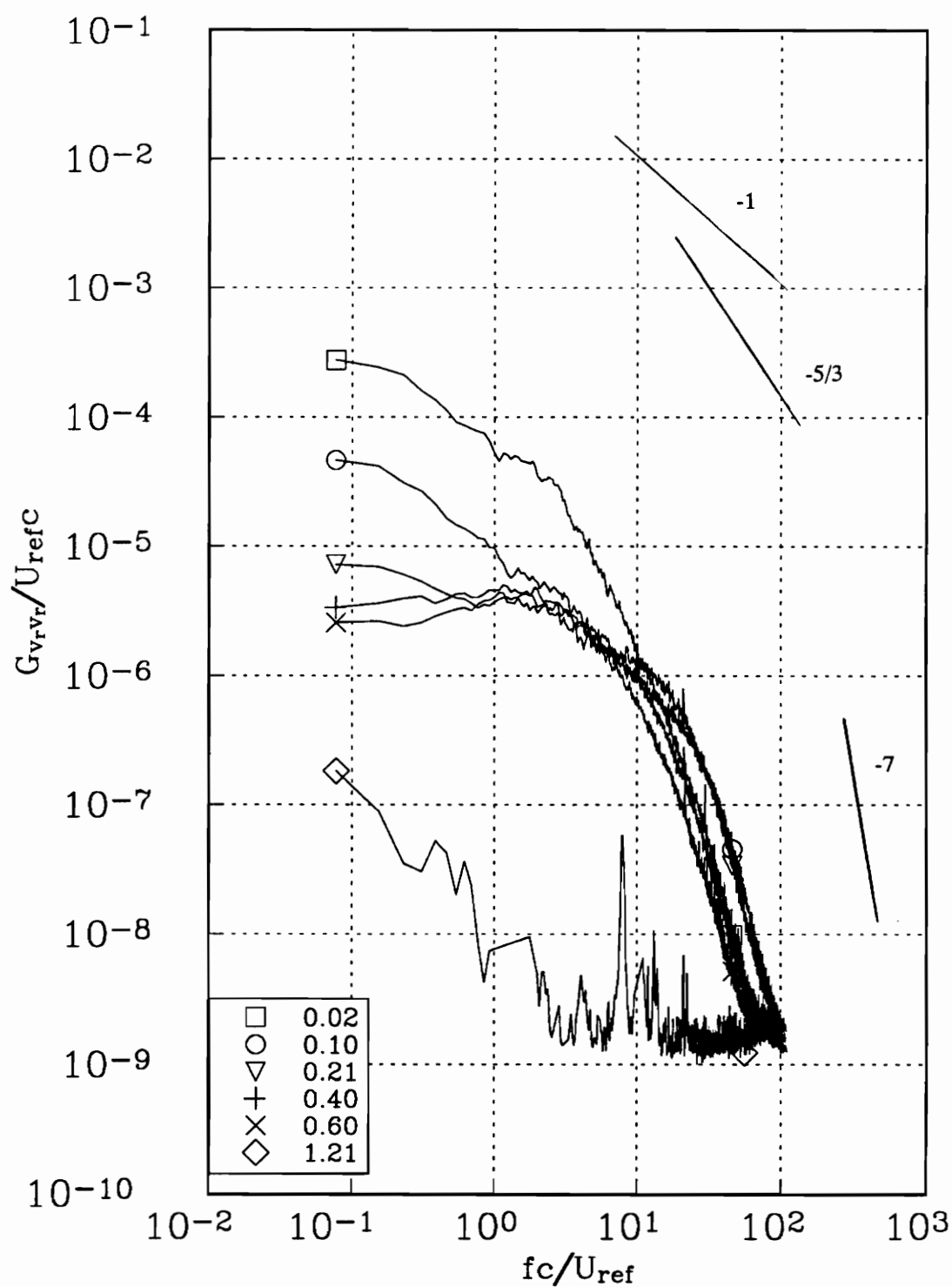


Figure 139c. v_r autospectra measured at representative radial locations along profile Hh for the co-rotating pair at $x/c=30$. Tic marks in figure 136 indicate measured r/c locations.

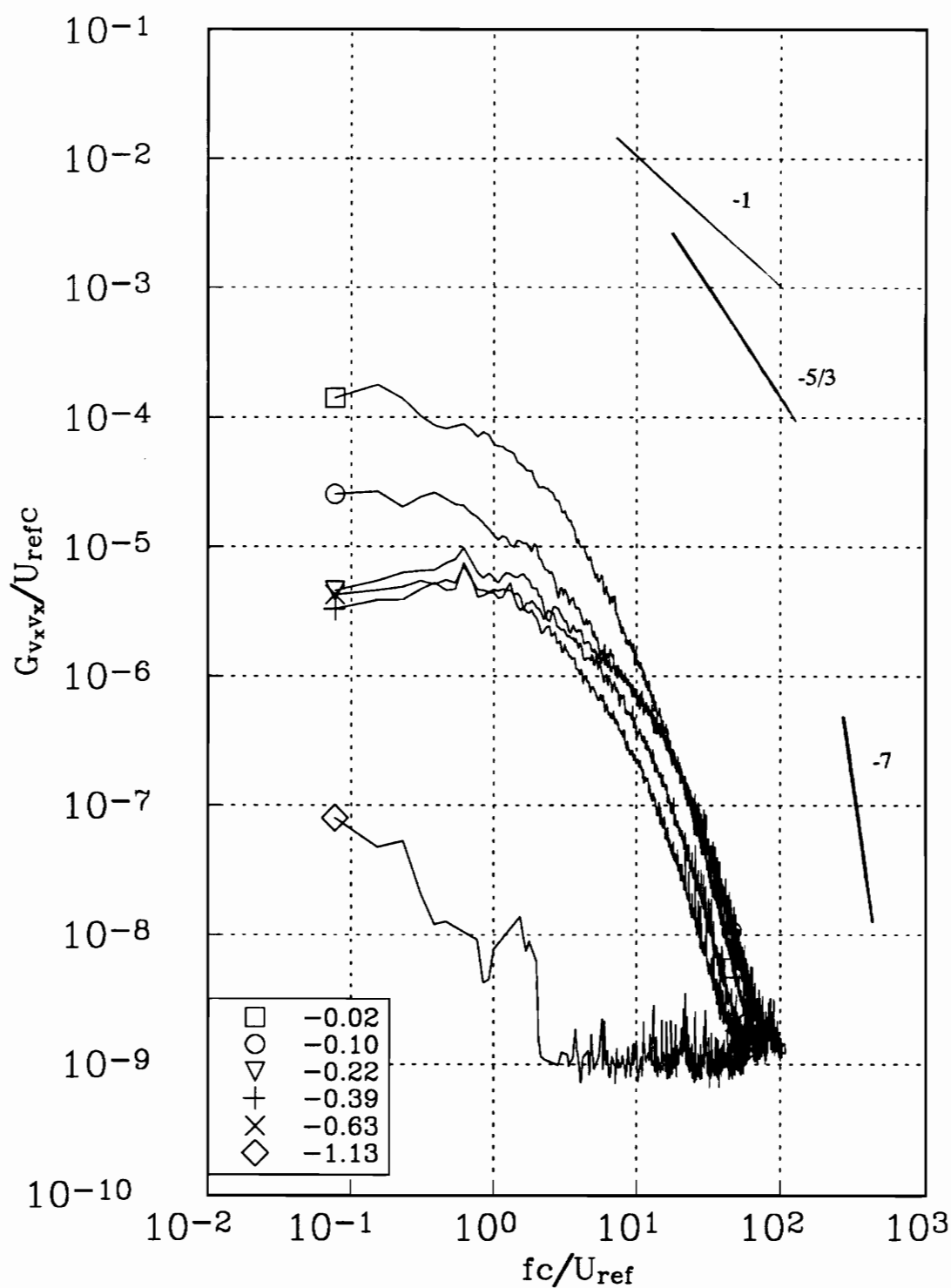


Figure 140a. v_x autospectra measured at representative radial locations along profile Hh for the co-rotating pair at $x/c=30$. Tic marks in figure 136 indicate measured r/c locations.

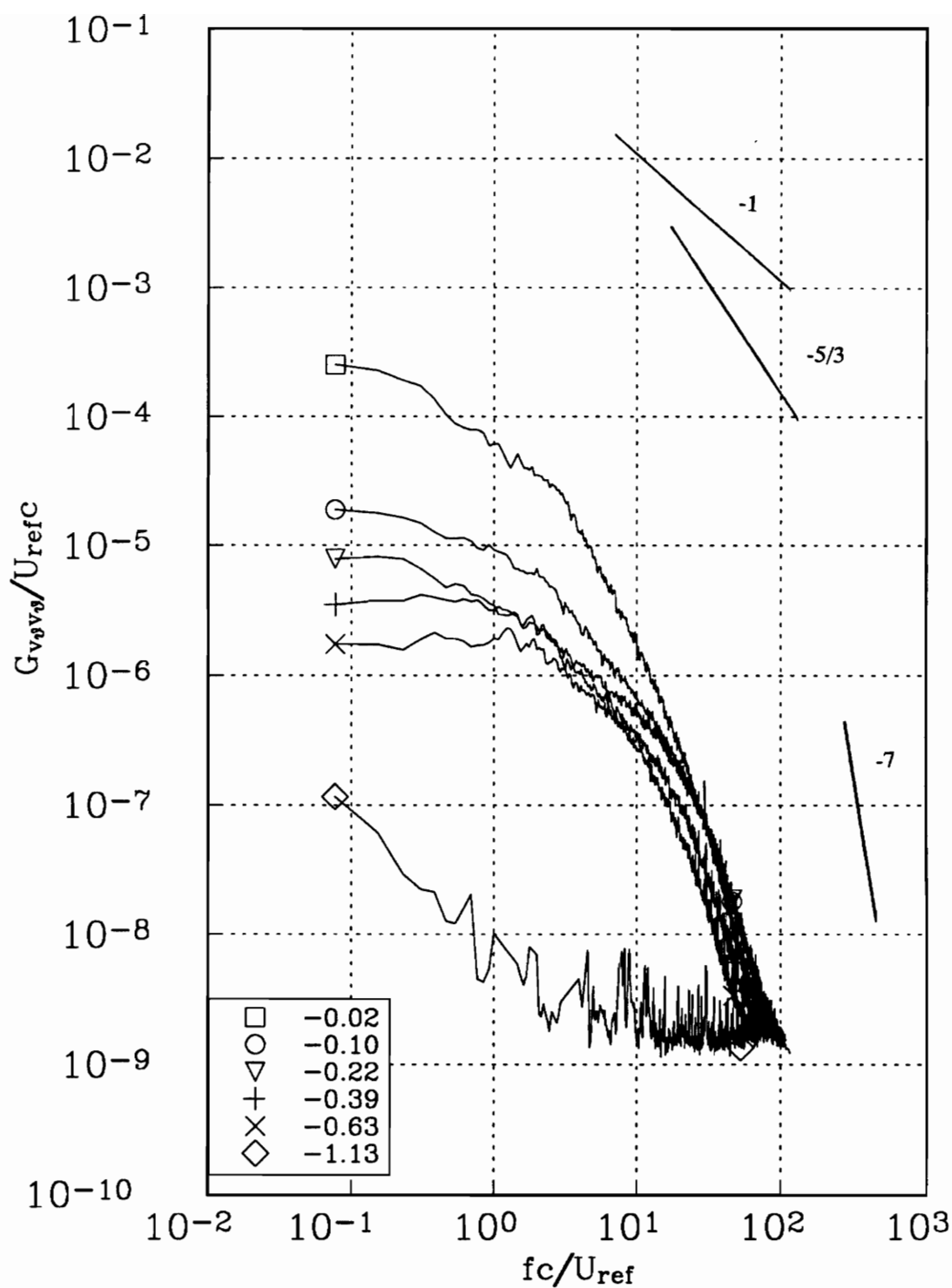


Figure 140b. v_θ autospectra measured at representative radial locations along profile Hh for the co-rotating pair at $x/c=30$. Tic marks in figure 136 indicate measured r/c locations.

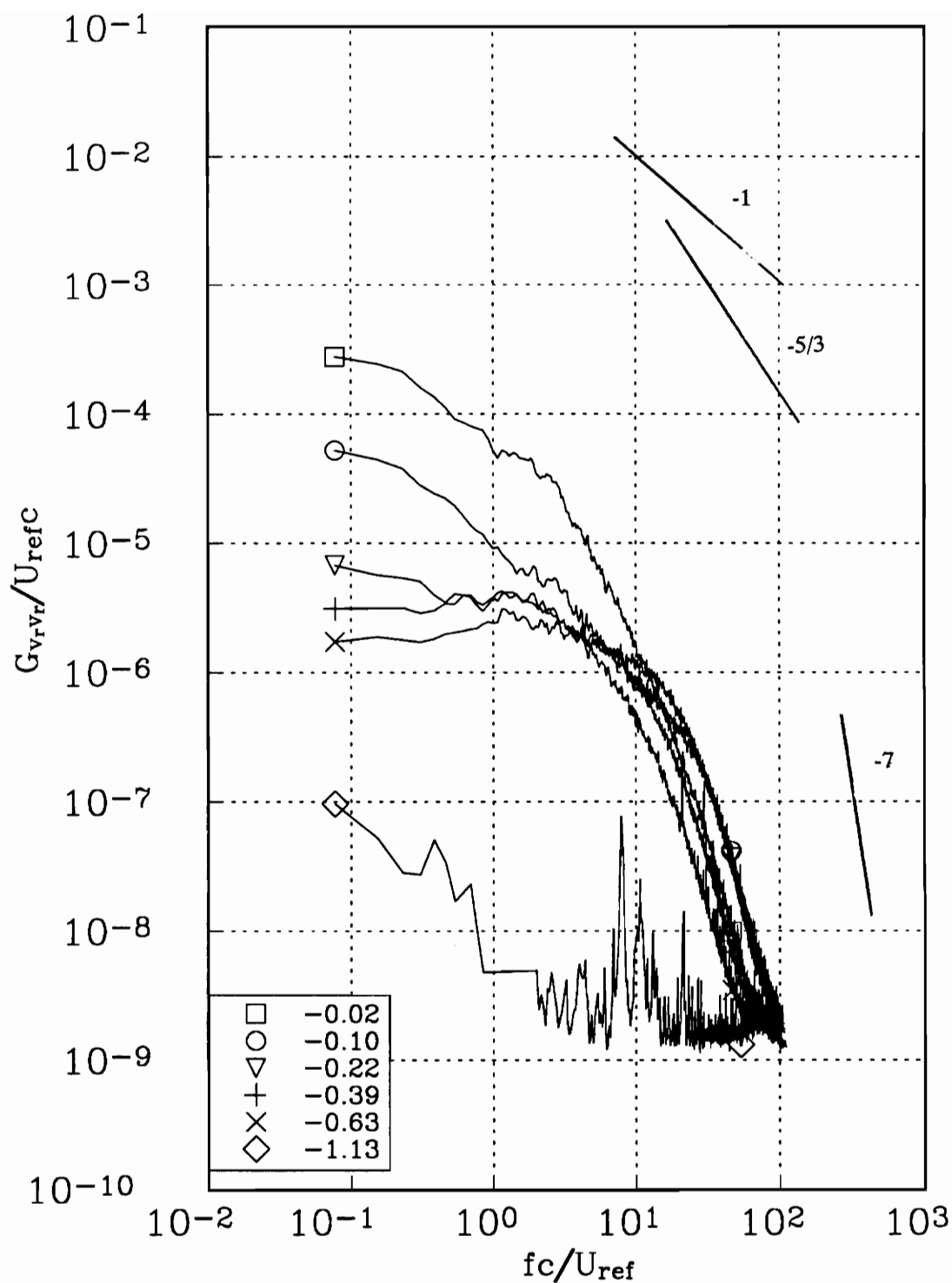


Figure 140c. v_r autospectra measured at representative radial locations along profile Hh for the co-rotating pair at $x/c=30$. Tic marks in figure 136 indicate measured r/c locations.

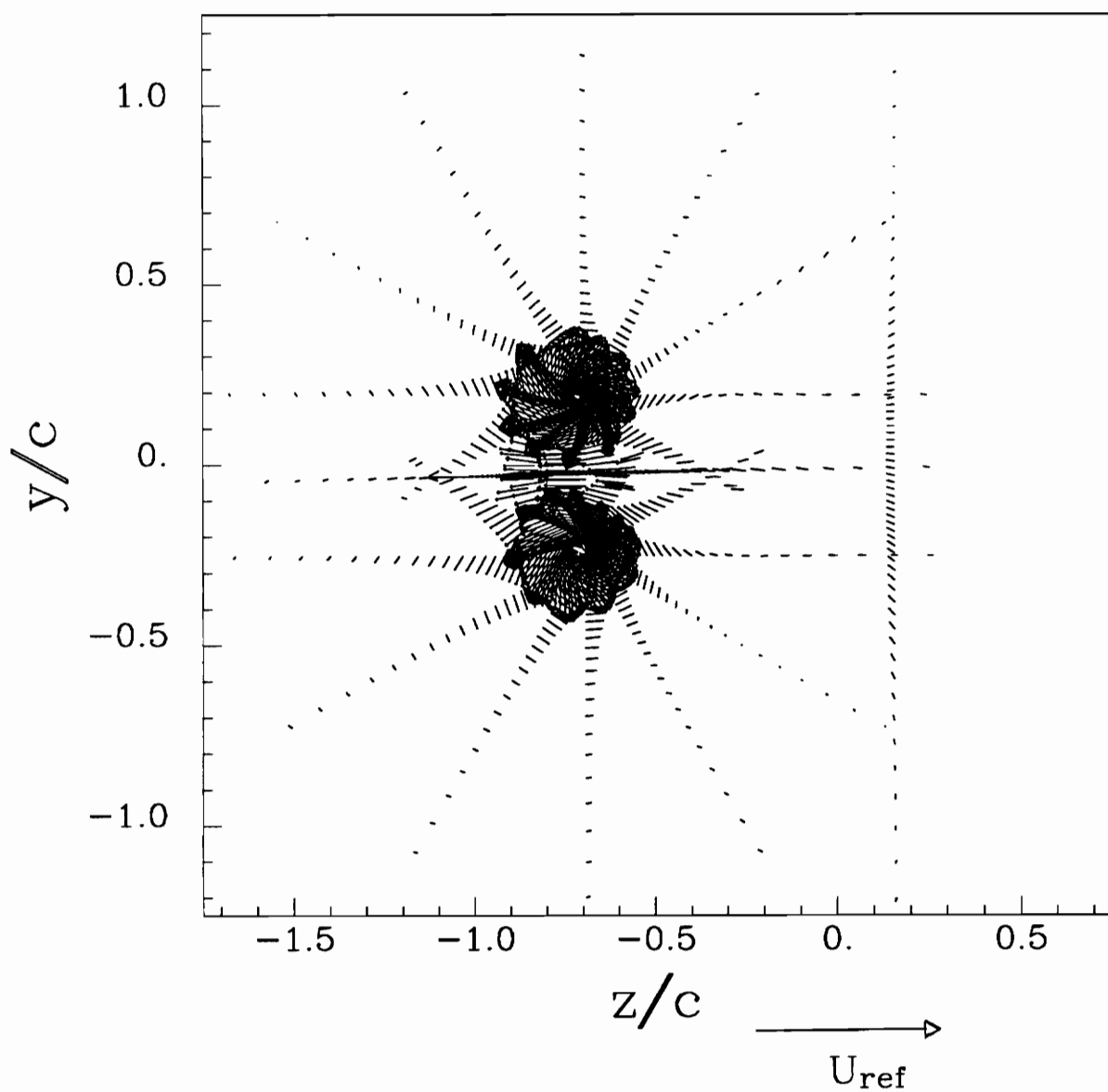
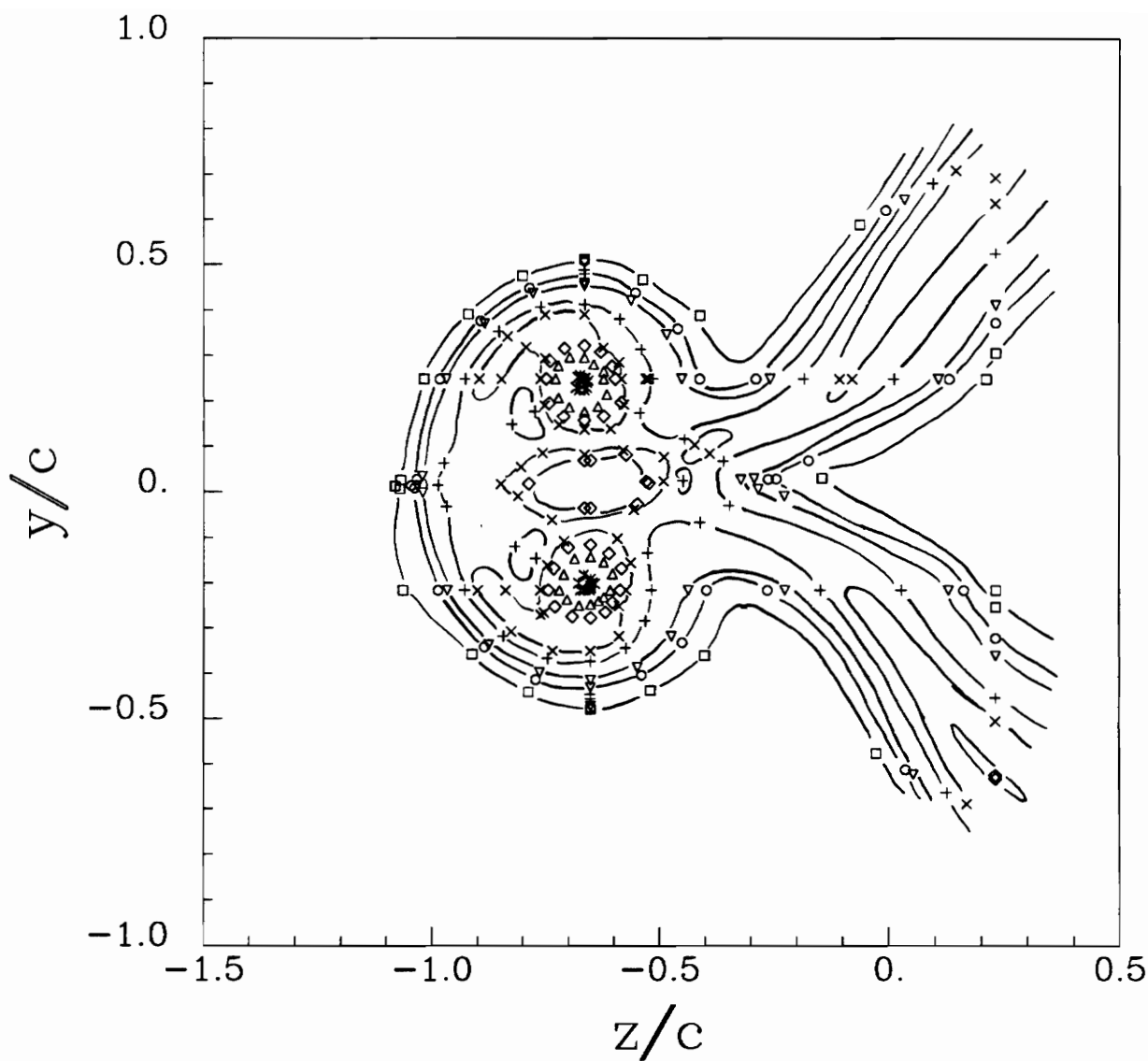
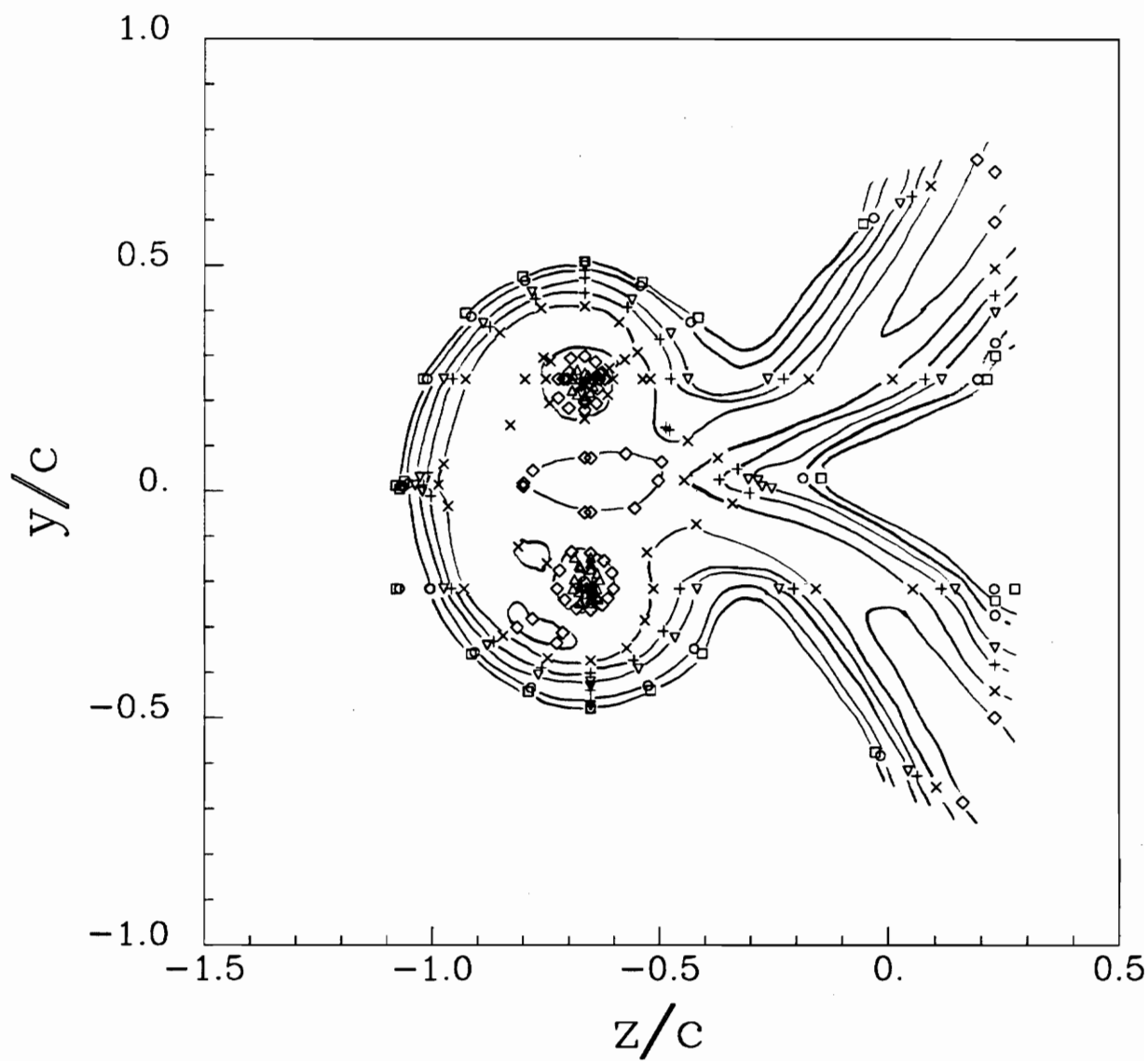


Figure 141. Mean secondary flow vectors of the counter rotating pair at $x/c=10$, angle of attack 5° , $Re_c=260,000$.



□	0.000010
○	0.000050
▽	0.000100
+	0.000300
×	0.000400
◇	0.000500
△	0.001000
*	0.005000

Figure 142. Contours of turbulent kinetic energy k/U_{ref}^2 for the counter rotating pair at $x/c=10$, angle of attack 5° , $Re_c=260,000$.



□	0.000005
○	0.000010
▽	0.000050
+	0.000100
×	0.000200
◇	0.000300
△	0.000500
*	0.001000

Figure 143. Contours of v_x^2/U_{ref}^2 for the counter rotating pair at $x/c=10$, angle of attack 5° , $Re_c=260,000$.

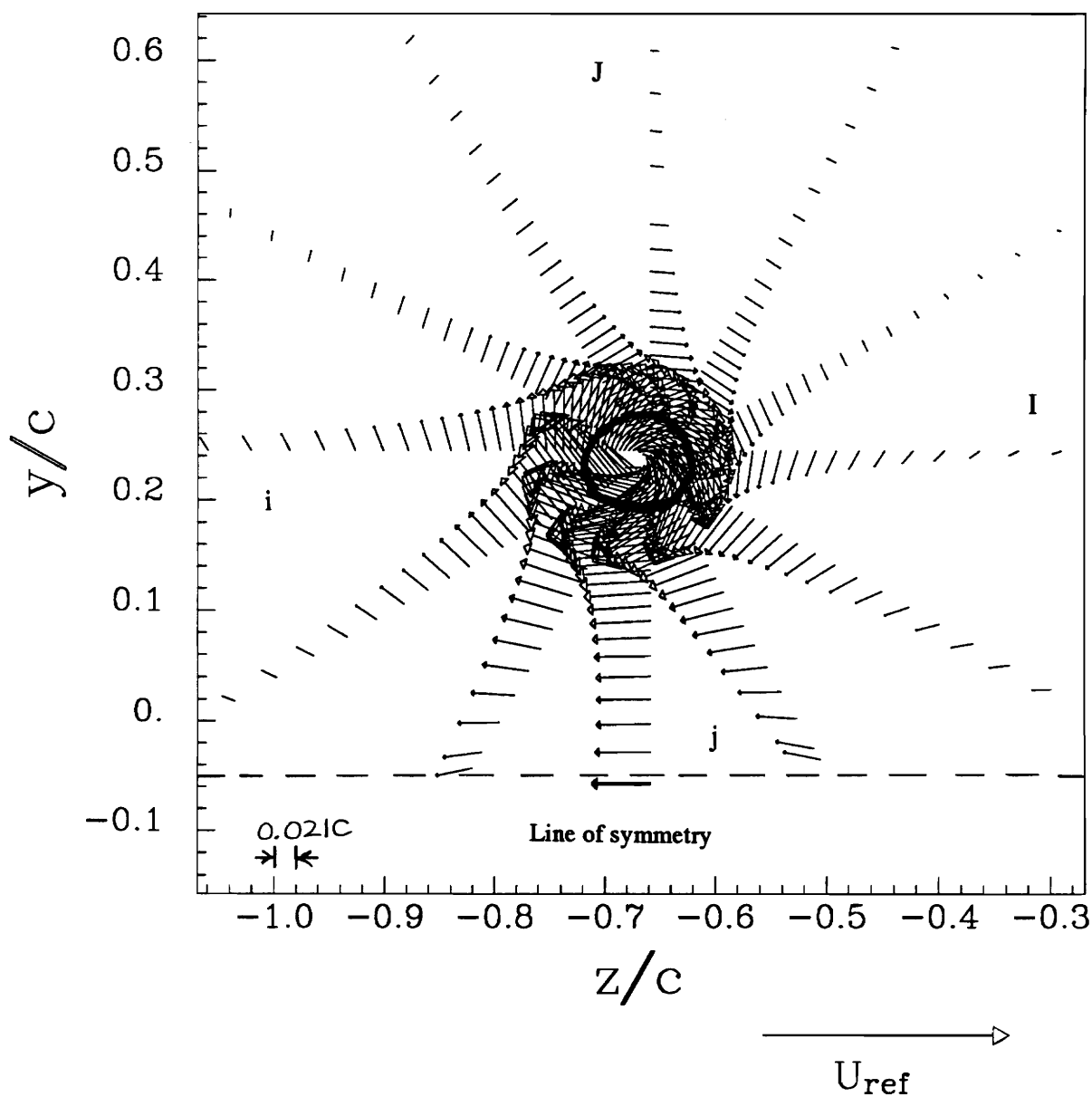


Figure 144. Core region showing mean secondary flows vectors for the upper counter rotating vortex at $x/c=10$, angle of attack= 5° , $Re_c=260,000$. Dotted line indicates core edge.

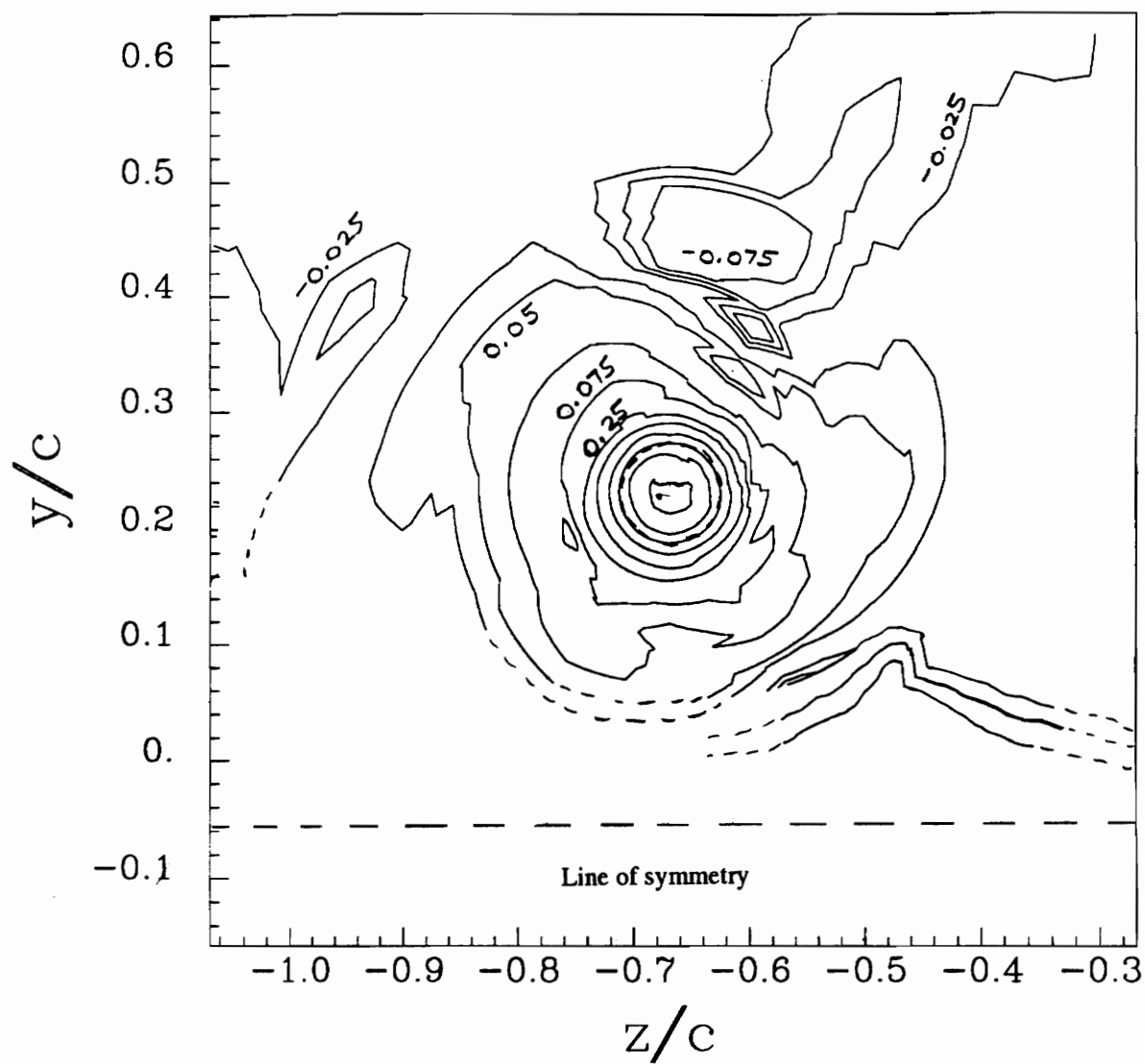


Figure 145. Core region showing contours of vorticity $\omega c/U_{\text{ref}}$ for the upper counter rotating vortex at $x/c=10$, angle of attack $=5^\circ$, $Re_c=260,000$. Dotted line indicates core edge.

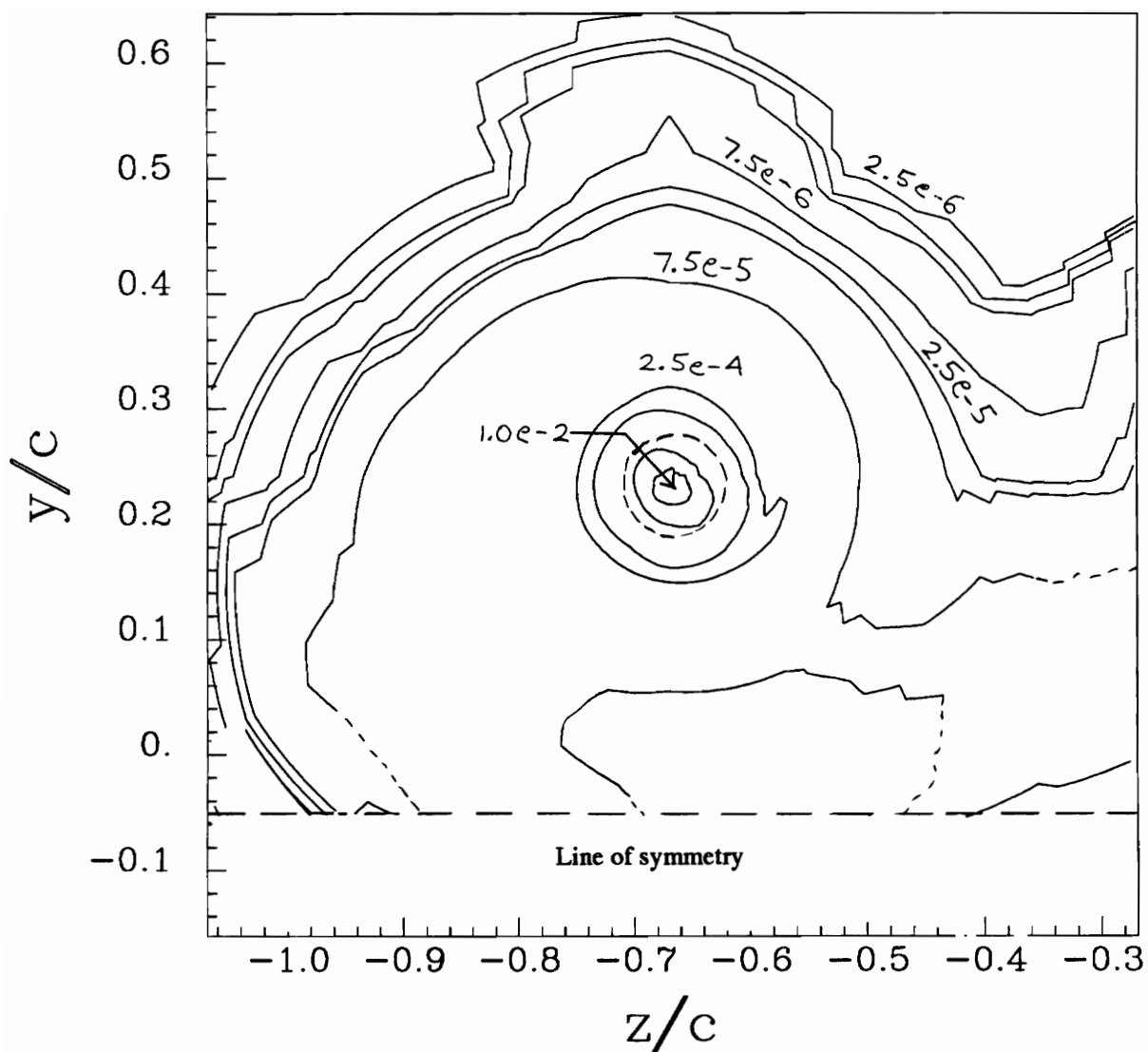


Figure 146. Core region showing contours of turbulent kinetic energy k/U_{ref}^2 for the upper counter rotating vortex at $x/c=10$, angle of attack= 5° , $Re_c=260,000$. Dotted line indicates core edge.

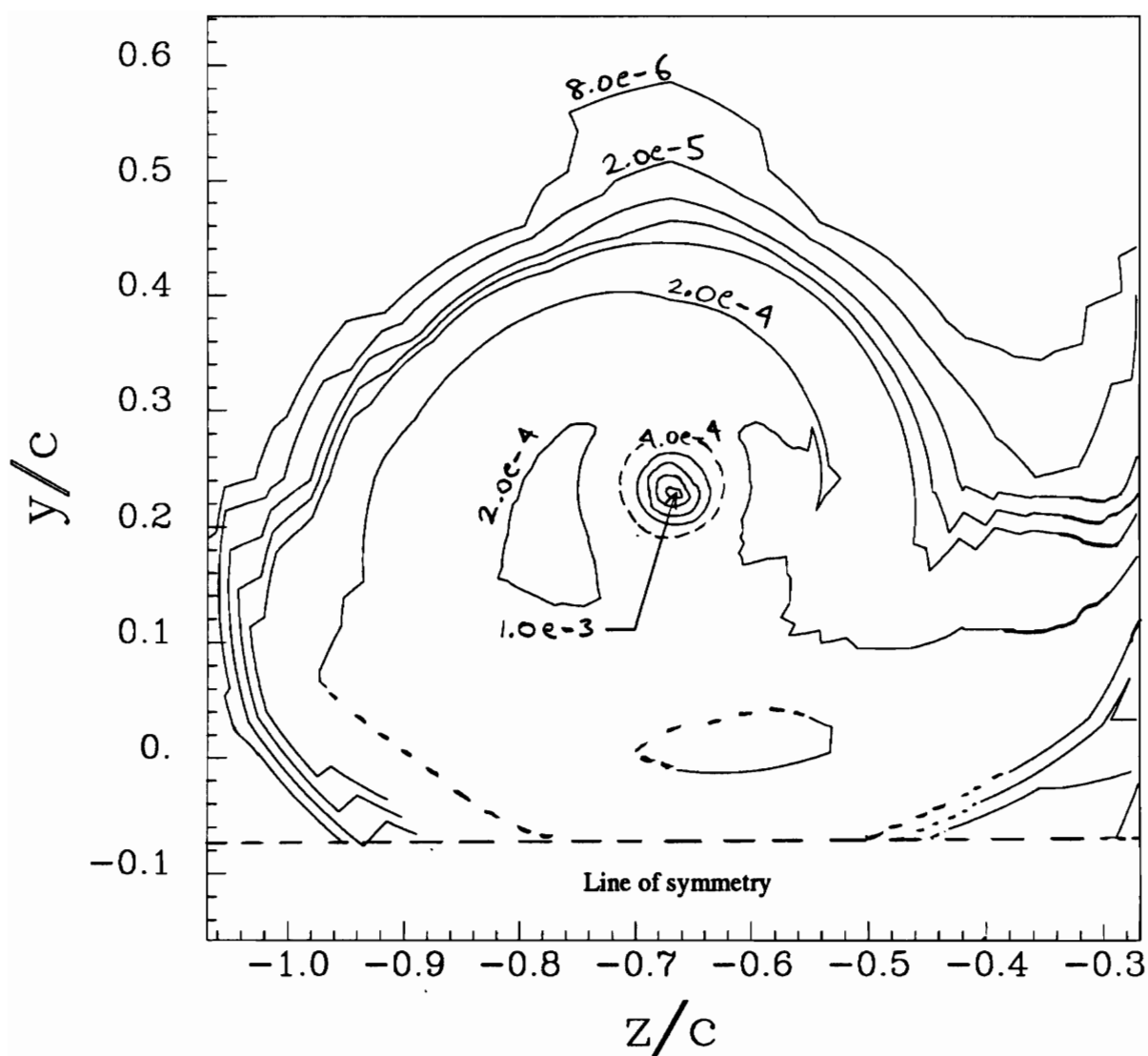


Figure 147. Core region showing contours of v_x^2/U_{ref}^2 for the upper counter rotating vortex at $x/c=10$, angle of attack= 5° , $Re_c=260,000$. Dotted line indicates core edge.

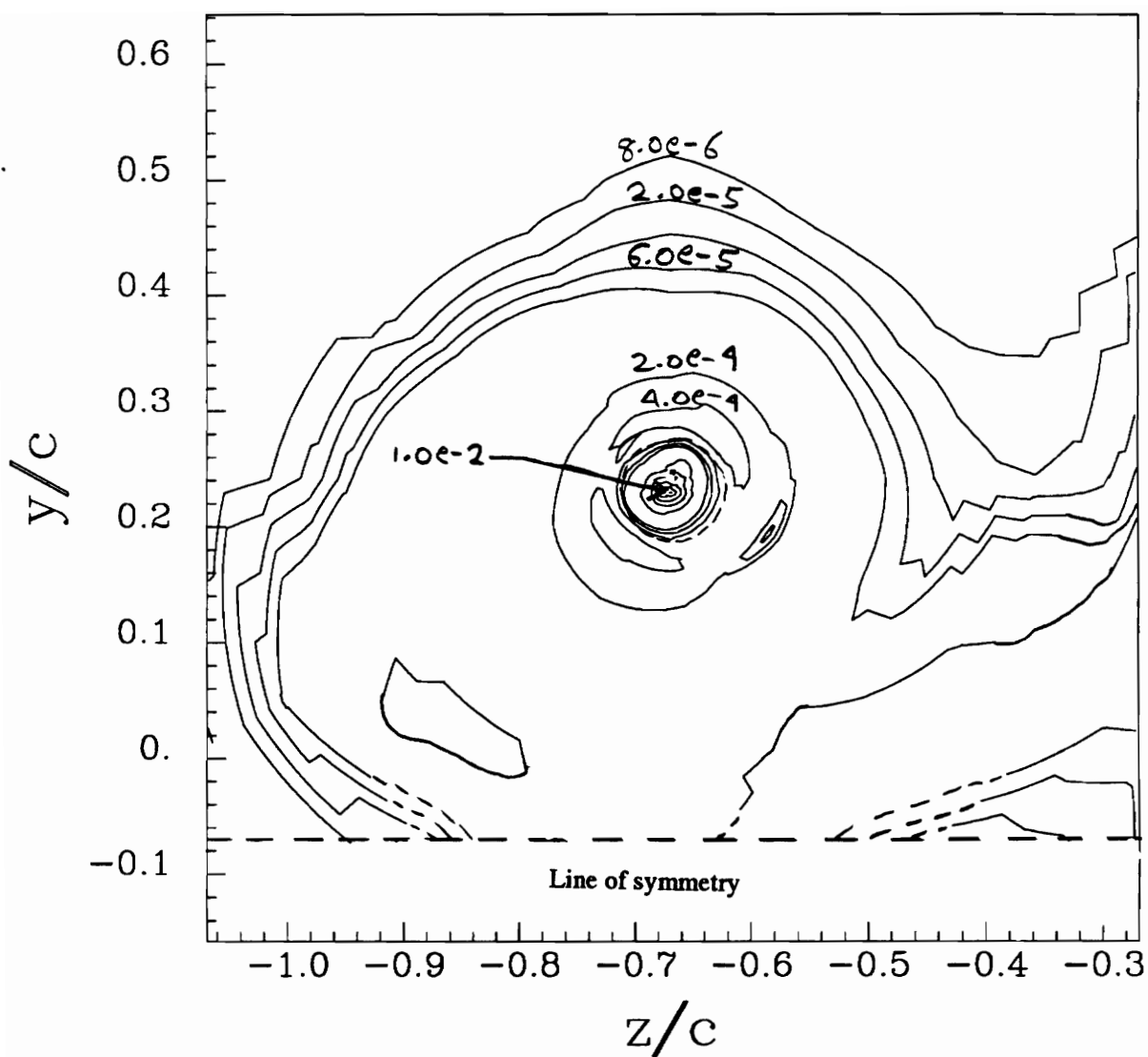


Figure 148. Core region showing contours of v_θ^2/U_{ref}^2 for the upper counter rotating vortex at $x/c=10$, angle of attack= 5° , $Re_c=260,000$. Dotted line indicates core edge.

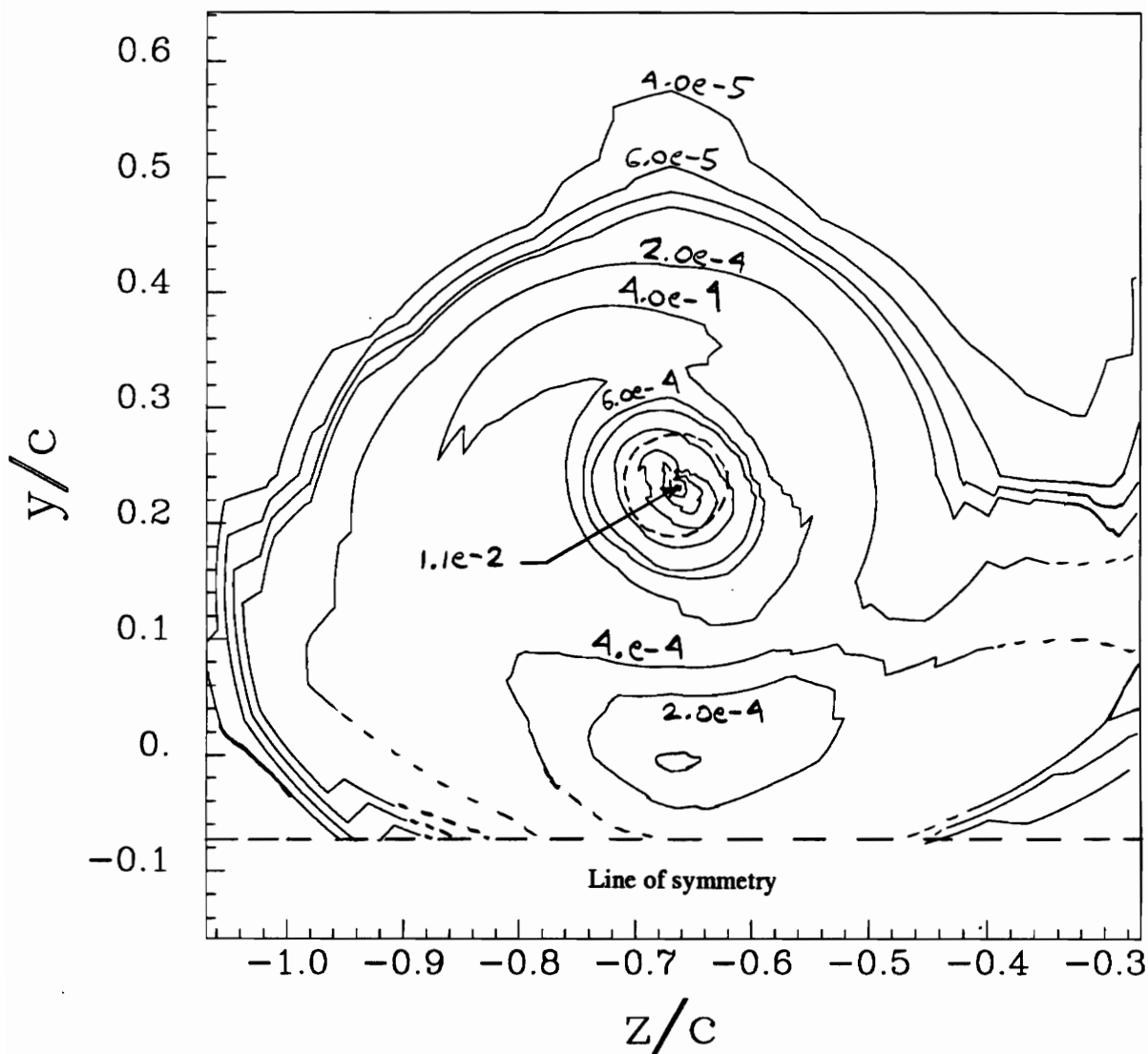


Figure 149. Core region showing contours of v_r^2/U_{ref}^2 for the upper counter rotating vortex at $x/c=10$, angle of attack= 5° , $Re_c=260,000$. Dotted line indicates core edge.

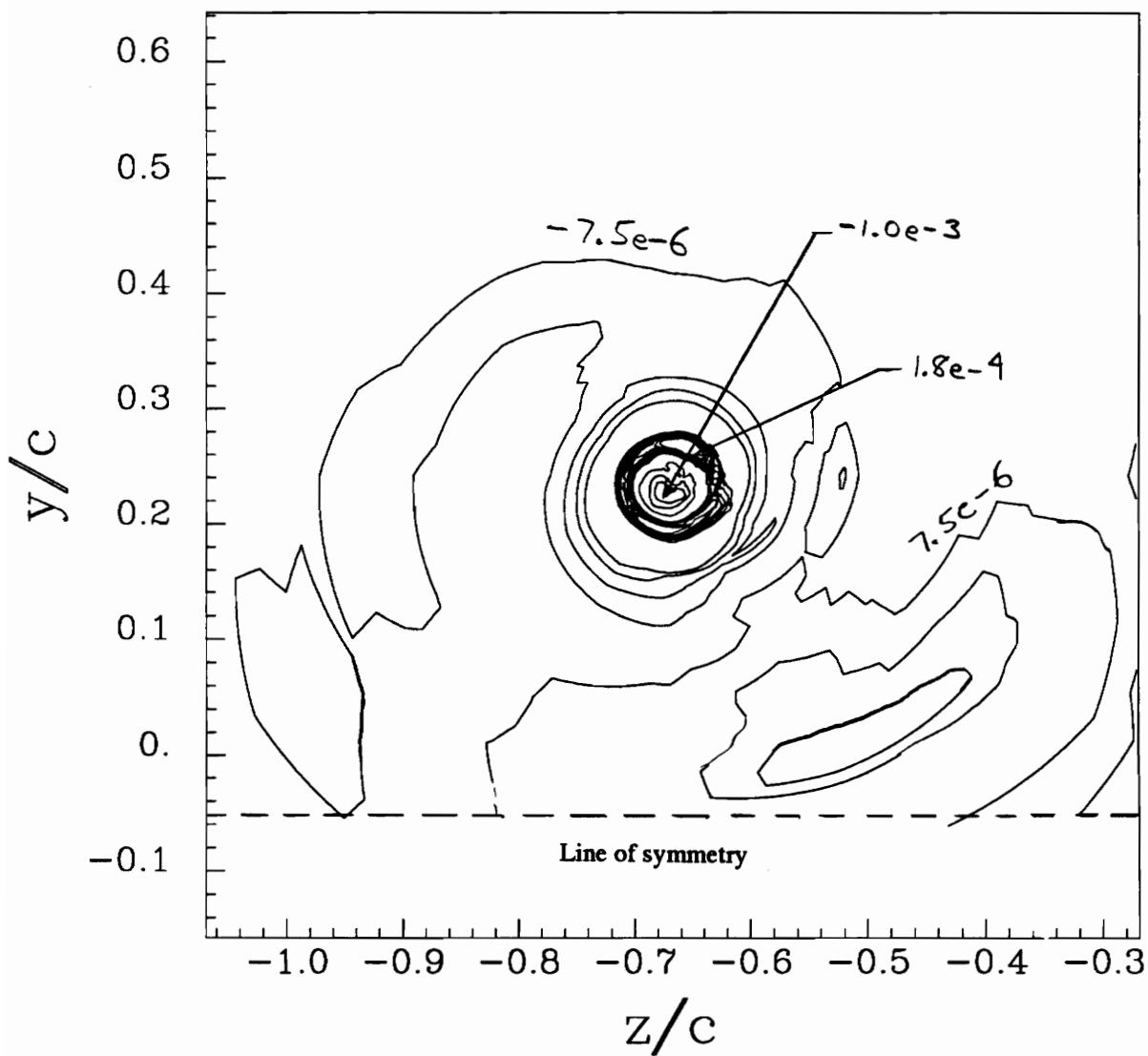


Figure 150. Core region showing contours of $v_x v_\theta / U_{ref}^2$ for the upper counter rotating vortex at $x/c=10$, angle of attack= 5° , $Re_c=260,000$. Dotted line indicates core edge.

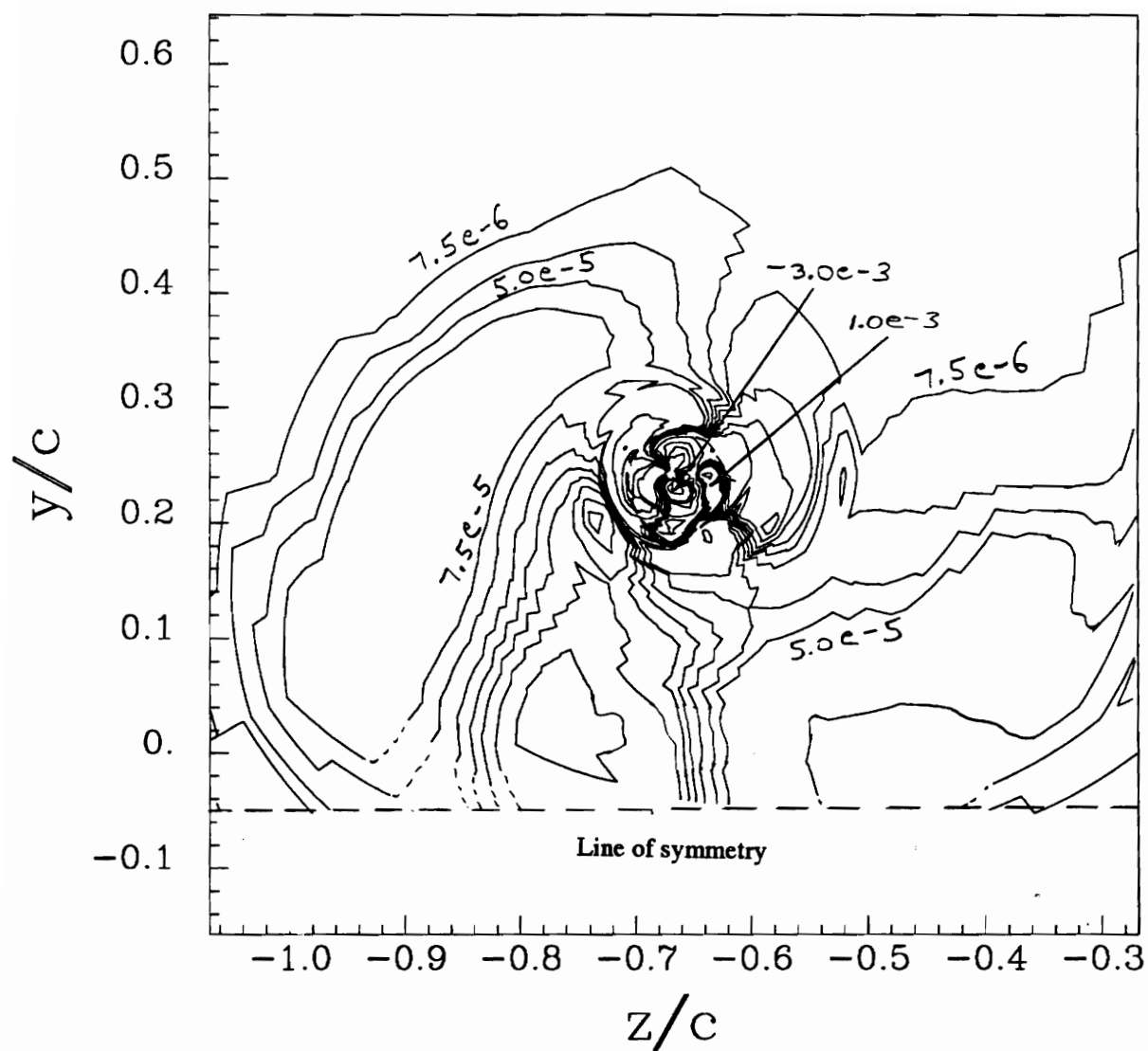


Figure 151. Core region showing contours of $v_{\theta}v_r/U_{ref}^2$ for the upper counter rotating vortex at $x/c=10$, angle of attack= 5° , $Re_c=260,000$. Dotted line indicates core edge.

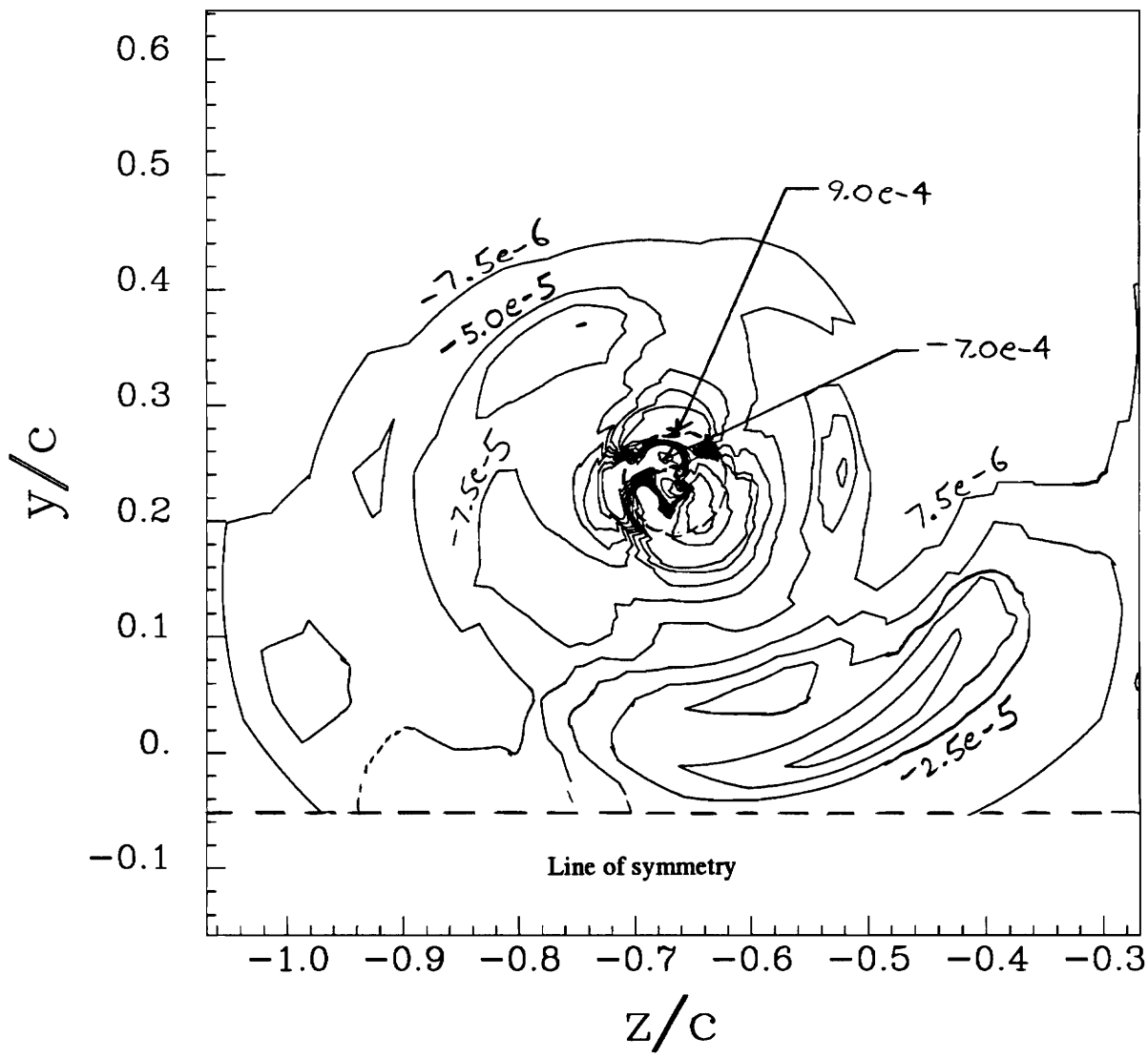


Figure 152. Core region showing contours of $v_x v_r / U_{ref}^2$ for the upper counter rotating vortex at $x/c=10$, angle of attack= 5° , $Re_c=260,000$. Dotted line indicates core edge.

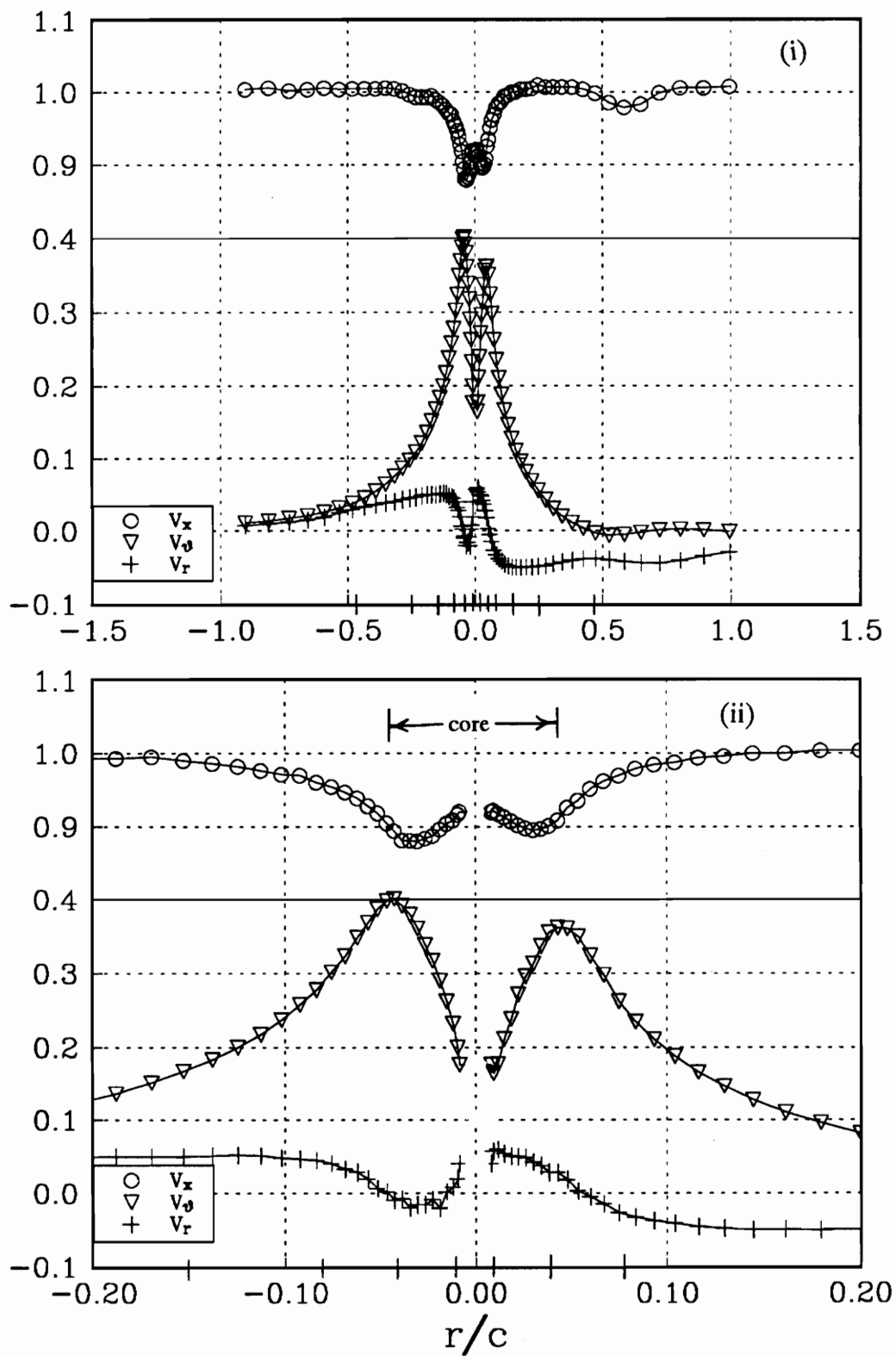


Figure 153a. Profile Ii mean velocities, measured parallel to the line of symmetry for the upper counter rotating vortex at $x/c=10$. (i) wake region, (ii) core region.

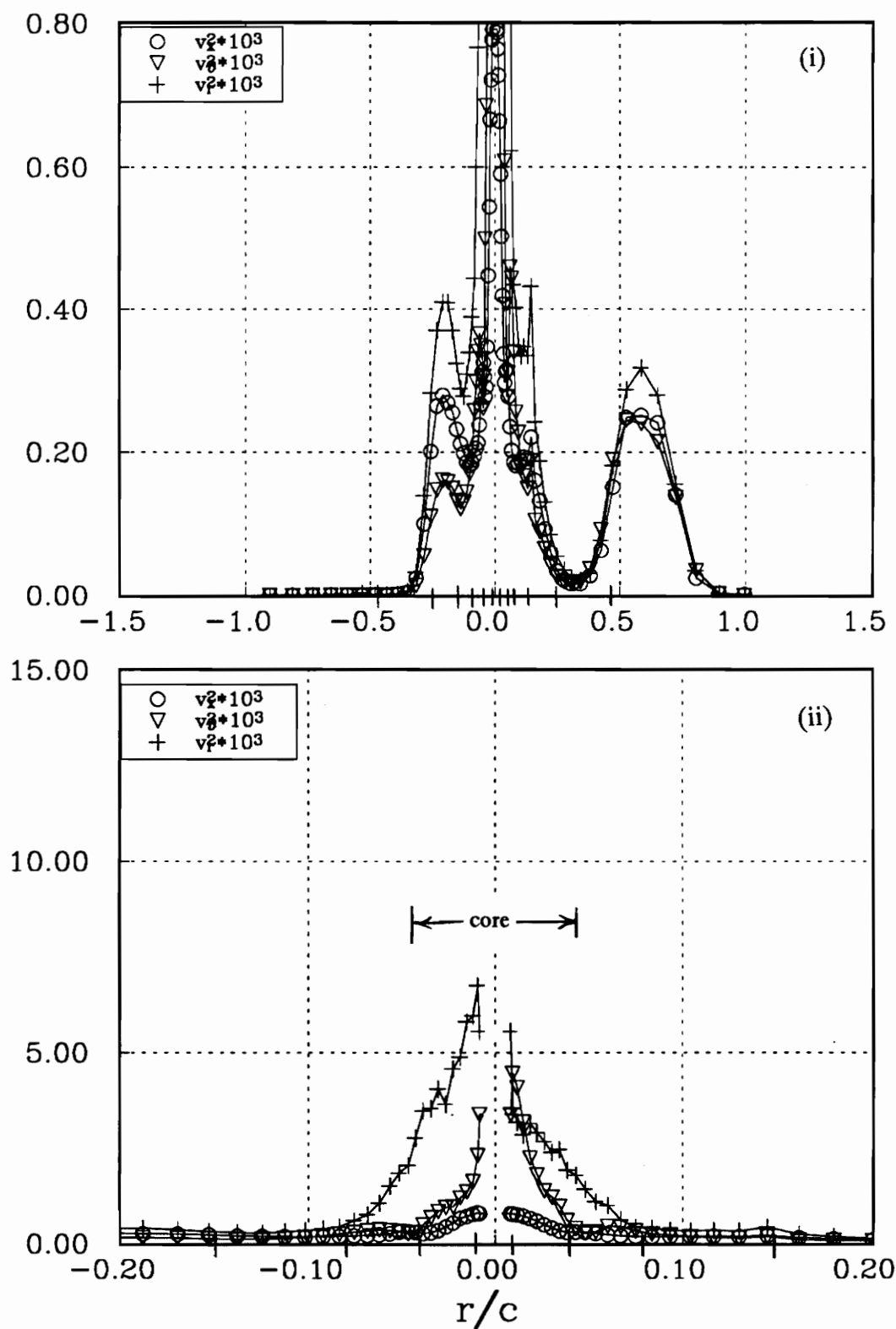


Figure 153b. Profile Ii normal stresses, measured parallel to the line of symmetry for the upper counter rotating vortex at $x/c=10$. (i) wake region, (ii) core region.

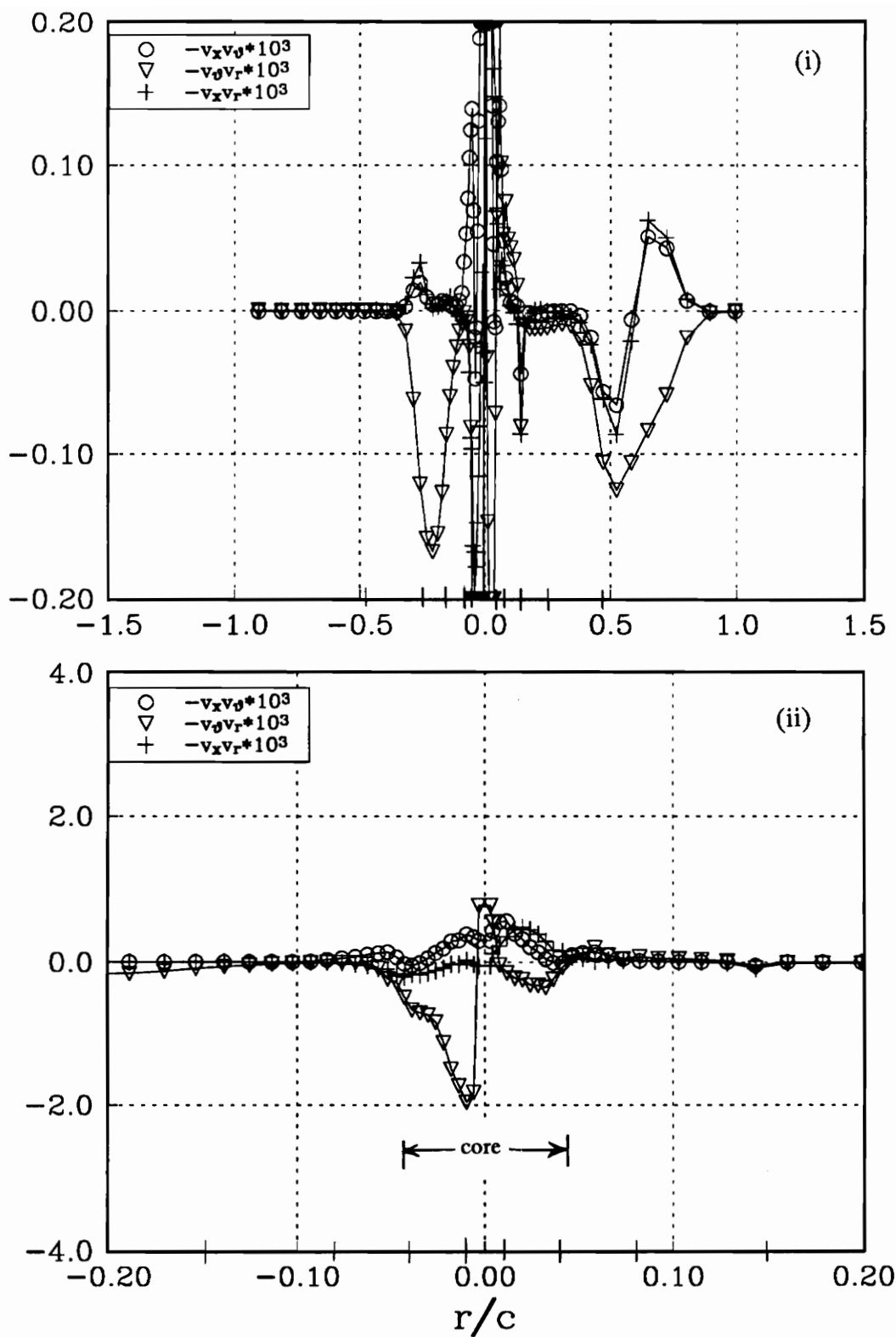


Figure 153c. Profile Ii shear stresses, measured parallel to the line of symmetry for the upper counter rotating vortex at $x/c=10$. (i) wake region, (ii) core region.

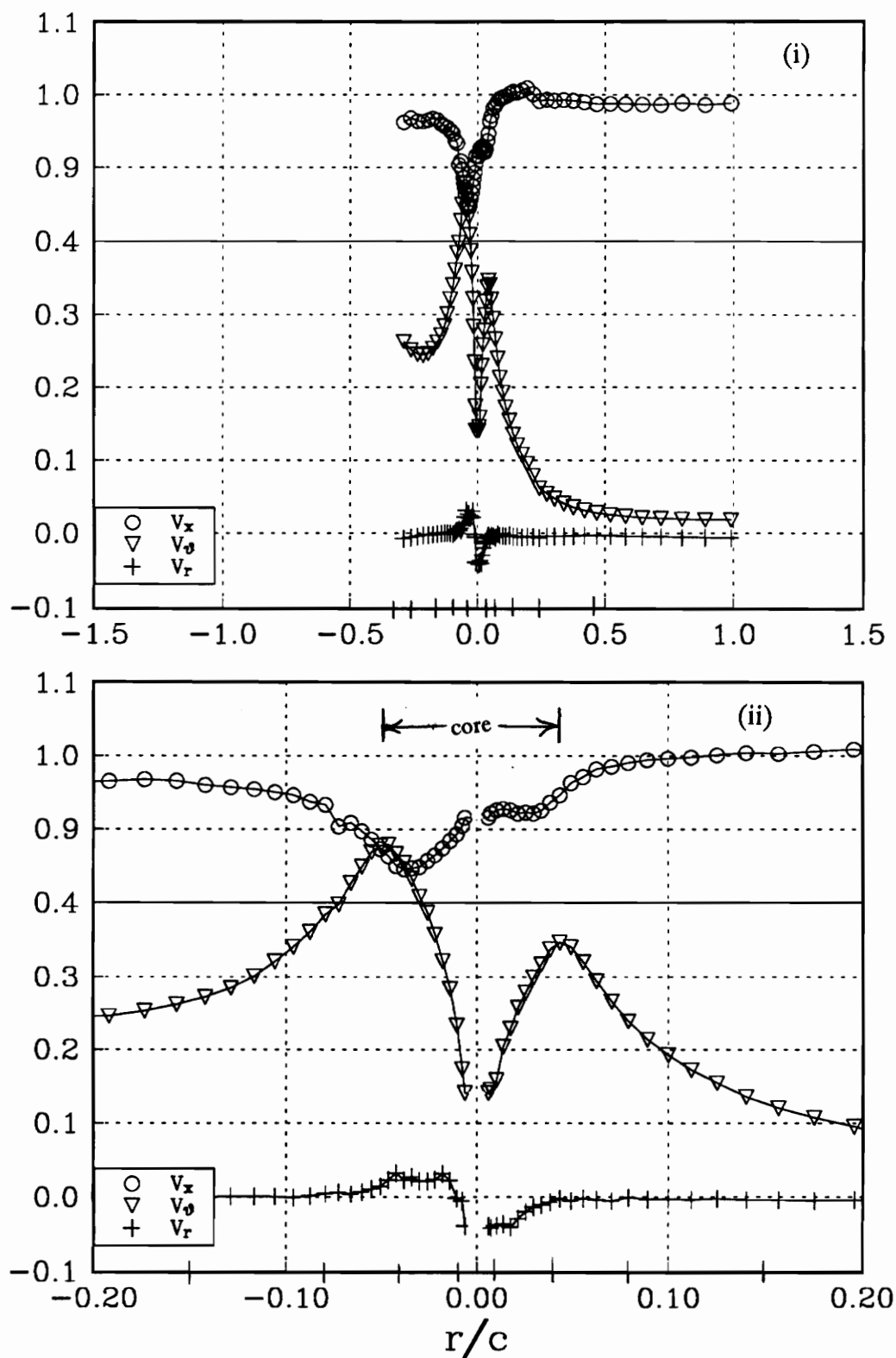


Figure 154a. Profile J mean velocities, measured perpendicular to the line of symmetry for the upper counter rotating vortex at $x/c=10$. (i) wake region, (ii) core region.

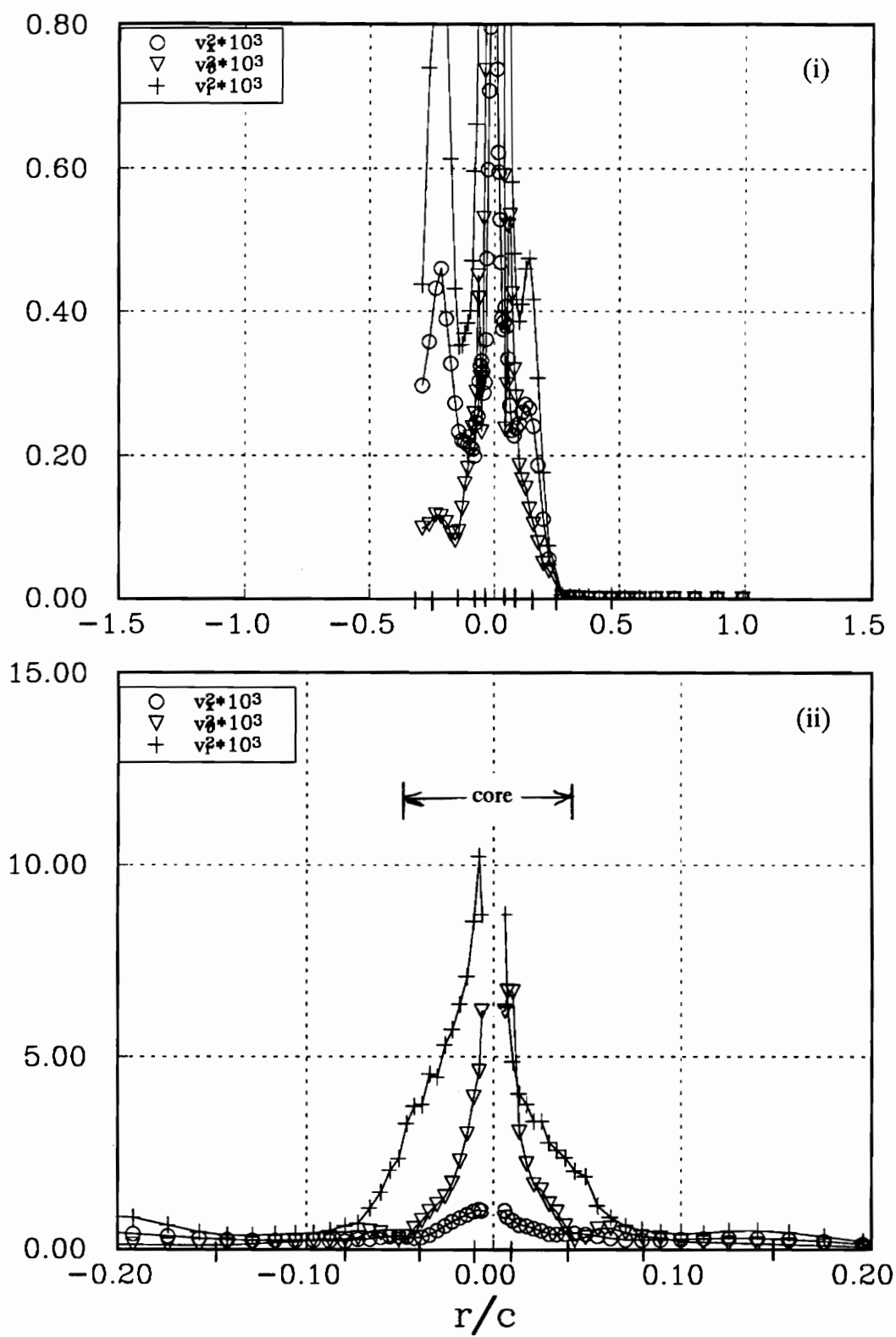


Figure 154b. Profile Jj normal stresses, measured perpendicular to the line of symmetry for the upper counter rotating vortex at $x/c=10$. (i) wake region, (ii) core region.

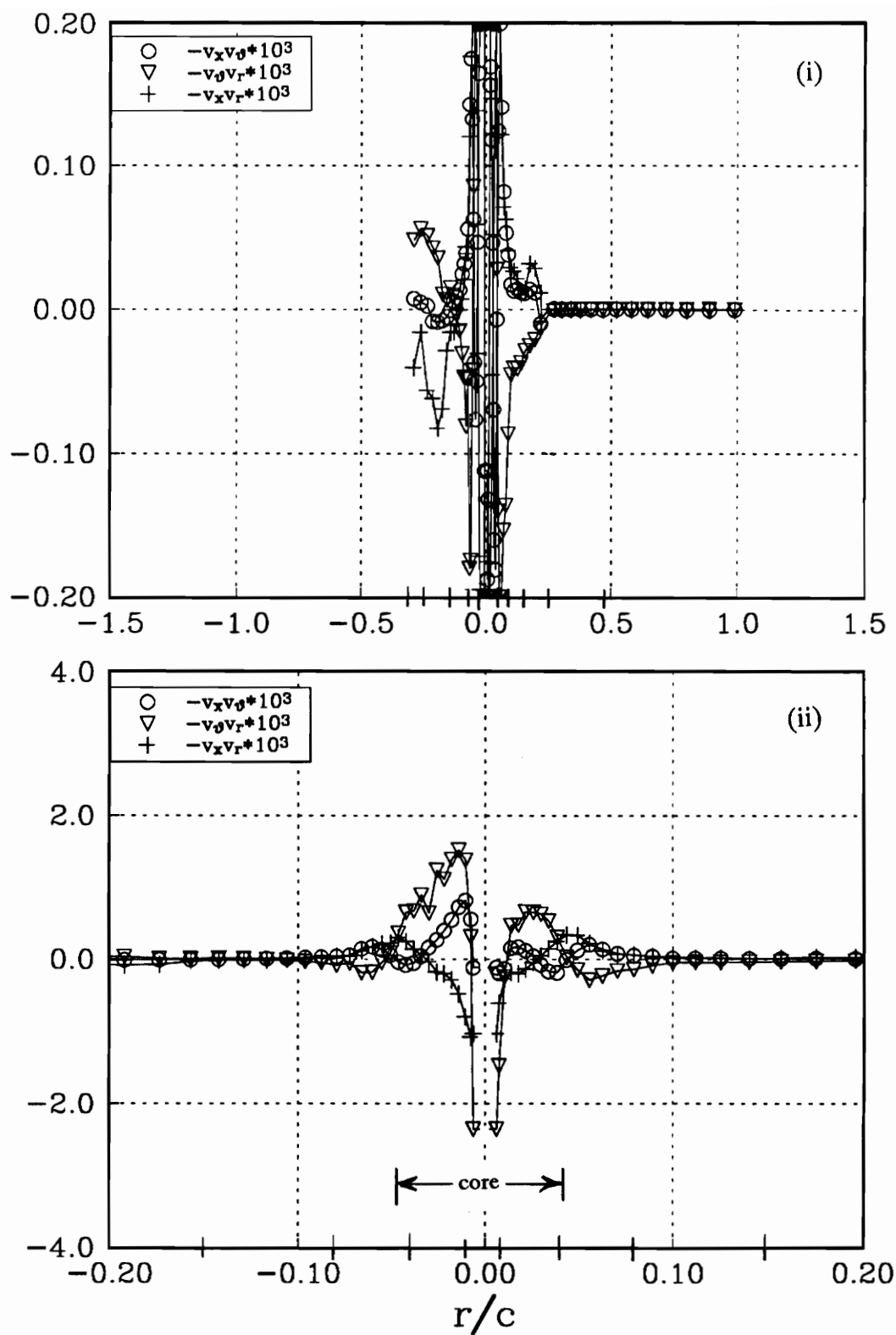


Figure 154c. Profile Jj shear stresses, measured perpendicular to the line of symmetry for the upper counter rotating vortex at $x/c=10$. (i) wake region, (ii) core region.

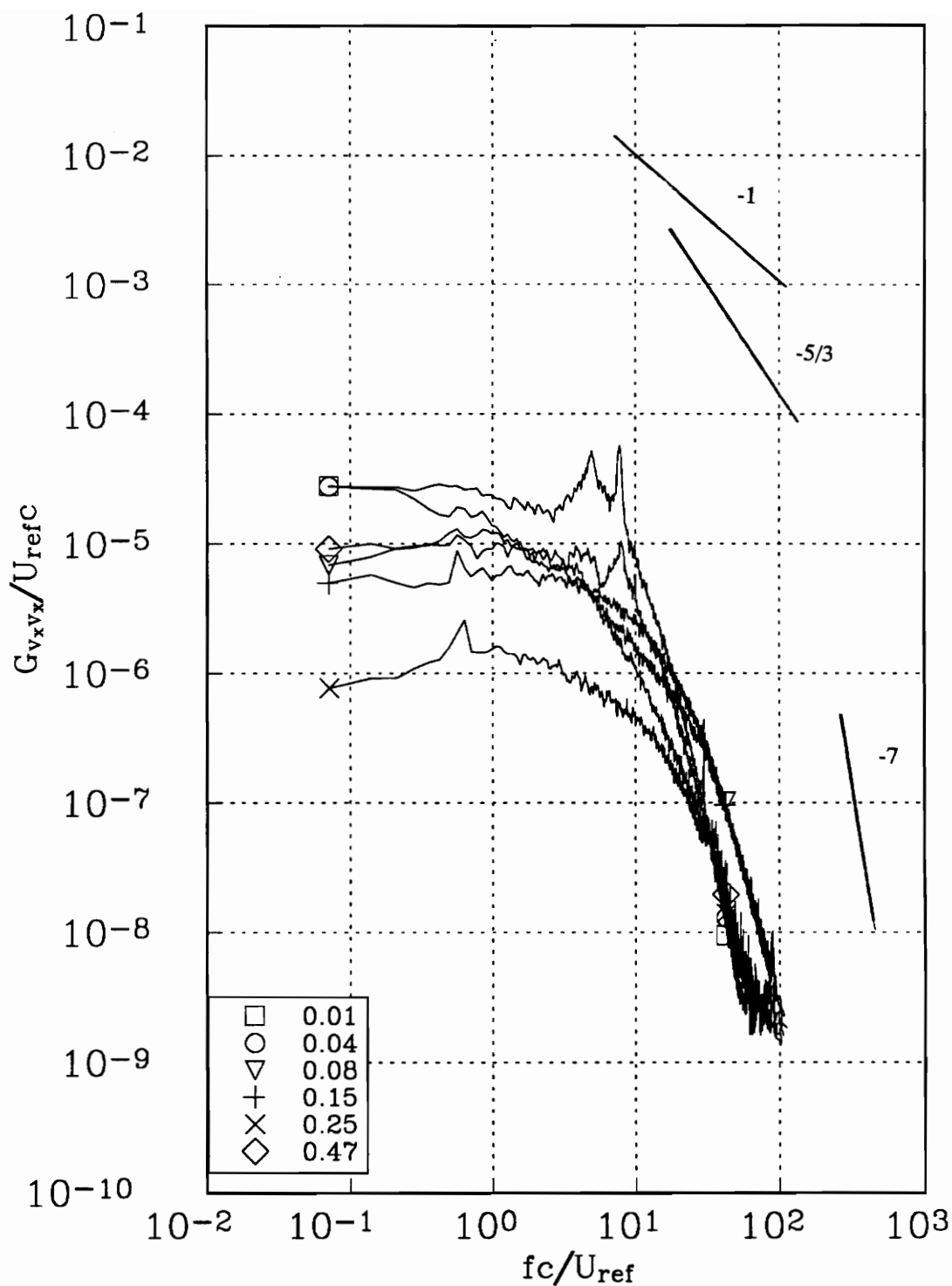


Figure 155a. v_x autospectra measured at representative radial locations along profile II for the upper counter rotating vortex at $x/c=10$. Tic marks in figure 153 indicate measured r/c locations.

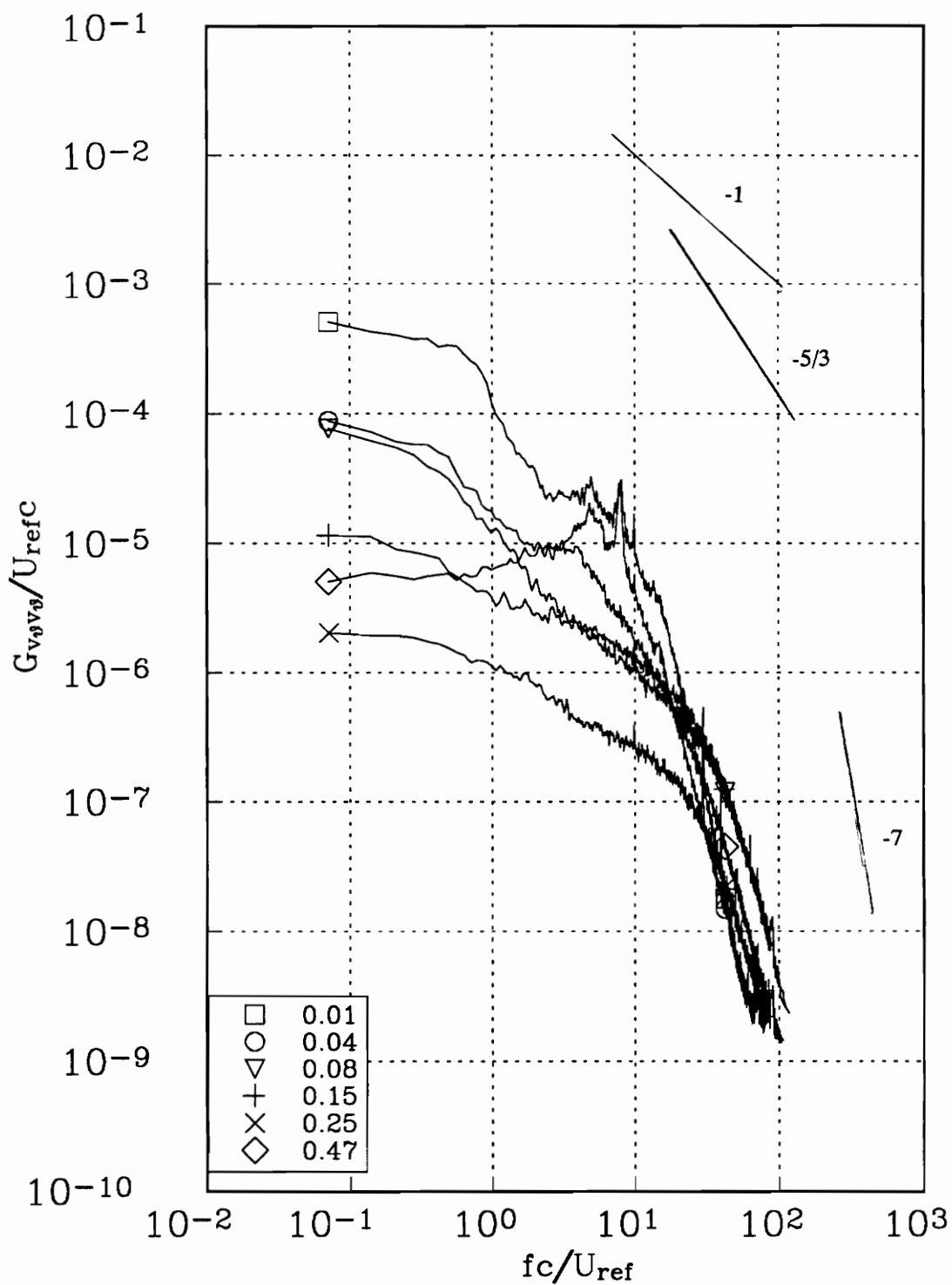


Figure 155b. v_θ autospectra measured at representative radial locations along profile II for the upper counter rotating vortex at $x/c=10$. Tic marks in figure 153 indicate measured r/c locations.

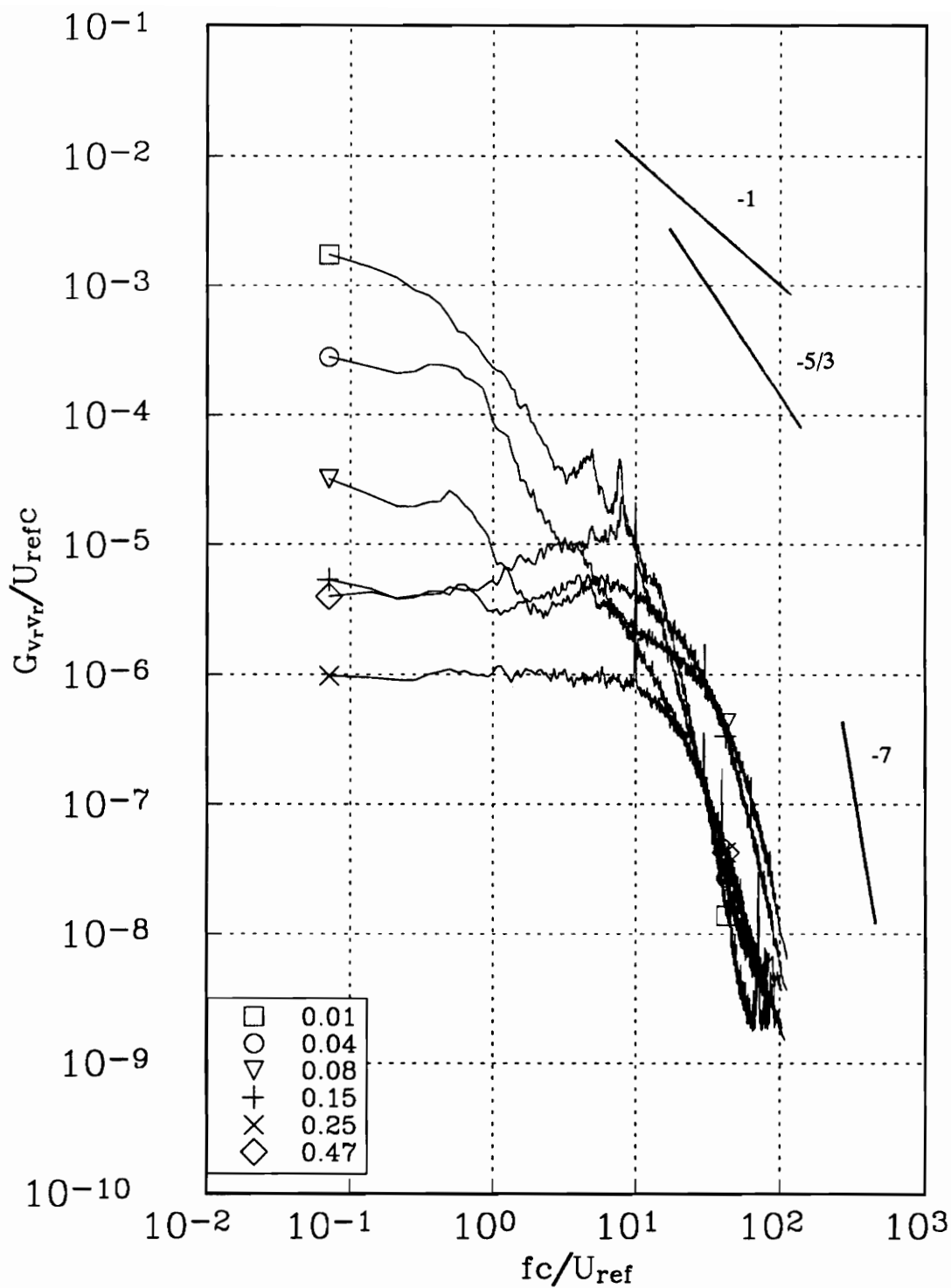


Figure 155c. v_r autospectra measured at representative radial locations along profile II for the upper counter rotating vortex at $x/c=10$. Tic marks in figure 153 indicate measured r/c locations.

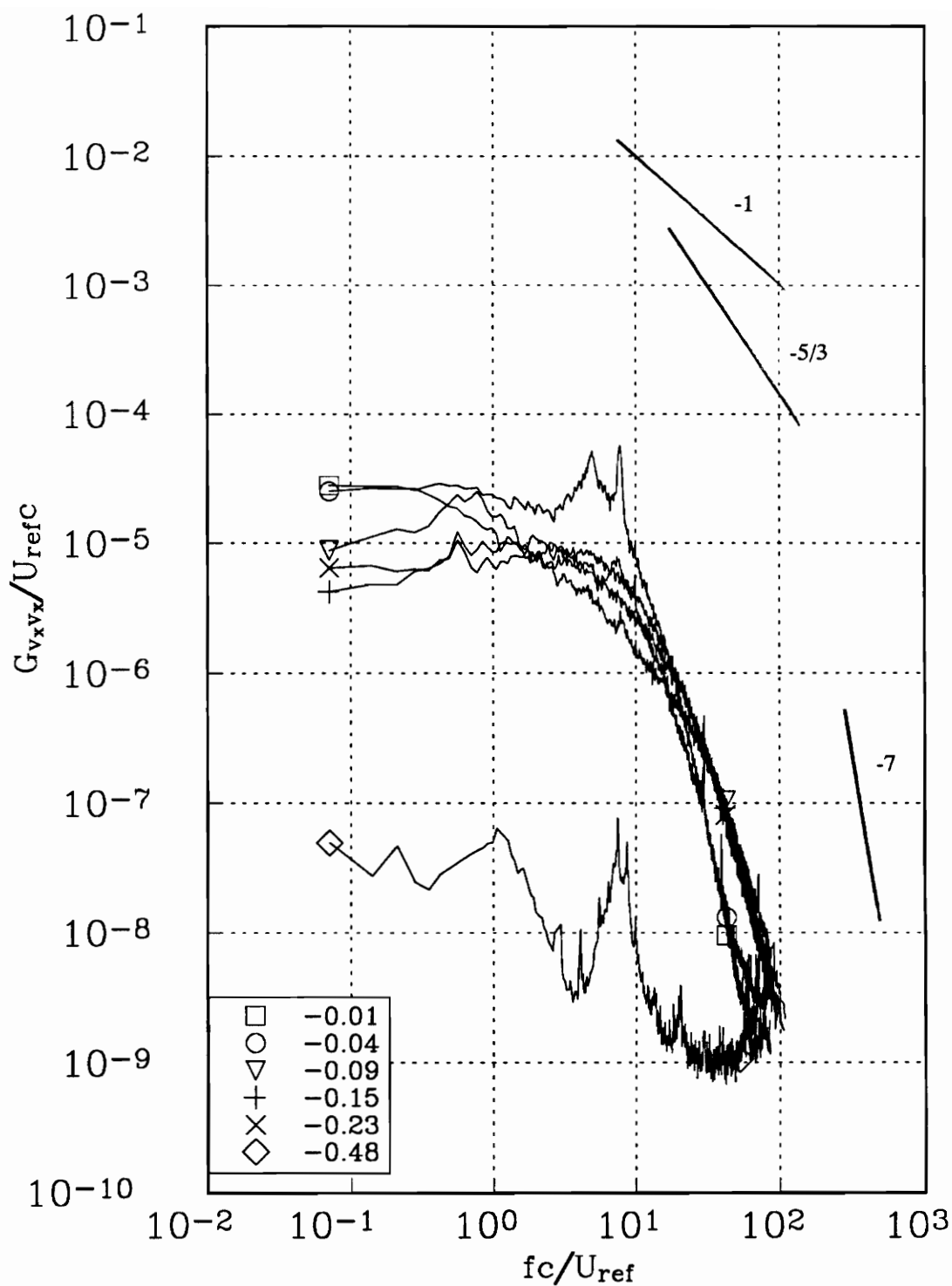


Figure 156a. v_x autospectra measured at representative radial locations along profile Ii for the upper counter rotating vortex at $x/c=10$. Tic marks in figure 153 indicate measured r/c locations.

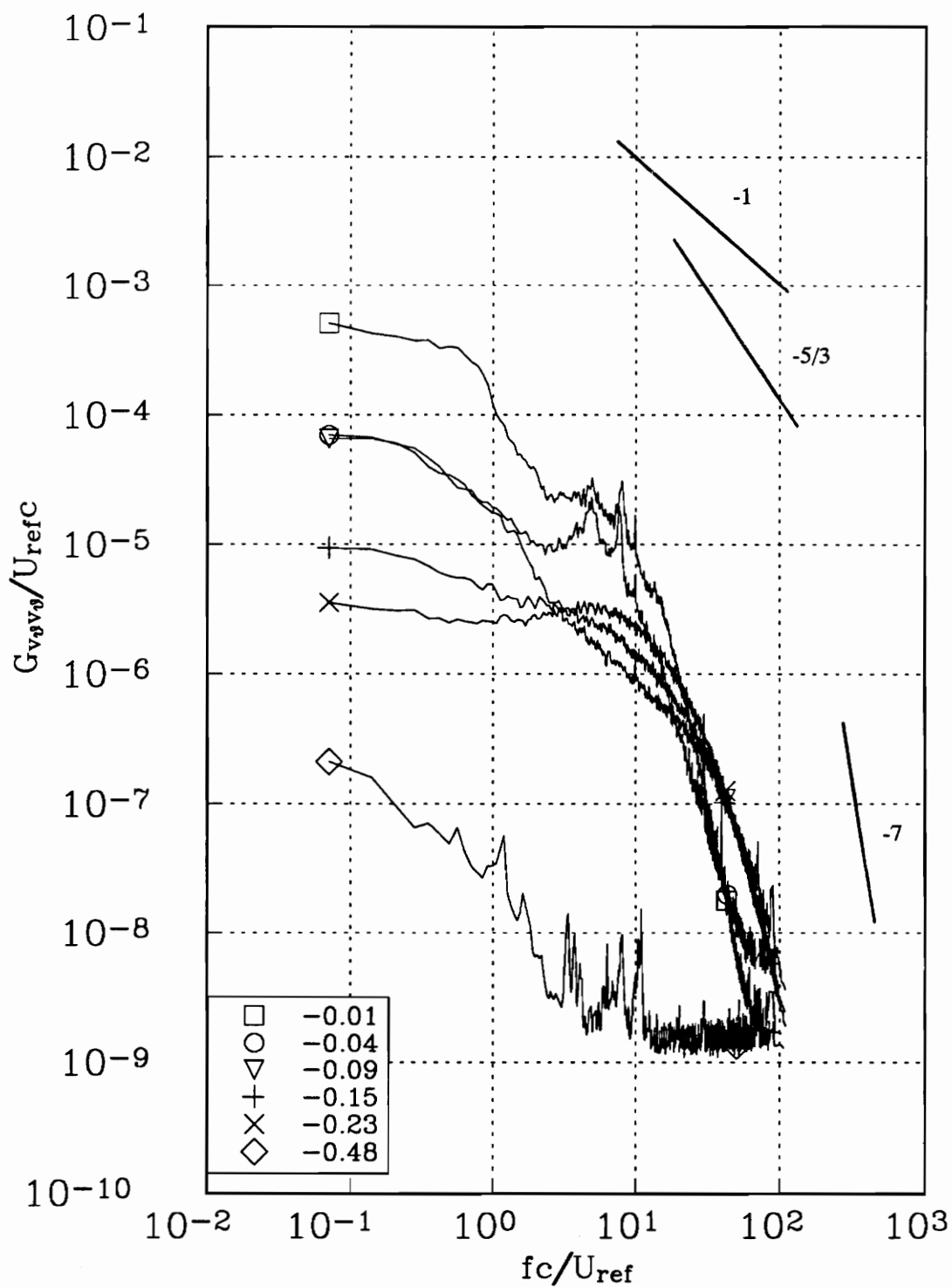


Figure 156b. v_θ autospectra measured at representative radial locations along profile II for the upper counter rotating vortex at $x/c=10$. Tic marks in figure 153 indicate measured r/c locations.

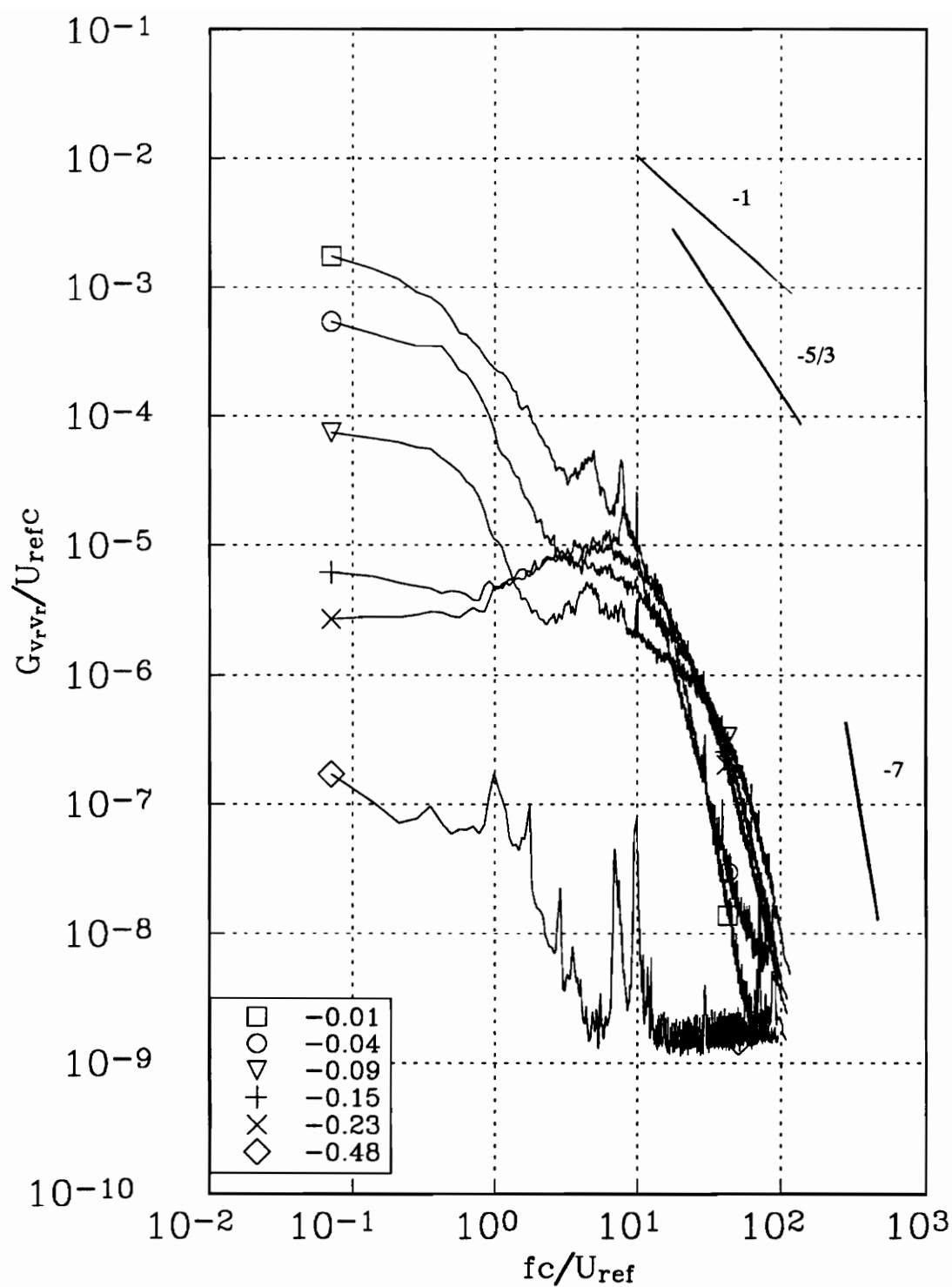


Figure 156c. v_r autospectra measured at representative radial locations along profile II for the upper counter rotating vortex at $x/c=10$. Tic marks in figure 153 indicate measured r/c locations.

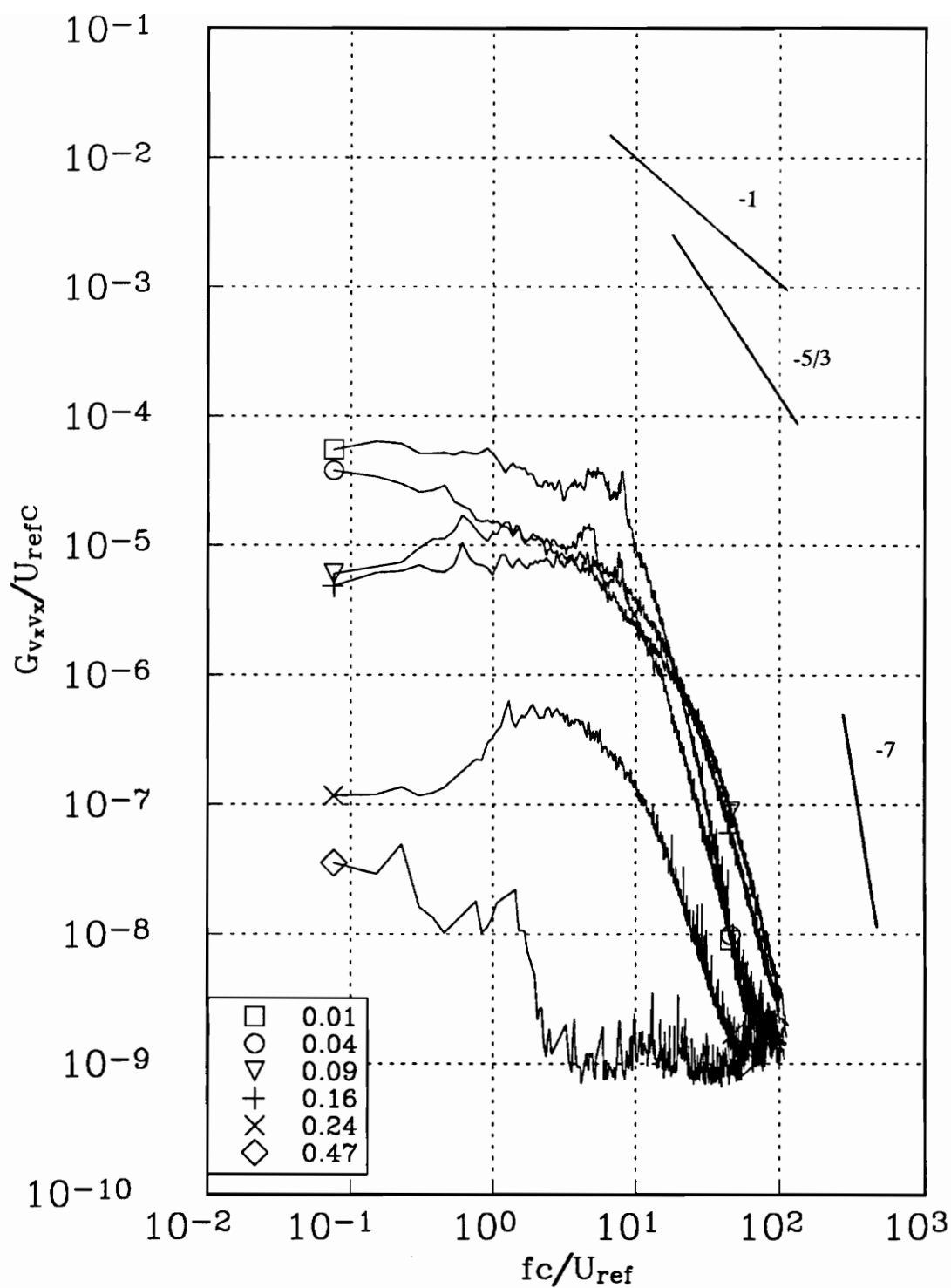


Figure 157a. v_x autospectra measured at representative radial locations along profile Jj for the upper counter rotating vortex at $x/c=10$. Tic marks in figure 154 indicate measured r/c locations.

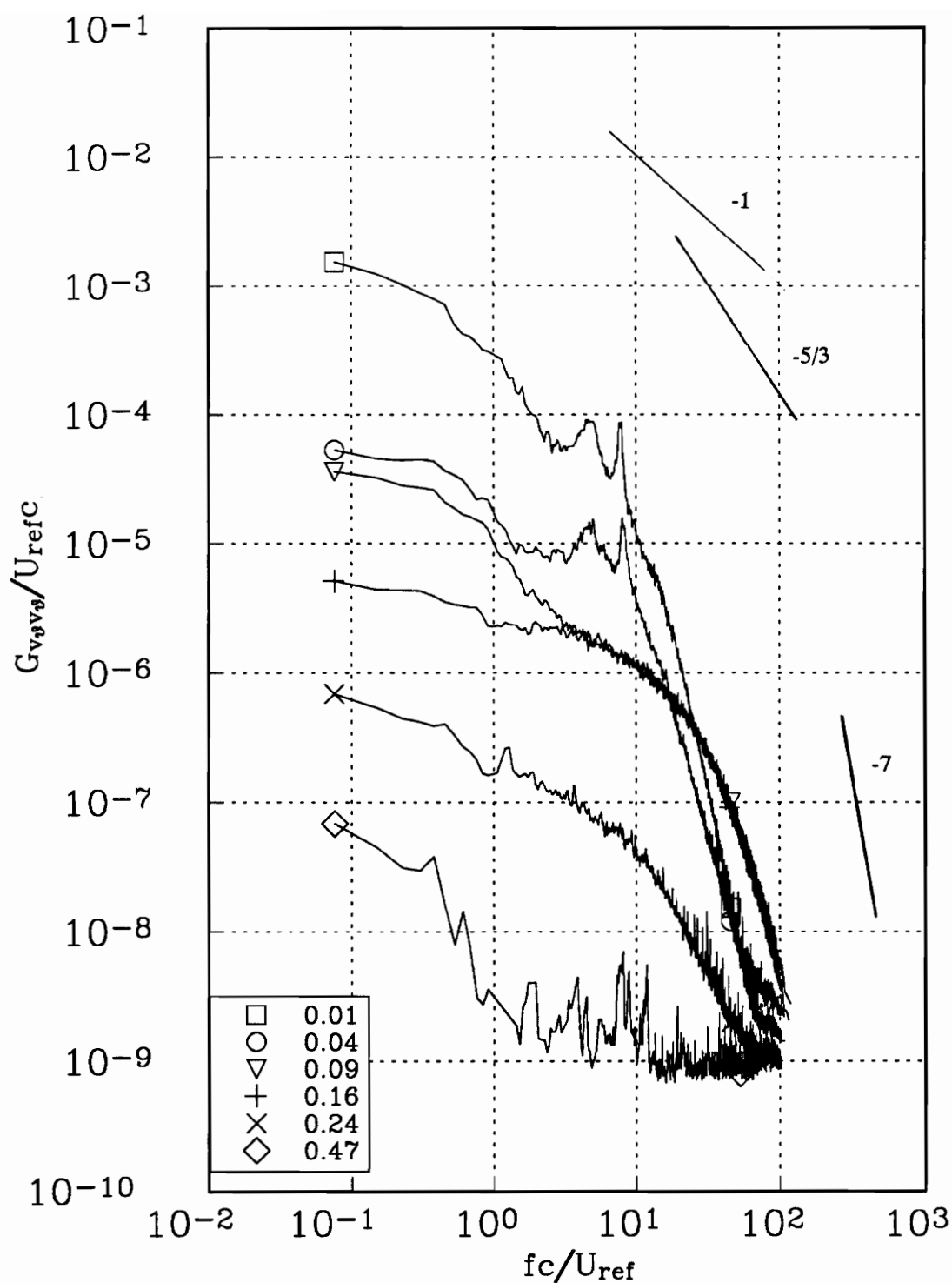


Figure 157b. v_θ autospectra measured at representative radial locations along profile Jj for the upper counter rotating vortex at $x/c=10$. Tic marks in figure 154 indicate measured r/c locations.

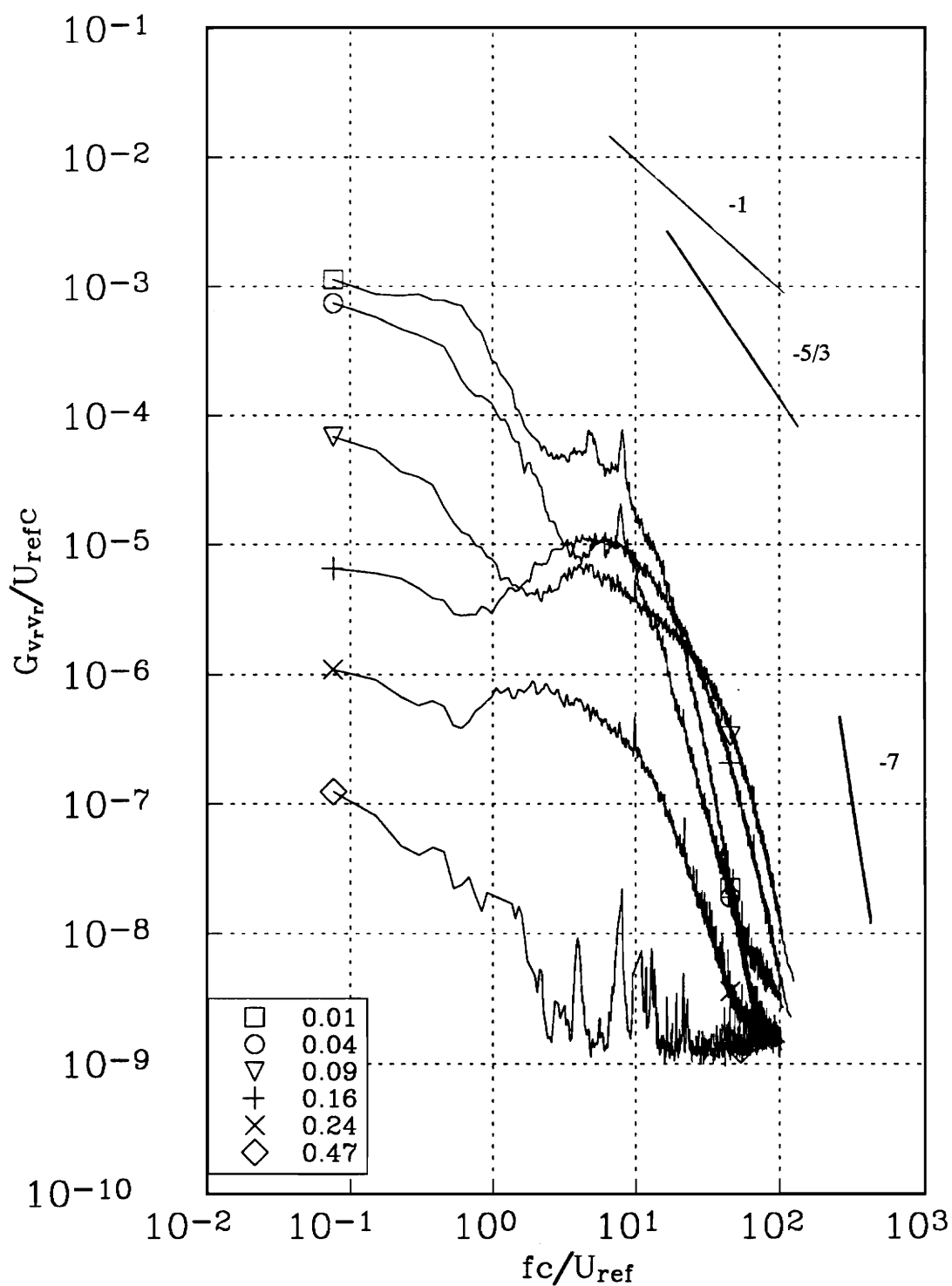


Figure 157c. v_r autospectra measured at representative radial locations along profile Jj for the upper counter rotating vortex at $x/c=10$. Tic marks in figure 154 indicate measured r/c locations.

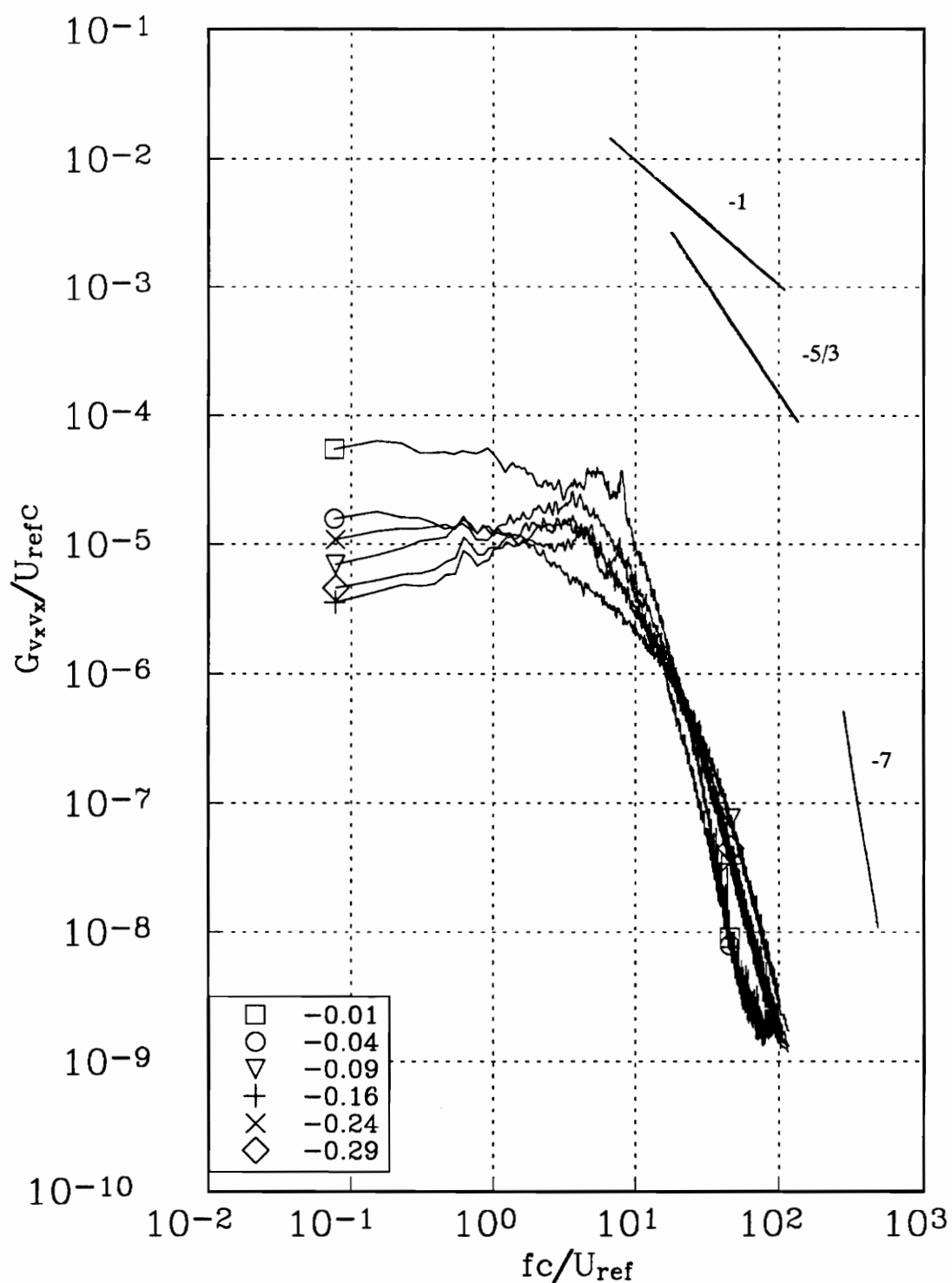


Figure 158a. v_x autospectra measured at representative radial locations along profile Jj for the upper counter rotating vortex at $x/c=10$. Tic marks in figure 154 indicate measured r/c locations.

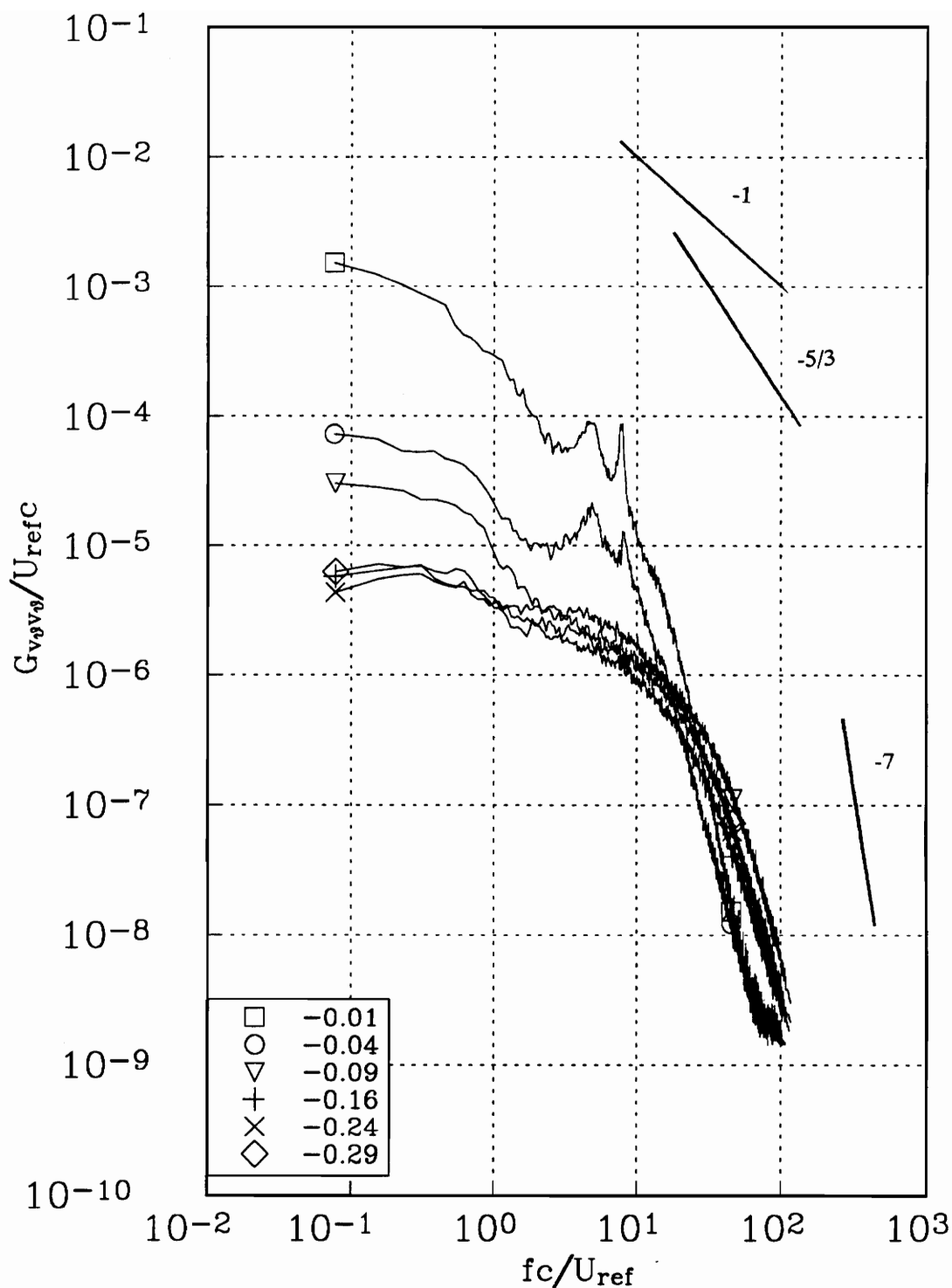


Figure 158b. v_0 autospectra measured at representative radial locations along profile Jj for the upper counter rotating vortex at $x/c=10$. Tic marks in figure 154 indicate measured r/c locations.

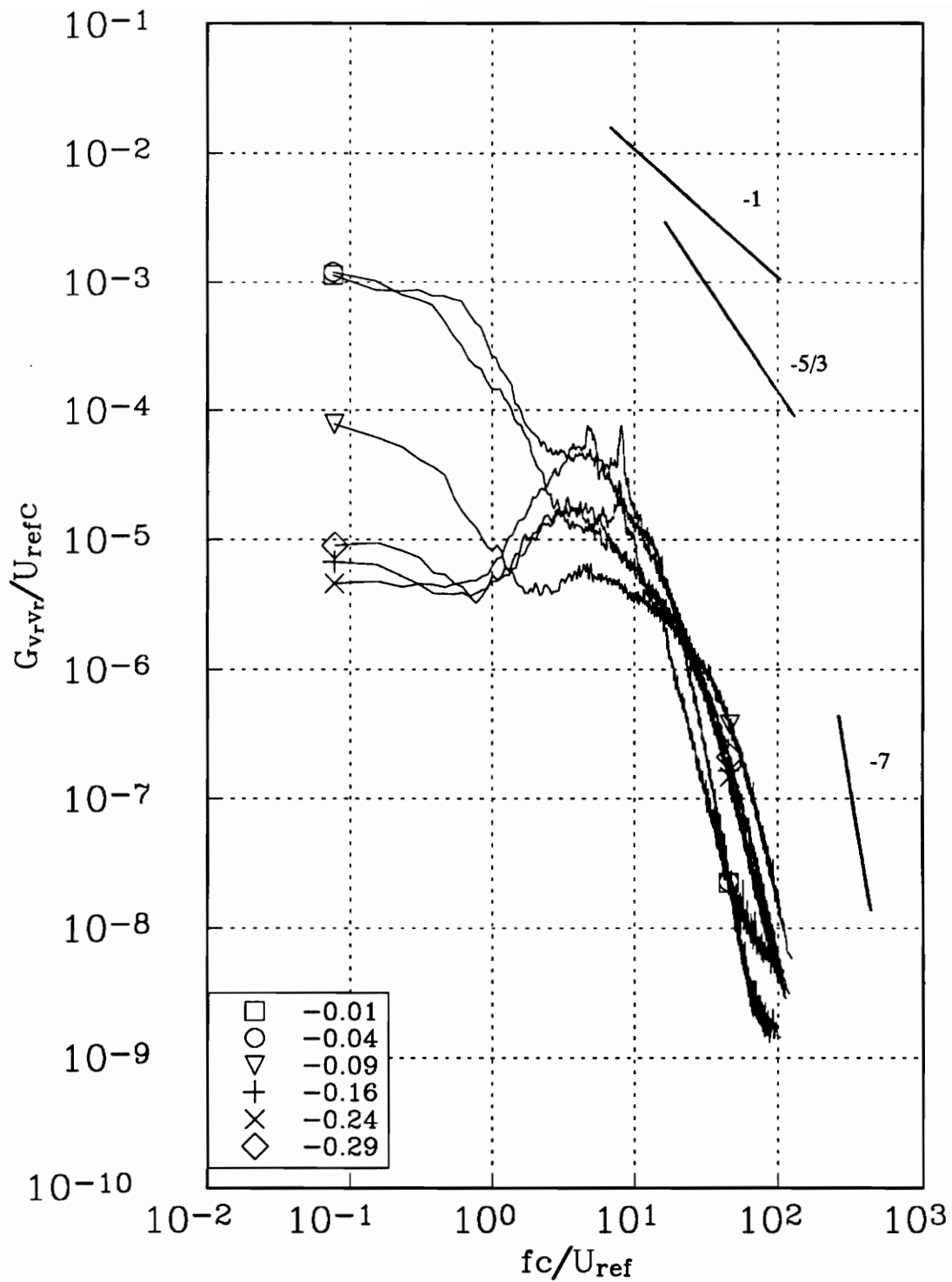


Figure 158c. v_r autospectra measured at representative radial locations along profile Jj for the upper counter rotating vortex at $x/c=10$. Tic marks in figure 154 indicate measured r/c locations.

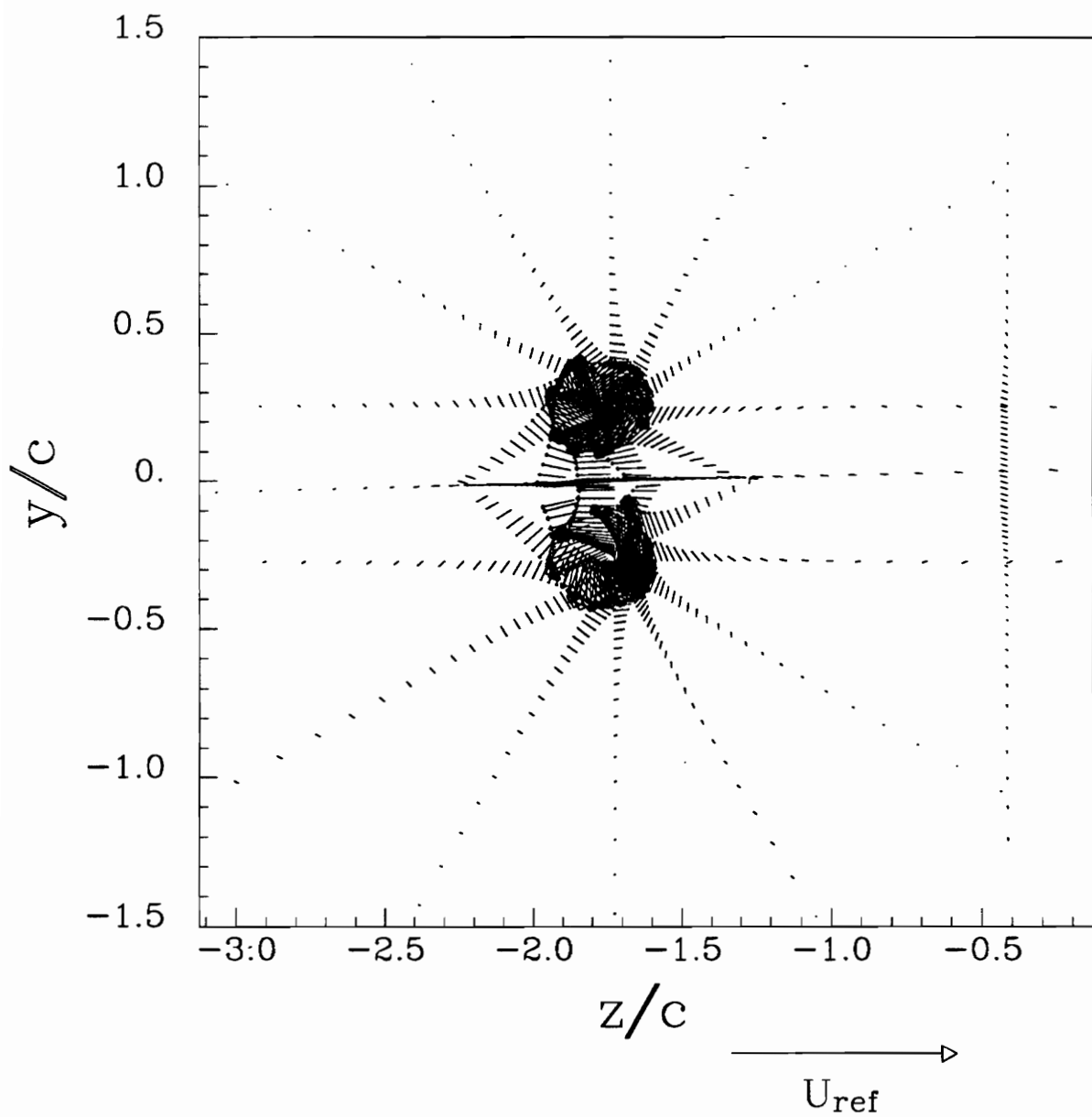
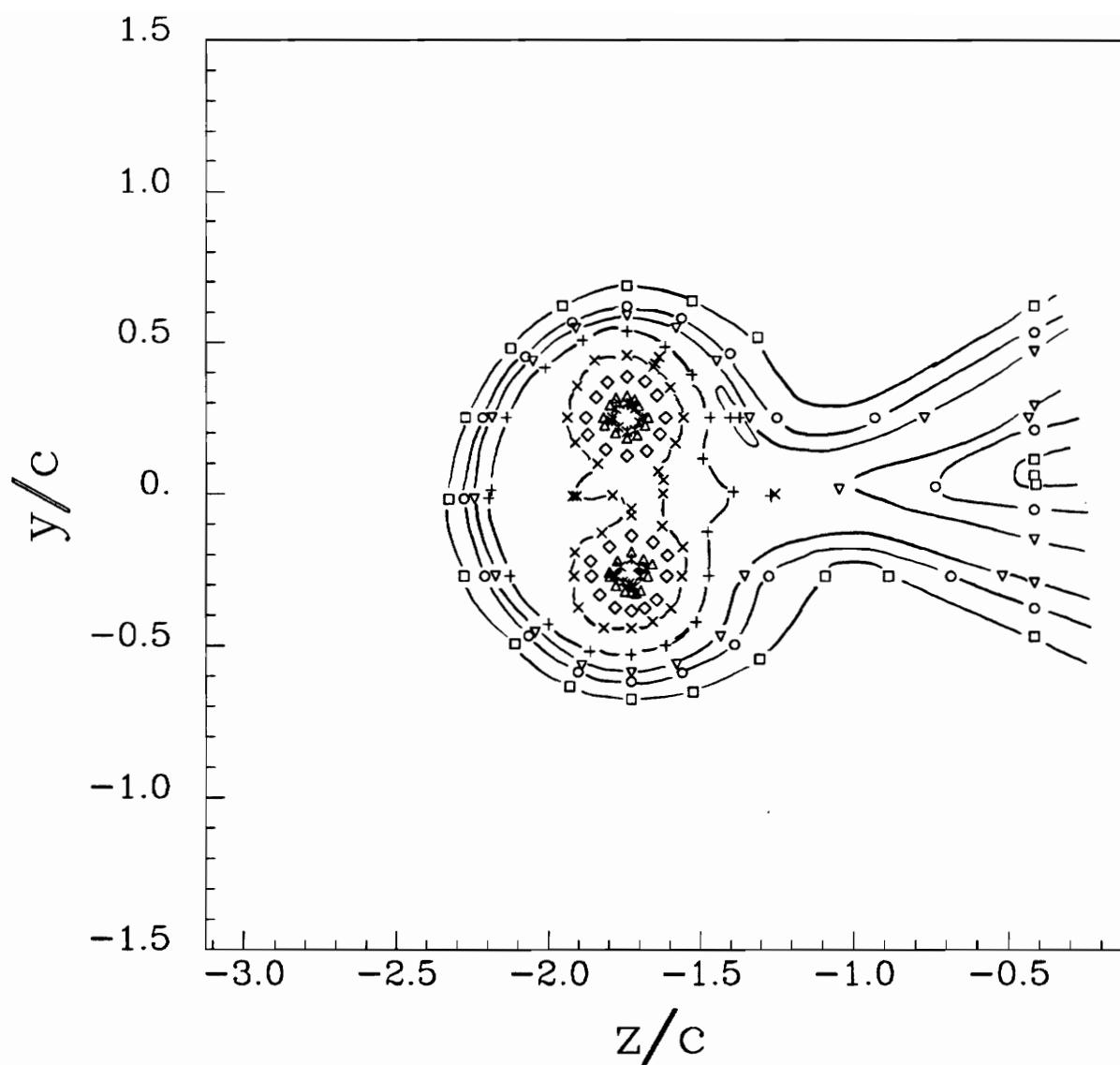
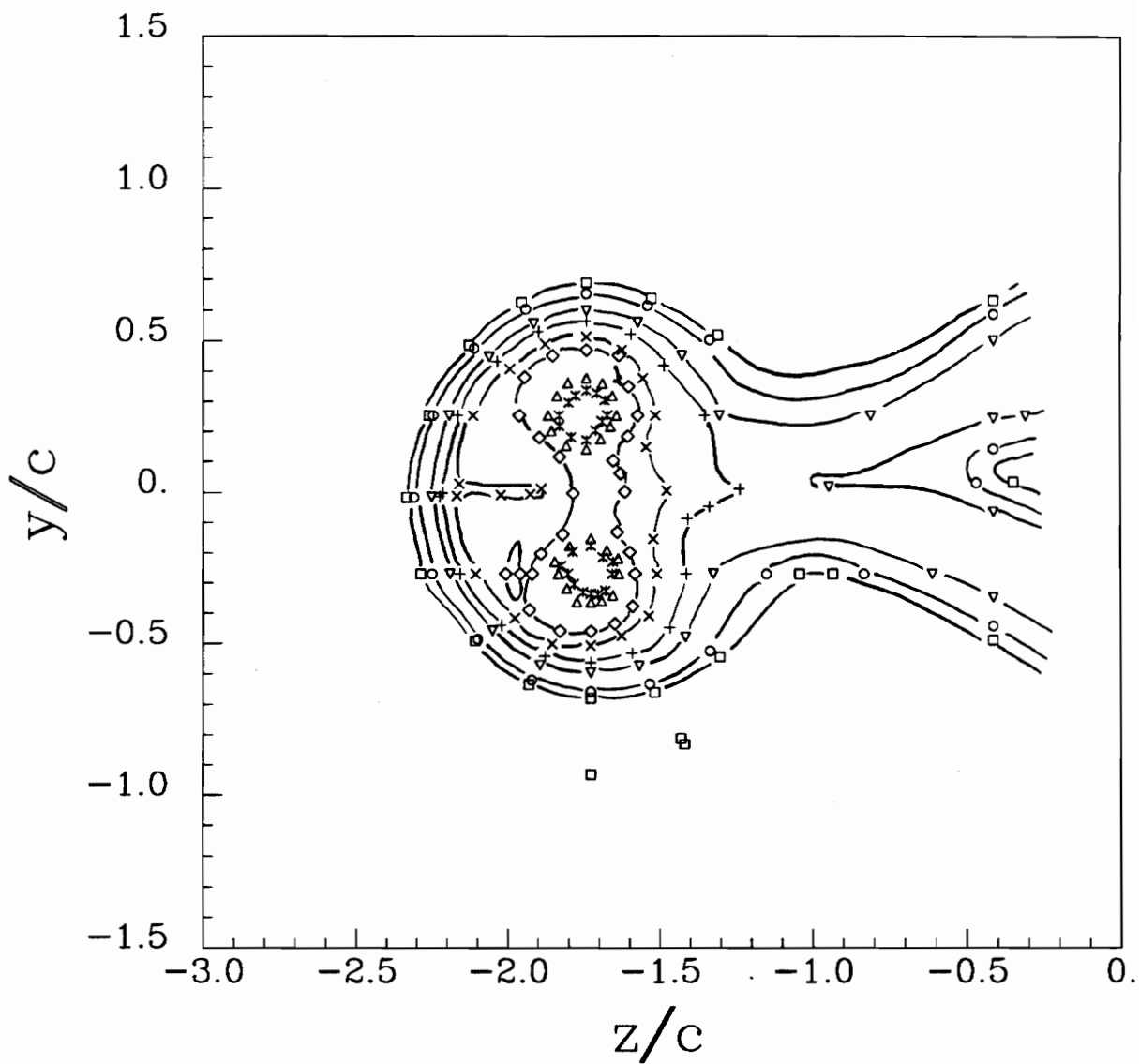


Figure 159. Mean secondary flow vectors of the counter rotating pair at $x/c=30$, angle of attack 5° , $Re_c=260,000$.



□	0.000010
○	0.000050
▽	0.000100
+	0.000250
×	0.000500
◇	0.001000
△	0.005000
*	0.010000

Figure 160. Contours of turbulent kinetic energy k/U_{ref}^2 for the counter rotating pair at $x/c=30$, angle of attack 5° , $Re_c=260,000$.



□	0.000005
○	0.000010
▽	0.000050
+	0.000100
×	0.000200
◇	0.000300
△	0.000500
*	0.001000

Figure 161. Contours of v_x^2/U_{ref}^2 for the counter rotating pair at $x/c=30$, angle of attack 5° , $Re_c=260,000$.

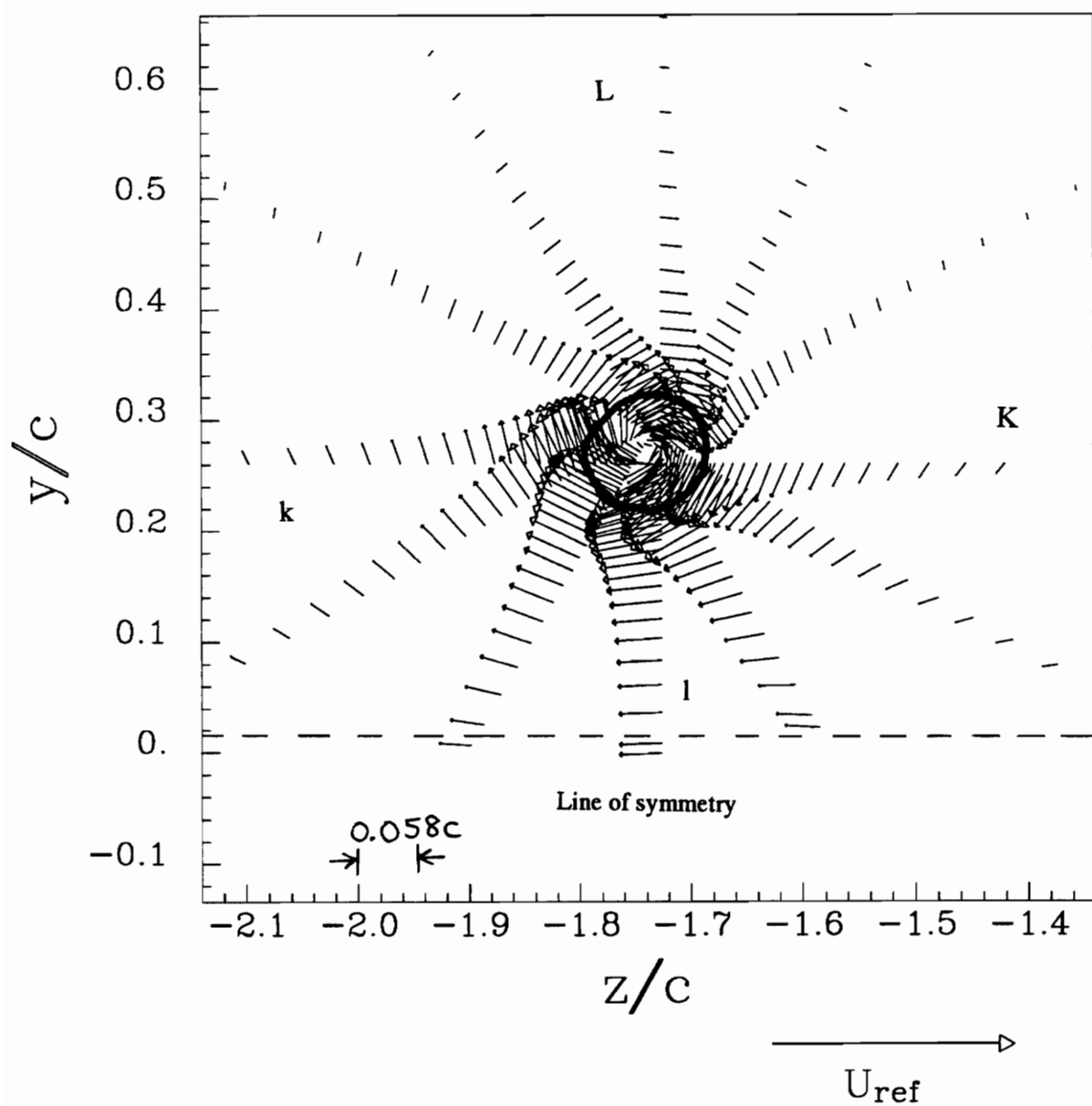


Figure 162. Core region showing mean secondary flows vectors for the upper counter rotating vortex at $x/c=30$, angle of attack= 5° , $Re_c=260,000$. Dotted line indicates core edge.

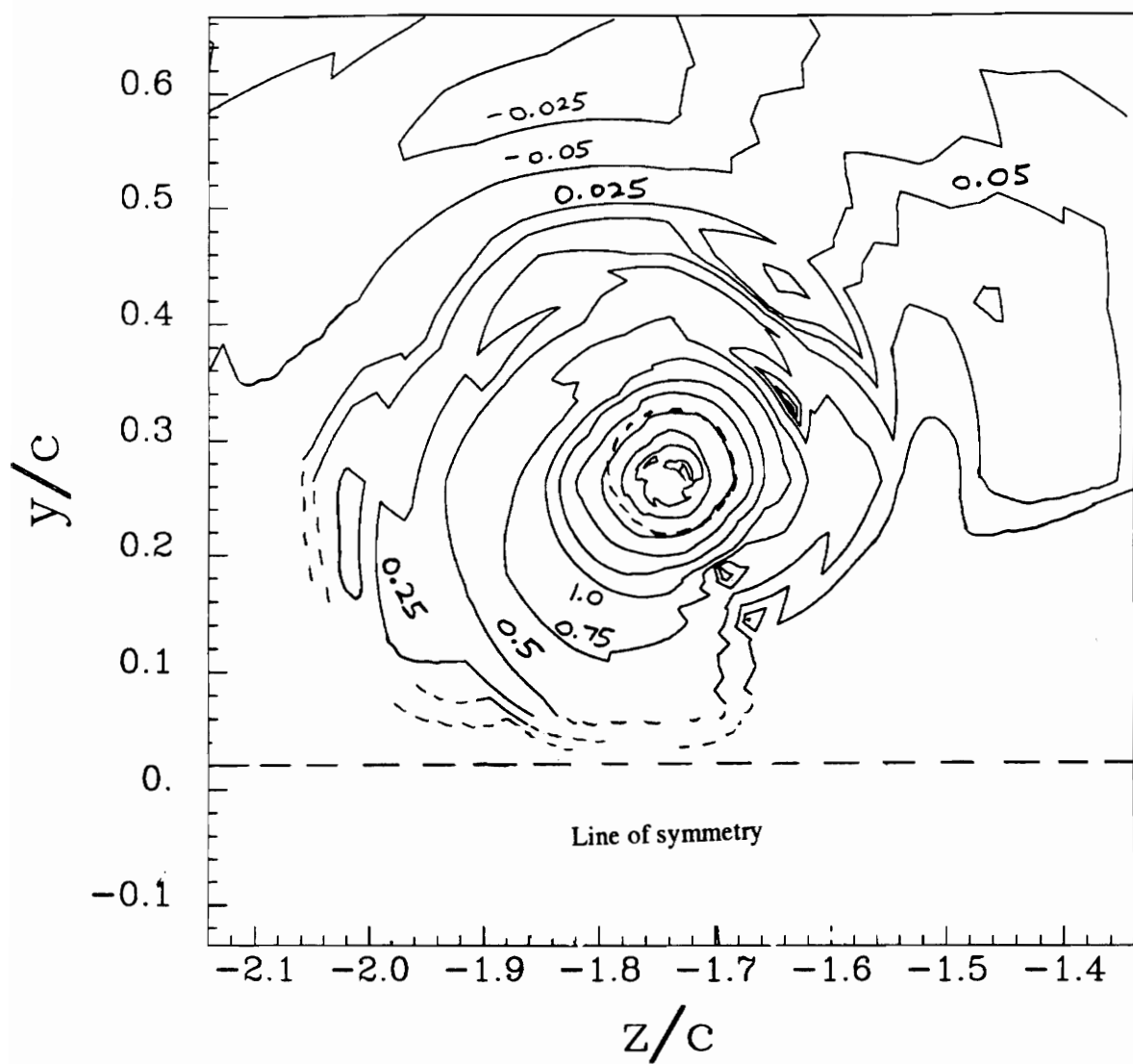


Figure 163. Core region showing contours of vorticity $\omega c/U_{ref}$ for the upper counter rotating vortex at $x/c=30$, angle of attack $=5^\circ$, $Re_c=260,000$. Dotted line indicates core edge.

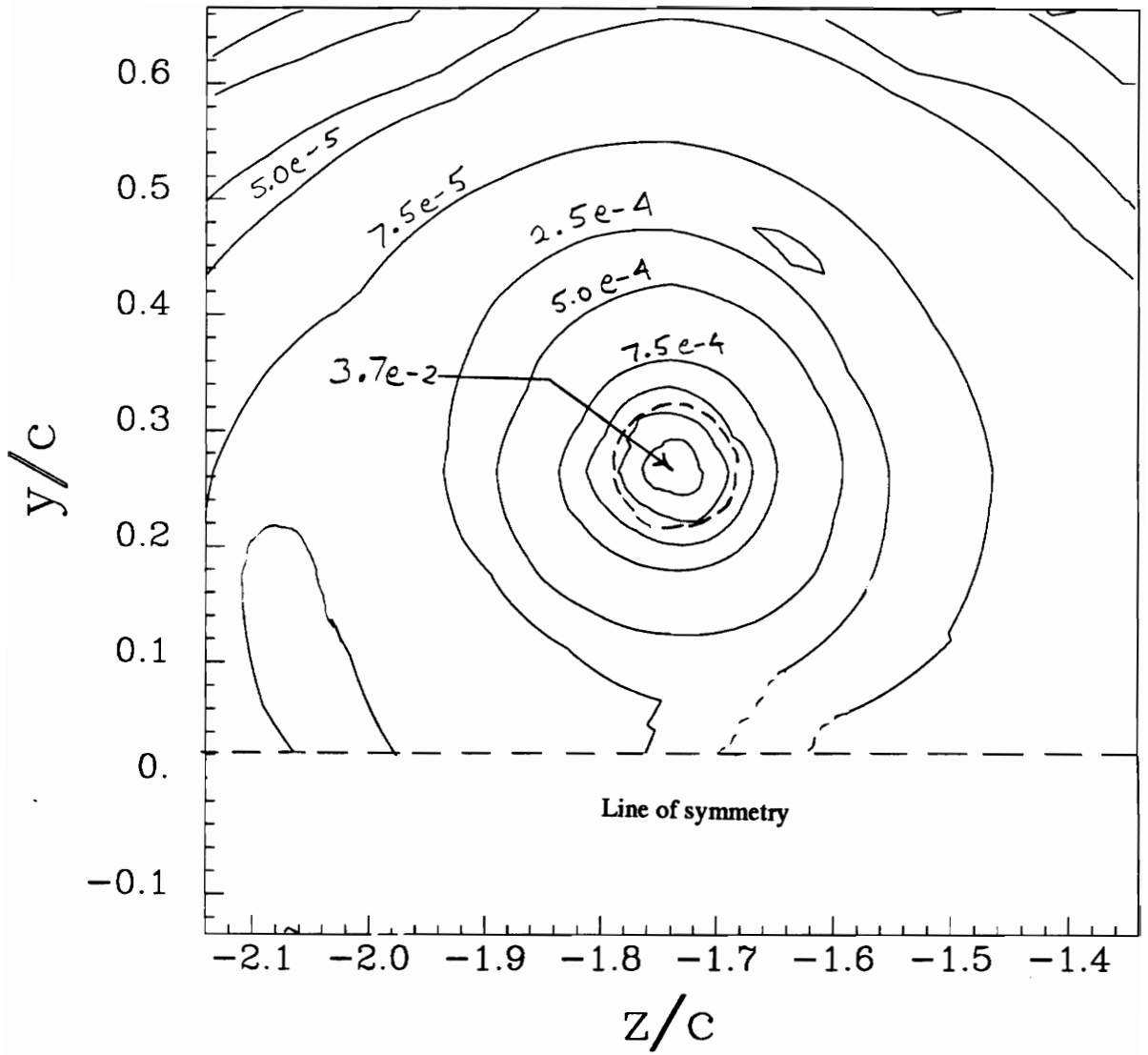


Figure 164. Core region showing contours of turbulent kinetic energy k/U_{ref}^2 for the upper counter rotating vortex at $x/c=30$, angle of attack= 5° , $Re_c=260,000$. Dotted line indicates core edge.

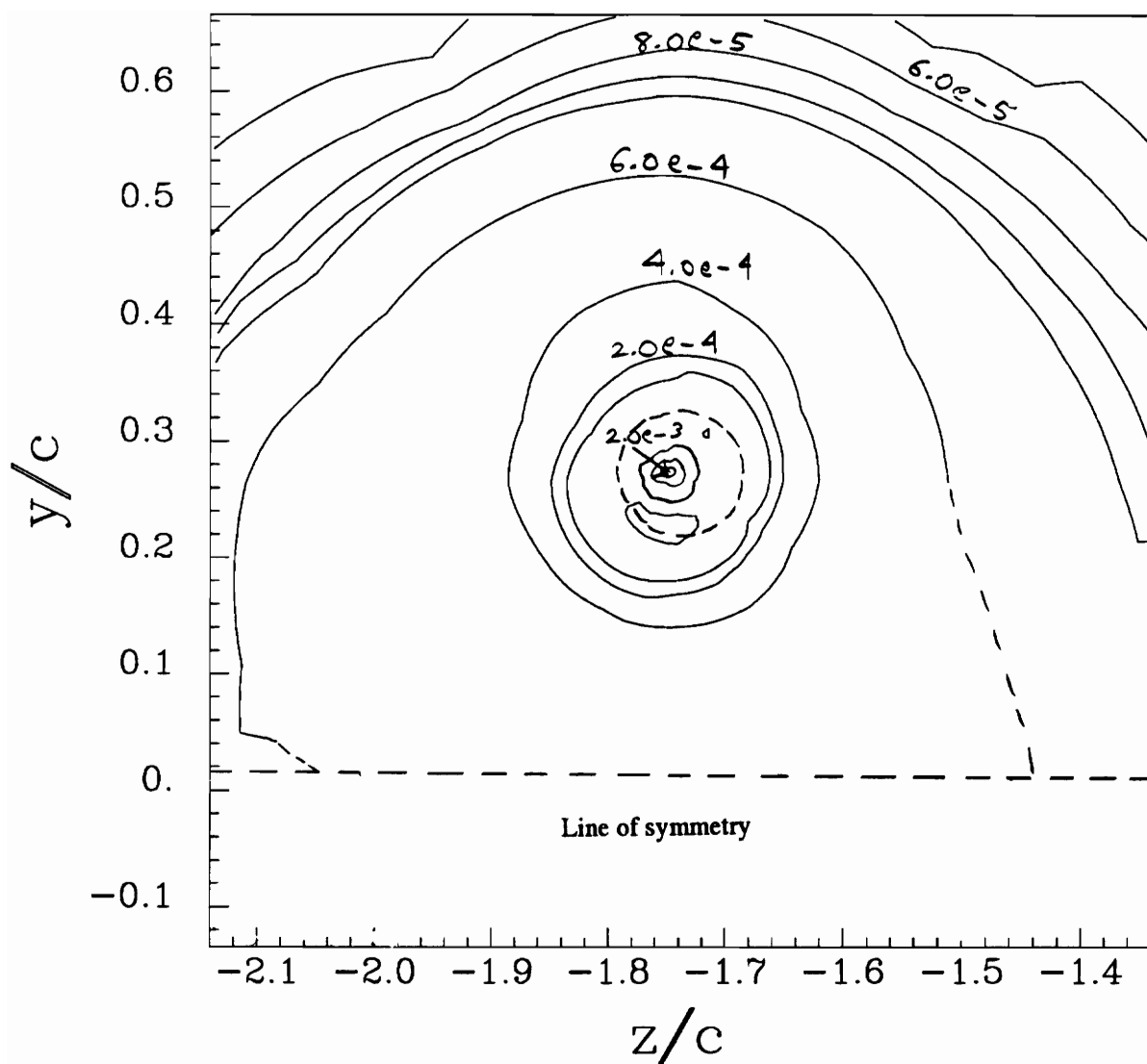


Figure 165. Core region showing contours of v_x^2/U_{ref}^2 for the upper counter rotating vortex at $x/c=30$, angle of attack= 5° , $Re_c=260,000$. Dotted line indicates core edge.

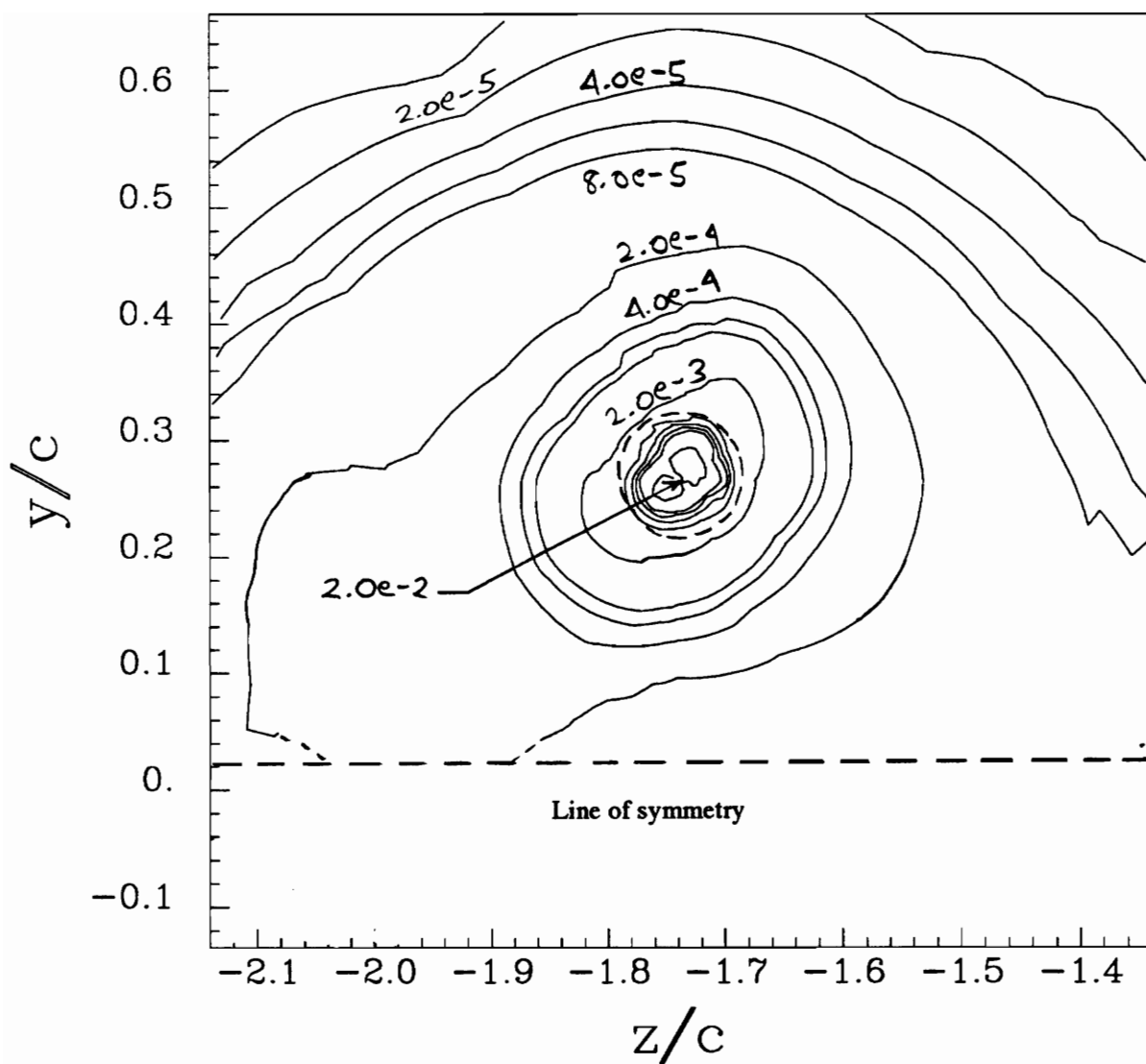


Figure 166. Core region showing contours of v_θ^2/U_{ref}^2 for the upper counter rotating vortex at $x/c=30$, angle of attack= 5° , $Re_c=260,000$. Dotted line indicates core edge.

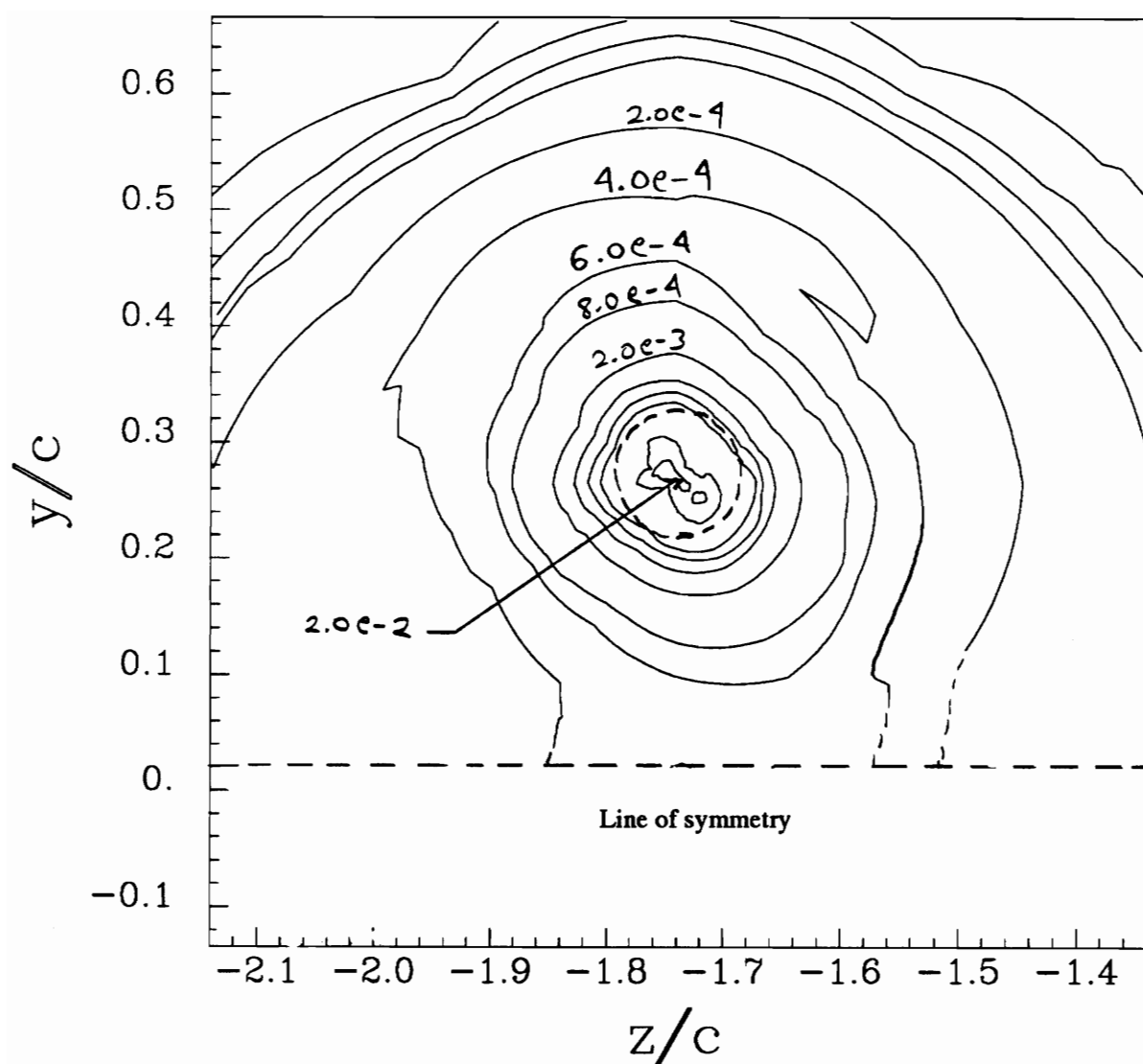


Figure 167. Core region showing contours of v_r^2/U_{ref}^2 for the upper counter rotating vortex at $x/c=30$, angle of attack= 5° , $Re_c=260,000$. Dotted line indicates core edge.

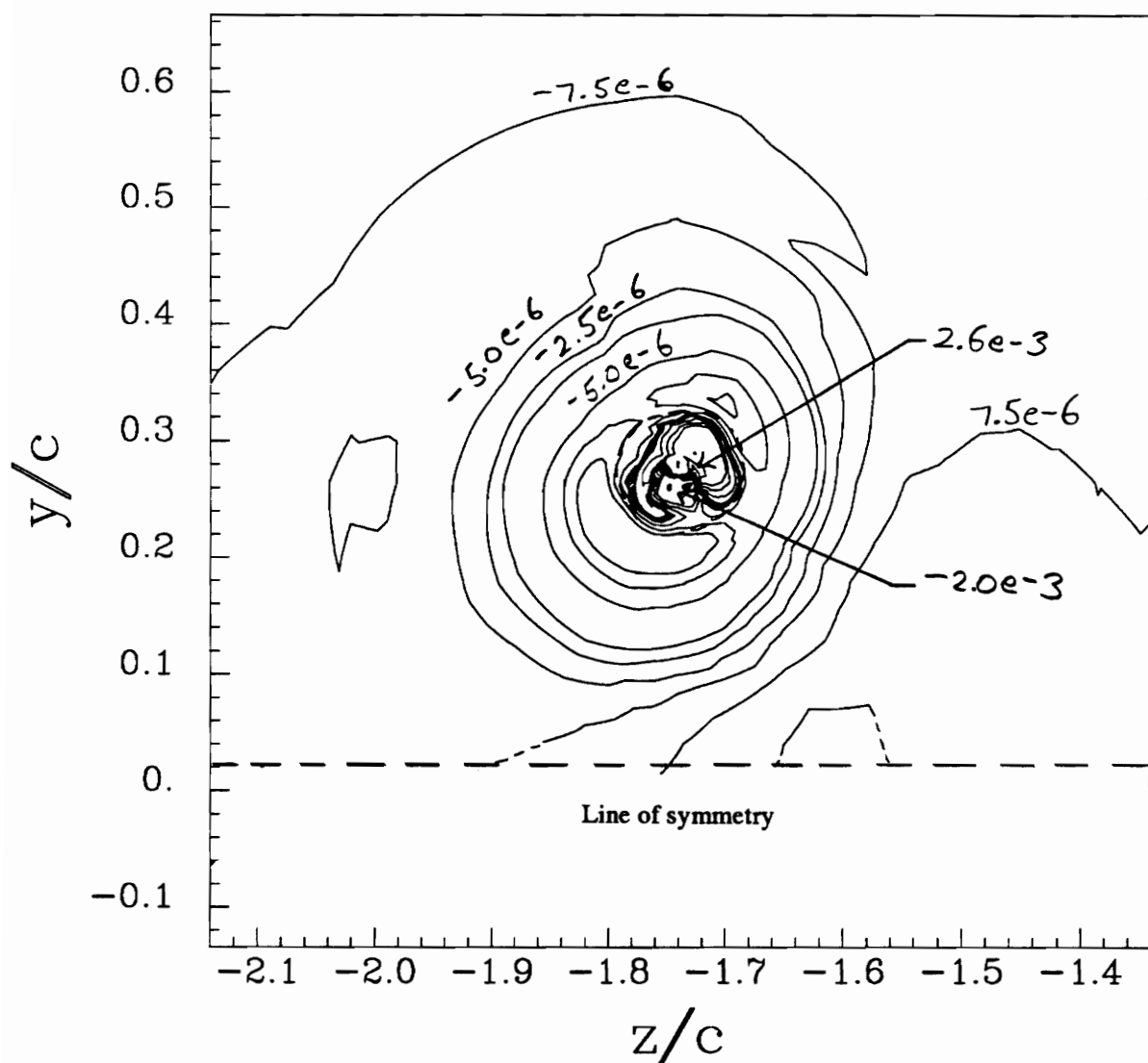


Figure 168. Core region showing contours of $v_x v_\theta / U_{ref}^2$ for the upper counter rotating vortex at $x/c=30$, angle of attack= 5° , $Re_c=260,000$. Dotted line indicates core edge.

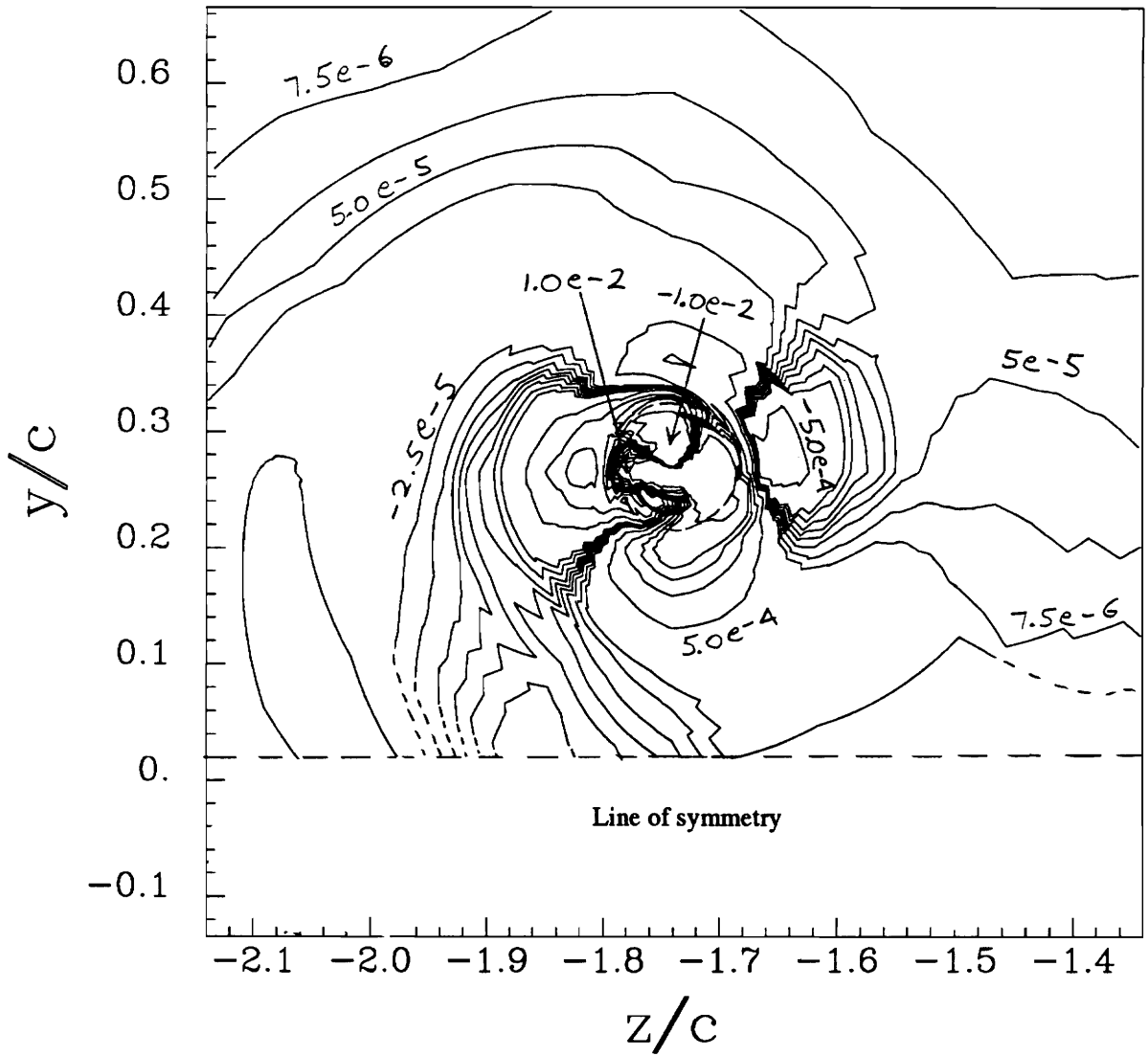


Figure 169. Core region showing contours of $v_\theta v_r / U_{ref}^2$ for the upper counter rotating vortex at $x/c=30$, angle of attack= 5° , $Re_c=260,000$. Dotted line indicates core edge.

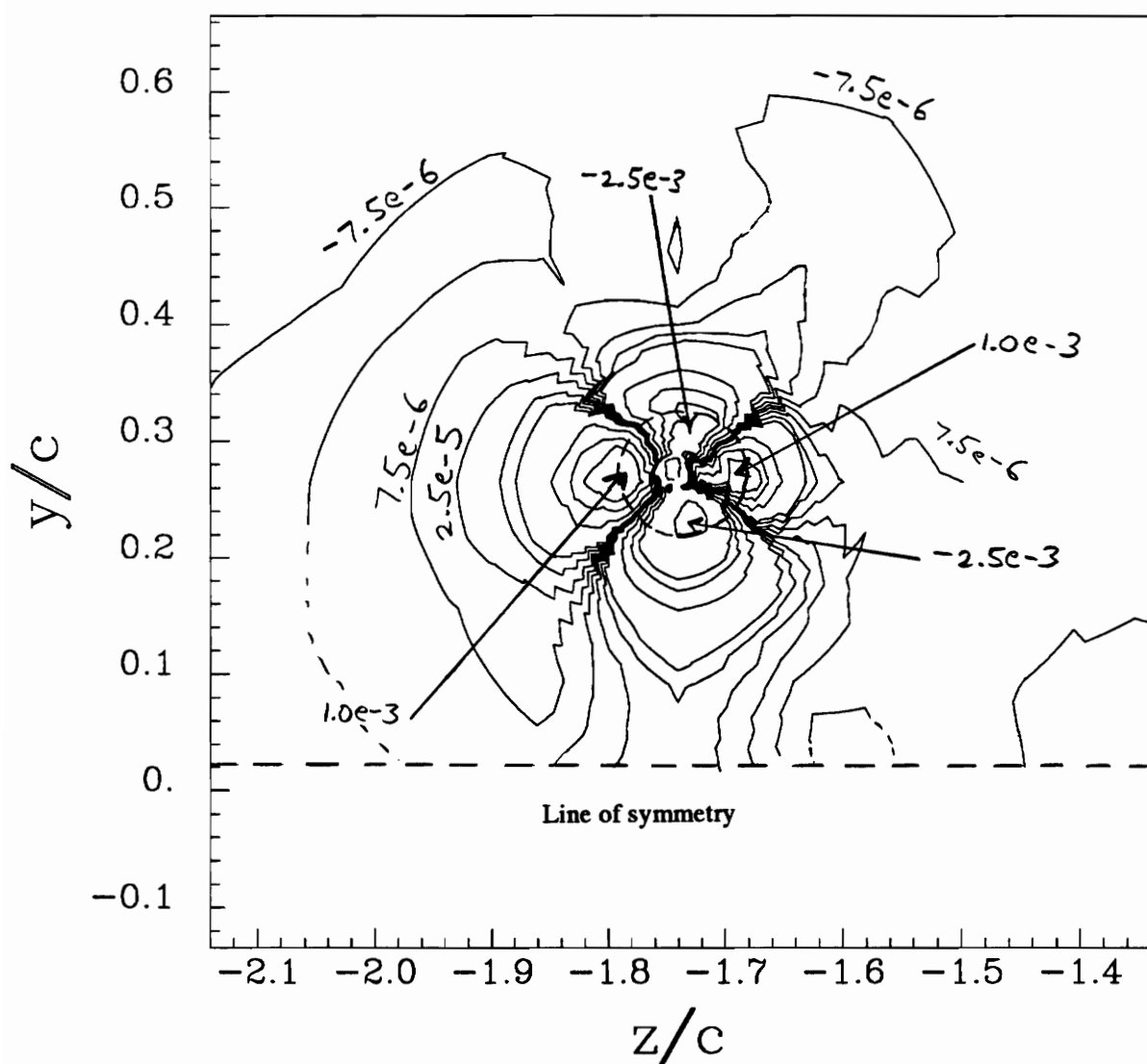


Figure 170. Core region showing contours of $v_x v_r / U_{ref}^2$ for the upper counter rotating vortex at $x/c=30$, angle of attack= 5° , $Re_c=260,000$. Dotted line indicates core edge.

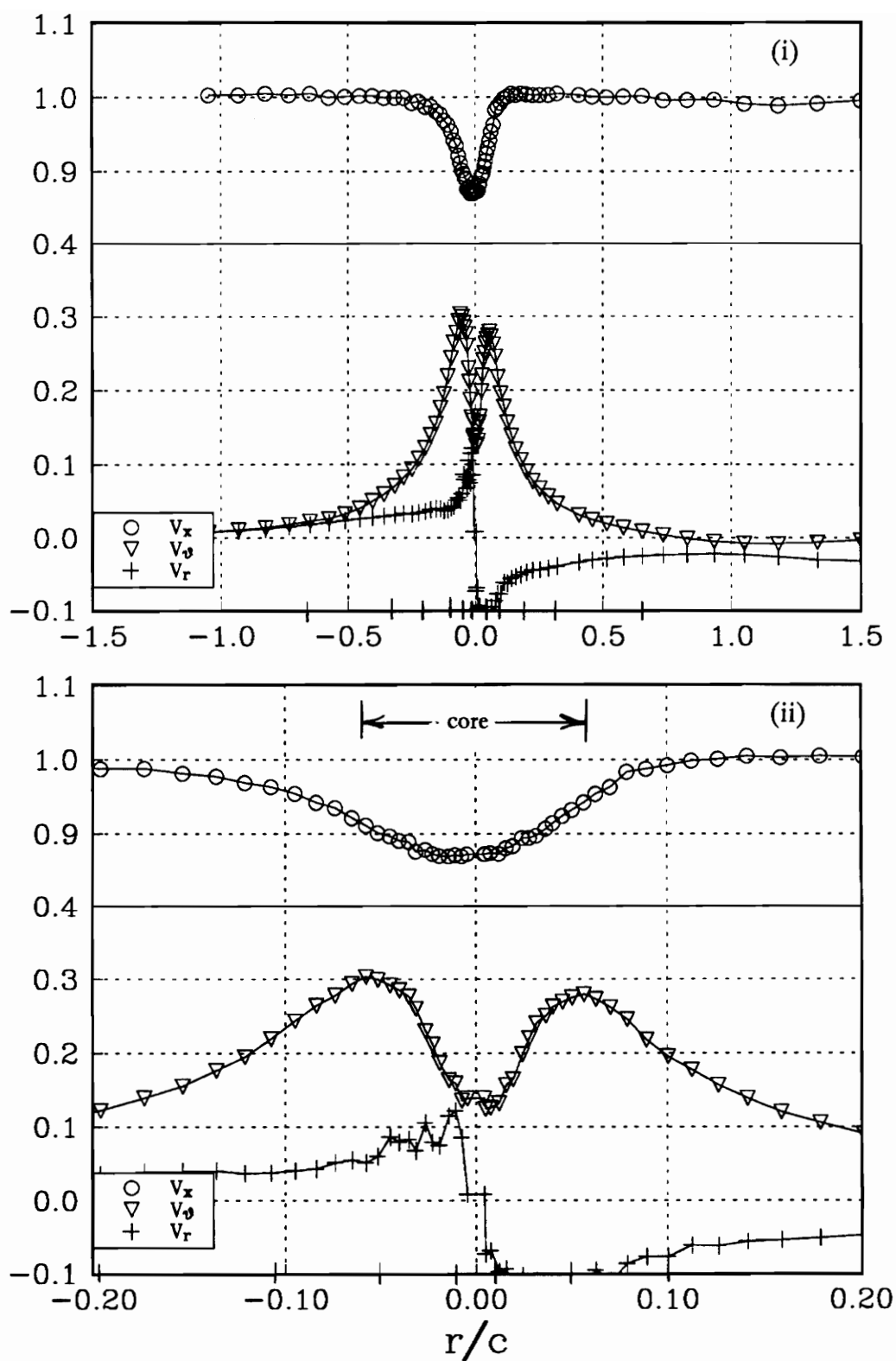


Figure 171a. Profile Kk mean velocities, measured parallel to the line of symmetry for the upper counter rotating vortex at $x/c=30$. (i) wake region, (ii) core region.

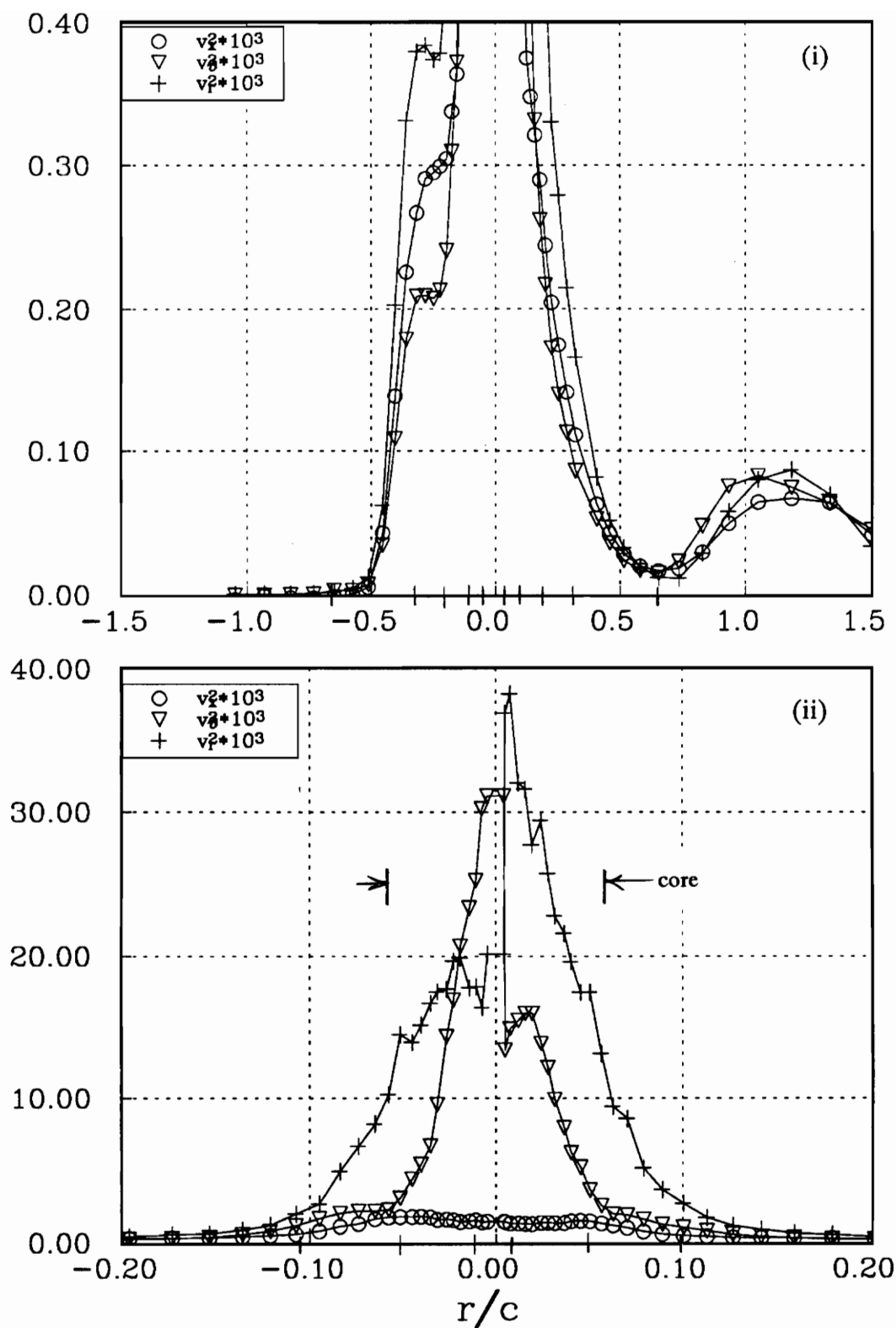


Figure 171b. Profile Kk normal stresses, measured parallel to the line of symmetry for the upper counter rotating vortex at $x/c=30$. (i) wake region, (ii) core region.

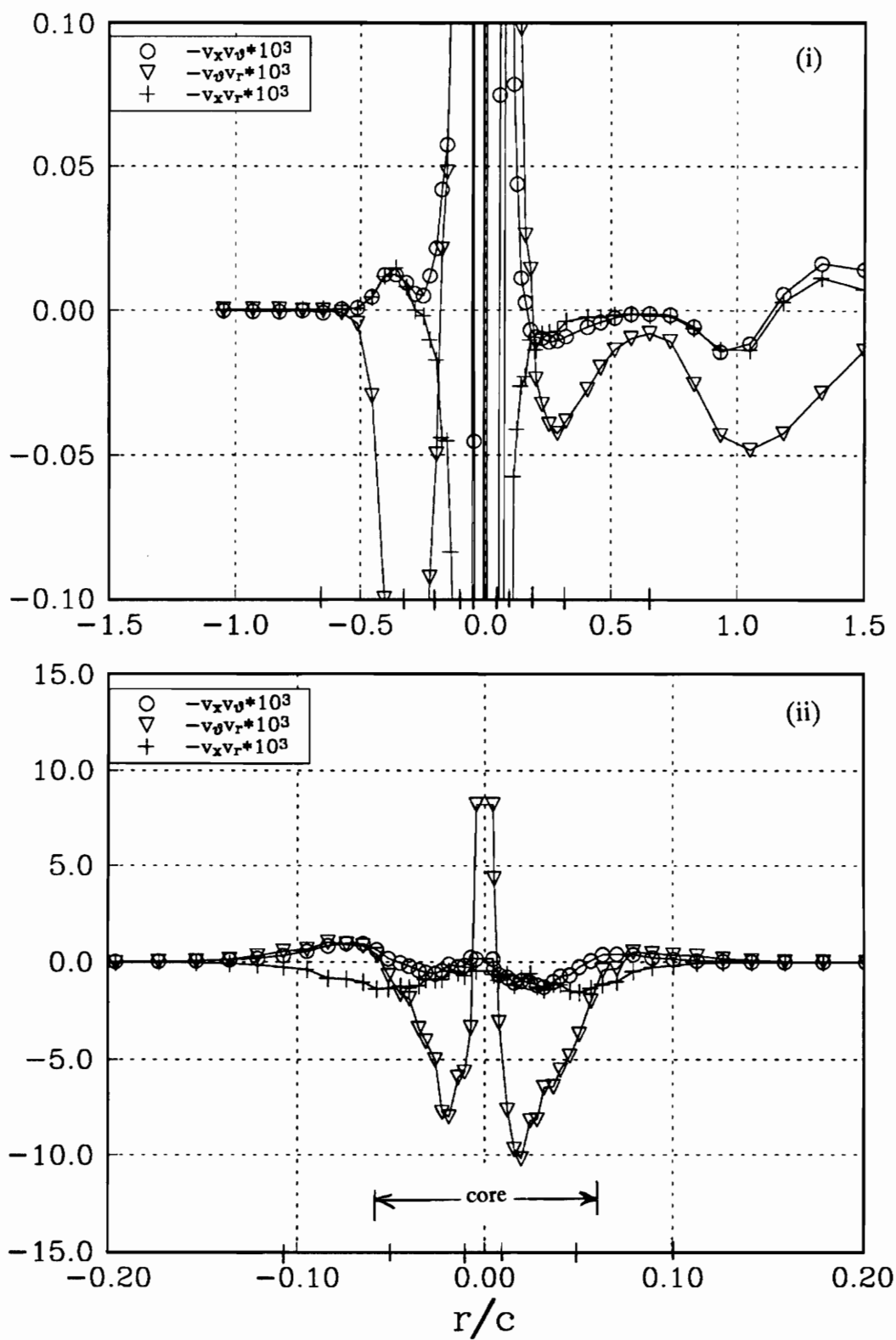


Figure 171c. Profile Kk shear stresses, measured parallel to the line of symmetry for the upper counter rotating vortex at $x/c=30$. (i) wake region, (ii) core region.

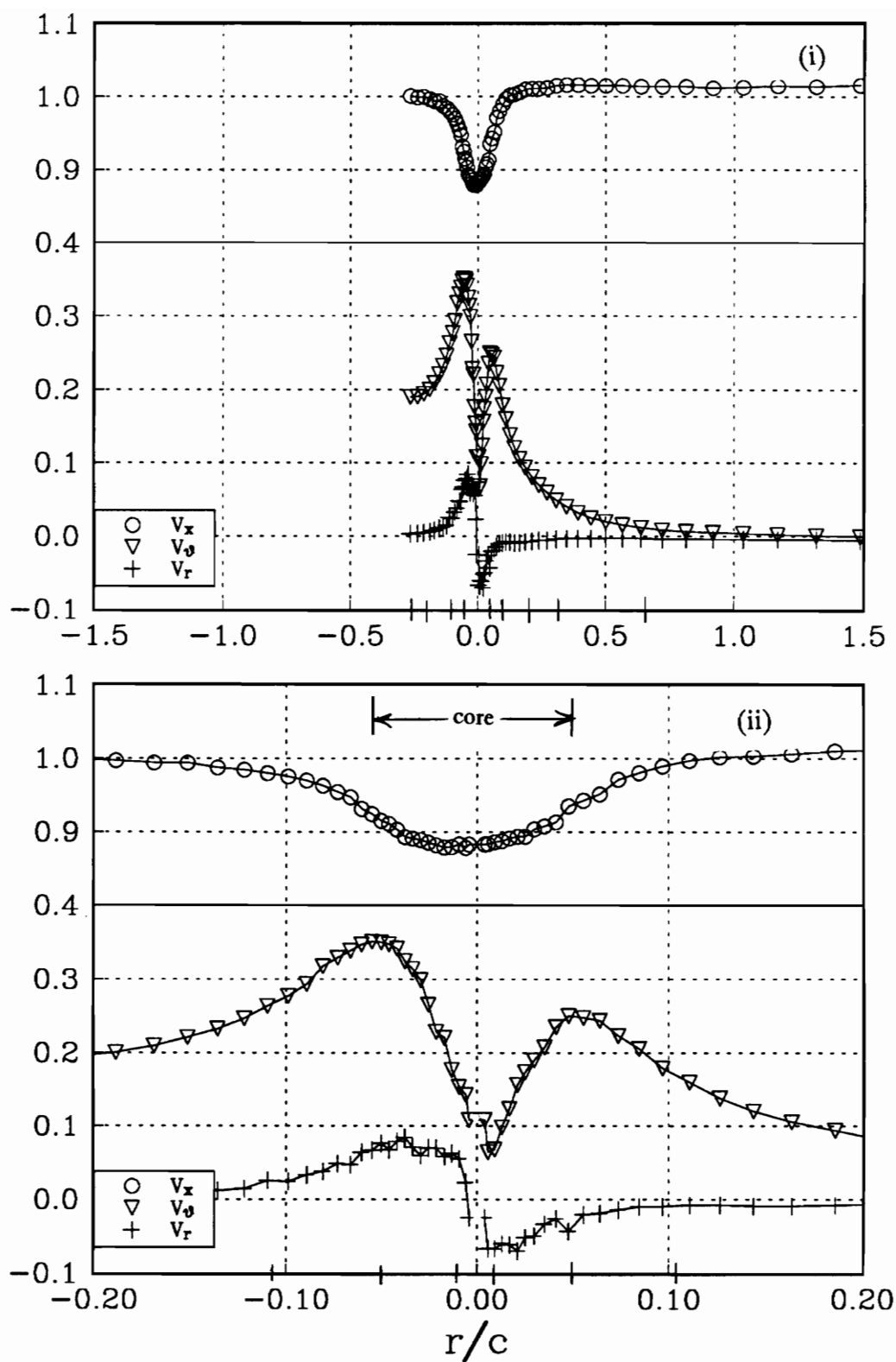


Figure 172a. Profile LI mean velocities, measured perpendicular to the line of symmetry for the upper counter rotating vortex at $x/c=30$. (i) wake region, (ii) core region.

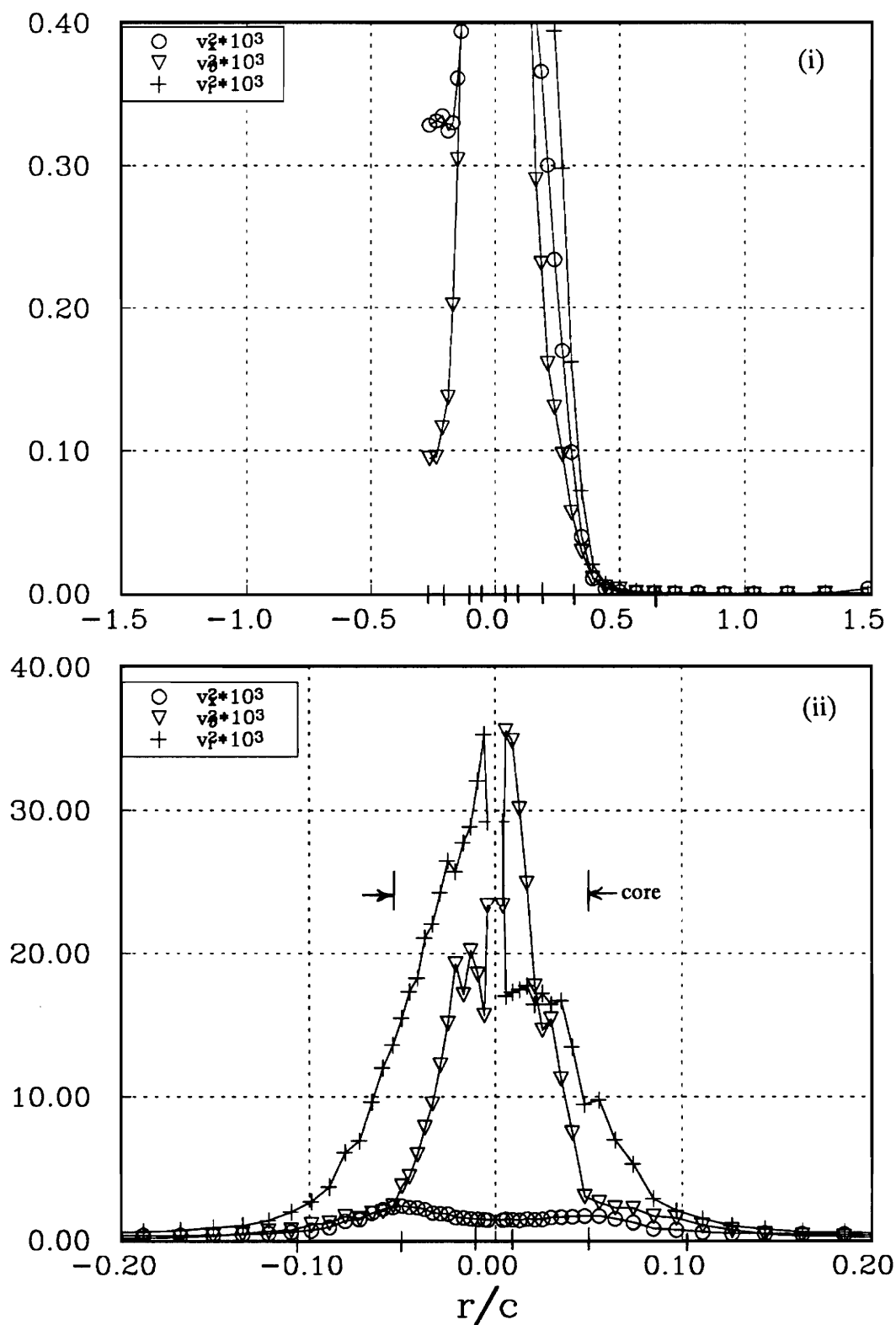


Figure 172b. Profile Ll normal stresses, measured perpendicular to the line of symmetry for the upper counter rotating vortex at $x/c=30$. (i) wake region, (ii) core region.

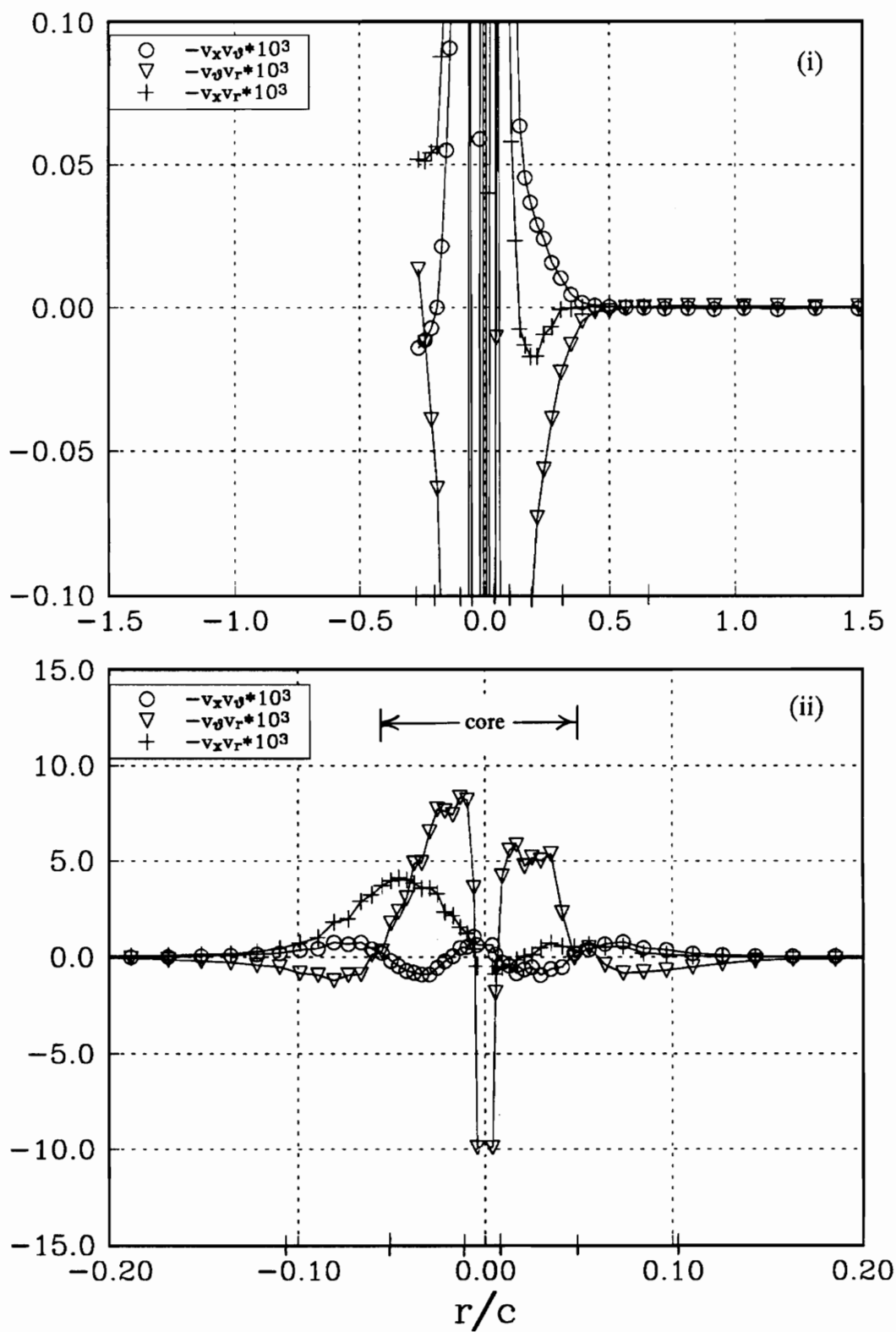


Figure 172c. Profile L1 shear stresses, measured perpendicular to the line of symmetry for the upper counter rotating vortex at $x/c=30$. (i) wake region, (ii) core region.

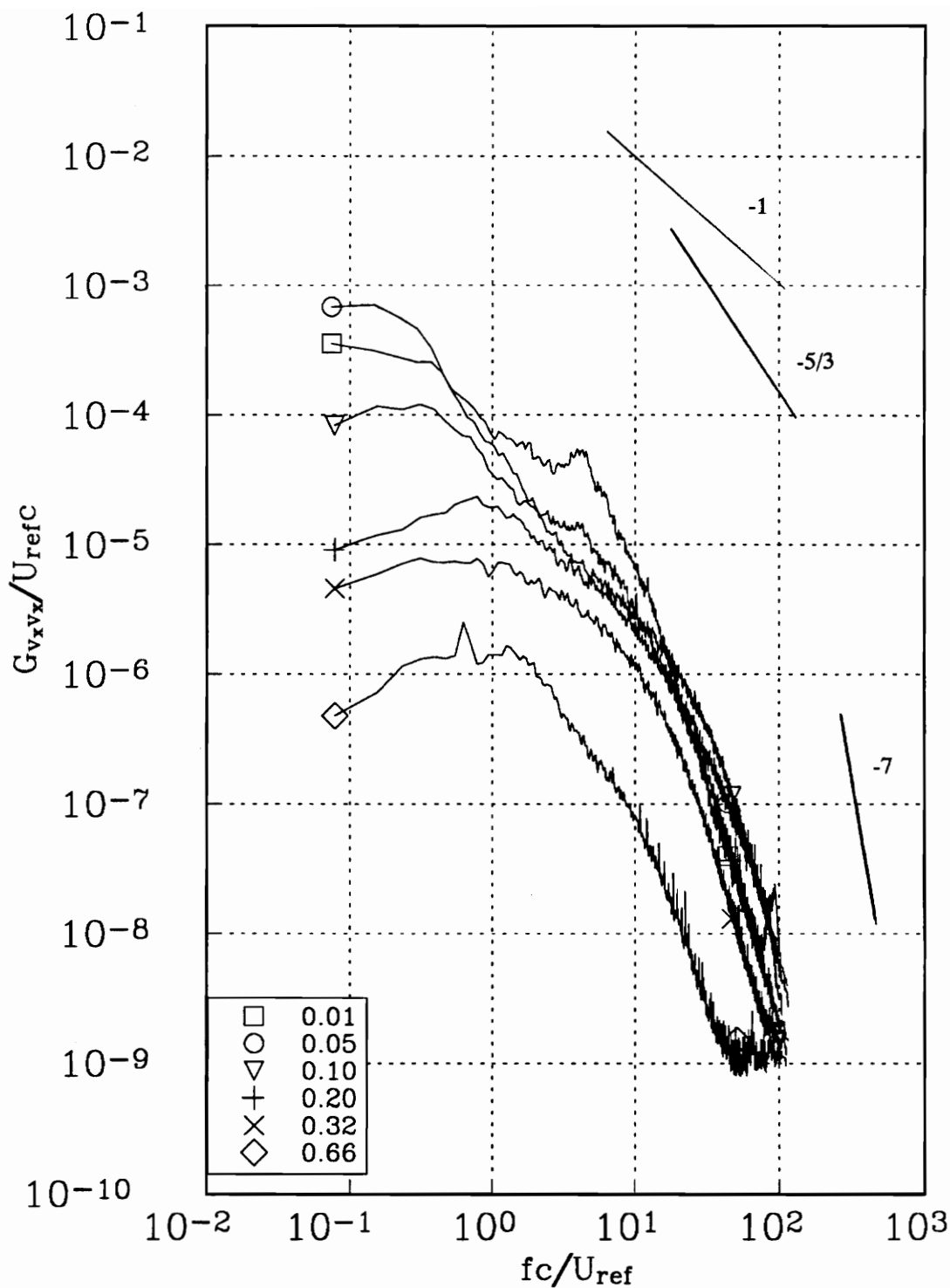


Figure 173a. v_x autospectra measured at representative radial locations along profile Kk for the upper counter rotating vortex at $x/c=30$. Tic marks in figure 171 indicate measured r/c locations.

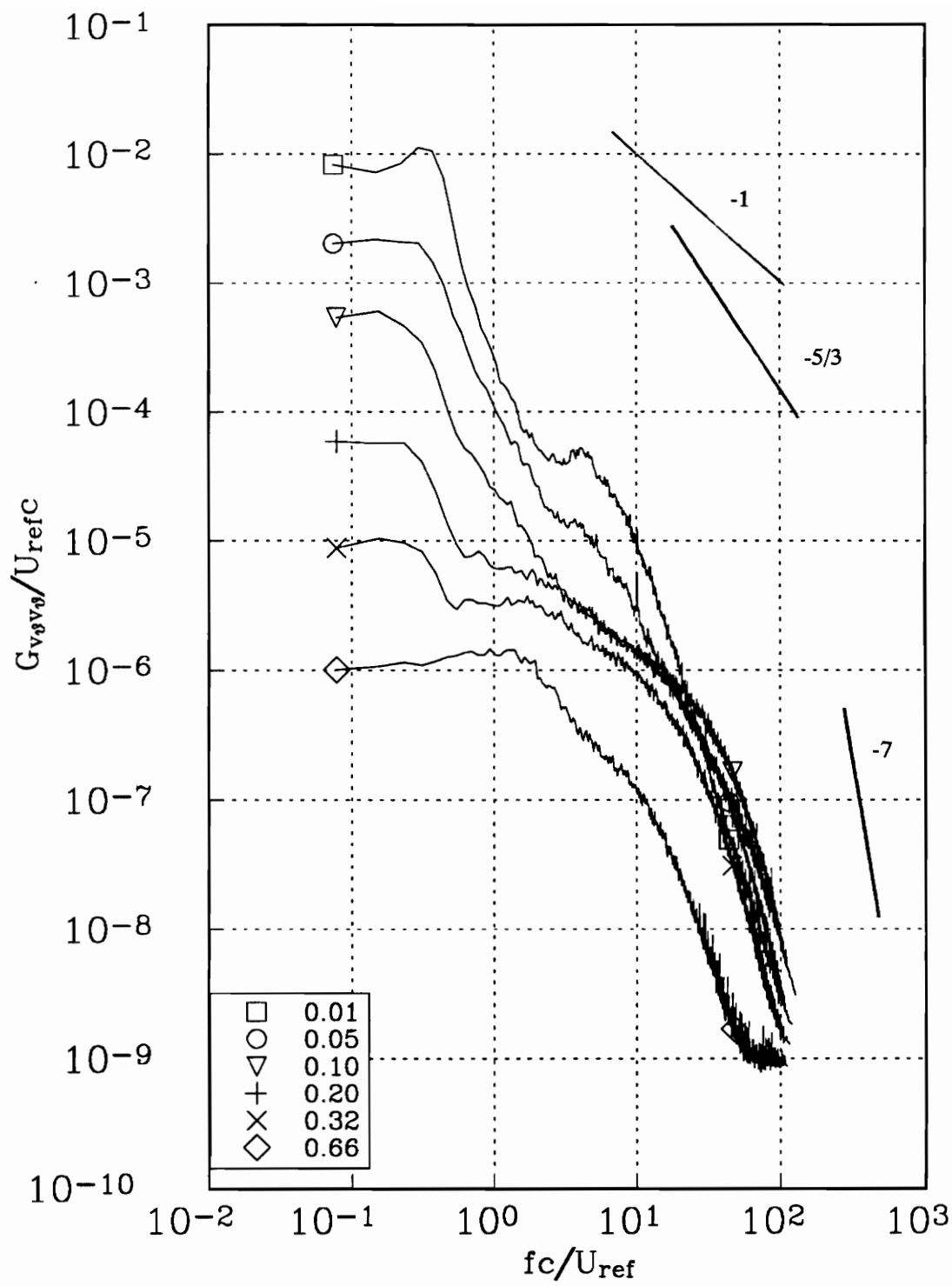


Figure 173b. v_θ autospectra measured at representative radial locations along profile Kk for the upper counter rotating vortex at $x/c=30$. Tic marks in figure 171 indicate measured r/c locations.

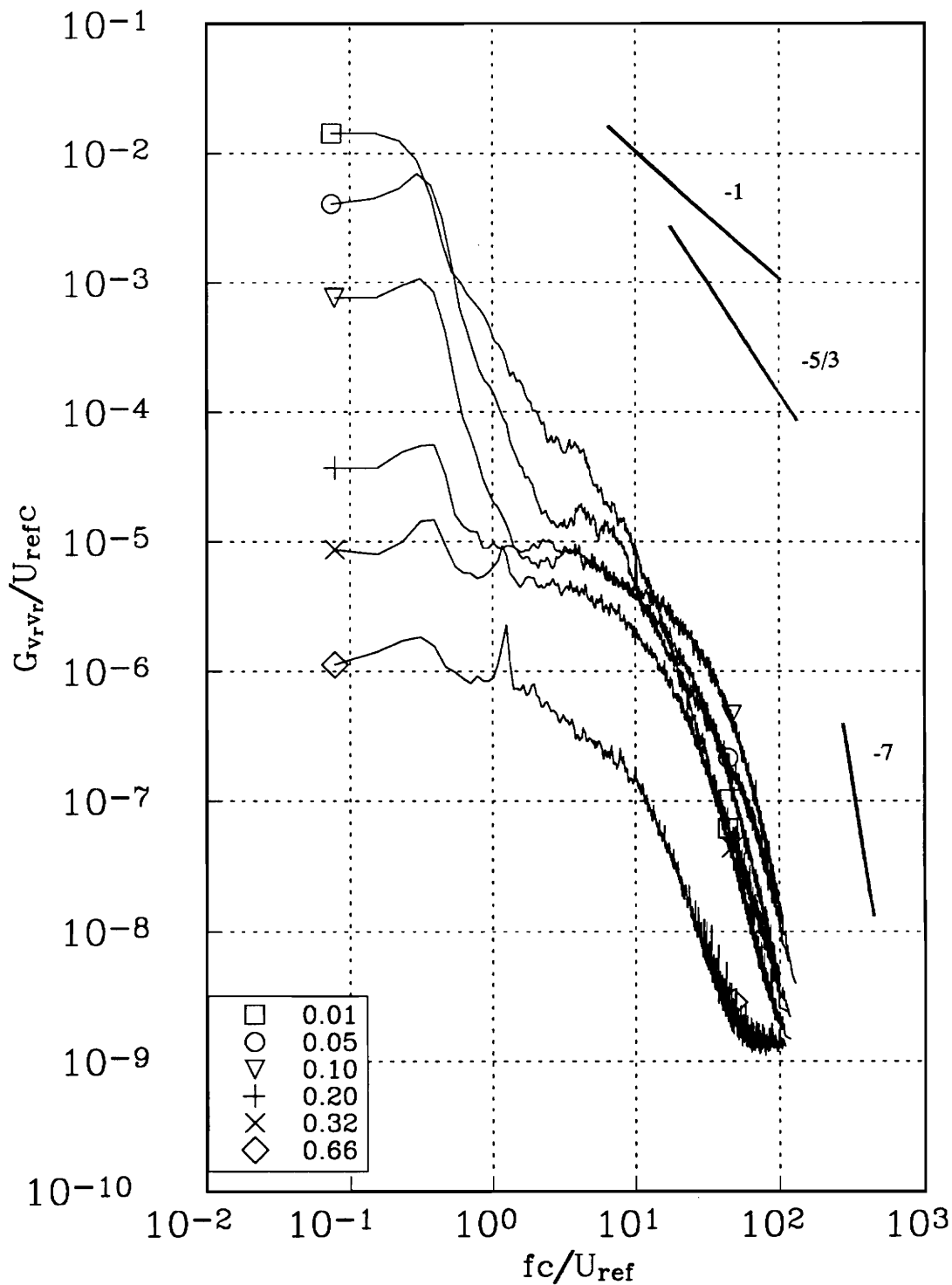


Figure 173c. v_r autospectra measured at representative radial locations along profile Kk for the upper counter rotating vortex at $x/c=30$. Tic marks in figure 171 indicate measured r/c locations.

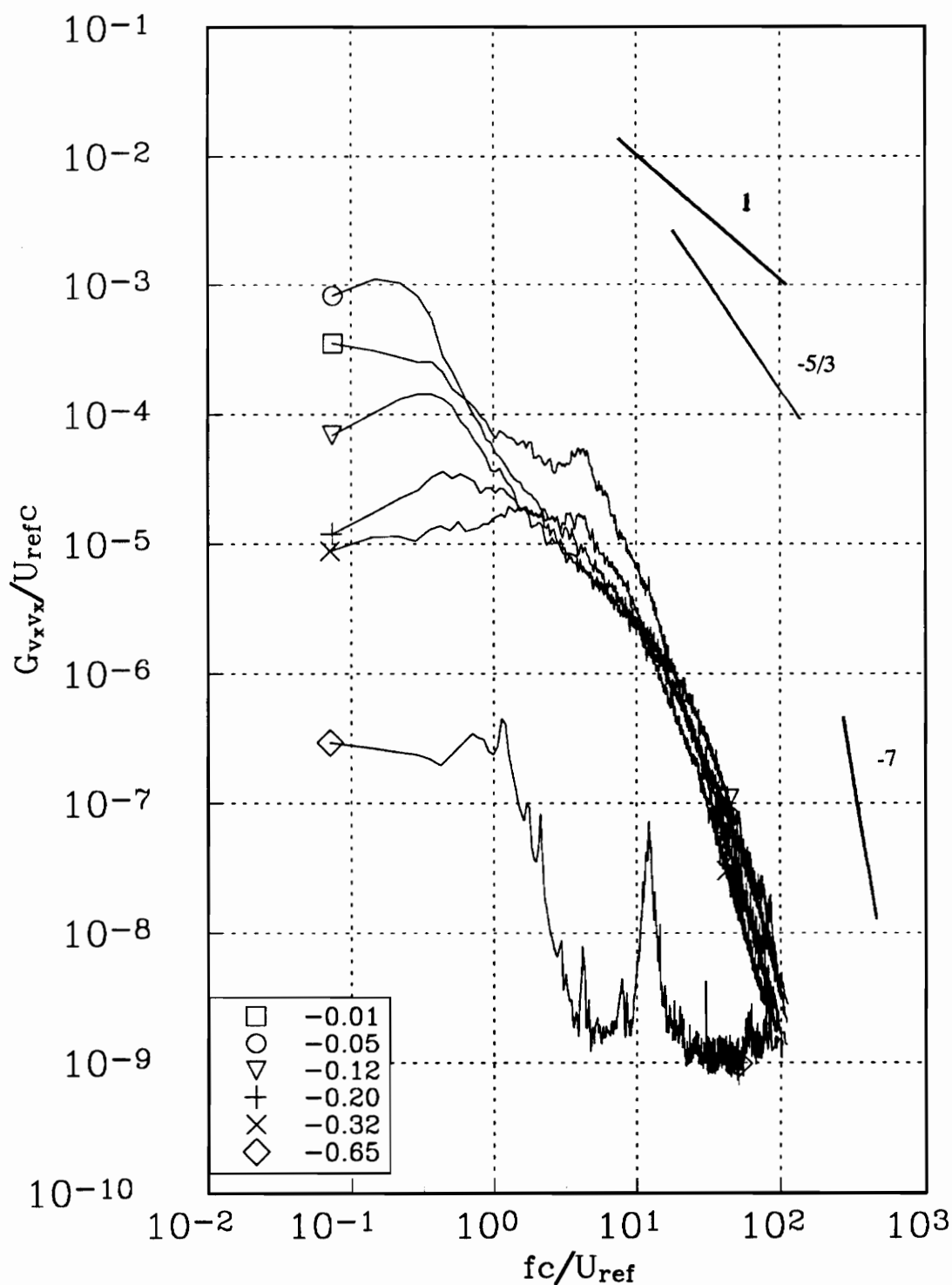


Figure 174a. v_x autospectra measured at representative radial locations along profile Kk for the upper counter rotating vortex at $x/c=30$. Tic marks in figure 171 indicate measured r/c locations.

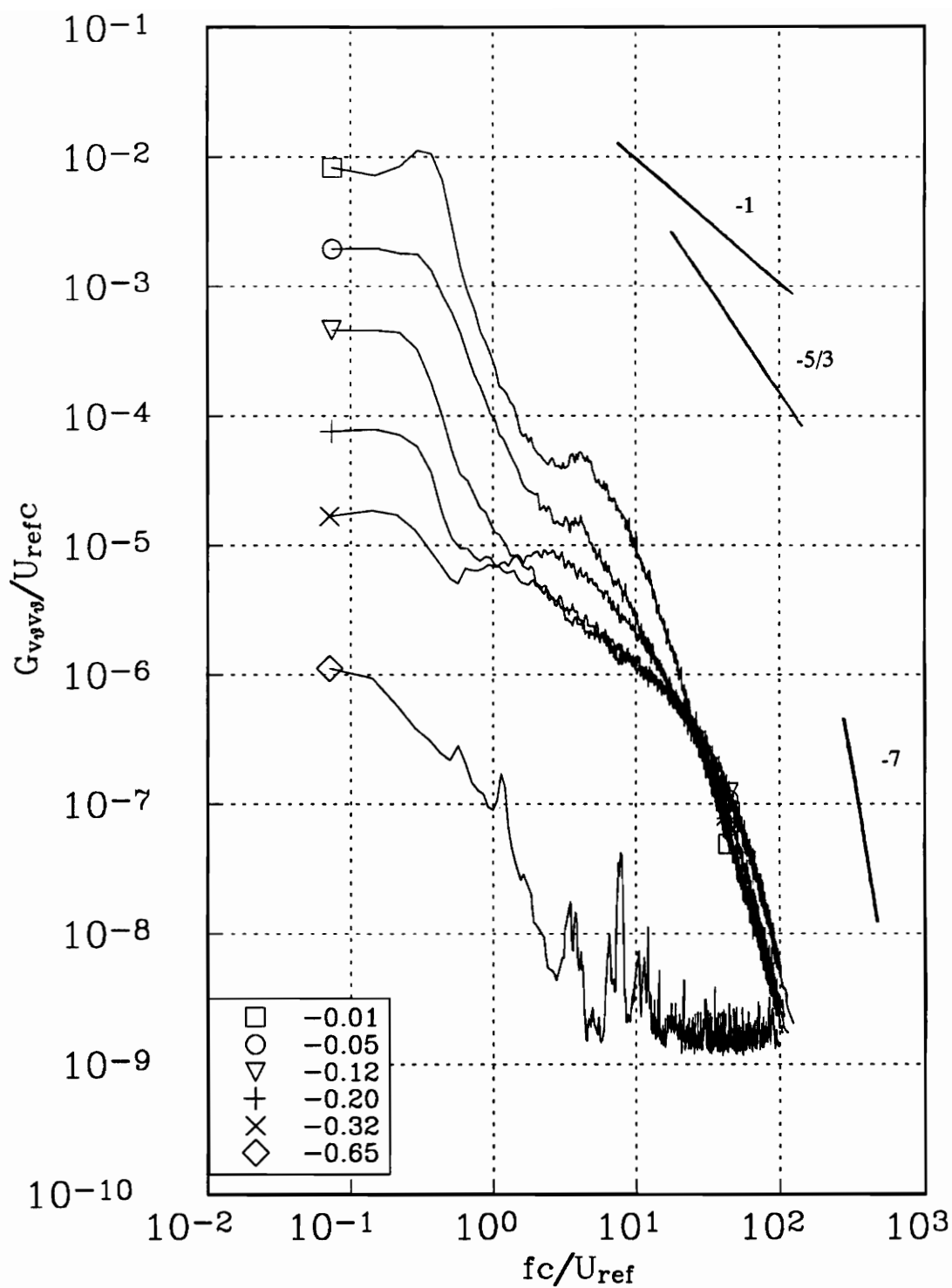


Figure 174b. v_{θ} autospectra measured at representative radial locations along profile Kk for the upper counter rotating vortex at $x/c=30$. Tic marks in figure 171 indicate measured r/c locations.

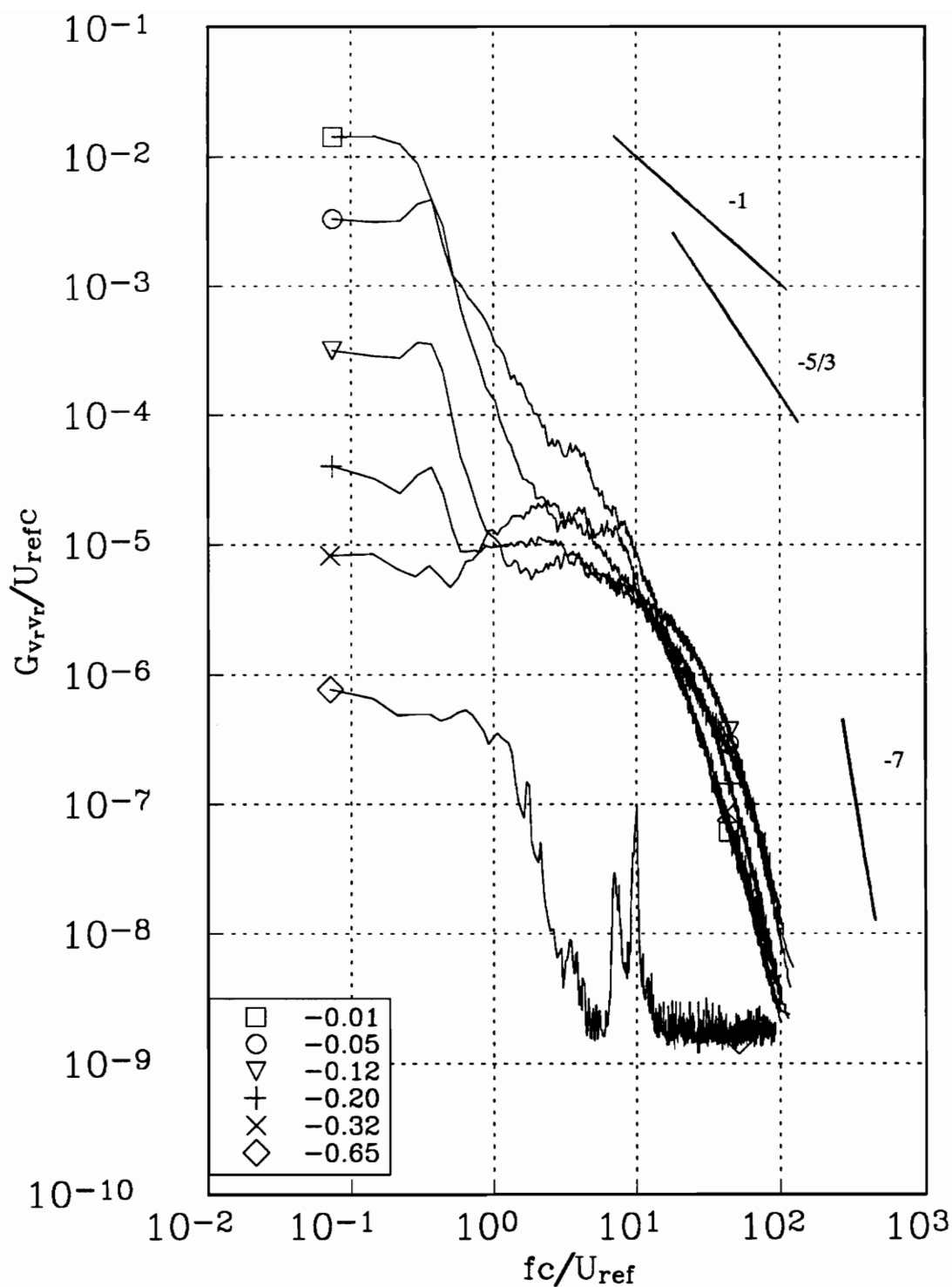


Figure 174c. v_r autospectra measured at representative radial locations along profile Kk for the upper counter rotating vortex at $x/c=30$. Tic marks in figure 171 indicate measured r/c locations.

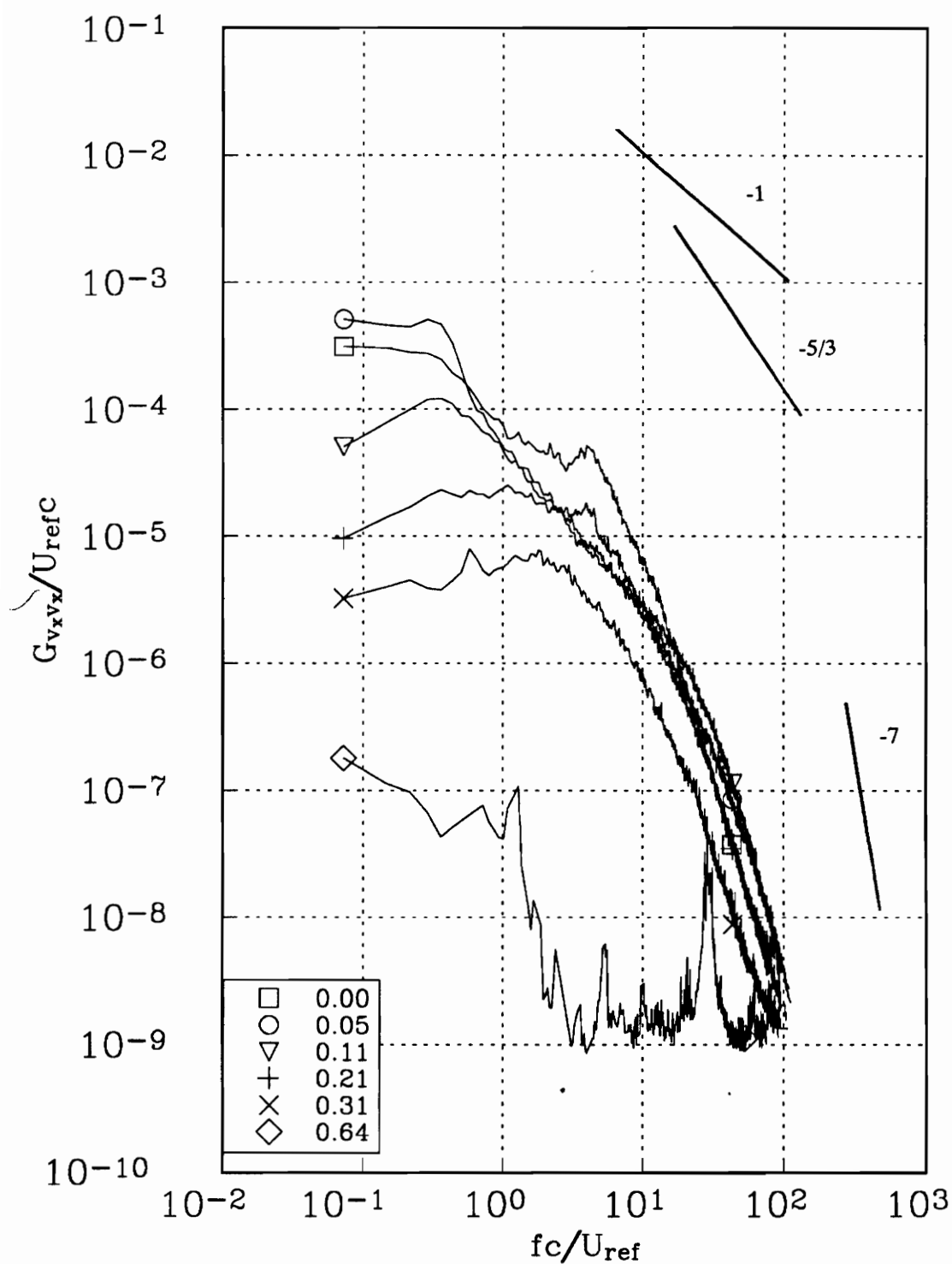


Figure 175a. v_x autospectra measured at representative radial locations along profile L1 for the upper counter rotating vortex at $x/c=30$. Tic marks in figure 172 indicate measured r/c locations.

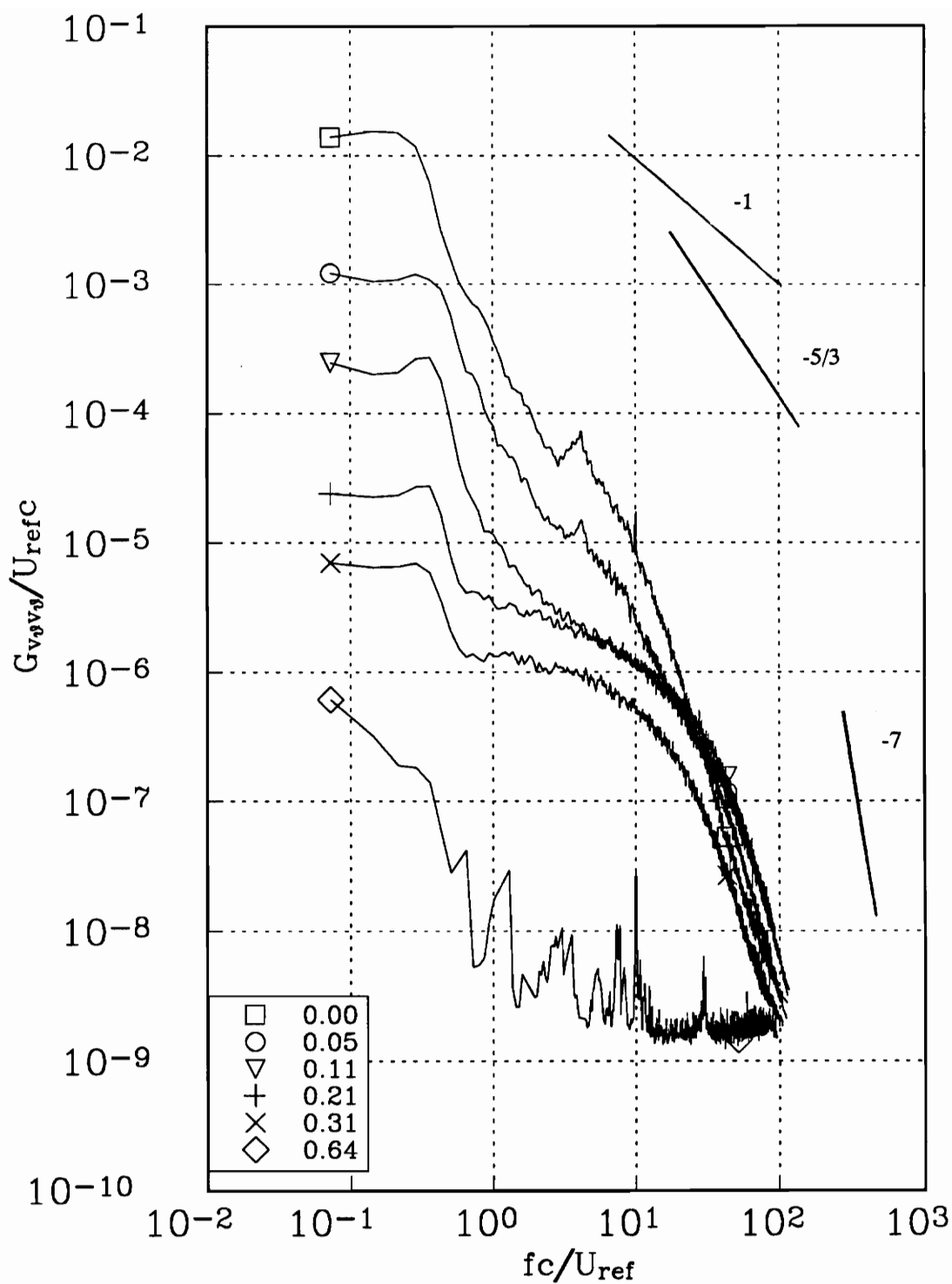


Figure 175b. v_θ autospectra measured at representative radial locations along profile LI for the upper counter rotating vortex at $x/c=30$. Tic marks in figure 172 indicate measured r/c locations.

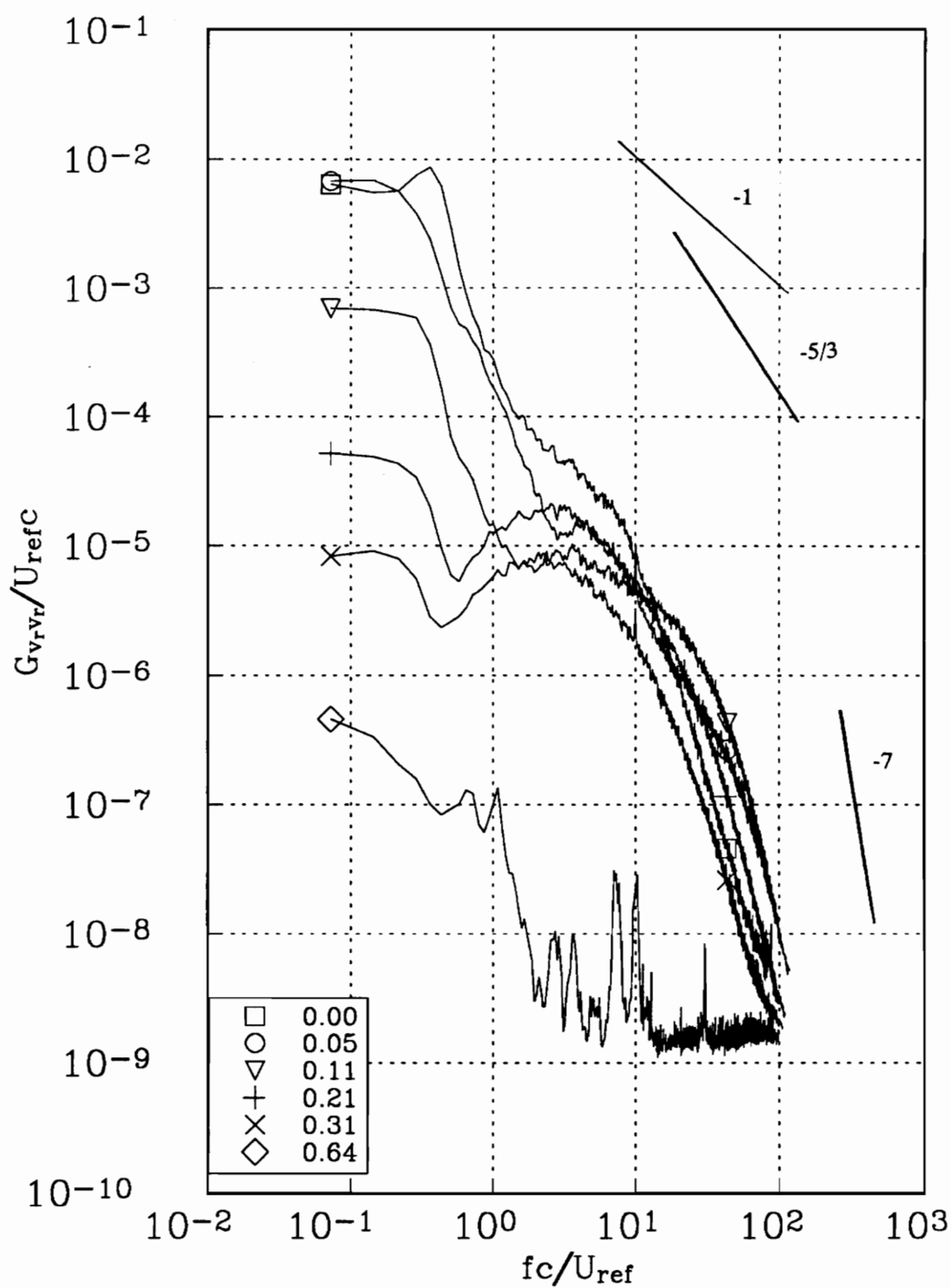


Figure 175c. v_r autospectra measured at representative radial locations along profile L1 for the upper counter rotating vortex at $x/c=30$. Tic marks in figure 172 indicate measured r/c locations.

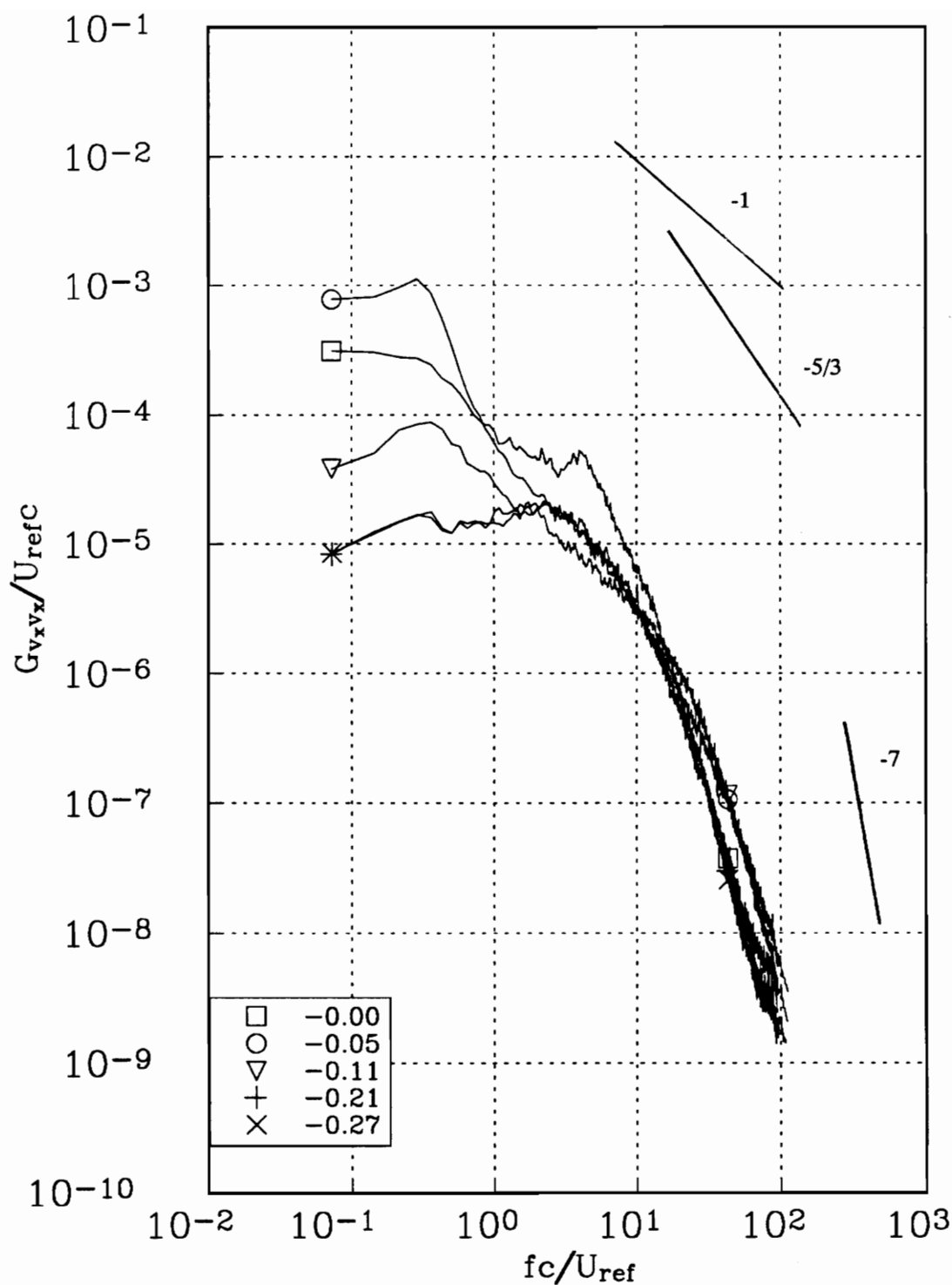


Figure 176a. v_x autospectra measured at representative radial locations along profile L1 for the upper counter rotating vortex at $x/c=30$. Tic marks in figure 172 indicate measured r/c locations.

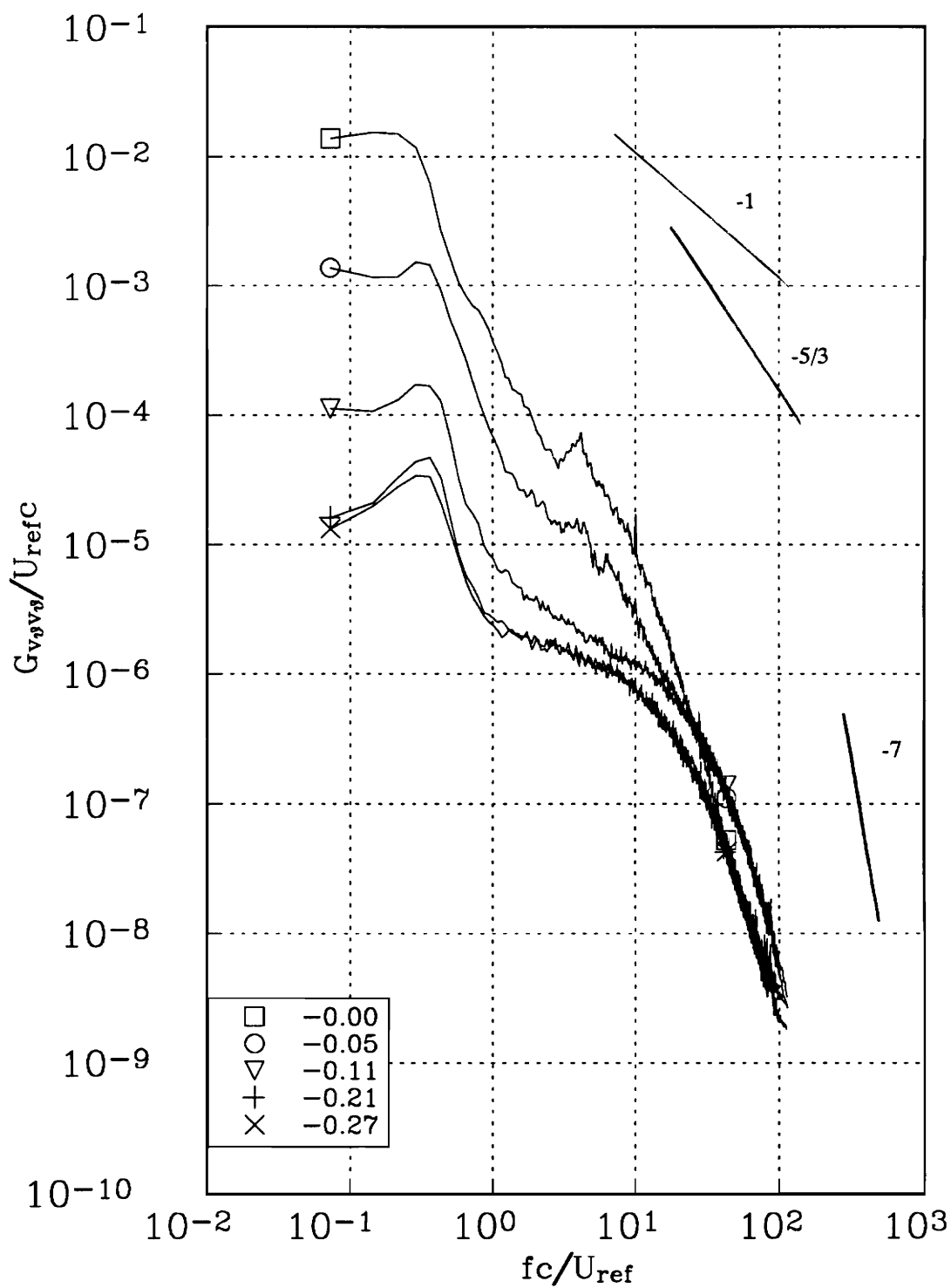


Figure 176b. v_θ autospectra measured at representative radial locations along profile LI for the upper counter rotating vortex at $x/c=30$. Tic marks in figure 172 indicate measured r/c locations.

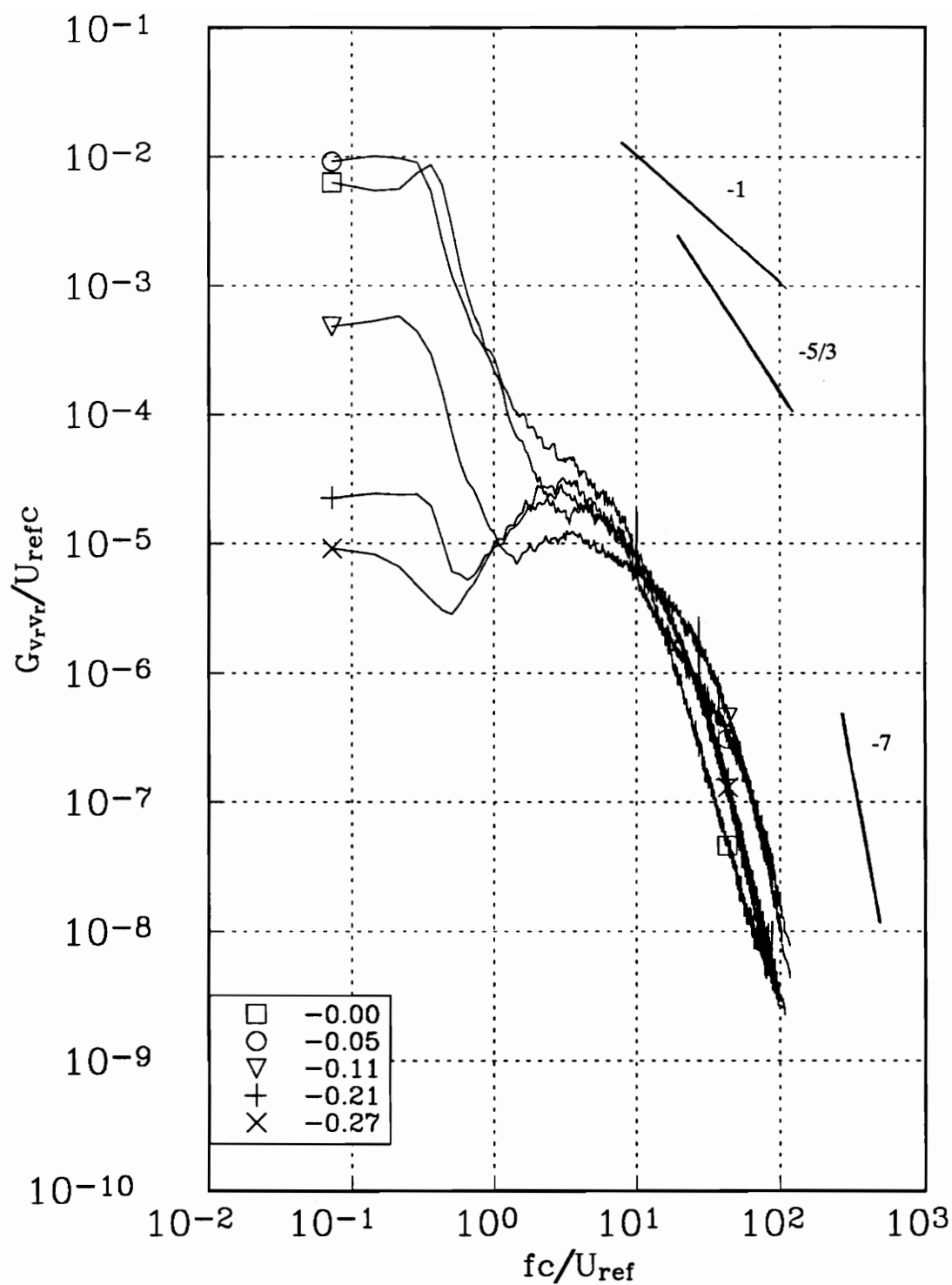


Figure 176c. v_r autospectra measured at representative radial locations along profile LI for the upper counter rotating vortex at $x/c=30$. Tic marks in figure 172 indicate measured r/c locations.

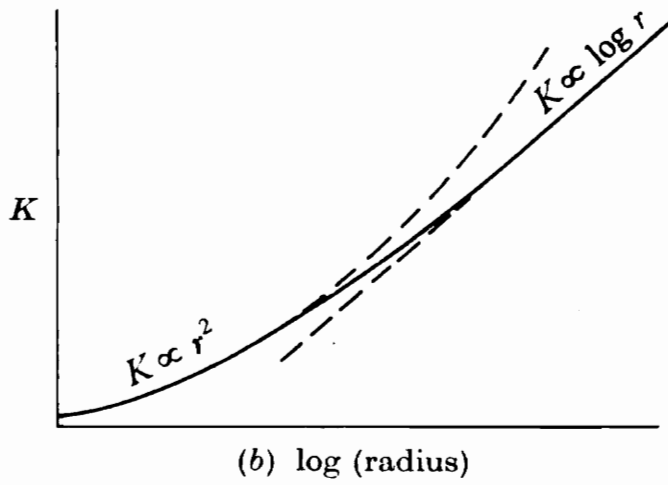
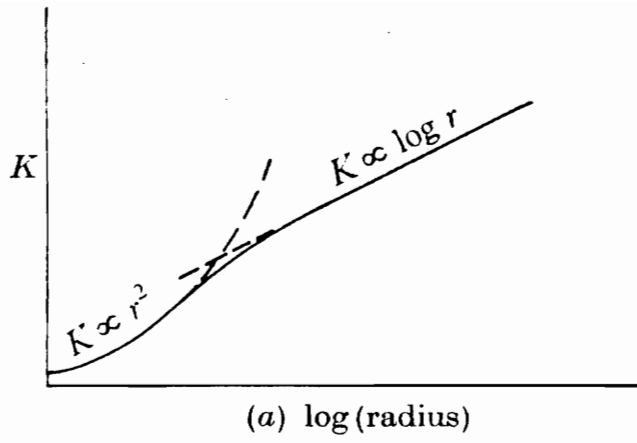


Figure 177. Hoffmann and Joubert's circulation profiles, (a) under developed case (i.e. viscosity dependent) and (b) fully developed case (i.e. viscosity independent).

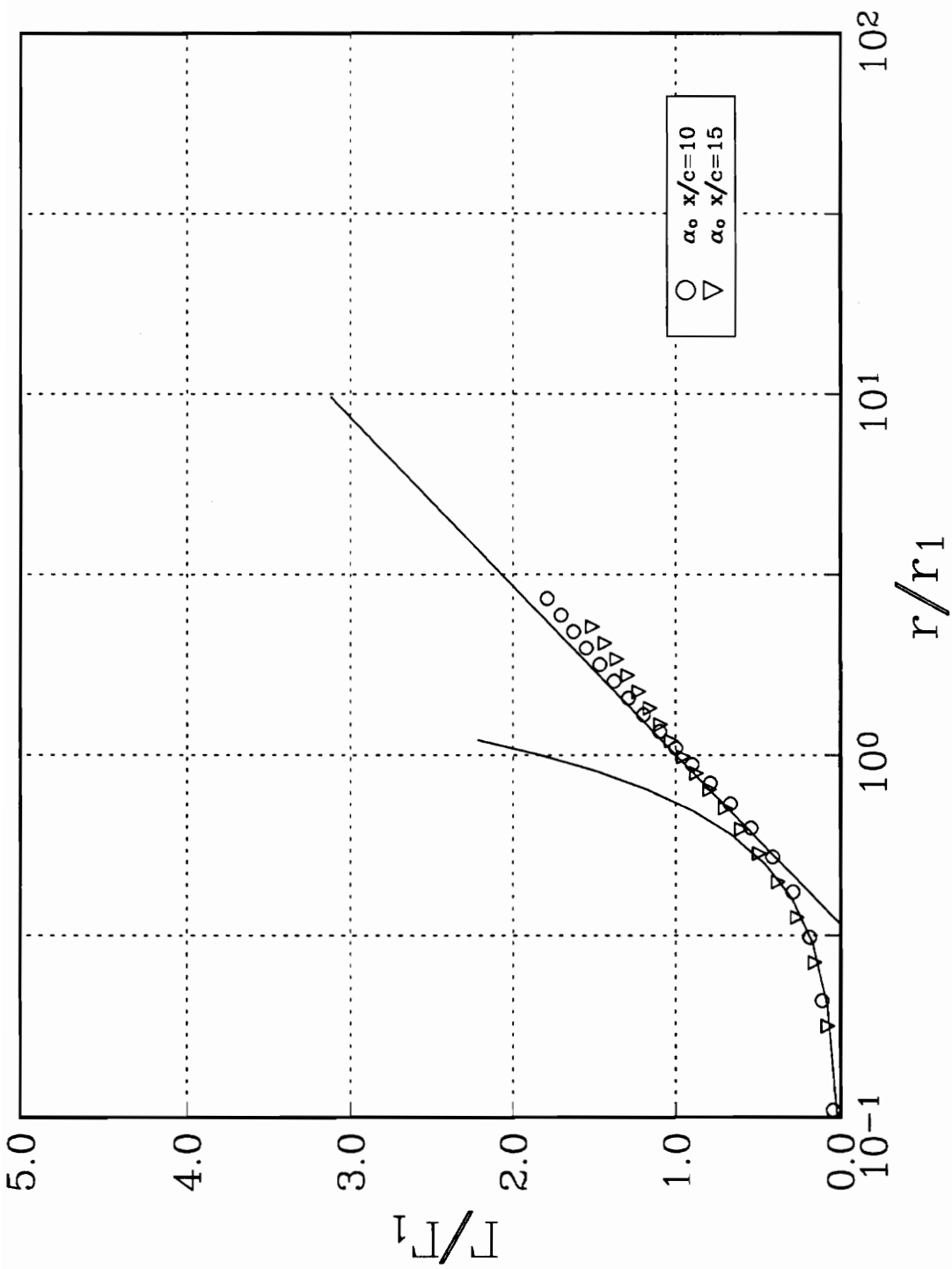


Figure 178. True circulation profiles for the co-rotating pairs at $x/c=10$ and 15 compared to Hoffmann and Joubert's circulation law.

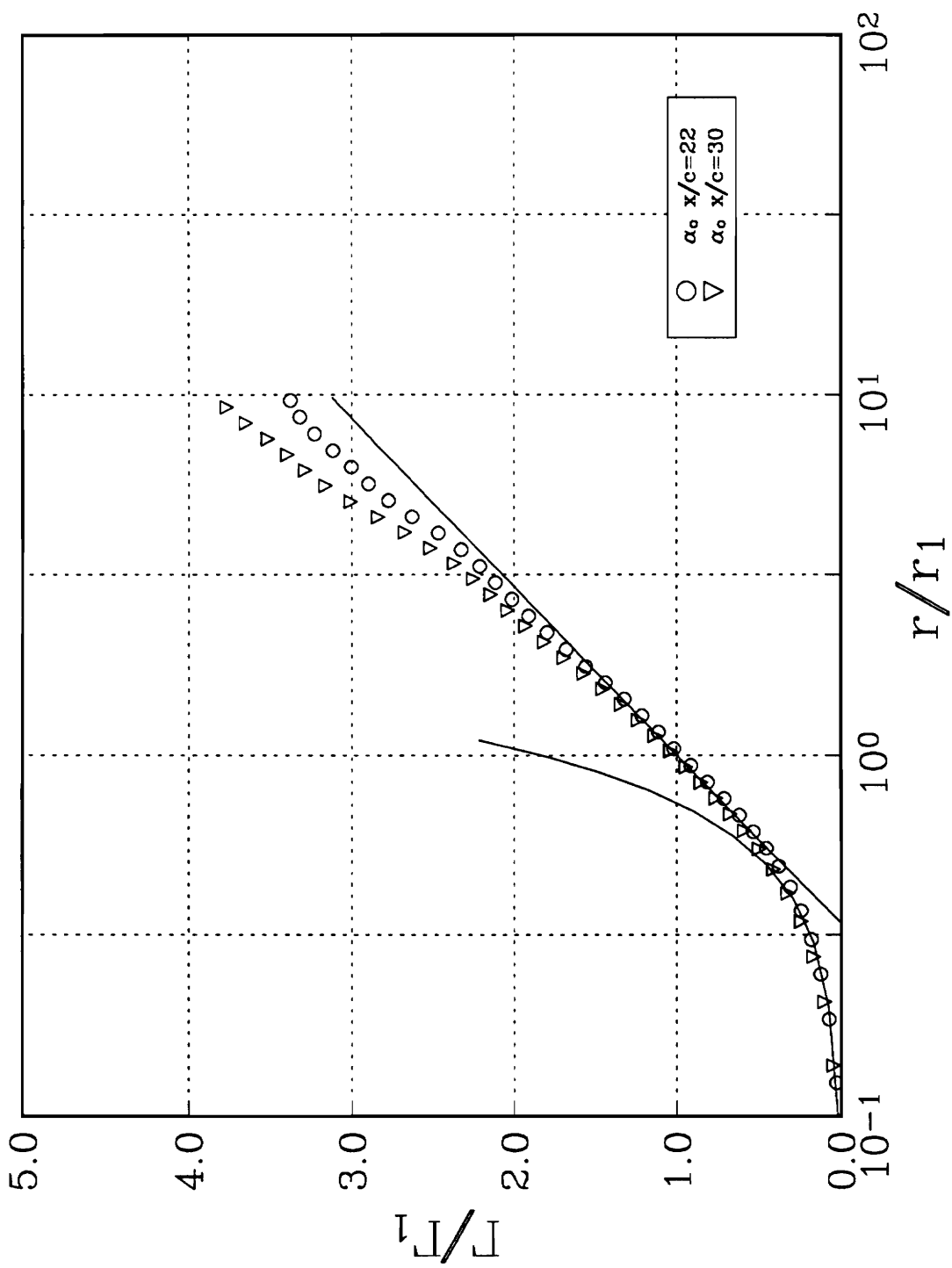


Figure 179. True circulation profiles for the co-rotating pairs at $x/c=22$ and 30 compared to Hoffmann and Joubert's circulation law.

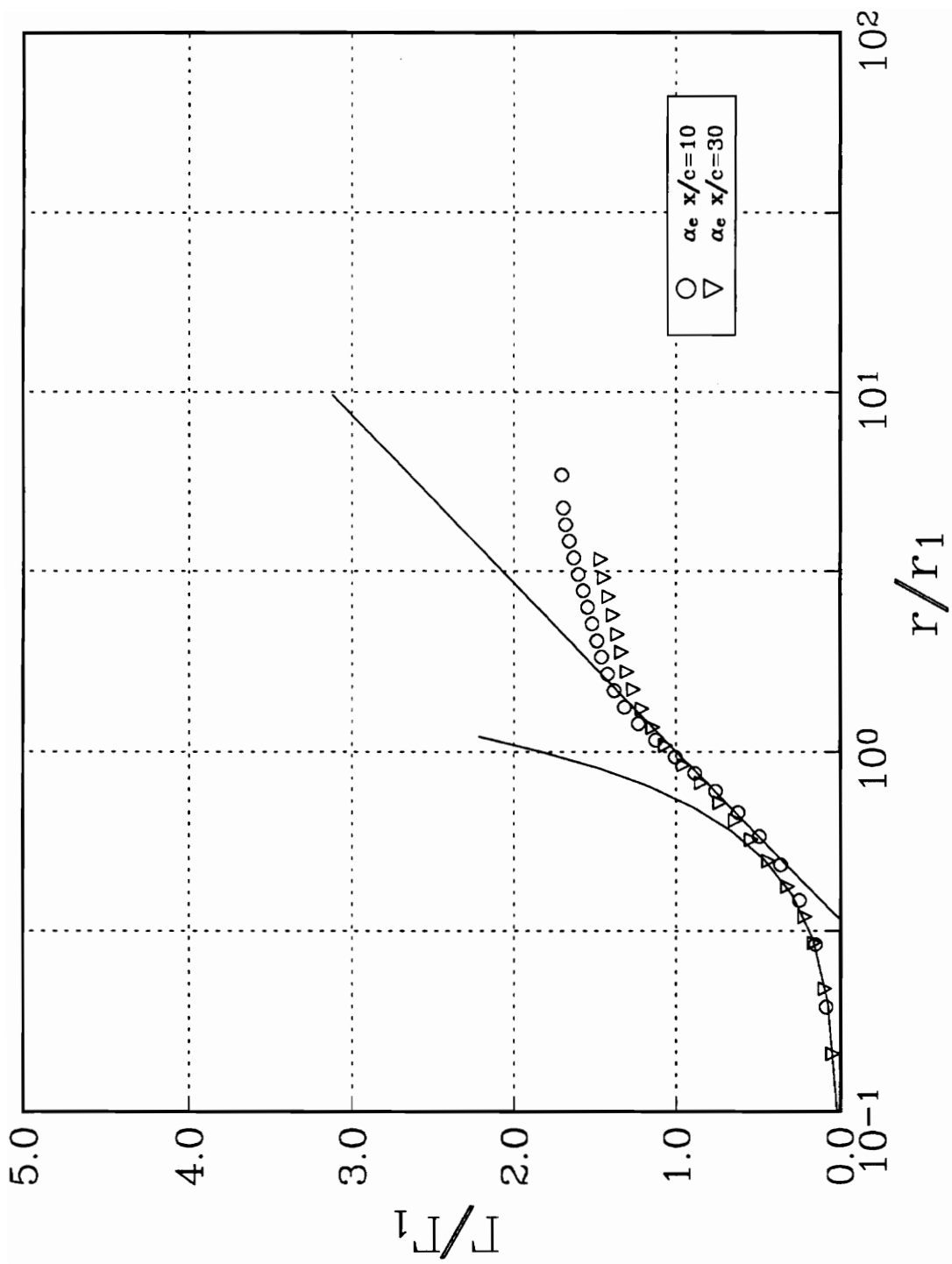


Figure 180. True circulation profiles for the counter rotating pairs at $x/c=10$ and 30 compared to Hoffmann and Joubert's circulation law.

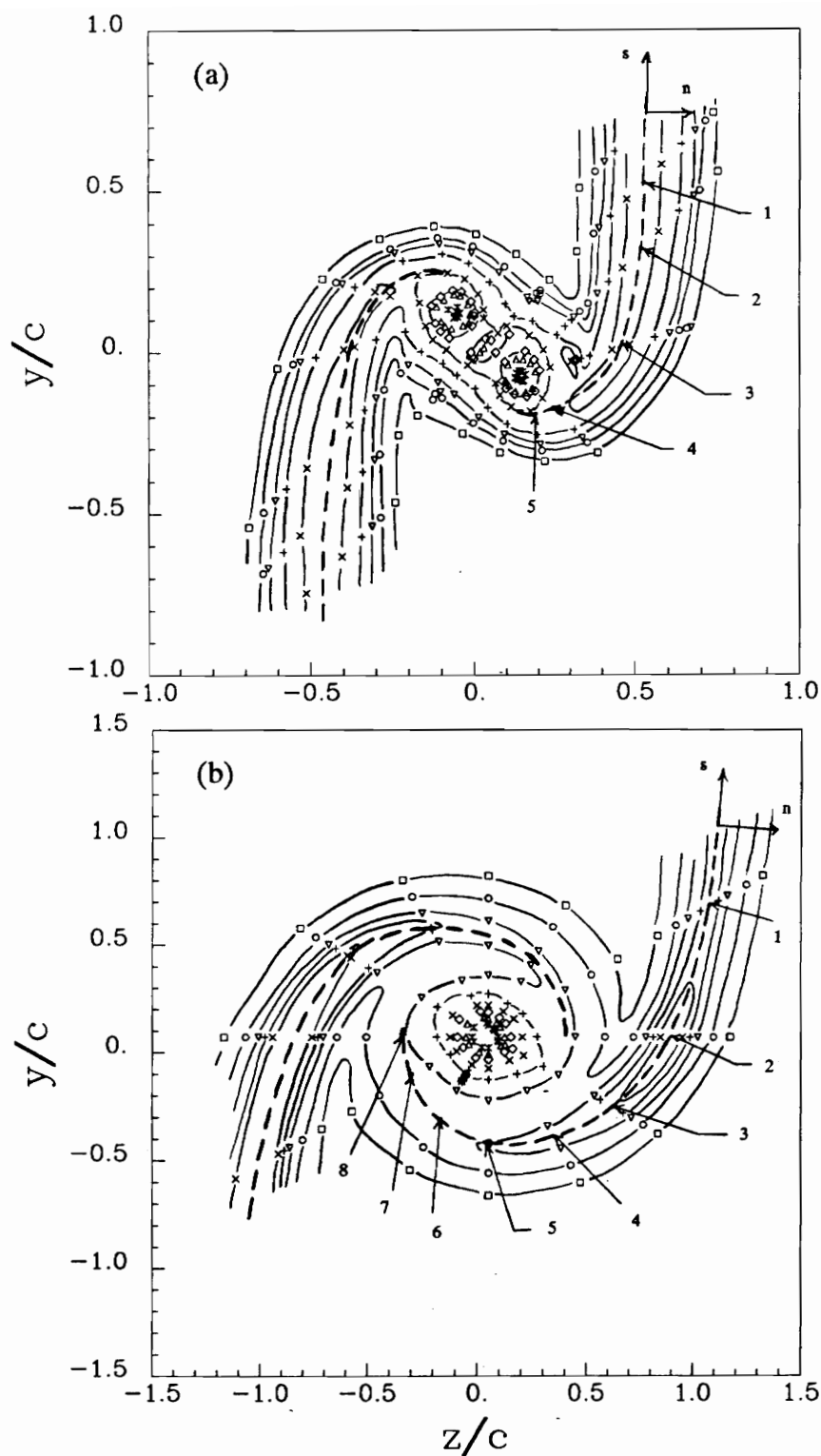


Figure 181. Turbulent kinetic energy contours showing shear layer coordinate system and representative stations for the co-rotating pairs at (a) $x/c=10$ and (b) $x/c=30$. Dotted line indicates center of spiral wake.

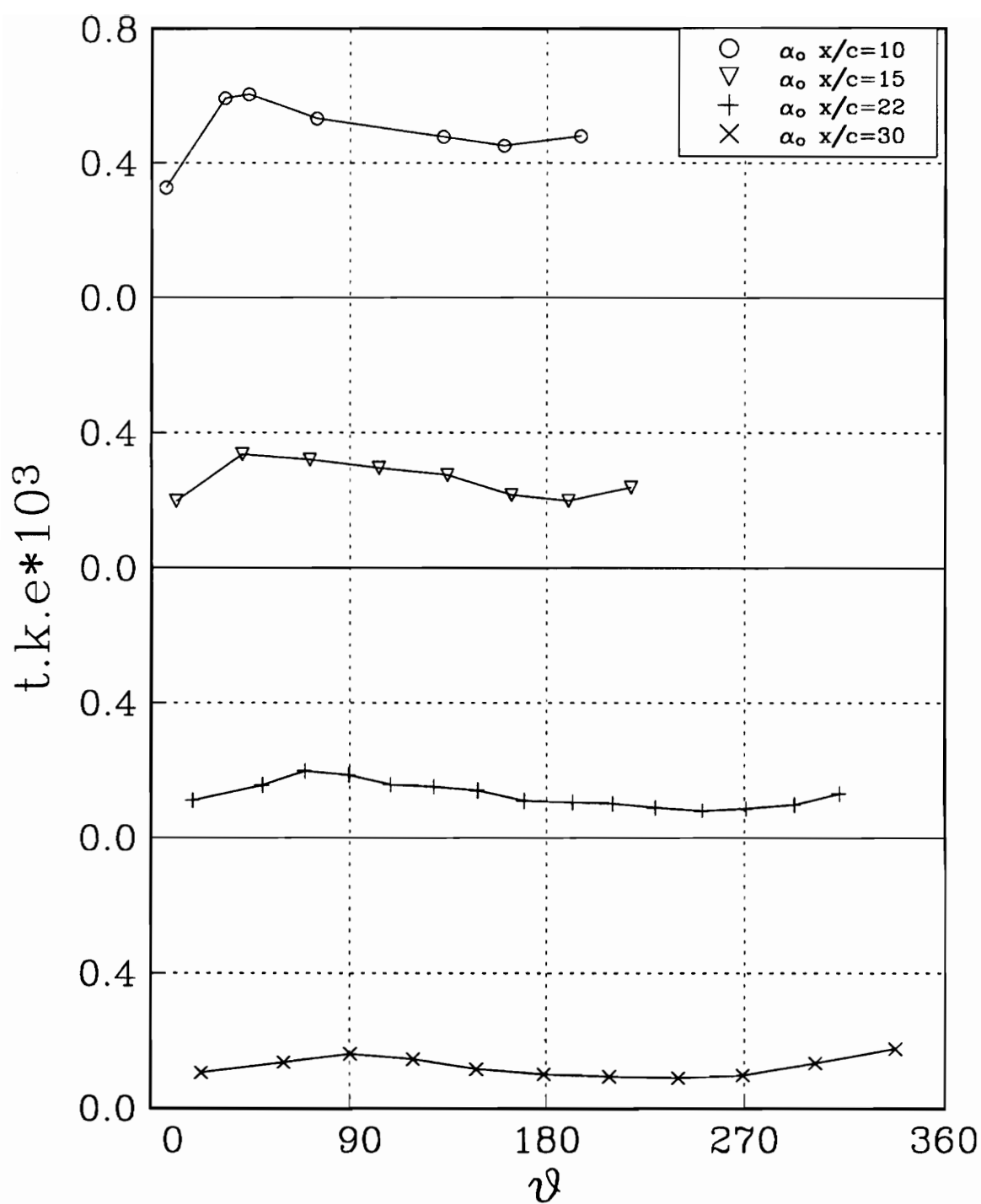


Figure 182. Turbulent kinetic energy in the wake centerline for the co-rotating pairs.

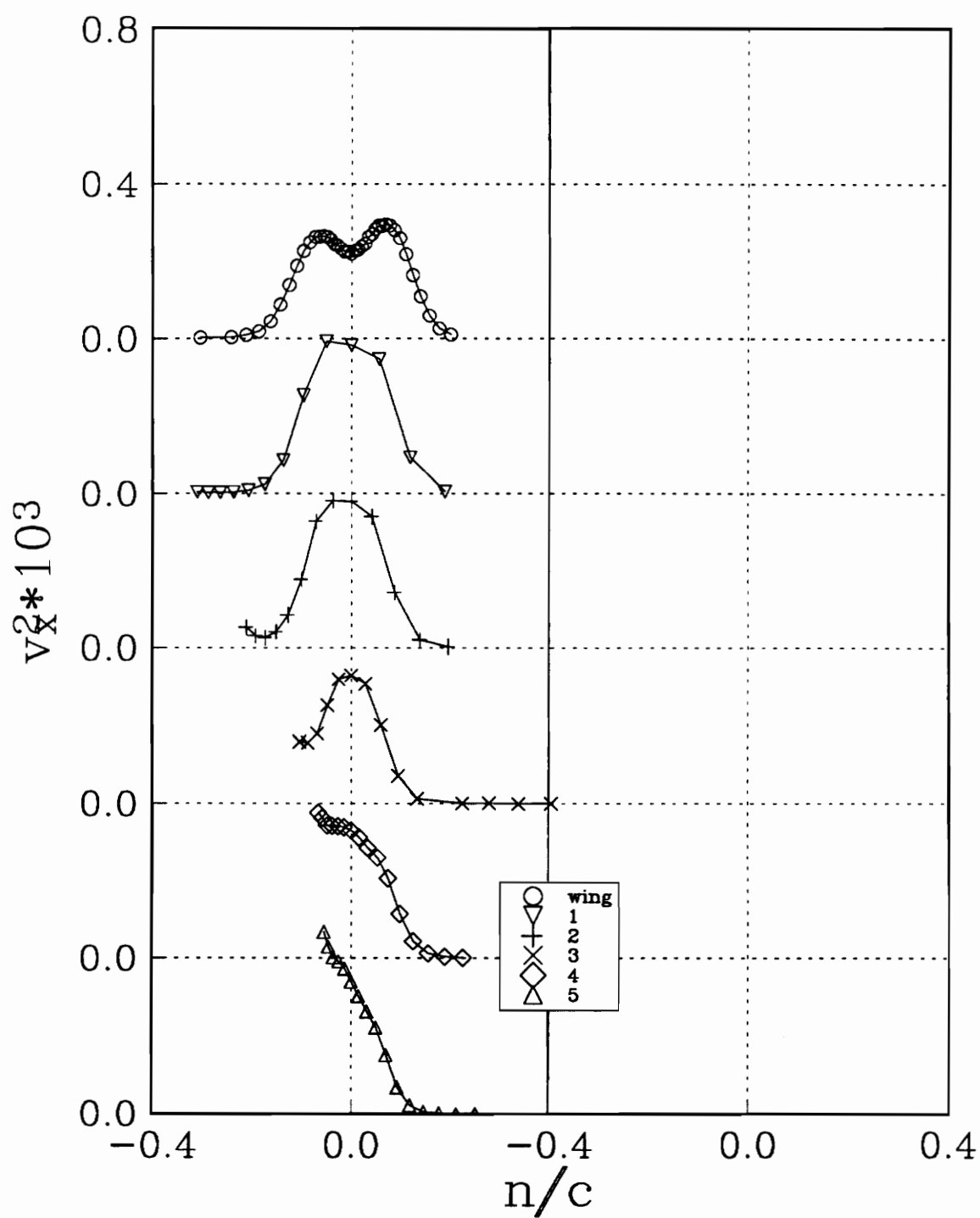


Figure 183a. v_x^2 profiles for the co-rotating case at $x/c=10$. Stations are indicated in figure 181.

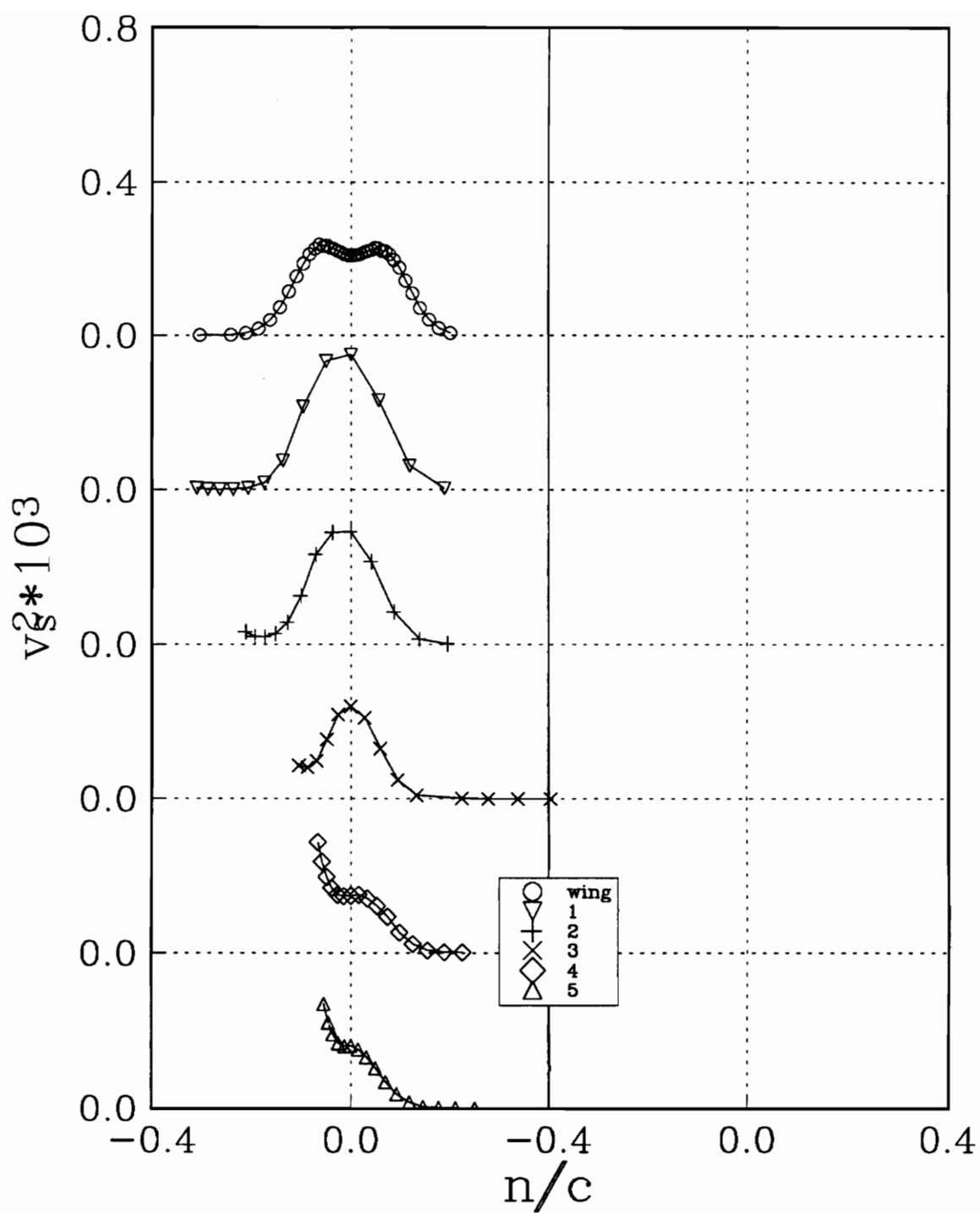


Figure 183b. v_s^2 profiles for the co-rotating case at $x/c=10$. Stations are indicated in figure 181.

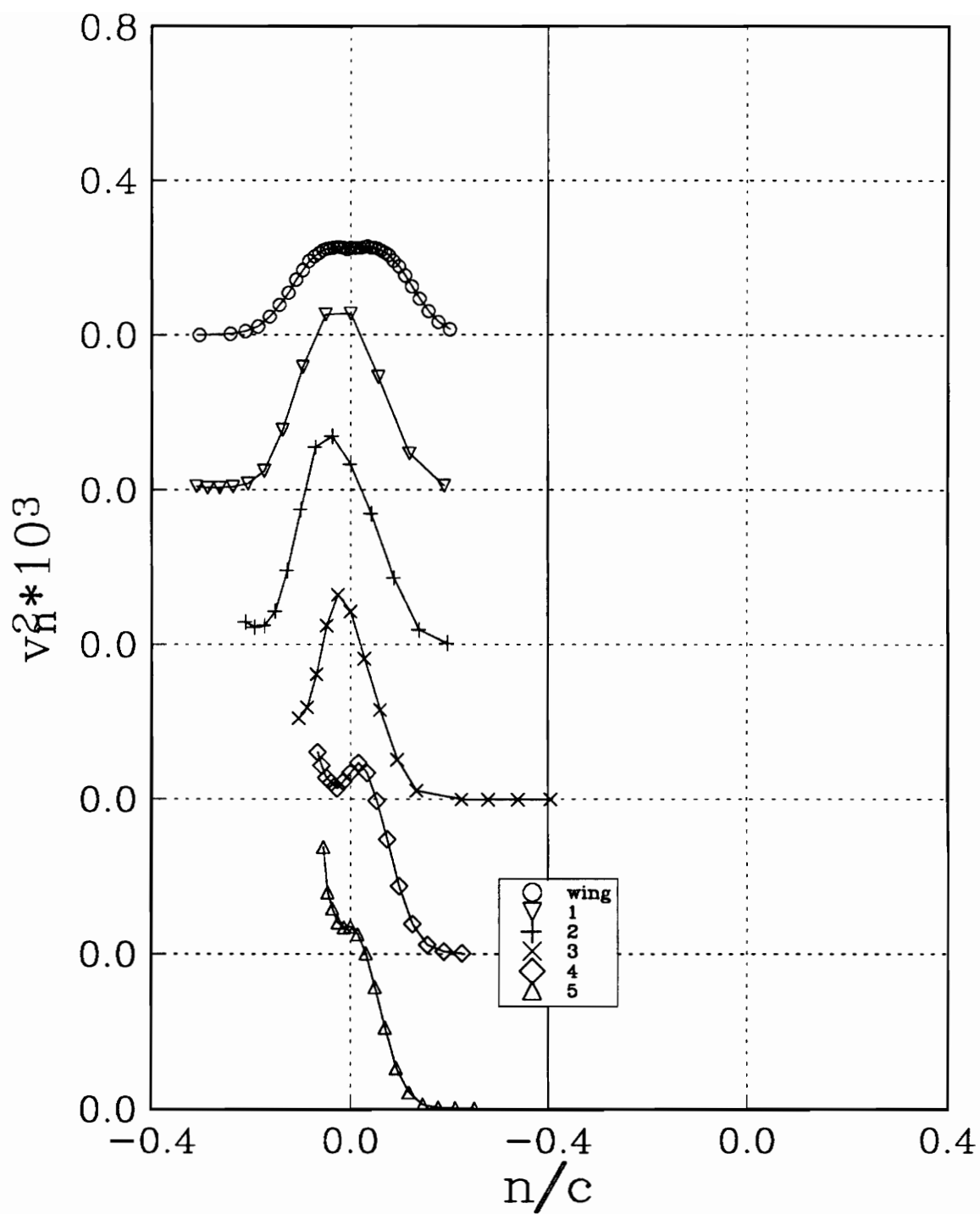


Figure 183c. v_n^2 profiles for the co-rotating case at $x/c=10$. Stations are indicated in figure 181.

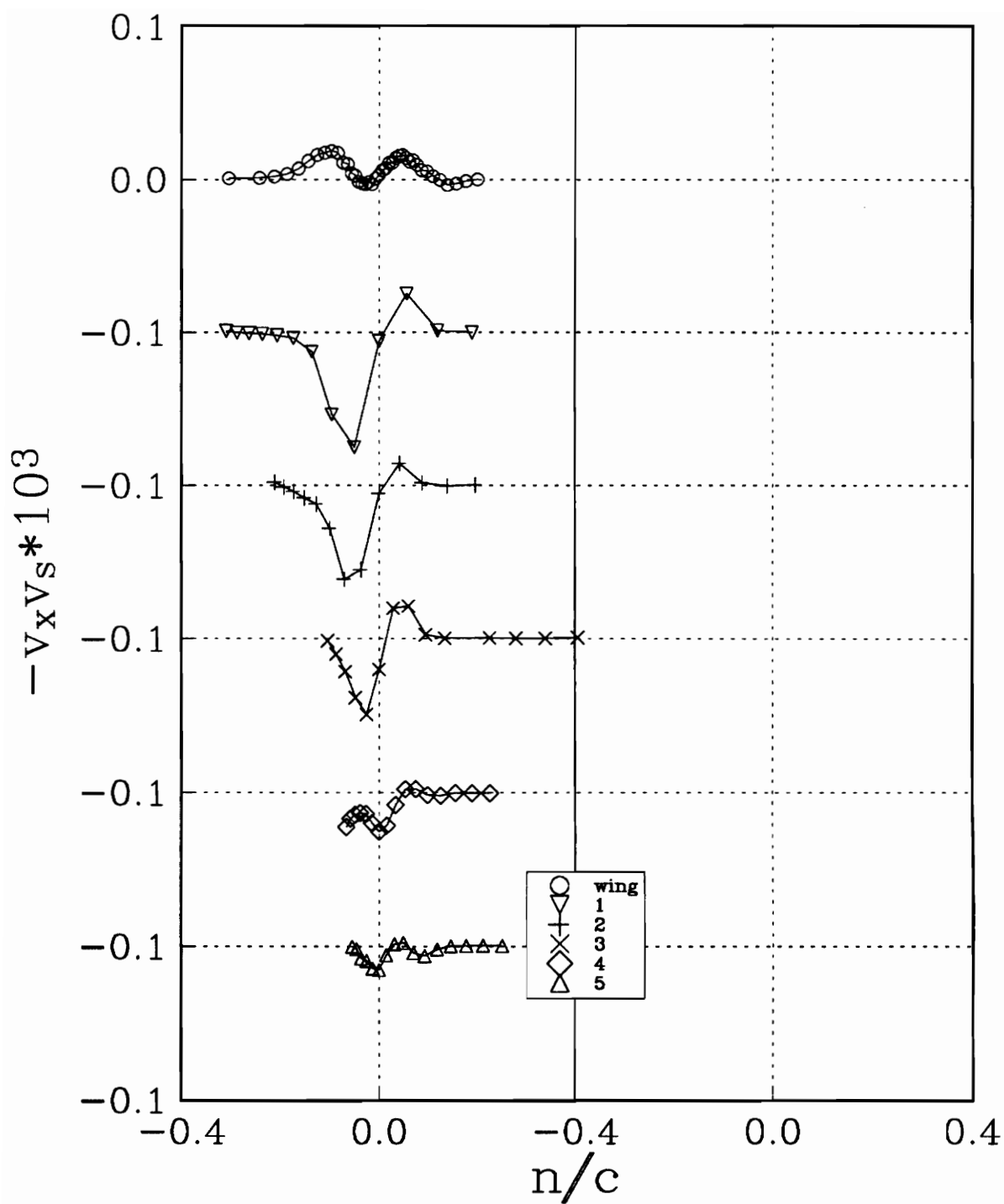


Figure 183d. $v_x v_s$ profiles for the co-rotating case at $x/c=10$. Stations are indicated in figure 181.

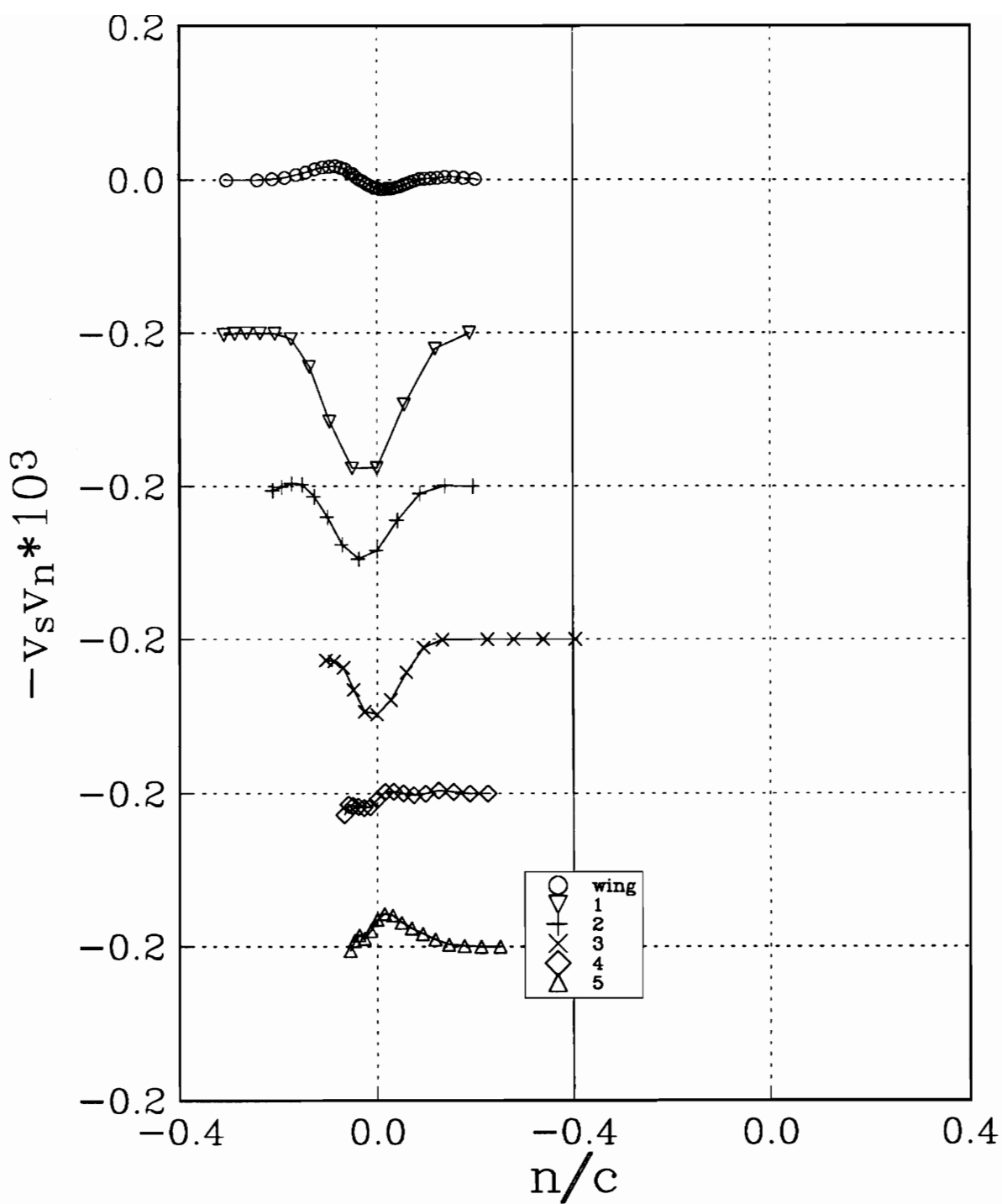


Figure 183e. $v_s v_n$ profiles for the co-rotating case at $x/c=10$. Stations are indicated in figure 181.

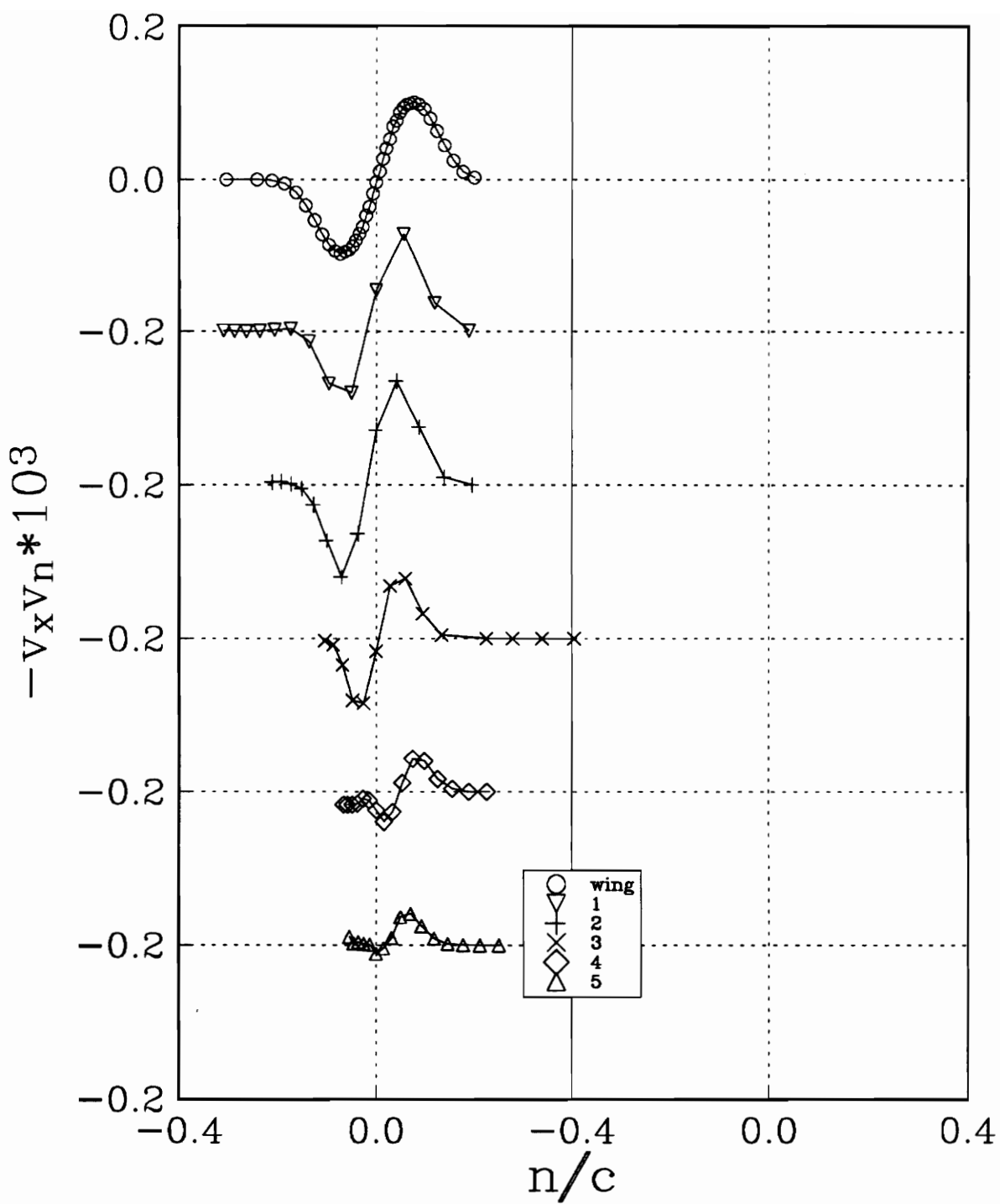


Figure 183f. $v_x v_n$ profiles for the co-rotating case at $x/c=10$. Stations are indicated in figure 181.

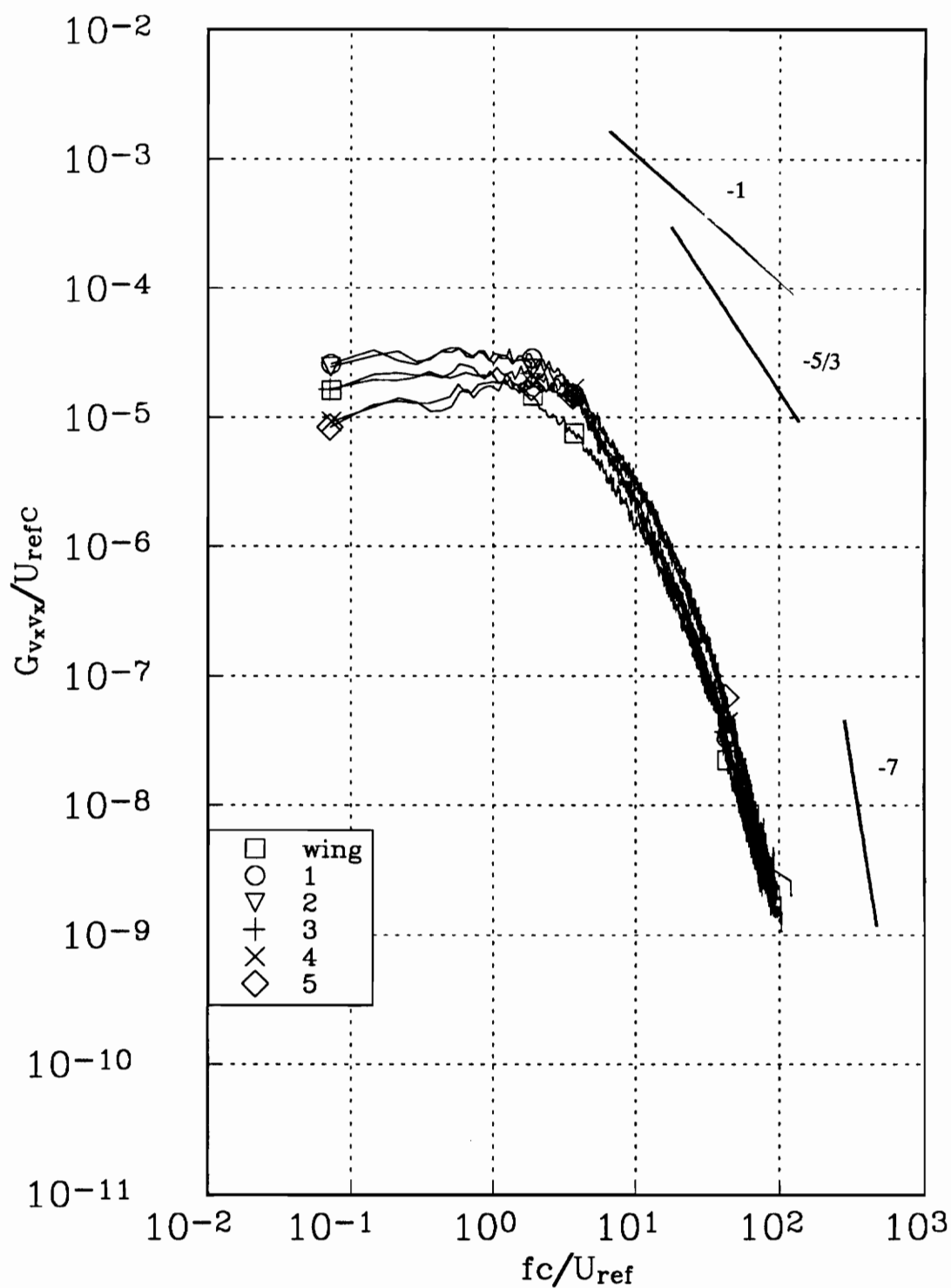


Figure 184a. v_x autospectra in the center of the wake for the co-rotating case at $x/c=10$. Stations are indicated in figure 181.

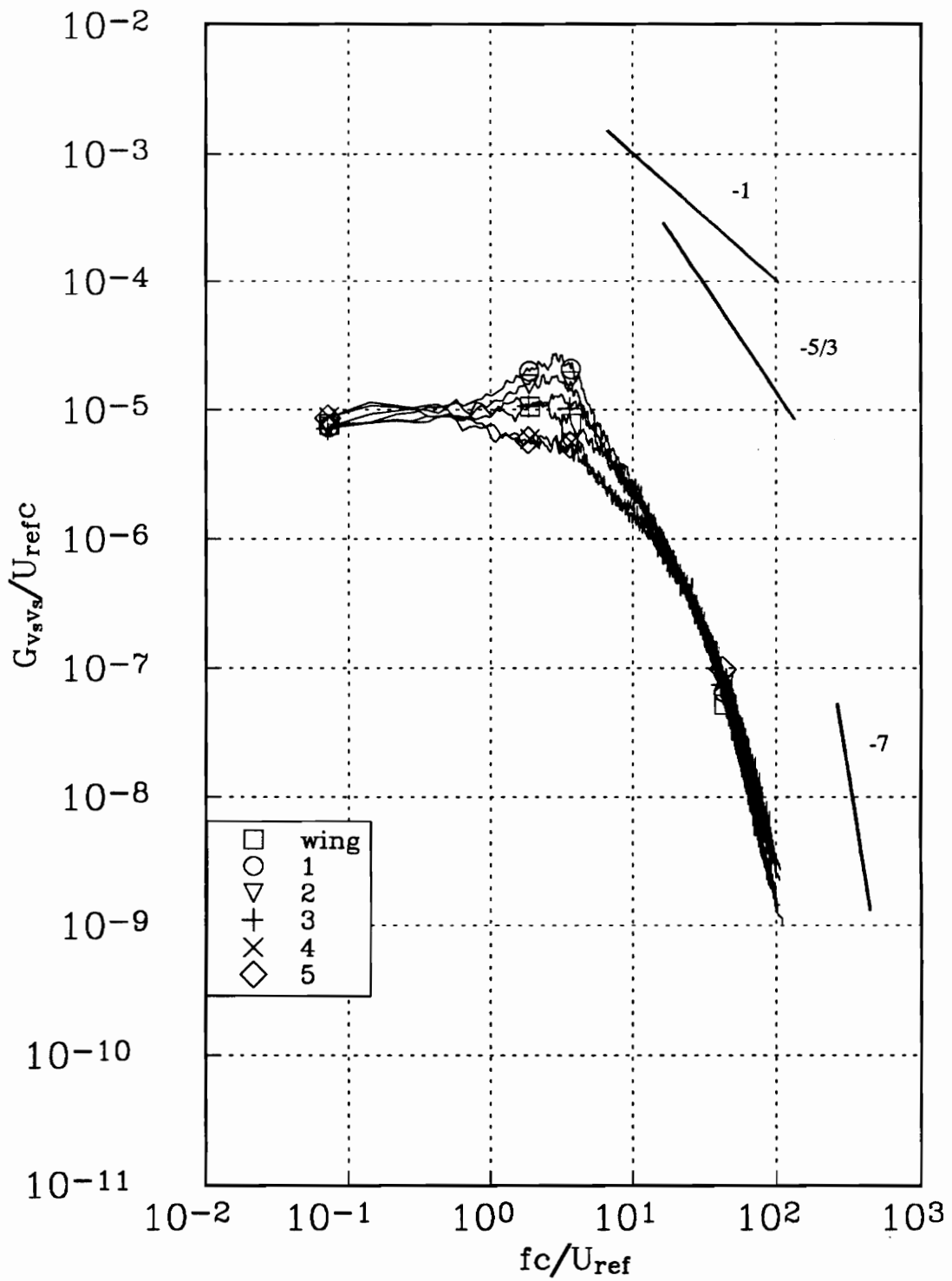


Figure 184b. v_s autospectra in the center of the wake for the co-rotating case at $x/c=10$. Stations are indicated in figure 181.

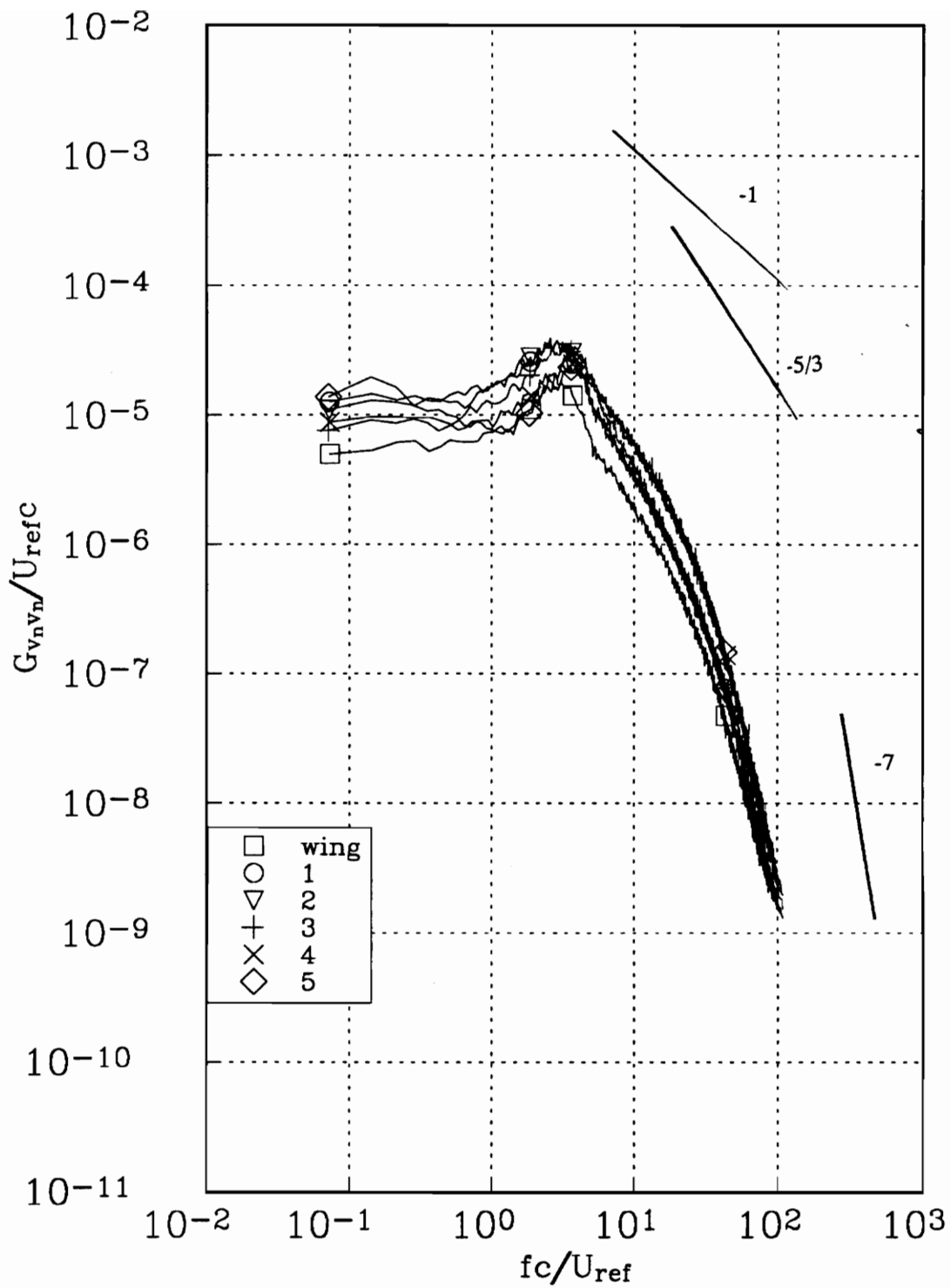


Figure 184c. v_n autospectra in the center of the wake for the co-rotating case at $x/c=10$. Stations are indicated in figure 181.

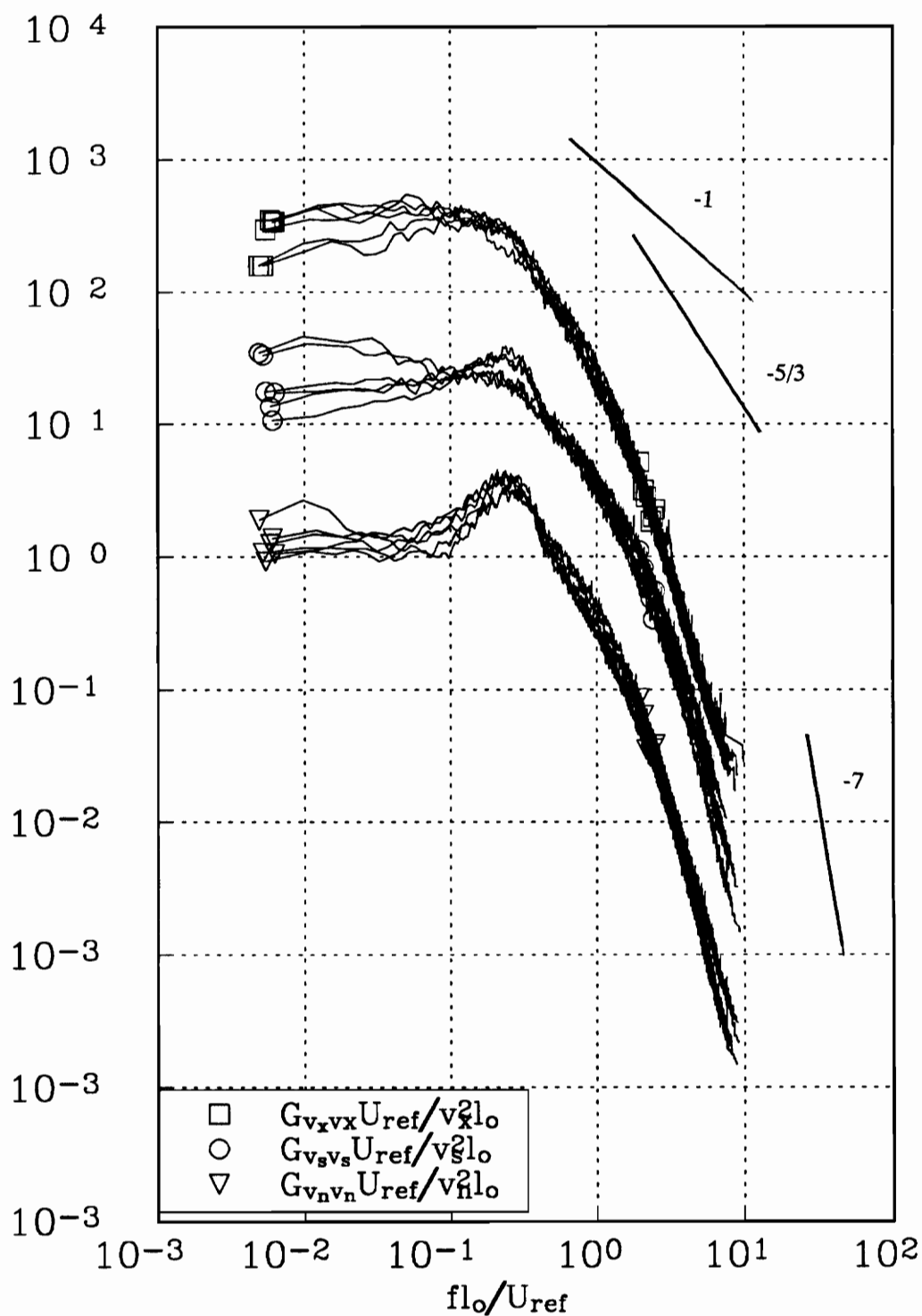


Figure 185. Autospectra in the center of the wake for the co-rotating case at $x/c=10$. Normalized by the local wake length scale L_0 .

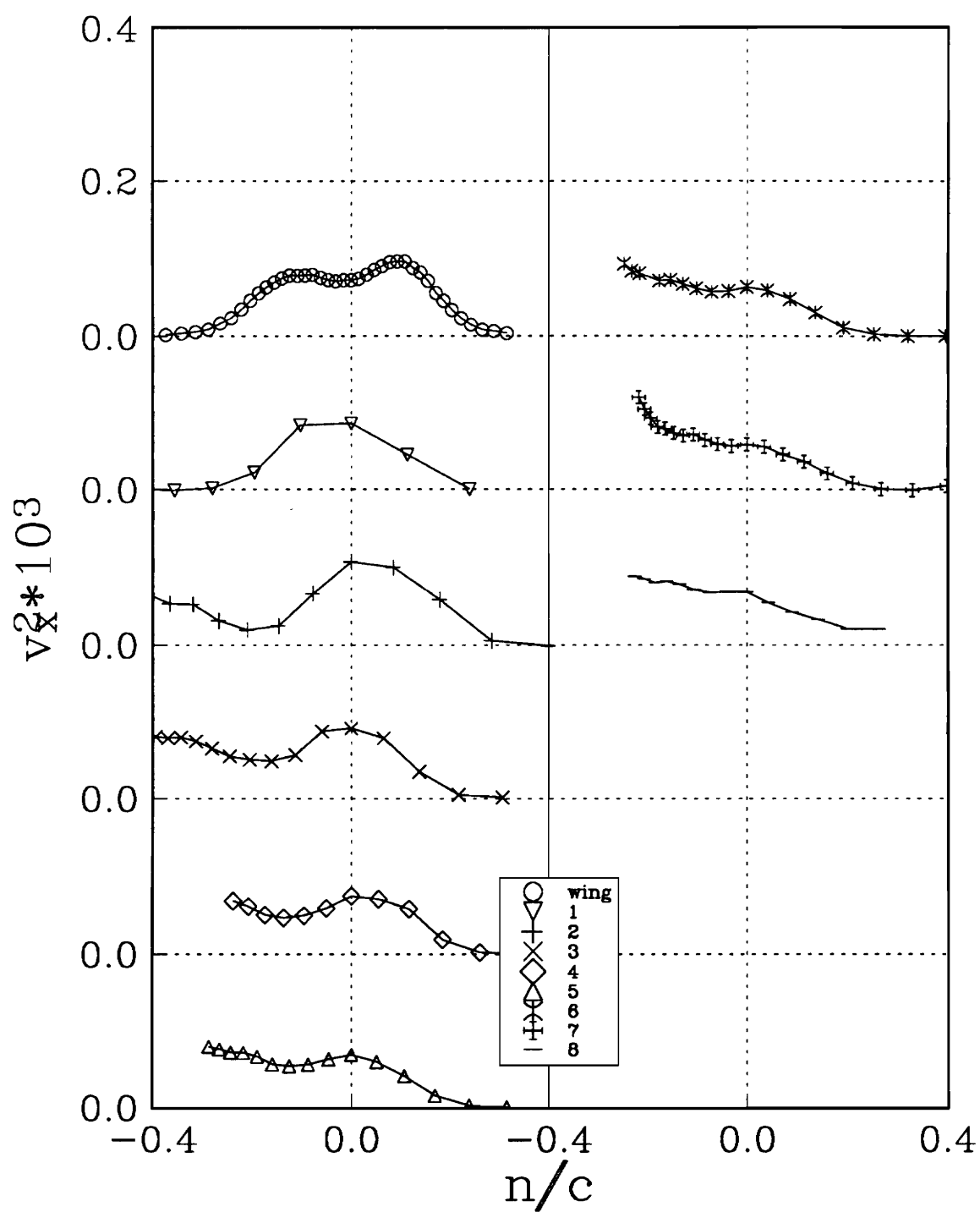


Figure 186a. v_x^2 profiles for the co-rotating case at $x/c=30$. Stations are indicated in figure 181.

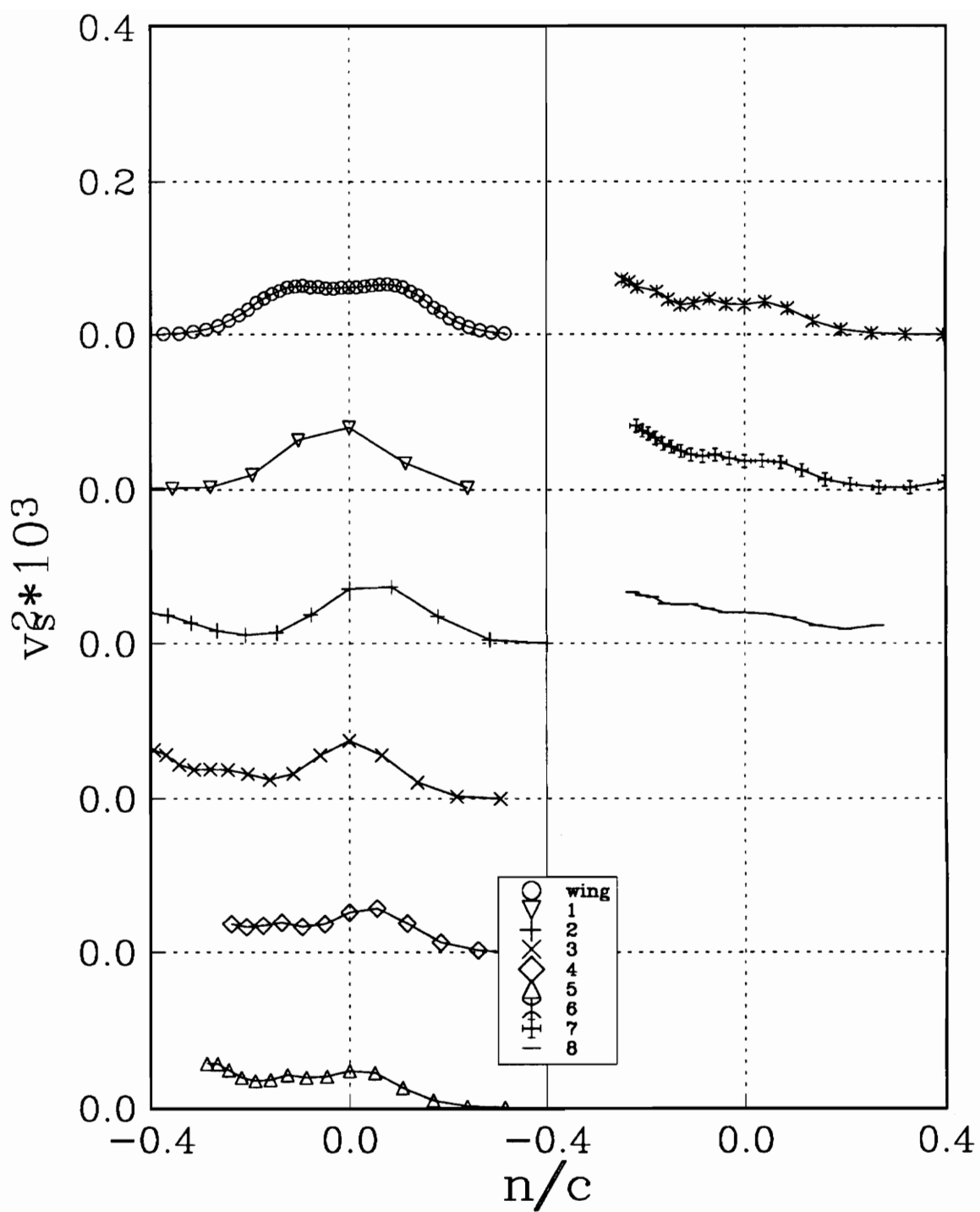


Figure 186b. v_s^2 profiles for the co-rotating case at $x/c=30$. Stations are indicated in figure 181.

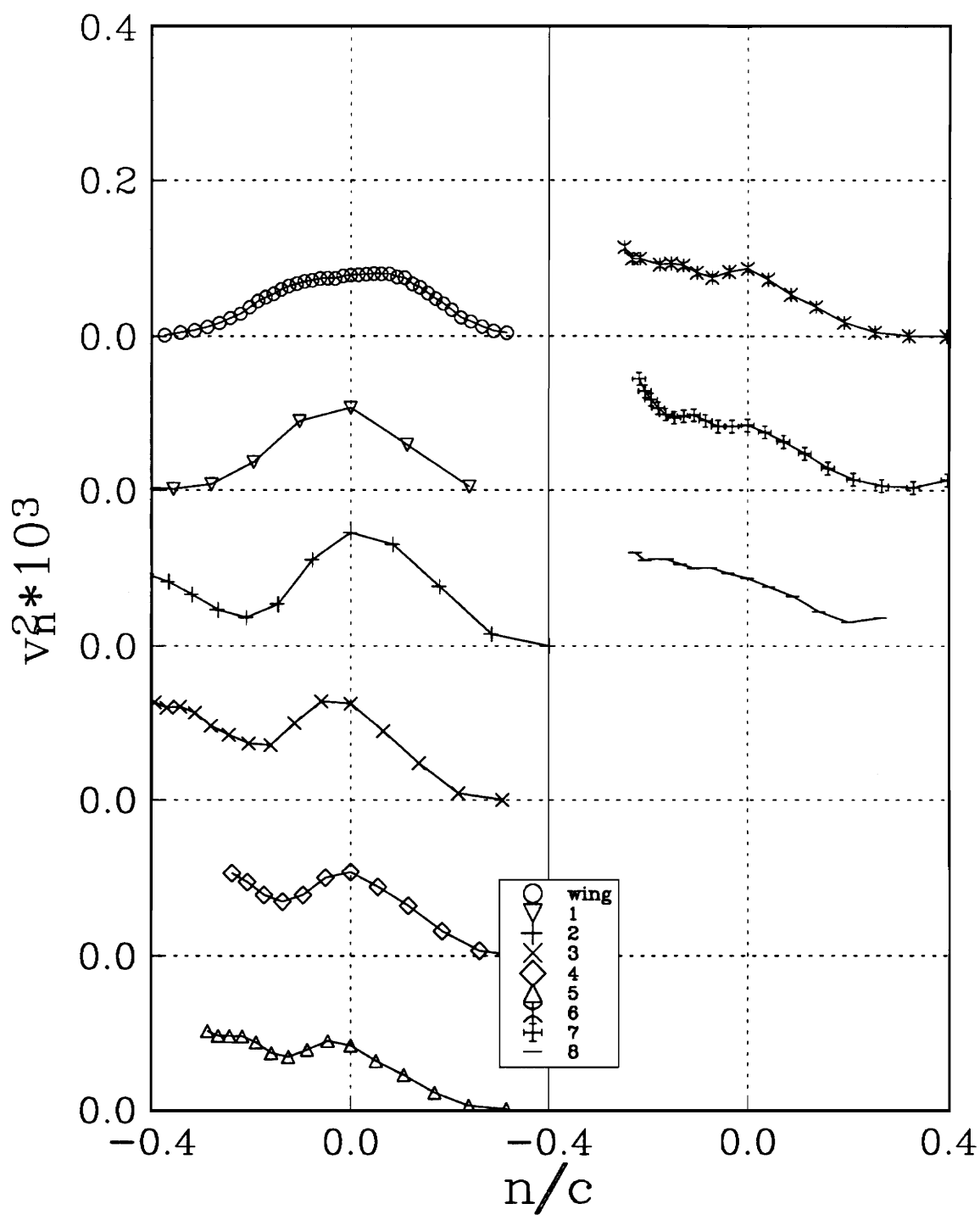


Figure 186c. v_n^2 profiles for the co-rotating case at $x/c=30$. Stations are indicated in figure 181.

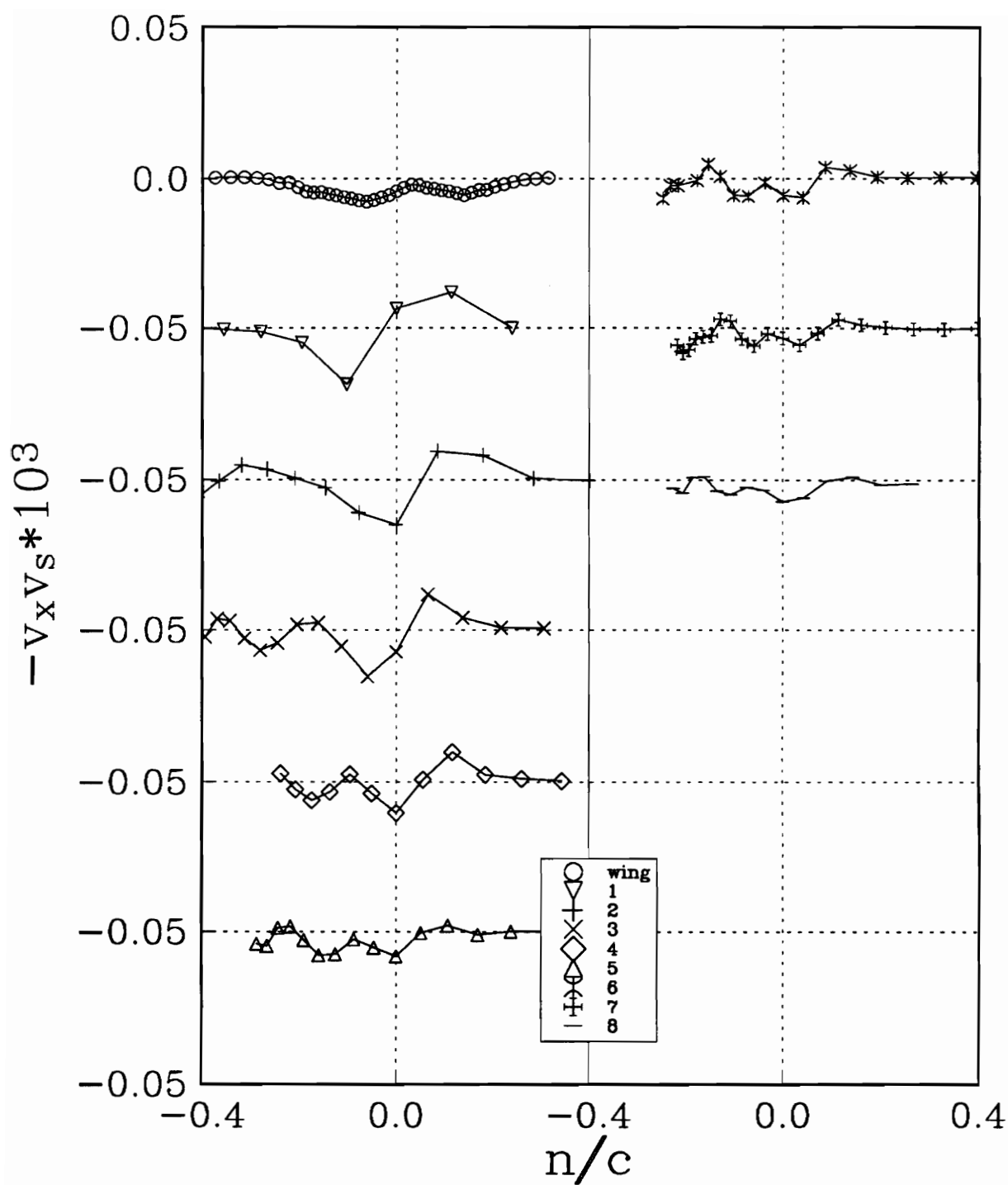


Figure 186d. $v_x v_s$ profiles for the co-rotating case at $x/c=30$. Stations are indicated in figure 181.

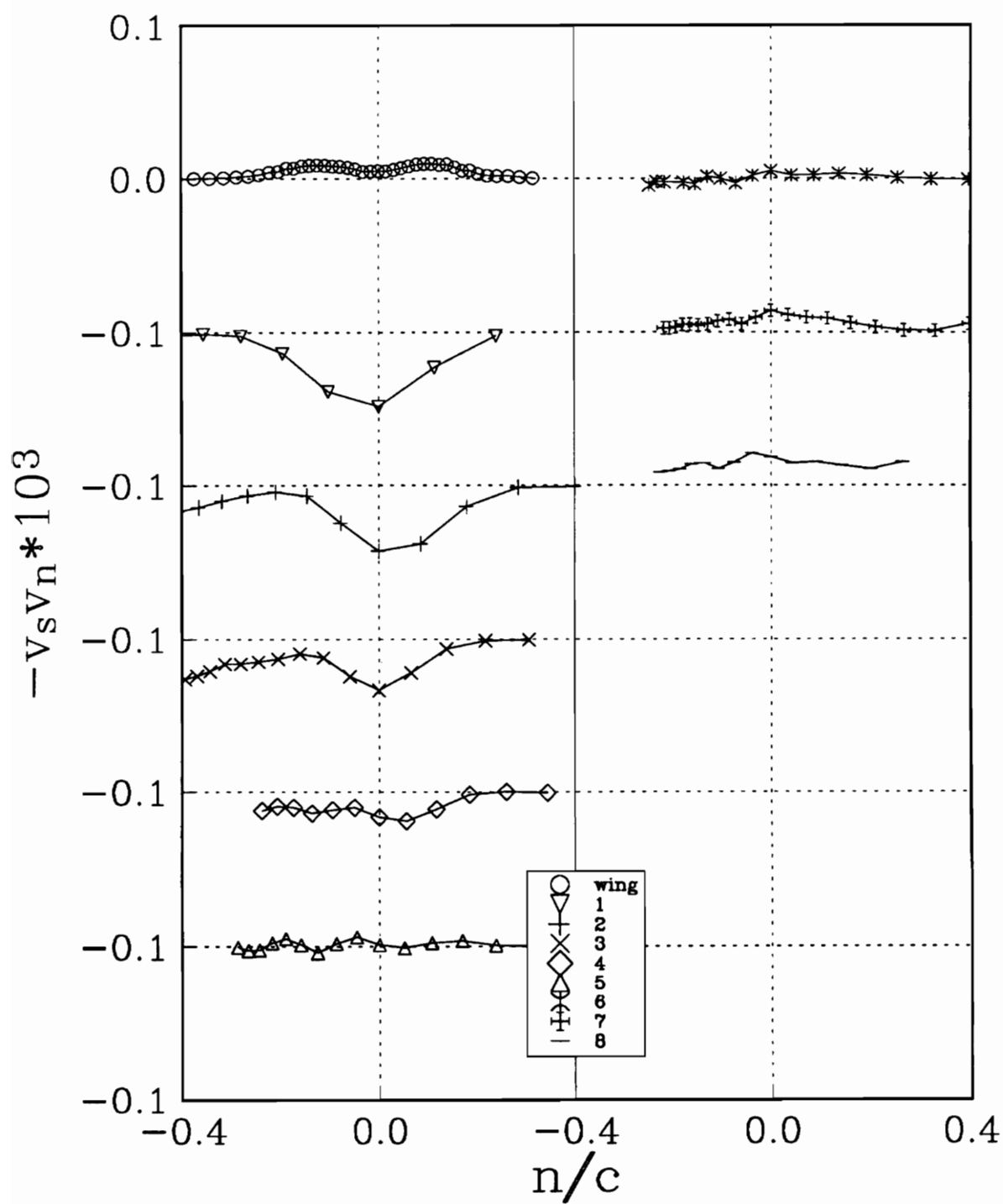


Figure 186e. $v_s v_n$ profiles for the co-rotating case at $x/c=30$. Stations are indicated in figure 181.

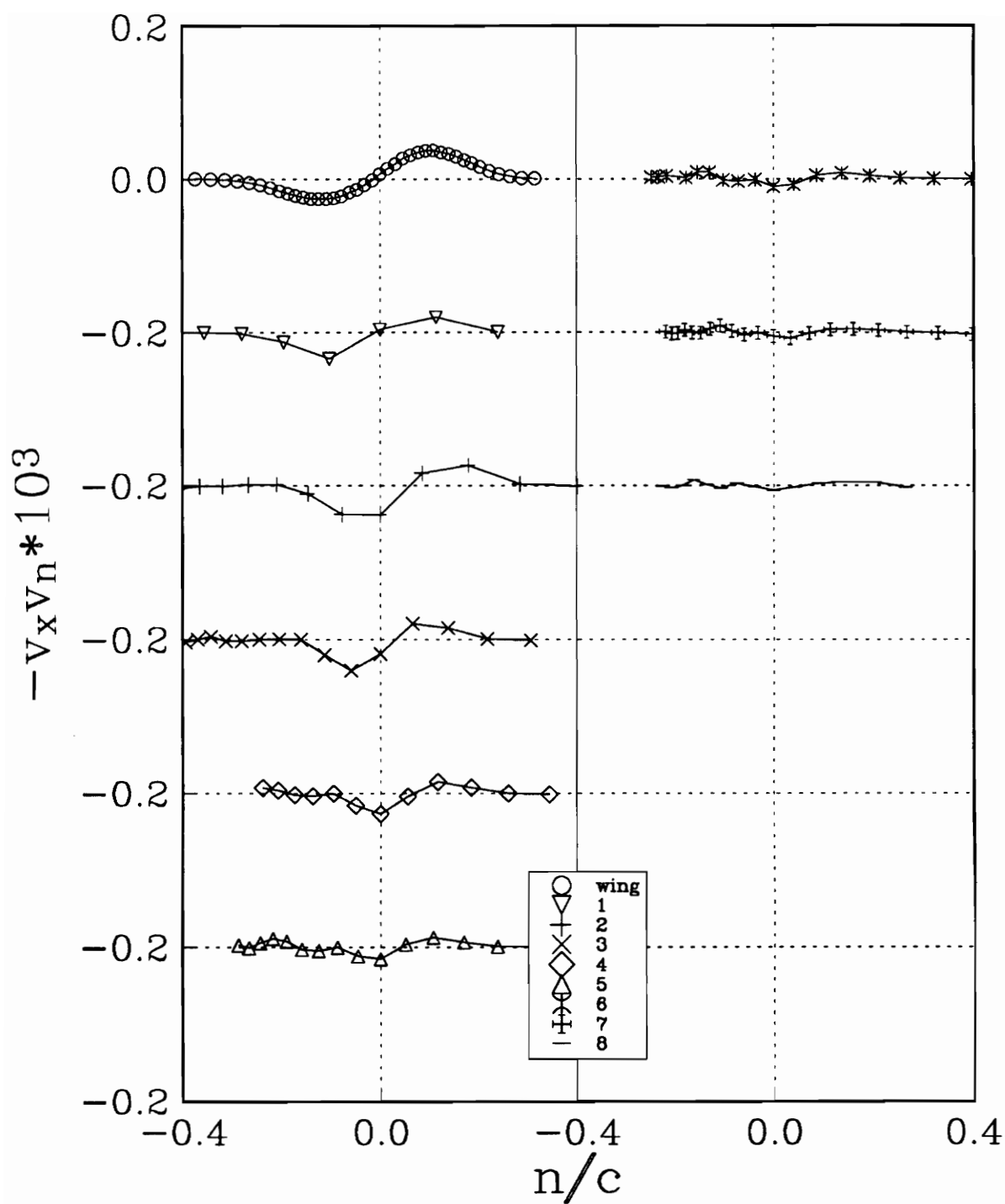


Figure 186f. $v_x v_n$ profiles for the co-rotating case at $x/c=30$. Stations are indicated in figure 181.

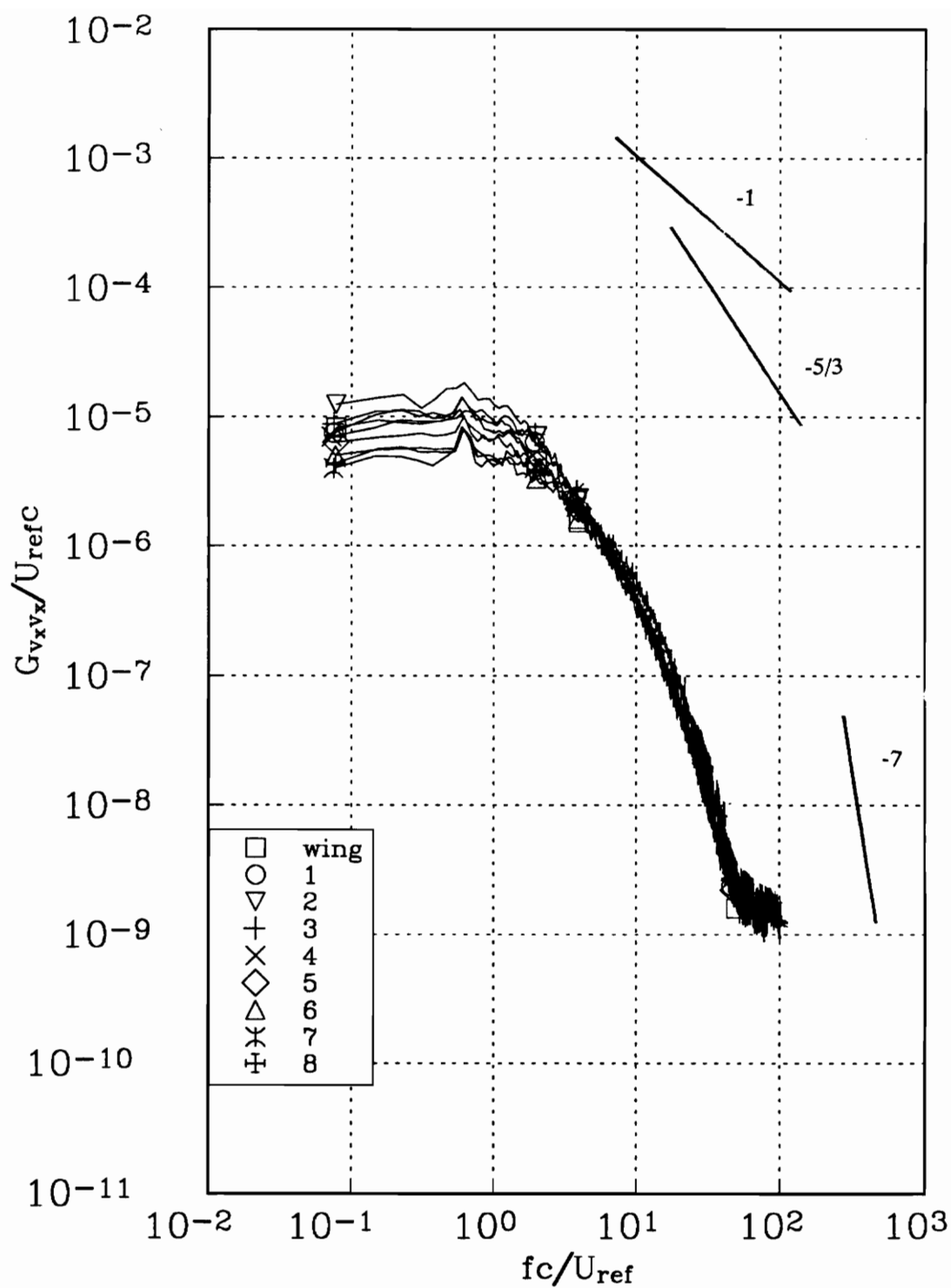


Figure 187a. v_x autospectra in the center of the wake for the co-rotating case at $x/c=30$. Stations are indicated in figure 181.

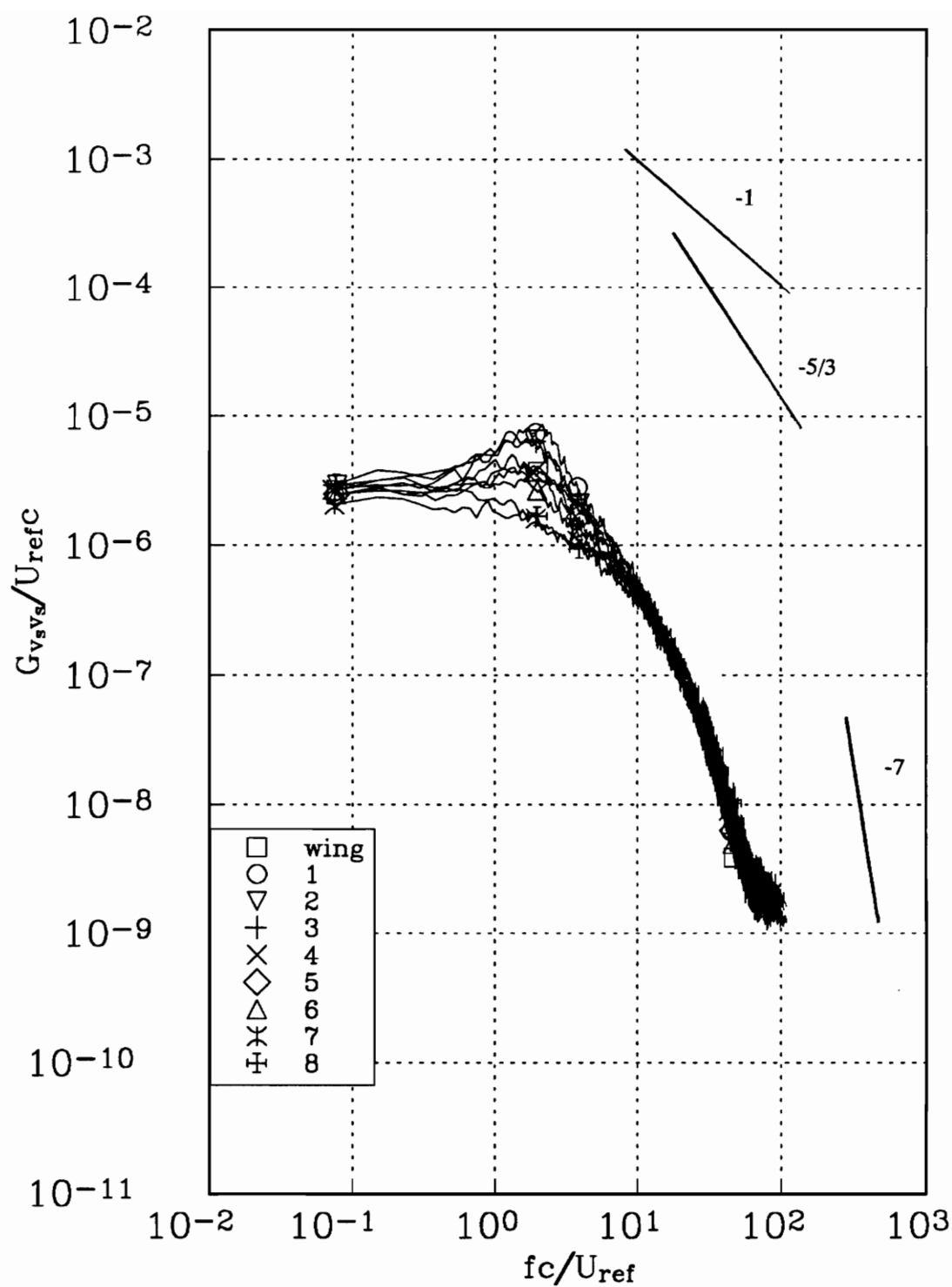


Figure 187b. v_s autospectra in the center of the wake for the co-rotating case at $x/c=30$. Stations are indicated in figure 181.

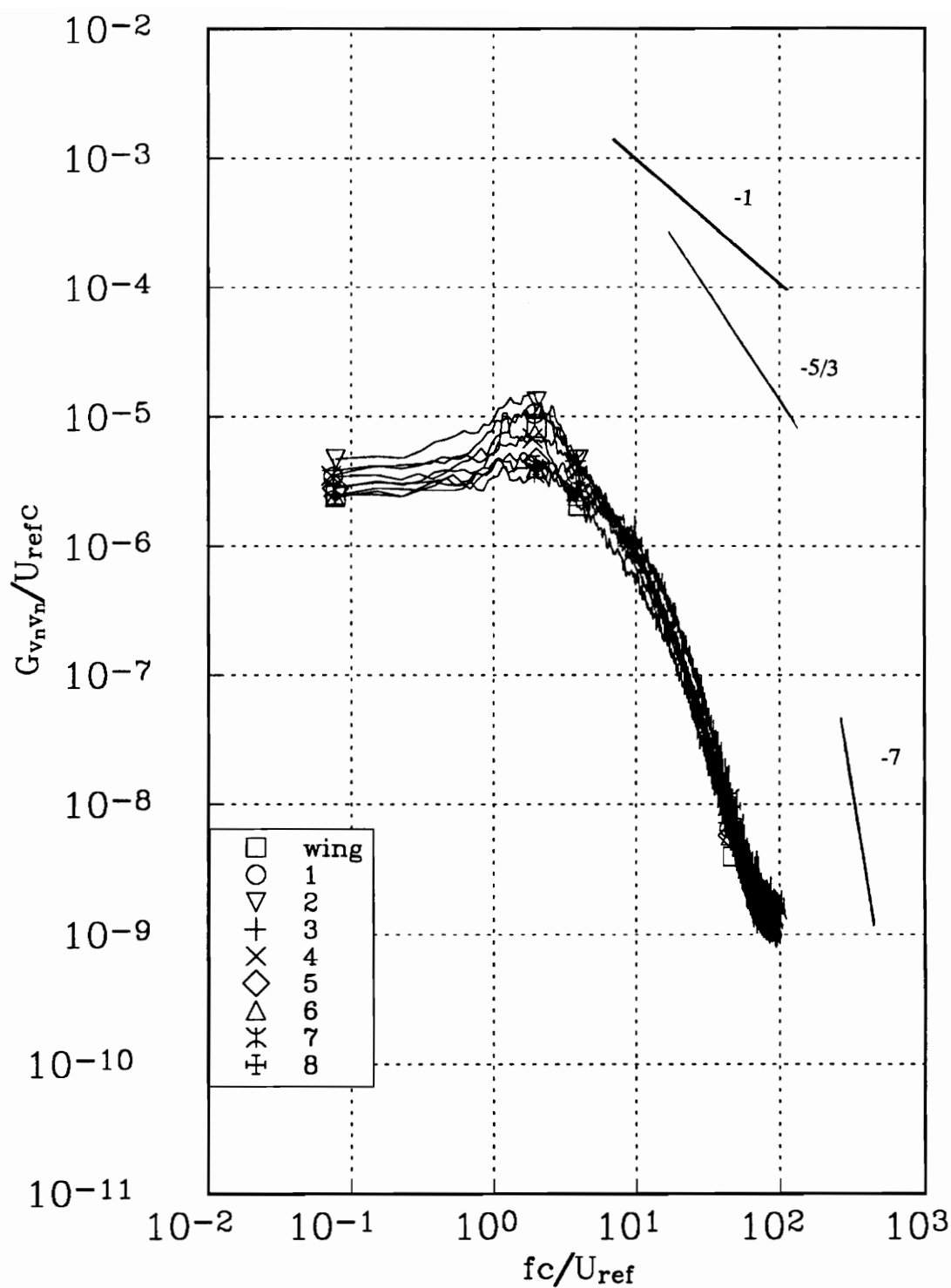


Figure 187c. v_n autospectra in the center of the wake for the co-rotating case at $x/c=30$. Stations are indicated in figure 181.

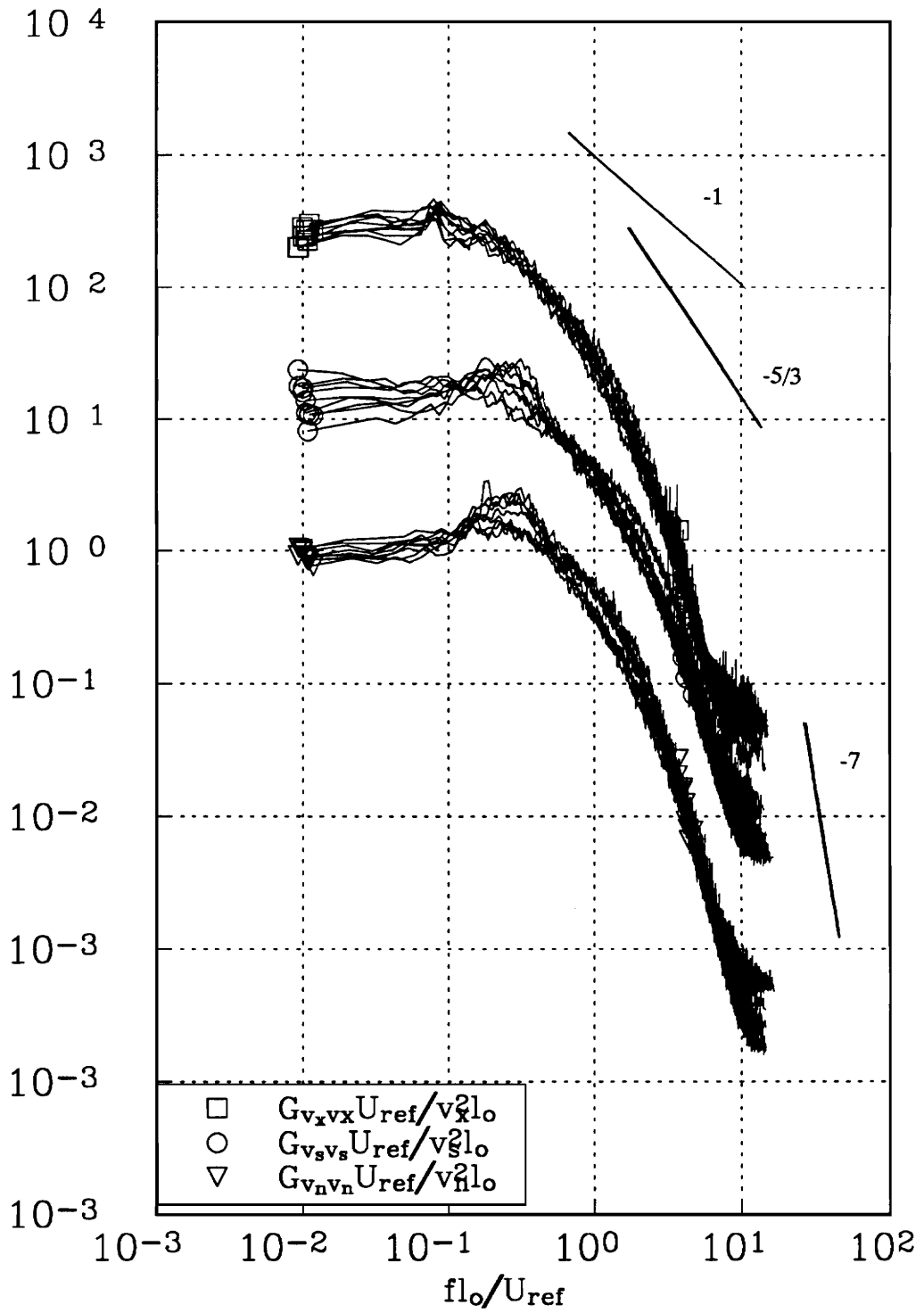


Figure 188. Autospectra in the center of the wake for the co-rotating case at $x/c=30$. Normalized by the local wake length scale L_0 .

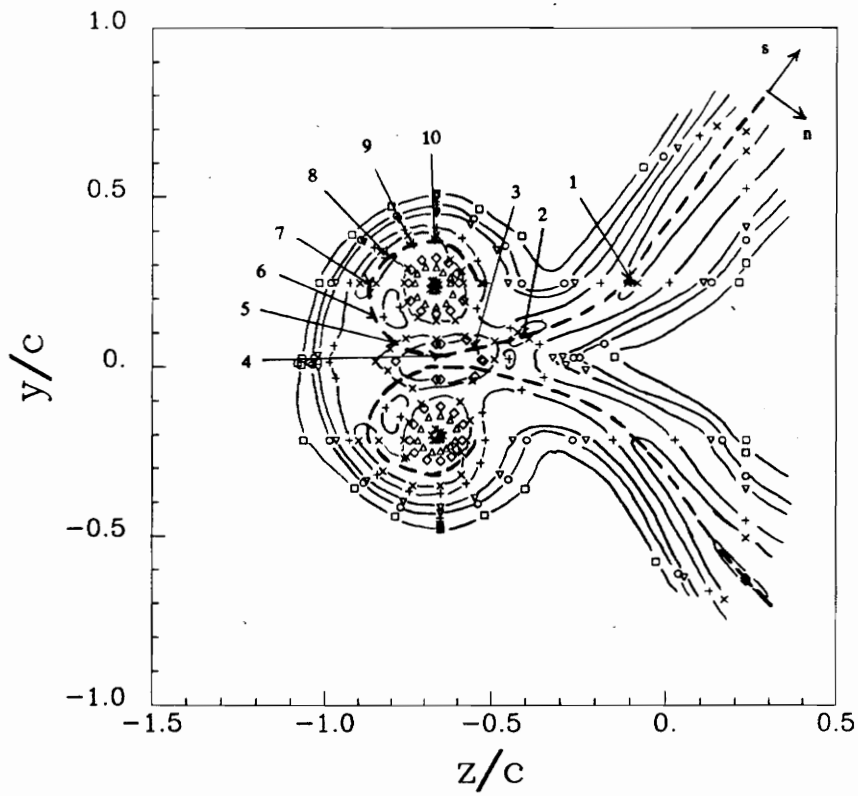


Figure 189. Turbulent kinetic energy contours showing shear layer coordinate system and representative stations for the counter rotating pair at $x/c=10$. Dotted line indicates center of spiral wake.

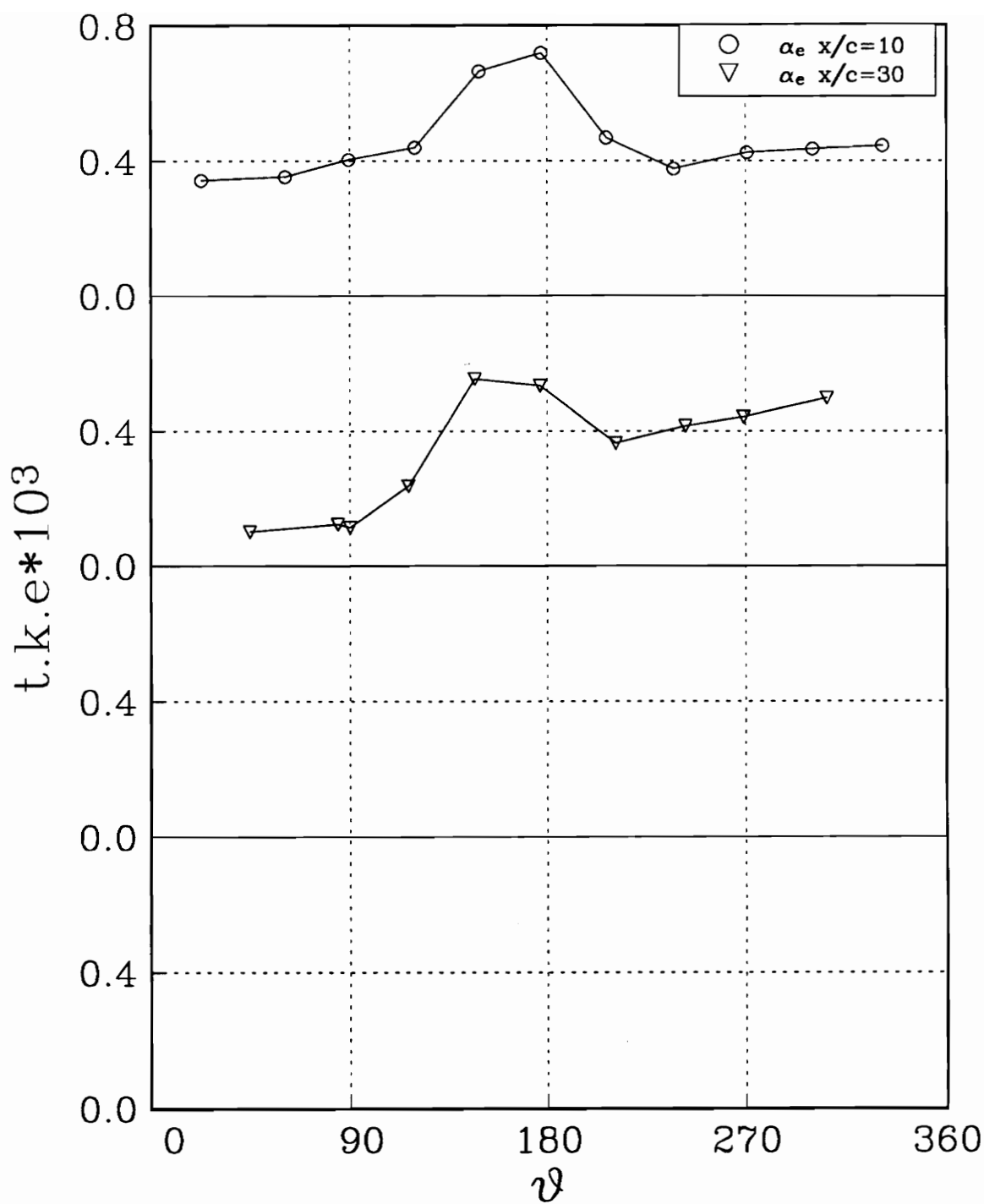


Figure 190. Turbulent kinetic energy in the wake centerline for the counter rotating pairs.

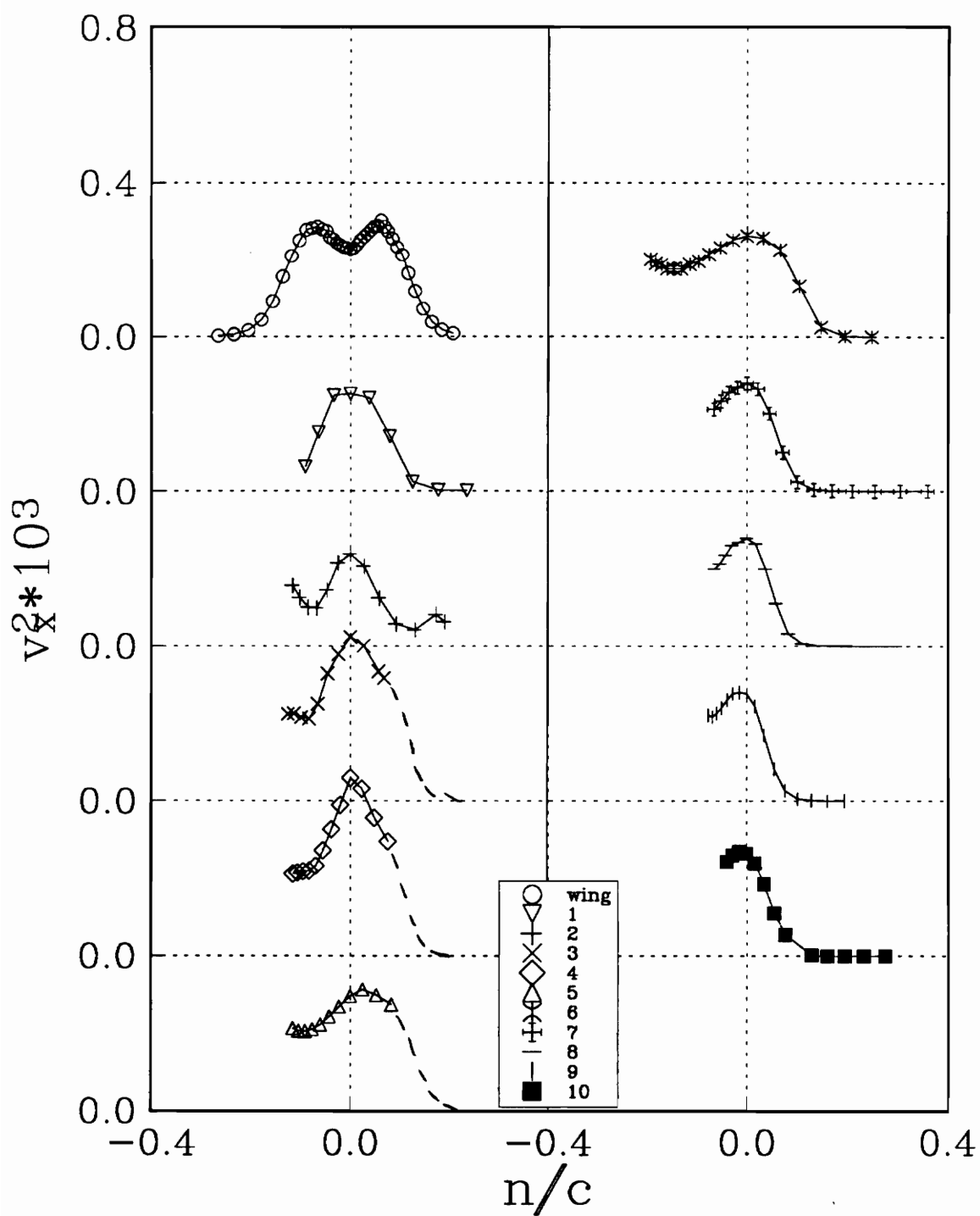


Figure 191a. v_x^2 profiles for the counter rotating case at $x/c=10$. Stations are indicated in figure 189.

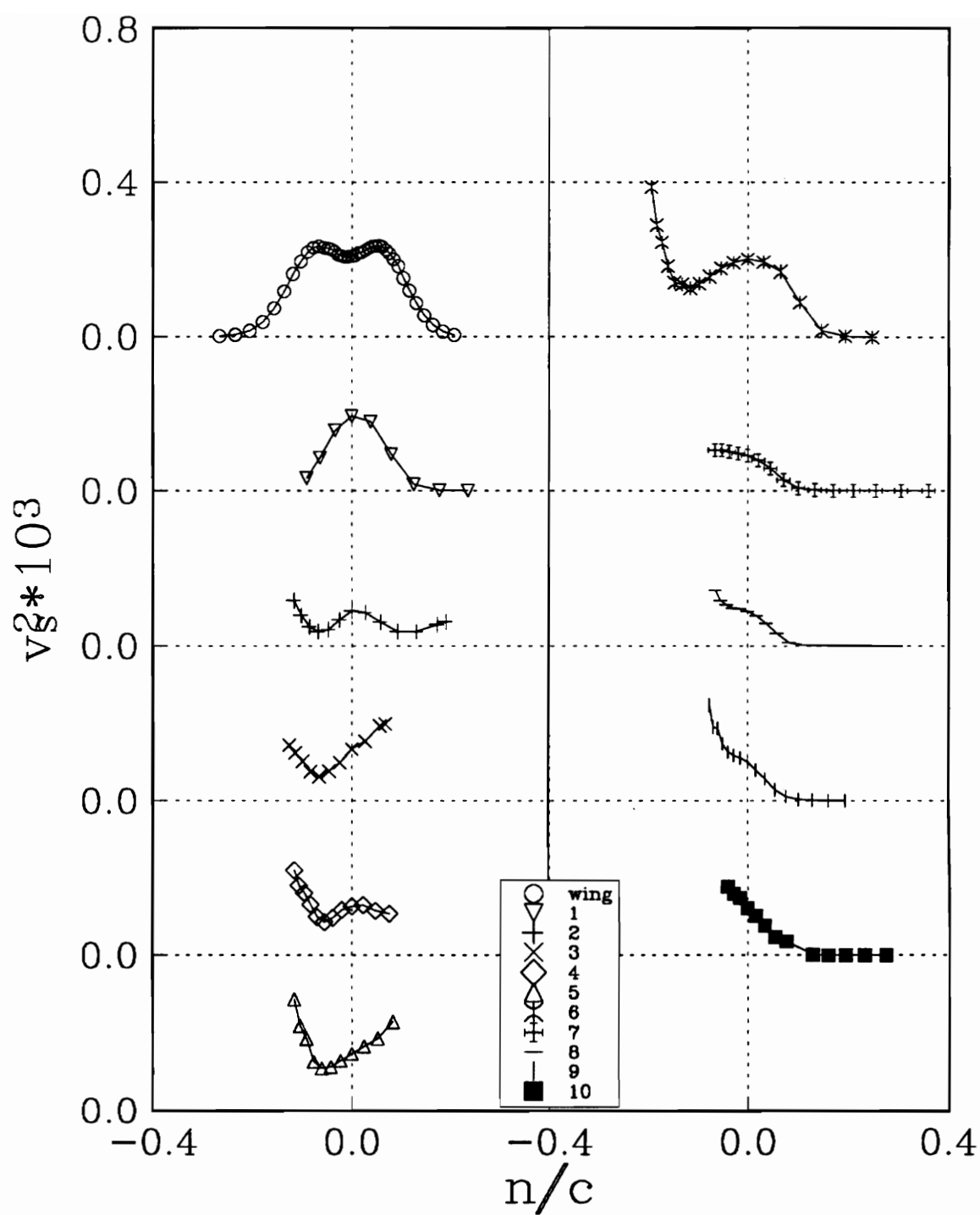


Figure 191b. v_s^2 profiles for the counter rotating case at $x/c=10$. Stations are indicated in figure 189.

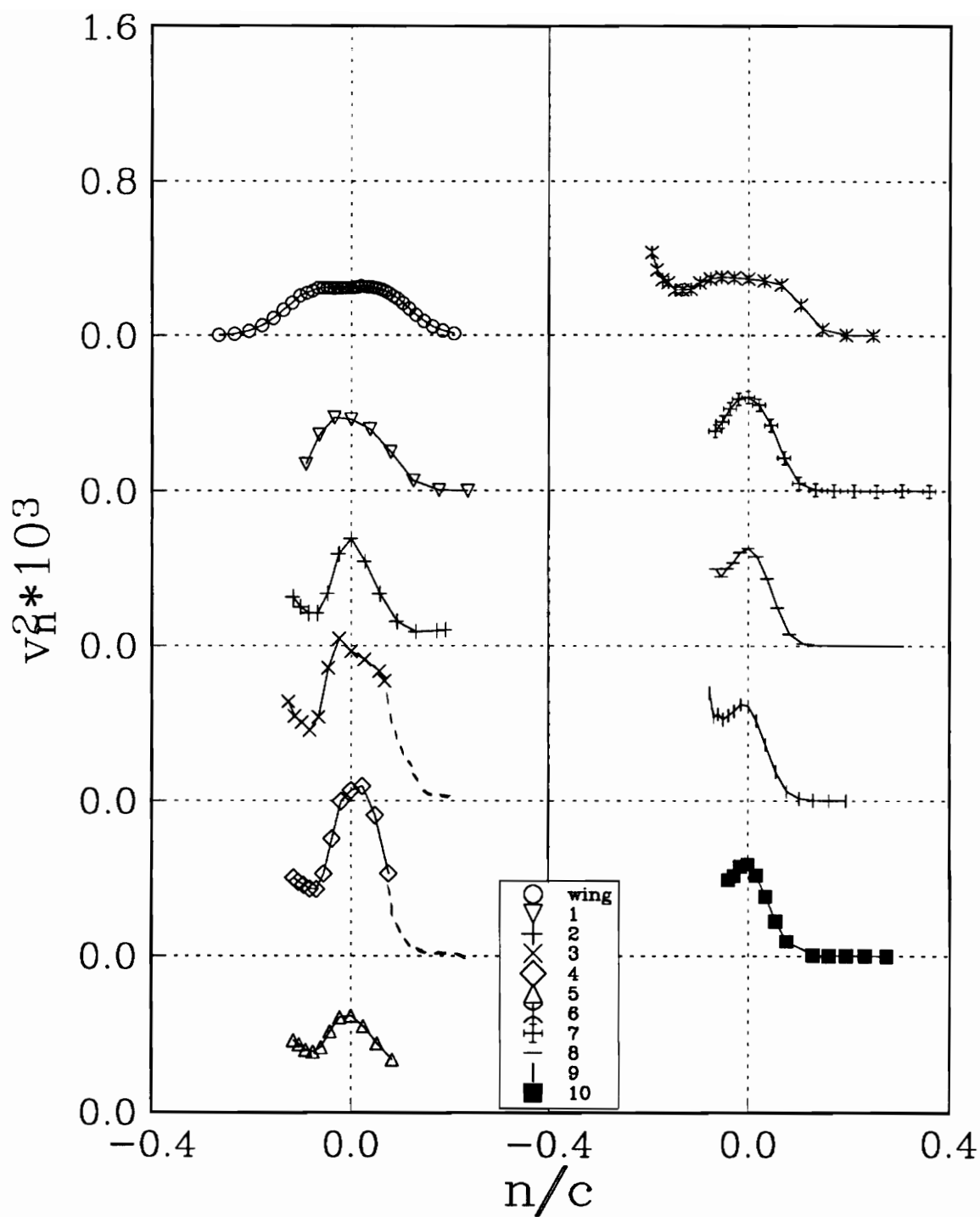


Figure 191c. v_n^2 profiles for the counter rotating case at $x/c=10$. Stations are indicated in figure 189.

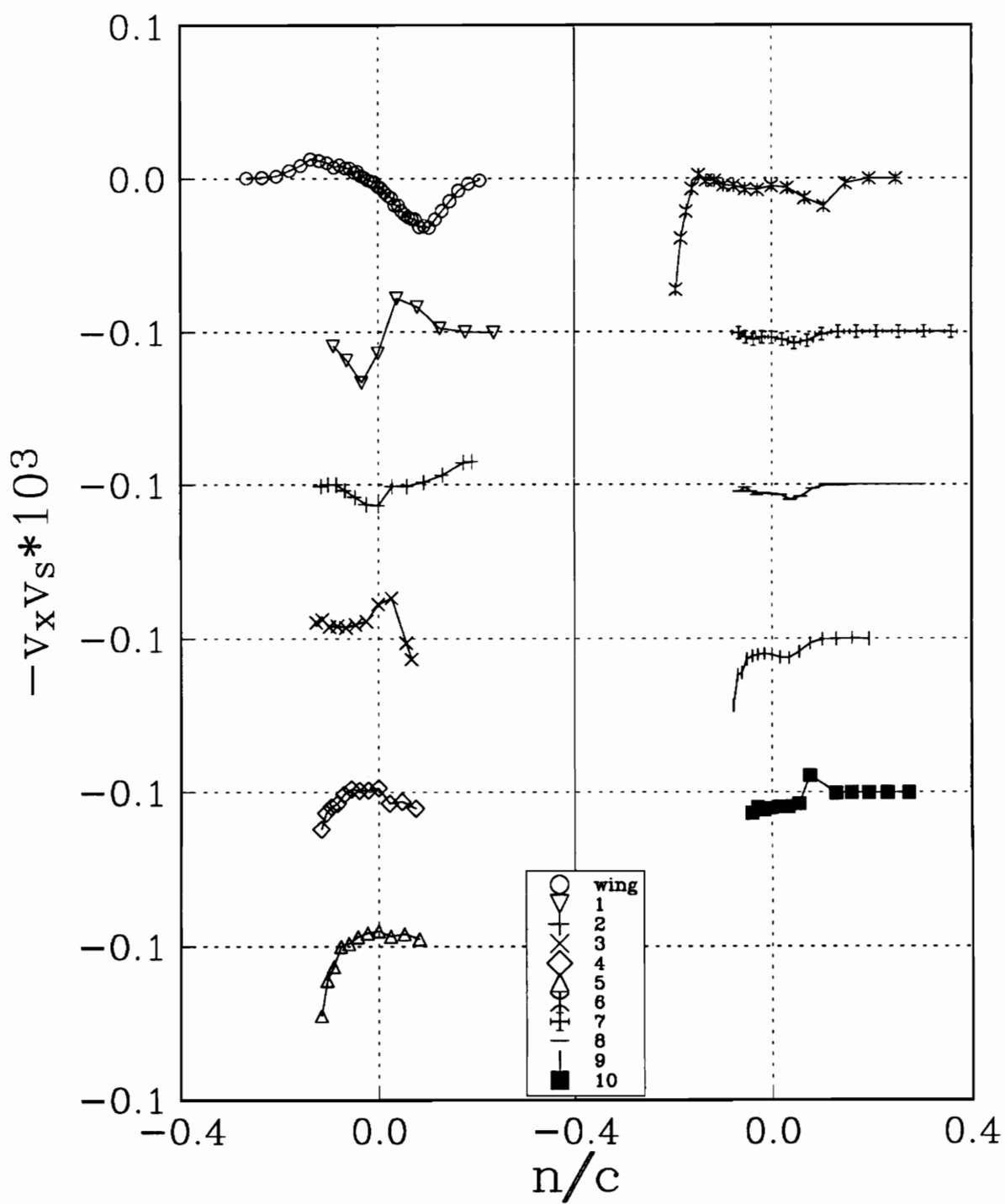


Figure 191d. $v_x v_s$ profiles for the counter rotating case at $x/c=10$. Stations are indicated in figure 189.

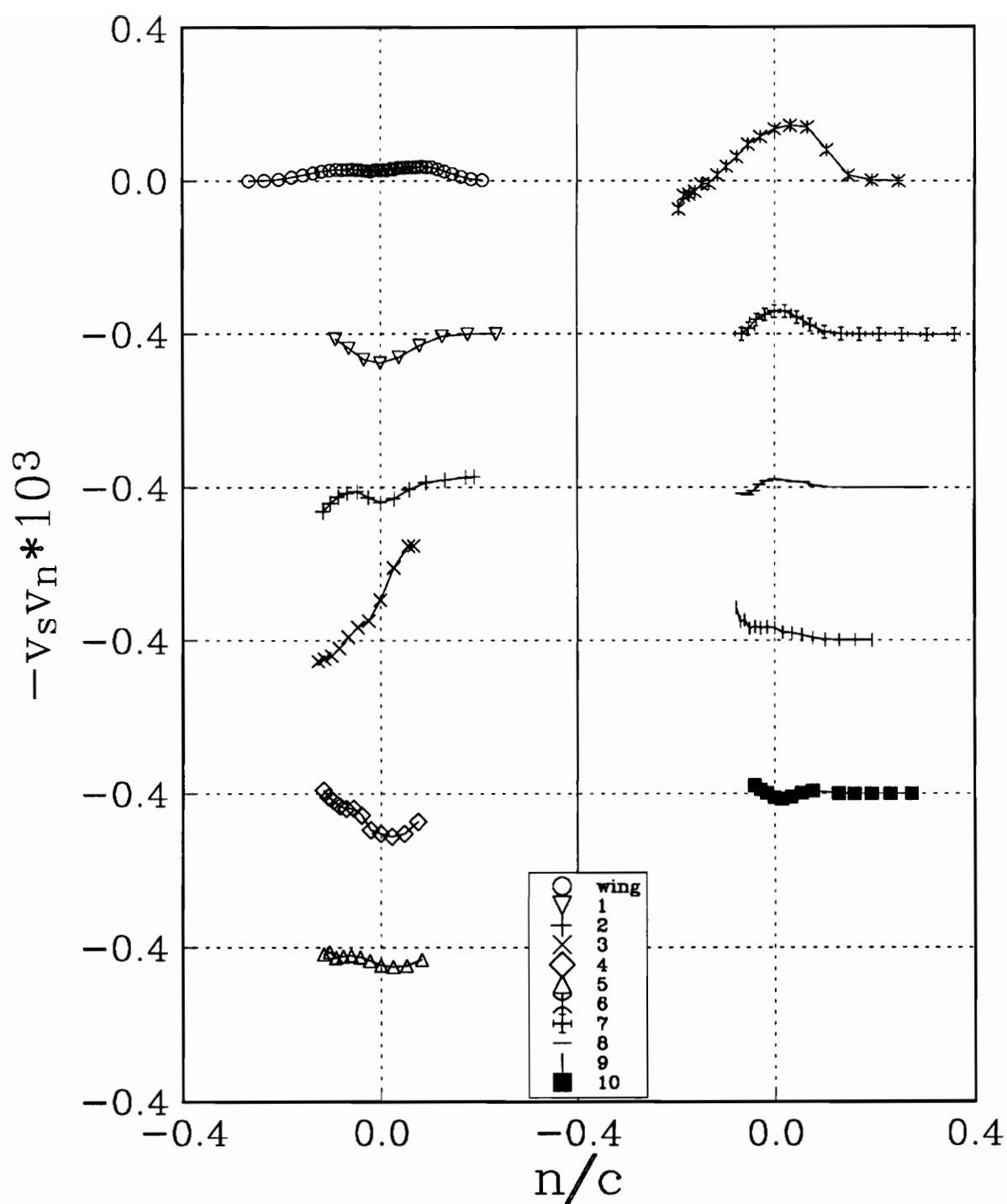


Figure 191e. $v_s v_n$ profiles for the counter rotating case at $x/c=10$. Stations are indicated in figure 189.

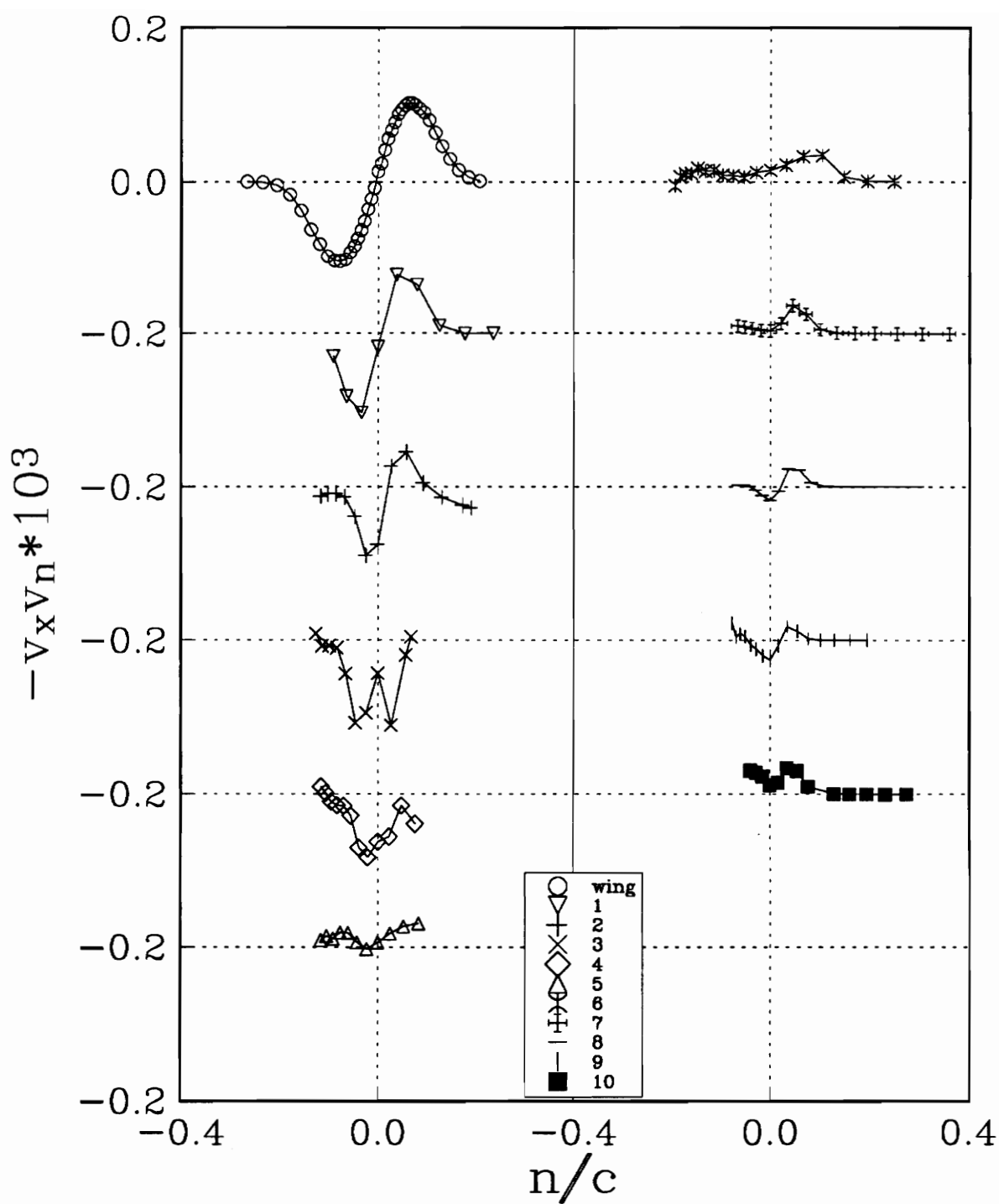


Figure 191f. $v_x v_n$ profiles for the counter rotating case at $x/c=10$. Stations are indicated in figure 189.

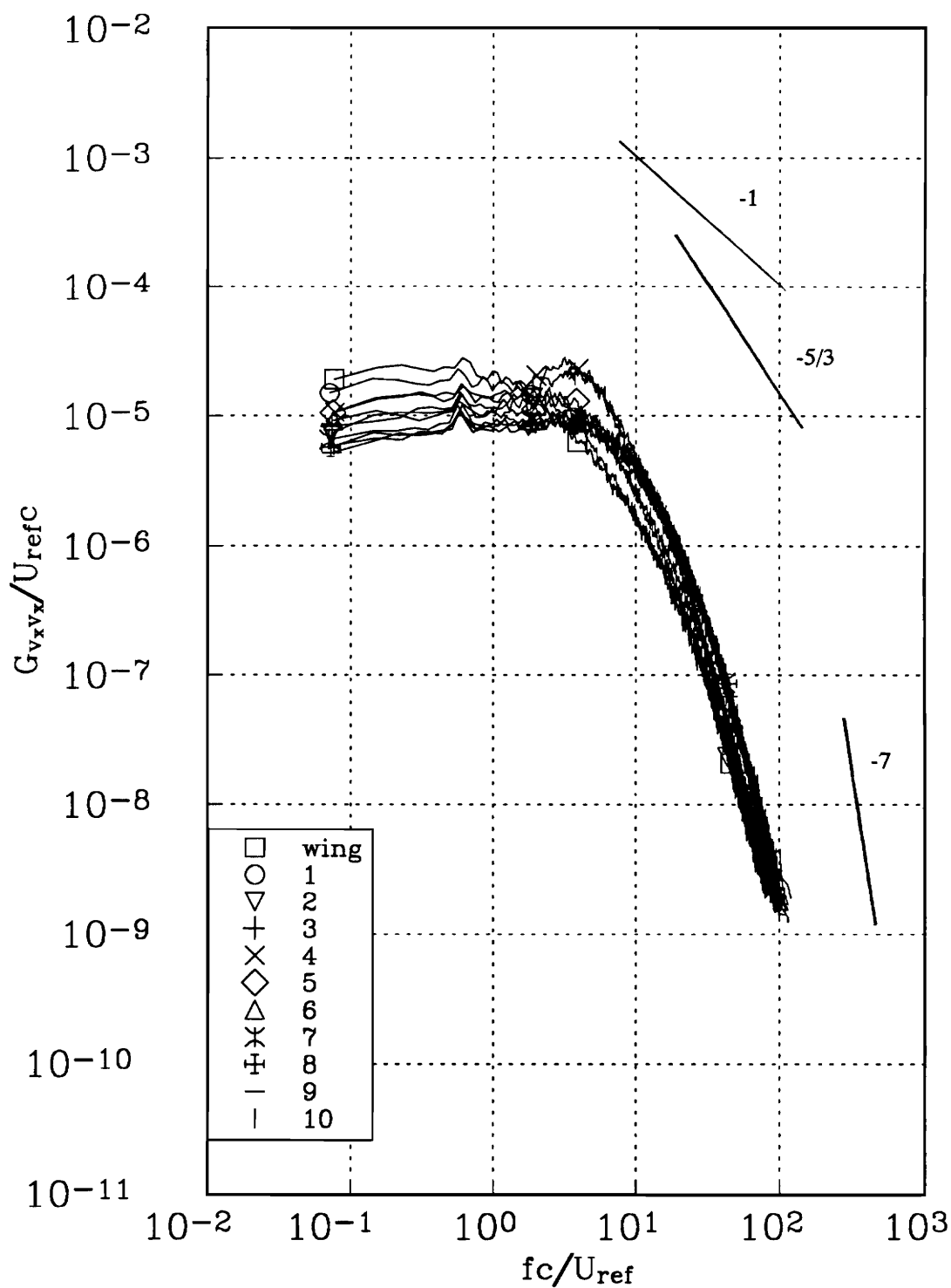


Figure 192a. v_x autospectra in the center of the wake for the counter rotating case at $x/c=10$. Stations are indicated in figure 189.

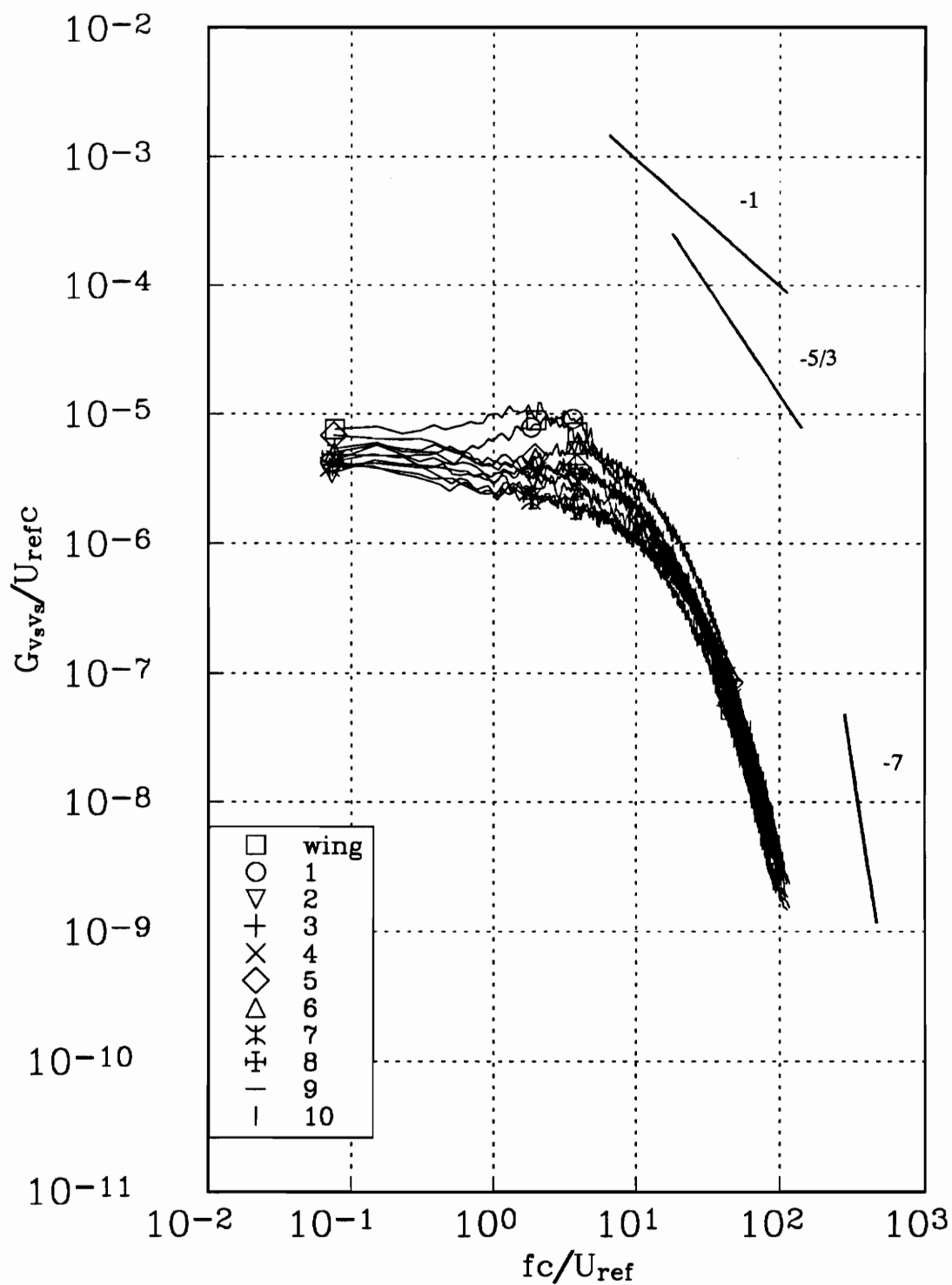


Figure 192b. v_s autospectra in the center of the wake for the counter rotating case at $x/c=10$. Stations are indicated in figure 189.

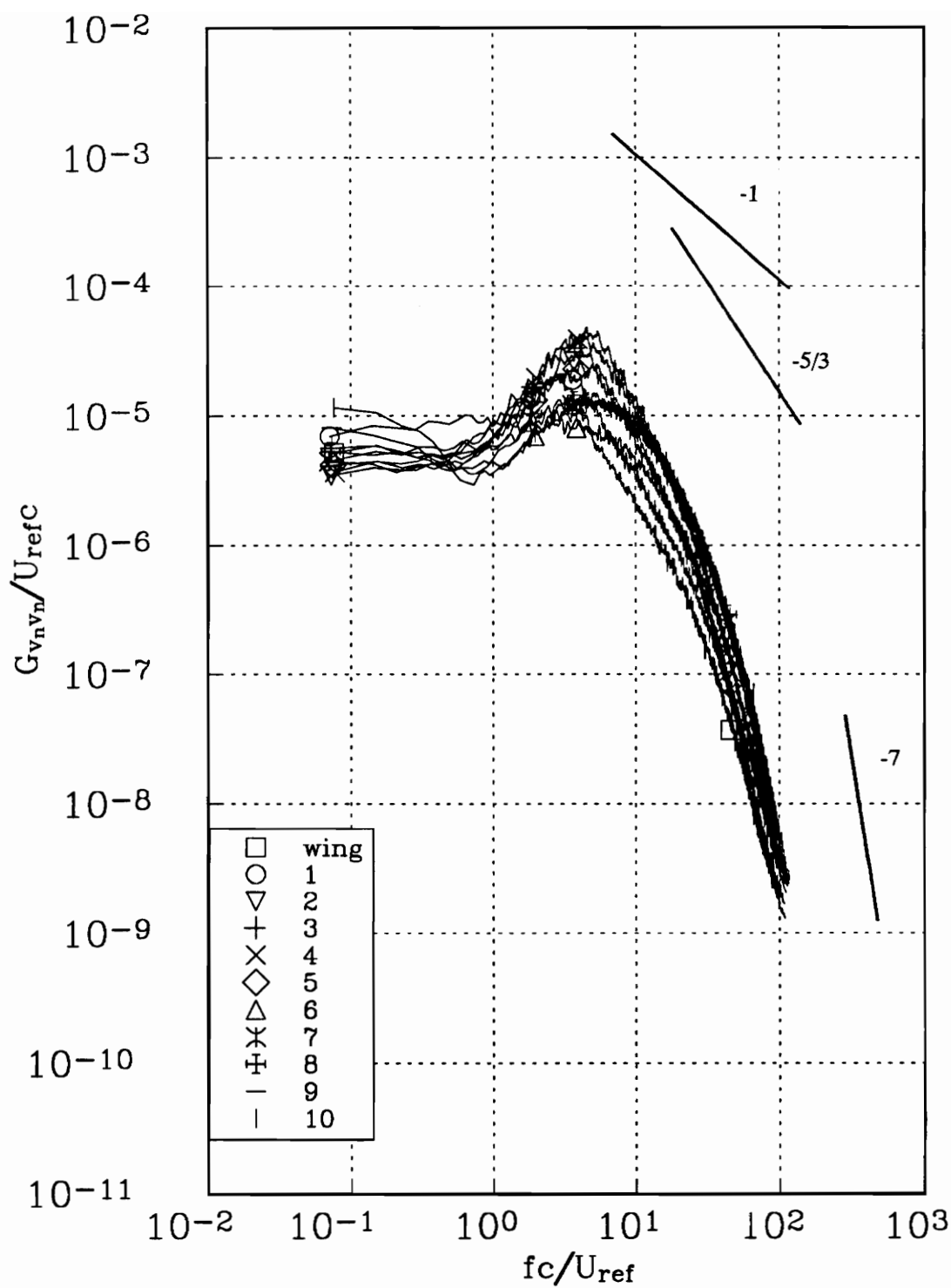


Figure 192c. v_n autospectra in the center of the wake for the counter rotating case at $x/c=10$. Stations are indicated in figure 189.

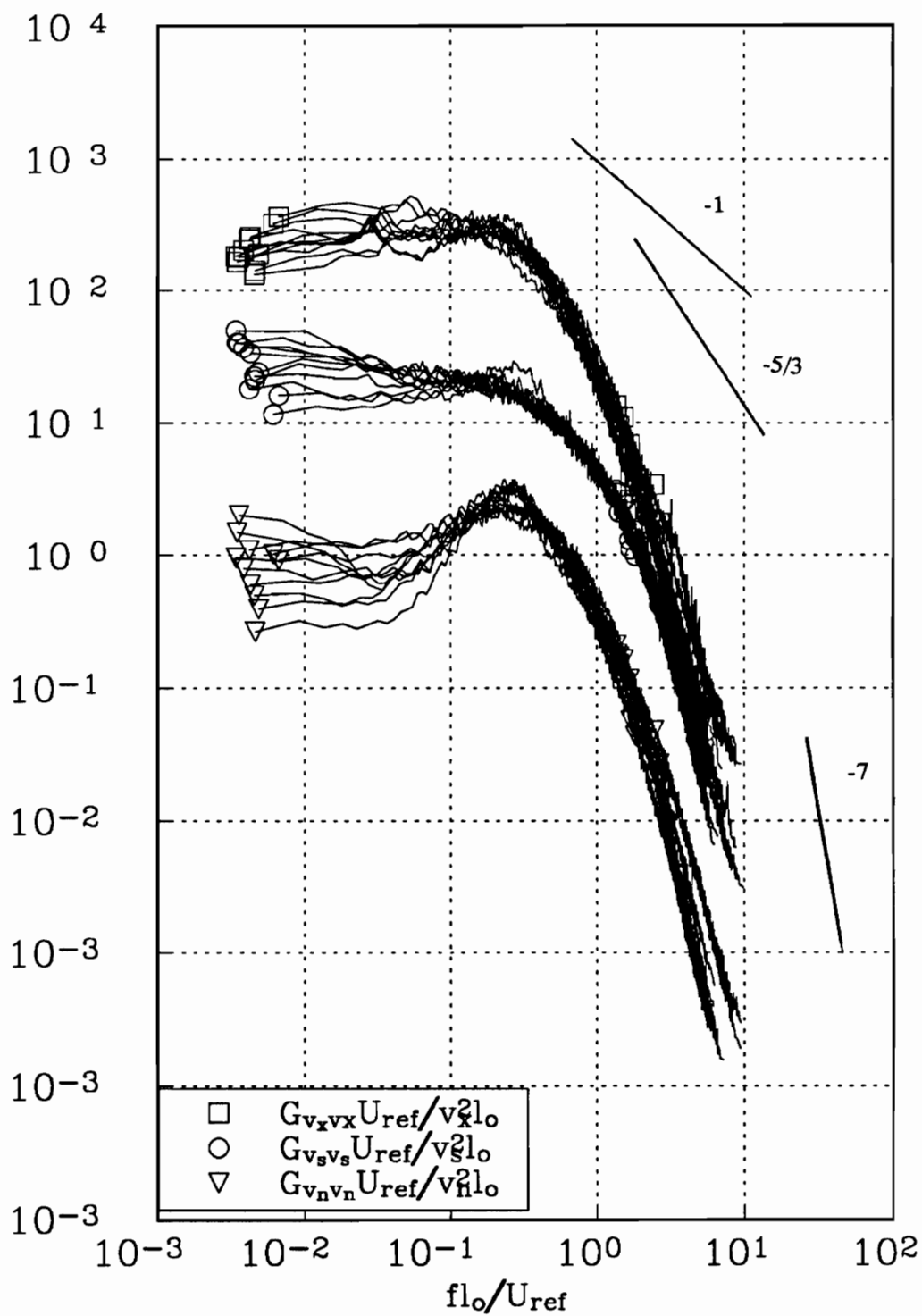
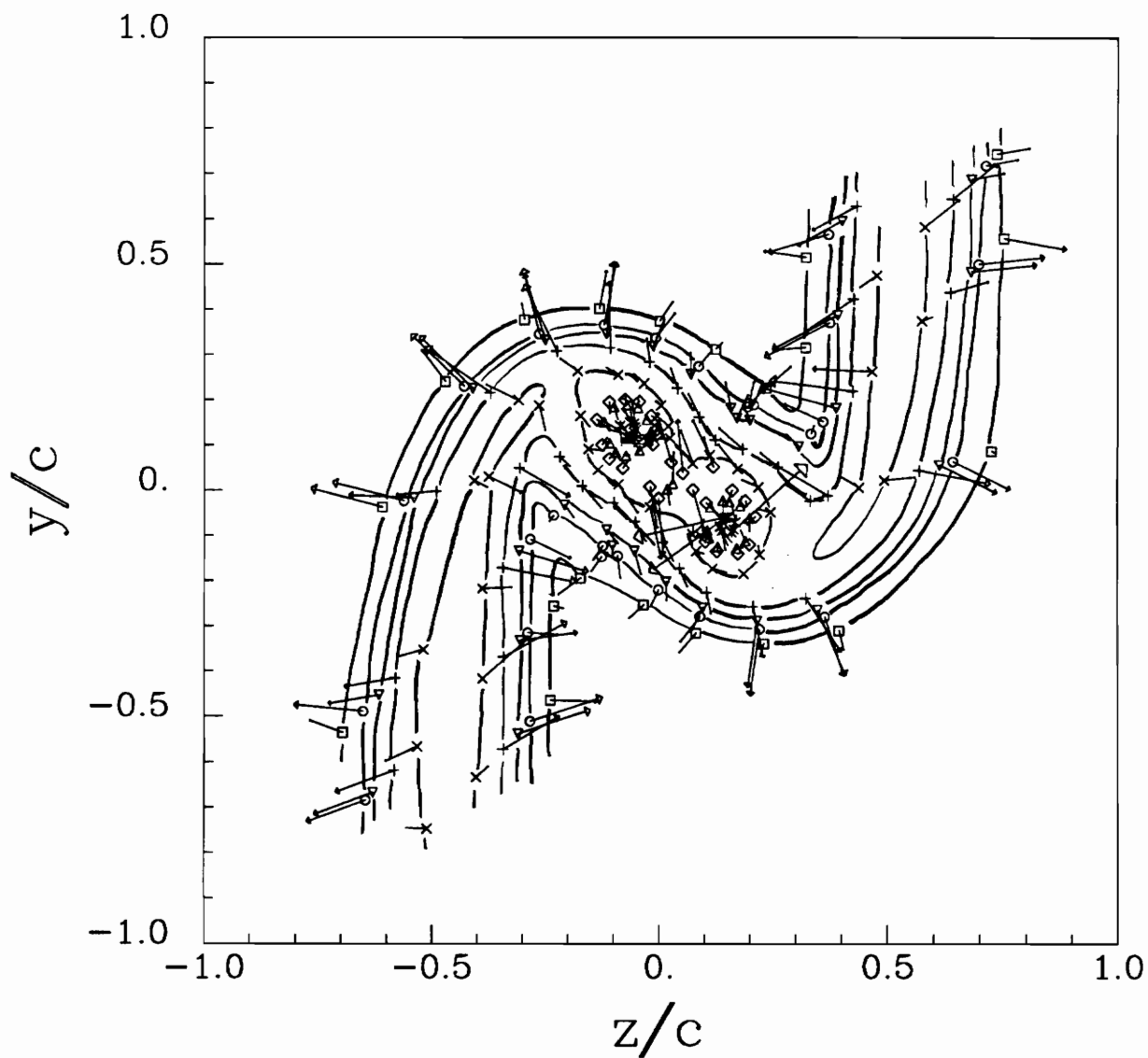
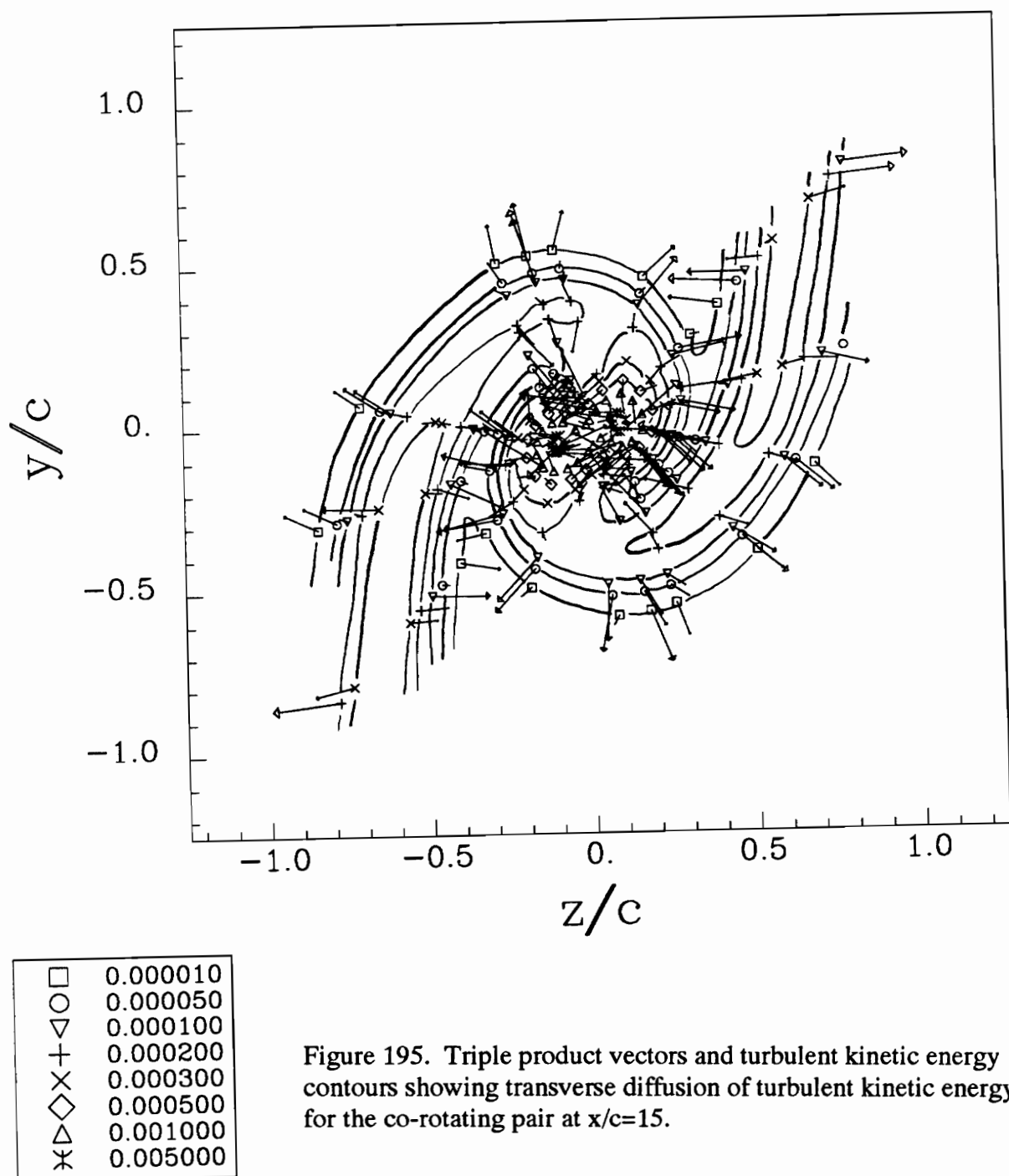


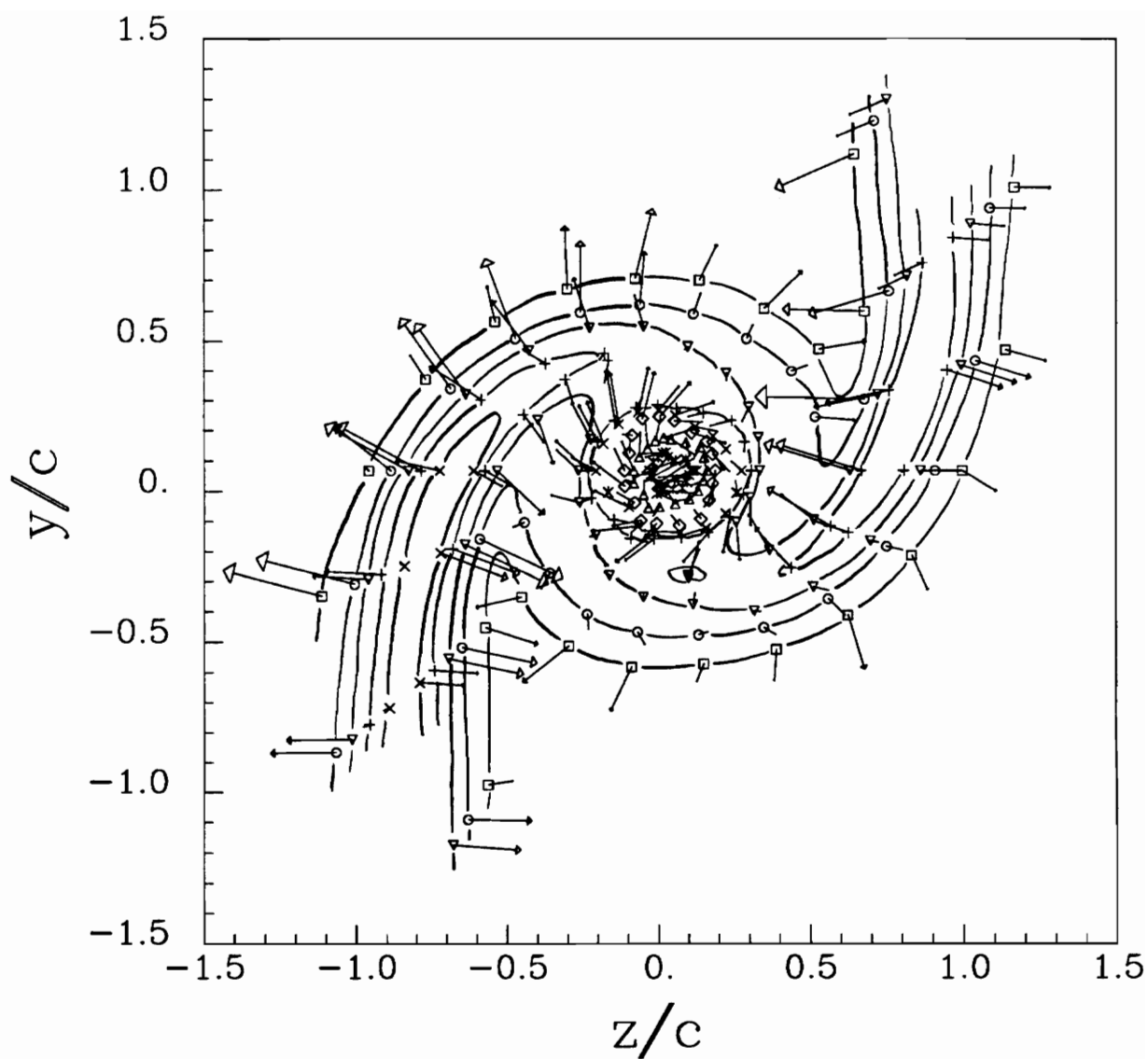
Figure 193. Autospectra in the center of the wake for the counter rotating case at $x/c=10$. Normalized by the local wake length scale L_0 .



□	0.000010
○	0.000050
▽	0.000100
+	0.000250
×	0.000500
◇	0.000750
△	0.001000
*	0.005000

Figure 194. Triple product vectors and turbulent kinetic energy contours showing transverse diffusion of turbulent kinetic energy for the co-rotating pair at $x/c=10$.





□	0.000010
○	0.000050
▽	0.000100
+	0.000150
×	0.000200
◇	0.000300
△	0.000500
*	0.001000

Figure 196. Triple product vectors and turbulent kinetic energy contours showing transverse diffusion of turbulent kinetic energy for the co-rotating pair at $x/c=22$.

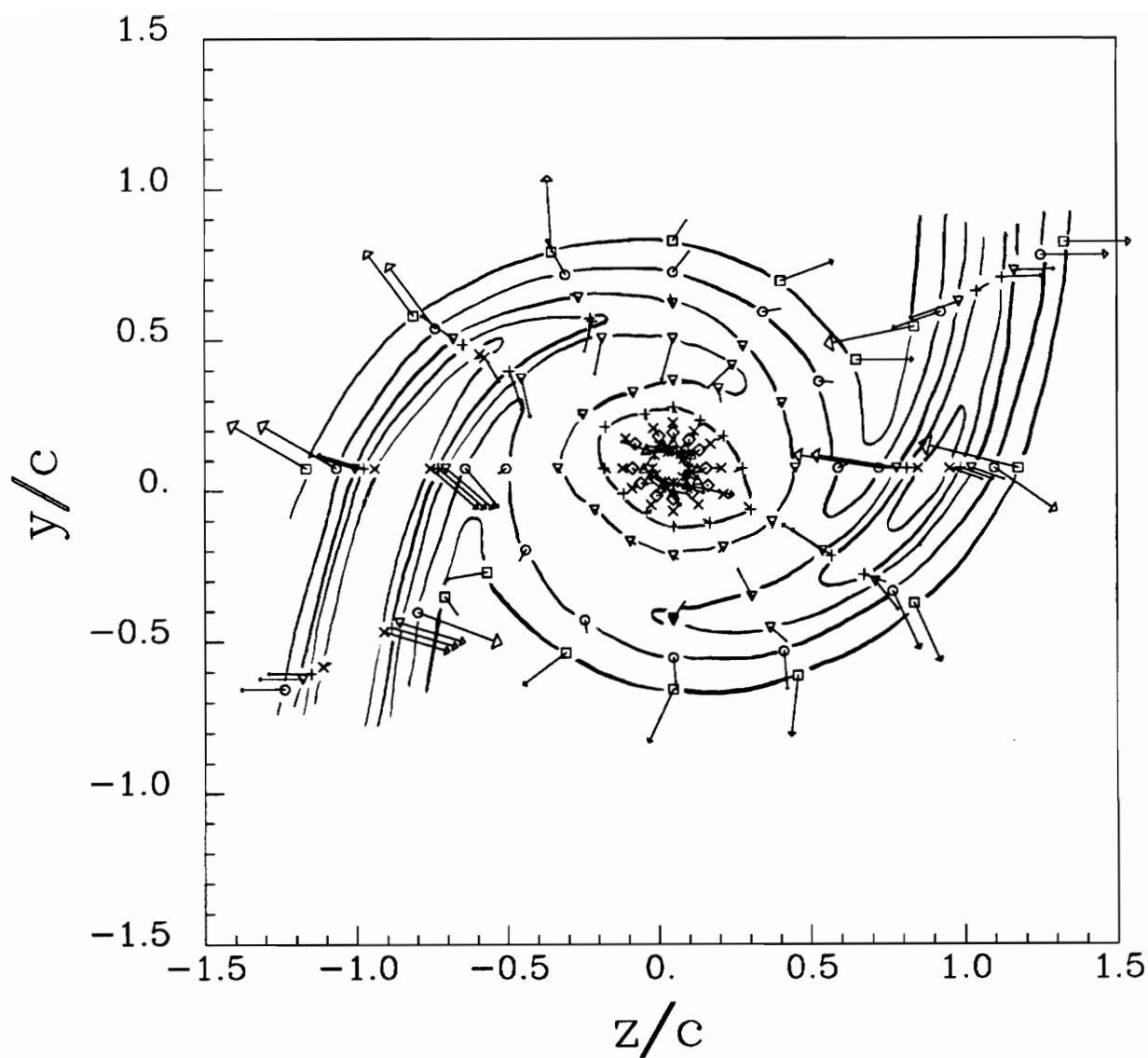
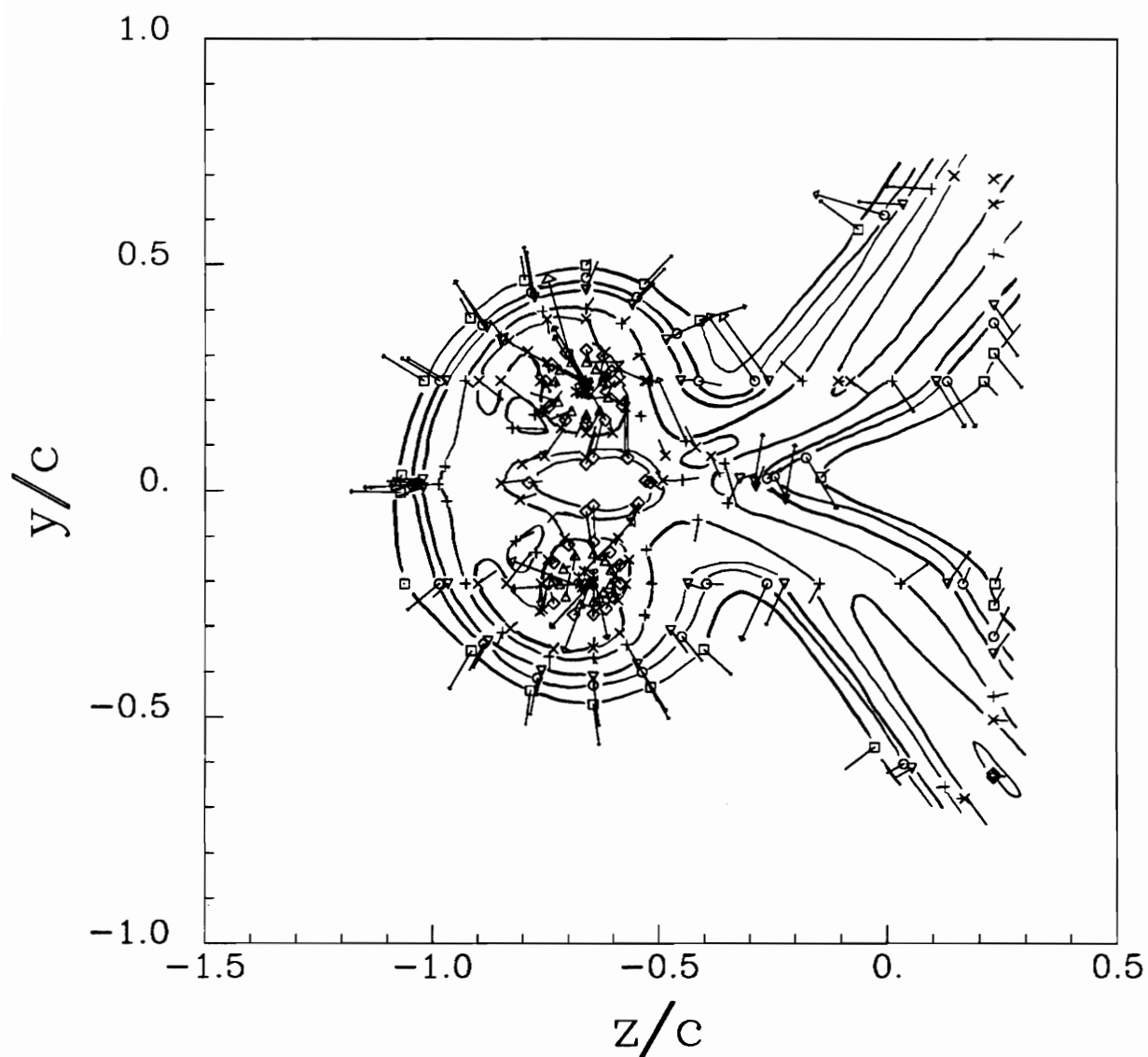
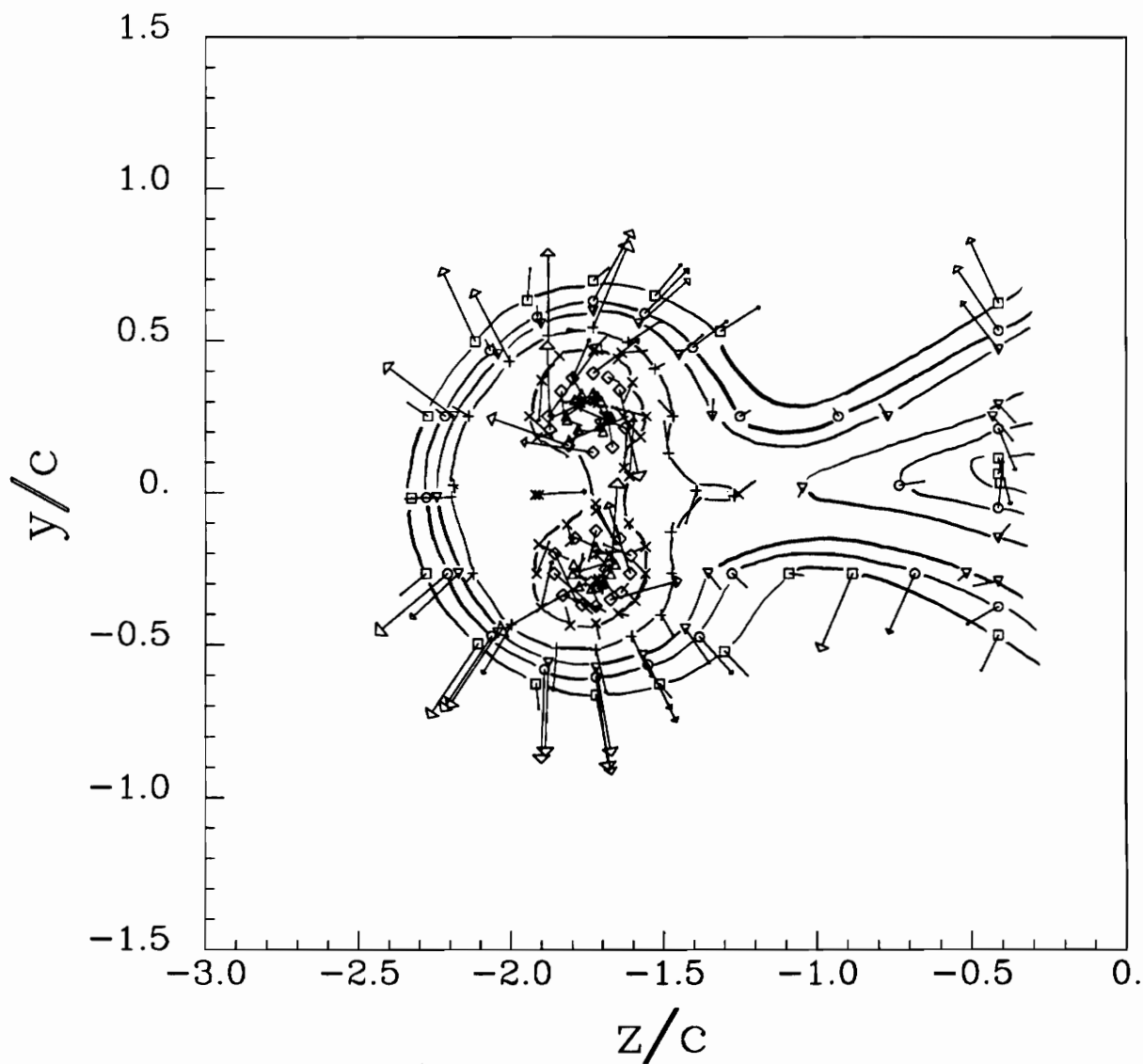


Figure 197. Triple product vectors and turbulent kinetic energy contours showing transverse diffusion of turbulent kinetic energy for the co-rotating pair at $x/c=30$.



□	0.000010
○	0.000050
▽	0.000100
+	0.000300
×	0.000400
◇	0.000500
△	0.001000
*	0.005000

Figure 198. Triple product vectors and turbulent kinetic energy contours showing transverse diffusion of turbulent kinetic energy for the counter rotating pair at $x/c=10$.



□	0.000010
○	0.000050
▽	0.000100
+	0.000250
×	0.000500
◇	0.001000
△	0.005000
*	0.010000

Figure 199. Triple product vectors and turbulent kinetic energy contours showing transverse diffusion of turbulent kinetic energy for the counter rotating pair at $x/c=30$.

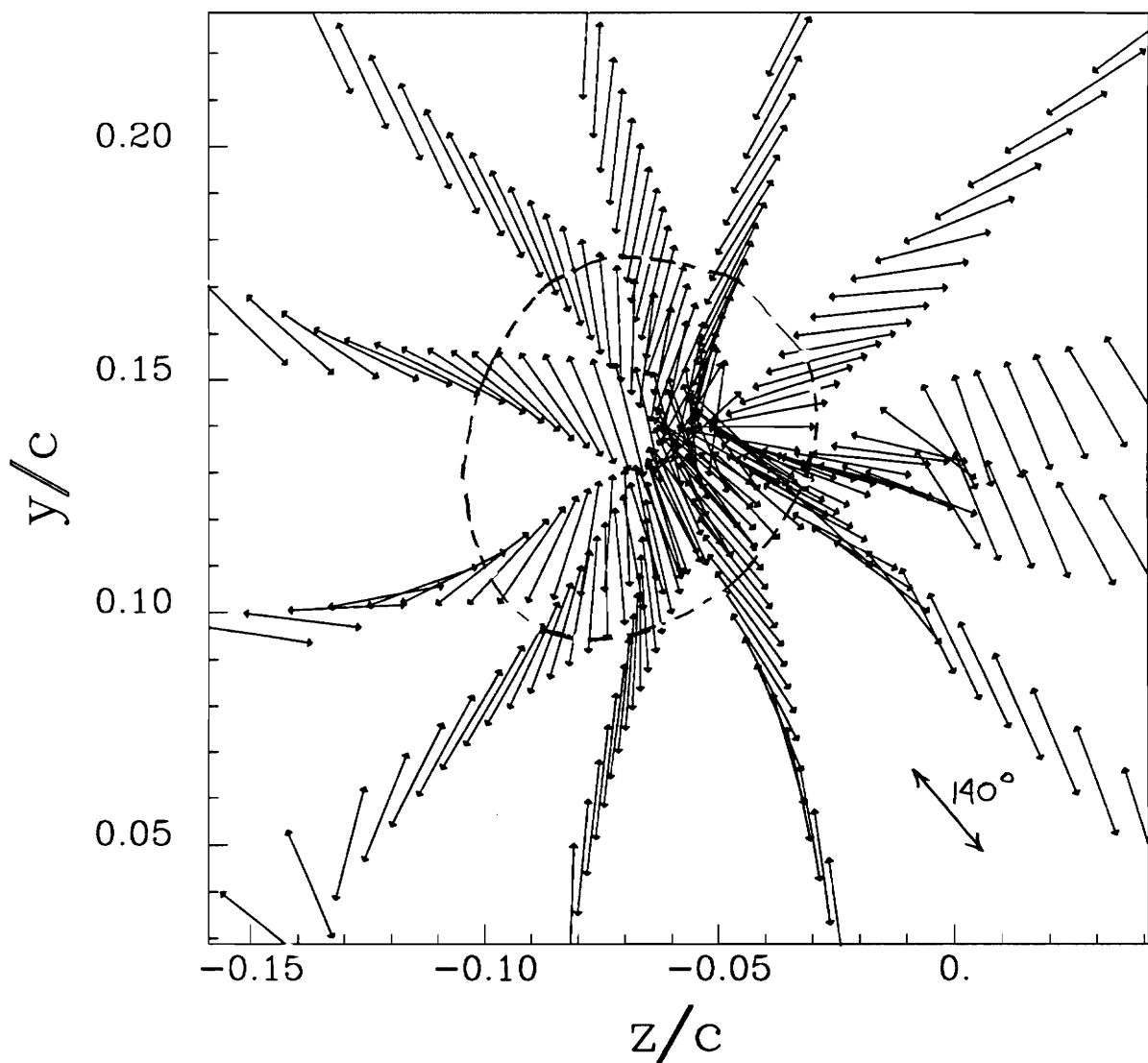


Figure 200. Principal stress direction vectors in the core region for the upper co-rotating vortex at $x/c=10$. Angle indicates probable direction of movement with dotted line showing edge of core.

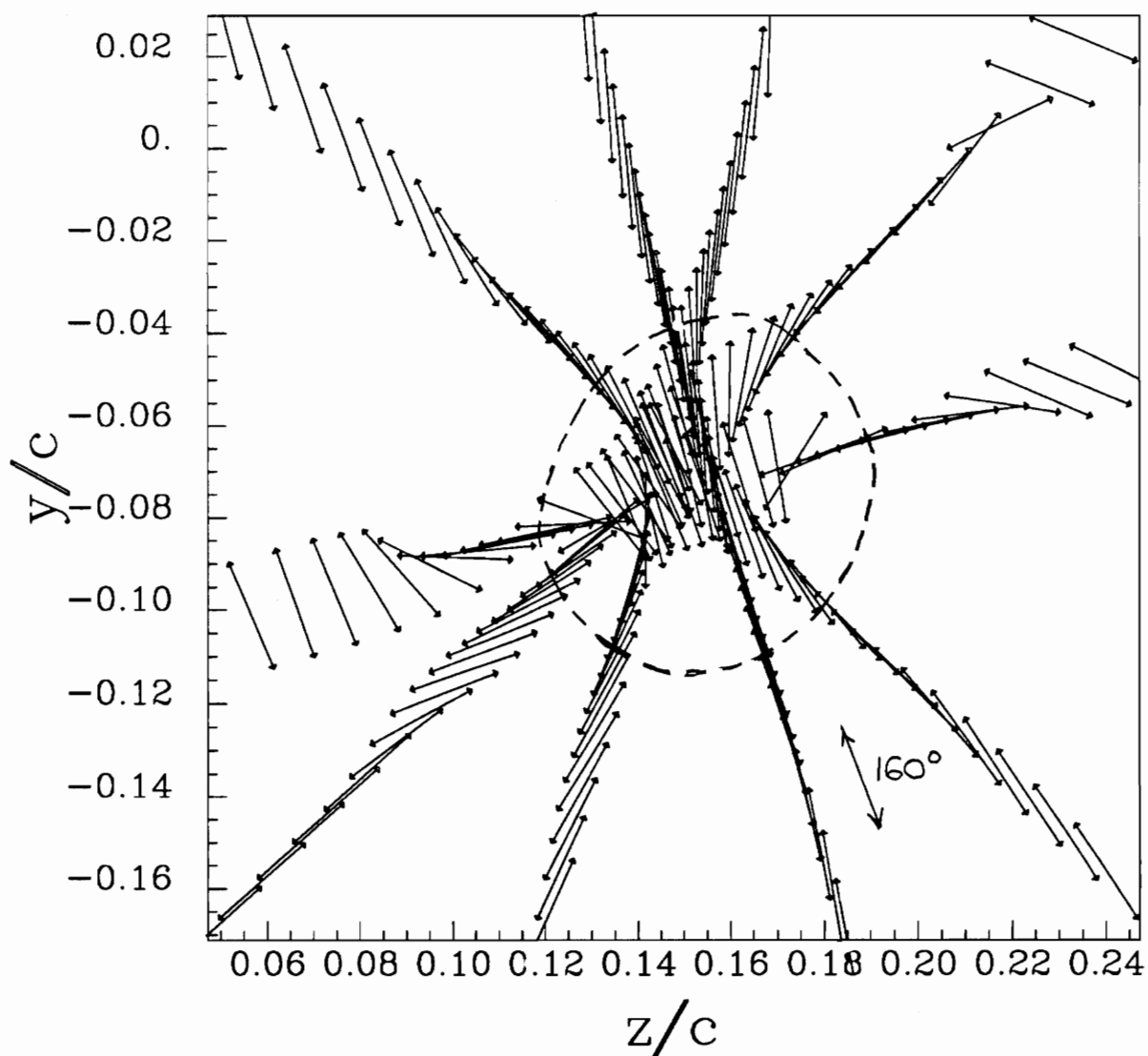


Figure 201. Principal stress direction vectors in the core region for the lower co-rotating vortex at $x/c=10$. Angle indicates probable direction of movement with dotted line showing edge of core.

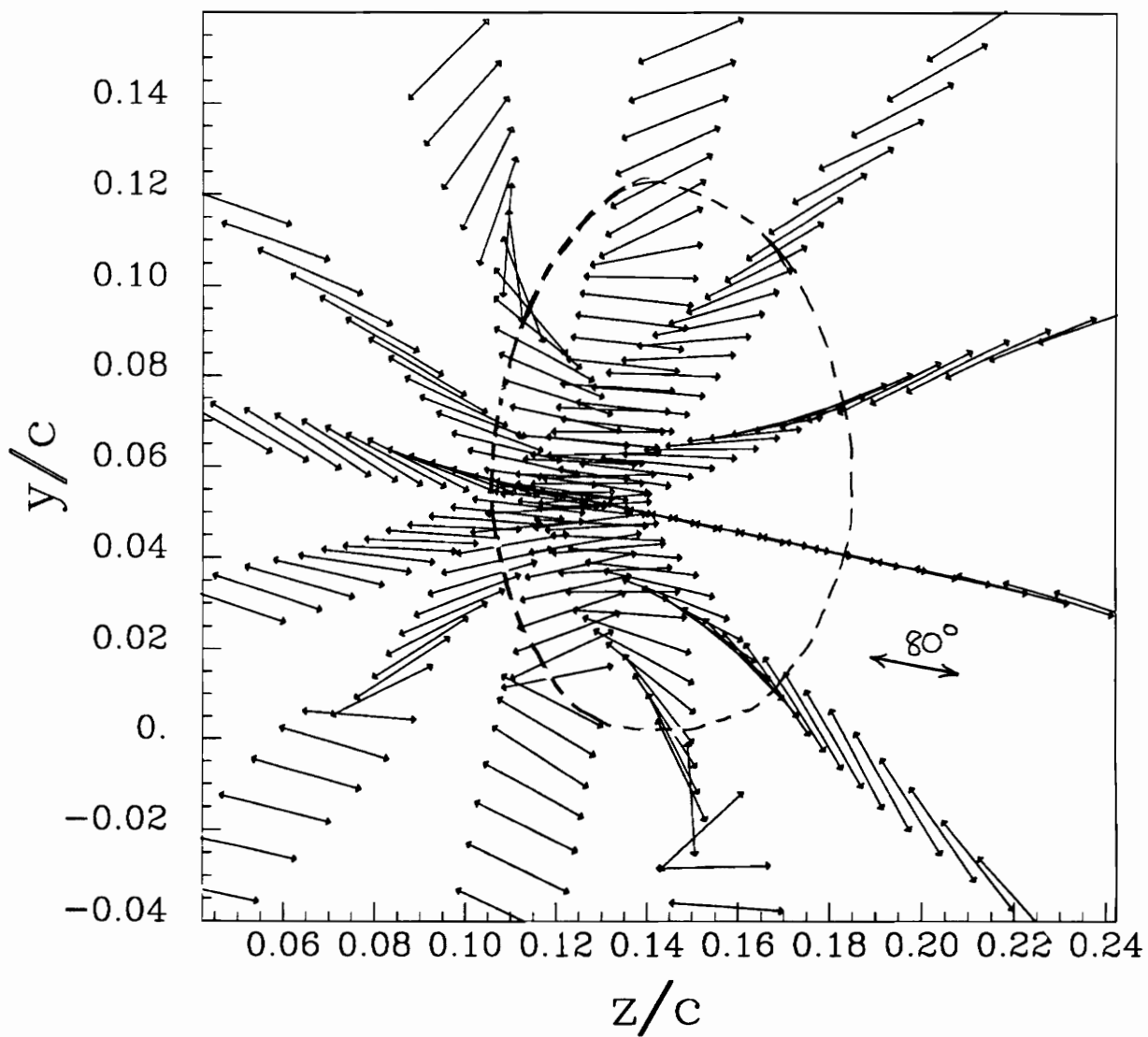


Figure 202. Principal stress direction vectors in the core region for the upper co-rotating vortex at $x/c=15$. Angle indicates probable direction of movement with dotted line showing edge of core.

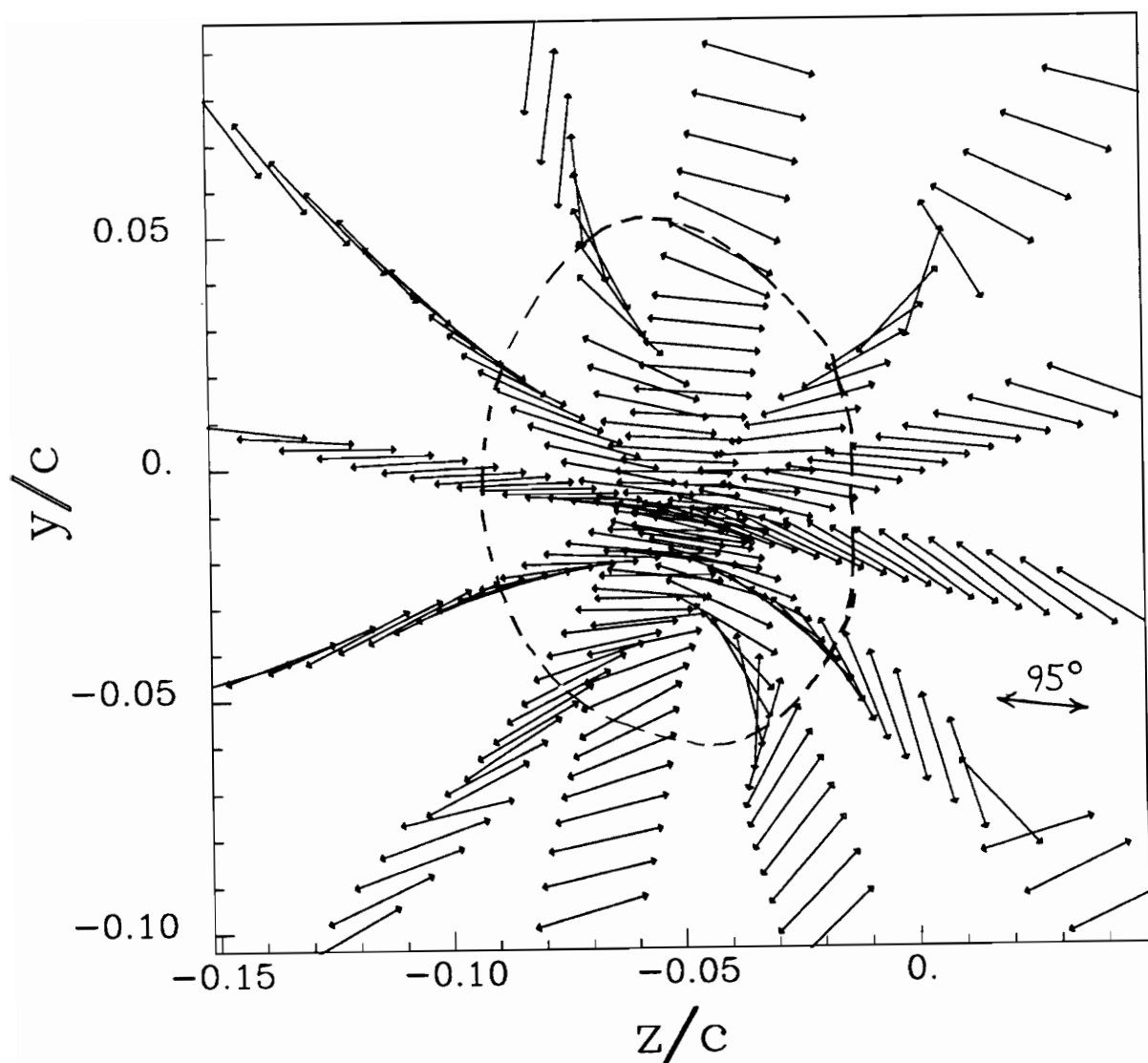


Figure 203. Principal stress direction vectors in the core region for the lower co-rotating vortex at $x/c=15$. Angle indicates probable direction of movement with dotted line showing edge of core.

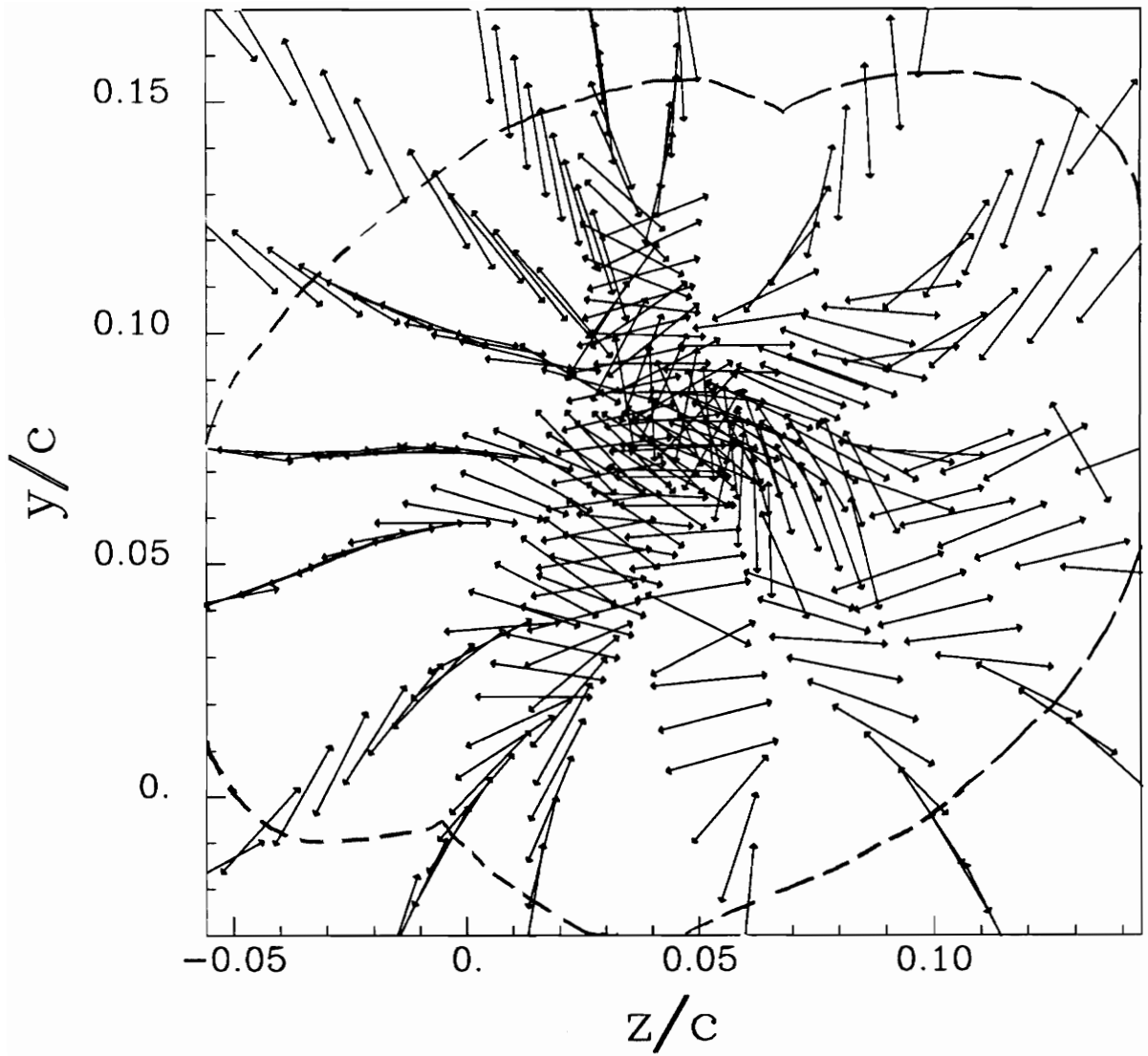


Figure 204. Principal stress direction vectors in the core region for the co-rotating vortex at $x/c=22$. Angle indicates probable direction of movement with dotted line showing edge of core.

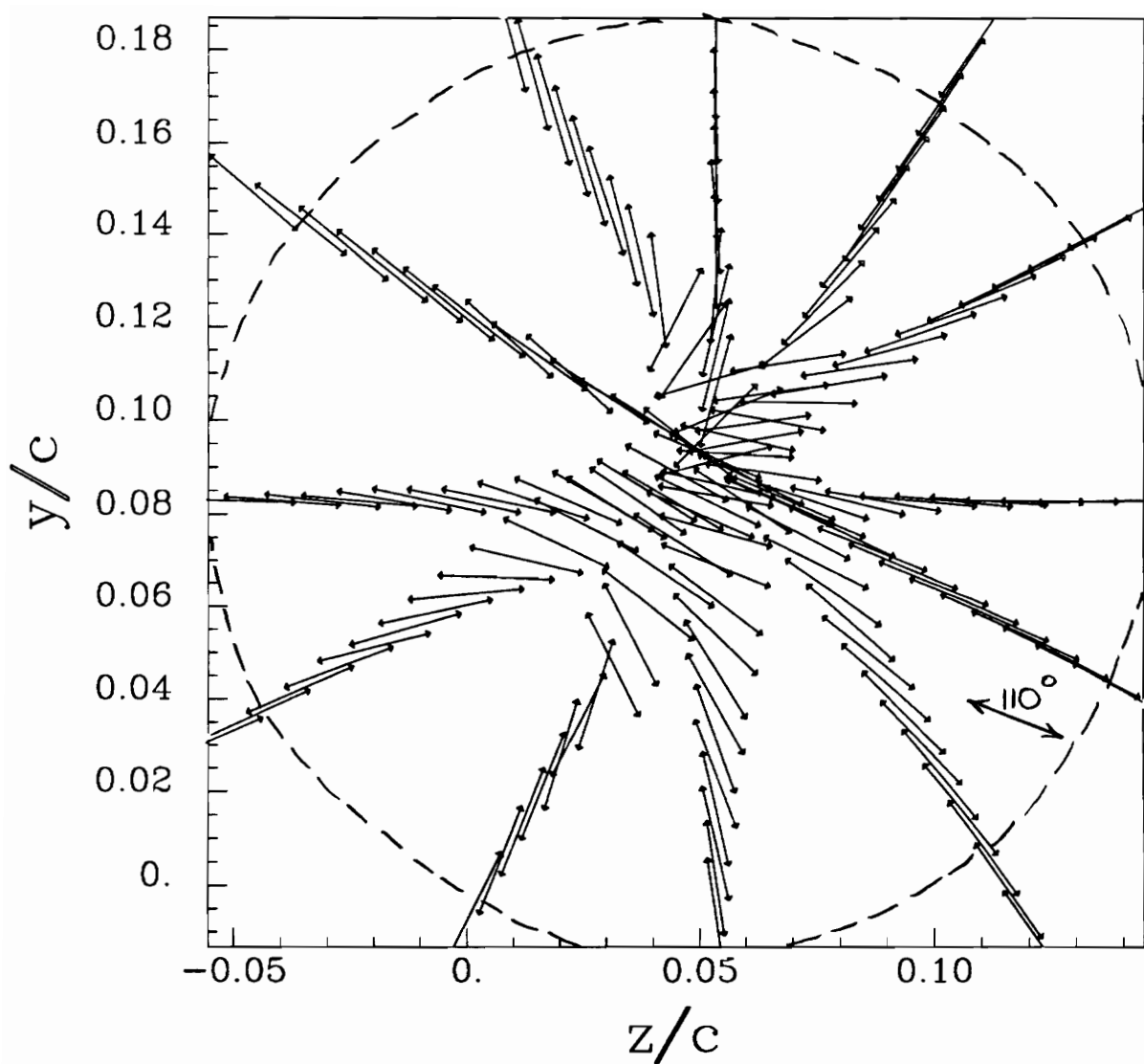


Figure 205. Principal stress direction vectors in the core region for the co-rotating vortex at $x/c=30$. Angle indicates probable direction of movement with dotted line showing edge of core.

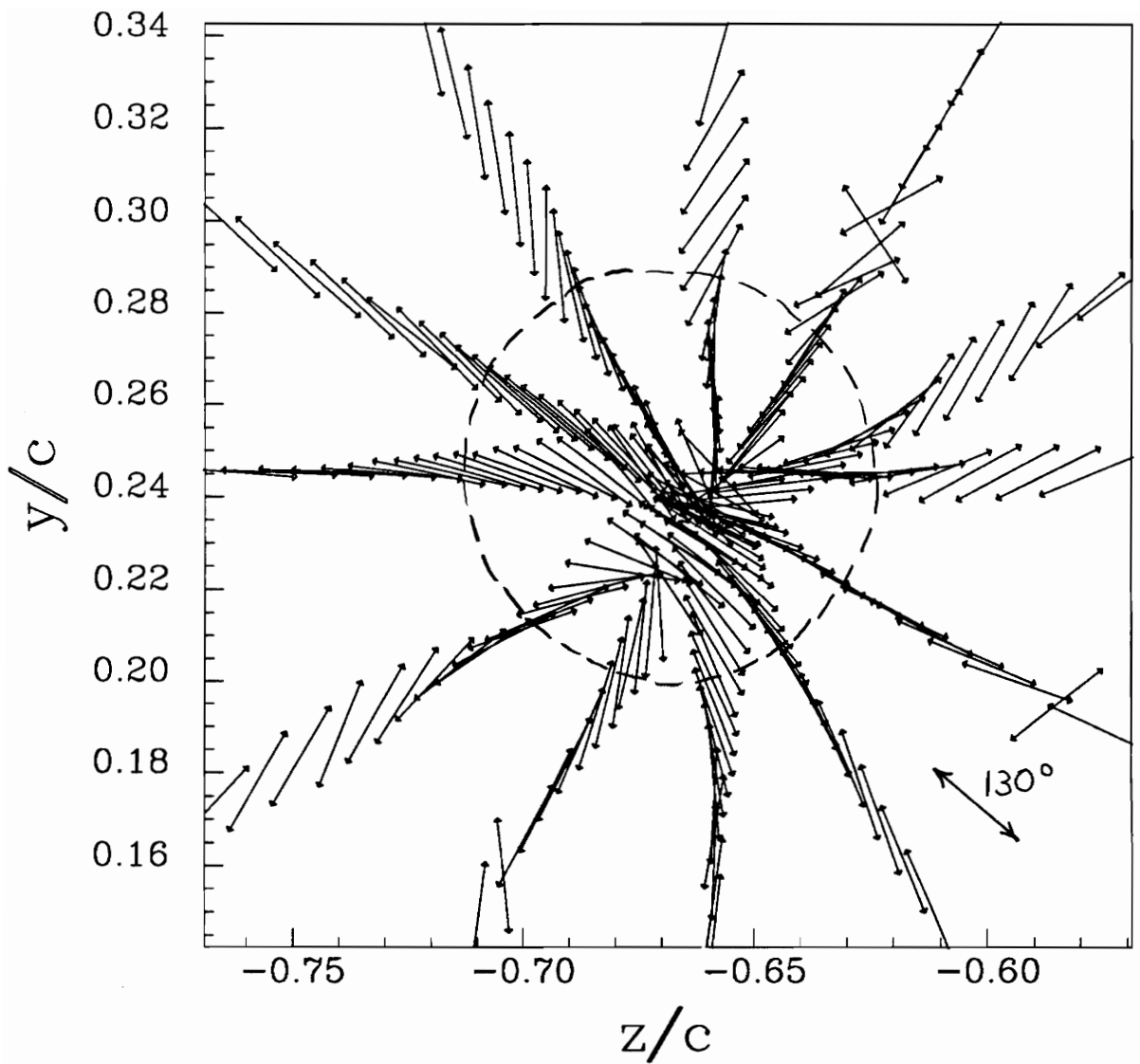


Figure 206. Principal stress direction vectors in the core region for the upper counter rotating vortex at $x/c=10$. Angle indicates probable direction of movement with dotted line showing edge of core.

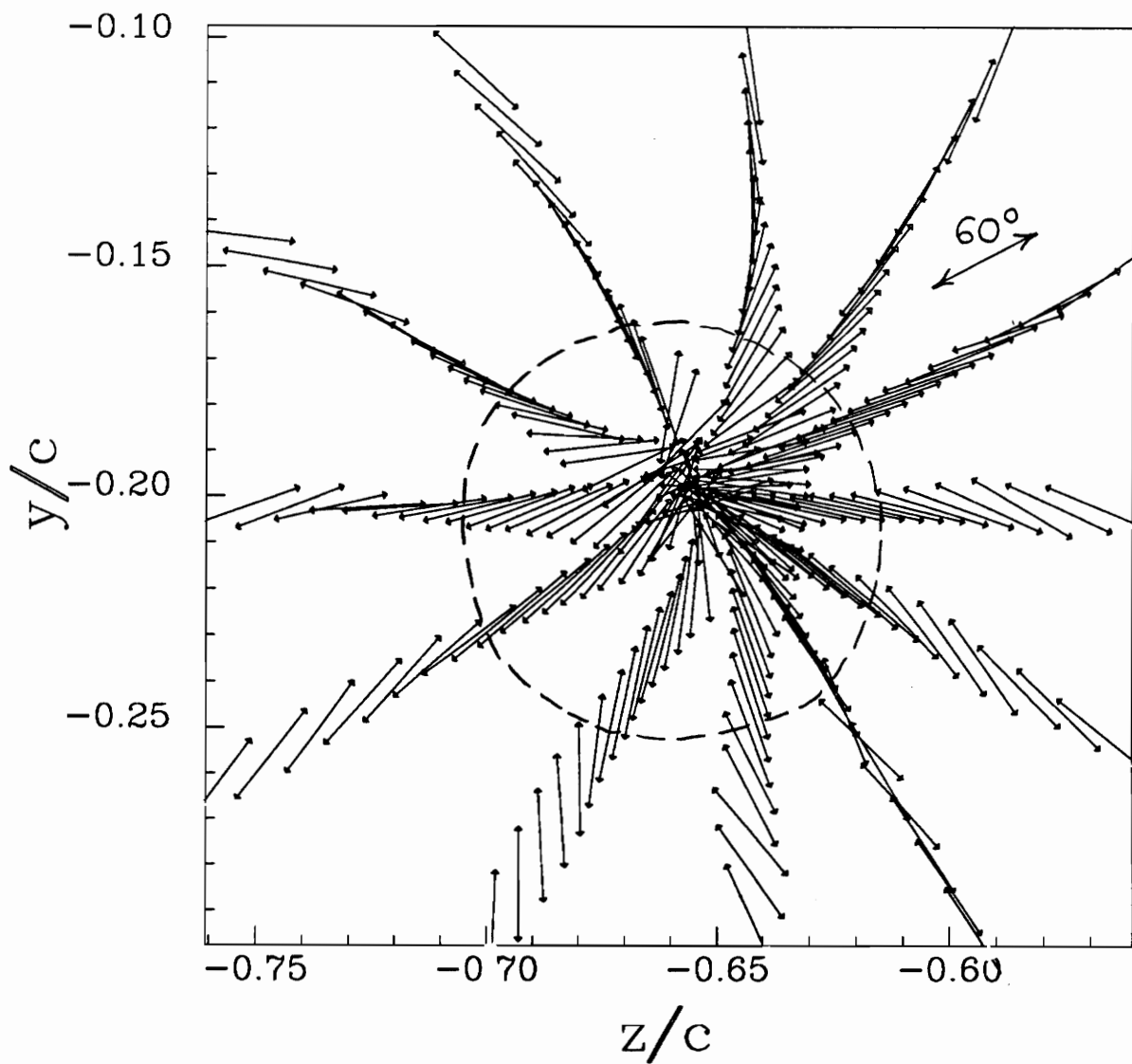


Figure 207. Principal stress direction vectors in the core region for the lower counter rotating vortex at $x/c=10$. Angle indicates probable direction of movement with dotted line showing edge of core.

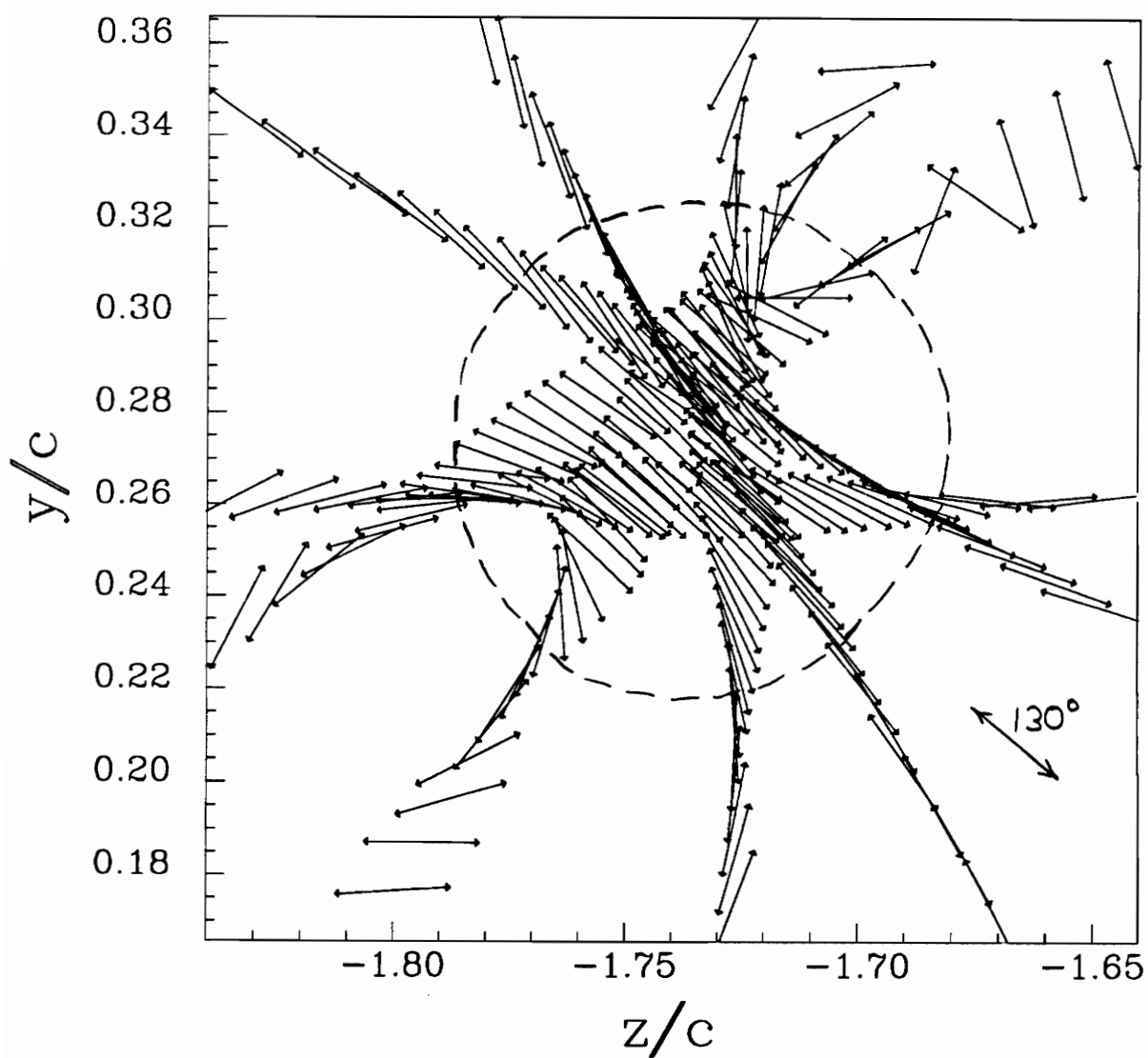


Figure 208. Principal stress direction vectors in the core region for the upper counter rotating vortex at $x/c=30$. Angle indicates probable direction of movement with dotted line showing edge of core.

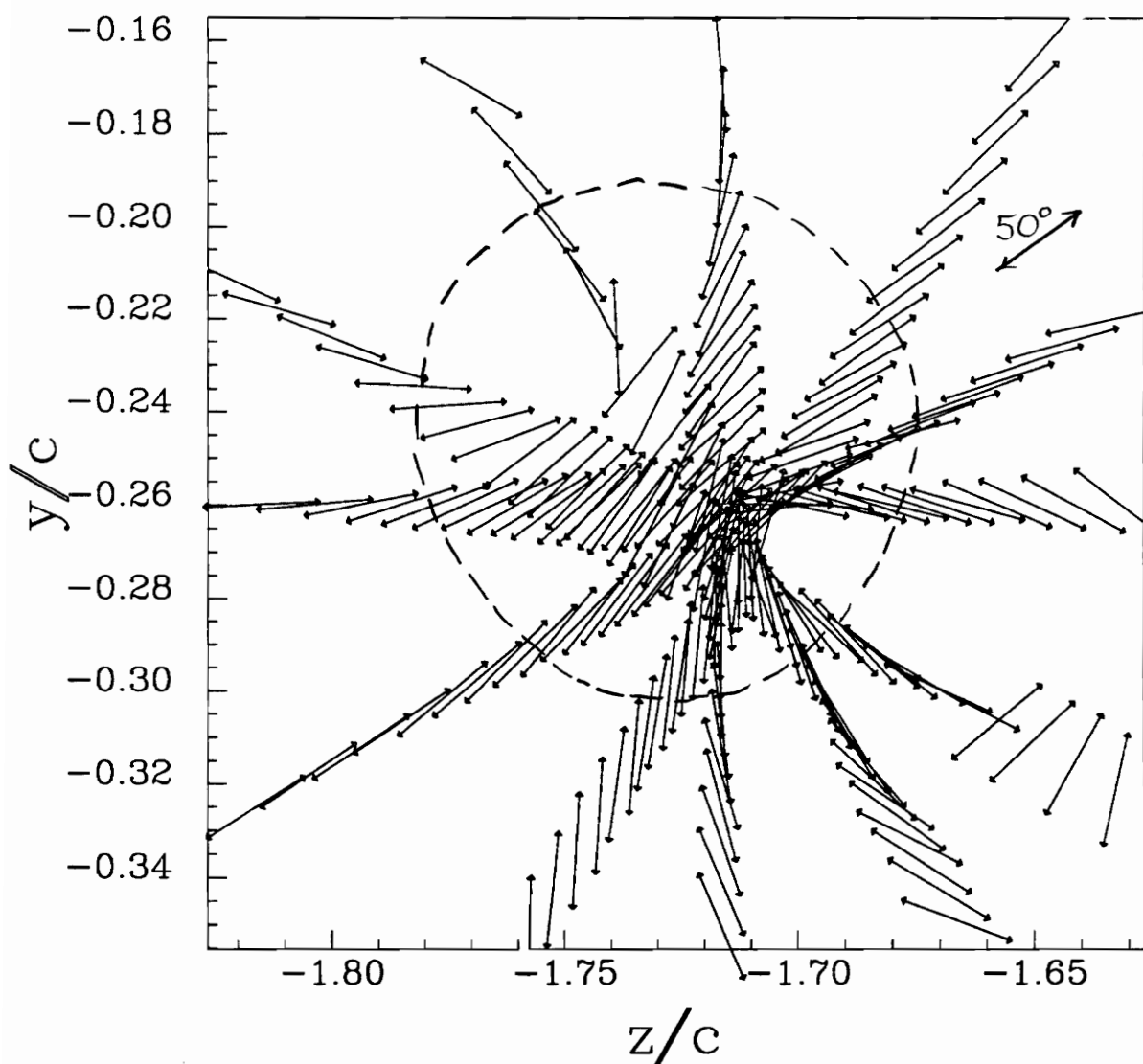


Figure 209. Principal stress direction vectors in the core region for the lower counter rotating vortex at $x/c=30$. Angle indicates probable direction of movement with dotted line showing edge of core.

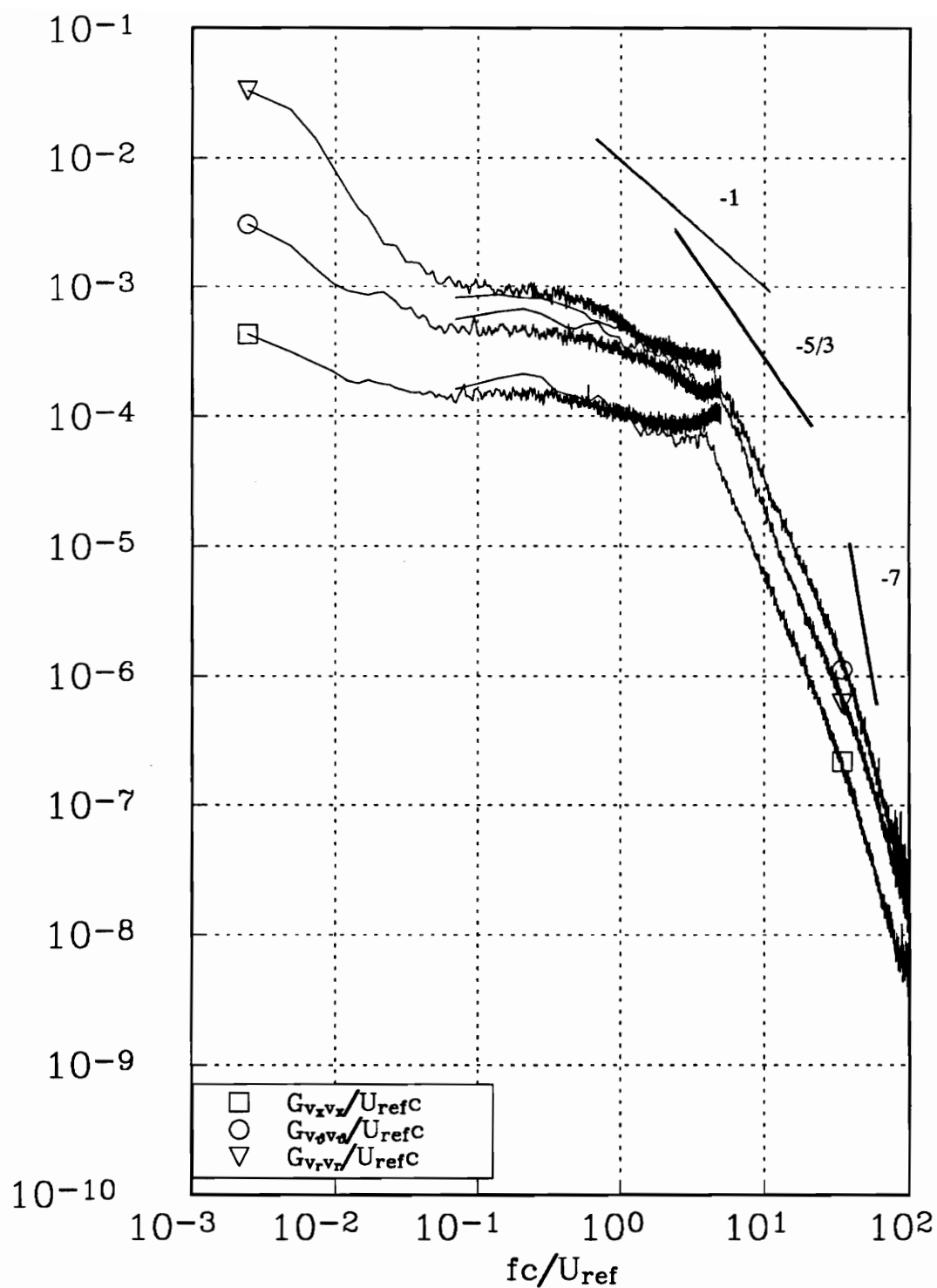


Figure 210. Long time average autospectra measured in the core region of the upper co-rotating vortex at $x/c=10$.

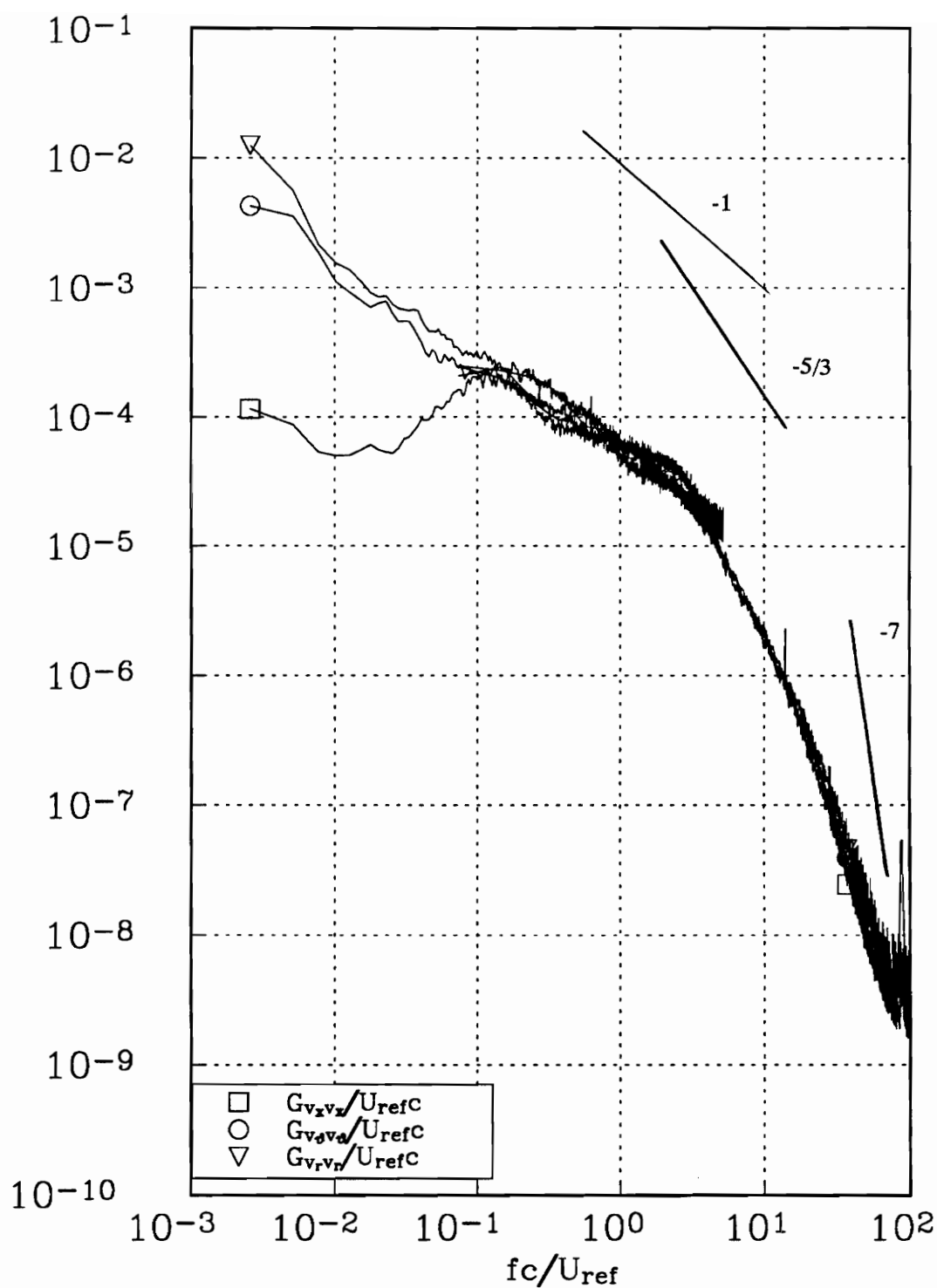


Figure 211. Long time average autospectra measured in the core region of the co-rotating vortex at $x/c=30$.

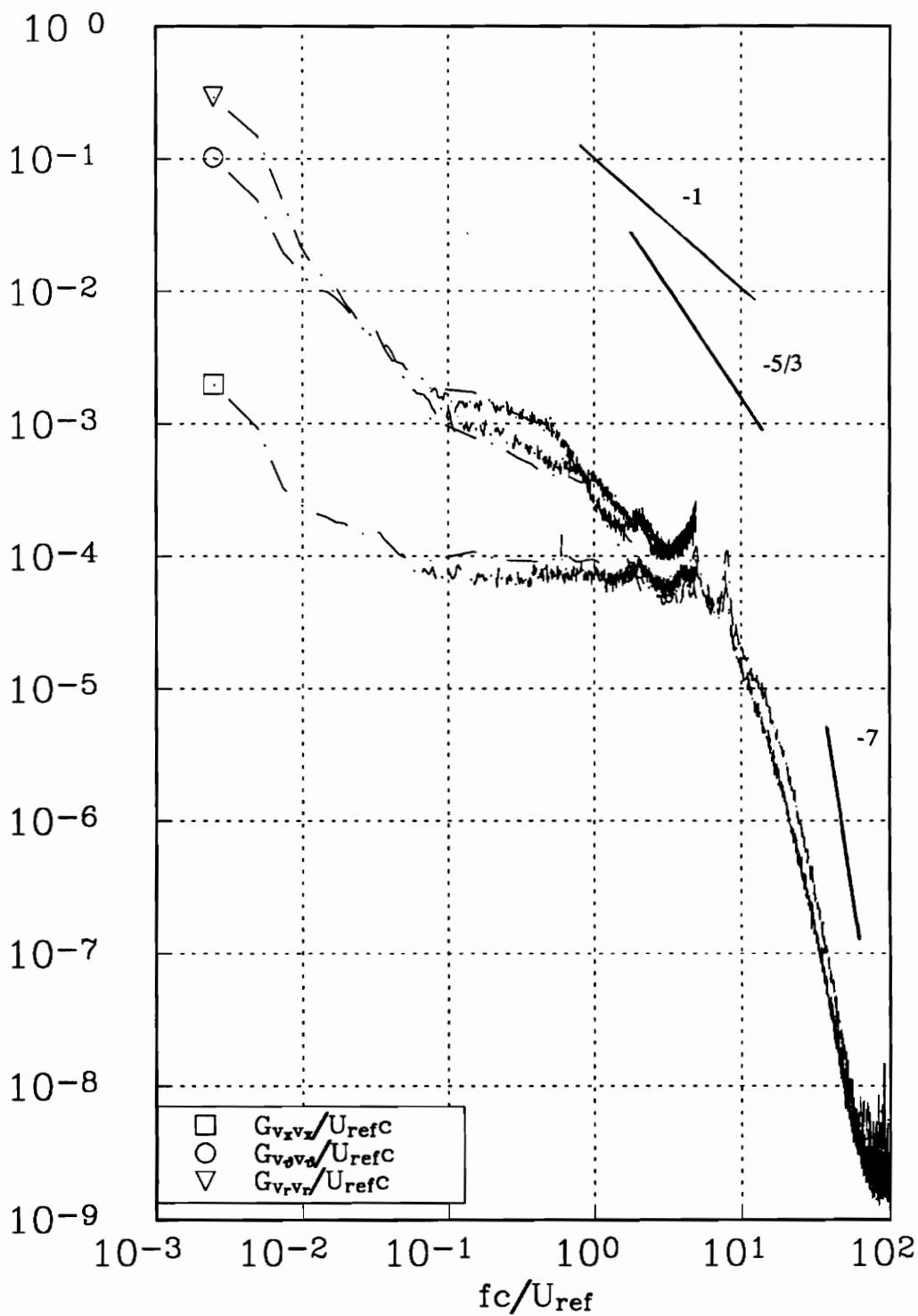


Figure 212. Long time average autospectra measured in the core region of the upper counter rotating vortex at $x/c=10$.

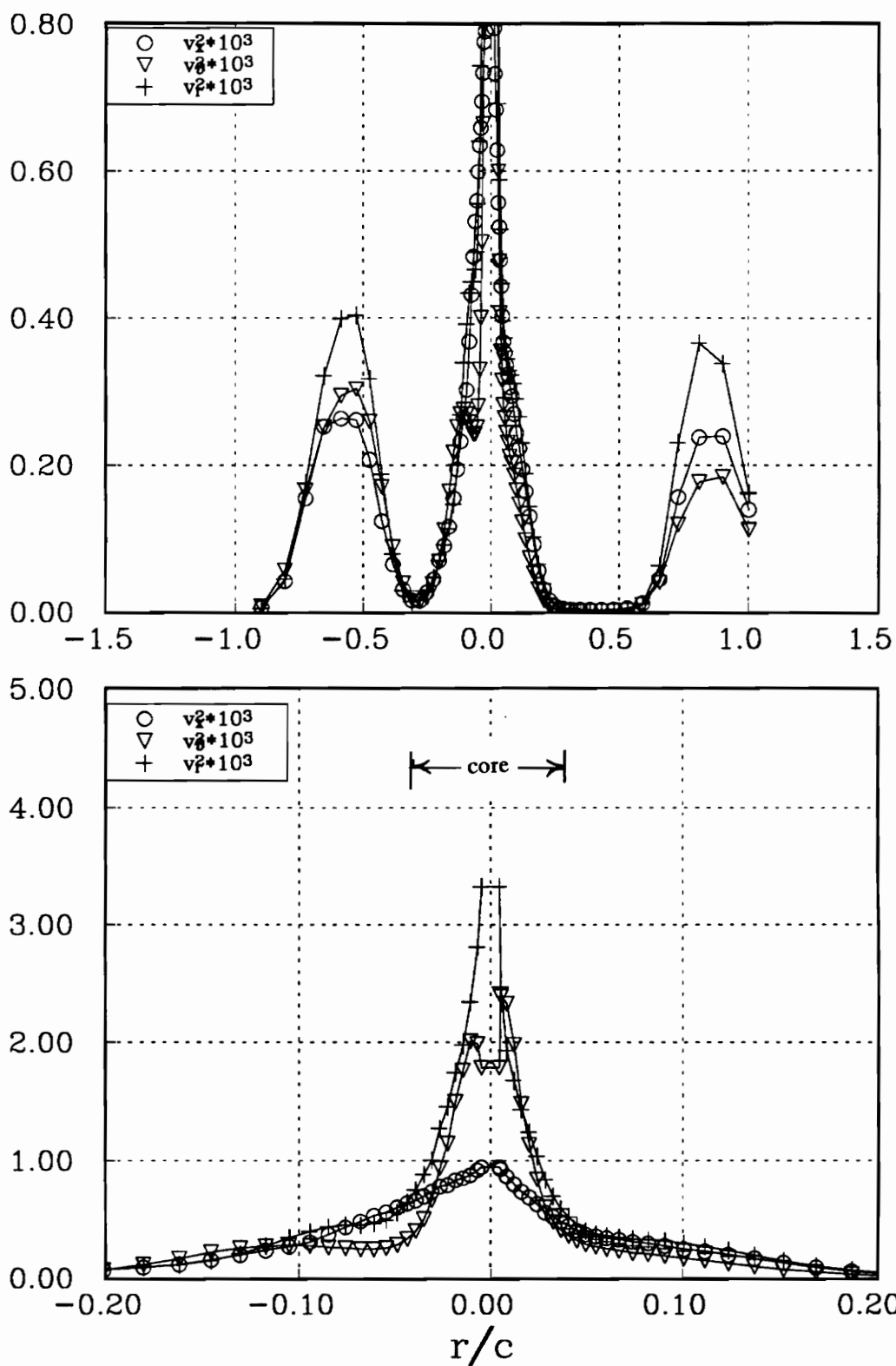


Figure 213a. Profile Aa showing normal stresses high passed filtered at a frequency of $fc/U_{ref}=1.5$ for the co-rotating pair at $x/c=10$.

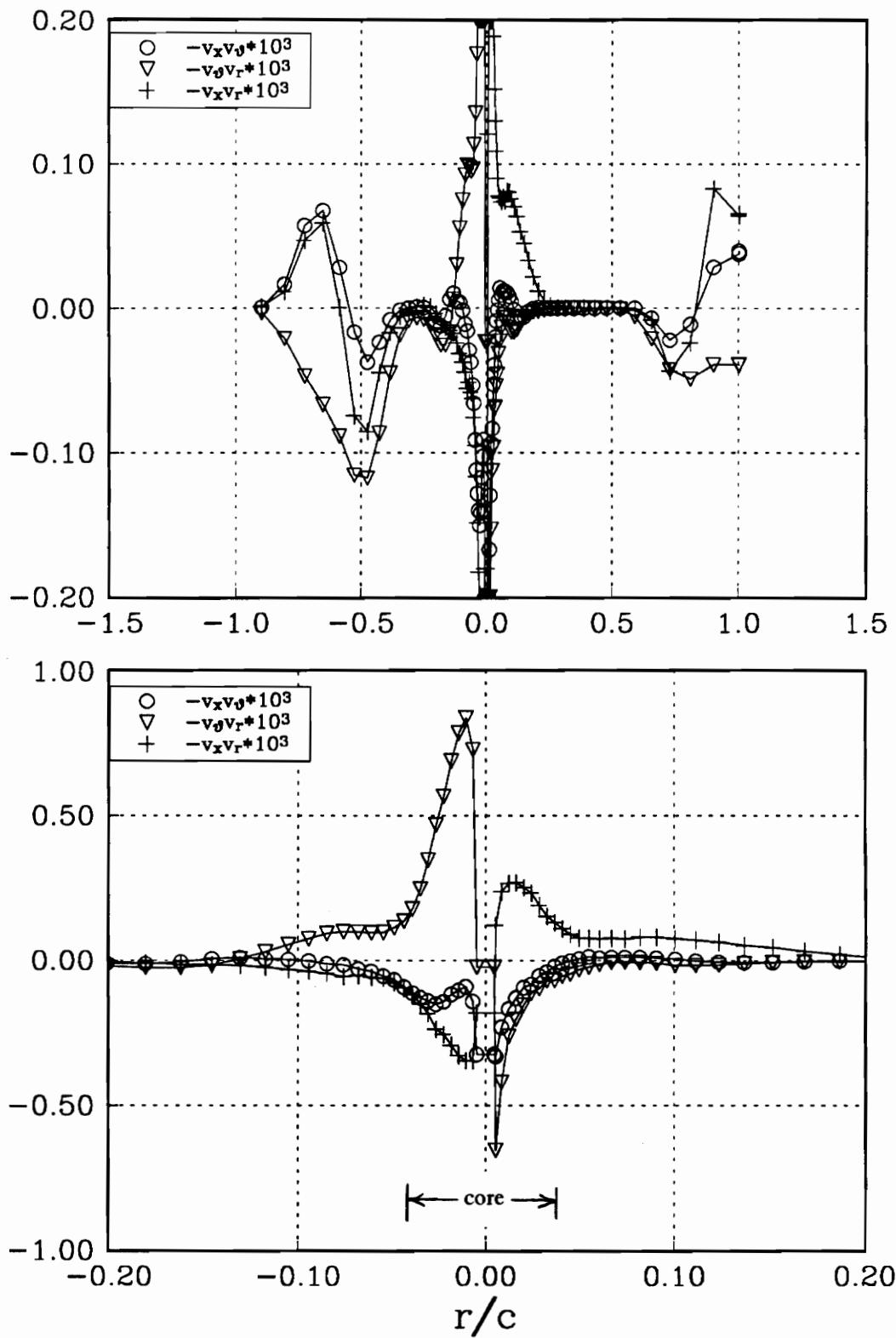


Figure 213b. Profile Aa showing shear stresses high passed filtered at a frequency of $fc/U_{ref}=1.5$ for the co-rotating pair at $x/c=10$.

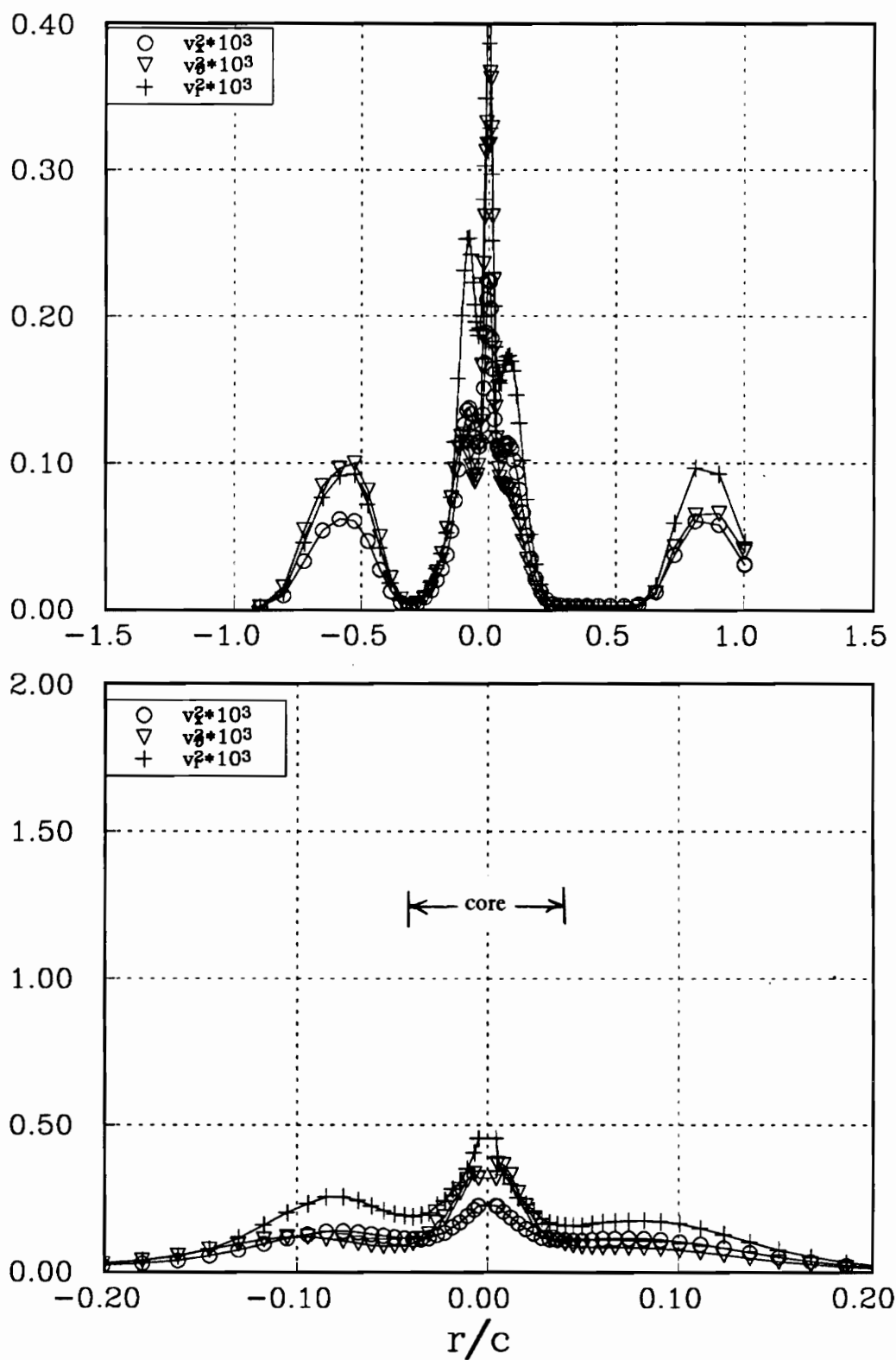


Figure 214a. Profile Aa showing normal stresses high passed filtered at a frequency of $fc/U_{ref}=7.0$ for the co-rotating pair at $x/c=10$.

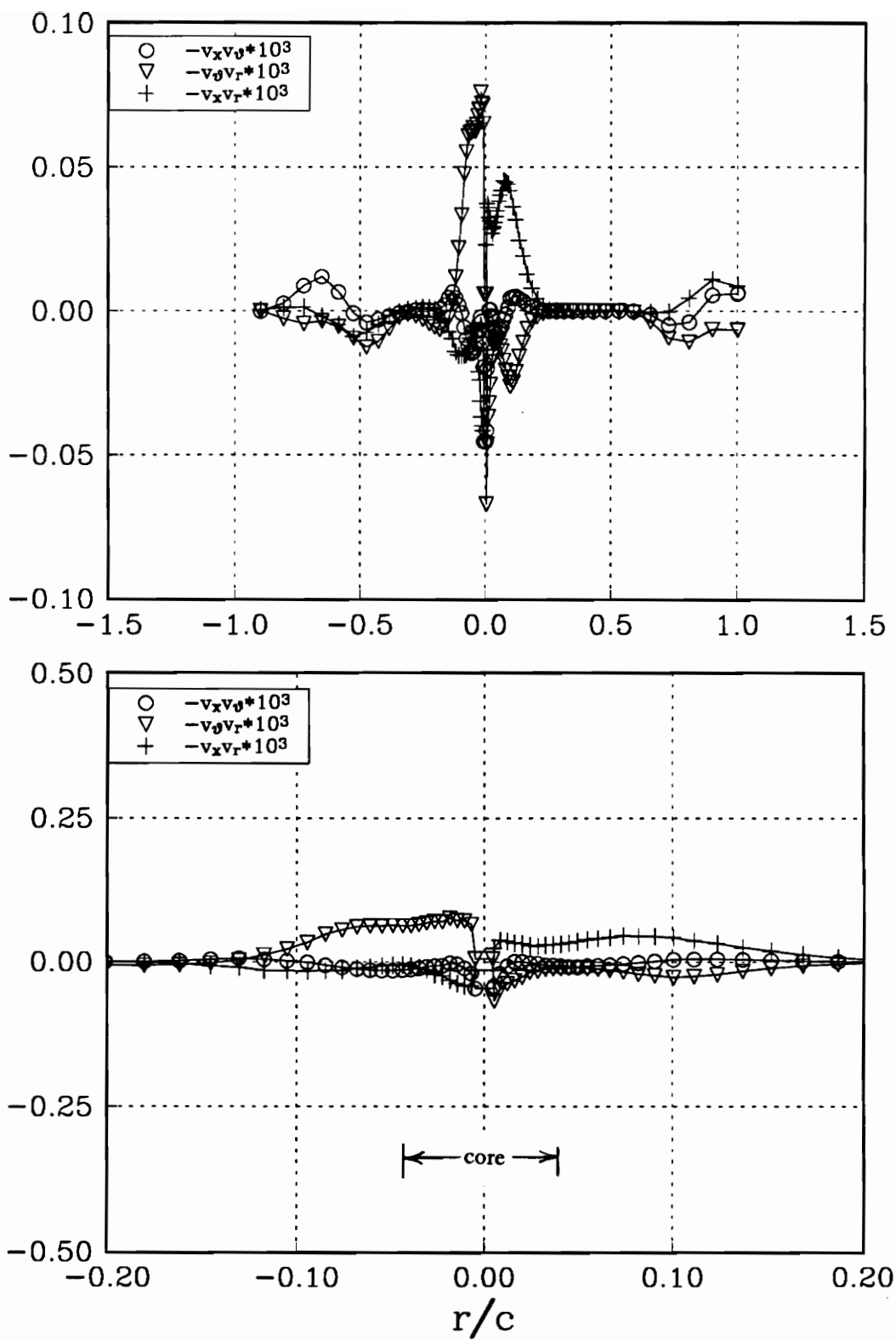


Figure 214b. Profile Aa showing shear stresses high passed filtered at a frequency of $fc/U_{ref}=7.0$ for the co-rotating pair at $x/c=10$.

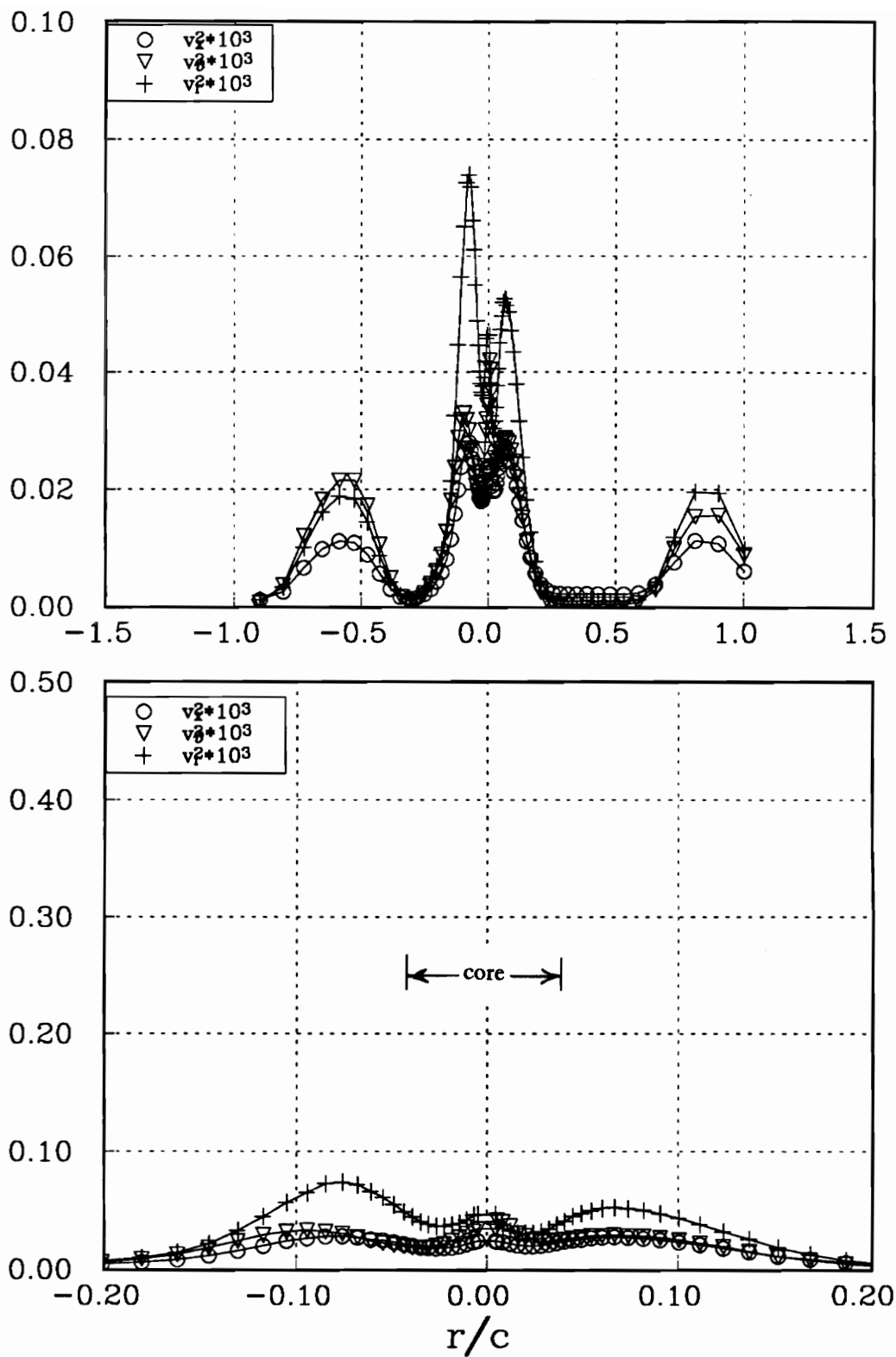


Figure 215a. Profile Aa showing normal stresses high passed filtered at a frequency of $f_c/U_{ref}=20.0$ for the co-rotating pair at $x/c=10$.

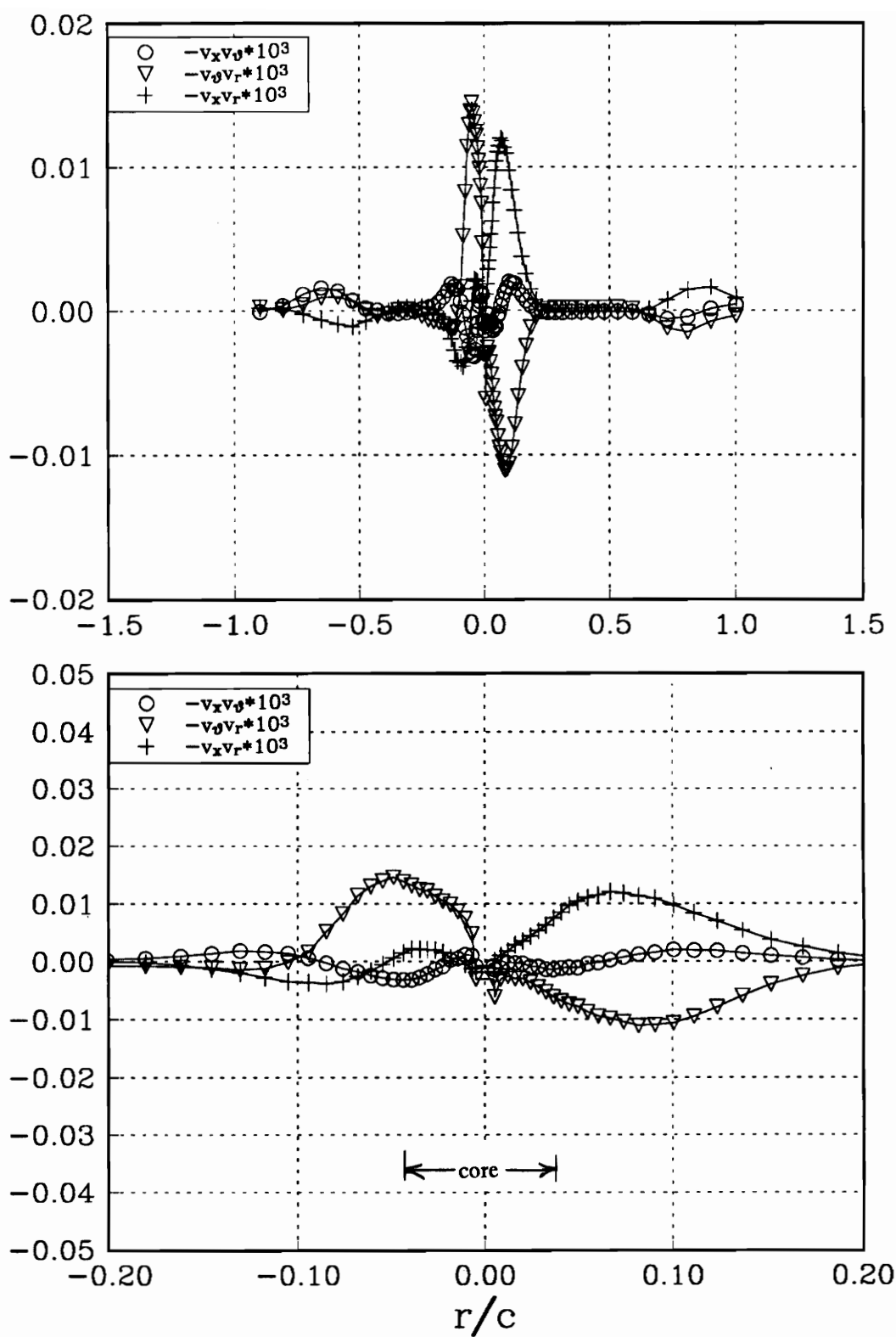


Figure 215b. Profile Aa showing shear stresses high passed filtered at a frequency of $fc/U_{ref}=20.0$ for the co-rotating pair at $x/c=10$.

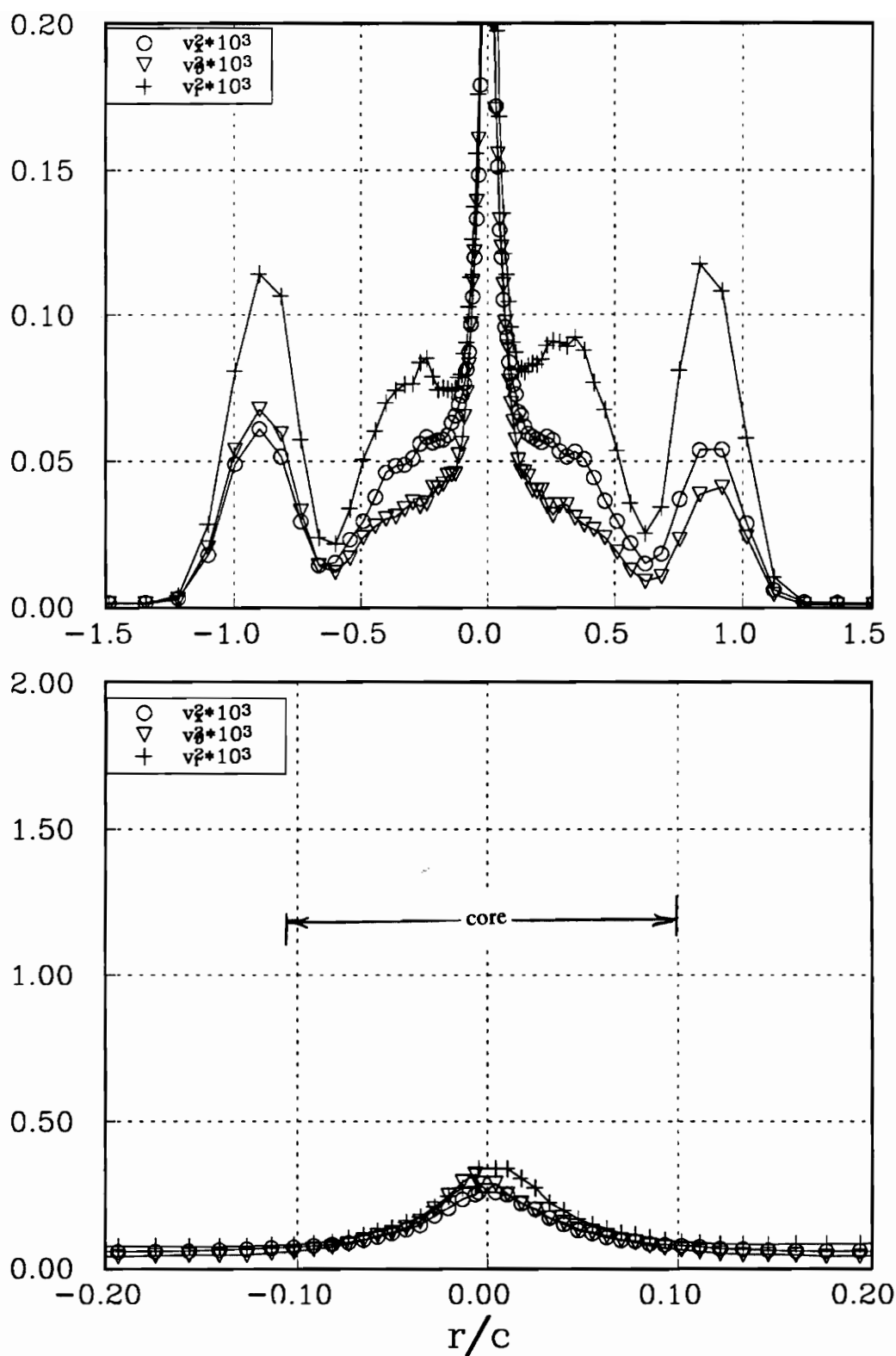


Figure 216a. Profile Gg showing normal stresses high passed filtered at a frequency of $f_c/U_{ref}=1.5$ for the co-rotating pair at $x/c=30$.

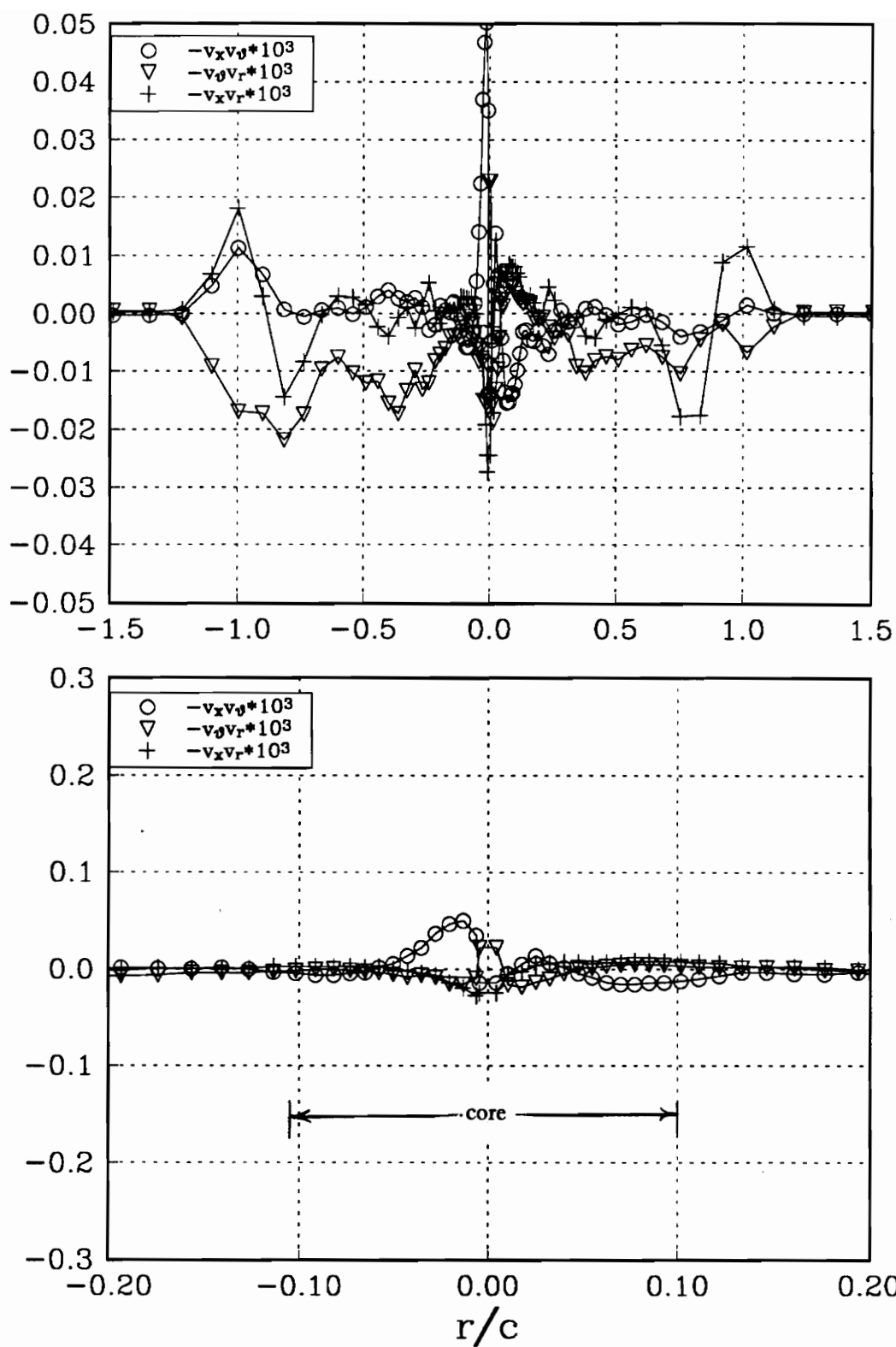


Figure 216b. Profile Gg showing shear stresses high passed filtered at a frequency of $fc/U_{ref}=1.5$ for the co-rotating pair at $x/c=30$.

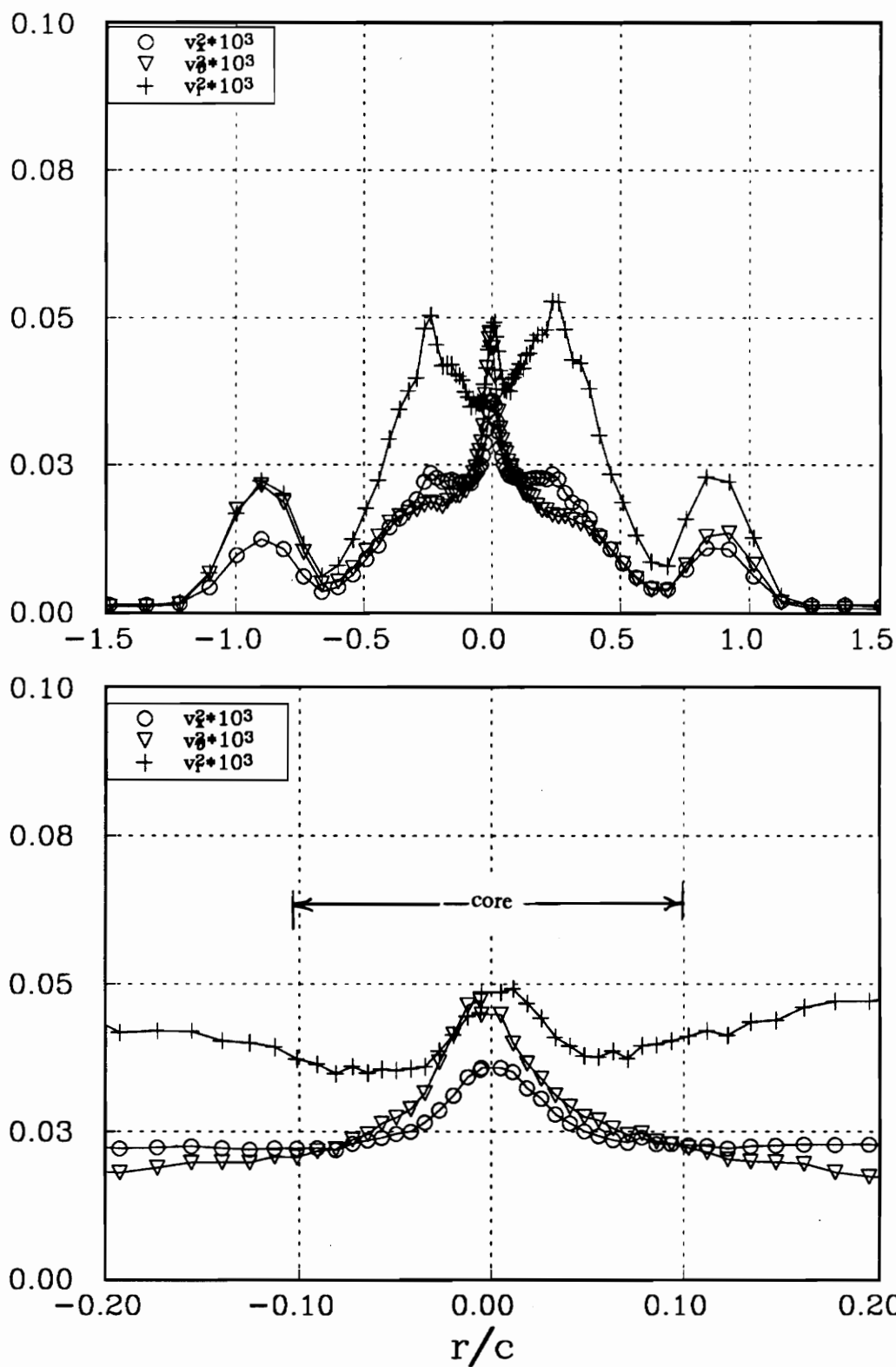


Figure 217a. Profile Gg showing normal stresses high passed filtered at a frequency of $fc/U_{ref}=7.0$ for the co-rotating pair at $x/c=30$.

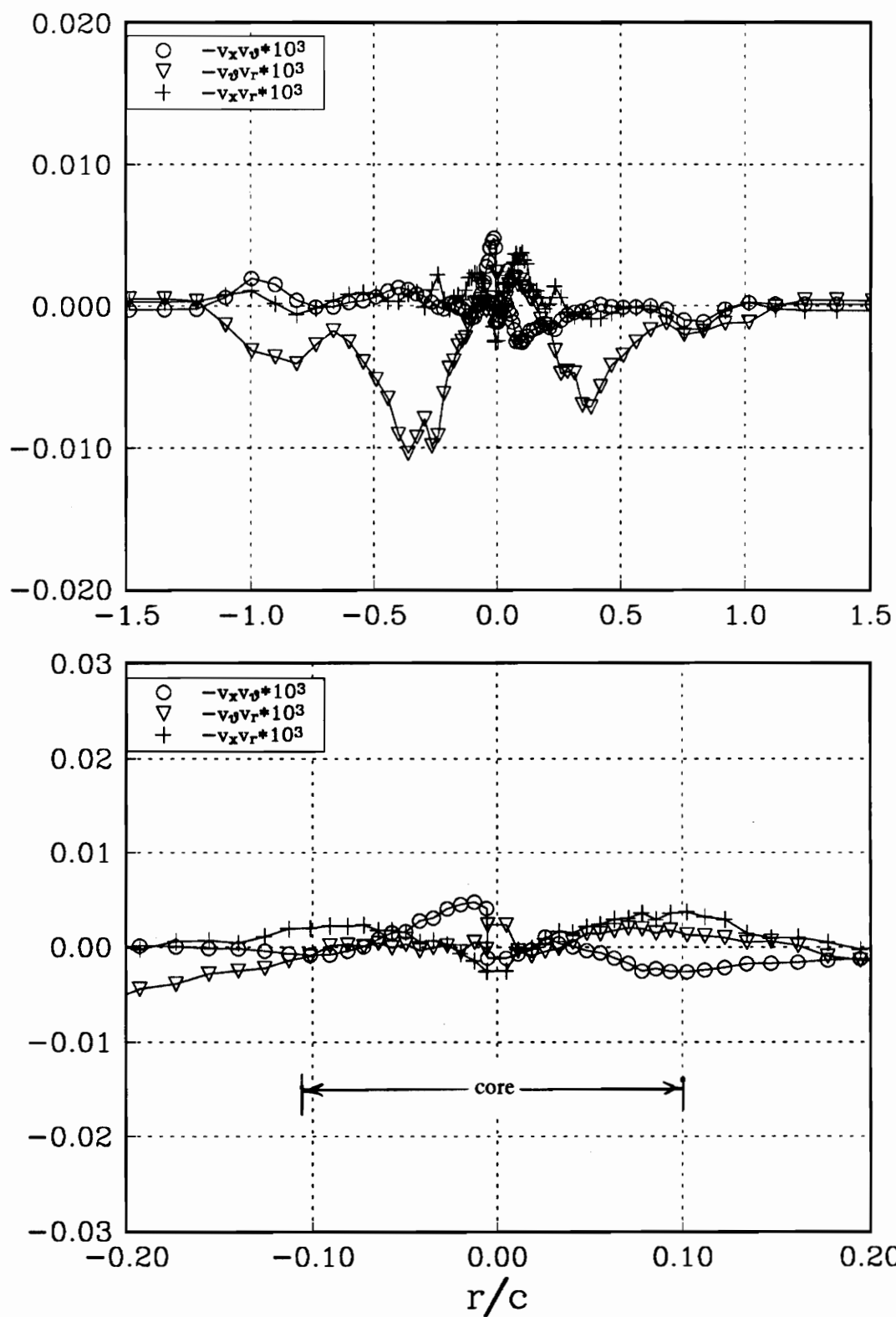


Figure 217b. Profile Gg showing shear stresses high passed filtered at a frequency of $fc/U_{ref}=7.0$ for the co-rotating pair at $x/c=30$.

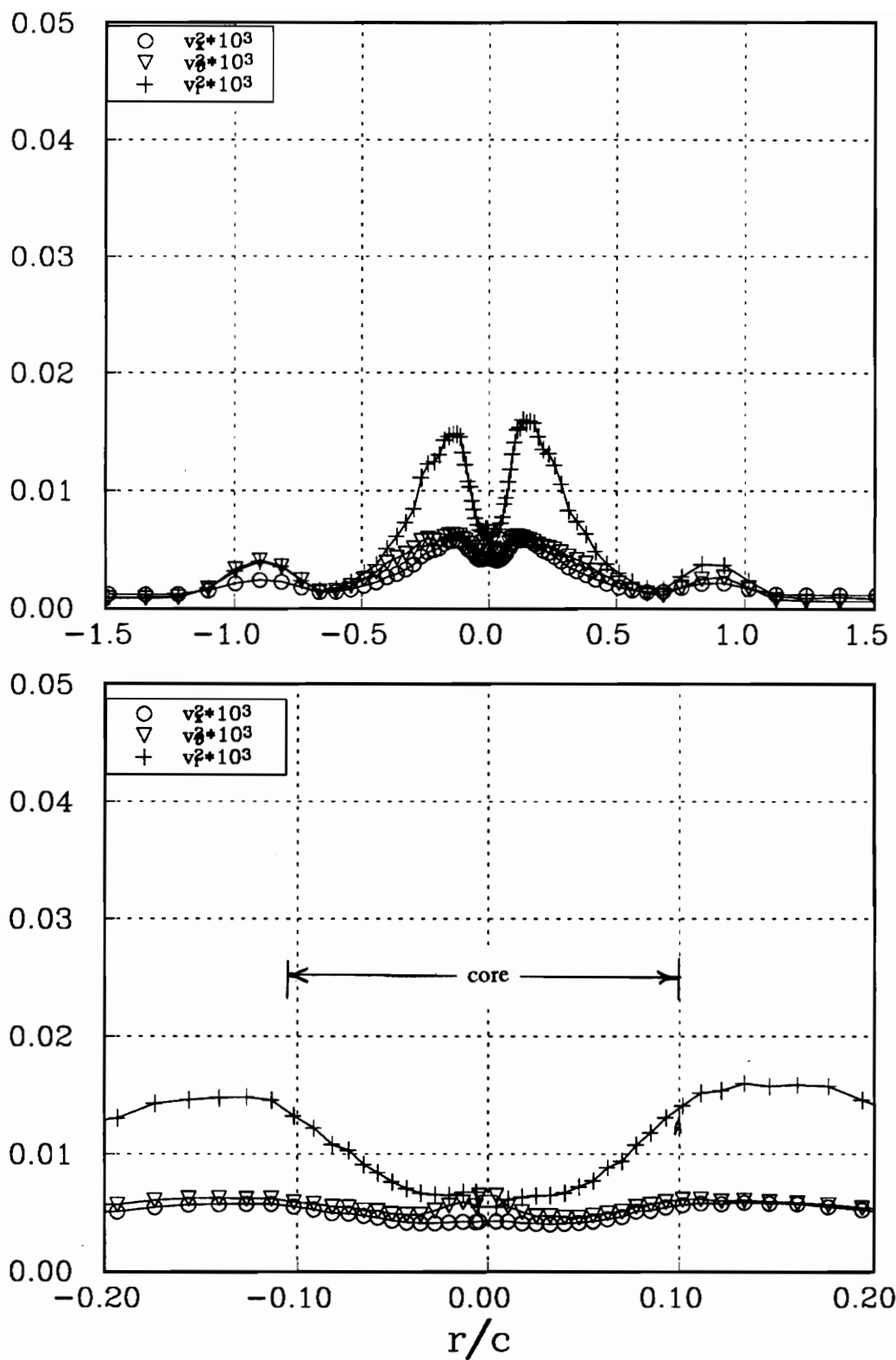


Figure 218a. Profile Gg showing normal stresses high passed filtered at a frequency of $fc/U_{ref}=20.0$ for the co-rotating pair at $x/c=30$.

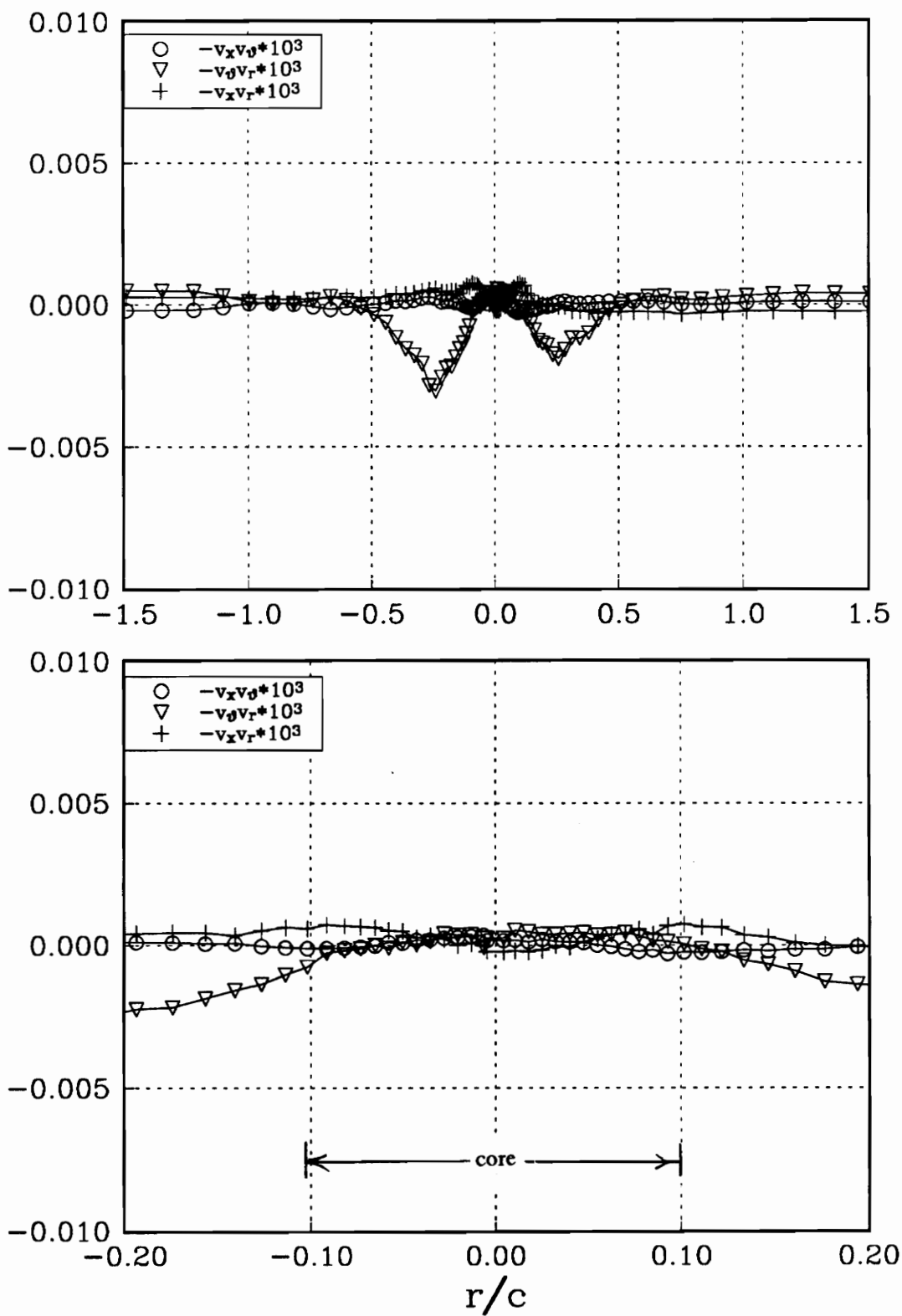


Figure 218b. Profile Gg showing shear stresses high passed filtered at a frequency of $fc/U_{ref}=20.0$ for the co-rotating pair at $x/c=30$.

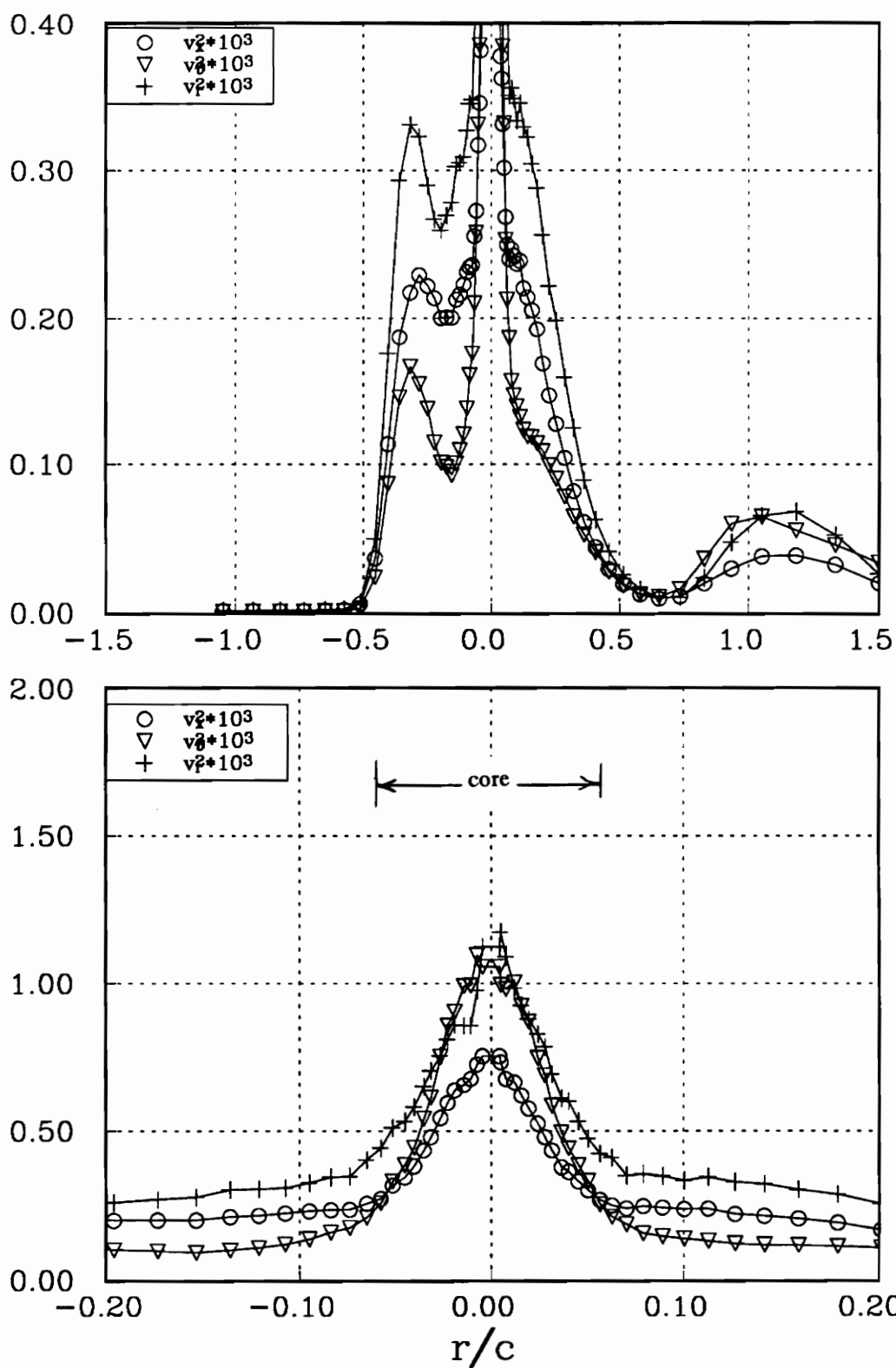


Figure 219a. Profile Kk showing normal stresses high passed filtered at a frequency of $fc/U_{ref} = 1.5$ for the counter rotating pair at $x/c = 30$.

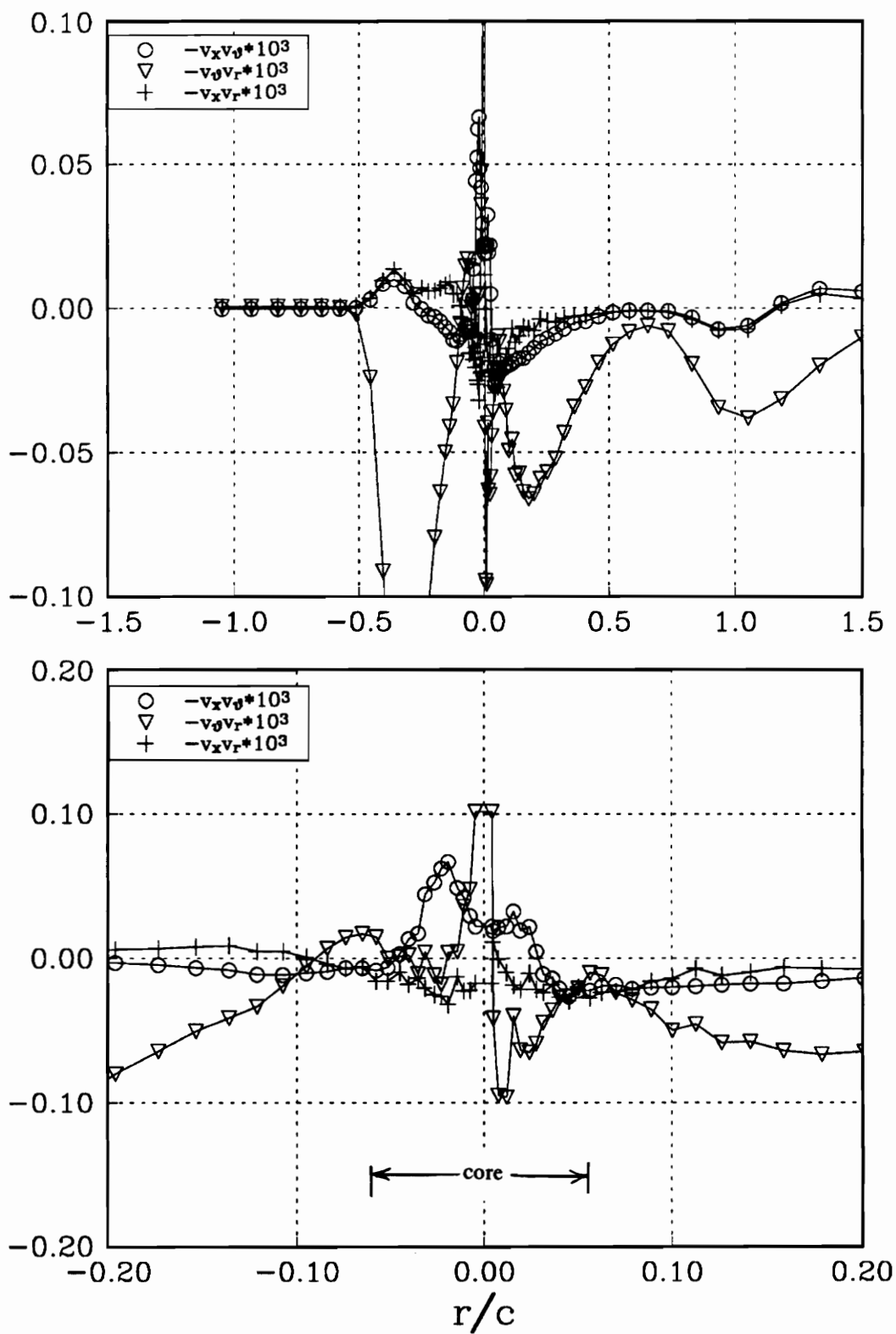


Figure 219b. Profile Kk showing shear stresses high passed filtered at a frequency of $fc/U_{ref}=1.5$ for the counter rotating pair at $x/c=30$.

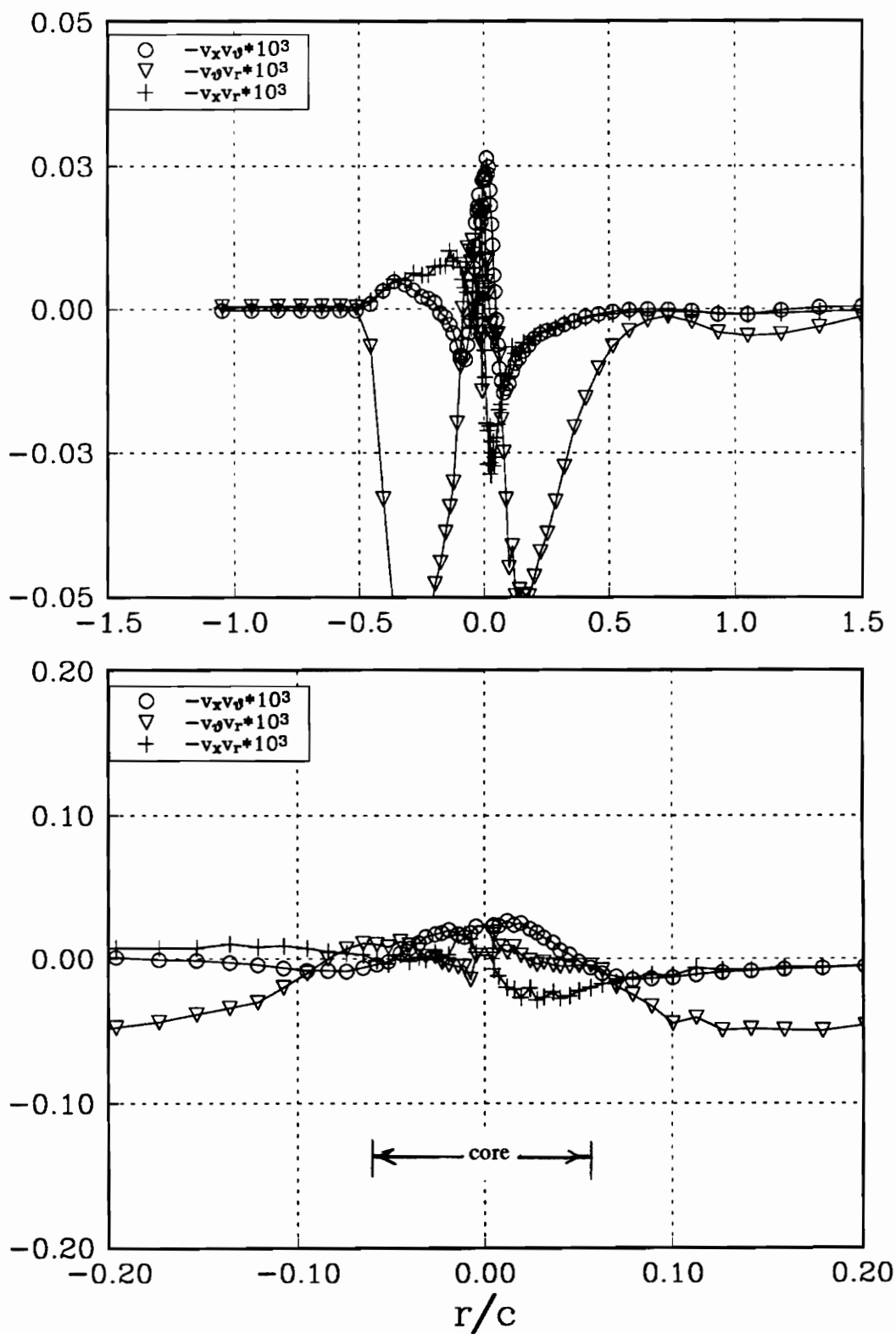


Figure 220a. Profile Kk showing normal stresses high passed filtered at a frequency of $f_c/U_{ref}=7.0$ for the counter rotating pair at $x/c=30$.

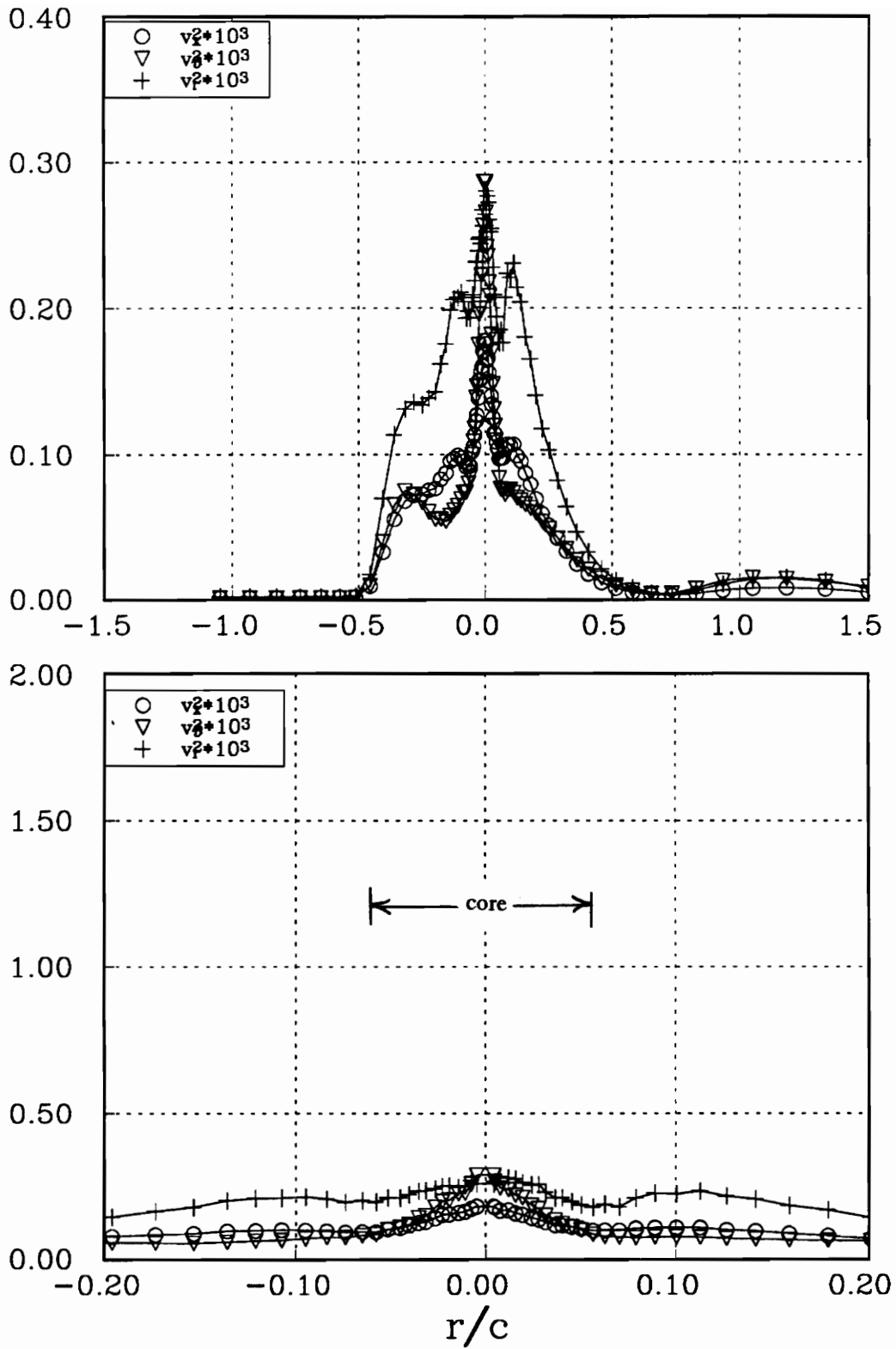


Figure 220b. Profile Kk showing shear stresses high passed filtered at a frequency of $fc/U_{ref}=7.0$ for the counter rotating pair at $x/c=30$.

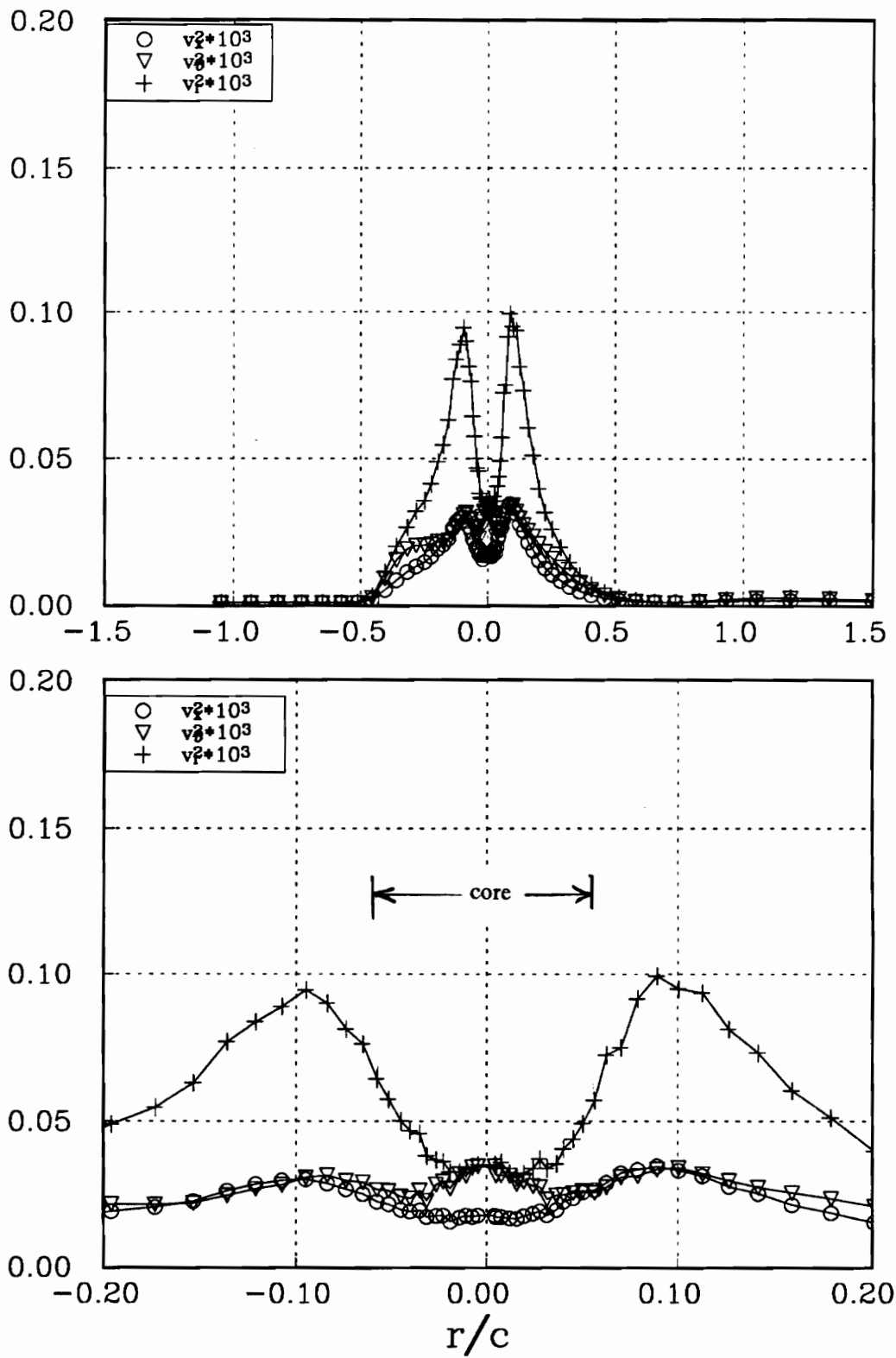


Figure 221a. Profile Kk showing normal stresses high passed filtered at a frequency of $fc/U_{ref}=20.0$ for the counter rotating pair at $x/c=30$.

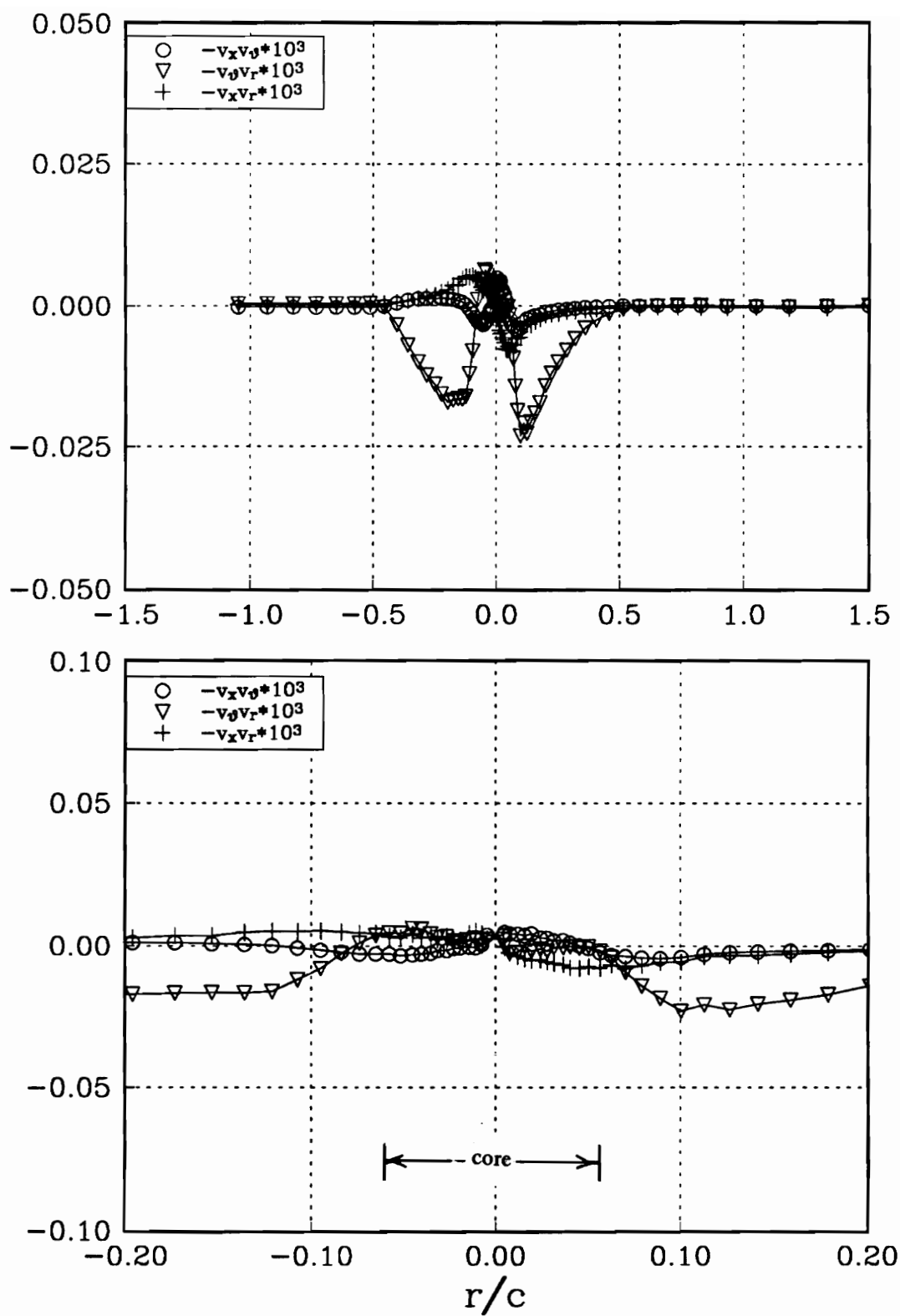


Figure 221b. Profile Kk showing shear stresses high passed filtered at a frequency of $f_c/U_{ref}=20.0$ for the counter rotating pair at $x/c=30$.

Vita

The author was born on October 1, 1966 in Newport News, Virginia. He graduated from Tabb High School in June 1984. For the next two years he ran his own construction company then entered Thomas Nelson Community College in June 1986. He earned a A.S degree in General Engineering and entered Virginia Polytechnic Institute and State University in July 1988. He received a B.S degree in Aerospace Engineering in May 1990 and stayed at VPI to pursue graduate studies in Aerospace Engineering.

A handwritten signature in cursive script, appearing to read "J. H. Zoller". The signature is written in black ink on a white background.